

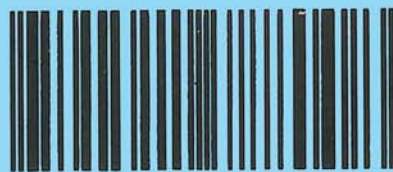
# IIUM ENGINEERING JOURNAL

**Volume 25**

**Number 1**

**January 2024**

ISSN 1511-788X



9 771511 788008



**IIUM  
Press**

**INTERNATIONAL ISLAMIC UNIVERSITY MALAYSIA**

**ISSN: 1511-788X E-ISSN: 2289-7860**

**<http://journals.iium.edu.my/ejournal>**



# IIUM ENGINEERING JOURNAL

Volume 25, Issue 1, January 2024  
<https://doi.org/10.31436/iiumej.v25i1>

---

## Copyright Notice

**Consent to publish:** The Author(s) agree to publish their articles with IIUM Press.

**Declaration:** The Author(s) declare that the article has not been published before in any form and that it is not concurrently submitted to another publication, and also that it does not infringe on anyone's copyright. The Author(s) holds the IIUM Press and Editors of the journal harmless against all copyright claims.

**Transfer of copyright:** The Author(s) hereby agree to transfer the copyright of the article to IIUM Press, which shall have the non-exclusive and unlimited right to publish the article in any form, including in electronic media. For articles with more than one author, the corresponding author confirms that he/she is authorized by his/her co-author(s) to grant this transfer of copyright.

**The IIUM Engineering journal follows the open access policy.**

All articles published open access will be immediately and permanently free for everyone to read, download, copy and distribute for noncommercial purposes.



IIUM Engineering Journal at <https://journals.iium.edu.my/ejournal> is licensed under a [Creative Commons Attribution-NonCommercial 4.0 International License](https://creativecommons.org/licenses/by-nc/4.0/).

---

## IIUM ENGINEERING JOURNAL EDITORS

---

### **CHIEF EDITOR**

Ahmad Faris Ismail, IIUM, Malaysia

### **TECHNICAL EDITOR**

Sany Izan Ihsan, IIUM, Malaysia

### **EXECUTIVE EDITOR**

AHM Zahirul Alam, IIUM, Malaysia

### **ASSOCIATE EDITOR**

Nor Farahidah Za'bah, IIUM, Malaysia

### **LANGUAGE EDITOR**

Lynn Mason, Malaysia

### **COPY EDITOR**

Hamzah Mohd. Salleh, IIUM, Malaysia

### **MALAY TRANSLATOR**

Nurul Arfah Che Mustapha, IIUM, Malaysia

### **EDITORIAL BOARD MEMBERS**

Abdullah Al-Mamun, IIUM, Malaysia

Abdumalik Rakhimov, IIUM, Malaysia

Aishah Najiah Bt. Dahnel, IIUM, Malaysia

Alya Naili Binti Rozhan, IIUM, Malaysia

Norsinnira Bt. Zainul Azlan, IIUM, Malaysia

Hanafy Omar, Saudi Arabia

Hazleen Anuar, IIUM, Malaysia

Konstantin Khanin, University of Toronto, Canada

Ma'an Al-Khatib, IIUM, Malaysia

Meftah Hrairi, IIUM, Malaysia

Mohamed B. Trabia, United States

Mohammad S. Alam, Texas A&M University-Kingsville, United States

Mustafizur Rahman, National University Singapore, Singapore

Ossama Abdulkhalik, Michigan Technological University, United States

Mohamed Hadi Habaebi, IIUM, Malaysia

Mohd. Sultan Ibrahim Bin Shaik Dawood, IIUM, Malaysia

Muhammad Ibn Ibrahimy, IIUM, Malaysia

Nor Fadhillah Mohamed Azmin, IIUM, Malaysia

Waqar Asrar, IIUM, Malaysia

### **AIMS & SCOPE OF IIUMENGINEERING JOURNAL**

The **IIUM Engineering Journal**, published biannually (January and July), is a carefully refereed international publication of International Islamic University Malaysia (IIUM). Contributions of high technical merit within the span of engineering disciplines; covering the main areas of engineering: Electrical and Computer Engineering; Mechanical and Manufacturing Engineering; Automation and Mechatronics Engineering; Material and Chemical Engineering; Environmental and Civil Engineering; Biotechnology and Bioengineering; Engineering Mathematics and Physics; and Computer Science and Information Technology are considered for publication in this journal. Contributions from other areas of Engineering and Applied Science are also welcomed. The IIUM Engineering Journal publishes contributions under *Regular papers and Invited review papers*. It also welcomes contributions that address solutions to the specific challenges of the developing world, and address science and technology issues from an Islamic and multidisciplinary perspective.

### **REFEREES' NETWORK**

All papers submitted to IIUM Engineering Journal will be subjected to a rigorous reviewing process through a worldwide network of specialized and competent referees. Each accepted paper should have at least two positive referees' assessments.

### **SUBMISSION OF A MANUSCRIPT**

A manuscript should be submitted online to the IIUM-Engineering Journal website at <https://journals.iium.edu.my/ejournal>. Further correspondence on the status of the paper could be done through the journal website.

---

---

## INTERNATIONAL ADVISORY COMMITTEE

A. Anwar, United States  
Abdul Latif Bin Ahmad, Malaysia  
Farzad Ismail, USM, Pulau Pinang, Malaysia  
Hanafy Omar, Saudi Arabia  
Hany Ammar, United States  
Idris Mohammed Bugaje, Nigeria  
K.B. Ramachandran, India  
Kunzu Abdella, Canada  
Luis Le Moyne, ISAT, University of Burgundy, France  
M Mujtaba, United Kingdom  
Mohamed Al-Rubei, Ireland  
Mohamed B Trabia, United States  
Syed Kamrul Islam, United States  
Tibor Czigany, Budapest University of Technology and Economics, Hungary  
Yiu-Wing Mai, The University of Sydney, Australia.

Published by:



IIUM  
Press

**IIUM Press,**

International Islamic University Malaysia  
Jalan Gombak, 53100 Kuala Lumpur, Malaysia  
Phone (+603) 6421-5014, Fax: (+603) 6421-6298

Whilst every effort is made by the publisher and editorial board to see that no inaccurate or misleading data, opinion or statement appears in this Journal, they wish to make it clear that the data and opinions appearing in the articles and advertisement herein are the responsibility of the contributor or advertiser concerned. Accordingly, the publisher and the editorial committee accept no liability whatsoever for the consequence of any such inaccurate or misleading data, opinion or statement.

ISSN 1511 - 788X



9 771511 788008

**IIUM Engineering Journal**

ISSN: 1511-788X E-ISSN: 2289-7860

# IIUM ENGINEERING JOURNAL

Volume 25, Issue 1, January 2024  
<https://doi.org/10.31436/iiumej.v25i1>

## Table of Contents

COPYRIGHT ..... i

EDITORIAL..... ii

### CHEMICAL AND BIOTECHNOLOGY ENGINEERING

- 2585: THE INFLUENCE OF PLANT GROWTH REGULATORS AND LIGHT SUPPLY ON BITTER CASSAVA CALLUS INITIATION FOR STARCH PRODUCTION ..... 1  
*Noor Illi Mohamad Puad, Soumayat Ali Ibrahim Mze, Azlin Suhaida Azmi and Muhammad Yusuf Abduh*
- 2629: INVESTIGATION OF ENHANCED ELECTROCOAGULATION-MEMBRANE PROCESS FOR WATER RECLAMATION FROM PALM OIL MILL EFFLUENTS ..... 12  
*Amina Tahreen, Mohammed Saedi Jami, Fathilah Ali, Nik Rashida Nik Abdul Ghani and Radhia Nedjai*
- 2732: CHARACTERISATION OF POMACEA CANALICULATA EGGS TREATED WITH PROTEASE ..... 26  
*Noor Hasyierah Mohd Salleh, Nurhadijah Zainalabidin and Siti Noor Hajar Md Latip*
- 2748: GROWTH REVIVAL OF GREY OYSTER (*PLEUROTUS PULMONARIUS*) POWDER CULTURE MUSHROOM FROM THE EFFECT OF SPRAY DRYING TEMPERATURE ..... 40  
*Zarina Zakaria, Fatihah Aziz, Mohd Sharizan Md Sarip and Noor Hasyierah Mohd Salleh*
- 2882: BIPHASIC CRUDE PALM OIL DECHLORINATION: EFFECT OF VOLUME RATIO AND CONCENTRATION OF SODIUM SILICATE TO HYDROXIDE ION DISTRIBUTION ..... 47  
*Zulfa Kurnia Umani Hari, Syamsul Bahari Abdullah, Saidatul Shima Jamari, Che Rahmat Che Mat and Mohd Sabri Mahmud*
- 2932: ADSORPTION PERFORMANCE OF FIXED-BED COLUMNS FOR THE REMOVAL OF PHENOL USING BAOBAB FRUIT SHELL BASED ACTIVATED CARBON ..... 59  
*Radhia Nedjai, Nassereldeen Kabbashi, Md Zahangir Alam, Ma'an Alkhatib, Amina Tahreen and Abdullah Al Mamun*

### CIVIL AND ENVIRONMENTAL ENGINEERING

- 2829: INFLUENCE OF CURING CONDITIONS ON THE EARLY STRENGTH OF LOW TEMPERATURE BELITE CEMENTS ..... 72  
*Sambo Gwandu Haliru and Rodiah Zawawi*
- 2847: THE EFFECT OF INDUSTRIAL AND WASTE FIBERS ON CONCRETE STRENGTH AND STRUCTURAL BEHAVIOR OF RC SHORT COLUMNS..... 87  
*Maryam H. Naser, Mayadah W. Falah, Fatimah H. Naser, Mohammed Salah Nasr, Tameem Mohammed Hashim and Ali Abdulhussein Shubbar*
- 2870: KEY SUCCESS FACTORS IN ROAD MAINTENANCE MANAGEMENT PROJECTS (A CASE STUDY OF MAYSAN PROVINCE, IRAQ) ..... 102  
*Milad Ghanbari and Zaid Khalid Hasani*
- 2959: EFFECTS OF SOIL ERODIBILITY ON RIVERBANK EROSION AND FAILURES ..... 115  
*Nur Aqilah Mohd Rosli, Saerahany Legori Ibrahim and Siti Hajar Yusoff*
- 2969: COMPARISON OF THE MECHANICAL PERFORMANCE OF DENSE GRADING AND POROUS GRADING MIXTURE UTILIZED WITH CRUMB RUBBER MODIFIED BINDER..... 128  
*Noor Yusriah Esa, Wan Nur Aifa Wan Azahar, Norhidayu Kasim and Nur Khairiyah Basri*
- 2983: MIXING SEQUENCE EFFECT OF CEMENT COMPOSITES WITH CARBON FIBRES ..... 142  
*Elizer Nevall Anthony, Ahmad Nurfaidhi Rizalman, Anand Ryan Thurairajah, S.M. Iqbal, S. Zainal and Muhd Fauzy Sulaiman*
- 2997: STRATEGIES TO REDUCE THE NUMBER OF SEVERELY INJURED VICTIMS IN ADOLESCENT MOTORCYCLE RIDERS ..... 153  
*Pada Lumba, Anton Ariyanto and Ahmad Fathoni*

## **ELECTRICAL, COMPUTER AND COMMUNICATIONS ENGINEERING**

---

2716: OPTIMAL CLUSTERING OF WIRELESS MULTIPATHS BY UNIFORM MANIFOLD APPROXIMATION AND PROJECTION-ASSISTED DBSCAN .....	167
<i>Emmanuel Trinidad and Lawrence Materum</i>	
2727: MOBILE GAS SENSING FOR LABORATORY INFRASTRUCTURE .....	178
<i>Raduan Sarif, Mohammed Faeik Ruzaij Al-Okby, Thomas Roddelkopf and Kerstin Thuro</i>	
2796: SPECTROSCOPY DATA CALIBRATION USING STACKED ENSEMBLE MACHINE LEARNING .....	208
<i>Mahmud Iwan Solihin, Chan Jin Yuan, Wan Siu Hong, Liew Phing Pui, Chun Kit Ang, Wafa Hossain and Affiani Machmudah</i>	
2898: COMPACT CPW 4X4 MIMO ANTENNA FOR WI-FI 6 (IEEE802.11.AX) AND 5G (NR77/NR78/NR79) COMMUNICATIONS .....	225
<i>Noora Salim, Mandeep J. Singh and Amer T. Abed</i>	
2913: PHOTOVOLTAIC MODULE TEMPERATURE ESTIMATION MODEL FOR THE ONE-TIME-POINT DAILY ESTIMATION METHOD .....	237
<i>Kinfatt Wong, Robiah Ahmad, Kushsairy Abdul Kadir and Norulhusna Ahmad</i>	
2914: ADVANCING SYSTEM INTEGRATION: VERILOG-BASED HARDWARE IMPLEMENTATION OF AN ASIC INTERFACE FOR THREE AMBA PROCESSORS .....	253
<i>Mohammad Iqbal Rahman Rokon, S.M.A. Motakabber, AHM Zahirul Alam, Gazi Zahirul Islam, Mohammad Abdulmatin and Md. Mahmud</i>	
3093: EXTENDABLE HIGH-GAIN DC-DC CONVERTER FOR STORAGE BATTERY AND PHOTOVOLTAIC CELL .....	263
<i>Khadiza Akter, S. M. A. Motakabber, AHM Zahirul Alam and Siti Hajar Binti Yusoff</i>	

## **MATERIALS AND MANUFACTURING ENGINEERING**

---

2811: THIOL FUNCTIONALIZED GOLD NANOBIPYRAMIDS-BASED PLASMONIC SENSOR FOR GLUCOSE DETECTION .....	274
<i>Natasya Salsabiila, Marlia Morsin, Muhammad Hanif, Suratun Nafisah, Nur Liyana Razali, Iwantono</i>	
2925: INVESTIGATION OF THE PROPERTIES OF LITHIUM-CONTAINING CERAMICS BASED ON LOW-PLASTIC CLAY .....	291
<i>Lubov Filippova, Anastasiya Akimova, Evgeniy Pikalov and Oleg Selivanov</i>	

## **MECHATRONICS AND AUTOMATION ENGINEERING**

---

2820: A WHEELCHAIR SITTING POSTURE DETECTION SYSTEM USING PRESSURE SENSORS .....	302
<i>Muhammad Annuar Alhadi Mohamad Yusoff, Nor Hidayati Diyana Nordin and Nur Liyana Azmi</i>	
2838: POWER OF ALIGNMENT: EXPLORING THE EFFECT OF FACE ALIGNMENT ON ASD DIAGNOSIS USING FACIAL IMAGES .....	317
<i>Mohammad Shafiul Alam, Muhammad Mahbubur Rashid, Ahmed Rimaz Faizabadi and Hasan Firdaus Mohd Zaki</i>	



# THE INFLUENCE OF PLANT GROWTH REGULATORS AND LIGHT SUPPLY ON BITTER CASSAVA CALLUS INITIATION FOR STARCH PRODUCTION

NOOR ILLI MOHAMAD PUAD<sup>1\*</sup>, SOUMAYAT ALI IBRAHIM MZE<sup>1</sup>,  
AZLIN SUHAIDA AZMI<sup>1</sup> AND MUHAMMAD YUSUF ABDUH<sup>2</sup>

<sup>1</sup>*Department of Chemical Engineering and Sustainability,  
Kulliyah of Engineering, International Islamic University Malaysia, Kuala Lumpur, Malaysia*

<sup>2</sup>*School of Life Sciences and Technology, Institut Teknologi Bandung,  
Jalan Ganesha, No. 10, Bandung, 40132 Indonesia*

\*Corresponding author: [illi@iium.edu.my](mailto:illi@iium.edu.my)

(Received: 26 August 2022; Accepted: 26 June 2023; Published on-line: 22 December 2023)

**ABSTRACT:** The application of cassava starch in the biopolymers industry has been growing significantly due to its low cost, good oxygen barrier in the dry state, and biodegradability. Plant culture technology is an alternative to traditional propagation as it does not require large areas for production, has a higher rate of multiplication, and produces disease-free plants. However, the application of cassava callus culture for starch production is limited. This study focuses on identifying the significant culture parameters for a maximum Rayong cultivar cassava callus growth and evaluation of its starch content. Cassava stems petiole and leaf explants were cultured on MS medium containing different combinations of 2,4-D (8, 12, and 15 mg/L) and BAP (1, 3, and 5 mg/L) under three light conditions (0, 16, and 24 h). The screening of the most influential parameter was done using the 2-level Factorial Design in Design Expert v13 by analyzing the frequency of callus formation. All leaf explant turned brown with no callus induction. The highest frequency of callus formation derived from stem petiole explant was achieved by the combination of 8 mg/L 2,4-D and 1 mg/L BAP under the light condition (75%) followed by 8 mg/L 2,4 D + 1 mg/L BAP under the dark condition (50%). Based on the ANOVA analysis, the individual supply of 2,4-D and BAP respectively, have a negative effect on callus formation while the combination of 2,4-D and BAP has a positive effect. Light supply did not significantly affect cassava callus formation. The amount of starch in the cassava callus was then investigated using an iodine test which yielded 0.21% of the total weight of the callus (0.0101g). The amount of starch is relatively low considering that the callus was not grown under the optimum condition for starch production. The findings of this study open prospects for future research in cassava cultures in favor of starch production.

**ABSTRAK:** Penggunaan kanji ubi kayu dalam industri biopolimer telah meningkat secara mendadak disebabkan oleh faktor kosnya yang rendah, rintangan oksigen yang baik dan sifat keterbiodegradasi. Teknologi kultur tisu tumbuhan merupakan alternatif kepada pembiakan secara tradisional yang mana teknologi ini tidak memerlukan kawasan penanaman yang luas, penghasilan yang lebih singkat dan menghasilkan tumbuhan bebas penyakit. Walau bagaimanapun, kajian mengenai penggunaan kanji dari kultur ubi kayu masih belum meluas. Kajian ini bertujuan mengenal pasti parameter penting dalam pertumbuhan maksimum kalus kultivar ubi kayu Rayong dan kandungan kanjinya. Eksplan dari tangkai petiol dan daun ubi kayu dikulturkan dalam medium MS yang mengandungi pelbagai kombinasi hormon tumbuhan 2,4-D (8, 12 dan 15 mg/L) dan BAP (1, 3 dan 5 mg/L) di bawah tiga tempoh masa pencahayaan (0, 16 dan 24 jam). Saringan parameter paling berpengaruh dilakukan menerusi reka bentuk faktorial 2-peringkat perisian Design Expert v13 melalui analisa frekuensi

pembentukan kalus. Semua eksplan daun telah bertukar dari hijau ke perang dan tidak menunjukkan induksi kalus. Bagi eksplan batang daun, frekuensi pembentukan kalus tertinggi diperoleh dari kombinasi 8 mg/L 2,4-D dan 1 mg/L BAP di bawah pencahayaan 24 jam (75%) diikuti dengan 8 mg/L 2,4 D + 1 mg/L BAP di bawah pencahayaan malap (50%). Berdasarkan analisis ANOVA, medium 2,4-D dan BAP masing-masing menunjukkan kesan negatif kepada pembentukan kalus, sementara kombinasi 2,4-D dan BAP memberikan kesan positif. Dapatan ini menunjukkan bahawa pencahayaan tidak signifikan terhadap pembentukan kalus kultur ubi kayu. Kandungan kanji di dalam kalus ubi kayu kemudiannya diuji dengan larutan iodin, dan menunjukkan dapatan sebanyak 0.21% dari berat kalus (0.0101 g). Secara relatif, nilai ini adalah rendah memandangkan eksperimen ini bukan dihasilkan di bawah keadaan optimum bagi pembentukan kanji. Hasil kajian ini membuka peluang kepada kajian-kajian lain di masa hadapan dalam penghasilan kanji dari kultur tisu ubi kayu.

---

**KEYWORDS:** *cassava; callus culture; 2,4-dichlorophenoxyacetic acid (2,4-D); 6-benzylaminopurine (BAP); light*

## 1. INTRODUCTION

The application of cassava (*Manihot esculenta* Crantz) starch in the biopolymers industry has been growing significantly due to its availability (particularly in seed and tuber plants), low-cost, good oxygen barrier in the dry state, renewability, and biodegradability [1]. Cassava starch has also gained large popularity as a starch source because of its low gelatinization temperature, high binding capacity, and viscosity [2]. For the manufacturing of a sustainable and efficient bioproduct raw material, bitter cassava is preferred over sweet cassava as it has high starch content, high production yield, and high chemical defense. The exploitation of 30% of waste from bitter cassava can be self-sufficient as a feedstock requirement for food, medical and packaging industries [3]. In accordance with that, it is estimated that the global cassava starch market will reach USD 8.1 billion in the next five years (2023-2027) [4].

However, cassava starch usage is facing some limitations in terms of mass propagation. The increase in demand requires several thousand hectares of arable land, which is limited since there is a decline in empty lands due to economic development. Moreover, traditional cassava cultivation records high pest and disease invasions, and requires long periods of cultivation [5,6]. Therefore, as an alternative, plant tissue culture has been used as a substitute for traditional propagation as it has been proven to remediate insufficient propagation and provide disease-free cassava plants. Additionally, *in vitro* cultivation is not dependent on geographical, seasonal, and environmental variations as it controls the plant's environment (nutrient media, physical factors, growth hormones, and aseptic condition) [7].

Among different types of plant tissue culture, callus culture is the most widely used due to its pluripotency. Although this culture is comprised of cells that have no specific function, this culture plays an important role in plant culture technology as it is being used as the starter for other cultures. For instance, this culture is used to initiate cell suspension culture which is frequently used in plant transformation studies or large-scale secondary metabolite production. Moreover, callus culture is also very crucial in the regeneration of plants as well as plant organ production. Callus culture can regenerate any part of the plant with the use of a suitable plant growth hormone [8]. The established conditions such as nutrient media and plant growth regulators (PGRs) influence highly on the callus culture induction and growth.

To our best knowledge, reports on cassava callus culture for starch production are still scarce. Most studies aimed to provide an effective callus induction based on the effect of different PGRs as well as alternative genetic modification to provide rapid production of the

cassava plant [8-10]. Moreover, no report is yet available specifically for the Rayong cultivar which was used in this study. Rayong cultivar is a bitter type of cassava, with a high starch content, wide adaptability to different environmental conditions, and high yield potential [11]. Thus, this study aimed to identify the effect of PGRs and light supply on the initiation of Rayong cultivar callus culture and preliminary evaluation of its starch content.

Plant growth regulators (PGRs) are hormones that affect the growth and development of a plant. In the case of callus growth, the major PGRs that influence its development are auxin and cytokinin. 2,4-dichlorophenoxyacetic acid (2,4-D) has been reported as the most effective auxin for cassava callus formation [8,12]. For cytokinin, thidiazuron (TDZ) induced a higher percentage of callus formation followed by 6-Benzylaminopurine (BAP) and kinetin. It is concluded that TDZ induced the formation of indole-3-acetic acid (IAA) in the cell which helps callus formation [9]. However, whether the combination of auxin and cytokinin on cassava callus initiation and growth might have a positive impact has yet to be reported. Therefore, this study explored the effect of combining 2,4-D (8, 12, and 15 mg/L) and BAP (1, 3, and 5 mg/L) on cassava callus initiation.

Moreover, light supply, as another culture parameter, was also investigated. Cassava callus culture can grow in both dark and light conditions, at a temperature of 25-28 °C within 1 month [8-9,12]. Light supply influenced the initiation time of the culture *i.e.* white-light exposure culture initiates faster callus formation than the dark culture. Accordingly, continuous light, 16-h light, and continuous dark conditions were chosen as the range for the light supply parameter. Cassava callus culture was initiated according to these parameters with constant monitoring of the process for 30 days with an interval of 3 days of sampling. A 2-level factorial design in Design Expert v13 (Stat-Ease, Inc., USA) was used for the experimental design and screening purposes. Finally, an iodine test was conducted for the preliminary evaluation of starch amount in the induced cassava callus.

## 2. MATERIALS AND METHODS

### 2.1 Materials

The explants (leaves and stem petiole) were obtained from the cassava trees (Rayong cultivar) planted at International Islamic University Malaysia. Ethanol was purchased from HmbG Chemicals, Germany while sodium hypochlorite was purchased from Bendosen, Malaysia. Both TWEEN® 20 and Gelrite were purchased from Sigma-Aldrich, UK. Murashige and Skoog (MS) basal medium, sucrose, casein hydrolysate were purchased from Duchefa, Netherlands. Meanwhile, hydrochloric acid (HCl), 2,4-D, and BAP were purchased from R&M Chemicals, UK. Sodium hydroxide (NaOH) was from Merck, UK.

### 2.2 Surface Sterilization of Cassava Explants

The surface sterilization procedure was adapted and modified based on Puad et al. [13]. Leaves and stem petioles of the Rayong cultivars were washed with antibacterial detergent for 5 min followed by washing with 50% thiram solution under continuous shaking for 1 hour. Each washing was followed by 3 rinses of distilled water. Next, the explants were soaked in 70% ethanol for 5 min, then bleached with 5.75% sodium hypochlorite with 2-3 drops of TWEEN® 20 for 10 min. After each soaking, the explants were rinsed at least three times with sterile distilled water [9,12]. The sterile explants were cut into small pieces of 5 mm which were inoculated in a media plate (4 explants per plate).

## 2.3 Preparation of Culture Media

The media preparation used was done following the method proposed by Puad & Tang [14]. The media contained 4.4 g/L of MS basal medium, 30 g/L of sucrose, 0.05 g/L of casein hydrolysate, 2.5 g/L of Gelrite, and 0.75 mL of plant protection mixture (PPM). The media was adjusted to a pH of 5.7 using 1 M of NaOH and 1 M of HCl and sorted following different combinations of 2,4-D and BAP concentration as presented in Table 1.

Table 1: Combinations of different concentrations of 2,4-D and BAP used in the study

No.	Combinations of 2,4-D: BAP (mg/L)
1	8:1
2	8:5
3	12:3
4	15:1
5	15:5

Then, the media were autoclaved at 121°C, 15 psi for 20 min and let to cool down till they reached 40 °C. The sterile explants were placed on the media, in sterile conditions and the cultures were incubated under three light conditions which are continuous light supply (24 h), 16-h light exposure, and continuous dark condition (0 h). The frequency of callus formation was the response used to evaluate the rate of callus formation during a period of 30 days.

## 2.4 Experimental Design

Using Design Expert v13, a 2-level factorial design was set up based on 3 different factors which are 2,4-D (8, 12, 15 mg/L), BAP (1, 3, 5 mg/L), and light exposure period (0-24 h) using cool-white fluorescent tube lights (2500 lm) resulting in 27 runs. The design was replicated two times for two different explants (cassava leaf and stem petiole). Each experiment was conducted in triplicate. Table 2 presents the design summary of the experiment. The effect of three factors was tested through the ANOVA analysis of the frequency of callus formation.

Table 2: The range of three factors for 2-level factorial design experiments

Factor	Name	Units	Low	Middle	High
A	2,4 D	mg/L	8	12	15
B	BAP	mg/L	1	3	5
C	LIGHT	h	0	16	24
Response	Frequency of callus formation	%			

## 2.5 Analytical Procedures

### 2.5.1 Callus Growth

During the 30 days of the incubation period, the observation on the frequency of callus formation was recorded every 3 days. The frequency of cassava callus formation was calculated using Eq. (1):

$$\text{Frequency of callus formation}(\%) = \frac{\text{Explants produced callus}}{\text{Total cultured explants}} \times 100 \quad (1)$$

### 2.5.2 Starch Content in Callus

The extraction of starch from the 0.0102 g of callus obtained from the initiation of the cassava callus culture was done following the method described in Reddy & Bhotmange [15]. The callus was dried in an oven (Memmert GmbH, Germany) for 48 h at 70 °C and then finely ground using a mortar and pestle. The protein molecules were removed by dispersing the callus in 0.153 mL of distilled water. The solution was adjusted to a pH of 10 by adding a few drops of NaOH and mixing moderately for 1 hour. Then, the starch was extracted by 3 sequential centrifugations at 5000 rpm for 30 min each. For each centrifugation, the supernatant was discarded, and the pellets were treated with 0.0306 mL of NaOH. The starch was resuspended in a mixture of 90% ethanol and NaOH for 1 hour at 80°C and let to cool to room temperature before adding distilled water to a volume of 10 mL. This last step was also performed with 0.10 g of commercial starch for the preparation of the standard starch solution.

To measure the starch content of the callus, a standard curve was constructed using different concentrations of commercial starch solution *i.e.*, 8, 16, 24, 32, 40%. The absorbance at 620 nm was recorded. Eq. (2) was generated from the starch standard curve where  $Y$  is the absorbance of starch solution and  $X$  is the percentage of starch standard solution (%). Eq. (2) was then used to calculate the percentage of starch in the sample solution before the amount of starch (g) in the callus was determined using Eq. (3).

$$Y = 0.0138X + 0.0179 \quad (2)$$

$$\text{Amount of starch (g)} = \frac{X \times \text{initial amount of callus}}{100} \quad (3)$$

## 3. RESULTS AND DISCUSSION

### 3.1 Callus Induction from Cassava Leaf Explants

After 1 month, it was observed that there were no calluses induced for any types of PGRs and concentrations derived from the cassava leaf explants. Instead, the leaf explants turned brown, and no response was observed (no callus initiation, no contamination) indicating that the explants were dead (Fig. 1). This could have been caused by the fact that the explants were soaked in 70% ethanol for 5 min during the sterilization of the explants. Indeed, ethanol is an excellent sterilization chemical, yet it is extremely phytotoxic to the plant cells when exposed for a long period time. According to Bello et al. [16], exposing *Solnacio biafrae* explant with ethanol for 20 s gave a high survival rate compared to 3 min and 5 min, respectively. The exposition period of the explant to ethanol is different for each plant and from different parts of the same plant [17]. As an example, leaf cells have less lignified thin cell walls except the leaf epidermis [12]. The thinness of the leaf cell wall might be one of the reasons why the leaf explant could not withstand our sterilization technique. Thus, to obtain a 'clean and live' leaf explant, further study on the sterilization of each type of explant needs to be developed and taken account to avoid loss of the explants, time, and material.

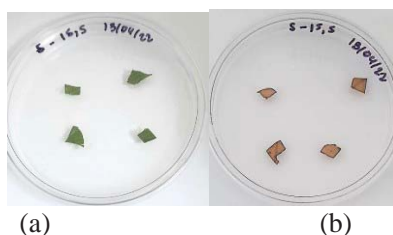


Fig. 1: Initiation of cassava callus on MS medium from leaf explant. (a) Day 1, (b) Day 30.

### 3.1 Callus Induction from Cassava Stem Petiole Explants

#### 3.1.1 Frequency of Callus Formation

Data tabulated in Table 3 clearly shows that callus was successfully induced from the combination of the first combination (8 mg/L of 2,4-D and 1 mg/L BAP) in both light conditions (75% to 0%) and dark conditions (50%) while explants placed in 12 mg/L 2,4-D and 3 mg/L BAP; 15 mg/L 2,4-D and 1 mg/L BAP; and 15 mg/L 2,4-D and 1 mg/L BAP induced very little callus (25%) to no callus induction (0%), respectively. Table 3 also demonstrates that the callus induction occurred from day 12 to day 24 in which faster growth was observed under the continuous light condition (24 h) compared to the dark condition (0 h). These results indicated that the combination and concentration of 2,4-D and BAP, as well as the light conditions, have an influence on the cassava callus growth and a lower concentration of auxin (2,4-D) and cytokinin (BAP) (8 mg/L 2,4-D + 1 mg/L) is favorable for cassava callus initiation.

Table 3: Summary of cassava callus initiation with different concentrations of 2, 4-D and BAP, and light conditions

Run	Factor A: 2,4D [mg/L]	Factor B: BAP [mg/L]	Factor C: LIGHT [h]	Callus induction [day]	Response: Frequency of callus formation [%]
1	8	5	0	24	25
2	15	5	24	-	0
3	8	1	24	14	50
4	8	5	24	-	0
5	15	5	0	-	0
6	15	1	0	-	0
7	15	1	24	-	0
8	8	1	0	14	25
9	12	3	16	24	25
10	8	5	24	27	25
11	8	1	0	24	50
12	15	5	0	-	0
13	15	5	24	-	0
14	8	1	24	16	50
15	15	1	24	-	0
16	8	5	0	24	50
17	15	1	0	-	0
18	12	3	16	-	0
19	8	5	24	-	0
20	8	1	0	24	50
21	15	5	24	-	0
22	15	5	0	-	0
23	8	5	0	-	0
24	12	3	16	-	0
25	8	1	24	12	75
26	15	1	0	-	0
27	15	1	24	-	0

### 3.1.2 ANOVA analysis

The ANOVA analysis of the stem petiole shows that the *p-value* for the model was less than 0.05, and the F-value was 28.51 which indicates that the model was significant (Table 4). The significant model terms were factors A, B and AB. Factor C (light condition) was part of the residuals since it is less significant (no effect on the model). Moreover, the difference between the adjusted R<sup>2</sup> and the predicted R<sup>2</sup> was less than 0.2 and R<sup>2</sup> was 0.8029 which was a higher value indicating a high degree of correlation between the experimental and predicted data. Hence it could be deduced that the model has a high degree of significance [18]. The equation of the design as shown in Eq. (4) suggests that a lower value of factor A and B, respectively results in a higher frequency of callus formation while a higher value of factor AB will give a higher frequency of callus formation.

Table 4: ANOVA analysis of cassava callus growth from the stem explants

Source	Sum of Squares	Degree of freedom	Mean square	F-value	p-value	
<b>Model</b>	10458.73	4	2614.68	28.51	<0.0001	Significant
<b>A- 2,4-D concentration (mg/L)</b>	5162.14	1	5162.14	42.58	<0.0001	
<b>B- BAP concentration (mg/L)</b>	2604.17	1	2604.17	21.48	0.0001	
<b>AB</b>	2604.17	1	2604.17	21.48	0.0001	
<b>Residual</b>	2546.19	21	121.25			
<b>Lack of fit</b>						Not significant
<b>Pure error</b>						
<b>Cor Total</b>	12916.67	26				

R<sup>2</sup> = 0.8029, Adj - R<sup>2</sup> = 0.7747, Pred - R<sup>2</sup> = 0.6771

$$\text{Frequency of callus formation (\%)} = +129.21919 - 8.64981A - 22.32143B + 1.48810AB \quad (4)$$

The results of this study opposed the previous studies which reported that a higher concentration of auxin and cytokinin is favorable for callus growth while a lower concentration of auxin and cytokinin favors organ culture growth [8,9]. However, the BAP concentration range used in this study (1 mg/L to 5 mg/L) is not within the BAP concentration range (0.1 mg/L to 1 mg/L) used in Faye et al. [9], which may cause the differences. The contradiction of the results obtained could also be due to the cultivar type and explant used. Fletcher et al. [12] proposed that different explants and cultivars react differently to different concentrations of PGR. In their study using different cassava cultivars available in Ghana, among the 3 concentrations of 2,4-D used *i.e.*, 8, 12, and 15 mg/L, 2,4-D at 8 mg/L achieved a better callus growth of *Afisiafi* cultivar for both leaf (75%) and bark (25%). In addition, for the *Afebankye* cultivar, the leaf explant gave a better result for 8 mg/L 2,4-D (75%) while the stem petiole supplemented with 12 mg/L 2,4-D achieved 45% of callus formation. However, for *Tuaka* cultivars the percentage of formed callus from the explants such as leaf, stem petiole, and buds did not change significantly at any of the three 2, 4-D concentrations (below 20%). Based on this, it can be proposed that the stem petiole explant from the Rayong cultivar resulted in better callus growth at a lower concentration of 2,4-D (8 mg/L).

Besides that, this study explored the effect of combining the 2,4-D and BAP at various concentrations on cassava callus initiation which so far has not been reported. It is reported that the combination of 2 mg/L 2,4-D and 0.1 mg/L BAP gave the best callus induction for two rice varieties, Basmati-370 and Basmati-385 [19]. The same results were described for different

plants such as *Brassica napus* and *Piper betle* L. var Nigra [20,21]. Thus, it can be deduced that for a combination of 2,4-D and BAP, the growth of the callus was favored by a lower concentration of auxin and cytokinin, and the type of plant, cultivars as well as explants significantly influenced the concentration of auxin and cytokinin.

Table 5: Light condition for different cassava cultivars

Type of cultivars	Type of explants	Light condition	Reference
Rayong	Leaf	Continuous light, 16-h light, continuous dark	This study
	Stem petiole		
Not available	Leaf	16-h light (white cooling fluorescent lamps)	[8]
	Stem		
	Root		
Doku	Leaf	Continuous dark	[12]
Afisiafi	Stem petiole		
Afebankye	Buds		
Soya	Not available	1 <sup>st</sup> incubation: Continuous dark	[9]
Niargi		2 <sup>nd</sup> incubation in 13-h light (light intensity of 4000 lux)	
Cololi			
Cacau			
Cacau roja			

Although the effect of the light is not significant to the callus growth based on the ANOVA results, it could still be observed that the cassava callus induced faster and had a higher frequency of callus formation under 24 hours of light exposure (started on the 12<sup>th</sup> day after inoculation) compared to the continuous dark condition (started on the 24<sup>th</sup> day). Callus formed under light condition have a frequency between 75% to 0% while the callus formed under total darkness gave a frequency between 50% to 0%. So far, studies related to the influence of light conditions on cassava callus culture are still scarce and different light conditions have been used to induce cassava callus culture as shown in Table 5. However, it is found that dark conditions are suitable for the initiation of rice callus culture while light exposure is suitable for its proliferation [22]. The results of this study partially conflicted with Chutipaijit [22] since the callus growth under 24 h light exposure recorded a better callus induction (75%) compared to the callus grown under continuous dark (50%), and 16h/8 light exposure (25%). On the other hand, a study by Ozarowski [23] on tobacco plants reported similar results to this study. The leaf blade of Motihari achieved 97.20% of callus formation under light condition. It was justified that the irregularities of reported results depend on the plant cultivar and type of explant used [23].

### 3.2 Preliminary Analysis of Starch Content in Callus

The amount of starch in cassava callus was determined using the cassava standard curve obtained from the quantitative iodine test performed on commercial cassava starch. The measured absorbance of the callus sample was 0.021 AU which corresponds to 0.22% of starch. This amount is relatively small compared to the standard amount (4.4 % starch) highlighted in Carciofi et al. [24]. The difference in value could be due to starch loss during the purification process. This statement is in line with our observation. Indeed, the small amount of callus obtained (0.0102 ±0.0002 g) went through several processes that need to be meticulously performed such as the separation of the supernatant and pellets during centrifugation. This

process could cause some of the desired product to be washed off along with the supernatant if not carefully performed. Thus, the accuracy of the results is highly biased. For future work, the selection of the starch extraction process from cassava callus culture should be thoroughly studied.

Another reason that could cause the small amount of starch content in our cassava callus is due to the phase of callus growth (induction phase, proliferation phase or regeneration phase). A callus cycle comprises 3 phases: the induction phase (dedifferentiation and division of the explants of the cells), the proliferation phase (rapid division of the cells), and the regeneration phase (differentiation of the cells and organogenesis). It is reported that the callus accumulates sugar (glucose and starch) in the proliferation phase of the cycle for the regeneration phase as the callus will require large energy for organogenesis and to equilibrate the level of free soluble sugars to counterbalance the osmotic potential in the medium [25]. In this study, the callus was obtained from a 3-week-old subculture which means it was still in the early stage of proliferation explaining why the accumulation of the starch was lower as the callus did not accumulate enough starch for its regeneration phase.

Moreover, the callus obtained was smaller in size and yellow in color (Fig. 2). Those physical attributes indicate a low regenerable cultivar which is known to have small amounts of sucrose, glucose, and starch content [26]. For rice callus, it is stated that the TN1 cultivars, which are non-regeneratable (NR), produce small and yellowish callus lacking glucose, sucrose, and starch content in both the callus induction phase and regeneration phase while the ANT39 cultivars, highly regeneratable (HR) cultivars, produce large, compact, and whitish callus which have high glucose, sucrose, and starch content in the callus induction phase but low sugar (glucose and starch) content in the regeneration phase. So far, no report regarding the regeneration of the cassava Rayong cultivars has been conducted. Thus, a conclusive statement cannot be provided since different plants have different attributes although they have the same capability to produce starch.



Fig. 2: Starch harvested from the callus induced from cassava stem explant in MS media with 8 mg/L of 2,4-D and 1 mg/L BAP.

#### 4. CONCLUSION

It was found that the concentration of the PGRs as well as their combination highly affect the frequency of callus formation while the light condition has less to no significance on callus induction. It was also found that a lower concentration of 2,4-D and BAP are favorable to callus formation (8 mg/L 2,4-D: 1 mg/L BAP). Regarding the evaluation of the starch content in the cassava culture using an iodine test, it was found that the callus accumulates only 0.22 % of starch which is below the standard value of various callus (4.4%) and might be due to loss of starch during the purification process of the starch or the fact that the callus was in the early

stage of the callus cycle (early proliferation stage) or the regeneration power of the cultivar (NR cassava lack of starch content). Hence, more research is required to provide conclusive reasons for the lack of starch in the cassava callus culture. To improve the study of cassava callus initiation for starch production, it is highly recommended to select a sterilization technique that is suitable for all types of explants and to select a fast and effective extraction technique and starch analysis method for the evaluation of the amount of starch in cassava callus. It is hoped that this study will help in selecting the parameters for optimizing the culture conditions for cassava callus establishment towards starch production.

## ACKNOWLEDGEMENT

We would like to acknowledge the Ministry of Higher Education Malaysia for funding this project under the Fundamental Research Grant Scheme (FRGS/1/2021/STG01/UIAM/02/2). In addition, the authors are grateful to the management of the International Islamic University Malaysia (IIUM) for a research fund (RMCG20-018-0018) for this work. Department of Chemical Engineering and Sustainability, Kulliyah of Engineering, IIUM for providing the laboratory facilities to conduct this study. We also thanked NGP Technology Sdn. Bhd. for providing us with cassava cuttings to be planted at IIUM and then used as the explants to initiate cassava cultures.

## REFERENCES

- [1] Tan SL. (2015) Cassava – Silently, The Tuber Fills. *UTAR Agriculture Science Journal*, 1(2): 12-24.
- [2] Li S, Cui Y, Zhou Y, Luo Z, Liu J, Zhao M. (2017) The industrial applications of cassava: current status, opportunities and prospects. *Journal of the Science of Food and Agriculture*, 97(8): 2282-2290. <https://doi.org/10.1002/JSFA.8287>
- [3] Tumwesigye KS, Oliveira JC, Namuwaya S, Sousa-Gallagher MJ. (2021) Cassava Biomaterial Innovations for Industry Applications. In (Ed.), *Cassava - Biology, Production, and Use*. IntechOpen. <https://doi.org/10.5772/intechopen.97493>
- [4] Cassava Starch Market, Consumption & Global Forecast. Available: <https://www.renub.com/cassava-starch-market-p.php>
- [5] Howeler R, Cain P, Trumbore L, Hidajat SU. (2012) The challenge of large-scale cassava production. *Sustainable Cassava Production in Asia for Multiple Uses and for Multiple Markets Proceedings 9th Regional Cassava Workshop*, 313-321.
- [6] NurulNahar E, Tan, SL. (2012) Cassava mini-cuttings as a source of planting material, *J. Trop. Agric. and Fd. Sc.*, 40(1): 145-151.
- [7] Hussain A, Ahmed I, Nazir H, Ullah I. (2012) Plant Tissue Culture: Current Status and Opportunities. *Recent Advances in Plant in Vitro Culture*, 37(3): 5-30. <https://doi.org/10.5772/50568>
- [8] Abdalla N, Ragab M, El-Miniawy S, Taha H. (2013) Callus induction, regeneration and molecular characterization of cassava (*Manihot esculenta* Crantz). *Journal of Applied Sciences Research*, 9: 3781-3790.
- [9] Faye A, Sagna M, Kane PD, Sane D. (2015) Effects of different hormones on organogenesis in vitro of some varieties of cassava (*Manihot esculenta* Crantz) grown in Senegal. *African Journal of Plant Science*, 9(8): 305-312. doi:<https://doi.org/10.5897/AJPS2014.1243>
- [10] Mahdi H, Edward R. (2018) In vitro propagation of selected Malaysia cassava (*Manihot esculenta* Crantz) varieties by using nodal explants. *Malaysian Applied Biology*, 47(1): 1-5.
- [11] Prammanee S, Kamprerasart K, Salakan S, Sriroth K. (2010) Growth and starch content evaluation on newly released cassava cultivars, Rayong 9, Rayong 7 and Rayong 80 at different harvest times. *Kasetsart J.*, 44: 558-563.

- [12] Fletcher EKA, Amoako TNE, Twumasi P. (2011) Effect of 2,4-D, explants type and cultivar on the callogenesis expression of cassava (*Manihot esculenta* Crantz) in Ghana. *African Journal of Biotechnology*, 10(46):9396-9401. <https://doi.org/10.5897/ajb10.2115>
- [13] Puad NIM, Sofri NSNM, Amid A, Azmi AS. (2022) Optimization of Surface Sterilization Method and Initiation of Bitter Cassava Callus Culture. *Biological and Natural Resources Engineering Journal*, 6(1): 47-59.
- [14] Puad NIM, Tang CW. (2015) A simple and Easy Method for Preparing Solid and Liquid Media for Plant Culture. *Experimental Methods in Modern Biotechnology* (vol. 3). IIUM Press, Malaysia.
- [15] Reddy DK, Bhotmange MG. (2013) Isolation of Starch from Rice (*Oryza sativa* L.) and its Morphological Study using Scanning Electron Microscopy. *International Journal of Agriculture and Food Science Technology*, 4(9): 859-866.
- [16] Bello OA, Esan EB, Obembe OO. (2018) Establishing surface sterilization protocol for nodal culture of *Solanecio biafrae*. *IOP Conference Series: Earth and Environmental Science*, 210: 012007. <https://doi.org/10.1088/1755-1315/210/1/012007>
- [17] Hesami M, Naderi R, Tohidfar M, Yoosefzadeh-Najafabadi M. (2019) Modeling and Optimizing in vitro Sterilization of Chrysanthemum via Multilayer Perceptron-Non-dominated Sorting Genetic Algorithm-II (MLP-NSGAI). *Frontiers in Plant Science*, 10. <https://doi.org/10.3389/fpls.2019.00282>
- [18] Anderson MJ, Whitcomb PJ. (2015) Two-level Factorial Design. *DOE Simplified: Practical Tools for Effective Experimentation*, [www.statease.com](http://www.statease.com).
- [19] Ullah H, Ullah I, Jadoon SA, Rashid H. (2007) Tissue culture techniques for callus induction in rice. *Sarhad J. Agric*, 23(1), 81-86.
- [20] Bano AS, Khattak AM, Basit A, Alam M, Shah ST, Ahmad N, Gilani SAQ, Ullah I, Anwar S, Mohamed HI. (2022) Callus Induction, Proliferation, Enhanced Secondary Metabolites Production and Antioxidants Activity of *Salvia moorcroftiana* L. as Influenced by Combinations of Auxin, Cytokinin and Melatonin. *Brazilian Archives of Biology and Technology*, 65: e22210200. <https://doi.org/10.1590/1678-4324-2022210200>
- [21] Junairiah J, Purnomo P, Utami ESW, Ni'matuzahroh N, Sulistyorini, L. (2018) Callus Induction of Piper betle L. Var Nigra Using 2,4-Dichlorofenoxyacetic Acid and 6-Benzil Aminopurin. *Biosaintifika: Journal of Biology & Biology Education*, 10(3): 588-596. doi:<https://doi.org/10.15294/biosaintifika.v10i3.15962>
- [22] Chutipaijit S, Sutjaritvorakul T. (2018) Titanium dioxide (TiO<sub>2</sub>) nanoparticles induced callus induction and plant regeneration of indica rice cultivars (suphanburi1 and suphanburi90). *Digest Journal of Nanomaterials and Biostructures*, 13(4): 1003-1010.
- [23] Ozarowski M. (2011) Influence of the physico-chemical factors, plant growth regulators, elicitors and type of explants on callus cultures of medicinal climbers of *Passiflora* l. L. *Herba Polonica*, 57(4): 58-75.
- [24] Carciofi M, Blennow A, Nielsen MM, Holm PB, Hebelstrup KH. (2012) Barley callus: a model system for bioengineering of starch in cereals. *Plant Methods*, 8(1): 1-10. <https://doi.org/10.1186/1746-4811-8-36>
- [25] Efferth T. (2019) Biotechnology Applications of Plant Callus Cultures. *Engineering*, 5(1): 50-59. <https://doi.org/10.1016/j.eng.2018.11.006>
- [26] Lee ST, Huang WL. (2013) Cytokinin, auxin, and abscisic acid affects sucrose metabolism conduce to de novo shoot organogenesis in rice (*Oryza sativa* L.) callus. *Botanical Studies*, 54(1): 1-11. <https://doi.org/10.1186/1999-3110-54-5>

# INVESTIGATION OF ENHANCED ELECTROCOAGULATION-MEMBRANE PROCESS FOR WATER RECLAMATION FROM PALM OIL MILL EFFLUENTS

AMINA TAHREEN, MOHAMMED SAEDI JAMI\*,  
FATHILAH ALI, NIK RASHIDA NIK ABDUL GHANI AND RADHIA NEDJAI

*Department of Chemical Engineering and Sustainability,  
Kulliyah of Engineering, International Islamic University Malaysia, Kuala Lumpur, Malaysia*

\*Corresponding author: [saedi@iium.edu.my](mailto:saedi@iium.edu.my)

*(Received: 18 October 2022; Accepted: 7 September 2023; Published on-line: 1 January 2024)*

**ABSTRACT:** The process of electrocoagulation (EC) enhanced with adsorbent addition, as a pre-treatment for ultrafiltration membrane, is widely unexplored in oil palm-based wastewater treatment. Utilizing predetermined EC operational parameters and a defined activated carbon (AC) dosage for biotreated palm oil mill effluents (BPOME), membrane fouling was studied during crossflow membrane filtration at 0.5 bar transmembrane pressure and 1 kDa membrane pore size. The dominant fouling mechanism in membrane filtration without EC-AC pretreatment of BPOME, was cake formation, which was determined through Hermia's pore blocking models. However, after EC-AC pre-treatment, the membrane fouling was mitigated. Moreover, the pre-treatment process, AC assisted EC, sustainably enhanced the final treated effluent quality in addition to enhancing fouling mitigation in the subsequent membrane filtration. The removal of Total Suspended Solids (TSS), turbidity and color were nearly 100% and Chemical Oxygen Demand (COD) was 99.7% removed with final value of  $5 \pm 1$  mg/L, which is within the range of reusable water standards.

**ABSTRAK:** Proses elektrokoagulasi (EC) yang ditingkatkan dengan bahan penyerap, adalah pra-rawatan bagi membran penuras ultra. Walau bagaimanapun ianya masih belum luas diterokai dalam sistem rawatan air buangan berasaskan kelapa sawit. Menggunakan pakai parameter operasi EC pra-tentu dan dos karbon aktif tentu (AC) bagi bio-rawatan efluen kilang kelapa sawit yang terawat (BPOME), mendakan membran telah dikaji menggunakan teknik penurasan membran aliran silang pada tekanan transmembran 0.5 bar dan saiz liang membran 1 kDa. Mekanisme mendakan membran kotoran dominan dalam penurasan membran tanpa pra-rawatan EC-AC BPOME, adalah pembentukan kek, iaitu terhasil melalui model penyumbatan liang Hermia. Walau bagaimanapun, selepas pra-rawatan EC-AC, mendakan kotoran membran dapat dikurangkan. Tambahan, proses pra-rawatan AC-EC, secara mampan dapat menambah kualiti akhir efluen terawat selain dapat meningkatkan mitigasi kotoran mendakan dalam penurasan membran seterusnya. Penyingkiran Total Pepejal Terampai (TSS) adalah 99.7%, kekeruhan dan warna adalah hampir 100%. Keperluan Oksigen Kimia (COD) tersingkir sebanyak 99.7% dengan nilai akhir sebanyak  $5 \pm 1$  mg/L, iaitu dalam julat piawaian air boleh guna semula.

**KEYWORDS:** *electrocoagulation; membrane filtration; activated carbon; membrane fouling*

## 1. INTRODUCTION

Sustainable wastewater treatment technology is a highly sought objective of the current global trend of the industrially flourishing oil palm industry. With advances in technology and global demands, the palm oil production limits tend to increase with time. However, the environmental impact of the rising industrial works and production is often partially or completely overlooked. Over time, the detrimental effects of high industrial wastewater discharge, loss of marine ecosystems, overuse of fresh water supply and environmental pollution can collectively cause a massive global downfall of the public health, the ecosystem, as well as the economy [1].

There are ongoing efforts to sustainably reclaim water from industrial effluents to cut down the overuse of fresh water supply and its global annual decline. Although most processes depicted good outcome on pollutant removal efficiency with extensive use of chemicals, oxidants, processes requiring large footprints, and complex water treatment processes, there is a crucial need for considering economic sustainability and environmental friendliness. Therefore, electrocoagulation (EC) is captivating researchers towards developing a low footprint-based technology with simplicity and versatility in pollutant removal across various wastewater types, and with low sludge production while mitigating harmful chemical-based treatments [2]. Moreover, hybrid technologies have emerged for water reclamation for industrial reuse [3]. Membrane technology is such a booming field in water treatment with its low footprint and selective pollutant rejection ability [4].

However, water reclamation based on membrane technology is costly and faces obstacles with inevitable fouling (pore blocking) at the membrane surfaces causing an overtime loss of flux which can be overcome by physical or chemical washing to regain original membrane functionality [5]. However, EC integration as pre-treatment for membrane process can potentially enhance wastewater treatment for water reclamation as it removes colloidal pollutants through charge destabilization, allowing a major cut down of pollutants entering the membrane. Consequently, fouling could be minimized to an extent of reversibility, helping to extend membrane functionality for an extensively long period of time and avoiding constant membrane replacements. Although chemical coagulation pre-treatment generally enhanced membrane filtration, there is a potential for EC based integrated processes to replace chemical coagulation as EC has proven to be more environmentally friendly and economical, with lower sludge production and easier operation avoiding harsh chemicals [6].

However, there are limited studies that explored EC-membrane processes enhanced with activated carbon for water reclamation from industrial wastewater. Palm oil industries treat their organic-matter-rich effluents and discharge the final effluent known as biotreated palm oil mill effluents (BPOME). BPOME is a dark brown and turbid looking wastewater, which is rich in organic matter, released in settling ponds as the final effluent. This study aims to investigate the potential of hybrid EC-membrane process with activated carbon (AC) addition to reclaim water from BPOME.

## 2. METHOD

BPOME was collected from the final discharge pond in a palm oil mill based in Negeri Sembilan, Malaysia. To prevent degradation due to naturally occurring biological activity, the collected sample was stored at 4 °C. The EC process was carried out with pre-optimized operating conditions of current, initial pH, and time of 1.75 A, 6, and 15 minutes just as the study carried out in [7] following the same setup, anode surface area (10.93 cm<sup>2</sup>), interelectrode distance (10 mm), and the same reactor (200 ml capacity beaker) and direct current supply unit

from Twintex (TP-2303K, Taiwan). This study incorporated further modification by activated carbon (AC) addition of 1 wt% as the study by [8].

The wastewater characterizations included COD, color, and total suspended solids (TSS) before and after EC using a spectrophotometer (HACH DR 5000, USA) according to American Public Health Association (APHA) standards [9]. A DRB 200 Reactor (HACH DRB 200, USA) was used to heat the COD vials (2 hours for 150°C) before COD measurement. The initial pH of the samples was controlled with 5% HCl and 0.1 M NaOH solutions with a pH meter (Mettler Toledo, MP220 model, USA). A multi-meter (HACH sensION5, USA) was used to measure the TDS, conductivity, and salinity of the wastewater samples. Turbidity of the samples was measured using a standard nephelometric method with a turbidity meter (EXTECH Instruments TB400, Taiwan). For separation of flocs after EC treatment, 0.45  $\mu\text{m}$  pore sized filter papers were used.

After EC, the treated BPOME was further treated with an ultrafiltration membrane. Crossflow filtration mode is one of the ways of physically reducing the concentration polarization and fouling rate by delaying the cake build up, varying the feed flow hydrodynamics [10]. Furthermore, membrane backwash via chemical cleaning contributes to removal of reversible fouling, whereas irreversible fouling diminishes the membrane performance over time, leading to membrane replacement [11]. However, having the influent feed pre-treated (i.e., EC in this study) to remove maximum possible colloids and pollutants, is one of the best ways to achieve fouling mitigation [5]. The approach of [12] was used to run the ultrafiltration membrane experiment in a crossflow mode of operation. The schematic diagram of the membrane filtration system set up used in this work is shown in Fig. 1. Before beginning the experiment, the membrane was soaked overnight in distilled water to remove impurities left over from the manufacturing processes or additives used in preserving and stabilizing the membrane. The next day, the membranes were wetted out again by circulating distilled water at 2.0 bars for 30-60 minutes. This procedure helped in preventing membrane compaction during permeation. The distilled water flux was measured before each experiment with a clean membrane at a pressure within 1 to 2 bars.

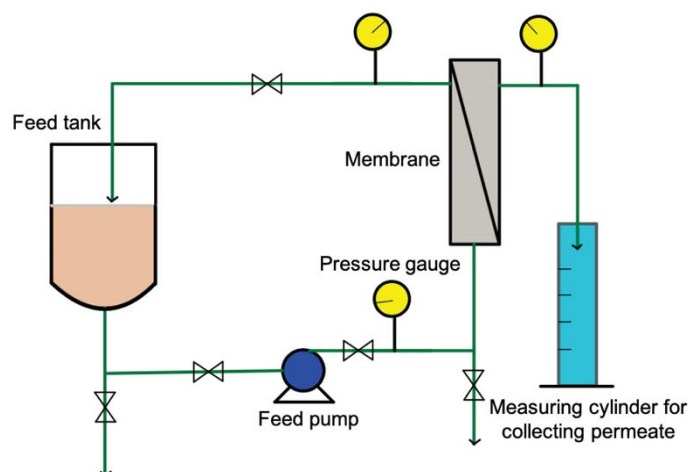


Fig.1. Schematic diagram of the crossflow filtration setup, adapted from [13].

A polyethersulfone membrane with a Molecular Weight Cut-Off (MWCO) of 1 kiloDaltons (kDa) and transmembrane pressure (TMP) of 0.5 bar was investigated on its ability to remove COD from the EC treated BPOME. These parameters resulted in the best permeate quality (highest removal of color, COD, and turbidity) in BPOME ultrafiltration in the study

reported by [12], that employed the same crossflow membrane filtration system. A lower TMP, contributed to the highest % COD removal, which was also indicated by the work of [14], where a higher applied pressure led to an enhanced gel layer formation that blocked the incoming organic matter from passing through, consequently reducing the removal of COD, color, and turbidity. The final permeate after crossflow ultrafiltration was characterized to determine the final removal efficiency in terms of COD, turbidity, TSS, and color, and were compared with reusable water standards.

After each experimental run, chemical cleaning was performed by passing 1 N NaOH at 1 bar (TMP) through the filtration membrane to preserve the integrity of the membrane. Additionally, the permeate volume collected was plotted against time to observe the flux. Next, the linearized pore blocking model equations (Table 1) were employed to fit the data, to determine the dominant pore blocking model, where  $J$ ,  $J_0$  and  $t$  represent the flux, initial flux, and time respectively, and  $K_{cb}$ ,  $K_s$ ,  $K_i$  and  $K_c$  represent the pore blocking constants for complete, standard, intermediate, and cake filtration models, in Eq. (1) to Eq. (4), respectively.

Table 1: Linearized pore blocking equations for membrane filtration [15]

Pore blocking model	Linearized equation
Complete	$\ln J^{-1} = \ln J_0^{-1} + K_{cb}t$ (1)
Standard	$J^{0.5} = J_0^{0.5} + K_s t$ (2)
Intermediate	$J^{-1} = J_0^{-1} + K_i t$ (3)
Cake filtration	$J^{-2} = J_0^{-2} + K_c t$ (4)

The energy consumption of the treated BPOME volume, at optimized conditions, was calculated with Eq. (5) and Eq. (6) in Table 5 for EC and membrane filtration, respectively. The symbols  $I(A)$ ,  $U(V)$  and  $t(\text{hours})$  represent the current applied, resulting voltage, and the time of EC operation, respectively. The flux  $J$  (L/(m<sup>2</sup>.min)), effective membrane surface area of 0.1 m<sup>2</sup> and transmembrane pressure, TMP (bar), are the parameters for the membrane filtration energy consumption in Eq. (6).  $V$  represents the working volume (m<sup>3</sup>) for EC and permeate volume (m<sup>3</sup>) for crossflow filtration.

Although COD removal was monitored after the EC process, concerns remain for the possibility of the presence of aluminum ions from the aluminum cathode in the final treated water. Aluminum contamination can be detrimental to human health as it has been known to increase the risk of dementia and Alzheimer's disease [16]. Therefore, the final treated effluent was tested for the presence of aluminum and possible trace metals to observe the impact of the EC and EC membrane process on BPOME. The ICP-MS technique is greatly beneficial for water analysis to determine trace metals, due to its sensitivity and the ability of multi-element detection, hence, the USEPA have employed this technique for water and waste analyses [17].

### 3. RESULTS AND DISCUSSION

With the EC optimized parameters and addition of powdered AC, the treated effluent quality was enhanced to the extent of fouling mitigation in the subsequent crossflow membrane filtration step of the hybrid process. The best outcome was achieved with 1 wt. % addition of AC in the EC reactor, and the removal of TSS, turbidity and color were nearly 100 % and COD was removed 99.7% with final average value of 5 mg/L, which lie within the range of process water standards (in terms of the stated key parameters, namely COD, TSS, turbidity, and color, as in the scope of this study).

Implementing the method carried out previously in [8], BPOME was treated with EC assisted with 1 wt% of AC addition. The resulting treated wastewater was used for studying pore blocking behavior in crossflow membrane filtration. Not all COD was removed, and a considerable amount of COD was left in the EC treated solution alone. However, with AC addition, the fastest removal % noted was of TSS from BPOME for all concentrations of powdered AC added, followed by turbidity, color, and COD. The combined action of the adsorption of colloids by both AC along with the metal coagulants generated from the Aluminum metal anode in the EC reactor, greatly enhanced the efficiency of the EC process, that contributed to a much higher pollutant removal rate. Membrane pore blocking studies were performed to further study the mechanism of the fouling in membrane ultrafiltration of BPOME for both with and without EC-AC pre-treatment.

### 3.1 Membrane Pore Blocking Study without EC-AC Pre-Treatment

The linearized pore blocking equations by [15], listed in Table 1, have been employed in this work to establish the prominent fouling mechanism prevailing in the crossflow filtration step. The linearized pore blocking models contribute not only to establish the dominant fouling mechanism taking place to explain the flux decline in the ultrafiltration membrane but also significantly contribute to the scale up design in the industrial scale, providing the pore blocking constant values [18]. Moreover, understanding the fouling mechanism enables the devising of antifouling strategies to overcome the loss of flux and preserve membrane integrity for longer time. Based on the linearized pore blocking model plots observed in Fig. 2 to Fig. 5, the trendlines after 10 minutes, beyond initial stage of crossflow operation, represent the relationship between the permeate flux with time with the respective pore blocking model. The pore blocking constants, along with the  $R^2$  and  $J_0$  (y-intercept) of each model, are summarized in Table 2, depicting the fitness of the experimental data with different pore blocking models.

Table 2: Summary of pore blocking constants,  $R^2$  and  $J_0$

	Pore blocking model	Pore blocking constant	$J_0$ (intercept) $L/m^2 \cdot min$	$R^2$
1	Standard	$K_s = 0.0078$	0.3452	0.9534
2	Intermediate	$K_i = 0.0296$	0.3484	0.9605
3	Complete	$K_{cb} = 0.0083$	0.3425	0.9450
4	Cake filtration	$K_c = 0.2109$	0.3570	0.9708

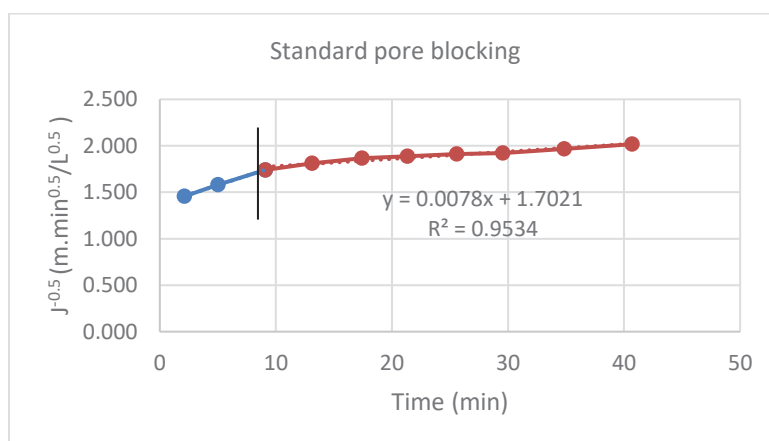


Fig. 2: Linearized plot for permeate flux vs time for standard pore blocking model.

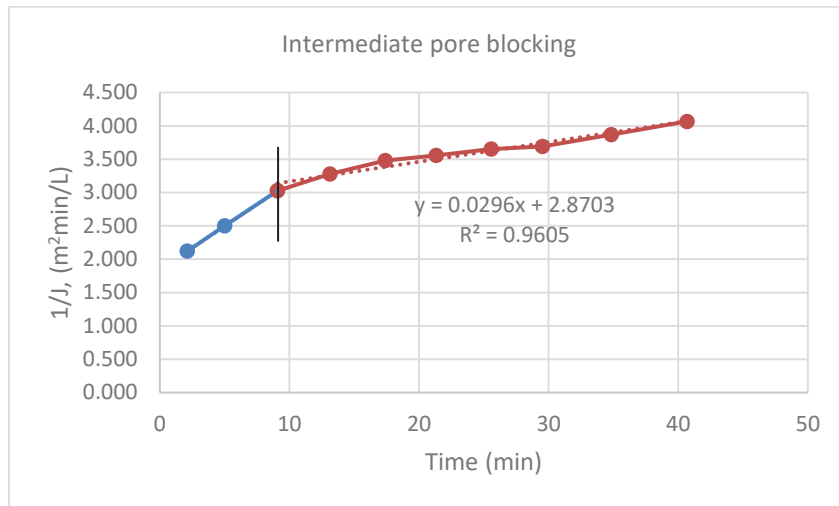


Fig. 3: Linearized plot for permeate flux vs time for intermediate pore blocking model.

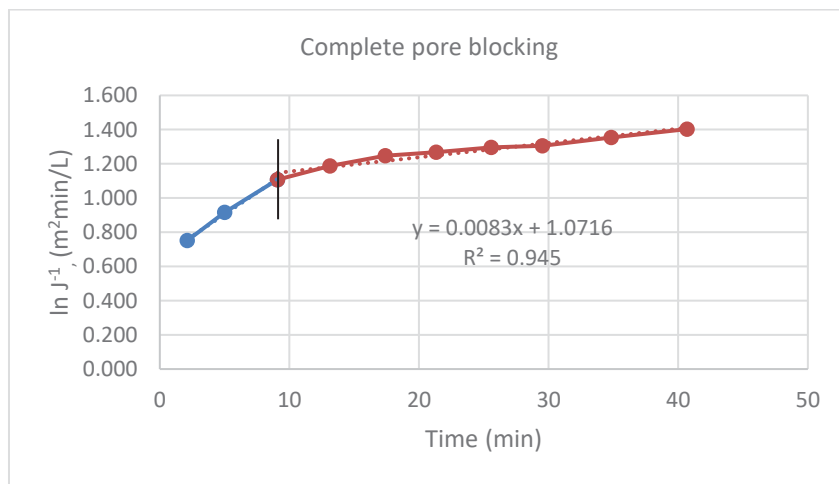


Fig. 4: Linearized plot for permeate flux vs time for complete pore blocking model.

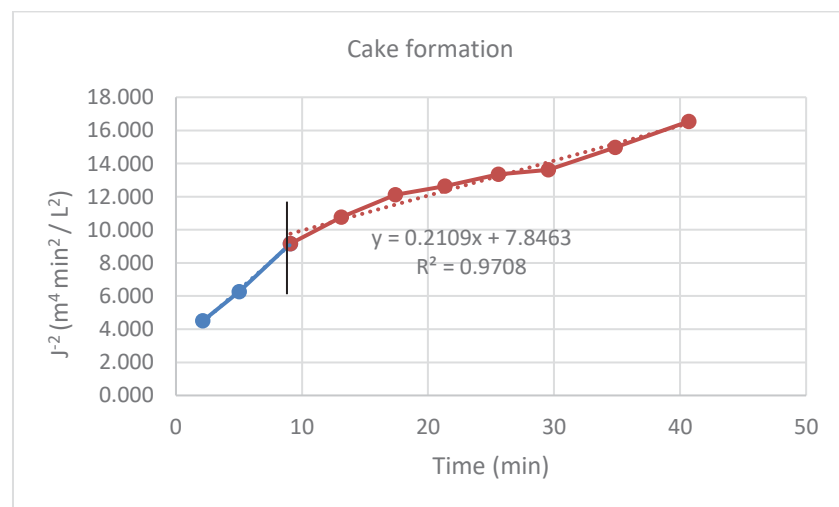


Fig. 5: Linearized plot for permeate flux vs time for cake filtration model.

The most suitable fouling model was determined by assessing the regression of the models (Table 2). With the highest  $R^2$  of 0.9708, cake filtration stood out as the dominating pore blocking mechanism in this study. After the cake filtration model, the intermediate pore blocking model depicted the next highest  $R^2$  of 0.9605. Therefore, the intermediate pore blocking contributed the most, leading towards the cake formation. This outcome of prevailing cake filtration fouling corresponds to the work of [14] where the membrane filtration depicted cake filtration as the dominant pore blocking mechanism for oil palm effluent, feedwater, and dairy wastewater respectively. Hence, overall, the conclusions established in these studies suggest the cake filtration model to be the most universal model that describes the fouling mechanism of wastewater membrane filtration.

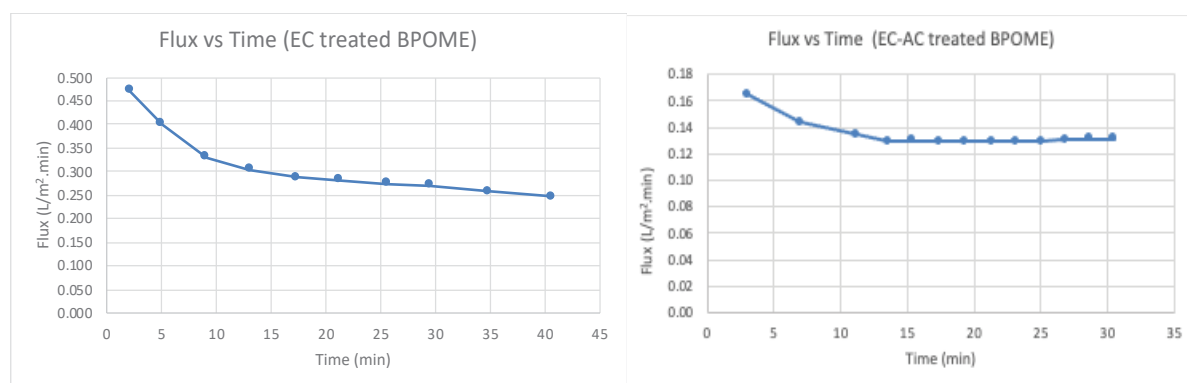


Fig. 6: Comparison of flux decline with and without EC-AC treatment.

Moreover, the flux decline in the ultrafiltration membrane was observed with and without EC-AC treated BPOME and is presented in Fig. 6. Notably, there is a decline in the flux after the initial phase of filtration, the flux was constant throughout, denoting no fouling took place as it was free from pollutants that cause membrane fouling for EC-AC treated BPOME ultrafiltration. To further explore the membrane fouling conditions, a membrane pore blocking study was carried out.

### 3.2 Membrane Pore Blocking Study with EC-AC Pre-Treatment

After collecting the EC (coupled with AC) treated BPOME, a crossflow ultrafiltration membrane was run with TMP 0.5 bar, effective membrane surface area of 0.1 m<sup>2</sup> and noting the time taken after every 100 mL volume of permeate achieved, freshwater flux was determined with deionized water, followed by BPOME.

As the observed permeate flux was nearly constant with time corresponding to the gradient of the linearized flux graphs for all the models (Fig. 7 to Fig. 10), it was concluded that the level of purity obtained in the EC with the addition of powdered AC prevented any type of fouling to take place in the crossflow filtration membrane. This result agrees with the notable work of [19], where incorporation of powdered AC pre-treatment by adsorption, significantly contributed to fouling mitigation along with pigment removal before carrying out membrane filtration. Therefore, exploring addition of powdered AC in this work, enhanced color removal in the EC process and greatly contributed to fouling mitigation of the subsequent crossflow membrane filtration in BPOME treatment.

### 3.3 Characterization of Permeate after Membrane Filtration

The permeate obtained after membrane filtration of BPOME pretreated with EC-AC, was characterized and compared with EPA standards for reusable water. The main parameters monitored for pollutant removal efficiency in this work were COD, turbidity, TSS, and color.

Besides, the final characterization of the permeate (Table 3) after the EC-membrane process, where EC was enhanced with addition of powdered AC in the reactor, 99.7% of COD was removed, with  $5 \pm 1$  mg/L of final COD value. Besides COD, almost 100% of TSS, color and turbidity were removed from the BPOME, with hybrid process. This water quality (based on color, TSS, COD, and turbidity) meets not only the standards of irrigation water but also process water for industrial reuse [20].

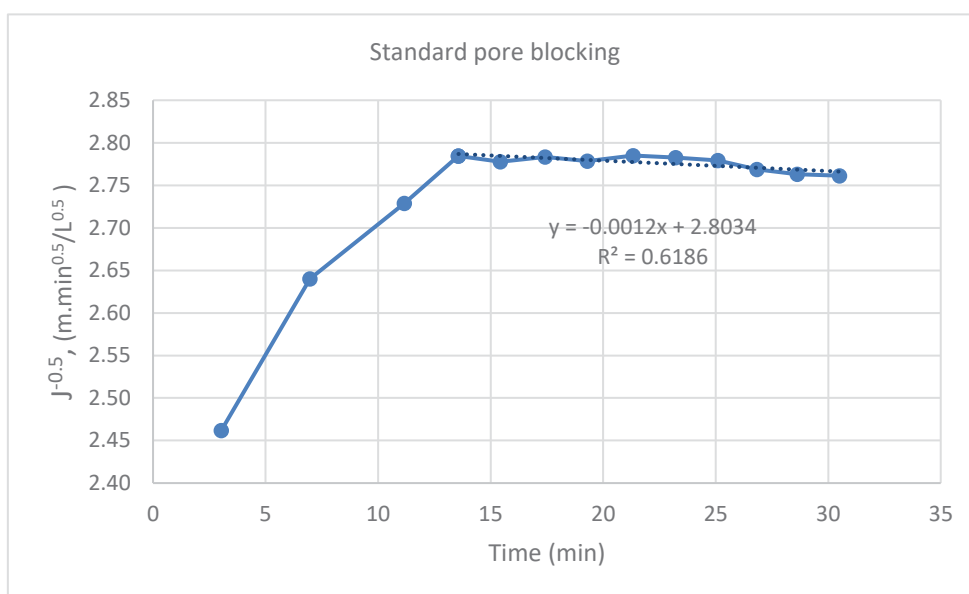


Fig. 7: Linearized plot for permeate flux vs time for standard pore blocking model for crossflow filtration of EC-AC treated BPOME.

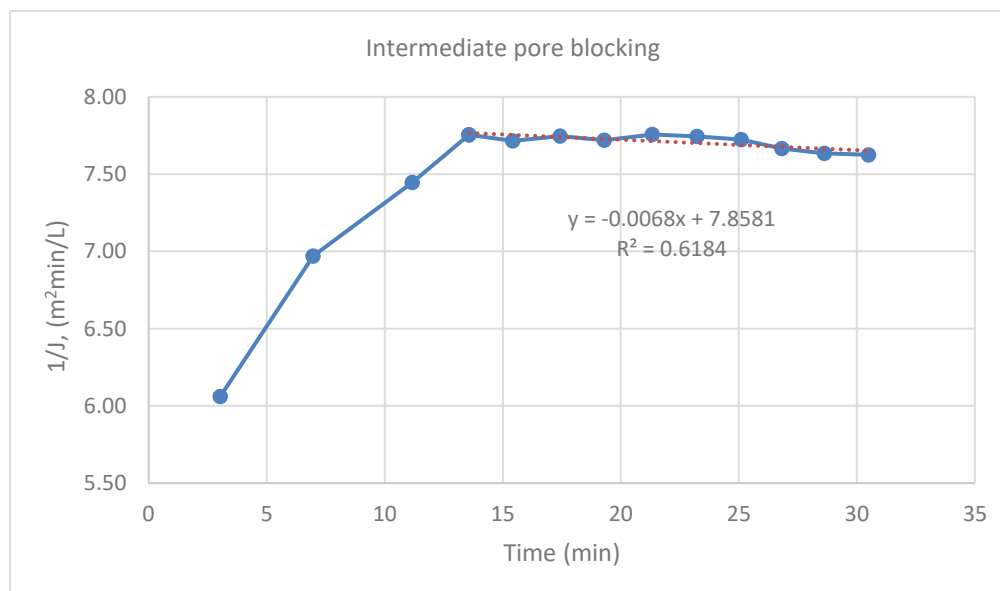


Fig. 8: Linearized plot for permeate flux vs time for intermediate pore blocking model for crossflow filtration of EC-AC treated BPOME.

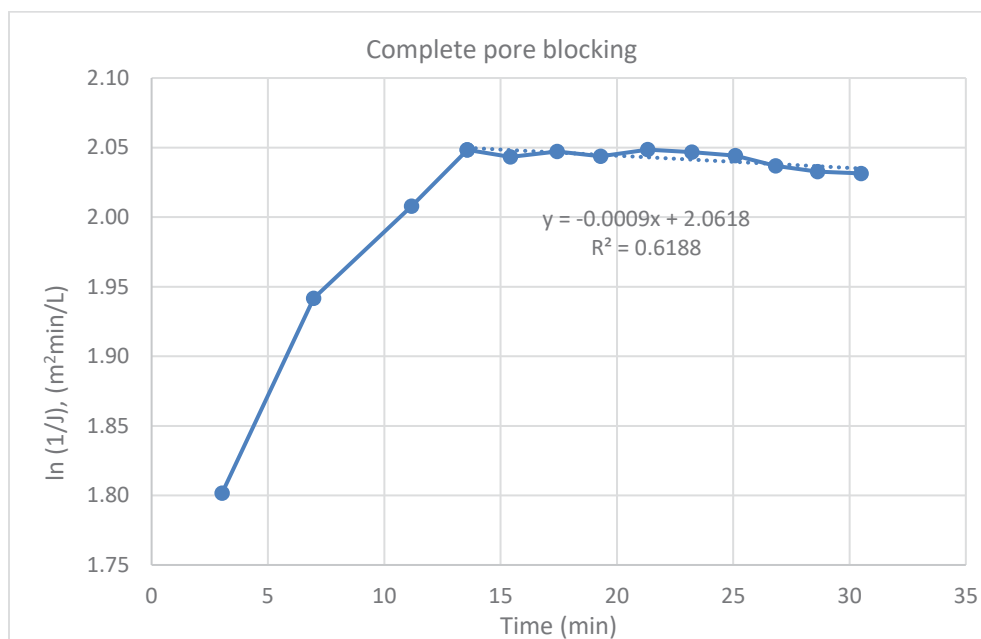


Fig. 9: Linearized plot for permeate flux vs time for complete pore blocking model for crossflow filtration of EC-AC treated BPOME.

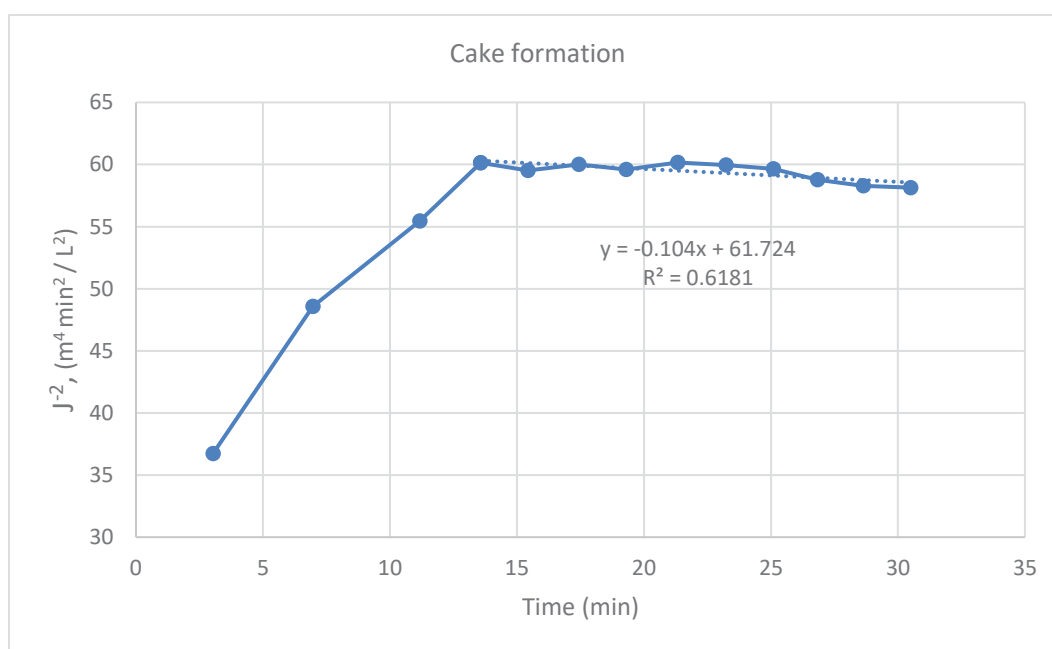


Fig. 10: Linearized plot for permeate flux vs time for cake formation model for crossflow filtration of EC-AC treated BPOME.

Table 3: Characterization of permeate after crossflow filtration of EC-AC treated BPOME

Parameters	Initial BPOME	Final permeate	Reusable limits (EPA)	Overall removal %
1 COD (mg/L)	1981	5±1	<30	99.7
2 Turbidity (NTU)	332	0.3	<2	99.9
3 TSS (mg/L)	192	0	<10-30	100
4 Color (PtCo)	2882	0	<5	100

After addition of powdered AC, the enhanced EC process with the destabilization of colloids with the action of AC adsorption enabled the removal of maximum TSS and turbidity, and a large quantity of COD and color. However, without AC addition, the resulting EC treated solution was not compatible enough to be treated with crossflow filtration to achieve process water COD. The physical observation of the treated BPOME at each stage is presented in Fig. 11. Notably, the final EC-AC treated output was transparent but not colorless and had a significant quantity of COD remaining without the addition of AC. However, with added AC, the EC process was enhanced with rapid removal of color, TSS and turbidity, with 100% color removal and maximum COD removal ( $5 \pm 1$  mg/L) subsequently after crossflow ultrafiltration membrane process. Therefore, the ability of the EC-membrane process to the sustainable water reclaim process from BPOME was proven in this study, after EC was enhanced with AC addition in the same EC reactor, incurring no additional unit operation and harsh oxidants.

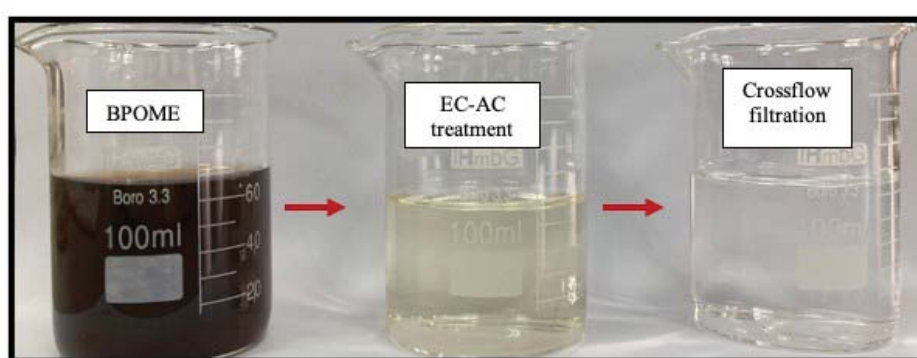


Fig. 11: Appearance of BPOME after EC (with AC addition) treatment and crossflow filtration.

Table 4: Concentration of trace metals in BPOME after EC and EC-membrane process

Metals	Initial concentration in BPOME, mg/L	Concentration after EC-membrane treatment, mg/L	Reusable EPA standard, mg/L [20]
Al	5.93	0.20	5
Fe	1.51	0.09	5
Cu	2.92	0.24	0.2
Zn	0.26	0.02	2
Ni	8.45	0.52	0.2
Cr	29.99	1.81	0.1
Pb	1.05	0.06	5
Co	0.62	0.03	0.05
Cd	0.03	0.00	0.01

According to the USEPA, 5 mg/L is the discharge limit for aluminum for water reuse in agriculture [20]. From the ICPMS analysis data presented in Table 4, EC-membrane process does not cause the possible leaking of aluminum ions in the final discharge from aluminum electrodes in EC. Moreover, the final concentration after the process is almost 97% less than the initial concentration in the BPOME sample, besides being lower than the EPA standard for reuse. Hence, it was confirmed that no possible aluminum contamination takes place in the treated effluent due to aluminum anode dissociation in EC. Rather, EC with AC assistance, removed over 90% of most of the trace metals present in the real BPOME, and additionally removed most of them to the reusable limits for irrigation water according to EPA guidelines

[20]. Investigating possible metal removal from BPOME was not in the scope of this research, but the finding supports the versatility of the EC process in removing various types of pollutants with its effective colloidal destabilization. Hence, the quality of EC being a sustainable environmentally friendly water treatment process is notably exhibited in this study, which corresponds to the work of [21].

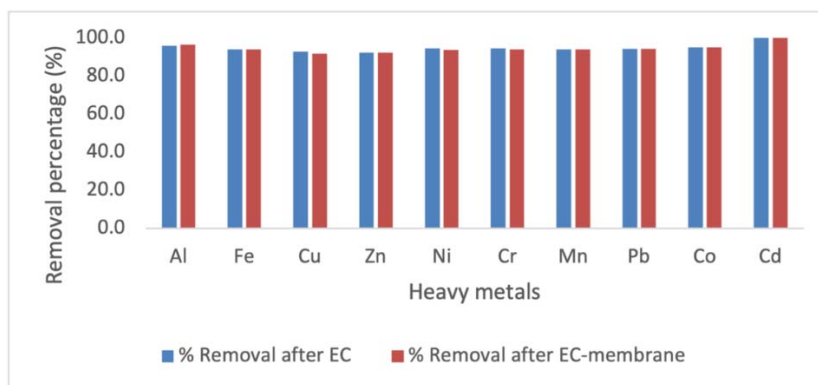


Fig. 12: Trace metal removal through ICPMS after EC and EC-membrane process on BPOME.

Figure 12 presents the percentage removal of trace metals namely Al, Fe, Cu, Zn, Ni, Cr, Mn, Pb, Co, and Cd, after EC and EC-membrane process on BPOME. The graph shows that EC alone removes the maximum possible percentage of trace metals, and no significant removal was observed after the ultrafiltration membrane. The coagulant formed from anode dissolution in EC results in the pollutant-coagulant complex formation after destabilization [2], hence separating it from the BPOME along with COD. Although the study aimed at COD removal from BPOME, the additional ICPMS result proved a subsequent removal of metals that were initially present in the wastewater. This occurrence of a versatile pollutant removal ability of EC from wastewater opens possibilities for further exploration of the process and its integration with other processes for a desired water purity for reusability in the industry as well as in the household or as drinking water. Besides the removal efficiency of the overall EC-membrane hybrid process, the energy consumption was evaluated in the following section.

### 3.4 Energy Consumption

The calculated energy consumption by the EC-membrane process is presented in Table 5.

Table 5: Energy consumption of EC-membrane process

Energy consumption	Formula	Results
EC	$\frac{I \times U \times t}{V}$ (5)	27.34 kWh/m <sup>3</sup>
Membrane filtration	$\frac{J \times A \times TMP}{V}$ (6)	0.0138 kWh/m <sup>3</sup>
<b>Total EC-membrane power consumption</b>		<b>27.354 kWh/m<sup>3</sup></b>

It is evident from this outcome, that EC is the process in the overall hybrid system that holds the main contributing role to the energy consumed in the overall hybrid process. As EC is primarily based on applied current for colloidal destabilization, it is predictable that it consumes the most energy to treat the volume of BPOME in this study. Though the power consumed varies based on reactor geometry, wastewater type, electrolyte conductivity and

pollutants present, a similar result was reported by [22], where maximum removal % of a specific pollutant (dye) was achieved from textile wastewater by EC treatment with a power consumption of 17.04 kWh/m<sup>3</sup>. However, working with a larger volume with addition of supporting electrolytes and employing multiple sacrificial anodes are reported to reduce power consumption in EC [23]. The resistance of the wastewater is a crucial determining factor of how much voltage is generated in the EC reactor, at a specified current.

When scaled up with respect to electrode surface area to volume ratio in a 500 ml beaker, at the same applied current, the voltage dropped to about 6.5 V. The energy requirement by EC can be minimized by scaling up the reactor volume, for instance with 2.5 L working volume, despite the low pollutant removal efficiency in EC on wastewater, a very low amount of energy was consumed (0.36 kWh/m<sup>3</sup>). Therefore, exploring the scale up of the EC reactor volume for a reduced power consumption is a strong recommendation to carry this study forward.

The energy consumed in the crossflow filtration process is mainly due to the pressure applied for the feed inlet, retentate and permeate flow. The pressure driving the overall process is denoted by the TMP (0.5 bar), the value of which was used in Eq. (6) to calculate the energy consumption. The energy consumed in the crossflow filtration of EC treated BPOME was 0.0138 kWh/m<sup>3</sup>, which is very small, and therefore, very economical for treating huge volume of feed [24]. Similar conclusion was made in the study by [25], where using an ultra-low TMP for crossflow filtration, significantly reduced the amount of energy consumed (<0.03 kWh/m<sup>3</sup>) for the ultrafiltration of oil/water emulsions. Further reduction of TMP leads to a much lower overall energy consumption, but the overall flux and time taken for the desired permeate volume are compromised.

The total energy consumption of the overall hybrid EC-membrane process was calculated to be 27.35 kWh/m<sup>3</sup>. As a small volume of BPOME had been treated as a batch process in the EC study, the energy consumed appears to be large in terms of per m<sup>3</sup> of treated sample. However, this can be combatted by scaling up the EC process to treat a larger BPOME volume. As BPOME undergoes natural biodegradation, its quality was not maintained completely constant throughout the experiment. However, storing the sample at 4°C helped to minimize biodegradation. The BPOME samples were characterized in every experiment and the average value was used to compare the overall treatment efficiencies. Besides, exploring the scale up of the EC reactor volume with multiple anodes for a more reduced power consumption is a recommendation to carry this study forward.

## 4. CONCLUSIONS

The fouling mechanisms in crossflow membrane filtration of BPOME were analyzed with and without adding powdered AC in the EC process prior to the membrane filtration. When powdered AC was coupled with the EC process in the BPOME treatment, fouling mitigation was noted. The final permeate obtained was 100% free of TSS and color, 99.9% of turbidity and 99.7% of COD, with a final COD value of 5±1 mg/L which met the agricultural and industrial water reuse standards. Further, the overall energy consumption (27.35 kWh/m<sup>3</sup>) largely resulted from EC, as it was solely based on application of direct current. Based on the small working volume used in this study, the high amount of energy consumption is reasonable, and can be overcome with effective scale up strategies, which is recommended to carry this research forward. Moreover, the subsequent removal of metals with EC, that were initially present in the wastewater, measured with ICP-MS, suggests possibilities of further exploration of the process for enhanced water reclamation from wastewater.

## ACKNOWLEDGEMENT

The authors express their gratitude to the Ministry of Higher Education (MOHE) Malaysia for granting a Fundamental Research Grant Scheme (FRGS), project no. FRGS/1/2019/TK02/UIAM/01/1 to support this work. The authors also express thanks to the International Islamic University Malaysia, Kulliyyah of Engineering, for the financial support under Kulliyyah of Engineering Merit Scholarship 2021 scheme.

## REFERENCES

- [1] Baggio G, Qadir M, Smakhtin V. (2021) Freshwater availability status across countries for human and ecosystem needs. *Science of the Total Environment*, 792: 148230. <https://doi.org/10.1016/j.scitotenv.2021.148230>.
- [2] Rakhmania, Kamyab H, Yuzir MA, Abdullah N, Quan LM, Riyadi FA, Marzouki R. (2022) Recent applications of the electrocoagulation process on agro-based industrial wastewater: a review. *Sustainability (Switzerland)*, 14(4): 1985. <https://doi.org/10.3390/su14041985>.
- [3] Xu J, Du Y, Qiu T, Zhou L, Li Y, Chen F, Sun J. (2021) Application of hybrid electrocoagulation–filtration methods in the pretreatment of marine aquaculture wastewater. *Water Science and Technology*, 83(6): 1315-1326. <https://doi.org/10.2166/wst.2021.044>.
- [4] Elma M, Rahma A, Pratiwi AE, Rampun ELA. (2020) Coagulation as pretreatment for membrane-based wetland saline water desalination. *Asia-Pacific J. Chemical Engineering*, 15: 1-7. <https://doi.org/10.1002/apj.2461>.
- [5] Tahreen A, Jami MS. (2021) Advances in antifouling strategies in membrane ultrafiltration: a brief review. *J. Advanced Research in Materials Science*, 76(1): 10-16. <https://doi.org/https://doi.org/10.37934/arms.76.1.1016>.
- [6] Padmaja K, Cherukuri J, Anji Reddy M. (2020) A comparative study of the efficiency of chemical coagulation and electrocoagulation methods in the treatment of pharmaceutical effluent. *J. Water Process Engineering*, 34: 101153. <https://doi.org/10.1016/j.jwpe.2020.101153>.
- [7] Tahreen A, Jami MS, Ali F, Yasin NMF, Ngabura M. (2021) Promising potential of electro-coagulation process for effective treatment of biotreated palm oil mill effluents. *Pollution*, 7(3): 617-632. <https://doi.org/10.22059/poll.2021.320645.1034>.
- [8] Tahreen A, Jami MS, Ali F. (2021) Activated carbon assisted electrocoagulation process for treating biotreated palm oil mill effluent. *IOP Conference Series: Materials Science and Engineering*, 1192: 012026. <https://doi.org/10.1088/1757-899x/1192/1/012026>.
- [9] APHA. (2002) Standard Methods for the Examination of Water and Wastewater.
- [10] Song L, Elimelech M. (1995) Theory of concentration polarization in crossflow filtration. *J. Chemical Society, Faraday Transactions*, 91: 3389-3398. <https://doi.org/10.1039/FT9959103389>.
- [11] Ezugbe EO, Rathilal S. (2020) Membrane technologies in wastewater treatment: A review. *Membranes*, 10(5): 89. <https://doi.org/10.3390/membranes10050089>.
- [12] Idrisa MA, Jami MS, Muyibi SA. (2010) Tertiary treatment of biologically treated palm oil mill effluent (POME) using UF membrane system: Effect of MWCO and transmembrane pressure. *International J. Chemical and Environmental Engineering*, 1(2).
- [13] Li HB, Shi WY, Zhang YF, Liu DQ, Liu XF. (2014) Effects of additives on the morphology and performance of PPTA/PVDF in situ blend UF membrane. *Polymers*, 6: 1846-1861. <https://doi.org/10.3390/polym6061846>.
- [14] Ahmad MA, Zainal BS, Jamadon NH, Yaw TCS, Abdullah LC. (2020) Filtration analysis and fouling mechanisms of PVDF membrane for POME treatment. *J. Water Reuse and Desalination*, 10: 187-199. <https://doi.org/10.2166/wrd.2020.101>.
- [15] Kumar RV, Goswami L, Pakshirajan K, Pugazhenth G. (2016) Dairy wastewater treatment using a novel low-cost tubular ceramic membrane and membrane fouling mechanism using pore blocking models. *J. Water Process Engineering*, 13: 168-175. <https://doi.org/10.1016/j.jwpe.2016.08.012>.

- [16] Rondeau V, Commenges D, Jacqmin-Gadda H, Dartigues JF. (2000) Relation between aluminum concentrations in drinking water and Alzheimer's disease: An 8-year follow-up study. *American J. Epidemiology*, 152(1):59-66. <https://doi.org/10.1093/aje/152.1.59>.
- [17] Creed J, Brockhoff C, Martin TD. (1994) Method 200.8 Determination of trace elements in waters and wastes by Inductively Coupled Plasma-Mass Spectrometry. US Environmental Protection Agency, 4: 1-57.
- [18] Haindl S, Stark J, Dippel J, Handt S, Reiche A. (2020) Scale-up of microfiltration processes. *Chemie Ingenieur Technik*, 92(6): 746-758. <https://doi.org/10.1002/cite.201900025>.
- [19] Zhang Y, Fu B, Wang X, Ma C, Lin L, Fu Q, Li S. (2020) Algal fouling control in low-pressure membrane systems by pre-adsorption: Influencing factors and mechanisms. *Algal Research*, 52: 102110. <https://doi.org/10.1016/j.algal.2020.102110>.
- [20] Crook J, Ammerman D, Okun D, Matthews R. (2012) EPA Guidelines for Water Reuse.
- [21] Nidheesh PV, Khan FM, Kadier A, Akansha J, Bote ME, Mousazadeh M. (2022) Removal of nutrients and other emerging inorganic contaminants from water and wastewater by electrocoagulation process. *Chemosphere*, 307. <https://doi.org/10.1016/j.chemosphere.2022.135756>.
- [22] Ghernaout D, Al-Ghonamy AI, Messaoudene NA, Aichouni M, Naceur MW, Benchelighem FZ, Boucherit A. (2015) Electrocoagulation of Direct Brown 2 (DB) and BF Cibacete Blue (CB) using aluminum electrodes. *Separation Science and Technology (Philadelphia)*, 50(9): 1413-1420. <https://doi.org/10.1080/01496395.2014.982763>.
- [23] Barhoumi A, Ncib S, Chibani A, Brahmi K, Bouguerra W, Elaloui E. (2019) High-rate humic acid removal from cellulose and paper industry wastewater by combining electrocoagulation process with adsorption onto granular activated carbon. *Industrial Crops and Products*, 140: 111715. <https://doi.org/10.1016/j.indcrop.2019.111715>.
- [24] Cowan JAC, Mactavish F, Brouckaert CJ, Jacobs EP. (1992) Membrane treatment strategies for red meat abattoir effluents. *Water Science Technology*, 25: 137-148.
- [25] Barambu NU, Bilad MR, Huda N, Abdul N, Nordin H, Bustam MA, Doyan A, Roslan J. (2021) Effect of membrane materials and operational parameters on performance and energy consumption of oil/water emulsion filtration. *Membranes*, 11: 370. <https://doi.org/10.3390/membranes11050370>.

## CHARACTERISATION OF *POMACEA CANALICULATA* EGGS TREATED WITH PROTEASE

NOOR HASYIERAH MOHD SALLEH<sup>1\*</sup>, NURHADIJAH ZAINALABIDIN<sup>2</sup>  
AND SITI NOOR HAJAR MD LATIP<sup>3</sup>

<sup>1</sup>Faculty of Chemical Engineering & Technology, Universiti Malaysia Perlis,  
Kangar, Perlis, Malaysia

<sup>2</sup>Faculty of Mechanical Engineering & Technology, Universiti Malaysia Perlis,  
Kangar, Perlis, Malaysia

<sup>3</sup>Sustainable Crop Protection Research Group, University Technology MARA,  
Shah Alam, Selangor, Malaysia

\*Corresponding author: [hasyierah@unimap.edu.my](mailto:hasyierah@unimap.edu.my)

(Received: 2 February 2023; Accepted: 19 October 2023; Published on-line: 1 January 2024)

**ABSTRACT:** *Pomacea canaliculata* is a type of freshwater snail that has become a major pest in paddy fields, as it feeds on young paddy leaves and stems, thus, posing a serious threat to paddy production. It was named one of the world's top 100 worst invasive species, with serious consequences for the environment, human health, and the social economy. Their hatchability rate is high, which explains their global distribution worldwide. Therefore, it is vital to manage their hatchability to prevent their population from expanding further by understanding the protection that permits the eggs to survive. *P. canaliculata* eggs are covered with a thin layer of cuticle that is rich in protein to protect the embryo during the hatching process. The biological treatment with protease enzyme successfully hydrolysed the protein cuticle layer, lowering the percentage of hatchability. Disruption of the protein cuticle may have an impact on conductivity, water loss, hatching time, protein content, and other factors. However, documentation of the protease effect on the protein cuticle is scarce. Therefore, the goal of this study is to evaluate the protease treatment on the protein cuticle of *P. canaliculata* eggs physically (conductivity, water loss, and morphological analysis) and chemically (cuticle protein content, protein breakdown, and amino acid profile). Physical characterisation revealed that protease-treated eggs have higher conductivity and water loss than the control egg. Images taken with a light microscope (LM) and a scanning electron microscope (SEM) revealed changes in cuticle structure, which explained the protease-induced cuticle hydrolysis. Chemical characterisation revealed a decrease in cuticle protein content, hydrolysis of protein to a small size, and changes in amino acid composition. The physical and chemical analyses strongly suggested that protease can damage the cuticle protein, thus, preventing the eggs from hatching.

**ABSTRAK:** *Pomacea canaliculata* adalah sejenis siput air tawar yang telah menjadi perosak utama di sawah padi, kerana ia memakan daun dan batang padi yang muda, sekaligus menimbulkan ancaman serius kepada pengeluaran padi. Ia disenaraikan antara 100 spesis invasif utama dunia dengan kesan serius pada alam sekitar, kesihatan manusia dan sosio-ekonomi. Kadar penetasannya adalah tinggi, meningkatkan penyebaran mereka secara global di seluruh dunia. Oleh itu, adalah sangat penting untuk mengawal populasi ini daripada terus berkembang dengan memahami perlindungan yang membenarkan telur untuk hidup. Telur *P. canaliculata* dilapisi dengan lapisan kutikel nipis yang kaya dengan protein bagi memberi perlindungan untuk embrio semasa proses penetasan. Rawatan biologi dengan enzim protease telah berjaya menghidrolisis lapisan kutikel protein, sekaligus mengurangkan peratusan penetasan. Gangguan terhadap lapisan kutikel protein mungkin memberi kesan pada konduktiviti, kehilangan air, tempoh penetasan, kandungan protein dan faktor lain. Walau

bagaimanapun, kesan protease ke atas kutikel protein adalah kurang. Oleh itu, objektif kajian ini adalah mengkaji rawatan protease ke atas kutikel protein telur *P. canaliculata* secara fizikal (konduktiviti, kehilangan air, dan analisis imej kutikel) dan secara kimia (kandungan protein kutikel, pecahan protein dan profil asid amino). Ciri fizikal menunjukkan telur yang dirawat protease mempunyai konduksi dan kehilangan air tinggi berbanding telur kawalan. Imej yang diambil dengan mikroskop cahaya (LM) dan mikroskop pengimbas elektron (SEM) mendedahkan perubahan dalam struktur kutikel, yang menjelaskan hidrolisis kutikel yang disebabkan oleh protease. Ciri kimia menunjukkan penurunan kandungan protein kutikel, saiz kecil pada hidrolisis protein, dan perubahan pada kandungan asid amino. Analisis fizikal dan kimia mencadangkan bahawa protease merosakkan protein kutikel, oleh itu menghalang telur daripada menetas.

---

**KEYWORDS:** *physical characterisation; chemical characterisation; biopesticide; P. canaliculata; eggs*

## 1. INTRODUCTION

*Pomacea canaliculata* is one of the most devastating pests in the rice farming sector because of its voracious hunger for young paddy leaves and stems [1]. It was named one of the world's top 100 worst invasive species, with serious consequences for the environment, human health, and the social economy. In February 2023, authorities in Perak, Malaysia, seized 10,125 pax of a banned chemical (fentin acetate) used to control *P. canaliculata*. The arrest of the banned chemical reflects the presence of many *P. canaliculata* in paddy plots and a lack of safety awareness among farmers. The preference of fentin acetate is due to the efficiency and fast action in controlling the *P. canaliculata* even though it is highly toxic to the environment and thus prohibited in the country.

Besides high population, *P. canaliculata* also has a high fecundity and hatchability rate, with females producing 200 to 300 eggs per week, resulting in 8,000 viable eggs per year, with 80% hatchability [1]. Therefore, managing their hatchability is essential to prevent population expansion. Water spraying, egg submersion, plant extracts, enzymes, physical collection, regulating temperature and light, and sustained release of niclosamide-gelatine are some of the techniques used to manage the hatching [2-6]. Control through its eggs is easier than control of the snail itself due to ease of locating eggs based on their bright red colour, fragility at this stage, and immobility. However, hatching control must be implemented quickly before the eggs hatch in 12-14 days.

The eggs are covered by a protective layer for embryo survival during the hatching process. Thus, the disruption of the protective layer covering the eggs consequently exposed the embryos to harsh environments and reduced their chances of hatching. A thin protective layer of tissue covering the egg, known as the cuticle, protects it from being dehydrated or infected [7]. Therefore, disruption of the cuticle will affect the hatching process. It has been shown that cuticle disruption by a biological agent, protease, which specifically targets the cuticle, successfully inhibits 86% of hatchability [5]. The disruption of the cuticle may affect its physical and chemical factors, such as ion conductivity, water loss, protein content, and other factors, which in turn affect hatchability. However, how far the treatment affects those factors is under-discovered. Therefore, an understanding of the relationship between protease and cuticle protease in terms of chemical and physical characteristics is necessary for a better hatching control strategy for *P. canaliculata*.

This paper discusses the physical and chemical changes in the cuticle upon protease application in order to explore its role in suppressing hatchability among *P. canaliculata* eggs.

The physical characteristics of *P. canaliculata* eggs treated with protease included conductivity, water loss, image analysis, and morphological analysis. Chemical characterisation included cuticle protein responses, protein breakdown by SDS-PAGE, and amino acid profiling. The results are important in explaining the role of protease in damaging the protection around these eggs, thus, promoting mortality as one way to manage snail breeding.

## 2. MATERIALS AND METHODS

### 2.1 Collection of *P. canaliculata* Eggs

About 50 masses of fresh eggs of *P. canaliculata* were collected weekly from a river bank in Simpang Empat, Perlis, Malaysia. The chosen sampling area has a high population of *P. canaliculata* colonies, as evidenced by collective groups of bright red eggs found on vegetation, leaves, and floating objects (stakes, twigs, and bottles) above the water's surface. Because the eggs were laid at night, the sampling was done early in the morning to minimise discrepancies. These eggs have the following characteristics: a soft eggshell, milky red colour, and mucus on the surface. The eggs that were mucus-free and a little hard on the eggshell were not considered for sampling. During the experiments, the masses of eggs were kept in an open incubator (62 × 40 × 46 cm) filled with tap water and kept at room temperature of 27 °C to create a humid environment as previously described by Meyer-Willere and Santos-Soto with slight modifications [8]. The humid condition was demonstrated by observing the condensation process.

### 2.2 Physical Characterisation Studies

#### 2.2.1 Conductivities Studies

The conductivity study was performed according to the method described by Peebles et al. with slight modifications [9]. Approximately 5 g of 3-day-old eggs were placed into a small basket (4 × 2 cm) before immersing in protease solution from *Aspergillus oryzae* (Sigma-Aldrich, USA) ranging from 2.5, 5 and 10 U/mL for 30 min. The protease was diluted using a phosphate buffer solution at pH 7. Each experiment was conducted in triplicate. The eggs were then rinsed several times with distilled water to remove any protease residue. Then, the protease-treated eggs and untreated eggs (control) were immersed in two separate beakers filled with 100 mL of distilled water. The conductivity of each beaker was measured every 2 hrs using a conductivity meter (EcoScan CON 6, Eutech Instruments).

#### 2.2.2 Water Loss in *P. canaliculata* Eggs

Further assessment of the effect of protease on *P. canaliculata* eggs was conducted by measuring water loss based on slight modifications of the method reported previously [9]. Several clutches of 3-day-old *P. canaliculata* eggs were weighed into 0.5 g each before placing them in 15 × 30 cm containers. These containers were then labelled and treated with 1 mL of water (negative control), 5 and 10 U/mL of protease, and 0.02 M ethylenediamine tetraacetic acid, EDTA (positive control). Based on a preliminary study conducted previously, high protease concentrations had a significant effect on the water loss of *P. canaliculata* eggs. Therefore, a high protease concentration range (0, 5, 10 U/mL) was chosen to observe its effect on water loss in the eggs. This also reflects the actual implementation where high protease is required to maintain efficiency. After 10 min of protease treatment, the samples were dried for several minutes and weighed again. These eggs, labelled as day 1, were placed in a desiccator with 75% relative humidity (RH), which was achieved using saturated Na<sub>2</sub>CO<sub>3</sub> (Merck, Malaysia) in distilled water. The desiccator was then placed in an oven at 30 °C. The weight

of the samples was taken daily until day 8 and the eggs were kept in the desiccator until hatching time (approximately 12 days). This experiment was performed in triplicate. The water weight loss was calculated by dividing the daily weight by the initial weight of the eggs.

### **2.2.3 Image analysis**

A single egg was retrieved from the 3-day-old clutch before the clutch underwent treatment with 10 U/mL protease solution in phosphate buffer (0.02 M, pH 7). The untreated egg served as a control. Images of the single egg for both samples were captured from four different angles five times daily to ensure the accuracy of the results. The captured images were then analysed using the JIMAGE 1.4 software. The clutches (protease-treated and controlled) were then placed in the breeding chamber for incubation. The colour changes of both clutches were examined under a dissecting microscope (DBA 200, MOTIC, China) at 4× magnification.

### **2.2.4 Scanning Electron Microscope**

The eggshells of the 10 U/mL protease-treated sample and the control were prepared and loaded on the double tape of the specimen stub. Then, the eggshells were coated with platinum using an auto-fine coater (JFC-1600, Tokyo, Japan), and later, observed using the scanning electron microscope (SEM) under 1,000× magnification.

### **2.2.5 Statistical Analysis**

All data were analysed using Microsoft Excel 2010 with a probability level of less than 5% ( $p < 0.05$ ) was regarded as statistically significant and contributed to the analysis.

## **2.3 Chemical Characterisation Studies**

### **2.3.1 Response of Cuticle to Protease**

The cuticle protein response towards protease was studied by placing 5 g of 3-day-old eggs in a basket (5 × 3 cm), which were treated with different concentrations of 100 mL of protease (0-5 U/mL) and EDTA (0-0.08 M) for 30 min. The eggs were then rinsed using distilled water before being immersed in 100 mL of 0.5% SDS for 10 min [10]. The protein content of the removed cuticle in each treatment was determined directly at an absorbance of 280 nm, with 0.5% SDS as the blank. All analyses were conducted in triplicate. The absorbance data of protease treatment and EDTA as a positive control was reported in %.

### **2.3.2 Cuticle Protein Analysis Using SDS-PAGE**

The hydrolysis of cuticle protein after the protease treatment was evaluated based on SDS-PAGE analysis. The analysis was conducted to prove that the cuticle protein was broken down into a small fraction of protein. In this analysis, 5 g of 3-day-old eggs were loaded into a basket and treated with 5 mL of phosphate buffer (0.02 M, pH 7) in a beaker for 15 min, with gentle stirring and kept at 4 °C. Approximately 1 mL of the supernatant was treated with 0.02 mL of protease (20 U/mL) solution for 10 min at 37 °C. The SDS-PAGE analysis was conducted using a Bio-Rad kit (Bio-Rad Laboratories Inc., California). The samples were solubilised with SDS-sample buffer containing β-mercaptoethanol (BME) and boiled for 5 min at 95 °C before resolving with 10% SDS-PAGE. Precision Plus (Bio-Rad Laboratories Inc., California) was used as the protein marker. Electrophoresis was conducted for 1 hr at 100 V (Biorad Mini-protean II Electrophoresis System, Bio-Rad, California), and was stained with silver staining [11].

### 2.3.3 Amino acid Profile of Cuticle Protease-treated Egg

Amino acid profiling of cuticle protein was conducted using the acid hydrolysis method, as reported by Piecyk et al. with several modifications [12]. Approximately 2 g of 3-day-old eggs were treated; one sample with water (control) and one sample with 2.5 U/mL of protease for 30 min, and these samples were later dried. Next, the samples were placed into crucibles before being mixed with 5 mL of 6 M HCl, and these crucibles were heated at 100 °C for 24 hrs. Then, 2 mL of 10% isopropanol was mixed into the hydrolysed eggs before undergoing centrifugation at 8,000 rpm for 10 min. The filtrates obtained underwent amino acid analysis using EZ:faast™ kit (Phenomenex). This treatment was conducted in triplicate.

## 3. RESULTS AND DISCUSSION

### 3.1 Physical Characterisation of Protease-treated Eggs

#### 3.1.1 Conductivities of Protease-treated Eggs

Figure 1 shows that the conductivity of protease-treated eggs increases proportionally with protease concentration and is saturated at a protease concentration of more than 5 U/mL. The conductivity of the eggs following 2.5 U/mL of protease treatment was 14.9  $\mu\text{S/hr}$ , then increased to 16.5  $\mu\text{S/hr}$  following treatment with 10 U/mL of protease. The p-value is 0.01178 and is statistically significant. Due to the protease concentration being close between each concentration, only concentrations of 0 and 10 U/mL statistically affect the conductivity reading.

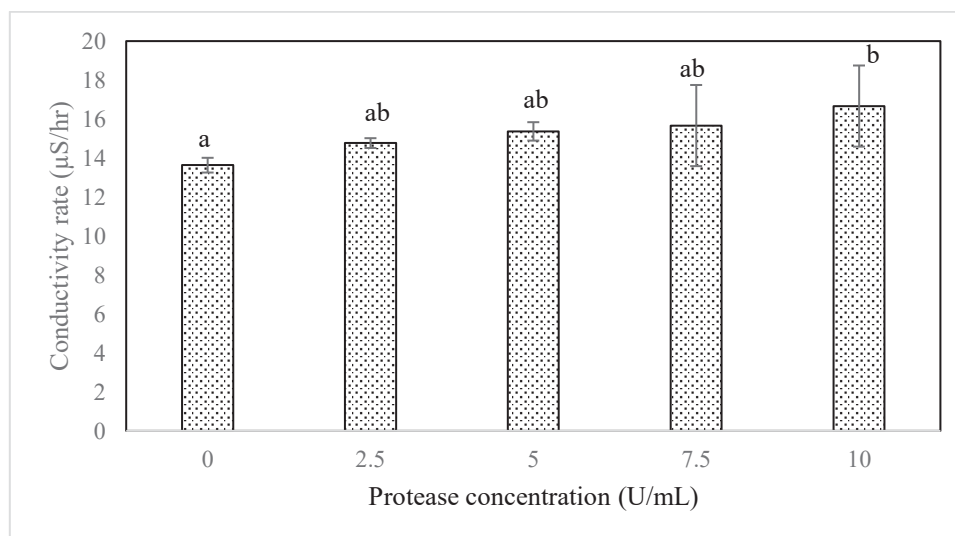


Fig. 1: Conductivity of *P. canaliculata* eggs following protease treatment.  
(Note: different superscripts signify significant mean differences)

Conductivity centration increased parallely with the protease treatment, thus demonstrating the action of protease in hydrolysing the cuticle protein. Initially, the cuticle was plugged into the eggshell pores, however, after protease treatment, it exposed the pores and increased the permeability of the eggs. Subsequently, more ions from the egg liquid, such as  $\text{Ca}^{2+}$ ,  $\text{K}^+$ ,  $\text{Na}^+$ , and  $\text{H}^+$  diffused out into the solution and increased the ionic strength. This passive diffusion occurred due to the concentration gradient, in which the ions in the inner part of the eggs have a higher concentration than the outer part, and obeyed Fick's law. A previous

study demonstrated the salting effect in food preservation, in which the film representing the membrane diffused inorganic salt solution ions,  $\text{Na}^+$  and  $\text{K}^+$ , into the biosolid [13].

It was reported that the increase in electrical conductivity was caused by a number of factors, including structural changes in the tissue and protopectin breakdown [14]. The excessive diffusion of ions from the interior egg liquid to the external environment demonstrated the changes in cuticle protein structure, thus affecting the hatching process.

### 3.1.2 Water Loss of Protease-treated Eggs

Protease treatment is also found to affect the rate of water loss in the eggs, as presented in Fig. 2. The water loss rate was faster in protease-treated eggs compared to negative control eggs (0 U/mL). An increment of 25% and 61% of water loss rate was recorded in the eggs following treatment with protease and EDTA (positive control), respectively. The protease treatment (0, 5, and 10 U/ mL) statistically affects the water loss, while protease 10 U/mL and EDTA as positive control work in a similar manner. The p-value for the analysis is  $7.6 \times 10^{-5}$  and is statistically significant.

The increment pattern of water loss indicated the effect of protease and EDTA in digesting the cuticle of *P. canaliculata* eggs, which reduced the barrier created by the cuticle and exposed the pores, resulting in high water loss rates. On the contrary, the negative control eggs possessed high-density cuticles that covered and blocked the pores, thus, creating a barrier from excessive water loss. The weight loss of these eggs was entirely dependent on the water vapor diffusion of albumen across eggshells and has been used as an indicator for successful hatchability in a variety of animal models [15].

In this current study, water loss in eggs was primarily caused by water evaporation through the eggshell; thus, removing the barrier formed by the cuticle and accelerating the evaporation of water from the cuticle. These results were consistent with findings reported by Galvez et al. in a study on removing the cuticle layer of an avian egg, which resulted in increased conductance and water loss [16]. Nonetheless, removing the cuticle using acetic acid, vinegar, and citric acid, particularly in the hatchery sector, has helped increase the water loss rate and improve quail egg hatchability. Although removing cuticles using a washing solution is a common practise in modern hatcheries to promote hatching, the conditions are different for snail eggs, which are sensitive to cuticle disruption.

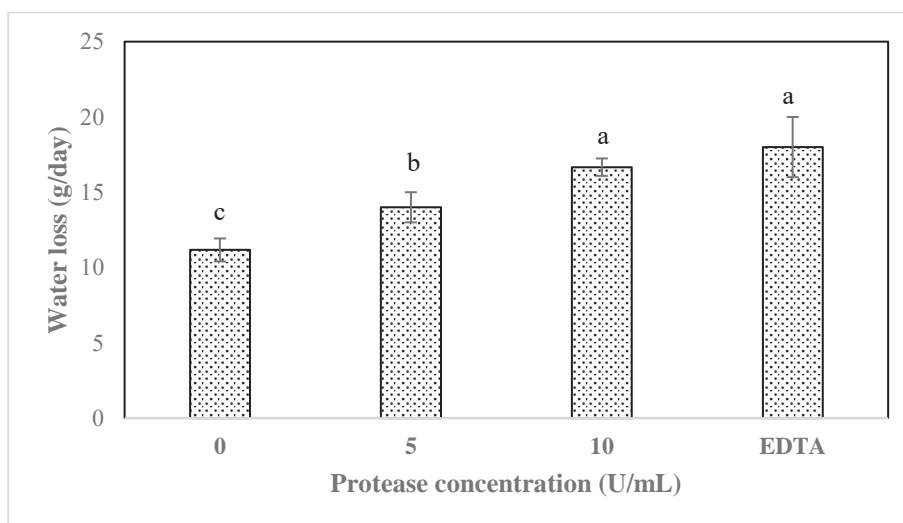


Fig. 2: Water loss in *P. canaliculata* eggs following protease treatment.  
(Note: different superscripts signify significant mean differences)

The permeability of the eggshell influences water vapour diffusion from the egg interior to the external environment. Initially, the eggshell has a tolerable permeability due to the presence of cuticle protein, which coats the wall of the pore interior from the eggshell exterior as a 'pore plug'. Its function is to regulate water vapour and electrical conductivity; however, the coating was removed after protease treatment, exposing the eggshell to the external environment and increasing its permeability. The high permeability thus allows excess water loss and an increase in electrical conductivity, consequently affecting the hatchability.

### 3.1.3 Image Analysis

The colour changes between the untreated (control) and protease-treated eggs (10 U/mL) were observed under a light microscope, as shown in Fig. 3. The control eggs showed variations in cuticle distribution and were red in colour from day 1 after oviposition until day 7. On day 8, the colour of the control eggs was a bit dull and became more intense as they passed day 9, which turned white on day 10, as an indicator of the hatching process (Fig. 3a).

The control eggs hatched on day 11. However, the eggs treated with protease appeared reddish in colour due to the absence of the cuticle and remained as they were until day 8, and then, some of the eggs turned dull in colour on day 9. The dull colour remained throughout the incubation period without any sign of hatching until day 11 (Fig. 3b).

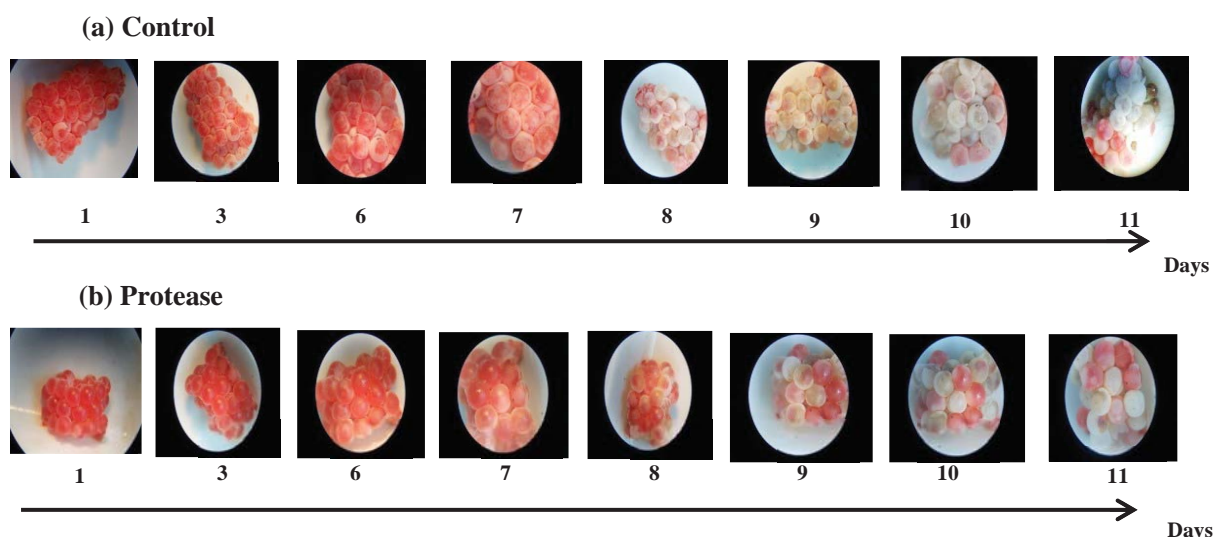


Fig. 3: Colour changes of *P. canaliculata* eggs: (a) control; and (b) protease-treated.

The eggs have a high red perivitelline fluid content during the early stages of embryo development, which provides nutrition for the growth of the embryo and influences the eggs to be red in colour. However, when hatching time approached, the liquidity of the perivitelline fluid began to decrease, thus, the eggshells turned white and became thinner. On the other hand, the volume of perivitelline fluid remained the same in the protease-treated eggs, and the eggshells remained red and thick, as no embryo was developing and no perivitelline fluid was taken up.

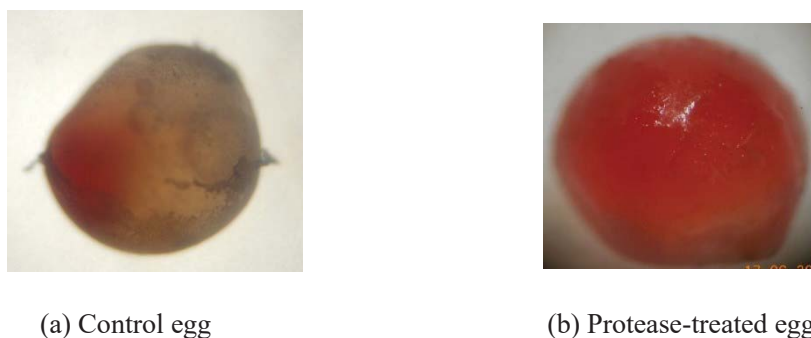


Fig. 4: The colour of (a) a control egg and (b) a protease-treated egg observed under a light microscope at 40× magnification.

The colour of a single control egg and a protease-treated egg was captured, and the effect of protease treatment is shown in Fig. 4 and 5, respectively. Particle analysis using JIMAGE was conducted to quantify the reddish areas caused by protease treatment in the captured images. The control egg showed a thin white layer of cuticle surrounding the egg. In contrast, due to protease treatment, the cuticle layer was diminished and exposed the protease-treated egg to become more reddish than the control egg, as well as leaving some swelling spots. Hence, protease has played a crucial role in disrupting the cuticle at this point, which promoted ion and water loss, and consequently, affected the hatching process. This observation was comparable to those made by Khan et al. in a study of the effect of *Paecilomyces lilacinus* treatment on *Meloidogyne javanica* eggs [17]. The protease and chitinase excreted by *Paecilomyces lilacinus* hydrolysed the vitelline and lipid layers of the *Meloidogyne javanica* eggs, allowing other metabolites to enter the eggs and resulting in a swelling effect.

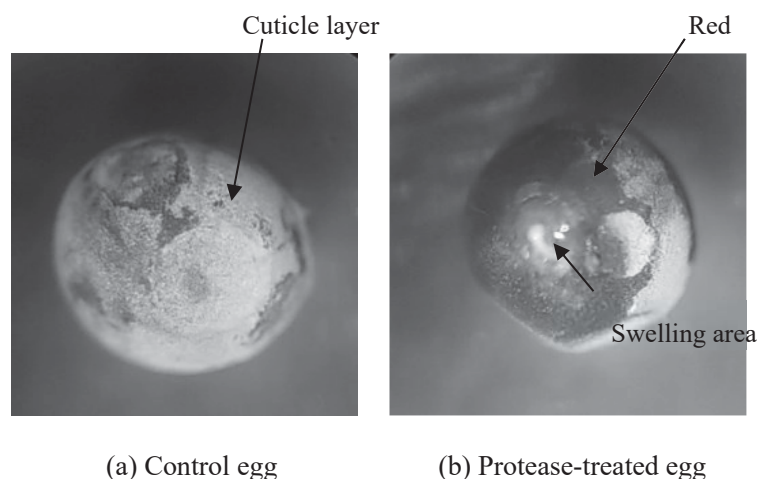


Fig. 5: The effect of protease treatment on *P. canaliculata* egg.

Particle analysis reveals that the red area increases linearly with increasing protease concentration, regardless of the age of the eggs (Fig. 6). Initially, the red area on the untreated eggs was 38%, which gradually increased to 84% following 10 U/mL of protease treatment. A high red zone indicated high cuticle layer digestion, which in turn affected the hatchability of *P. canaliculata* eggs. These results demonstrated that the cuticle layer was successfully thinned by the protease, which also made the red colour of the eggs more obvious.

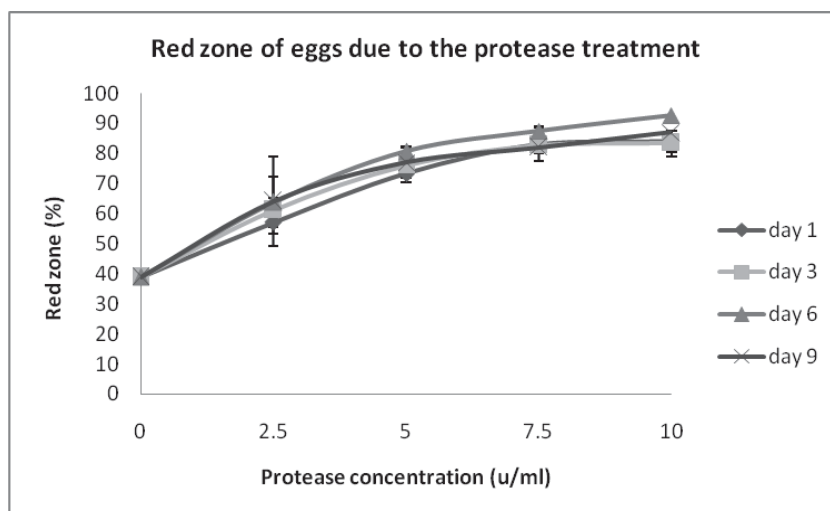


Fig. 6: Effect of protease treatment on the red zone development of *P. canaliculata* eggs.

### 3.1.4 Scanning Electron Microscope

The effect of protease treatment on cuticle protein is further confirmed through morphological analysis using scanning electron microscopy (SEM), as shown in Fig. 7.

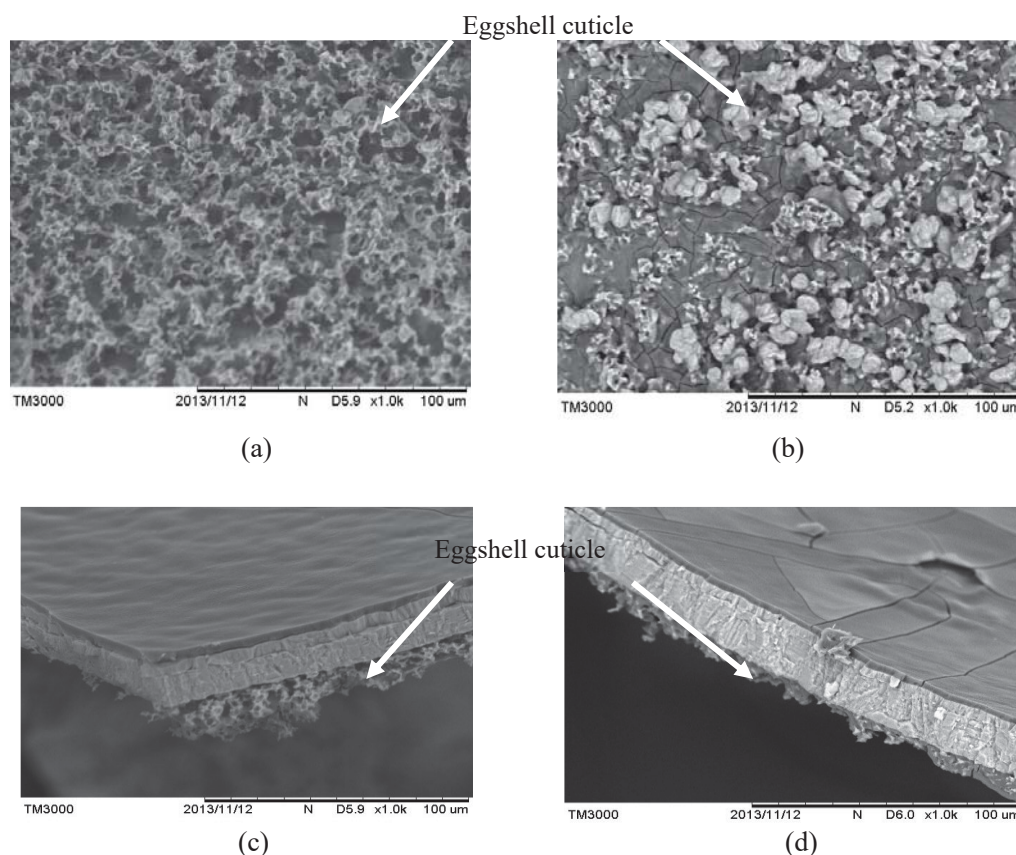


Fig. 7: SEM images of (a) control eggshell, (b) protease-treated eggshell, (c) cross-section of control eggshell, and (d) cross-section of protease-treated eggshell at 1,000 $\times$  magnification.

The morphology of the control egg shows a homogeneous distribution, fluffy surface, and high cuticle coverage across the eggshell surface (Fig. 7a). The protease-treated egg, on the

other hand, exhibits a heterogeneous distribution, rough surface, shrinkage, coagulation, low cuticle coverage, and some cracking patterns on the eggshell surface (Fig. 7b). The cross-section image of the eggshell reveals that the control eggshell has a thick layer of cuticle (Fig. 7c), in contrast to the thin layer of cuticle seen on the protease-treated eggs (Fig. 7d). The morphology of the control eggs indicated a healthy cuticle structure. The cuticle protects the embryo from microbial contamination by plugging the pores, while controlling gas exchange and water vapour loss during the hatching process. However, following protease treatment, the cuticle layer was destroyed as a ‘pore plug’ and became thin, as demonstrated by the cuticle coagulation appearance. The hydrolyzation of the cuticle protein reflects the changes not only in the protein content of the cuticle but also in the electrical conductivity and water loss, which are potent factors for the development of the embryo. The disruption of the cuticle reflects the failure of its role as the main defence agent for the fragile embryo, resulting in poor hatchability. Quanlin et al. reported a similar observation when treating avian eggs with EDTA for cuticle removal, in which the cuticle appeared rough [18].

### 3.2 Chemical Characterisation in Conductivities Studies

#### 3.2.1 Analysis of Cuticle Response to Protease Treatment

Cuticle protein levels decrease proportionally with increasing protease concentration, as shown in Fig. 9. The cuticle protein concentration has reduced from 100% to 29% following 5 U/mL of protease treatment. The cuticle protein of eggs treated with EDTA also showed a similar reduction pattern as those treated with protease. These analyses showed the function of protease in hydrolysing the cuticle protein. Other hydrolytic enzymes, such as chitinase and collagenases produced by other fungi have been reported to hydrolyse the cuticle of plant-parasitic nematode eggs [19].

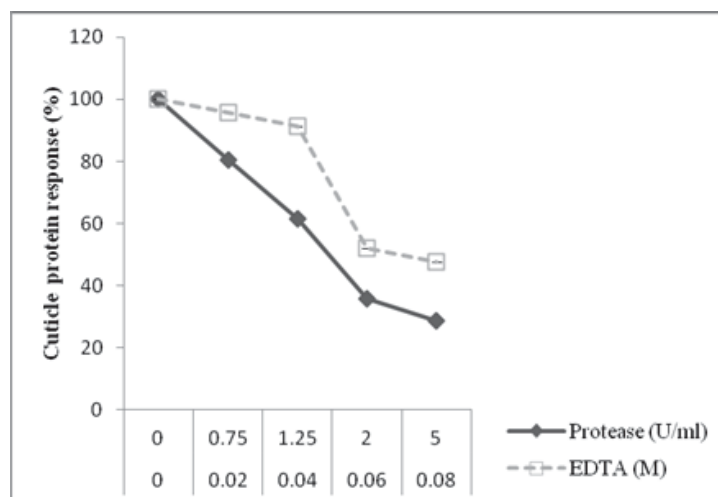


Fig. 9: The cuticle protein response due to protease action.

#### 3.2.2 Analysis of Cuticle Degradation Using SDS-PAGE

To further study protease action on cuticle protein, the SDS-PAGE analysis is conducted, as shown in Figure 10. The marker is shown on the left side of this figure. The analysis results showed that protease appeared in several estimated sizes of 80, 49.1, and 28 kDa. Casein (C) was used as a control since protease is involved in casein hydrolysis to tyrosine. Based on the findings, casein was approximately 20.6 kDa in size and appeared in a thick line, consequently being hydrolysed into a very fine line following protease treatment (C-E). The cuticle protein extracted with phosphate buffer (PBS) revealed several peptides with high

intensity at protein sizes ranging from 38.4 to 7.1 kDa. However, following protease cleavage (PBS-E), the cuticle protein was broken down to form small peptides in the PBS-E hydrolysates, with lower intensity of low molecular weight peptide fractions, namely 33, 15, and 8 kDa. On the other hand, the cuticle treated with phosphate buffer (prior to protease treatment) was identical to casein, C, at 20.6 kDa. However, following protease treatment, both PBS-E and CE showed no protein band at 20.6 kDa, which were possibly cleaved into even smaller protein sizes. These results clearly show that the cuticle protein of the eggs is completely hydrolysed by protease, as shown in Fig. 10.

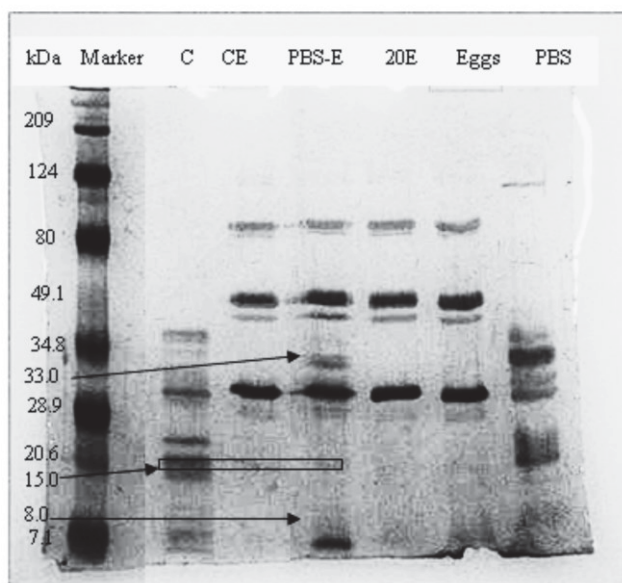


Fig. 10: The bands of SDS-PAGE for casein (C), casein treated with enzyme (CE), cuticle in phosphate buffer, treated with enzyme (PBS-E), 20 U/mL of protease (20E), cuticle protein treated with protease (Eggs), and cuticle extracted with phosphate buffer at pH 7 (PBS).

### 3.2.3 Analysis of Amino Acid Profile of the Treated Cuticle

The reduction in cuticle protein, as a response to protease, is supported by amino acid analysis results, as shown in Fig. 11.

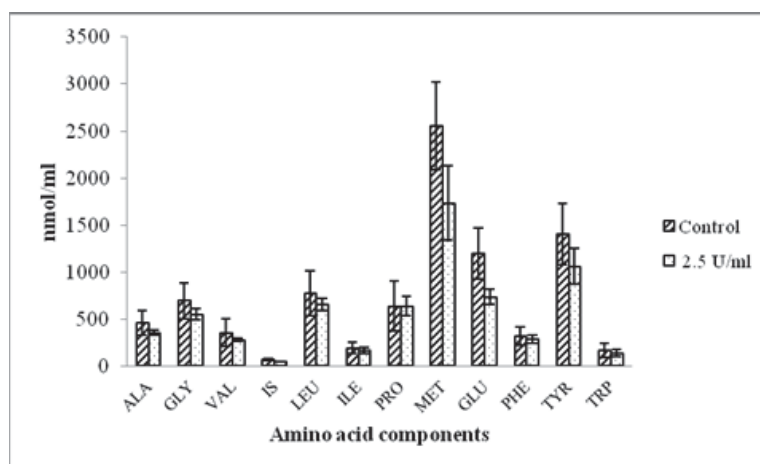


Fig. 11: The amino acid analysis of cuticle protein following protease treatment.

Based on Fig. 11, the cuticle protein of *P. canaliculata* eggs contains 11 major amino acid components, prominently methionine (2,500 nmol/mL), tyrosine (1,400 nmol/mL), and glutamine (1,200 nmol/mL), followed by other amino acids, namely leucine (800 nmol/mL), glycine (700 nmol/mL), and proline (600 nmol/mL). These amino acid groups were reduced in parallel with the increasing protease concentration following treatment, except for proline. The major amino acids that were reduced the most were tyrosine (68%) and methionine (54%). Tyrosine provides an excellent substrate for protease action. This could explain the increased protease action in hydrolysing amino acids in the cuticle protein. These findings showed several similarities with amino acids found in the eggshell of a land snail, *Cornu aspersum*, which contained leucine, tyrosine, lysine, and small amounts of methionine [20]. However, avian cuticles were found to be rich in glycine, lysine, aspartic acid, glutamic acid, tyrosine, and arginine. The diverse compositions of amino acids among different species are important in accommodating the growth requirements of the embryos.

The hydrolysis of cuticle protein by protease is depicted clearly by SDS-PAGE and amino acid profiling. The cuticle protein disintegrated into small fractions and changed in terms of amino acid concentration. The changes in the chemical content of cuticle protein thus play a major role in impaired cuticle function which in turn affects the hatchability. As a result, protease treatment influenced both the physical and chemical properties of cuticle protein during the hatching process. Protease enzyme treatment could be one option for controlling the *P. canaliculata* population through egg management.

#### 4. CONCLUSION

This study showed that the mechanism of protease was not only physically affecting the eggs, but also chemically through the disruption of their cuticle protein. Protease was found to coagulate the cuticle layer on the surface of the eggs, and increased conductivity and water loss rate, while causing swelling and highlighting the red colour of the eggs. The reduction of cuticle protein and protein breakdown showed the effectiveness of protease in digesting cuticle protein, which led to the un-hatchability of the eggs. The damage to the cuticle protein subsequently interrupted the functions of the cuticle in protecting the eggs from microbial penetration, dehydration, and gaseous exchange. As all crucial factors for embryo survival were affected by the disruption of the cuticle, consequently, the hatchability of the eggs was also affected. In conclusion, this study of the mechanism of protease action on *P. canaliculata* eggs has provided more knowledge for the management and control of the snail population. This study, however, was limited to the use of commercial protease on *P. canaliculata* eggs on a lab scale. However, it can be useful to have a basic understanding of the protease action against cuticle protein for field applications. It is suggested that synthesis protease from microbes or plants be used to reduce costs while still providing the same action to the cuticle protein. Future research should focus on the application of synthesized protease in the field, taking into account temperature, intact time, humidity, storage stability, spray method and other factors that may impair protease efficiency in eggs. The protease application is relevant in managing *P. canaliculata* population, beginning with the most vulnerable stage of its lifecycle, the egg. The management of eggs is simpler than the management of matured snails because their eggs are fragile and easy to locate due to their bright red colour. The potential of protease used as biopesticides for crop protection can't be denied. It can be used in liquid form and sprayed on the target, *P. canaliculata* egg. Therefore, the protection strategy by protease in managing *P. canaliculata* eggs can be a good alternative and can consequently facilitate the reduction of their distribution, and mitigate the damages done by these snails to protect paddy production from future extinctions.

## ACKNOWLEDGEMENT

The researchers would like to acknowledge the Ministry of Science, Technology and Innovation (MOSTI), Malaysia for the financial support under the Science Fund Grant (9005-00056), the Department of Agriculture, Perlis for the supporting data on snail invasion, and the Department of Chemical Engineering Technology, University Malaysia Perlis for the facilities and continuous support.

## REFERENCES

- [1] Marwoto RM, Isnaningsih NR, Joshi RC. (2018) The invasive apple snail (*Pomacea* spp) in Indonesia, Bio Web of Conferences, 35: 41-48. <https://doi.org/10.1051/bioconf/20201900014>
- [2] Wang Z, Tan J, Tan L, Liu J, Zhong L. (2012). Control the egg-hatching process of *Pomacea canaliculata* (Lamarck) by water spraying and submersion, Acta Ecologica Sinica, 32: 184-188. <https://doi.org/10.1016/j.chnaes.2012.04.008>
- [3] Wang J, Xing Y, Dai Y, Ki Y, Xiang W, Dai J, Xu F. (2022) A novel gelatin-based sustained release molluscicide for control of the invasive agricultural pest and disease vector *Pomacea canaliculata*, Molecules, 27: 4268. <https://doi.org/10.3390/molecules27134268>
- [4] Latip SNHM, Ibrahim R, Haiyee ZA. (2017) The antifeedant activity of essential oil from *Cymbopogon citratus* and *Piper bitle* for controlling golden apple snail, *Pomacea canaliculata*. J Fundamental of Applied Science, 9(6S): 39-49. <https://doi.org/10.4314/jfas.v9i6s.4>
- [5] Mohd Salleh NH, Zainalabidin N. (2017) Evaluation of protease enzyme on *Pomacea canaliculata* eggs. In: Saian R., Abbas, M. (eds) Proceedings of the second International Conference on the Future of ASEAN (ICoFA). 16-17 August 2017; Malaysia. Edited by Saian R. and Abbas MA, Springer; pp. 443-451. [https://doi.org/10.1007/978-981-10-8471-3\\_44](https://doi.org/10.1007/978-981-10-8471-3_44)
- [6] Zainalabidin N, Mohd Salleh NH, Dachyar A, Mohamed Zulkali MD. (2014) Application of *Bacillus thuringiensis* subs *kurstaki* as biological agents for disrupting Golden Apple Snail (*Pomacea canaliculata*) eggs and juveniles. Proceedings of International Conference of Engineering Management:25-26 Jan 2014; Perlis, Malaysia.
- [7] Wilsom PW, Suther CS, Bain MM, Icken W, Jones A, Quinlan-Pluck F, Olori V, Gautron J, Dunn IC. (2017) Understanding avian egg cuticle formation in the oviduct: a study of its origin and deposition. Biology of Reproduction, 97(1): 39-49. <https://doi.org/10.1093/biolre/iox070>
- [8] Meyer-Willere AO, Santos-Soto A. 2006. Temperature and light intensity affecting egg production and growth performance of the Apple snail *Pomacea patula* (Baker 1922), Advances en Investigaciaon Agropecuaria, 10: 41-58.
- [9] Peebles ED, Pansky T, Doyle SM, Boyle CR, Smith TW, Latour MA. (1998) Effects of dietary fat and eggshell cuticle removal on egg water loss and embryo growth in broiler hatching eggs. Poultry Science, 77(10): 1522-1530. <https://doi.org/10.1093/ps/77.10.1522>
- [10] Rose-Martel M, Du J, Hincke MT. (2012) Proteomic analysis provides new insight into the chicken eggshell cuticle. Journal Proteomics, 75(9): 2697-2706. <https://doi.org/10.1016/j.jprot.2012.03.019>
- [11] Chevallet, M., Luche, S., Rabilloud, T. (2006) Silver staining of proteins in polyacrylamide gels. Natural Protocol, 1(4): 1852-1858. <https://doi.org/10.1038/nprot.2006.288>
- [12] Piecyk M, Srama A, Bzducha A, Obiedzinsk M. (2007) Application of HPLC and GC/MS to quantification of phenylalanine in chosen kinds of food for particular nutritional uses. Acta Scientarium Polonorum Technologia Alimentaria, 6(2): 5-18. [http://www.food.actapol.net/volume6/issue2/1\\_2\\_2007.pdf](http://www.food.actapol.net/volume6/issue2/1_2_2007.pdf)
- [13] Cremasco H, Galvan D, Angilelli KG, Borsato D, de Oliveira AG. (2019) Influence of film coefficient during multicomponent diffusion-KCl/NaCl in biosolid for static and agitated system using 3D computational simulation. Food Science Technology (Campinas), 39 (1): 173-181. <https://doi.org/10.1590/fst.40917>

- 
- [14] Kulshreshtha G, D'Alba L, Dunn IC, Rehault-Godbert S, Rodriguez-Navarro AB, Hincke MT. (2022) Properties, genetics and innate immune function of cuticle in egg-laying species. *Front Immunology*, 13:838525. <https://doi.org/10.3389/fimmu.2022.838525>
- [15] Alsobayel AA, Almarshade MA, Albadry MA. (2013) Effect of breed, age and storage period on egg weight, egg weight loss and chick weight of commercial broiler breeders raised in Saudi Arabia. *Journal Saudi Social Agricultural Science*, 12(1): 53–57. <https://doi.org/10.1016/j.jssas.2012.06.003>
- [16] Galvez DV, Castro I, Morel PCH, Chua WH, Loh M. (2021) The eggshell structure in apteryx; form, function and adaptation for the production of a caviar substitute. *Ecology and Evolution*, 11(7): 3184-3202. <http://doi.org/10.1002/ece3.7266>
- [17] Khan AK, Williams L, Nevalainen HKM. (2004) Effects of *Paecilomyces lilacinus* protease and chitinase on the eggshell structure and hatching of *Meloidogyne javanica* juveniles. *Biological Control*, 31(3): 346-352. <https://doi.org/10.1016/j.biocontrol.2004.07.011>
- [18] Quanlin L, Kun W, Jiangxia Z, Congjiao S, Changrong G, Ning Y, Guiyun X. (2019) Nanostructural basis for the gloss of chicken eggshells. *Poultry Science*, 98(11): 5446-5451. <https://doi.org/10.3382/ps/pez329>.
- [19] Darwesh El-Hawary AS, El Kelany US, El Sherbiny GM. (2019) Nematicidal activity of thermostable alkaline protease produced by *Saccharomonaspora viridis* strain Hw G550. *Biotechnology Reproductive*, 24: e00386. <http://doi.org/10.1016/j.btre.2019.e00386>.
- [20] Mackowiak-Dryka MM, Szkucik K, Pyz-Lukasi R. (2020) Snail eggs as a raw material for the production of a caviar substitute. *Journal of Veterinary Research*, 64(4): 543-547. <https://doi.org/10.2478/jvetres-2020-0062>.

## BIPHASIC CRUDE PALM OIL DECHLORINATION: EFFECT OF VOLUME RATIO AND CONCENTRATION OF SODIUM SILICATE TO HYDROXIDE ION DISTRIBUTION

ZULFA KURNIA UMANI HARI<sup>1</sup>, SYAMSUL BAHARI ABDULLAH<sup>1</sup>,  
SAIDATUL SHIMA JAMARI<sup>1</sup>, CHE RAHMAT CHE MAT<sup>3</sup>  
AND MOHD SABRI MAHMUD<sup>1,2</sup>

<sup>1</sup>Faculty of Chemical and Process Engineering Technology, <sup>2</sup>Centre for Research in Advanced Fluid & Processes, Universiti Malaysia Pahang, 26300 Kuantan, Pahang, Malaysia

<sup>3</sup>Malaysian Palm Oil Board, 6, Persiaran Institusi, Bandar Baru Bangi, 43000 Kajang, Selangor

\*Corresponding author: mohdsabri@ump.edu.my

(Received: 29 May 2023; Accepted: 6 December 2023; Published on-line: 1 January 2024)

**ABSTRACT:** Dechlorination of crude palm oil (CPO) to prevent toxic contaminant formation inspired studies of applying alkaline in its treatments. This paper reports distribution of hydroxide ion ( $\text{OH}^-$ ) from sodium hydroxide (NaOH) and sodium silicate (SS) between aqueous solution and CPO under equilibrium systems to moderate its presence in CPO and minimize saponification. In this study,  $\text{OH}^-$  was determined through pH measurements, which also indicated sodium hydroxide (NaOH) presence. Filtered CPO was mixed with SS solution at room temperature in various volume ratios and SS concentrations under 800-rpm agitation before being settling down to form layers of liquids. The One-Factor-in-A-Time approach was used to optimize the ratio. Acid value test and GCMS analyses were used to determine free fatty acids. Calibration curve construction revealed 0.0818 of  $\text{OH}^-$  dissociation constant. SS solution could turn to acidic at  $6.344 \times 10^{-5}$  g/ml of concentration probably due to hydrated silica. Using 0.01 g/ml SS solution, volume ratios between CPO and SS solution spanning from 0.33 to 3 were all under alkaline conditions but decreasing  $\text{OH}^-$  concentration, where 2 liquid phases only appeared in the ratio of 2.33 and 3. Concentration of SS was then varied for the 2.33 volume ratio and a sigmoid trend of  $\text{OH}^-$  increase was evident. The McCabe-Thiele plot revealed  $\text{OH}^-$  equilibrium below operating line suggesting its extraction impossibility to CPO.

**ABSTRAK:** Penyahklorinan minyak sawit mentah (MSM) bertujuan mencegah pembentukan bahan cemar toksik telah mendorong penggunaan alkali dalam rawatan minyak itu. Manuskrip ini melaporkan taburan ion hidroksida ( $\text{OH}^-$ ) daripada sodium hidroksida dan sodium silikat (SS) antara larutan akueus dan MSM di bawah keadaan penampungan untuk mengurangkan kehadirannya dalam MSM bagi mengelakkan pembentukan sabun. Dalam kajian ini, kepekatan  $\text{OH}^-$  ditentukan melalui pengukuran pH, yang juga merupakan petunjuk kepada kewujudan NaOH. MSM yang ditapis dicampur dengan larutan SS pada suhu bilik dalam pelbagai nisbah isipadu dan kepekatan di bawah pengadukan 800 rpm sebelum diendapkan untuk membentuk lapisan cecair. Pendekatan Satu-Faktor-Sekali telah digunakan untuk mengoptimalkan nisbah tersebut. Ujian nilai asid dan analisis GCMS digunakan untuk menentukan kandungan asid lemak bebas. Penjanaian lengkung penentu-ukuran membolehkan pemalar pelepasan  $\text{OH}^-$  diperolehi iaitu 0.0818. Larutan SS boleh bertukar asid pada kepekatan  $6.344 \times 10^{-5}$  g/ml mungkin disebabkan silika yang terhidrasi. Dengan menggunakan larutan SS 0.01 g/ml, nisbah isipadu antara MSM dan larutan SS dari 0.33 ke 3 berkeadaan alkali dan menurun kepekatan hidroksida. 2 fasa cecair hanya wujud pada nisbah 2.33 dan 3. Kemudian kepekatan SS diubah-ubah untuk nisbah isipadi 2.33 itu

dan corak sigmoid hidroksida diperoleh. Plot McCabe-Thiele mendapati keseimbangan kepekatan hidroksida berada di bawah garisan operasi menunjukkan pengekstrakan adalah mustahil berlaku terhadap OH<sup>-</sup> ke dalam MSM.

---

**KEYWORDS:** *Dechlorination, crude palm oil, hydroxide, sodium silicate solutions, extraction.*

## 1 INTRODUCTION

Malaysian palm oil has been banned by European Union (EU) due to the issue of 3-monochloropropanediol (MCPD) ester and glycidyl esters. These two contaminants are carcinogenic. Thus, a requirement of 1.25-ppm and 1-ppm maxima are imposed respectively to enter their market. Many removal methods of the contaminants have been tested either in lab scale or industrial scale.

MCPD diesters are normally generated from triglycerides after their glycerol molecules have been attacked by chlorine or chloride in nucleophilic substitution reactions under acidic aqueous solution environment to form chloropropanols [1]. The production of 2-MCPD and 3-MCPD derivatives is in a five-atom cyclic carbocation intermediate mechanism or a three-member epoxide ring structure. Formation of MCPD fatty acid diester is usually by heating a mixture of triheptadecanoin and lindane (an organochlorine agent) and MCPD diester formation was found to be significant at 200°C and above, but not at temperatures between 100°C and 180°C. The observation could not be explained by any of the reported cation or glycidol mechanisms suggesting that under low moisture, high temperature conditions, 3-MCPD esters formation may have a new mechanism with chlorine. In this case, triglycerides and chlorine are probably precursors to the MCPD diester synthesis: cyclic acyloxonium or glycidyl ester 3-MCPD monoester and diester synthesis, beside acidity, catalyst and moisture [2].

Several efforts have been made by Malaysia Palm Oil Board (MPOB) to help local industries comply standard palm oil mill requirement such as cleaning palm oil fruits bunch before extraction [3-5], segregation of sterilizer condensate and empty fruit bunch streams from primary CPO production [6], liquid-liquid extraction with a polar solvent solution [7] and pre-treatment process using dechlorinating agent. Dechlorination of CPO is particularly a new approach as a result of a regulation implemented by MPOB in 2019 [8]. Enforcement of this regulation is however still pending because of the difficulty in getting a practical technique to conduct the dechlorination in mills as there are several forms of chlorine in CPO.

Currently available patent is by using magnesium silicate in CPO bleaching, which resulted in significant reduction of 3-MCPD ester in refined- bleached- deodorized palm oil in some refinery processes [2]. Magnesium chloride synthesized from the dechlorination reaction is water soluble. In general, reactions in an heterogenous system was usually deteriorated by mass transfer problems. In synthesis of a chemical process, liquid-liquid system is generally more practical and economical. CPO is currently washed by using raw water, but the supplied general raw water usually contains chlorine for killing germs and microbes. Thus, an additional dechlorination system must be applied to treat the raw water before the CPO washing. The amount of the treated water used to remove chlorine in CPO is a lot because of the solubility issue of organic chloride. Therefore, an alternative liquid-liquid system is in need to reduce the cost.

Dechlorination using alkaline has the potential to remove chlorine both in raw water and CPO, but hydroxides ( $\text{OH}^-$ ) can react with FFAs to form soap, which can unfortunately decrease the oil's quality. The presence of  $\text{OH}^-$  from common alkaline such as NaOH can be moderated in a liquid-liquid equilibrium by using sodium silicate (SS) that may behave like a buffer [9]. MPOB collaborates with us, in this regard, under a grant given by Ministry of Higher Education, Malaysia. Preliminary works of testing SS dilute solution in CPO were done, but no report was published due to inconsistent results. Issues with physical property of  $\text{OH}^-$  and NaOH dissociated from SS perhaps needs to be resolved. Therefore, the effect of the ratio between CPO and SS solution on the  $\text{OH}^-$  concentration needs to be investigated and optimized to achieve the desired level of chlorine. This study aimed to investigate the effect of the ratio between crude palm oil (CPO) and SS solutions, and the SS concentration on the  $\text{OH}^-$  concentration in the various mixtures. The results of this study can provide valuable information for the CPO dechlorinating process and improve the quality of the final product.

## 2 EXPERIMENTAL METHODS

### 2.1 Materials

CPO was collected at Felda Lepar Hilir 3. The CPO sample was then filtered and stirred to ensure homogeneity. SS powder supplied by Bendosen was diluted in deionized water and distilled water to prepare its solution. Analytical grade of iso-propyl alcohol and hexane supplied by HmBG Chemical was used for gas chromatography GCMS analyses. Absolute ethanol from Fluka was applied in FTIR analysis for cleaning lens and in pH measurement for cleaning the probe tips and pH buffer solutions of 4, 7, and 10 from Mettler Teledo were used in calibrating pH meter.

### 2.2 Experimental Design and Extraction Tests

CPO and SS solution were mixed at  $40^\circ\text{C}$  (equivalent temperature to clarifier in most mills) in the volume ratios that were varied based on One Factor at a Time (OFAT) in beakers. The beakers were attached with 1-mm scale graph paper to measure thickness of liquid layer as shown in Fig. 1. The volume ratios varied between 1:3 and 3:1, including replicates as suggested by Design Expert ver.7 software. The concentration of SS was 0.01 g/ml as proposed by Malaysian Palm Oil Board (MPOB) and the companies that applied SS in palm oil mills [10]. Mettler Teledo pH meter giving reading up to 2-decimal place was employed to measure pH after 12 h of mixing, from which  $\text{OH}^-$  concentrations were calculated and the response variable. Table 1 shows the ratio of the liquids in continual, fractional values within 100 ml of total volume for 7 points including replicates.

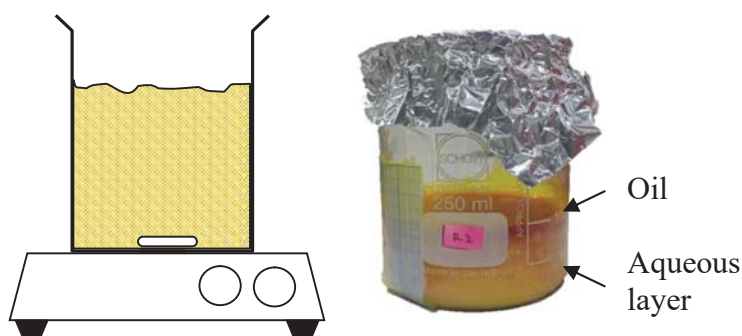


Fig. 1. Heated, stirred beaker for reactive mixing and settling of SS and CPO

Table 1. Volume Ratios between CPO and SS solution

Run	Volume Ratio of CPO TO SS	CPO (ml)	SS (ml)
1	3.00	75	25
2	1.67	62.5	37.5
3	0.33	25	75
4	0.33	25	75
5	2.33	70	30
6	1.00	50	50
7	3.00	75	25

The experiment was then repeated by varying the concentration of SS solution from 0.0004 g/ml to 0.25 g/ml. The volume ratio of CPO:SS solution was kept constant at 7:3 because the others did not remain 2 clear liquid layers. Table 2 shows the concentration of the SS within 100 ml of total volume for 7 points including replicates.

Table 2: Concentration of SS Solution

Run	Concentration of SS (g/ml)
1	0.0626
2	0.1252
3	0.0004
4	0.2500
5	0.0004
6	0.1875
7	0.2500

### 2.3 Dissociation of Hydroxide Ion from SS solution

Silica in low concentration of SS solution may pose acidic mixture due to bonding of silicon and oxygen at various structures [11]. The standard solutions of SS solution were prepared by using the half-serial dilution method [12] to avoid pipetting mistake. The dilution started with 0.01 g/ml of SS.

pH meter with 2-decimal point reading was preferably used to get immediate results. Other analysis methods, such as using titration would not get the actual OH<sup>-</sup> because of equilibrium shift during neutralization. The pH meter was calibrated by using three buffer solutions of different pH. Eq. (1) shows the dissociation of SS to form sodium hydroxide before OH<sup>-</sup> is formed in Eq. (2).



OH<sup>-</sup> from SS was calculated via the equation of pH [13]

## 2.4 Profile of Crude Palm Oil by using GC-MS

Initially, CPO was filtered by using hydrophobic syringe filter made of PTFE in a 0.45- $\mu\text{m}$  thickness and 25-mm diameter of a disc to separate suspended particle and aqueous solution. 1 mL of isopropyl alcohol or hexane solvent was mixed with 100  $\mu\text{L}$  of the filtered CPO in vials by using micropipette. A gas chromatography, Agilent 6890 model, equipped with mass spectrometry detector (GC-MS) was used to analyze the analytes. The oven of the GC was mounted with SGE BPX5 column with the dimension of 30-meter length, 0.025-mm diameter and 0.25- $\mu\text{m}$  film thickness. The oven temperature was raised from 40°C at 10 °C/min to 300°C and remained at that temperature for 5 min.

## 2.5 Acid value determination by using auto-titrator.

Free fatty acid is normally formed during CPO storage [14] and periodical analysis was done to check its content. The procedure followed the acid value analysis standard namely MPOB Test Method c2.7:2004 which is also equivalent to AOCS Te a-64(1997)[15]. Free fatty acid problematically forms soap with NaOH and its quantity could be determined from the acid value analysis. 0.1 mol/L potassium hydroxide (KOH) solutions were prepared by dissolving KOH pellets in distilled water by using 1-L volumetric flask. The KOH solution was then used as a titrant to the auto-titrator from Metrohm, 785 DMP Titrino model. pH electrode LL Solvotrode (8.109.1586) Metrohm AG 9101 Herisau was used as the probe. The room temperature was set at 28 °C. Initially, the system was calibrated with pH 7 buffer solution and the actual pH reading was set as the end point. The sample was prepared by diluting 5 ml of filtered CPO in 75 ml of isopropanol. The reading of pH and volume of KOH being used were recorded and analyzed. A blank test of isopropanol solvent was also included in the analysis. The titrations were repeated at least twice and the ceramic membrane of the pH probe was rinsed between the analysis runs by using absolute ethanol as this titration involved fatty liquid.

# 3 RESULTS AND DISCUSSION

Hydroxide ion is the key conjugate to sodium ion in NaOH that will be involved in the dechlorination reaction. The reaction was assumed to simultaneously occur when chloride was present in aqueous media or OH<sup>-</sup> diffused to the organic phase of CPO, but the results will not be the focus in this report. Preliminary characterization of chemical and physical properties in perspective of extraction are presented here to further design the concept of dechlorination later.

## 3.1 Dissociation of Hydroxide Ion from Sodium Silicate Solution

Information of pH on SS solution is necessary before its application to any liquid due to variety of silica structure from different suppliers and sensitivity of silicon to any presence of other ions, heat and light as a semiconductor element. Silica can form silicic acid in very dilute conditions. OH<sup>-</sup> was determined from pH readings using Eq. (3)[16].

$$C_{OH^-} = \frac{1 \times 10^{-14}}{10^{-pH}} \quad (3)$$

Fig. 2 shows pH of SS solution at various concentrations. Two trends of data were captured by different models. By using the nonlinear regression in SigmaPlot 10, data was

fitted ( $R^2 > 0.95$ ) with logarithmic Eq. (4) and quadratic Eq. (5) as respectively shown in Fig. 2(a) and (b).

$$pH = 13.8059 + 0.4218 \ln C_{SS} \quad (4)$$

$$pH = 6.99 - 157794.2C_{SS} + 2484503101.2C_{SS}^2 \quad (5)$$

where,  $C_{SS}$  denotes the concentration of SS solution in  $g\ ml^{-1}$ .

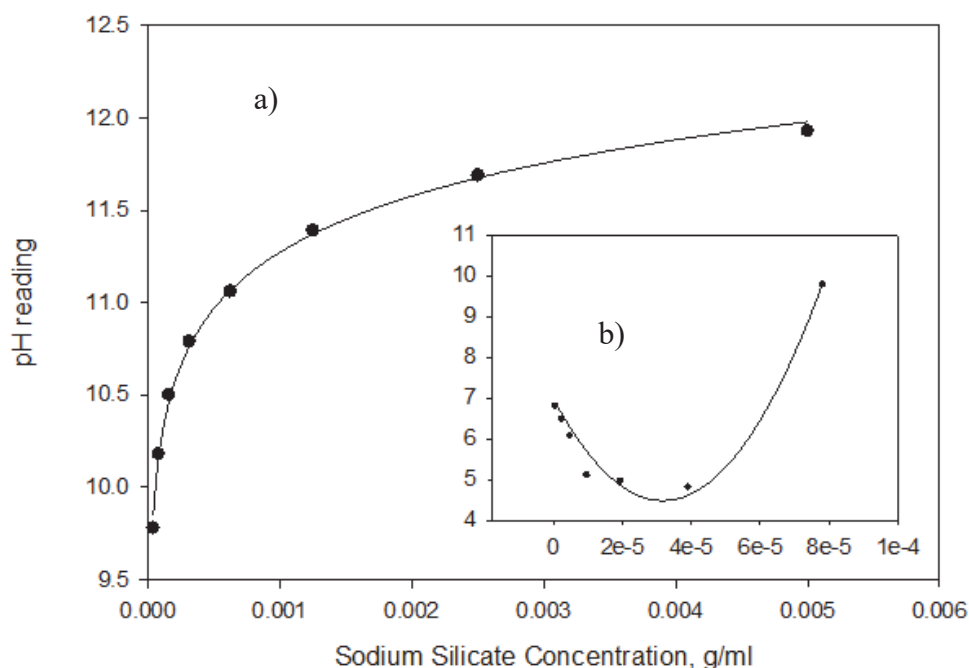


Fig. 2. pH at various SS concentrations

Based on the model, the logarithmic model of pH gives pH for 1 molar of SS 11 times lower than that of 1-M NaOH. This was probably the incomplete  $OH^-$  dissociation from SS at an equilibrium at room temperature. A further analysis on molarity of SS and  $OH^-$  revealed direct proportion in linear trendline from origin on their graph where its gradient is the dissociation constant of component,  $K_D$ , as shown in Eq. (6) at  $28^\circ C$ .

$$K_D = \frac{[OH^-]}{[Na_2SiO_3]} = 0.0818 \quad (6)$$

The model of the plot is, however, valid until  $6.344 \times 10^{-5}$  g/ml because pH dropped below pH 7 and formed a curve as shown in the small graph in Fig. 2. Hence, acid condition clearly appeared below this concentration. The quadratic model that fitted it has a minimum pH 4.48 at  $3.17 \times 10^{-5}$  g/ml prior to a decrease until pH 7 when the concentration is 0. Perhaps, several form of silica structure created the acidic condition [9] in the form of silanol (Si-O-H) functional or silicic acid ( $SiO_4^{4-}$ ) groups, thus silica falls under the category of acidic ligand, inorganic minerals and exhibits hydrophilic properties [17]. A comparison with pH of blank water indicated that about 10% difference in zero error of calibration revealed thus dissimilar standard reduction potential according to the Nernst equation for a pH measurement [18]. Therefore, the sample without SS would not be used as the reference in the calibration. Silica

from SS solution can be measured by using FTIR in the vibrational band in range between 1150 and 950  $\text{cm}^{-1}$ . However, upon checking, its zero error was above 1% and this method is not practical for dilute SS solution.

### 3.2 Crude Palm Oil Profile and Free Fatty Acid Content

Analyses of chromatogram using mass spectroscopy detector were initially conducted by diluting CPO samples with isopropanol, the common solvent in AOCS titration analysis [19], but the GCMS analyte formed unclear layer of different density after a few minutes left on the autosampler rack. Result of replicates were not consistent with their original samples. Solubility of oil impurities might be the issue. Hence, hexane was used and able to minimize deviation of results with replicate analyses. Fig. 3 shows the chromatographic analysis result of CPO using hexane solvent in GCMS. Palmitic acid, or n-hexadecanoic acid had 40.20 % of fat at retention time of 17.975 min. Oleic acid and stearic acid or octadecanoic acids had 46.76 % and 9.62 %, respectively. These results were supported by Montoya, Cochard [20], which were close to 50 % of fat in palm oil was saturated, including 44% palmitic acid (C16:0), 5% stearic acid (C18:0), and traces of myristic acid (C14:0). About 40% of the fatty acids were unsaturated, including 10% polyunsaturated linoleic acid (C18:2) and linolenic acid (C18:3). Nonetheless, from the chromatogram analysis results, separation of FFA and conjugated fatty acids in glyceride was not possible using the SGE BPX5 column. Comparison between the fatty acid QUAL results and FFA content from acid value titration showed large differences. From the acid value test, FFA content of the sample used in the GCMS analysis was only 7.9 %. That sample was 7 days after collection. Initial collection, it was about 3%.

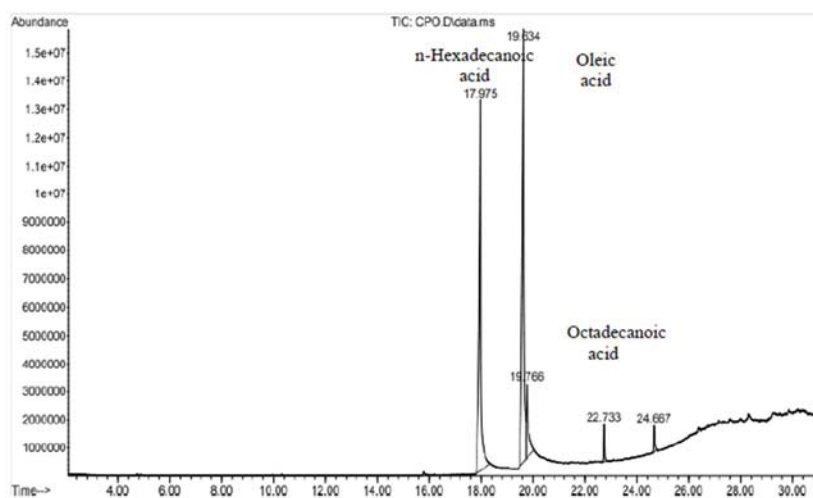


Fig. 3. Chromatogram of CPO Using GCMS

### 3.3 Effect of CPO-SS Volume Ratio

The pH reading decreased from 10.10 and plateaued out at 8.16 with the higher CPO volume. pH 8.16 was probably the value of buffering for SS in the mixture. The response of  $\text{OH}^-$  concentration on various volume ratios of CPO and SS from 1:3 to 3:1 is shown in Fig. 4. The increase in the ratio decreased the  $\text{OH}^-$  concentration, but no minimum at any pH was registered like the one previously resulted in the calibration curve at very low concentrations of SS probably due to the absence of acids from silica and free fatty acids (FFA). Pandey, Larroche [21] reported that pH of CPO was usually from 3.6 to 5.1, which is slightly acidic due to the presence of FFA from the hydrolysis of oil. In this study, the acid value analysis

revealed FFA content between 7.79 and 8 wt% in the CPO. Although this indicates that the oil samples degraded and its quality became off-spec for refinery process due to long storage in the experiment, pH remained above neutral with the presence of SS solution. The plot shows concave up decreasing shape.

One Factor Design (OFD) analysis was used to optimize the process and the correlation between concentration pH and the volume ratio is expressed in Eq. (7). This quadratic model was suggested among other polynomial models and parameters with the F value of 1.48 for Lack of Fit in Residual, indicating that this model significantly fitted the data.

$$[OH^-] = (11.94 + 11.4956\theta - 2.56373 \theta^2)10^{-5} \text{mol/L} \quad (7)$$

Where,  $\theta$  is volume ratio between CPO and SS. The above neutral and alkaline pH would not last.  $7.41 \times 10^{-5}$  mol/L, is the smallest concentration of  $OH^-$  could drop when CPO was more,  $Na_2O$  from SS was no longer available and hydrogen ion from acids or FFA became dominant, thus the buffering equilibrium had been breached.

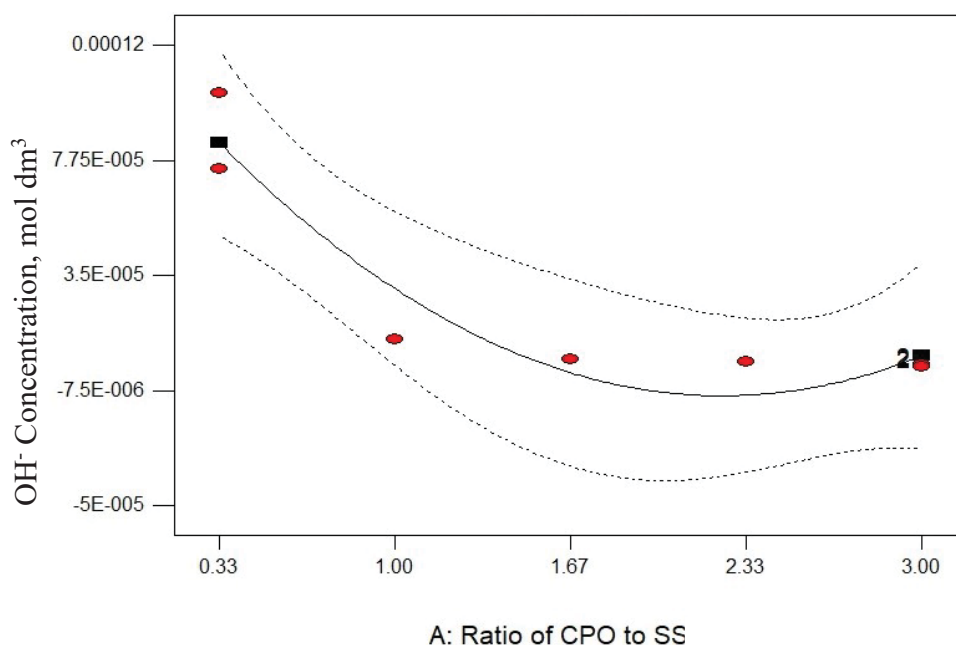


Fig. 4. The effect of volume ratio on  $OH^-$  concentration.

Compared to  $OH^-$  dissociation from NaOH (or ionization), distribution constant of  $OH^-$  from SS shown by Eq. (6) is relatively very low. Nevertheless, visibility of the second liquid phase was only evidenced at upper layer as shown in Fig. 1 from the CPO-SS volume ratio of 3:1 and 7:3. Table 2 shows the change of the volume ratio appeared after the mixture being settled for 12 h. The number of runs was not according to the sequence. The ratio dropped for about 67 to 78% from the original volume ratio due to the expansion of emulsion phase. This finding should be considered seriously if one intends to develop a liquid-liquid extraction as it will affect the liquid hold-up of the process. In this case, our painstaking experiment of  $OH^-$  extraction as the key reactant for dechlorination in the aqueous phase will be started from 7:3 and above. The volume ratio below 0.33 can also be considered, since at that ratio, the liquid was bulkily emulsified so that clearer aqueous phase can hopefully be obtained and separated from the oil phase.

Table 2: Effect of Mixing to Volume

Run	Volume Ratio	Volume Ratio after 12 h
4	0.33	Single phase
3	0.33	Single phase
6	1.00	Single phase
2	1.67	Unclear layering
5	2.33	0.76
7	3.00	0.74
1	3.00	0.67

### 3.4 Effect of SS Concentration

Concentration of SS is another factor that will affect the presence of OH<sup>-</sup>. In the OFAT analysis, pH increase was recorded as the concentration of SS increased, and the highest pH was 11.91 as shown in Fig. 5. However, no acidic condition was found. The quadratic model suggested by Design Expert was Eq. (8) and as shown in Fig. 5(a), could only fit 88.67% (R-squared) of the data while the regression using sigmoid model in Sigma Plot 10 as Eq. (9) in Fig. 5(b) could significantly fit 99.3%. Although the quadratic model was best suggested, the fitness of the model was below 95% and insignificant.

$$[OH^-] = (1.878 + 4.01C_{SS} + 2C_{SS}^2)10^{-3} \quad (8)$$

$$[OH^-] = \frac{0.0078}{1 + e^{\frac{0.1644 - C_{SS}}{0.0219}}} \quad (9)$$

Both models interestingly captured a downward curve, and the latter unveiled a trend that was symptomatic of autocatalysis. Dissociation of OH<sup>-</sup> might be more than what was previously shown in the calibration curve. This also indicates that Na<sub>2</sub>O was released more because of a reaction that consumed silicate, its conjugate in SS, started from 0.1644 g/ml, which is the middle point of the sigmoid graph. Undesired reactions other than dechlorination such as saponification and hydrolysis probably increase due to the OH<sup>-</sup> increase. This might justify why industries employed only 0.01 g/ml of SS solution in palm oil mills for oil extraction rate improvement.

### 3.5 McCabe Thiele Plot

Besides distillation column, McCabe Thiele method is also used to determine stages of mixer and settler for a solvent extraction process between two immiscible liquid phases. Fig. 6 shows two McCabe-Thiele plots for two volume ratios from the results of volume ratio study above that remained two layers of liquid phase after 12 h of settling. Volume ratios of CPO:SS can be interpreted as operating lines on the McCabe-Thiele graphs, which were also symbolized  $\theta$ . At  $\theta = 3$ , the equilibrium was  $3.62 \times 10^{-8}$  and  $1.13 \times 10^{-6}$  g/g of OH<sup>-</sup> in CPO

and SS solution respectively. At  $\theta = 2.33$ , both equilibria were from the same SS concentration, but they appeared at different points. This discrepancy might be due to different FFA content and other impurities that reacted with component of SS solution [22]. The equilibrium conditions of  $\text{OH}^-$  for both  $\theta$ s is all far below the operating lines, suggesting that at these volume ratios,  $\text{OH}^-$  is not likely extractive to CPO [23].

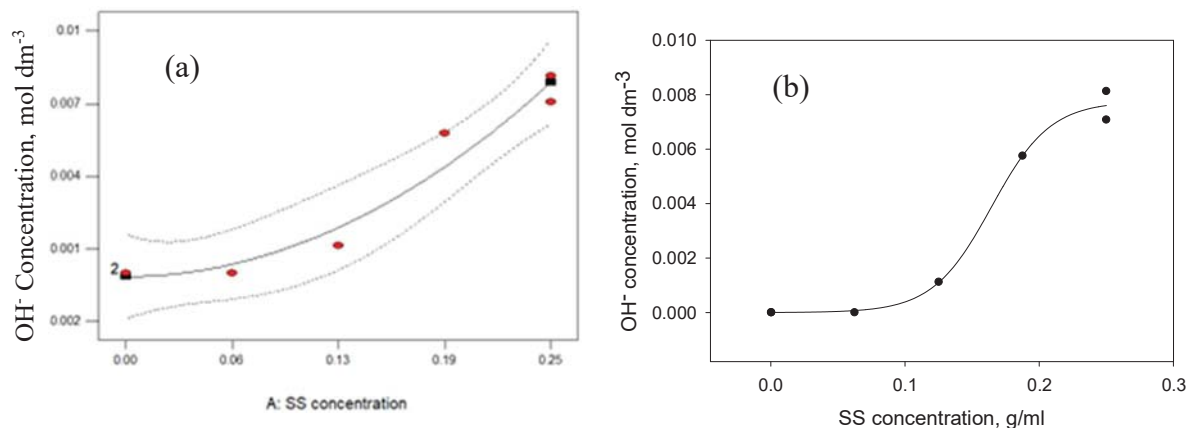


Fig. 5. The effect of SS concentration on  $\text{OH}^-$  concentration for the volume ratio of 2.33.

The SS solution was 0.01 g/ml and  $\text{OH}^-$  from dissociated NaOH was not extracted to CPO. Thus, possibility of undesired hydrolysis reactions consuming free fatty acids and glycerides, which are highly non-polar and do not dissolve in the aqueous phase is low. In the case of SS concentration variation, clear 2-layer liquid formed at concentration of 0.0004 g/ml. Emulsion layer formed at 0.0625 g/ml and others concentration started from 0.1252 g/ml till 0.25 g/ml the second layer became solidified.

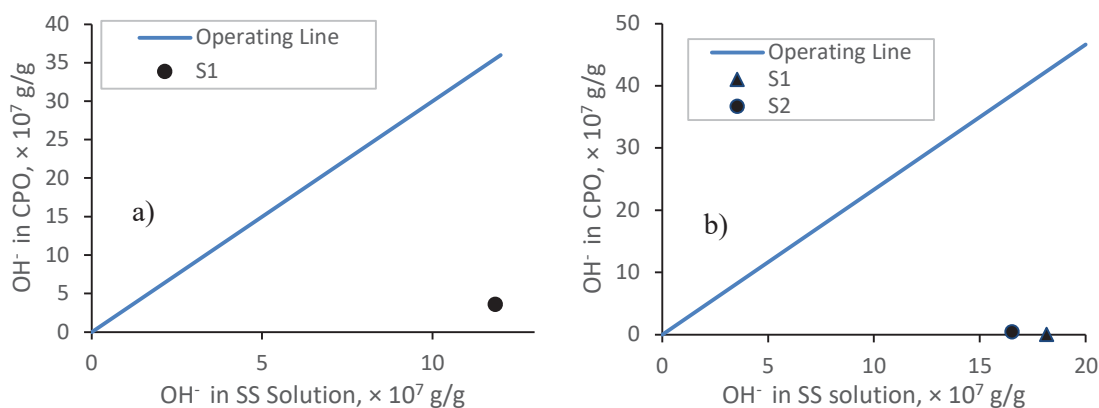


Fig. 6. McCabe-Thiele plot of solvent extraction for (a)  $\theta = 3$  and (b)  $\theta = 2.33$ .

## 4 CONCLUSION

The effect of mixing SS solution to CPO at various volume ratios was investigated where  $\text{OH}^-$  from NaOH that was dissociated from the SS solution was measured by using pH. The equilibrium condition for volume ratios of CPO:SS that secured biphasic condition were 7:3 and 3:1 and below the operating line according to McCabe-Thiele method, indicating that  $\text{OH}^-$  is not extractive. Only 0.004 g/ml concentration of SS formed 2 layers of liquid-liquid phase for OFAT varied concentration of SS. The acid values of the sample are 18.539 (mg

KOH/ g CPO) and 18.982 (mg KOH/ g CPO), for sample 1 and sample 2, respectively. The free fatty acid contents in both samples are 7.79% and 8.01 %. OH<sup>-</sup> concentration decreased following a quadratic model to the increase of volume ratios but it increased in a sigmoid model to the increase of SS concentration. The possible cause of these effects is detailed in the result discussion above.

## ACKNOWLEDGMENT

The author would like to express gratitude to all lab personnel at our faculty, plant managers of LCSB Lepar Hilir mill and FGVPIB Lepar Hilir Mill for the crude palm oil samples and the financial support given by the Ministry of Higher Education Malaysia under the fundamental research grant scheme numbered FRGS/1/2022/TK05/UMP/02/23 or RDU220114

## REFERENCES

- [1] Gao B, Li Y, Huang GYu L. (2019) Fatty Acid Esters of 3-Monochloropropanediol: A Review. *Annual Review of Food Science and Technology*. 10: 259-284. Available from: <https://www.annualreviews.org/doi/abs/10.1146/annurev-food-032818-121245>
- [2] Wei T, Liu W, Zheng Z, Chen Y, Shen M Li C. (2022) Bibliometric Analysis of Research Trends on 3-Monochloropropane-1,2-Diol Esters in Foods. *Journal of Agricultural and Food Chemistry*. 70: 15347-15359. Available from: <https://doi.org/10.1021/acs.jafc.2c06067>
- [3] Hilmi SMHS, Othman NH, Saporin N, Jahaya SS, Noor AMAsis AJ. (2019) Process for producing a refined palm fruit oil having a reduced 3-mcpd content. Available from: <https://patents.google.com/patent/WO2019027315A2/en>
- [4] Hassan NSM, Chew CLM, Tahir ZM, Amin Buhari Md Zain, Siran AJAM, Wok K, Yunus MFM, Jahaya SS, Rejab SAM, Mustaner MHilmi SMHS. (2019) An integrated oil extractor apparatus for sterilizing, digesting and pressing oil palm loose fruitlets. WO-2019216757-A1 Available from: <https://patents.google.com/patent/WO2019216757A1/en?q=WO-2019216757-A1>
- [5] Nizam AFAMahmud MS. (2021) Food quality assurance of crude palm oil: a review on toxic ester feedstock. *OCL*. 28: 23-37. Available from: <https://doi.org/10.1051/ocl/2021011>
- [6] Chew CLSaporin N. (2021) Principal Formation and Mitigations Strategies for 3-MCPDE in Palm Oil Processing. *Journal of Oil Palm and the Environment*. 12: 86-95.
- [7] Oey SB, van der Fels-Klerx HJ, Fogliano Vvan Leeuwen SPJ. (2022) Chemical refining methods effectively mitigate 2-MCPD esters, 3-MCPD esters, and glycidyl esters formation in refined vegetable oils. *Food Research International*. 156: 111137. Available from: <https://www.sciencedirect.com/science/article/pii/S0963996922001946>
- [8] Kadir APG, Penguatkuasaan Tambahan Syarat Lesen yang Dikenakan bagi Pemegang Lesen dalam Kategori Kilang Buah Kelapa Sawit (MF), Kilang Penapis (RF), Pengeksport Keluaran Kelapa Sawit (PX) dan Pengimport Keluaran Kelapa Sawit (PM): Keselamatan Makanan dan Minyak Sawit yang Berkualiti, in (9)04/C/PD/656/4 Jil. 5, Berhad, M.P.O., Editor 2019, MPOB: Bangi, Selangor, Malaysia.
- [9] Bajpai P, (2014) 7 - Chemicals Used in Deinking and Their Function\*\*Some excerpts taken from Bajpai, 2006 with kind permission from Pira International, UK, in *Recycling and Deinking of Recovered Paper*, Bajpai, P., Editor, Elsevier, Oxford; pp. 121-137. Available from: <http://www.sciencedirect.com/science/article/pii/B9780124169982000076>
- [10] III DD, Zhan HM, Hamid MFA, Idzhan NIMShukor MZ. (2017) Use of mineral salts to improve production of crude palm oil and controlling the oil lost. WO 2017/150965 A1: WO 2017/150965 A1
- [11] Dankert Fvon Hänisch C. (2021) Siloxane Coordination Revisited: Si–O Bond Character, Reactivity and Magnificent Molecular Shapes. *European Journal of Inorganic Chemistry*. 2021: 2907-2927. Available from: <https://chemistry-europe.onlinelibrary.wiley.com/doi/abs/10.1002/ejic.202100275>

- [12] Sapkota A. Serial Dilution- Definition, Formula, Calculator, Procedure, Uses. 2022 [cited 2023 12/5/2023]; Available from: <https://microbenotes.com/serial-dilution/>.
- [13] Ryen Caenn HCHDaGRG (2017) Evaluating Drilling Fluid Performance,
- [14] Ahmad Nizam AF, Muthiyah KMahmud MS. Free fatty acid formation in oil palm fruits during storage. in IOP Conference Series: Materials Science and Engineering. 2020. IOP Publishing, 991: 012009. Available from: <https://dx.doi.org/10.1088/1757-899X/991/1/012009>
- [15] Yeong SK, Idris ZHassan HA, (2012) 20 - Palm Oleochemicals in Non-food Applications, in Palm Oil, Lai, O.-M., Tan, C.-P., and Akoh, C.C., Editors., AOCS Press; pp. 587-624. Available from: <http://www.sciencedirect.com/science/article/pii/B978098189369350023X>
- [16] Ebbing DDGammon SD (2013) General Chemistry, Brooks/Cole Cengage Learning
- [17] Singh S, Wasewar K, Kansal SK, (2020) Low-cost adsorbents for removal of inorganic impurities from wastewater, in Inorganic Pollutants in Water, Devi, P., Singh, P., and Kansal, S.K., Editors., Elsevier; pp.173-203. Available from: <https://www.sciencedirect.com/science/article/pii/B978012818965800010X>
- [18] Shintani Y, Ogawa K, Saruya TKawarada H, Development of glassless all-solid-state pH sensor, Edition, Y.T.R.E., Editor 2017.
- [19] Kuntom A, Lin SW, Ai TY, Idris NA, Yusof M, Sue TTIbrahim NA (2005) MPOB Test Methods, Malaysian Palm Oil Board
- [20] Montoya C, Cochard B, Flori A, Cros D, Lopes R, Cuellar T, Espeout S, Syaputra I, Villeneuve P, Pina M, Ritter E, Leroy TBillotte N. (2014) Genetic Architecture of Palm Oil Fatty Acid Composition in Cultivated Oil Palm (*Elaeis guineensis* Jacq.) Compared to Its Wild Relative *E. oleifera* (H.B.K) Cortes.
- [21] Pandey A, Larroche C, Dussap C-G, Gnansounou E, Khanal SKRicke S (2019) Biogas Production From Industrial Effluents, Elsevier, Academic Press
- [22] Taifan GSPMaravelias CT. (2020) Integration of graphical approaches into optimization-based design of multistage liquid extraction. Computers & Chemical Engineering. 143: 107126. Available from: <https://www.sciencedirect.com/science/article/pii/S0098135420306256>
- [23] Barcelos TT, Martins M, Sousa RCoimbra JSdR. (2018) Liquid-Liquid Extraction of Neutral Lipids and Free Fatty Acids from Microalgae Oil. Journal of Chemical & Engineering Data. 63: 3391-3399. Available from: <https://doi.org/10.1021/acs.jced.8b00281>

## ADSORPTION PERFORMANCE OF FIXED-BED COLUMNS FOR THE REMOVAL OF PHENOL USING BAOBAB FRUIT SHELL BASED ACTIVATED CARBON

RADHIA NEDJAI<sup>1,2\*</sup>, NASSERELDEEN KABBASHI<sup>2</sup>, MD ZAHANGIR ALAM<sup>2</sup>,  
MA'AN ALKHATIB<sup>2</sup>, AMINA TAHREEN<sup>2</sup> AND ABDULLAH AL MAMUN<sup>3</sup>

<sup>1</sup>Department of Biology, Faculty of Science, Badji Mokhtar University, 23000 Annaba, Algeria

<sup>2</sup>Cataclysmic Management and Sustainable Development Research Group (CAMSDE),

Department of Civil Engineering, Kulliyah of Engineering,

International Islamic University Malaysia, Kuala Lumpur, Malaysia

<sup>3</sup>Bioenvironmental Engineering Research Center (BERC),

Department of Chemical Engineering & Sustainability, Kulliyah of Engineering,

International Islamic University Malaysia, Kuala Lumpur, Malaysia

\*Corresponding author: radiaradia19@gmail.com

(Received: 16 July 2023; Accepted: 9 October 2023; Published on-line: 1 January 2024)

**ABSTRACT:** A continuous adsorption study in a fixed-bed column using baobab fruit shell activated carbon (BF-AC) was investigated for phenol removal from an aqueous solution. Baobab fruit shell (BFS) was chemically activated using potassium hydroxide (KOH) at 700 °C in a nitrogen (N<sub>2</sub>) atmosphere. Scanning electron microscope (SEM), X-ray diffraction (XRD), and BET surface area analyses were performed for the characterization of BF-AC. Fixed-bed experiments were carried out and the effect of feed flowrate (10, 15, 20 mL/min) and bed height (5, 10, 15 cm) on the adsorption were investigated by evaluating the breakthrough curves. BET surface area of BF-AC was 1263 m<sup>2</sup>/g, indicating its well-developed pores and its good quality as an adsorbent. The findings showed that the exhaustion time ( $t_d$ ) and breakthrough time ( $t_b$ ) reduced as the flowrate augmented, while they increased as the bed height augmented. With the increase in the bed height and the flowrate, phenol solution volume treated was augmented. Also, BF-AC with bed height of 15 cm provided better elimination of phenol with carbon usage rate (CUR) of 1.74 g/L and empty bed contact time (EBCT) of 9.9 minutes. According to the findings, BF-AC is an effective adsorbent for removing phenol from aqueous solutions.

**ABSTRAK:** Kajian penjerapan berterusan menggunakan kulit buah baobab diaktifkan karbon (BF-AC) telah dikaji menggunakan pakai kolum lapisan tetap bagi penyingkiran fenol daripada larutan cecair. Kulit buah Baobab (BFS) diaktifkan secara kimia menggunakan kalium hidroksida (KOH) pada suhu 700 °C dalam atmosfera nitrogen (N<sub>2</sub>). Imbasan mikroskop elektron (SEM), pembelahan sinar-X (XRD), dan analisis permukaan BET dijalankan bagi pencirikan BF-AC. Eksperimen kolum lapisan tetap bagi mengkaji kesan penjerapan pada aliran suapan (10, 15, 20 mL/min) dengan ketinggian (5, 10, 15 cm) dinilai melalui lengkung bulus. Kawasan permukaan BET BF-AC adalah 1263 m<sup>2</sup>/g, menunjukkan liang yang elok terbentuk dan berkualiti baik sebagai penyerap. Penemuan ini menunjukkan bahawa puncak masa maksima ( $t_d$ ) dan masa terbaik ( $t_b$ ) berkurangan pada kadar aliran bertambah, sebaliknya ianya meningkat pada ketinggian bertambah. Dengan penambahan ketinggian katil dan kadar aliran, jumlah larutan fenol yang dirawat telah bertambah. Selain itu, BF-AC pada ketinggian 15 cm menunjukkan penghapusan fenol terbaik pada kadar penggunaan karbon (CUR) 1.74 g/L dan masa sentuhan kolum kosong (EBCT) 9.9 minit. Ini menunjukkan, BF-AC adalah penyerap yang berkesan bagi menyingkirkan fenol daripada larutan cecair.

**KEYWORDS:** adsorption; Baobab fruit shell; breakthrough curves; fixed-bed column; phenol

## 1. INTRODUCTION

Phenol is regarded as an environmental problem owing to its discharge in wastewater from a variety of industries, including petroleum refineries, petrochemicals, pharmaceuticals, pesticide manufacturing, resins, steel mills, coke manufacturing, paints, dye production, and mine discharge [1]. Currently, about 7.8 million tons of phenol are produced annually around the world, with production rates on the rise [2]. Phenol has been classified as a hazardous substance due to the potential danger it poses when it comes into contact with living organisms. United States Environmental Protection Agency (USEPA) has designated phenol as a priority pollutant due to its toxicity, with an allowed limit of 0.001 mg/mL and 0.1 mg/L in water supplies and wastewater, respectively [3].

Several methods have been used to remove phenol from aqueous solutions, involving ion-exchange [4], distillation [5], adsorption [6], chemical oxidation [7], extraction [8], coagulation [9], bio-degradation [10], and electro-chemical oxidation [11]. Adsorption has been shown in numerous studies to be a highly effective method for removing phenol from wastewater, and activated carbon (AC) has been frequently used as an adsorbent [3]. This method attracted a lot of attention because of its benefits, including ease of use, superior design flexibility, selectivity, high performance, no need for secondary purification, and the absence of undesirable by-product production [12,13]. Commercially available AC is an established and widespread adsorbent for the removal of various pollutants [14]. Despite its extensive use, AC remains an expensive material [1]. Moreover, saturated-AC regeneration is very tedious, difficult, and expensive [14]. This necessitates finding and developing inexpensive adsorbents from inexpensive and abundant raw materials.

Using lignocellulosic biomass as a raw material for the production of AC provides an alternative to conventional sources and is considered an effective way to discard massive waste quantities and reduce the cost of AC production as well. Lignocellulosic biomasses are cheap, plentiful, renewable, non-toxic, easily accessible, and eco-friendly [1]. Many lignocellulosic biomasses have been utilized as precursors to produce AC for phenol removal from wastewater. However, these studies were limited to fixed bed columns. Only a few studies have been carried out on fixed-bed investigations. This could be due to the restriction caused by a significant lack of an adsorbent material in substantial quantity [15]. Lignocellulosic biomasses that have been utilized to remove the phenol from wastewater in fixed-bed are *Lantana camara* [16], sugarcane bagasse [17], date palm [18], fox nutshell [19], corn cob [20], neem leaves [21], and rice husk [22]. These biomasses offer an alternative to traditional sources, which may serve as potential precursors to produce AC. As a result, to find a new renewable alternative source for AC, efforts have been made to produce AC from baobab fruit shell (BFS) by chemical activation [1,23-25].

Baobab fruit shell is a lignocellulosic residue of the baobab fruit, which is one of the most abundant agriculture wastes with an annual average amount of 30,285 tons [26]. BF-AC was utilized as an adsorbent for the removal of environmental pollutants, including heavy-metals [27,28], dyes [24,29], and phenolic compounds [1,23,25]. In order to remove the phenol from aqueous solutions, batch studies of the potential BF-AC have been conducted [1]. Phenol adsorption on BF-ACs adsorbents produced by chemical activation utilizing  $ZnCl_2$ , KOH, and  $H_3PO_4$  has also been reported [1]. The findings showed that the phenol adsorption rate by BF-ACs was rapid, and that AC treated with KOH could absorb more than 95% of phenol. The optimization of phenol removal on BF-AC has also been studied [23]. The results demonstrated

that BF-AC has high efficiency in the removal of phenol from aqueous solutions with an adsorption capacity of 196.86 mg/g [3,23]. The earlier studies were confined to batch studies only [1,3,23,25]. However, understanding the column mode adsorption pattern is necessary to suggest potential applications in the field.

However, the goal of the current research is to examine the ability of the BF-AC for the removal of phenol in a continuous fixed-bed adsorption column. Continuous flow conditions are regarded as necessary and effective in large-scale industrial wastewater treatment owing to their simplicity, convenient operation, handling, and regeneration capacity [30]. The current study investigated the effects of some operating factors on adsorption, including flowrate and bed height. Prior to using the BF-AC as an adsorbent, SEM, BET surface area, and XRD analyses were performed to characterize the material.

## 2. METHODOLOGY

### 2.1 Materials

In the current work, baobab fruit has been obtained from Sudan, at the end of the rainy season. Potassium hydroxide (KOH), hydrochloric acid (HCl), and phenol (C<sub>6</sub>H<sub>5</sub>OH) were acquired from Sigma-Aldrich (Malaysia). Nitrogen gas (99.95 %) was purchased from Fuelink Marketing Sdn. Bhd. (Selangor, Malaysia).

### 2.2 Methods

#### 2.2.1 Adsorbent Preparation

In the current work, baobab fruit was obtained from Sudan, at the end of the rainy season. Baobab fruit shells (BFS) were washed several times with distilled water. Wet BFS were dried in the oven before being milled and sieved into fine particles (< 1 mm). An amount of KOH was added to crushed BFS using a 1:2 impregnation ratio (IR) (BFS:KOH). Distilled water was added to the mixture in an amount equal to four times the total quantity of BFS and KOH mixture. The sample was stirred at 50 °C for 1 hr and then inserted in an oven at 100 °C and left overnight. Nitrogen gas (N<sub>2</sub>) was utilized for purging a quartz tube a few minutes before carbonization began. N<sub>2</sub> was kept in place throughout the activation and cooling processes. Sample carbonization was carried out for 1 hr at 700 °C. The product was placed in a desiccator to cool, then neutralized with a HCl solution (0.5 M, 50 mL), followed by a wash with warm distilled water (70 °C) until a constant pH of the washing solution was reached. BF-AC produced was dried in the oven at 110 °C.

#### 2.2.2 Characterization of BF-AC

The morphological structure of powdered BF-AC and its structural alterations that resulted from the chemical activation process were both seen using SEM (JEOL-IT 100). For X-ray Diffraction (XRD) analysis, a Bruker D2 phaser (Bruker AXS, Germany) was utilized. The porosity of the BF-AC was assessed using Quanta-chrome, Autosorb-1C, and a surface area analyzer in accordance with Brunauer-Emmett-Teller (BET) model through physical adsorption of N<sub>2</sub> (at 77 k).

#### 2.2.3 Adsorbate Preparation

An appreciable amount of phenol was dissolved in distilled water to prepare the stock solution of adsorbate (phenol) with a concentration of 150 mg/L.

### 2.2.4 Fixed-Bed Column Adsorption Studies

Column experiments were conducted utilizing a stainless-steel tube of 29 mm in diameter and 300 mm in height. The phenol solution was stored in a storage tank, where the tank had retained a steady depth of pollutant by recharging the tank to retain the pressure of the solution in the tank. The adsorbent was immersed in distilled water, then rinsed and poured several times for the removal of the fine particles. BF-AC was dried overnight at 110 °C and known quantities of activated carbon were placed into the column at various heights (5, 10, and 15 cm), which were measured before the tests. The columns were filled with distilled water, then preserved and immersed before filling the column with the phenol. Afterward, phenol solutions of 150 mg/L were pumped through the column bed, which would lower bed utilization as explicated using a peristaltic pump at various flowrates of 15, 10, and 20 mL/min [16]. Activated carbon weight was determined after it was filled into the column to the required height. Finally, the bed exhaustion time was determined by collecting treated phenol samples from the outlet at time intervals and measuring the remaining phenol. The flowrate was kept constant with a control valve at constant rates. Samples were collected from the collection port in the column at different time intervals. Residual concentrations of phenol were measured at 270 nm wavelength using a spectrophotometer. The experimental setup from this study of the column is shown in the schematic diagram (Fig. 1). Table 1 illustrates the range of each parameter that was utilized for this study. Each parameter used was specified depending on the information obtained in the literature review [16].

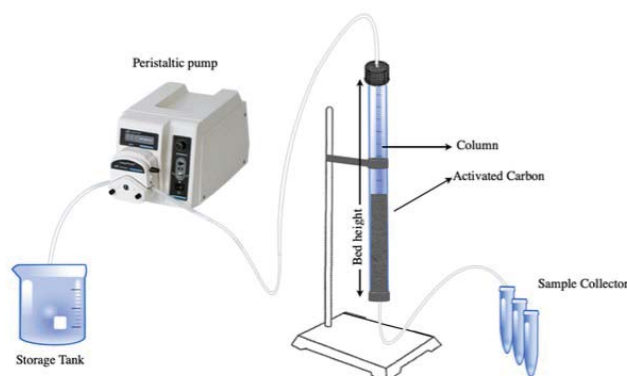


Fig. 1: Bed column experimental setup.

Table 1: Column operating parameters and conditions

Parameters	Variations
Column bed depth (cm)	30
Column diameter (cm)	2.9
Flowrate (mL/min)	10, 15, 20
Bed height (cm)	5, 10, 15
BF-AC mass (g)	5.5, 11, 16.5
Initial concentration of phenol (mg/L)	150

### 2.2.3 Fixed-Bed Adsorption Column Analysis

#### A: Columns Effluent Analysis

The concentration of residual phenol was utilized to determine the breakthrough curve graph by plotting the fractional ratio (Eq. 1) versus time.

$$f = \frac{C}{C_0} \quad (1)$$

where  $C_0$  is the initial concentration of phenol and  $C$  is the residual concentration of phenol.

### **B: Performance Evaluation of Adsorbent**

The breakthrough curve was plotted to determine the time needed to reach the breakthrough point ( $t_b$ ) and the time needed to reach the exhaust point ( $t_x$ ) using Eq. 2 and Eq. 3, respectively. The time for phenol to exhaust the mass transfer zone/active adsorption zone ( $t_\delta$ ) was determined using Eq. 4.

$$t_b = \frac{V_b}{Q} \quad (2)$$

$$t_x = \frac{V_x}{Q} \quad (3)$$

$$t_\delta = \frac{(V_x - V_b)}{Q} \quad (4)$$

Also, the specific throughput was determined with Eq. 5 to evaluate the BF-AC performance in the column. A water quantity that might be processed by BF-AC in liters/g was determined from a specified throughput and compared at a breakthrough time ( $t_b$ ) and at exhaustion ( $t_x$ ).

A specific throughput and the empty bed contact time (EBCT) were determined using the following equations:

$$\text{Specific throughput} = \frac{Q t_b}{M} \quad (5)$$

$$\text{EBCT} = \frac{V_f}{Q} = \frac{L \cdot A_F}{v \cdot A_F} = \frac{L}{v} \quad (6)$$

where EBCT is the contact time in the empty bed (h),  $V_f$  is the volume occupied by BF-AC media including porosity volume ( $\text{m}^3$ ),  $Q$  is the flowrate to adsorber (L/hr),  $A_F$  is the BF-AC area available for flow ( $\text{m}^2$ ),  $L$  is the BF-AC depth (m), and  $v$  is the superficial flow velocity ( $Q/A_F$ ) in (m/h).

Equation 7 was used to get the carbon use rate (CUR), which is the amount of BF-AC consumed throughout the treatment process (g/L).

$$\text{CUR} = \frac{M}{Q t_b} = \frac{1}{\text{specific throughput}} \quad (7)$$

The length of the mass transfer zone (MTZ) is typically a function of the hydraulic loading rate applied to the column and the characteristics of the adsorbent. If the loading rate is too great, the height of the MTZ will be larger than the AC bed depth, which results in pollutants not being completely removed by the column. Equation 8 was used to determine a MTZ ( $H_{MTZ}$ ) height [31].

$$H_{MTZ} = Z \left[ \frac{(V_E - V_B)}{V_E - f(V_E - V_B)} \right] \quad (8)$$

The bed column parameters, as well as its unit and formula, are presented in Table 2.

Table 2: Details fixed-bed column parameters

Packed bed column parameters	Formula	Unit
Volume at breakthrough ( $V_b$ )	$V_b = \frac{t_b}{Q}$	mL
Volume at exhaustion point ( $V_x$ )	$V_x = \frac{t_x}{Q}$	mL
Breakthrough time ( $t_b$ )	$t_b = \frac{V_b}{Q}$	min
Exhaustion time ( $t_x$ )	$t_x = \frac{V_x}{Q}$	min
Time taken to exhaust the mass transfer zone ( $t_\delta$ )	$t_\delta = \frac{(V_x - V_b)}{Q}$	min
Height of Mass Transfer Zone ( $H_{MTZ}$ )	$H_{MTZ} = Z \left[ \frac{(V_E - V_B)}{V_E - f(V_E - V_B)} \right]$	cm
Carbon Usage Rate (CUR)	$CUR = \frac{M}{Q t_b} = \frac{1}{\text{specific throughput}}$	g/L
Specific throughput	$\text{Specific throughput} = \frac{Q t_b}{M}$	mL/g
Empty bed contact time (EBCT)	$EBCT = \frac{V_f}{Q} = \frac{L \cdot A_F}{v \cdot A_F} = \frac{L}{v}$	min

### 3. RESULTS AND DISCUSSION

#### 3.1 BF-AC Characterization

For observing the physical surface morphology of BF-AC, the SEM technique was used. Figure 2 displays SEM micrographs of BF-AC produced at 1000 and 2500 magnifications. SEM micrographs show that the AC surface is highly porous with many irregular-shaped uneven pores. Higher porosity results in more surface area, which facilitates greater adsorbate removal from its aqueous solution [1]. The details are also described in our previous studies [3,25].

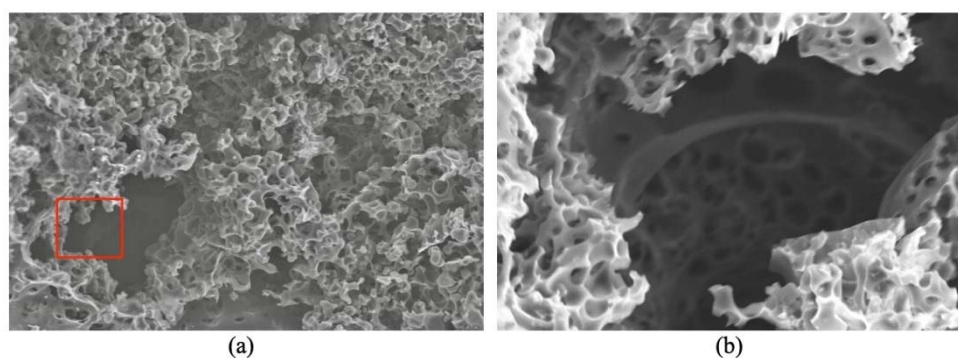


Fig. 2: SEM images of produced BF-AC magnification of (a) x1000, (b) x2500.

XRD analysis was performed in order to determine the crystalline composition of the prepared BF-AC. Figure 3 presents the XRD profile of BF-AC. The lack of a clearly defined peak for any aspect of the diffraction profile, as seen by the XRD spectrum, suggests that the BF-AC were not subjected to any mineral peaks. Similar findings and conclusions have been reached by several investigations [27,29].

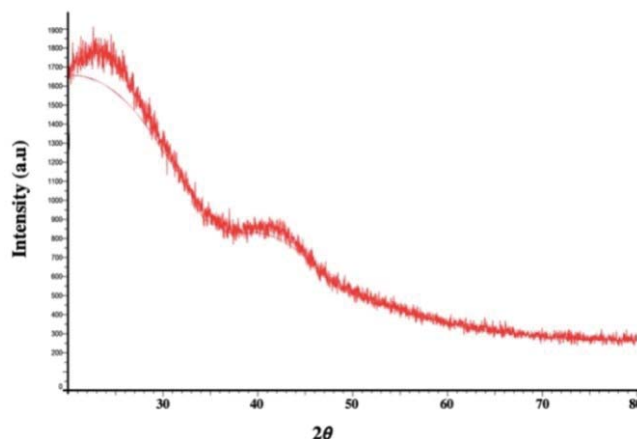


Fig. 3: X-Ray Diffraction pattern of BF-AC.

N<sub>2</sub> adsorption–desorption isotherms of produced BF-AC are displayed in Fig. 4. The adsorption isotherm is classified into Type I isotherm, which is microporous adsorbents (containing pores < 2 nm), according to IUPAC classification approach [32]. The findings confirmed the microporosity of BF-AC as indicated in Table 3 and are consistent with the pore size distribution curve.

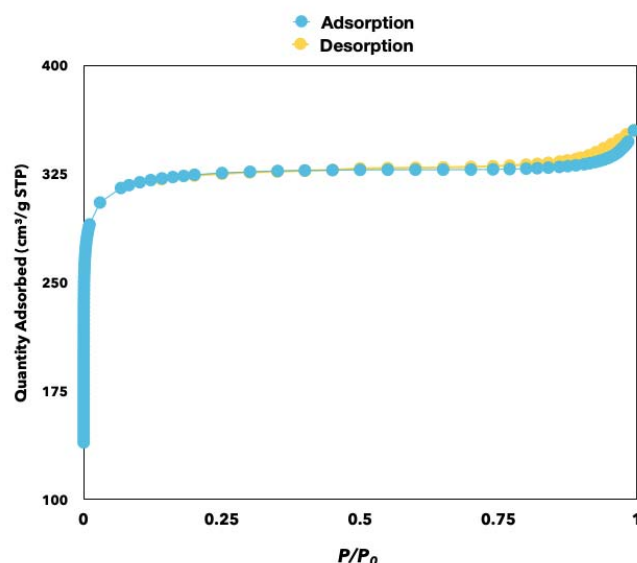


Fig. 4: N<sub>2</sub> adsorption–desorption isotherms of produced BF-AC.

Table 3 shows the pore volume, pore diameter, and BET surface area of BF-AC. The findings showed that BF-AC has a high surface area (1263 m<sup>2</sup>/g). With a particular micropore area of 1152 m<sup>2</sup>/g, a micropore volume of 0.453 cm<sup>3</sup>/g, an exterior surface area of 111.24 m<sup>2</sup>/g, and pore diameter of 1.74 nm, the BF-AC is clearly highly developed.

Table 3: The surface area and pore distribution of BF-AC.

Sample	BET specific surface area (m <sup>2</sup> /g)	Micropores area (m <sup>2</sup> /g)	External surface area (m <sup>2</sup> /g)	Average pore diameter (nm)	Total pore volume (cm <sup>3</sup> /g)	Volume of micropores (cm <sup>3</sup> /g)
BF-AC	1263.127	1152.886	111.24	1.739	0.549	0.4531

## 3.2 Fixed-Bed Adsorption Column Analysis

The experiments were carried out with varied bed heights (5, 10, 15 cm), varied flow rates (10, 15, 20 mL/min), and phenol concentration of 150 mg/L (evaluated by batch mode in our earlier study [3]). According to the experimental results, the corresponding breakthrough curves ( $C/C_0$ ) vs  $t$  were plotted for each observation.

### 3.2.1 Effect of Flowrate

The flowrate is a significant factor in the packed bed column adsorption process, which helps to predict the efficiency of the BF-AC. The breakthrough curves were investigated at various flowrates. The effects of flowrate on the phenol removal by BF-AC were investigated at different flowrates (10, 15 and 20 mL/min), whereas the phenol initial concentration and bed depth were kept constant at 150 mg/L and 5 cm, respectively. To achieve a bed height of 5 cm, 5.5 g BF-AC were poured into the column. The results obtained from the experiments were utilized for constructing the breakthrough curves ( $C/C_0$  vs time) for 5, 10, and 20 mL/min flowrates (Fig. 5).

From the breakthrough graphs, it is evident that as the flowrate increased, the breakthrough curves became steeper. The adsorbate residence time in the column decreased as the flowrate increased, which had an impact on how quickly the phenol aqueous solution left the column. This phenomenon could explain the pattern observed in the graph. Consequently, the BF-AC column effective adsorption capacity decreased, because the adsorbate solvents in the column did not have enough time to disseminate the solute into the pores of the adsorbent [33]. According to the results presented in Table 4, it can be noted that the exhaustion time ( $t_d$ ) and breakthrough time ( $t_b$ ) declined as the flowrate augmented [15,16,34]. The mass transfer zone length increased with the rise in flowrate, leading to quicker column saturation [16]. The best results at a low flowrate of 10 mL/min can be inferred. Other researchers reported similar findings [16,34].

By comparing the various flowrates, it becomes evident that the flowrate of 20 mL/min treated the highest volume, which was 6745 mL followed by the flowrate of 15 mL/min which was 5590 mL, followed by the flowrate of 10 mL/min with 4200 mL. So, the treated volume increased as the flow rate increased. During the column adsorption process, MTZ normally transfers from the influent end to the effluent end of the adsorbed bed. It means that the region of active adsorbent shifts to the effluent-end of the bed where the adsorbate has yet to be saturated, and this occurs after the adsorbent near the influent becomes saturated [35]. The low elimination of contaminants is done when the MTZ height is greater than the bed height [35,36]. From the results, the MTZ of the three different columns was higher than the bed height of 5 cm. It was also observed that MTZ decreased with increased flowrate. Similar remarks have been reported recently by Patel [37].

The rate of use of the adsorbent is often reported as a carbon use rate (CUR), which is an essential factor when column studies are scaled. Another significant parameter when the column activity is performed is the EBCT, which is the volume of the bed occupied by the adsorbent divided by the flowrate. According to the findings, the EBCT decreased as the flowrate rose. Similar observations were recently reported by Muthamilselvi et al. [14].

### 3.2.2 Effect of Bed Height

The effects of bed height on the phenol removal by BF-AC were also investigated in the range of 5, 10 and 15 cm, while the inlet of the phenol concentration and flowrate were kept constant at 150 mg/L and 20 mL/min, respectively. Figure 6 displays the graphs of phenol concentration vs time at various bed heights. The length of the bed (in which the phenol

aqueous solution flows) increases as the bed height increases. Comparing the various bed heights, the column bed height of 15 cm recorded 12296 mL of the treated volume, which was the highest volume treated. This obviously presented a higher capacity with 15 cm bed height. This was because, with a rising bed height, further binding sites were available for the adsorbate to diffuse through the pores of the adsorbent and as a consequence, the area of adsorption rose [16,30]. It was clearly observed that the breakthrough time ( $t_b$ ) and exhaustion time ( $t_x$ ) as the bed height augmented (Table 5). Other researchers have reported similar results [16,38].

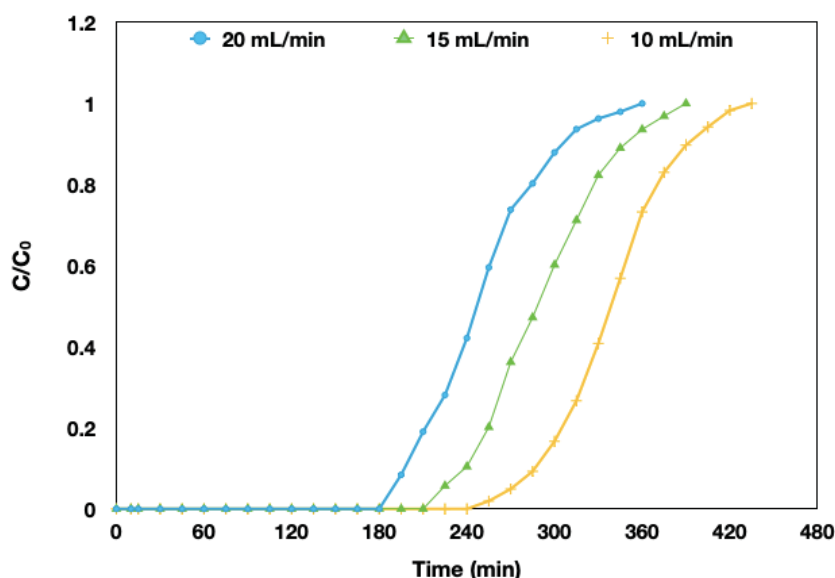


Fig. 5: Phenol adsorption breakthrough curves at various flowrates (10,15 and 20 mL/min), 5 cm bed height, and 150 mg/L initial phenol concentration.

Also, the bed height of 5 cm provided a low effluent due to its MTZ, which was greater than the bed height. Moreover, MTZ declined with the rise in bed height. Comparable observations were reported by Kapur & Mondal [39]. From Table 5, the BF-AC with a bed height of 15 cm was chosen owing to its greater phenol removal and the amount treated.

Table 4: Column adsorption parameters for phenol at different flowrates

Packed Bed Column Parameters	Flowrate (mL/min)		
	10	15	20
Initial phenol concentration (mg/L)	150	150	150
Bed depth (cm)	5	5	5
Volume treated (mL)	4200.31	5590.24	6745.08
Volume at breakthrough (mL)	2715.94	3328.33	3524.74
Volume at exhaustion point (mL)	4122.19	5471.19	6575.59
Breakthrough time, $t_b$ (min)	271.59	221.89	176.23
Exhaustion time, $t_x$ (min)	412.22	364.75	328.78
Time taken to exhaust the mass transfer zone, $t_\delta$ (min)	140.62	142.86	152.54
Height of Mass Transfer Zone, $H_{MTZ}$ (cm)	10.23	11.75	13.92
Carbon Usage Rate, CUR (g/L)	2.025	1.65	1.56
Specific throughput (mL/g)	493.80	605.15	640.86
Empty bed contact time, EBCT (min)	19.80	13.20	9.90

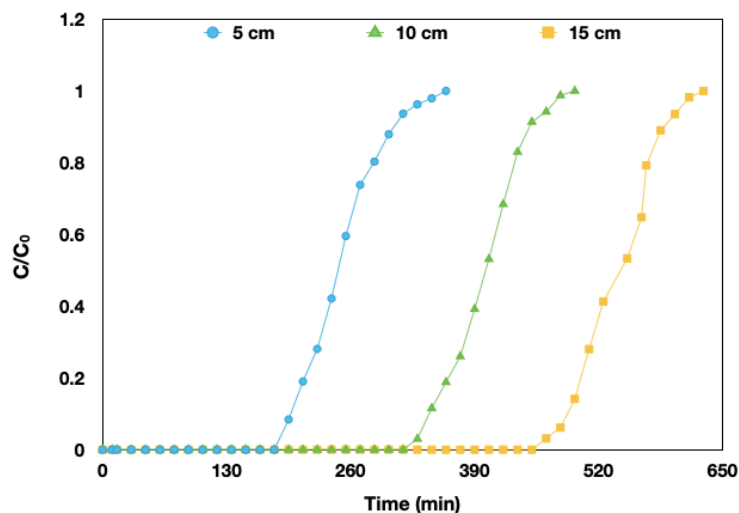


Fig. 6: Phenol adsorption breakthrough curves at various bed heights (5, 10 and 15 cm), 20 mL/min flowrate, and 150 mg/L initial phenol concentration.

Table 5: Bed column parameters for phenol at different bed heights

Packed Bed Column Parameters	Bed Height (cm)		
	5	10	15
Initial phenol concentration (mg/L)	150	150	150
Flowrate (mL/min)	20	20	20
Volume Treated (mL)	6745.08	9606.06	12296.12
Volume at breakthrough (mL)	3524.74	6727.27	9460.3
Volume at exhaustion point (mL)	6575.59	9454.55	12146.87
Breakthrough time, $t_b$ (min)	176.24	336.36	473.01
Exhaustion time, $t_x$ (min)	328.78	472.73	607.34
Time taken to exhaust the mass transfer zone, $t_\delta$ (min)	152.54	136.36	134.33
Height of Mass Transfer Zone, $H_{MTZ}$ (cm)	13.92	10.99	9.33
Carbon Usage Rate, CUR (g/L)	1.56	1.63	1.74
Specific throughput (mL/g)	640.86	611.57	573.35
Empty bed contact time, EBCT (min)	9.90	9.90	9.90

## 4. CONCLUSION

Activated carbon from baobab fruit shell was used to remove phenol from the aqueous solutions. The characterization studies confirm the adsorption behavior of prepared BF-AC with the BET surface area of 1263.127 m<sup>2</sup>/g. BF-AC has a large BET surface area and more pore volume, making it a practical and efficient way to remove phenol in a packed bed system. This study revealed that bed height and flowrate have a significant impact on breakthrough times and removal capacities. The removal of phenol was found to be favored by an increase in flowrate and bed height. The breakthrough time increased with an increase in bed height but decreased with an increase in flow rate. BF-AC with a bed height of 15 cm provided better elimination of phenol with CUR of 1.74 g/L and EBCT of 9.9 minutes. The AC prepared from the baobab fruit shell was promising for removing the phenol from the aqueous solution in a fixed bed column.

## REFERENCES

- [1] Nedjai R, Kabbashi, NA Alkhatib, MFR Alam, MZ. (2021) Removal of Phenol from Aqueous Solution by Adsorption onto Baobab Fruit Shell Activated Carbon : Equilibrium and Kinetics Studies. *J. Environ. Treat. Tech.*, 9: 686-697.
- [2] Rashed MN. (2013) Adsorption Technique for the Removal of Organic Pollutants from Water and Wastewater. *Org. Pollut. Monit. Risk Treat.*, 7: 167-194. <https://doi.org/10.5772/54048>.
- [3] Nedjai R, Kabbashi NA, Alam MZ, Al-Khatib MFR. (2021) Statistical Optimization of Adsorption Processes for the Removal of Phenol by Activated Carbon Derived from Baobab Fruit Shell. *IOP Conf. Ser. Mater. Sci. Eng.*, 1192: 012003. <https://doi.org/10.1088/1757-899x/1192/1/012003>.
- [4] Ochando-Pulido JM, González-Hernández R, Martínez-Ferez A. (2018) On the effect of the operating parameters for two-phase olive-oil washing wastewater combined phenolic compounds recovery and reclamation by novel ion exchange resins. *Sep. Purif. Technol.*, 195: 50-59. <https://doi.org/10.1016/j.seppur.2017.11.075>.
- [5] Mohamad Said KA, Ismail AF, Abdul Karim Z, Abdullah MS, Hafeez A. (2021) A review of technologies for the phenolic compounds recovery and phenol removal from wastewater. *Process Saf. Environ. Prot.*, 151: 257-289. <https://doi.org/10.1016/j.psep.2021.05.015>.
- [6] Qiu B, Shao Q, Shi J, Yang C, Chu H. (2022) Application of biochar for the adsorption of organic pollutants from wastewater: Modification strategies, mechanisms and challenges. *Sep. Purif. Technol.*, 300: 2023. <https://doi.org/10.1016/j.seppur.2022.121925>.
- [7] Peings V, Frayret J, Pigot T. (2015) Mechanism for the oxidation of phenol by sulfatoferrate(VI): Comparison with various oxidants. *J. Environ. Manage.*, 157: 287-296. <https://doi.org/10.1016/j.jenvman.2015.04.004>.
- [8] Liu J, Xie J, Ren Z, Zhang W. (2013) Solvent Extraction of Phenol with Cumene from Wastewater. *Desalin. Water Treat.*, 51: 3826-3831. <https://doi.org/10.1080/19443994.2013.796993>.
- [9] Ahmad, NSB, Mamun, AA, Nedjai, R. (2023). Assessment of expired coagulant for water treatment. In *AIP Conference Proceedings*. 2713(1). AIP Publishing. <https://doi.org/10.1063/5.0129719>.
- [10] Sharma NK, Philip L. (2014) Effect of cyanide on phenolics and aromatic hydrocarbons biodegradation under anaerobic and anoxic conditions. *Chem. Eng. J.*, 256: 255-267. <https://doi.org/10.1016/j.cej.2014.06.070>.
- [11] Bedoui A, Saad MEK, Elaloui E, Rabaoui N, Allagui MS, Moussaoui Y (2013). Anodic oxidation of o-nitrophenol on BDD electrode: Variable effects and mechanisms of degradation. *J. Hazard. Mater.*, 250: 447-453. <https://doi.org/10.1016/j.jhazmat.2013.02.027>
- [12] Jawad AH, Sabar S, Ishak MAM, Wilson LD, Norrahma ASS, Talari MK, Farhan AM. (2017) Microwave-Assisted Preparation of Mesoporous-Activated Carbon from Coconut (*Cocos nucifera*) Leaf by H<sub>3</sub>PO<sub>4</sub> Activation for Methylene Blue Adsorption. *Chem. Eng. Commun.*, 204: 1143-1156. <https://doi.org/10.1080/00986445.2017.1347565>.
- [13] Mofidian R, Barati A, Jahanshahi A, Shahavi MH. (2020) Fabrication of novel agarose–nickel bilayer composite for purification of protein nanoparticles in expanded bed adsorption column. *Chem. Eng. Res. Des.*, 159: 291-299. <https://doi.org/10.1016/j.cherd.2020.03.024>.
- [14] Muthamilselvi P, Karthikeyan R, Kapoor A, Prabhakar S. (2018) Continuous fixed-bed studies for adsorptive remediation of phenol by garlic peel powder. *Int. J. Ind. Chem.*, 9: 379-390. <https://doi.org/10.1007/s40090-018-0166-z>.
- [15] Vijayaraghavan K, Jegan J, Palanivelu K, Velan M. (2004) Removal of nickel(II) ions from aqueous solution using crab shell particles in a packed bed up-flow column. *J. Hazard. Mater.*, 113: 223-230. <https://doi.org/10.1016/j.jhazmat.2004.06.014>.
- [16] Girish CR, Murty VR. (2015) Adsorption of Phenol from Aqueous Solution Using Lantana camara, Forest Waste: Packed Bed Studies and Prediction of Breakthrough Curves. *Environ. Process.*, 2: 773-796. <https://doi.org/10.1007/s40710-015-0117-z>.

- [17] Allahkarami E, Dehghan Monfared D, Silva LFO, Dotto GL. (2023) Application of Pb–Fe spinel-activated carbon for phenol removal from aqueous solutions: fixed-bed adsorption studies. *Environ. Sci. Pollut. Res.*, 30: 23870-23886. <https://doi.org/10.1007/s11356-022-23891-z>.
- [18] Dalhat MA, Mu’Azu ND, Essa MH. (2021) Generalized decay and artificial neural network models for fixed-Bed phenolic compounds adsorption onto activated date palm biochar. *J. Environ. Chem. Eng.*, 9(1): 2023. <https://doi.org/10.1016/j.jece.2020.104711>.
- [19] Kumar A, Rout DR, Jena HM. (2022) Phosphoric acid modified activated carbon prepared from Fox nutshell for adsorption of phenol: batch and continuous studies. *Int. J. Environ. Anal. Chem.* 3099067. <https://doi.org/10.1080/03067319.2022.2158739>.
- [20] Iheanacho OC, Nwabanne JT, Obi CC, Onu CE. (2021) Packed bed column adsorption of phenol onto corn cob activated carbon: linear and nonlinear kinetics modeling. *South African J. Chem. Eng.*, 36: 80-93. <https://doi.org/10.1016/j.sajce.2021.02.003>.
- [21] Mandal A, Majumder A, Banik I, Ghosh K, Bar N, Das SK. (2021) Fixed-bed column study for removal of phenol by neem leaves – Experiment, MLR and ANN analysis. *Sustain. Chem. Pharm.*, 23: 100514. <https://doi.org/10.1016/j.scp.2021.100514>.
- [22] Lua AC, Jia Q. (2009) Adsorption of phenol by oil-palm-shell activated carbons in a fixed bed. *Chem. Eng. J.*, 150: 455-461. <https://doi.org/10.1016/j.cej.2009.01.034>.
- [23] Nedjai R, Kabbashi NA, Alam MZ, Alkhatib MFR. (2022) Optimisation of Activated Carbon Production from Baobab Fruit Shells by Chemical Activation with KOH for the Removal of Phenol. *Water Conserv. Manag.*, 6: 45-50. <https://doi.org/10.26480/wcm.01.2022.45.50>.
- [24] Nedjai R, Alkhatib MFR, Alam MZ, Kabbashi NA. (2021) Adsorption of Methylene Blue onto Activated Carbon Developed from Baobab Fruit Shell By Chemical Activation: Kinetic Equilibrium Studies. *IIUM Eng. J.*, 22: 31-49. <https://doi.org/10.31436/iiumej.v22i2.1682>.
- [25] Nedjai R, Kabbashi NA, Alam MZ, Al-Khatib MFR. (2021) Production and Characterization of Activated Carbon from Baobab Fruit Shells by Chemical Activation Using ZnCl<sub>2</sub>, H<sub>3</sub>PO<sub>4</sub> and KOH. *J. Phys. Conf. Ser.* 2129. <https://doi.org/10.1088/1742-6596/2129/1/012009>.
- [26] Nedjai R. (2021) Production and Characterization of Activated Carbon from Baobab Fruit Shell Via Chemical Activation for the Removal of Phenol, PhD thesis, Kulliyah of Engineering, International Islamic University Malaysia.
- [27] Vunain E, Kenneth D, Biswick T. (2017) Synthesis and characterization of low-cost activated carbon prepared from Malawian baobab fruit shells by H<sub>3</sub>PO<sub>4</sub> activation for removal of Cu(II) ions: equilibrium and kinetics studies. *Appl. Water Sci.*, 7: 4301-4319. <https://doi.org/10.1007/s13201-017-0573-x>.
- [28] Chigondo F, Nyamunda BC, Sithole SC, Gwatidzo L. (2013) Removal of lead (II) and copper (II) ions from aqueous solution by baobab (*Adononsia digitata*) fruit shells biomass. *IOSR Journal of Applied Chemistry*, 5(1): 43-50. DOI: 10.9790/5736-0514350
- [29] Vunain E, Biswick T. (2018) Adsorptive removal of methylene blue from aqueous solution on activated carbon prepared from Malawian baobab fruit shell wastes : Equilibrium , kinetics and thermodynamic studies and thermodynamic studies. *Sep. Sci. Technol.*, 54: 27-41. <https://doi.org/10.1080/01496395.2018.1504794>.
- [30] Lezehari M, Baudu M, Bouras O, Basly, JP. (2012) Fixed-bed column studies of pentachlorophenol removal by use of alginate-encapsulated pillared clay microbeads. *J. Colloid Interface Sci.*, 379: 101-106. <https://doi.org/10.1016/j.jcis.2012.04.054>.
- [31] Metcalf W. (2003) *Metcalf and Eddy wastewater engineering: treatment and reuse*. Wastewater Engineering: Treatment and Reuse McGraw Hill. New York, NY, 384.
- [32] Sotomayor FJ, Cychosz KA, Thommes M. (2018) Characterization of Micro/Mesoporous Materials by Physisorption: Concepts and Case Studies. *Acc. Mater. Surf. Res.*, 3: 34-50.
- [33] Kumar A, Jena HM. (2016) Removal of methylene blue and phenol onto prepared activated carbon from Fox nutshell by chemical activation in batch and fixed-bed column, *J. Clean. Prod.*, 137: 1246-1259. <https://doi.org/10.1016/j.jclepro.2016.07.177>.
- [34] Ahmad AA, Hameed BH. (2010) Fixed-bed adsorption of reactive azo dye onto granular activated carbon prepared from waste. *J. Hazard. Mater.*, 175: 298-303. <https://doi.org/10.1016/j.jhazmat.2009.10.003>

- [35] Bansal RC, Goyal M. (2005) Activated Carbon Adsorption. CRC press
- [36] Idris MA. (2010) Use of hybrid membrane system for the production of process water from biologically treated palm oil mill effluent (POME), PhD thesis, Kulliyah of Engineering, International Islamic University Malaysia.
- [37] Patel H. (2020) Batch and continuous fixed bed adsorption of heavy metals removal using activated charcoal from neem (*Azadirachta indica*) leaf powder. Sci. Rep., 10: 1-12. <https://doi.org/10.1038/s41598-020-72583-6>.
- [38] Chowdhury ZZ, Zain SM, Rashid AK, Rafique RF, Khalid K. (2013) Breakthrough curve analysis for column dynamics sorption of Mn(II) ions from wastewater by using *Mangostana garcinia* peel-based granular-activated carbon. J. Chem. 2013: 959761. <https://doi.org/10.1155/2013/959761>.
- [39] Kapur M, Mondal MK. (2016) Design and model parameters estimation for fixed-bed column adsorption of Cu(II) and Ni(II) ions using magnetized saw dust. Desalin. Water Treat., 57: 12192-12203. <https://doi.org/10.1080/19443994.2015.1049961>.

# INFLUENCE OF CURING CONDITIONS ON THE EARLY STRENGTH OF LOW TEMPERATURE BELITE CEMENTS

SAMBO GWANDU HALIRU<sup>1,2\*</sup> AND RODIAH ZAWAWI<sup>1</sup>

<sup>1</sup>Faculty of Built Environment, Universiti Malaya, Kuala Lumpur, Malaysia

<sup>2</sup>Department of Civil Engineering, Kebbi State University of Science and Technology, Aliero, Nigeria

\*Corresponding author: [sambo.halirugwandu@ksusta.edu.ng](mailto:sambo.halirugwandu@ksusta.edu.ng)

(Received: 11 April 2023; Accepted: 2 September 2023; Published on-line: 1 January 2024)

**ABSTRACT:** Low temperature belite cements are produced using techniques that stabilize the more reactive high temperature polymorphs of dicalcium silicate ( $C_2S$ ) to improve early strength, but the effect of curing conditions on them is not well studied. The focus of this work is to assess the improvement of their early strength in different curing conditions. During the synthesis of the cements at 1000 °C, the more reactive polymorphs,  $\alpha'$ - $C_2S$  and  $\beta$ - $C_2S$ , were stabilized using gypsum and hydrothermal treatment with potassium hydroxide. The phase composition of the synthesized cements was analysed using X-ray powder diffraction. The morphology and elemental composition of the  $C_2S$  crystals and hydrated pastes were determined using a scanning electron microscope equipped with an energy-dispersive X-ray system. Mortar samples were cured in different conditions that include hot air and hot water curing at 60 °C and 90 °C. The 28-day strength development, capillary water porosity, water absorption, and ultrasonic pulse velocity were tested. The formation of hydration products and strength was dependent on the type of  $C_2S$  polymorph. Curing at elevated temperatures improved the transport properties of mortars. Samples cured at 90 °C in hot air obtained the highest early strength. The presence of  $\alpha'$ - $C_2S$  and elevated curing temperatures significantly improve the early strength of the mortar samples.

**ABSTRAK:** Simen belite suhu rendah dihasilkan melalui teknik menstabilkan reaktif polimorf dikalsium silikat ( $C_2S$ ) bersuhu tinggi bagi meningkatkan kekuatan awal, tetapi kesan keadaan pengawetan ke atasnya tidak dikaji dengan baik. Fokus kerja ini adalah bagi menilai peningkatan kekuatan awal pada keadaan pengawetan berbeza. Sintesis simen pada suhu 1000 °C, iaitu pada polimorf lebih reaktif,  $\alpha'$ - $C_2S$  dan  $\beta$ - $C_2S$ , telah distabilkan menggunakan rawatan gipsum dan hidroturma dengan kalium hidroksida. Fasa komposisi simen tersintesis dianalisa menggunakan pembelauan serbuk sinar-X. Komposisi morfologi dan unsur kristal  $C_2S$  dan pes terhidrat ditentukan menggunakan pengimbas mikroskop elektron yang dilengkapi sistem sinar-X penyebar tenaga. Sampel mortar telah diawetkan dalam keadaan berbeza termasuk pengawetan udara panas dan air panas pada suhu 60 °C dan 90 °C. Perkembangan kekuatan keliangan kapilari air, penyerapan air, dan halaju nadi ultrasonik telah diuji pada hari ke 28. Pembentukan produk penghidratan dan kekuatan adalah bergantung kepada jenis polimorf  $C_2S$ . Pengawetan pada suhu tinggi meningkatkan sifat pengangkutan mortar. Sampel yang diawet pada 90 °C dalam udara panas memperoleh kekuatan awal tertinggi. Kehadiran  $\alpha'$ - $C_2S$  dan suhu pengawetan tinggi dengan ketara meningkatkan kekuatan awal sampel mortar.

**KEYWORDS:** *belite cements; dicalcium silicate; thermal curing; transport properties; porosity*

## 1. INTRODUCTION

Portland cement is the predominantly used binder in construction with an annual production of 4.1 gigatons in 2020, partly due to its utilization in concrete, the most used synthetic material in the world [1]. It is estimated that the global concrete stock is around 315 gigatons [2]. The vast usage of cement can be attributed to its high early strength and the availability of its primary raw materials (limestone and clay) in economic quantities across the continents. However, despite efforts to improve sustainability, the production of cement accounts for about 12 percent of total industrial energy consumption. It also consumes about 1.7 tonnes of raw materials and emits around 0.84 tonnes of carbon dioxide for every tonne of cement produced [3-5]. These are among the factors necessitating research in alternative binders such as belite cements.

Belite cements have similar raw materials and production processes as Portland cements but with lower environmental consequences. They both have similar compounds with the major difference being the percentage of the calcium silicates i.e., tricalcium silicate ( $C_3S$ ) and dicalcium silicate ( $C_2S$ ). Clinkers of Portland cements contain an average of 60 percent  $C_3S$  and 10 percent  $C_2S$  while those of belite cements are composed of 40–60 percent  $C_2S$  and 10–30 percent  $C_3S$  [2]. Producing belite clinkers emits 10–12 percent less carbon dioxide due to lesser demand for limestone. The average burning temperature of 1300 °C is also used which is almost 200 °C less than the clinkering temperature for Portland cements [6]. Furthermore, belite cements can be produced in a Portland cement factory, thus, making their large-scale production feasible [7]. They can also be covered by existing codes of practice such as EN 197-1 if they satisfy the requirements that include  $C_3S + C_2S > 66$  percent of total clinker [2].

Recent studies assessed the characteristics of  $C_3S$ -free belite cements that are produced at temperatures between 800 and 1200 °C [8-13]. Burning at low temperatures produces  $C_2S$  with smaller grain size that can accelerate hydration, and a porous crystalline structure capable of incorporating by-products [14]. The by-products are introduced by adding compounds such as gypsum and sodium fluoride as mineralizers or through hydrothermal treatment with alkaline solutions e.g., sodium hydroxide and potassium hydroxide [9,12,15]. The introduction of ions into the crystalline structure of the  $C_2S$  from these by-products and the fast cooling assists in stabilizing the more reactive high-temperature polymorphs of  $C_2S$ . There are five ( $\alpha$ ,  $\alpha'_h$ ,  $\alpha'_l$ ,  $\beta$ ,  $\gamma$ ) polymorphs of  $C_2S$  that are stable at different temperatures with distinct crystalline structures [16]. These polymorphs have different reactivity, with the  $\alpha'$ - $C_2S$  being the most hydraulic. The  $\alpha$ - $C_2S$  and  $\beta$ - $C_2S$  have moderate reactivity while the  $\gamma$ - $C_2S$  is the least reactive and the most stable polymorph [10].

During hydration, both  $C_3S$  and  $C_2S$  produce the same compounds, calcium silicate hydrates (C–S–H) gel and calcium hydroxide. However,  $C_3S$  hydrates faster than  $C_2S$ , and it is responsible for the high early strength and heat of hydration in Portland cements. Furthermore,  $C_3S$  can achieve about 78–80 percent hydration at 28 days under normal curing conditions while  $C_2S$  can achieve only 20–50 percent. But at full hydration  $C_3S$  produces 72.5 and 27.5 percent volume of C–S–H gel and calcium hydroxide respectively while  $C_2S$  produces 94.4 percent C–S–H gel and only 5.6 percent calcium hydroxide. This makes  $C_2S$  more durable and resistant to chemical attacks by producing more C–S–H gel that contributes to the strength and less calcium hydroxide which is the more reactive hydration product [2]. The low hydration heat in belite cements limits the possibilities of thermal cracking and increases their suitability in mass concrete production.

The major drawback in the wide acceptance of belite cements is their low early strength due to their slowed hydration. Accelerating the hydration process and hardening is necessary

for obtaining cement composites with sufficient early strength. The techniques used include elevating the hydration temperature in different curing processes such as steam curing, hot water curing, hot air curing, and autoclaving [17]. There is no agreement regarding which method is the most effective and the optimum curing temperature. Similarly, opinions on the delay time (the period between casting and application of heat) differ among the researchers. From the reviewed literature, three delay times were suggested: immediately after casting; after the initial set; and after a 24-hour delay [18].

Thermal acceleration of hydration in Portland cements is extensively studied but there is not enough data on belite cements. It was discovered that elevated curing temperatures can have a detrimental effect on Portland cements hydration that can cause a loss of long-term strength, a phenomenon called the crossover effect [19]. This is widely agreed to be caused by the non-uniform distribution of hydration products that creates cracks and a porous microstructure. This might vary between belite cements and Portland cements, as a study by Thomas et al. [20] reported a 25 percent increase and 21 percent decrease in compressive strength for belite cements and Portland cements, respectively, at 28 days when curing temperature was raised from 20 °C to 70 °C.

Although there are recent studies that were conducted to assess the effects of curing conditions on belite cements, they were conducted on cements produced at high temperatures that contained C<sub>3</sub>S [17,19]. The objective of this study is to produce C<sub>3</sub>S-free belite cements at low temperatures using waste materials and assess the effect of six curing conditions on early strength development. They include curing in saturated lime water, curing at room temperature (RT) and 85±5 percent relative humidity (RH), and hot water and hot air curing at 60 °C and 90 °C.

## 2. MATERIALS AND METHODS

### 2.1 Materials

The raw materials used in this study were cockle shells, rice husk ash (RHA), and calcined clay. They were all oven dried at 105 °C to constant mass, ground in a ball mill grinder, and screened through a sieve with 150 µm aperture [9,10,12,13,21]. The calcined clay was obtained by burning at 800 °C in an electric furnace with a 5 °C heating rate for 120 minutes. Figures 1 and 2 show the raw materials used in the study and particle size distribution of the fine aggregate used in mortar preparation, respectively. The chemical composition of the materials that was determined using X-ray fluorescence (XRF) is shown in Table 1.

### 2.2 Synthesis of Belite Cement

The raw meals were prepared to have a lime/silica (CaO/ SiO<sub>2</sub>) ratio of 2. The first group contained 55.18 percent cockle shell and 44.82 percent calcined clay with a lime saturation factor (LSF) of 0.61 while the second group was composed of 65.20 percent cockle shell and 34.80 percent RHA, and an LSF of 0.71. The chemical composition of the raw meals is shown in Table 2. Three batches of raw meals were prepared from each group with different treatment methods as shown in Table 3. A total of six batches of binary raw meals were prepared for this study.

The CH and RH precursors from the hydrothermal treatment were prepared from a dry mix of raw meals. The ground raw materials were added to a 0.6 M potassium hydroxide (KOH) solution at a liquid-to-solid ratio of 5:1. The mixture was stirred and heated at 100 °C using a magnetic stirrer at atmospheric pressure for four hours. The solution was then filtered through a Whatman filter paper to remove excess liquid before drying in an oven at 105 ± 5 °C

for three hours. The precursors were crushed and sieved to a particle size of less than 150  $\mu\text{m}$  before burning.

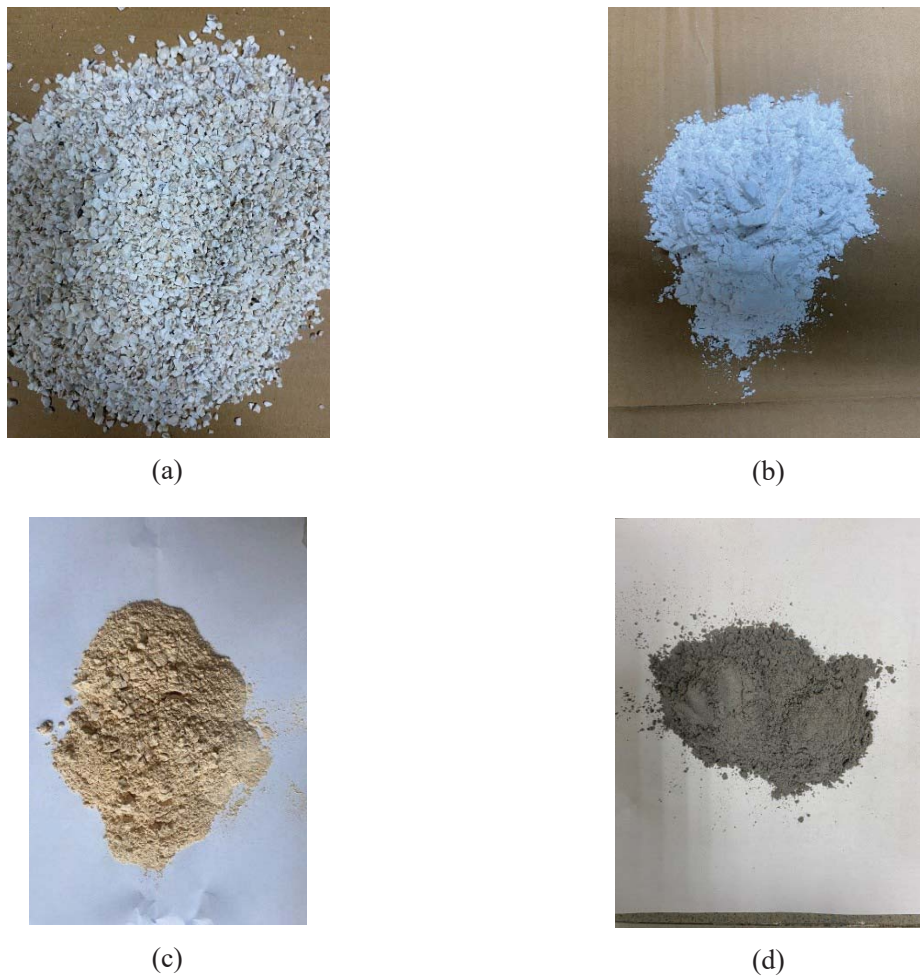


Fig. 1: Samples of (a) crushed cockle shell (b) ground cockle shell (c) calcined clay (d) rice husk ash.

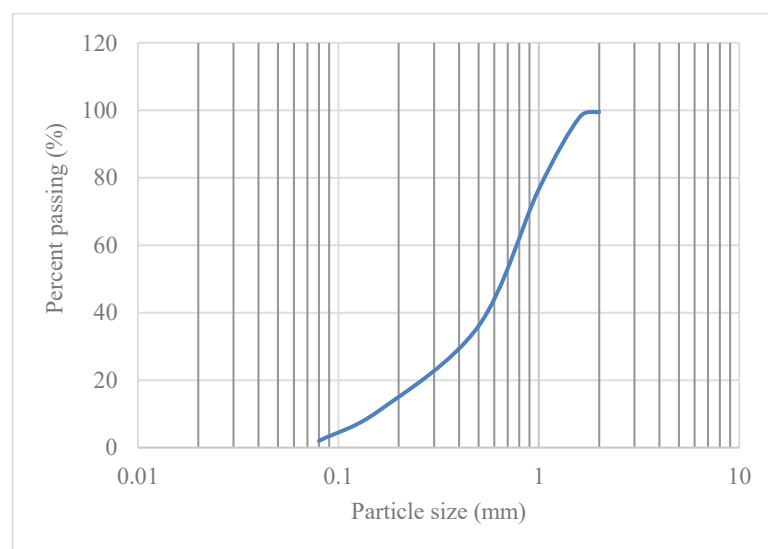


Fig. 2: Particle size distribution of fine aggregate.

Table 1: Chemical composition of raw materials (percent)

Oxide	Cockle shell	Clay	RHA
SiO <sub>2</sub>	-	60.07	92.40
Fe <sub>2</sub> O <sub>3</sub>	0.34	8.68	0.44
Al <sub>2</sub> O <sub>3</sub>	-	20.69	-
CaO	97.59	0.21	1.11
K <sub>2</sub> O	0.26	3.34	5.12
MnO	-	-	0.12
TiO <sub>2</sub>	-	1.02	-
BaO	-	4.35	-
ZnO	-	-	0.08
SrO	0.54	-	-
LOI	1.27	1.64	0.73

The raw meals were calcined in alumina-based crucibles in a laboratory furnace at 1000 °C for three hours followed by rapid air cooling down to room temperature. The products were ground in a ball mill grinder and sieved to a particle size of less than 53 µm.

Table 2: Chemical composition of raw meals (percent)

Oxide	Clay based	RHA based
SiO <sub>2</sub>	26.92	32.16
Fe <sub>2</sub> O <sub>3</sub>	4.08	0.37
Al <sub>2</sub> O <sub>3</sub>	9.27	-
CaO	53.94	64.02
K <sub>2</sub> O	1.64	1.95
MnO	-	0.04
TiO <sub>2</sub>	0.46	-
BaO	1.95	-
ZnO	-	0.03
SrO	0.30	0.35
LOI	1.44	1.10

Table 3: Binders and their treatment method

Binder ID	Raw materials	Treatment
CN	Cockle shells and clay	No treatment (control)
CG	Cockle shells and clay	2% dihydrate gypsum (CaSO <sub>4</sub> ·2H <sub>2</sub> O)
CH	Cockle shells and clay	Hydrothermal treatment in 0.6 M KOH
RN	Cockle shells and RHA	No treatment (control)
RG	Cockle shells and RHA	2% dihydrate gypsum (CaSO <sub>4</sub> ·2H <sub>2</sub> O)
RH	Cockle shells and RHA	Hydrothermal treatment in 0.6 M KOH

### 2.3 Testing Methods

The X-ray diffraction (XRD) patterns of all the synthesized products were obtained using an Empyrean PANalytical XRD diffractometer (Cu K $\alpha$  1.54060Å, 5–70° 2 $\theta$  range, 0.0260

step). The microstructure, morphology, and elemental analysis of the belite crystals and pastes were examined using a Quanta FEG 650 scanning electron microscope (SEM) equipped with an energy-dispersive X-ray (EDX) system. The pastes were prepared with water-to-binder ratio of 0.4, and the samples were coated using gold sputtering. The mortars were prepared according to EN 196-1 [22] using sand-to-cement ratio of 3 and water-binder ratios ranging from 0.66–0.75. They were cast in 50 mm cube moulds and demoulded after 24 hours. The mortars were cured in water and tested at 28 days for compressive strength. Compressive strength test was conducted using a 2000 kN compression machine and a loading rate of 0.4 kN/s. The pulse velocities through the mortars were measured using a direct transmission method between the transmitter and receiver transducers. The test was conducted on the samples before the compressive strength test.

The samples containing calcined clay (CN, CG, and CH) were selected and further tested for their early compressive strength and transport properties in different curing conditions, including elevated temperature curing. The elevated temperature curing was for a period of 48 hours after demoulding and then subsequent curing in saturated conditions until testing. The curing ID was assigned based on the name of the binder used, curing temperature, and curing method. The curing age was added as a suffix, with 7 and 28 signifying testing at 7 and 28 days, respectively. Table 4 shows the curing IDs and conditions for the samples prepared using the CN binder, and Fig. 3 shows the curing conditions of the samples.

Table 4: Curing conditions of samples

Curing ID	Curing condition
CNRLW7, CNRLW28	Saturated lime water at RT
CNRST7, CNRST28	RT and 85±5% RH
CN60W7, CN60W28	60 °C in hot water
CN60A7, CN60A28	60 °C in hot air
CN90W7, CN90W28	90 °C in hot water
CN90A7, CN90A28	90 °C in hot air

The capillary water porosity was determined using the water displacement method. After curing, the mass of the saturated samples was measured both in air ( $m_{sat}$ ) and while fully submerged in water ( $m_{sub}$ ). The samples were oven dried at 105 °C until constant mass and the mass was measured again ( $m_{dry}$ ). The capillary water porosity was measured using Eq. (1). The water absorption coefficient was obtained using the partial immersion method in accordance with EN ISO 15148 [23]. The three sides of the dried samples from the capillary water porosity were coated with hot paraffin wax and placed on supports with the water at a 5mm level from the bottom of the sample. The increase in mass of the samples was measured at different time intervals until the difference between two successive measurements was less than 1%. The increase in mass per face area (in  $\text{kg}/\text{m}^2$ ) was plotted against the square root of the weighing time (in seconds), and the water absorption coefficient was calculated from the graph.

$$\text{capillary water porosity (\%)} = \frac{m_{sat} - m_{dry}}{m_{sat} - m_{sub}} \times 100 \quad (1)$$



Fig. 3: Curing conditions in (a) saturated conditions, (b) saturated lime water, (c) hot air and (d) hot water.

### 3. RESULTS AND DISCUSSION

#### 3.1 XRD Analysis

All the obtained belite cements contained different polymorphs of  $C_2S$  due to the influence of their treatment method. The XRD patterns of the belite cements in Fig. 4 and Fig. 5 show that  $\beta$ - $C_2S$  is the most common hydraulic phase in all the binders as was obtained by several previous researchers [8-12]. The diffractograms show that  $\alpha'$ - $C_2S$  peaks are only present in the belite cements that were produced from the precursors that were hydrothermally treated with KOH i.e., in Fig. 4c and Fig. 5c for CH and RH, respectively. The stabilization of  $\alpha'$ - $C_2S$  can be attributed to the presence of potassium ions introduced from the treatment.

Belite cements from raw meals without any treatment and those containing 2 percent gypsum only had peaks of  $\beta$ - $C_2S$ . The XRD patterns of CG and RG, in Fig. 4b and Fig. 5b, respectively, indicate that they contain more peaks of  $\beta$ - $C_2S$  than CN and RN (Fig. 4a and Fig. 5a respectively). This is due to the presence of  $SO_3$  ions from the addition of gypsum that favours the stabilization of  $\beta$ - $C_2S$ . It was reported by Zhao et al. [15] that at a high percentage of gypsum (up to 4 percent), the  $SO_3$  ions stabilize the higher temperature polymorphs such as

$\alpha'$ -C<sub>2</sub>S. However, Mazouzi et al. [9] suggest the presence of SO<sub>3</sub> ions in high quantities favours only  $\beta$ -C<sub>2</sub>S and can sometimes prevent the stabilization of other polymorphs.

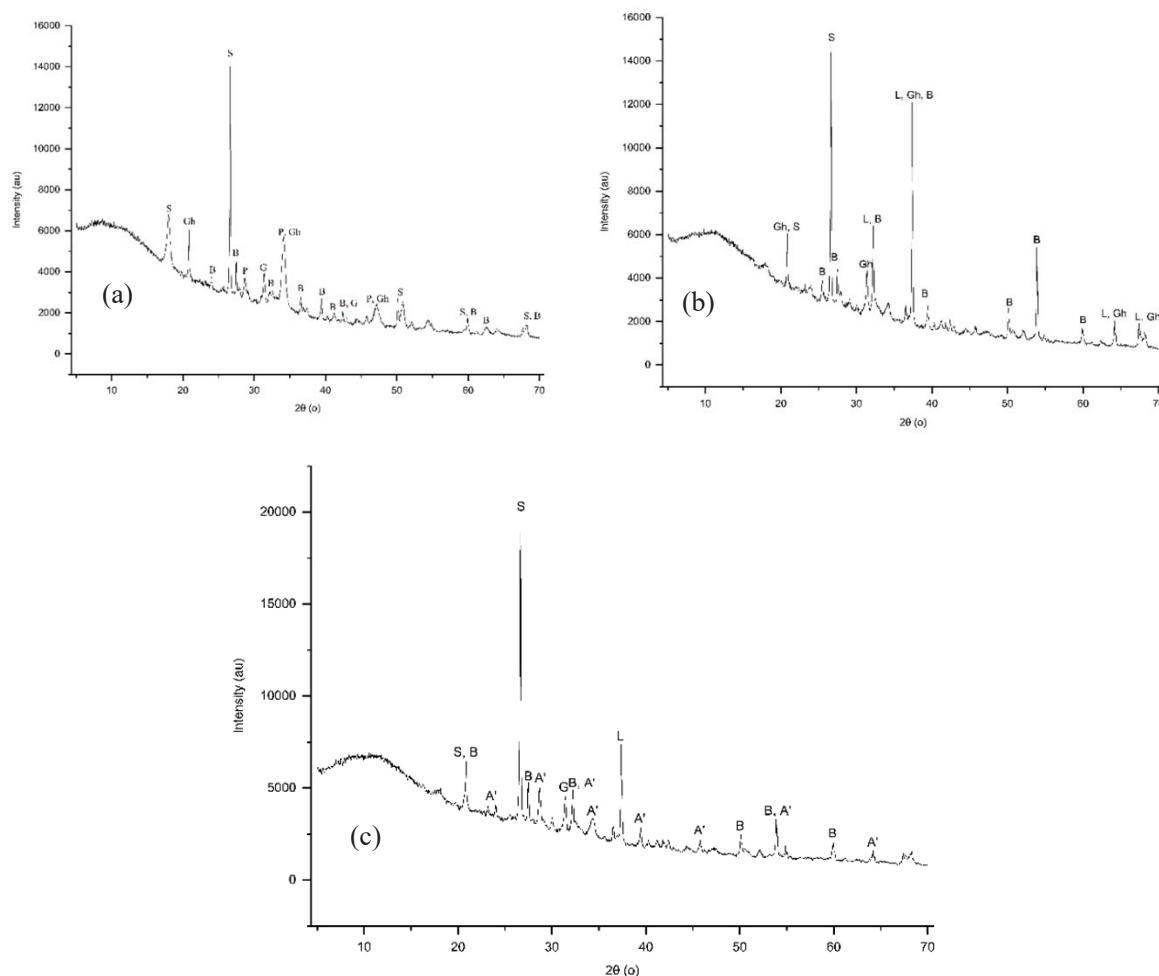


Fig. 4: XRD patterns of belite cements (a) CN (b) CG (c) CH (A':  $\alpha'$ -C<sub>2</sub>S; B:  $\beta$ -C<sub>2</sub>S; G:  $\gamma$ -C<sub>2</sub>S; S: SiO<sub>2</sub>; L: lime; Gh: gehlenite; P: portlandite).

There were also other compounds that were formed in the belite cements that include  $\gamma$ -C<sub>2</sub>S, wollastonite, and gehlenite that are undesirable. Although  $\gamma$ -C<sub>2</sub>S can be activated by grinding, it is largely regarded as an inert compound when compared to  $\alpha'$ -C<sub>2</sub>S and  $\beta$ -C<sub>2</sub>S. The presence of wollastonite signifies the incomplete reaction of calcium, and it has very poor hydraulic properties. Gehlenite is obtained through a reaction between calcium oxide and dehydroxylated clay minerals. It poorly reacts with water, and thereby has little hydraulic value.

### 3.2 Scanning Electron Microscopy (SEM) and Energy-dispersive X-ray (EDX) Analysis

The SEM analysis of CN and CH binders in Fig. 6a and Fig. 6c, respectively, show that the belite crystals obtained have an irregular shape with a particle size of less than 10  $\mu$ m which is in agreement with the findings of other studies [8,9]. The binders are expected to have improved hydraulic reactivity due to their small particle size. The microstructures of the hydrated pastes cured at 60 °C in hot air are shown in Fig. 7a and Fig. 7c for CN and CH, respectively. The C-S-H obtained in both pastes has a flake-like morphology. However, the CH paste produced a denser microstructure compared to the CN paste, which can be attributed

to the faster hydration of the  $\alpha'$ -C<sub>2</sub>S compared to the  $\beta$ -C<sub>2</sub>S. The EDX analysis of the cements (Fig. 6b and Fig. 6d) and pastes (Fig. 7b and Fig. 7d) for the red circled spots showed that the major elements present are calcium, oxygen, silicon, and aluminium. The large amount of aluminium is due to the chemical composition of the clay used as raw material. There were also minor insertions of elements such as iron, potassium, magnesium, and sodium which can substitute calcium and create a disorder in the crystal lattice of the C<sub>2</sub>S that might lead to improved hydration and hydraulic activity [8].

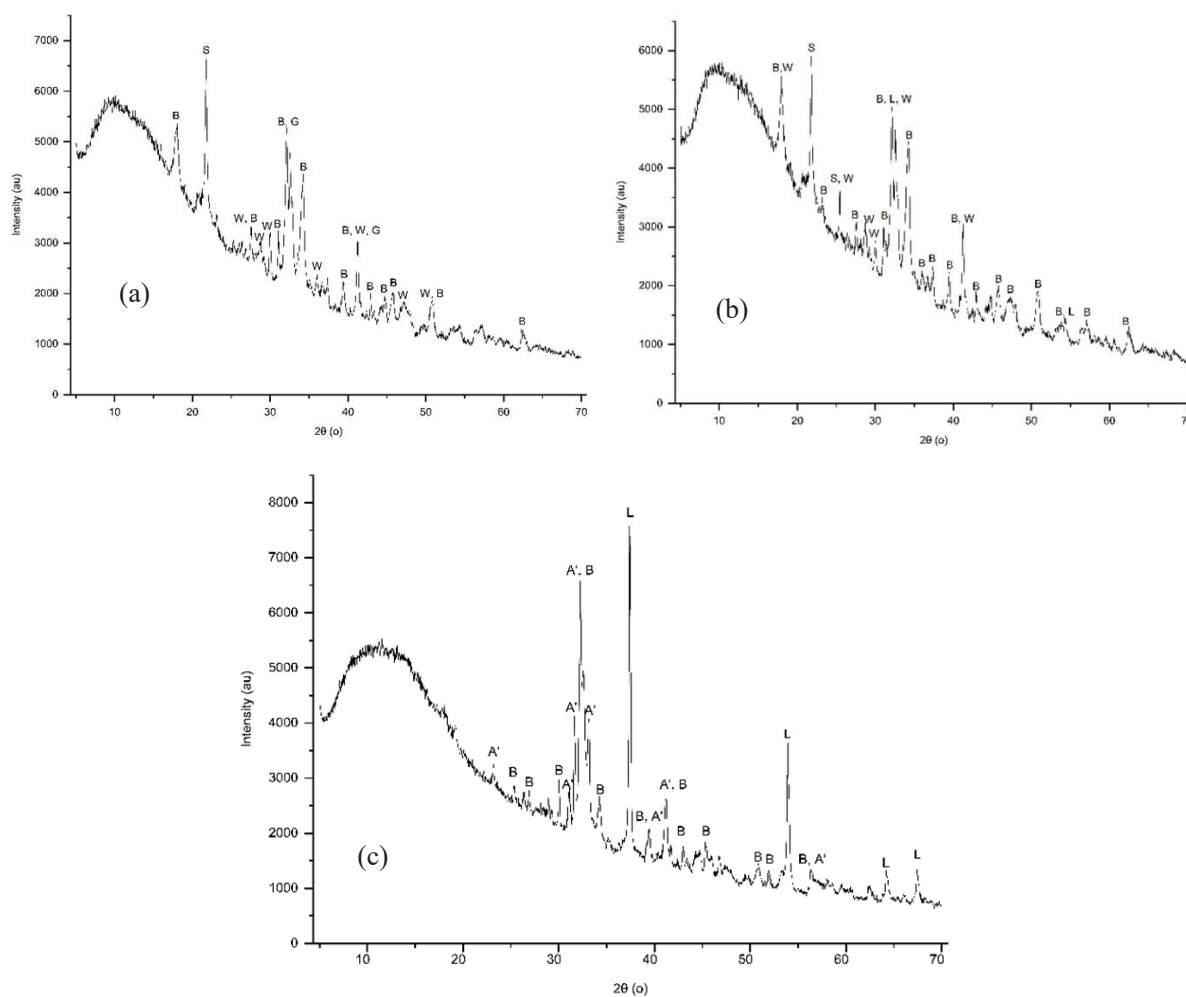


Fig. 5: XRD patterns of belite cements (a) RN (b) RG (c) RH (A':  $\alpha'$ -C<sub>2</sub>S; B:  $\beta$ -C<sub>2</sub>S; G:  $\gamma$ -C<sub>2</sub>S; S: SiO<sub>2</sub>; L: lime; W: wollastonite; P: portlandite).

### 3.3 Compressive Strength

The results of compressive strengths are presented in Fig. 8. The development of strength can be observed to increase with increased curing age except for the samples cured at 90 °C (both hot air and hot water). The mortars cured at room temperature, in saturated conditions and lime water, had a moderate increase in strength. The strength development is significantly affected by the treatment method of raw meals, [10,12] and curing temperatures [18,19]. It can be observed that the binders that were treated hydrothermally obtained the highest strengths at all curing ages and methods. This reaffirms the higher reactivity of  $\alpha'$ -C<sub>2</sub>S over  $\beta$ -C<sub>2</sub>S. The samples containing gypsum exhibited slightly higher strength than the control due to the SO<sub>3</sub>

ions stabilizing more  $\beta$ - $C_2S$ . The increase in compressive strength of the CNRST28 sample with respect to CHRST28 and CGRST28 samples is 213 percent and 110 percent respectively.

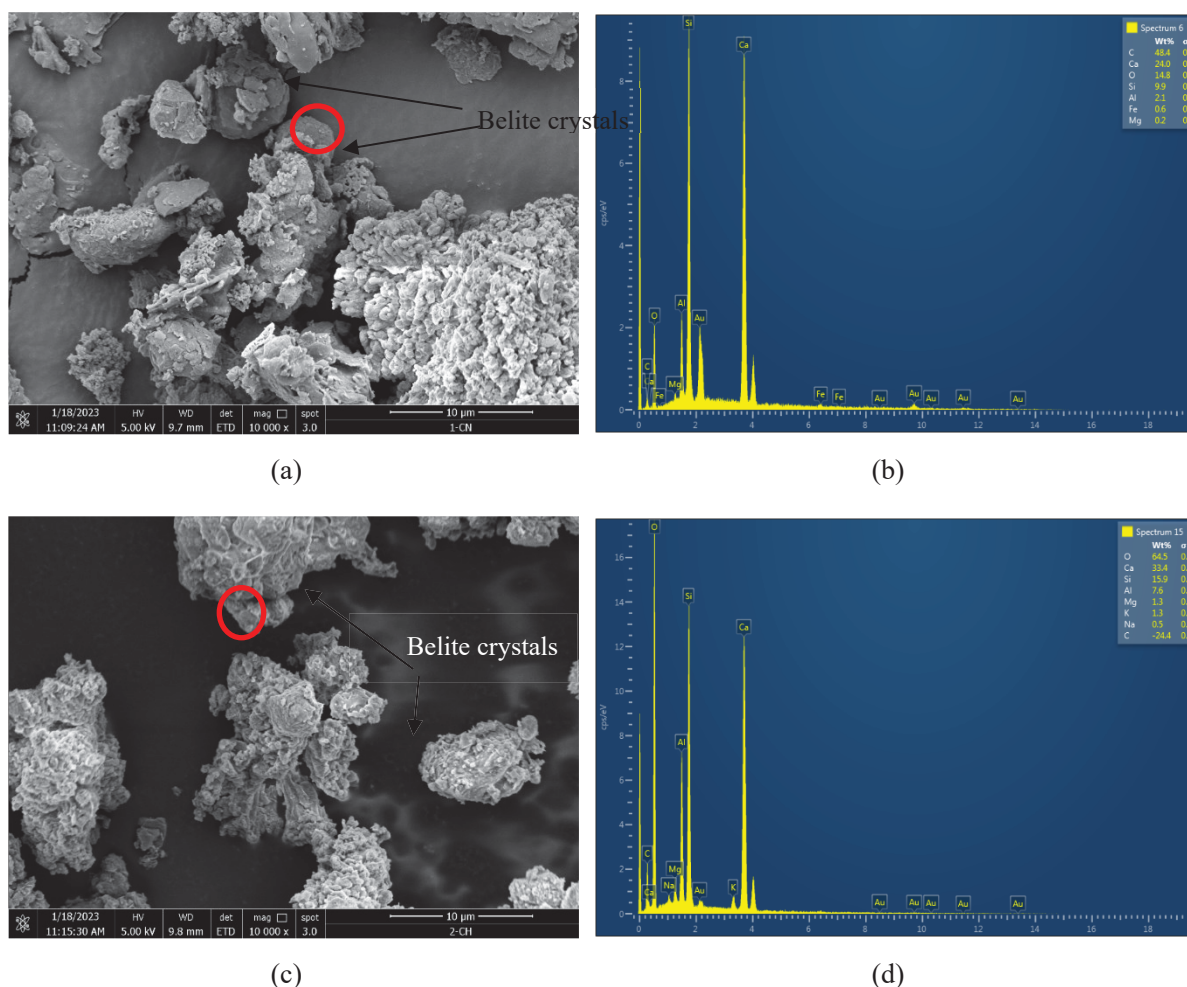


Fig. 6: SEM and EDX results of synthesized cements (a and b) CN (c and d) CH.

The strength after 7 days of curing increased with increasing curing temperatures. The CH90A7 obtained the highest 7-day strength due to the high reactivity of the  $\alpha'$ - $C_2S$  and curing temperature. However, the presence of a crossover effect was observed at 28 days in all samples cured at 90 °C, and there was a strength decrease of 9.8 percent between CH90A7 and CH90A28. From the compressive strengths obtained, the most preferred method of elevated temperature curing cannot be deduced between hot water and hot air curing methods. However, it can be concluded that a curing temperature of 90 °C is detrimental to the long-term strength of low temperature belite cements.

### 3.4 Ultrasonic Pulse Velocity (UPV) Test

The results of the UPV test conducted on the samples at 28 days are presented in Fig. 9. It can be observed that samples cured at room temperature obtained values between 3.11 and 3.91 km/s. The CHRLW28 and RHRLW28 samples had the highest UPV values of 3.91 and 3.84 km/s respectively which can be classified as 'good'. This can be attributed to the faster hydration of  $\alpha'$ - $C_2S$  that produces a compact structure that reduced porosity and water absorption.

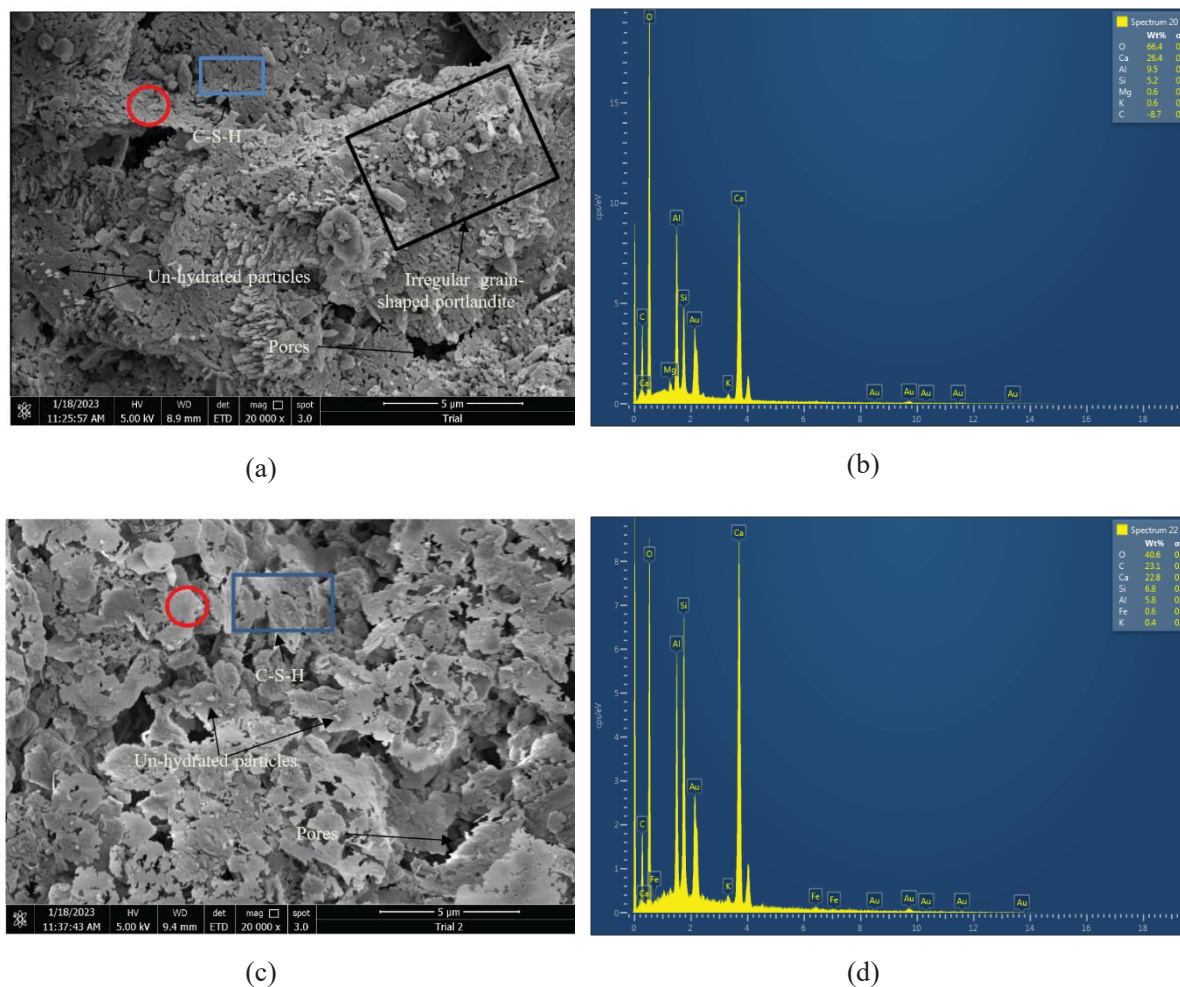


Fig. 7: SEM and EDX results of synthesized cement pastes cured at 60 °C, (a and b) CN (c and d) CH.

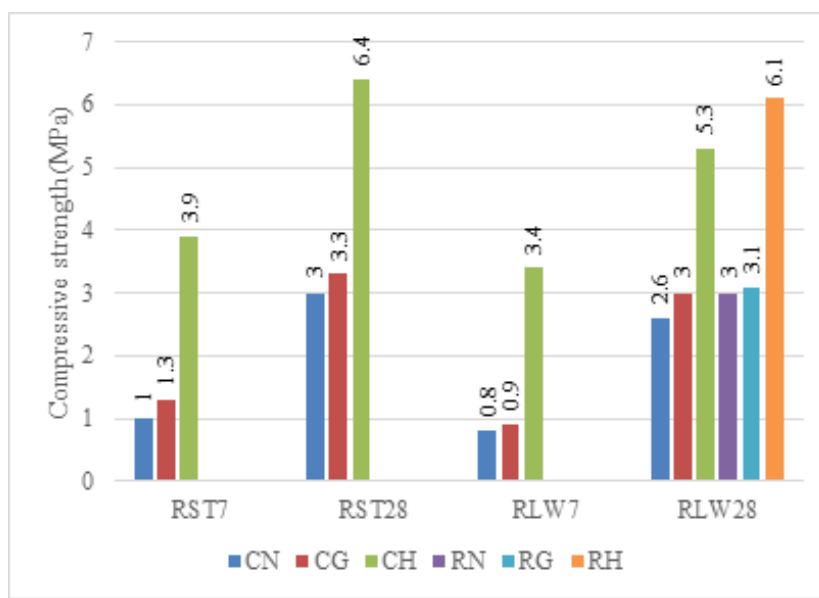
The mortar samples made from CN, CG, RN, and RG binders all had UPV values between 3.0 and 3.5 km/s which classifies them in the ‘medium’ category. This is due to the low reactivity of  $\beta$ -C<sub>2</sub>S, hence, the slow hydration that led to the formation of fewer hydration products that can reduce porosity. The UPV values for all the samples cured at 90 °C, and CN60A28 and CG60A28 (samples cured in hot air at 60 °C) are all below 3.0 km/s. This can be because of the presence of flaws in the samples that may be due to the self-desiccation and rapid non-uniform formation of hydration products that resulted in internal cracking and the creation of pores.

Although other samples cured at 60 °C have values that place them in the ‘medium’ category, their long-term durability is still uncertain. The lowest values at all curing temperatures were obtained from samples cured in hot air due to more loss of internal water. Hence, curing in hot air will produce samples that will have high drying shrinkage that can negatively affect the durability of the samples.

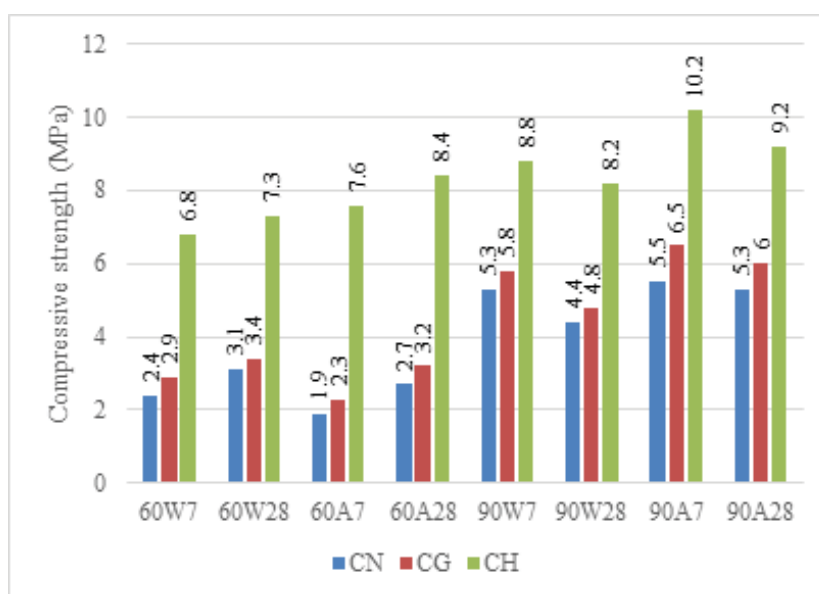
### 3.5 Effective Water Porosity and Water Absorption Coefficient

The results from the capillary water porosity and water absorption coefficient tests are presented in Fig. 10a and Fig. 10b, respectively. It can be observed from Fig. 10a that mortars prepared from the CH binder had the lowest capillary porosity at all curing conditions while those from the CN binder had the highest. This is due to the formation of a dense and porous microstructure by the CH and CN binders, respectively [18]. The results for the water

absorption coefficient test in Fig. 10b show an opposite trend with mortars from the CH binders having the least coefficient of water absorption. The water absorption coefficient decreases with an increase in both curing temperature and capillary water porosity. Also, the samples cured in hot water had a lower coefficient of water absorption than those cured in hot air at the same temperature. This can be due to the difference in microstructure, as the samples cured in hot water might have a more uniform production of hydration compounds. It is evident that both properties are affected by the nature of hydration compounds formed.



(a)



(b)

Fig. 8: Compressive strength development of samples cured at (a) room temperature, and (b) elevated temperature.

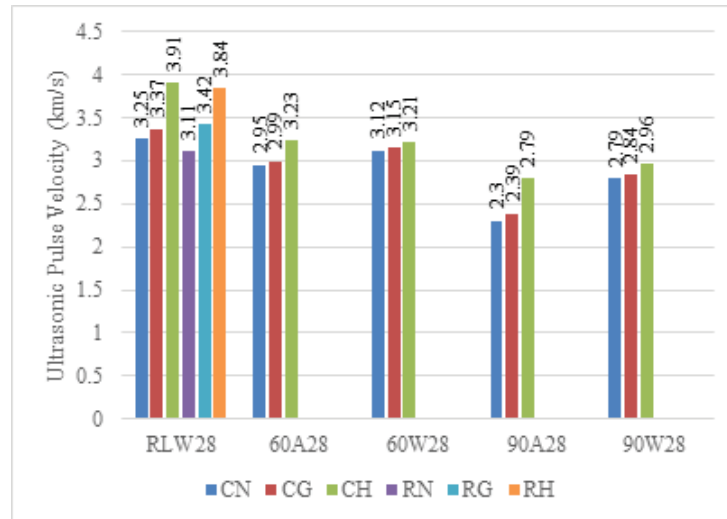
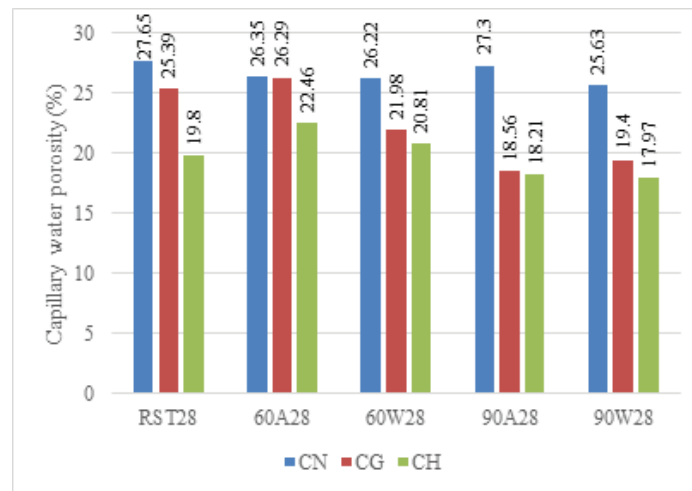
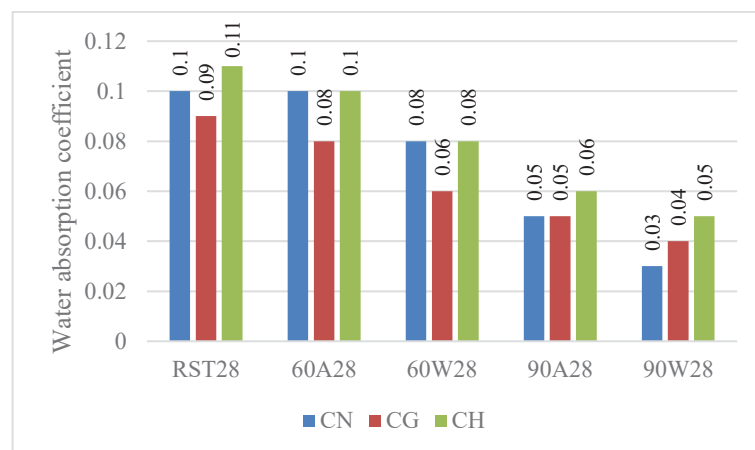


Fig. 9: UPV values of mortars with different curing conditions.



(a)



(b)

Fig. 10: Transport properties of mortars curing (a) capillary water porosity, and (b) water absorption coefficient.

## 4. CONCLUSION

The effect of curing conditions on the early strength of low temperature belite cements was assessed in this study from which these conclusions can be drawn:

- The development of early strength of low temperature belite cements is highly dependent on the curing temperature.
- Although the highest early strengths were obtained at a curing temperature of 90 °C, lower temperatures within the range of 60 °C are more suitable for improving the early strength of these mortars.
- The delay period of 24 hours reduced the loss of strength due to the crossover effect, and the loss is only visible in the 28 days strength of samples cured at 90 °C.
- The presence of the  $\alpha'$ -C<sub>2</sub>S polymorph is shown to have a beneficial effect on hydration and strength development at all curing conditions.
- Elevated temperature curing has a positive effect on the capillary water porosity and water absorption of these mortars.

## REFERENCES

- [1] Garside M. (2021) Cement production worldwide from 1995 to 2020. Available: [<https://www.statista.com/statistics/1087115/global-cement-production-volume/>].
- [2] Cuesta A, Ayuela A, Aranda MAG. (2021) Belite cements and their activation. *Cement and Concrete Research*, 140: 106319. <https://doi.org/10.1016/j.cemconres.2020.106319>
- [3] Alsop PA. (2019) *The cement plant operations handbook for dry-process plants*. Surrey, Tradeship Publications Ltd.
- [4] Harrison T, Jones MR, Lawrence D. (2019) 8 - The Production of Low Energy Cements. In *Lea's Chemistry of Cement and Concrete*. 5th edition. Edited by Hewlett PC, Liska M. Oxford, Butterworth-Heinemann: pp 341-361.
- [5] International Energy Agency. (2021) Cement. Available [<https://www.iea.org/reports/cement>].
- [6] Gawlicki M. (2020) Belite in cements with low emission of CO<sub>2</sub> during clinker formation. *Cement Wapno Beton*, 25(5): 348-357. [doi.org/10.32047/CWB.2020.25.5.1](https://doi.org/10.32047/CWB.2020.25.5.1)
- [7] Popescu CD, Muntean M, Sharp JH. (2003) Industrial trial production of low energy belite cement. *Cement and Concrete Composites*, 25(7): 689-693. [https://doi.org/10.1016/S0958-9465\(02\)00097-5](https://doi.org/10.1016/S0958-9465(02)00097-5)
- [8] Kacimi L, Cyr M, Clastres P. (2010) Synthesis of  $\alpha'$ -L-C<sub>2</sub>S cement from fly-ash using the hydrothermal method at low temperature and atmospheric pressure. *Journal of Hazardous Materials*, 181(1): 593-601. <https://doi.org/10.1016/j.jhazmat.2010.05.054>
- [9] Mazouzi W, Kacimi L, Cyr M, Clastres P. (2014) Properties of low temperature belite cements made from aluminosilicate wastes by hydrothermal method. *Cement and Concrete Composites*, 53: 170-177. <https://doi.org/10.1016/j.cemconcomp.2014.07.001>
- [10] Duvallat TY, Mahmoodabadi M, Oberlink AE, Robl TL, Jewell RB. (2022) Production of  $\alpha'$ H-belite-CSA cement at low firing temperatures. *Cement and Concrete Composites*, 134: 104820. <https://doi.org/10.1016/j.cemconcomp.2022.104820>
- [11] Moudar J, Agourrame H, El Fami N, Diouri A, Taibi M. (2022) Stabilization and characterization of dicalcium silicate belite phase by metallic zinc. In *Proceedings of 3rd International Congress on Materials & Structural Stability*. Edited by Diouri A, Sonebi M, Saadi M, Khachani N, Ait Ahsaine H, *Material Today: Proceedings*: pp 1442-1446.
- [12] Bouzidi MA, Tahakourt A, Bouzidi N, Merabet D. (2014) Synthesis and Characterization of Belite Cement with High Hydraulic Reactivity and Low Environmental Impact. *Arabian Journal for Science and Engineering*, 39(12): 8659-8668. <https://doi.org/10.1007/s13369-014-1471-2>

- [13] Pimraksa K, Hanjitsuwan S, Chindapasirt P. (2009) Synthesis of belite cement from lignite fly ash. *Ceramics International*, 35(6): 2415-2425. <https://doi.org/10.1016/j.ceramint.2009.02.006>
- [14] Kotsay G, Jaskulski R. (2020) Belite cement as an ecological alternative to Portland cement - a review. *Materials Structures Technology*, 2(1): 70-76. [10.31448/mstj.02.01.2019.70-76](https://doi.org/10.31448/mstj.02.01.2019.70-76)
- [15] Zhao Y, Lu L, Wang S, Gong C, Huang Y. (2013) Modification of Dicalcium Silicates Phase Composition by BaO, SO<sub>3</sub> and MgO. *Journal of Inorganic and Organometallic Polymers and Materials*, 23(4): 930-936. <https://doi.org/10.1007/s10904-013-9873-2>
- [16] Bye G, Livesey P, Struble L. (2011) *Portland Cement*. London, ICE Publishing.
- [17] Morales-Cantero A, De la Torre AG, Cuesta A, Fraga-Lopez E, Shirani S, Aranda MAG (2020) Belite hydration at high temperature and pressure by in situ synchrotron powder diffraction. *Construction and Building Materials*, 262: 120825. <https://doi.org/10.1016/j.conbuildmat.2020.120825>
- [18] Federowicz K, Figueiredo VA, Al-kroom H, Abdel-Gawwad HA, Abd Elrahman M, Sikora P. (2020) The Effects of Temperature Curing on the Strength Development, Transport Properties, and Freeze-Thaw Resistance of Blast Furnace Slag Cement Mortars Modified with Nanosilica. *Materials*, 13(24): 5800. <https://www.mdpi.com/1996-1944/13/24/5800>
- [19] Shirani S, Cuesta A, Morales-Cantero A, De la Torre AG, Olbinado MP, Aranda MAG. (2021) Influence of curing temperature on belite cement hydration: A comparative study with Portland cement. *Cement and Concrete Research*, 147: 106499. <https://doi.org/10.1016/j.cemconres.2021.106499>
- [20] Thomas JJ, Ghazizadeh S, Masoero E. (2017) Kinetic mechanisms and activation energies for hydration of standard and highly reactive forms of  $\beta$ -dicalcium silicate (C2S). *Cement and Concrete Research*, 100: 322-328. <https://doi.org/10.1016/j.cemconres.2017.06.001>
- [21] Yang Z, Tao X, Wang G, Li W. (2022) Study on Preparation of Low Heat High Belite Clinker from Waste Mortar and Its Modification. *Materials*, 15: 3196. <https://www.mdpi.com/1996-1944/15/9/3196>
- [22] British Standard Institution. (2016) BS EN 196-1:2016 Methods of testing cement - Part 1: Determination of strength. London.
- [23] British Standard Institution. (2003) BS EN ISO 15148:2002+A1:2016 Hygrothermal performance of building materials and products. Determination of water absorption coefficient by partial immersion. London.

## THE EFFECT OF INDUSTRIAL AND WASTE FIBERS ON CONCRETE STRENGTH AND STRUCTURAL BEHAVIOR OF RC SHORT COLUMNS

MARYAM H. NASER<sup>1</sup>, MAYADAH W. FALAH<sup>2</sup>, FATIMAH H. NASER<sup>1</sup>,  
MOHAMMED SALAH NASR<sup>3\*</sup>, TAMEEM MOHAMMED HASHIM<sup>2</sup>  
AND ALI ABDULHUSSEIN SHUBBAR<sup>4</sup>

<sup>1</sup>College of Engineering, Al-Qasim Green University, Babylon, Iraq

<sup>2</sup>Building & Construction Techniques Engineering Department,  
Al-Mustaqbal University College, Babylon, Iraq

<sup>3</sup>Technical Institute of Babylon, Al-Furat Al-Awsat Technical University, Babylon, Iraq

<sup>4</sup>School of Civil Engineering and Built Environment, Liverpool John Moores University,  
Liverpool, UK

\*Corresponding author: mohammed.nasr@atu.edu.iq

(Received: 25 April 2023; Accepted: 2 September 2023; Published on-line: 1 January 2024)

**ABSTRACT:** Concrete is a brittle substance; thus, it is reinforced with rebars and fibers to enhance its ductility. On the other hand, the presence of waste from various industries negatively impacts the environment. The ongoing reconstruction in Iraq has resulted in an abundance of locally produced rebar-connecting wire (RCW) and copper electric wire (CEW) waste. To minimize the environmental impact of these wastes, they can be reused in other industries, such as the concrete industry. Few studies have dealt with concrete's structural and mechanical properties containing these local residues. Therefore, this study included an experimental investigation of concrete columns with and without various types of industrial and waste fibers. Two types of industrial fibers (macro hooked-end; CH, and micro straight; CS) steel fibers and two types of waste fibers (RCW and CEW) were utilized. Six reinforced concrete (RC) columns ( $150 \times 150 \times 450 \text{ mm}^3$ ) were cast: one control column without fibers and five columns with fibers. The fiber content within the columns was fixed at 0.75% of the concrete volume. The cracks pattern, load-deflection behavior and concrete strain for RC columns were investigated. Moreover, the mechanical properties in terms of compressive, splitting tensile, and flexural strengths tests were also conducted. The results revealed that all types of fibers used improved the mechanical and structural properties of the concrete. Moreover, although the hybrid synthetic fibers gave the best improvement compared to the reference sample, the waste fibers (especially RCW) showed a significant improvement that reached 30.91% in relation to the ultimate load and (10.1, 10.8 and 14.4%) in relation to the compressive, tensile, and flexural strengths respectively.

**ABSTRAK:** Konkrit adalah material rapuh; oleh itu ianya dikuatkan dengan besi dan fiber bagi menguatkan kekuatannya. Dalam masa sama, kehadiran bahan buangan dalam pelbagai industri memberi kesan negatif kepada persekitaran. Penstrukturan semula Iraq yang sedang berlangsung memberi kesan kepada kebanjiran bahan buangan seperti besi penghubung litar (RCW) dan litar elektrik tembaga (CEW) buatan tempatan. Bagi mengurangkan kesan pencemaran terhadap alam sekitar,

bahan-bahan ini boleh diguna balik dalam industri berbeza, seperti industri konkrit. Terdapat banyak kajian terhadap buangan tempatan yang melibatkan struktur bahan konkrit dan sifat mekanikal. Oleh itu, kajian ini merupakan kajian eksperimen pasak konkrit dengan atau tanpa pelbagai jenis industri dan fiber buangan. Dua jenis fiber industri iaitu fiber besi (mikro hujung-penyangkut; CH dan mikro lurus; CS) dan dua jenis fiber buangan (RCW dan CEW) dipakai. Enam RC pasak konkrit ( $150 \times 150 \times 450 \text{ mm}^3$ ) dihasilkan: satu pasak kawalan tanpa fiber dan lima pasak dengan fiber. Kandungan fiber dalam pasak di tetapkan pada 0.75% isipadu konkrit. Corak rekahan, ciri-ciri kesan beban dan tekanan konkrit pada pasak RC dikaji. Tambahan, kajian terhadap ciri-ciri mekanikal berdasarkan tekanan, rekahan tensil dan kekuatan anjalan telah dijalankan. Dapatan kajian menunjukkan kesemua fiber yang digunakan menambah baik ciri-ciri mekanikal dan struktur konkrit. Tambahan lagi, walaupun fiber sintetik hibrid menunjukkan paling baik berbanding sampel contoh, fiber buangan (terutama RCW) menunjukkan pembaharuan ketara mencapai 30.91% berbanding beban maksimum dan masing-masing menunjukkan 10.1, 10.8 dan 14.4% pada tekanan, rekahan tensil dan kekuatan anjalan.

---

**KEYWORDS:** *industrial and waste fibers; RC columns; mechanical properties; structural behavior*

## 1. INTRODUCTION

Concrete is a vastly employed building substance all over the world [1]. However, it begins to lose its bearing capacity as cracks start and gradually continues with the growth of cracks which may eventually lead to failure. Normal concrete is characterized by its low tensile and cracking resistance and limited ductility [2]. Therefore, different types of fibers (such as natural, synthetic and steel fibers) are integrated into the concrete to improve the mechanical characteristics and resistance against cracking of cement-concrete composites [3,4]. Concrete made with steel fiber has been efficiently used in precast products, slabs on grade, architectural panels, shotcrete, marine structures, thin and thick repairs, structures in seismic zones, crash barriers, hydraulic structures, foundations, and many other structures [5]. Depending on its properties, the utilization of fibers in a concrete structural member may enhance ductility performance and limit the crack generation and overall strength and toughness [6,7]. Moreover, fiber-reinforced concrete can improve the compressive behavior of concrete pillars. This improvement is attributed to the effect of confinement of these fibers, which leads to superior performance in terms of resistance and ductility compared to ordinary concrete [8]. In this context, several previous studies investigated the effect of fibers on reinforced concrete columns. Some of these studies [9-11] have found that adding steel fibers increased the strength of columns and showed higher levels of ductility when compared with columns that did not contain steel fibers. Mahdi [12] presented an analytical and experimental evaluation of the ductility and strength of high-performance and normal concrete columns with/without polypropylene and steel fibers confined by tie reinforcement. It was found that adding fibers to high-performance and normal concrete short columns improves their behavior and increases the ultimate strength. Moreover, the results showed that the percentage increase in the peak strength when breaking the fixed steel fiber volume decreases slightly with the increase in the aspect ratio of the fibers. Balanji et al. [13] researched the behavior of hybrid steel fiber-reinforced (HSF) high-strength concrete circular columns under various loading situations. The hybrid steel fiber is composed of a mixture of fine and large steel fibers. Results demonstrated that reinforced concrete columns with HSF realized higher ductility and strength under

different loading conditions than RC columns without HSF. Also, it was revealed that the cracks of the concrete cover were delayed due to the presence of fibers.

On the other hand, the use of metallic waste fibers, especially steel ones, in concrete and their comparison with industrial fibers have been investigated in the literature. For example, Domski et al. [14] conducted an experimental study to investigate the impact of waste steel fibers (WSF) from tire recycling on concrete properties and compared the results with conventional engineered steel fibers (ESF). The results indicated that the concrete containing WSF achieved higher ductility and tensile strength than that made with ESF. Moreover, Samindi et al. [15] researched the mechanical performance of concrete produced with waste (recovered from tires) and manufactured steel fibers. It was found that the compressive strength of concrete was improved by 17–20% in the presence of manufactured fibers compared to 5–12% enhancement for waste fibers. Moreover, a similar ductile behavior was observed for both types of fibers when used separately at a rate of 0.5%. Furthermore, Sofi and Gopu [16] explored the compressive, splitting tensile and flexural characteristics of concrete made from industrial and waste fibers (electrical waste glass fiber, EWGF, and electrical waste copper wire fiber, EWCWF). Results revealed that the industrial, EWGF and EWCWF fibers improved the compressive, splitting tensile and flexural strengths by (42.6%, 81.6% and 46.1%), (15.35%, 90.1 and 31.7%) and (23.76, 46.4 and 38.8%), respectively.

The volume of fibers in a mixture plays a crucial role in determining its various properties. A study conducted by Soulioti et al. [17] focused on the mechanical behavior of reinforced concrete that was reinforced with steel fibers of varying geometries (hooked ends and waved) and volumes (0.5%, 1%, and 1.5%). The findings showed that the mechanical properties, flexural toughness, and peak strength of the concrete improved as the fiber content increased. Additionally, the geometry of the fibers was found to have a significant impact on the material's mechanical performance. On the other hand, Gao et al. [18] studied the compressive behavior of RC columns under uniaxial compression in recycled aggregate concrete incorporated steel fibers in proportions of 0.5%, 1%, and 1.5% (by volume). They found that the optimum percentage for steel fiber was 1%. A study was conducted by Attia [19] to investigate the impact of different types (steel and polypropylene) and amounts of fibers (0.5% and 0.75%) with different aspect ratios (100 and 667) on the strength of RC columns. The results indicated that adding fibers, particularly at a percentage of 0.75% with an aspect ratio of 100, improved the mechanical properties and structural behavior of the concrete columns.

The waste, especially solid waste, constitutes a problem facing governments in developing countries because of its negative impact on the environment. It occupies large areas in landfills in addition to the fact that its decomposition takes a long time. Therefore, one of the methods to reduce this environmental damage is to reuse the waste in other industries (for example, concrete manufacturing) and convert it into valuable materials. Among these waste materials are rebar-connecting wires (RCW) and copper electric wires waste (CEW). These wastes are produced locally (in Iraq) in significant quantities as a result of the reconstruction of destroyed buildings due to wars and military operations in recent years. Few studies have dealt with using these local wastes as fibers in concrete. Moreover, few studies have examined four distinct types of fibers and compared them in terms of mechanical and structural performance. Furthermore, limited studies have dealt with the mechanical behavior of concrete columns containing hybrid fibers and compared it with the control (fiber-free) and that containing synthetic or waste fibers. In addition, the significance of this research stands out as it enhances sustainability and the management of solid waste by transforming non-valuable materials into valuable ones that can be utilized successfully in the construction industry. Accordingly, this study aims to investigate the mechanical and structural properties of reinforced concrete

columns containing locally produced (RCW and CEW) fibers along with industrial hooked-end and straight steel fibers. The results of the study are considered promising, not only in improving the above properties but also contributing to enhancing the production of green concrete as a result of reusing these wastes and reducing their harmful environmental impact.

## 2. EXPERIMENTAL WORK

### 2.1 Properties of Concrete Materials

The components used in the production of the concrete mixtures for plain and reinforced specimens were lime cement, natural fine and coarse aggregates, superplasticizer, and tap water. The cement was CEM II/A-L-42.5R in type and conformed to BS EN 197-1 [20]. Tables 1 and 2, respectively, illustrate the physical and chemical characteristics of the cement.

Table 1: Chemical analysis of the cement

Oxide, %	Percentage by Weight
CaO	59.89
SiO <sub>2</sub>	20.8
Al <sub>2</sub> O <sub>3</sub>	5.50
Fe <sub>2</sub> O <sub>3</sub>	5.1
MgO	3.81
Free CaO	0.67
SO <sub>3</sub>	1.8
Loss on Ignition	2.2
Insoluble Residue	1.1

Table 2: Physical properties of the cement

Physical Properties	Test Results	
Specific Gravity	3.15	
Fineness (Blaine) (m <sup>2</sup> /kg)	346	
Time of Setting (Vicat) (minute)	Initial time	180
	Final time	205
Compressive Strength (MPa)	3 days	20.50
	7 days	27.00

The fine aggregate (natural sand) met Iraqi Standard No.45, zone 2 [21]. The fineness modulus of sand was 2.94. Natural gravel with a maximum size of 10 mm was employed as a coarse aggregate. The sieve analysis results of fine and coarse aggregates are presented in Tables 3 and 4, respectively. SikaViscocrete-5930, which conformed to ASTM C494 (types F and G) [22], was utilized as a workability adjuster. Four types of steel fibers (see Fig. 1) were added to the concrete mixtures to improve their properties. Two types of these fibers are considered conventional (purchased from the market): one was macro hooked-end (CH), and the other was micro straight-end (CS). In contrast, the other types of fibers were waste. The source of one of the waste fibers was from the rebar-connecting wires (RCW), and the other was from the copper electric wires waste (CEW). The wires were cut to the required size manually. The properties of all types of fibers are given in Table 5.

Table 3: The sieve analysis results of the fine aggregate

Sieve Size (mm)	Passing %	Limits of the Iraqi Standard, Zone 2
10	100	100
4.75	100	90-100
2.36	82.5	75-100
1.18	60.9	55-90
0.60	49.4	35-59
0.30	11.3	8-30
0.15	2.3	0-10

Table 4: The sieve analysis results of the fine aggregate

Sieve Size (mm)	Passing, %	Limits of the Iraqi Standard
14	100	100
9.5	100	85-100
4.75	20.7	0-25
2.36	2.5	0-5

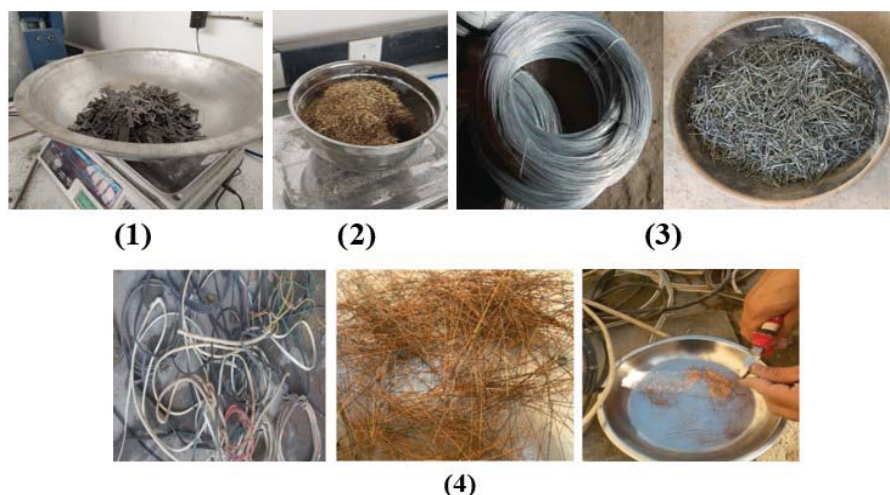


Fig. 1: The fibers used (1) CH; (2) CS; (3) RCW; and (4) CEW.

Table 5: The properties of fibers

Fiber Designation	Tensile Strength (MPa)	Density (kg/m <sup>3</sup> )	Length (mm)	Diameter (mm)	Aspect ratio (L/D)
CH	1300	7500	35	0.5	70
CS	2300	7860	13	0.2	65
RCW	510	7500	20	0.8	25
CEW	387	8760	10	0.17	59

## 2.2 Mix proportions, Casting, and Curing

The mix proportions that were adopted for this study were 1:1.25:2 (cement: sand: gravel) with a W/C ratio of 0.35. For the concrete mixes, all parameters were fixed except for the type of fibers. The fibers were added in proportions of 0.75% by volume of concrete. One reference mix (control), four mixtures containing a single type of fiber (CH, CS, RCW, or CEW) and

one mix incorporating hybrid fibers (CH + CS) were executed for this study. For the hybrid fibers mixture, the addition percentage for each the micro and macro steel fibers was 0.375% (0.75% in total). Table 6 shows the details of mix proportions for all mixes. After mixing, the fresh concrete was cast in standard and column molds. After about 24 hours of casting, specimens were lifted from molds. Thereafter, the specimens were placed in water until the testing time (28 days).

Table 6: Mix proportion details of concrete mixes

Mix Designation	Fiber Type	Cement (kg/m <sup>3</sup> )	Sand (kg/m <sup>3</sup> )	Gravel (kg/m <sup>3</sup> )	Fiber, %	Super-Plasticizer (kg/m <sup>3</sup> )	Water (kg/m <sup>3</sup> )
M1	---	450	563	900	0.75	4.5	157.5
M2	CH	450	563	900	0.75	4.5	157.5
M3	CS	450	563	900	0.75	4.5	157.5
M4	CH+CS	450	563	900	0.375+0.375	4.5	157.5
M5	RCW	450	563	900	0.75	4.5	157.5
M6	CEW	450	563	900	0.75	4.5	157.5

### 2.3 Reinforced Concrete Specimens

This study included the preparation and testing of six columns under static load. The cross-section for all columns was 150 × 150 mm, and the columns have a total length of 450 mm. The columns were reinforced with four (Ø6 mm) longitudinal bars and Ø4 @ 50 mm stirrups. Figure 2 shows the details of the geometry and reinforcement of the columns.

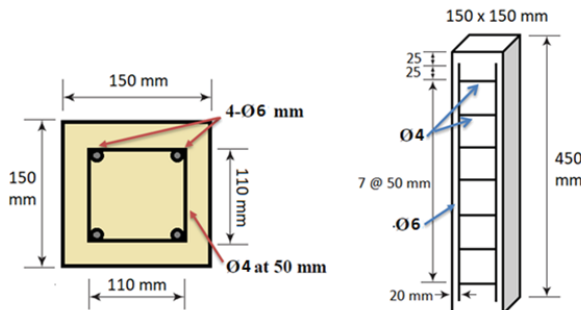


Fig. 2: Geometry and reinforcement details of the tested specimens.

Six samples were cast for this study: one control column without steel fibers for comparison with other columns, and five specimens containing 0.75% steel fibers with different types: macro, micro, and hybrid (conventional and waste). All columns are identified in Table 7.

Table 7: Designation of the RC Columns

Column Name	Identification of Fibers
C1	Column without fibers
C2	Column with macro steel fibers
C3	Column with micro steel fibers
C4	Column with hybrid (50% macro+ 50% micro) steel fibers
C5	Column with rebar-connecting waste wires
C6	Column with copper electric waste wires

Deformed steel bars (6 and 4 mm) in diameter were used as shown in Fig. 3. Bars of size Ø6 mm were utilized as a longitudinal reinforcement and bars of size Ø4 mm were used as a stirrup reinforcement. Table 8 shows the results of testing steel reinforcement according to ASTM A615 [23].

Table 8: Strength of steel reinforcement used.

Nominal Diameter (mm)	4	6
Fy (MPa)	412	423



Fig. 3: Steel reinforcement of RC columns.

## 2.4 Tests

Several mechanical tests were performed for this study. The mechanical test types and specimen details are presented in Table 9. The modulus of elasticity was determined depending on (ACI 363R) [24] from Eq. 1:

$$E_c = 3320 \sqrt{f_c'} + 6900 \quad (1)$$

Besides, reinforced concrete (RC) columns were tested for crack pattern, ultimate load, load-deflection and strain behavior.

Table 9: Mechanical tests details

Test	Specimen shape	Dimensions, mm	Standard
Compressive strength	Cube	150×150×150	BS 1881 Part 116 [25]
Splitting tensile strength	Cylinder	100×200	ASTM C496 [26]
Modulus of rupture	Prism	100×100×400	ASTM C78 [27]

## 3. RESULTS AND DISCUSSION

### 3.1 Mechanical Properties

#### 3.1.1 Compressive strength

The results of the compression test for all the mixtures are shown in Fig. 4. The results generally showed that the added fibers of all types improved compressive strength. The percentage of improvement was within the range of 3.9 to 27% compared to the reference mixture (without fibers). This is due to these fibers' role in arresting the growth of cracks within the concrete matrix [28]. Moreover, the results clearly showed that the best compressive strength (59.34 MPa, which represents a 27% improvement related to plain concrete) was

recorded when using hybrid fibers. The reason for this behavior can be attributed to the fibers' ability to restrict cracking on both the micro and macro levels [29]. Furthermore, the waste fibers gave an improvement of 3.9% for RCW fibers and 10.1% for CEW fibers, which represented (especially for CEW fibers) a significant increase related to the reference sample.

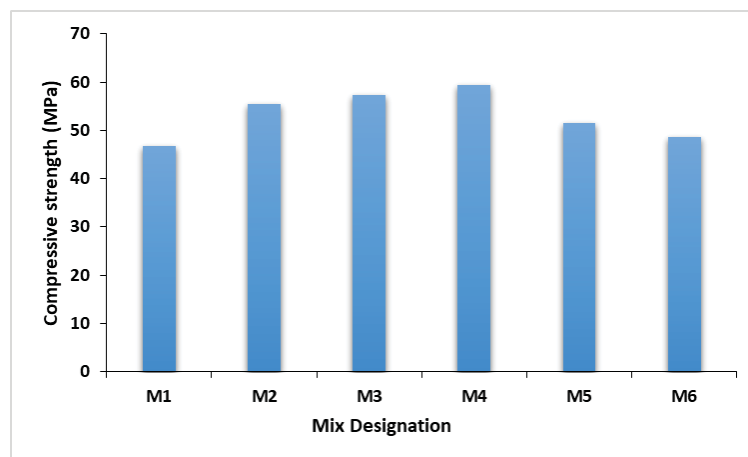


Fig. 4: Compressive strength results of plain and fiber reinforced specimens.

### 3.1.2 Splitting Tensile Strength

Figure 5 presents the splitting tensile strength of concrete cylinders. The results illustrated, as in the case of the compressive strength test, that the presence of fibers contributed to an increase in the tensile strength of concrete in proportions differing according to the type of fibers. Also, the highest improvement value (35.3%) was obtained after using the hybrid fibers (CH+CS), followed by the hooked-end fibers. The ability of hybrid fibers to effectively bridge cracks, and thus the micro-mechanical features of crack bridging, work from the stage of damage development to after final loading [30]. On the other hand, the increase in the tensile strength in the hooked-end fibers mixture results from the increase in the value of the bonding strength between the fibers and the concrete due to the hooked ends [31]. Furthermore, the waste fibers showed strength exceeding the reference mixture by 10.8 and 7% for CH and CS fibers, respectively, which indicates the ability of these fibers to bridge the cracks and increase the collapse resistance of the concrete.

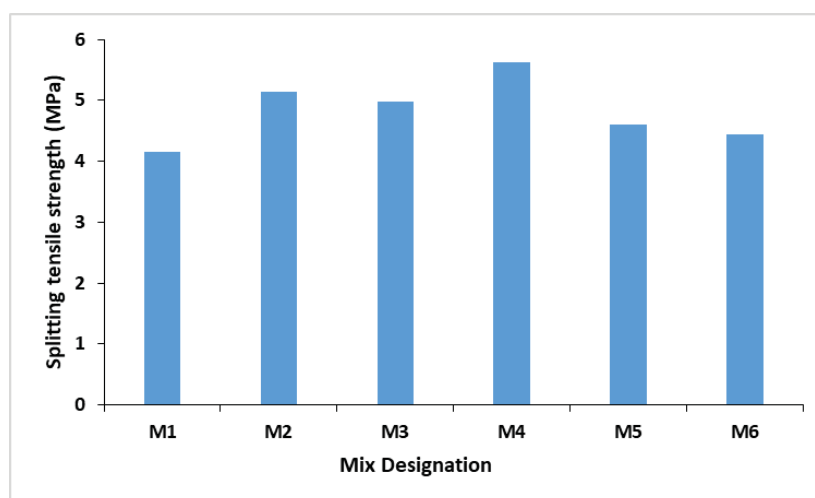


Fig. 5: Splitting tensile strength results of concrete mixtures.

### 3.1.3 Flexural Strength

The results of flexural strength for the reference and fiber-reinforced mixes are displayed in Fig. 6. In general, the flexural strength results were in the same trend as the compressive and tensile strength tests. Where the mixtures incorporating fibers demonstrated higher strength than those without them. Moreover, the mixture containing the hybrid of micro and macro fibers recorded the highest flexural strength (improvement percentage was 37.3%). The improvement in flexural length of the hybrid fiber-based concrete is due to the ability of the fine steel fibers to control micro-cracking in the early stages of loading and hooked-end fibers are larger, providing a bridge mechanism across large (macro) cracks [32]. Also, the waste fibers increased strength by 11.2% and 14.4% (over the control sample) for CH and CS fibers, respectively. This indicates the effectiveness of crack-bridging action for these waste fibers.

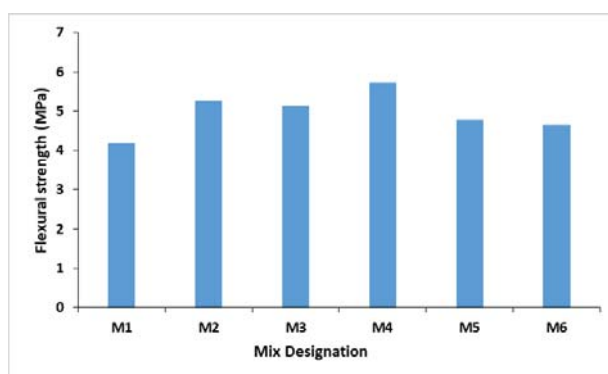


Fig. 6: Flexural strength results of concrete mixtures.

Furthermore, according to the above, it can be noticed that the CH fibers had a superior performance than CS fibers in compressive, splitting tensile and flexural strengths tests. The reason beyond that may be attributed to the bond increasing between the fibers and concrete matrix as a results of fiber length (CH fibers are twice as long as CS fibers) [33].

## 3.2 Flexural Properties of RC Columns

### 3.2.1 First Crack and Cracks Pattern

The load was applied to the centerline of the columns as previously described. The member condition, cracks extension, behavior, or any damage from loading to failure was observed. Concrete cracks were observed to show the damage process during each column's testing phases. Table 10 and Fig. 7, respectively, show the results of first crack loads and crack patterns for all columns.

Table 10: First crack load, ultimate load and deflection results

Column	Fiber Type	First Crack Load (kN)	Ultimate Load (kN)	Increase Rate in Ultimate Load %	Max. Deflection (mm)
C1	---	335.37	619.61	-----	1.10
C2	CH	404.99	794.19	28.18	1.79
C3	CS	410.34	883.72	42.63	2.22
C4	CH+CS	471.13	914.21	47.54	2.01
C5	RCW	398.14	811.12	30.91	1.64
C6	CEW	404.12	784.23	26.56	1.48

The results of the control (without steel fibers) column (C1) showed that the first crack was observed at (335.37 kN). Upon further loading, new cracks extending on both sides to deform the column, were recorded. As the loading increased, cracks appeared in the concrete at the column supports. With continued loading, the deformation of the column grew. Finally, the concrete split and failed in shear on all four sides at the bottom of the column.



Fig. 7: Crack patterns for columns with different steel fibers.

On the other hand, the presence of fibers delayed the appearance of the first crack compared to the reference sample. Where the results showed that the presence of hybrid fibers (C4) contributed to improving the load of the first crack by 40.48%, while the waste fibers (RCW; C5, and CEW; C6) showed superiority in the load of the first crack by 18.72 and 20.50%, respectively compared to the reference column. Furthermore, the results indicated that the primary cracks were noticed at the beginning of loading for fibers containing columns. As the load increased, new cracks extended from both sides in the center of the column depth. Because of shearing, new cracks extended diagonally at the top of the column. As the loading continued, new cracks also showed up in the column and the concrete cover breakage happened in the mid-span. The width of the main crack increased at the mid-span of the column. Finally, the column failed.

Moreover, in the case of the control column without steel fiber, the failure was mainly caused by cracks spreading parallel to the direction of the load through the coarse aggregate particles, known as a splitting crack. It was also found that the failure pattern under compressive load is a combination of tensile split failure and shear failure when adding the fibers to reinforced concrete columns. The presence of fiber changed how the reinforced concrete columns failed from a brittle to a more ductile failure. For columns with fibers, the vertical cracks that appeared in tested specimens were generally held together by the fibers. Also, the implication of fibers prevented the concrete from spalling. The cracks were distributed uniformly and extended along the length of the member. Their number is more, which indicates the usefulness of using these fibers in the distribution of stresses along the column [34]. This indicates the increase in ultimate strength and ductility of columns made with fiber.

### 3.2.2 Load – Deflection Behavior

Figure 8 shows load–deflection curves (the values can be seen in Table 10) of the specimens used in this study. In general, it was found that adding metallic fibers to reinforced concrete columns increased the ultimate load compared to fiber-free columns. Furthermore, the column behavior containing fibers had more deformability and ductility than those without fibers. These results agree with those in the literature [35].

Additionally, results revealed that specimen **C1** (the control) gave a lower value in ultimate load when compared with other columns with fiber. Also, it exhibited a brittle failure mechanism, while the reinforced concrete columns with metallic fiber were quite ductile in the compression test (which was observed through the development of cracks and the final shape of columns in addition to the values of the ultimate loads at the failure). Hence, the fibers have been very successful in confining concrete internally.

Moreover, column **C4**, made with hybrid (CH+CS) fibers, showed significant enhancement in ultimate load and ductility compared to other metallic fiber types. The ultimate load of the hybrid fiber-based column was superior to the control one by 47.63%. This behavior can be interpreted as follows [36]; under loading, the microfibers avoid expansion of the structure by bridging the microcracks. Once the microfibers are affected, the larger fibers will continue to bridge the cracks until the damage is corrected, which enhances the load-deflection property. Furthermore, waste fibers enhanced the RC columns' load-carrying capacity. The recorded load improvements for RCW and CEW, respectively, were 30.91% and 26.56% compared to the control column, which indicates the efficiency of these fibers in bridging cracks and improving the load-deformation behavior.

Also, it was found that short fibers had a greater effect on the primary part of matrix cracking. Thus, it contributes more to enhancing the strength of the composite compared to long fibers. Thereby, the initiation and propagation of primary cracks are controlled by short fibers earlier and more actively than long fibers. Accordingly, short fibers appear larger in number as a result of their proximity to each other [37].

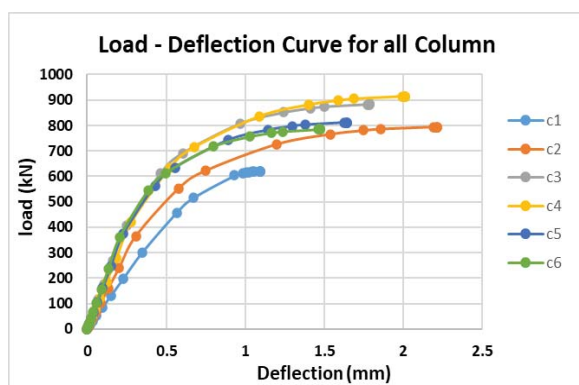


Fig. 8: Load – deflection curves for columns with and without fibers.

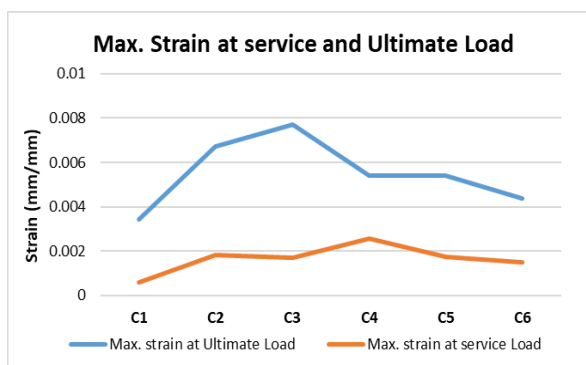


Fig. 9: Maximum strain at service and ultimate loads for all columns.

### 3.2.3 Concrete Strains

The strain in the concrete was measured at different load levels, at mid-span for all columns, using demec discs located 50 mm along the column length. It was measured using a Digital Vernier Caliper. The concrete strain at service and ultimate loads are presented in Fig. 9. Results revealed that a similar behavior with low strain values for all columns was observed,

consistent with the high stiffness of the uncracked section. When the crack occurred, the differences between them increased significantly.

It was observed that the maximum compressive strain  $\epsilon_{\max}$  at ultimate load (Pu) ranged between 0.0034 to 0.0077 while the maximum strain  $\epsilon_{\max}$  at service load (at 0.7 Pu) from 0.00056 to 0.0025 as shown in Fig. 9. The maximum strain  $\epsilon_{\max}$  at service load values were below the normal ones prescribed by the American Code of Practice (ACI Committee 363),  $\epsilon_{cu}$ , which is 0.003. Figure 10 shows the strain distribution of concrete for all columns in different load stages.

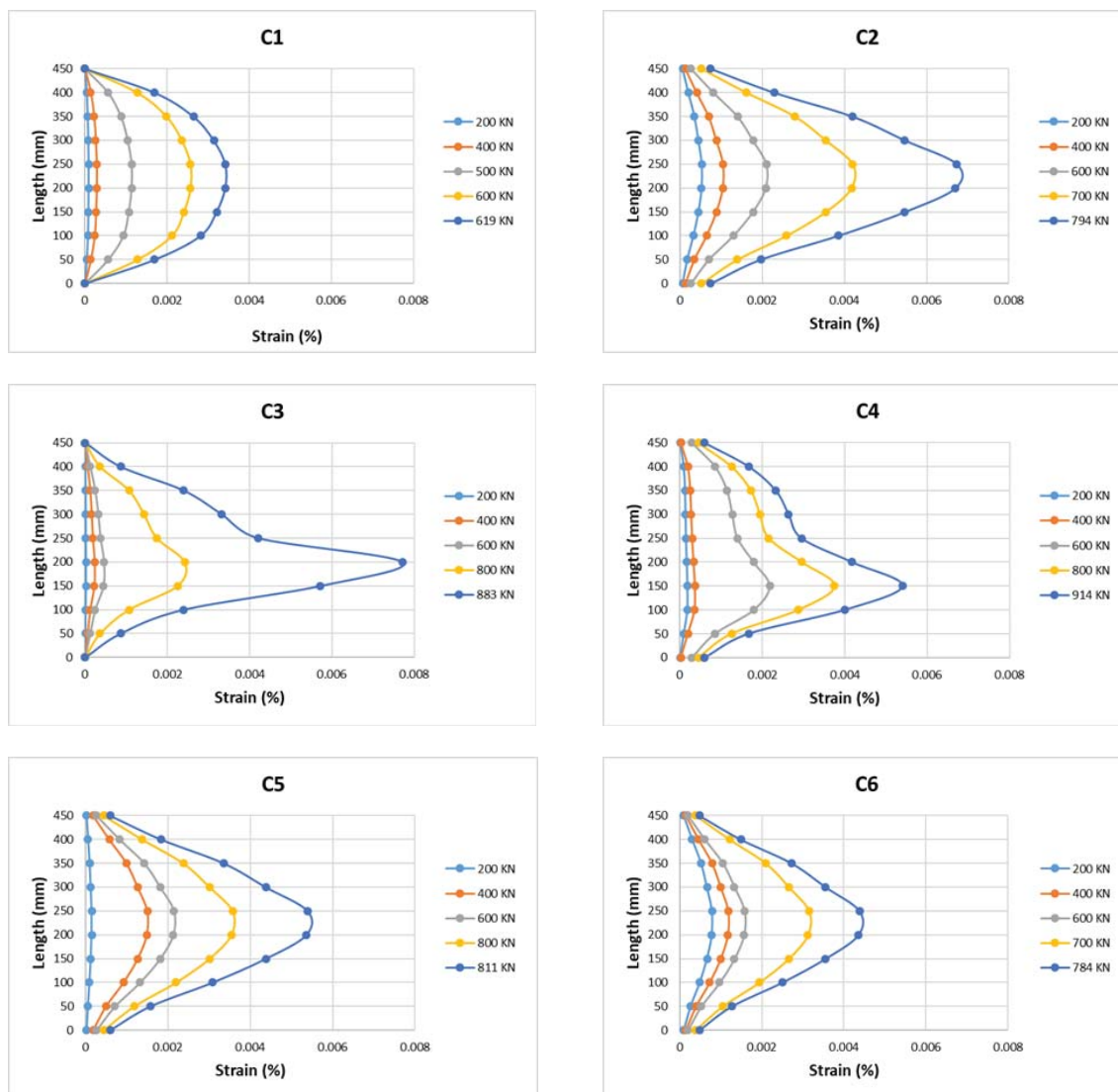


Fig. 10: Concrete strain distribution for all columns in different load stages.

## 4. CONCLUSIONS

According to what was obtained in this experimental study for RC columns with different types of metallic fibers under static loading, the conclusions shown below can be stated:

1. Industrial and waste fibers showed a clear improvement in the mechanical properties of concrete, where the percentages of increments were within the ranges of 3.9-27%,

- 7-35.5%, and 11.2-37.3% for compressive, splitting tensile, and flexural strengths, respectively.
2. The most remarkable improvement for industrial fibers was recorded in the mixture containing hybrid fibers, while for waste fibers, RCW fiber-based mixture showed better performance than CEW in the all-mechanical examinations performed.
  3. The behavior of the columns with metallic fibers was more deformable than columns without fibers. Moreover, in the presence of industrial and waste fibers, the distribution of cracks was uniform and extended along the member length, and its number was greater.
  4. The column with hybrid steel fiber had a load-carrying capacity greater than the control column by about 47.54 %. On the other hand, the improvements for waste fibers-based columns were 30.91% and 26.56% for RCW and CEW fibers, respectively.
  5. The maximum strain  $\epsilon_{\max}$  at service load (at 0.7 ultimate loads) was between 0.00056 to 0.0025, less than the allowable strain according to ACI Committee 363 (0.003) for all columns.

In summary, considering all mechanical and structural tests, it is noted that the best performance was recorded when using hybrid fibers (macro and microfibers). Despite this, the waste fibers recorded a clear improvement in all concrete properties, and the performance of (RCW) was better than (CEW) compared to the reference sample. Moreover, waste disposal is another benefit of using these fibers, as it contributes to reducing environmental damage and thus is considered a promising solution in the field of green concrete technology.

## ACKNOWLEDGEMENT

The authors give their heartfelt thanks to Al-Mustaqbal University College for providing technical support for this research.

## REFERENCES

- [1] Nasr MS, Hussain TH, Najim WN. (2018) Properties of Cement Mortar Containing Biomass Bottom Ash and Sanitary Ceramic Wastes as a Partial Replacement of Cement. *International Journal of Civil Engineering and Technology (IJCIET)*, 9(10): 153-165.
- [2] Tokoda A, Chagweda F. (2020) Formulation Of Fiber Reinforced Concrete. Abou Bekr Belkaid University - Tlemcen, Algeria
- [3] Khan K, Ahmad W, Amin MN et al. (2022) Compressive Strength Estimation of Steel-Fiber-Reinforced Concrete and Raw Material Interactions Using Advanced Algorithms. *Polymers*, 14(15): 3065.
- [4] Cao M, Khan M. (2021) Effectiveness of multiscale hybrid fiber reinforced cementitious composites under single degree of freedom hydraulic shaking table. *Structural Concrete*, 22(1): 535-549.
- [5] Hadi MNS. (2007) Using fibres to enhance the properties of concrete columns. *Construction and Building Materials*, 21(1): 118-125.
- [6] Smarzewski P. (2019) Analysis of failure mechanics in hybrid fibre-reinforced high-performance concrete deep beams with and without openings. *Materials*, 12(1): 101.
- [7] Abdulridha SQ, Nasr MS, Al-Abbas BH, Hasan ZA. (2022) Mechanical and structural properties of waste rope fibers-based concrete: An experimental study. *Case Studies in Construction Materials*, 16e00964.

- [8] Rivera JE, Eid R, Paultre P. (2021) Influence of synthetic fibers on the seismic behavior of reinforced-concrete circular columns. *Engineering Structures*, 228111493. doi: <https://doi.org/10.1016/j.engstruct.2020.111493>.
- [9] Hadi MNS. (2009) Reinforcing concrete columns with steel fibres. *Asian Journal of Civil Engineering*, 10(1): 79-95.
- [10] Ikponmwosa EE, Salau MA. (2011) Effect of short steel fibre reinforcement on laterized concrete columns. *Journal of Sustainable Development*, 4(1): 230.
- [11] Al-Shamma YM. (2011) Strength and Ductility of Confined Steel Fiber Reinforced Concrete Short Columns. MSc. Struct. Eng. Al-Mustansiriya Univ. Baghdad 113
- [12] Mahdi ZR. (2012) Behavior of fiber reinforced high performance concrete columns. Sc Thesis Univ. Technol. Baghdad Iraq
- [13] Balanji EKZ, Sheikh MN, Hadi MNS. (2016) Performance of high strength concrete columns reinforced with hybrid steel fiber under different loading conditions.
- [14] Domski J, Katzer J, Zakrzewski M, Ponikiewski T. (2017) Comparison of the mechanical characteristics of engineered and waste steel fiber used as reinforcement for concrete. *Journal of Cleaner Production*, 15818-28. doi: <https://doi.org/10.1016/j.jclepro.2017.04.165>.
- [15] Samarakoon SMSMK, Ruben P, Wie Pedersen J, Evangelista L. (2019) Mechanical performance of concrete made of steel fibers from tire waste. *Case Studies in Construction Materials*, 11e00259. doi: <https://doi.org/10.1016/j.cscm.2019.e00259>.
- [16] Sofi A, Gopu GN. (2019) Influence of steel fibre, electrical waste copper wire fibre and electrical waste glass fibre on mechanical properties of concrete. In: IOP Conf. Ser. Mater. Sci. Eng. IOP Publishing. p 12023.
- [17] Soulioti D V, Barkoula NM, Paipetis A, Matikas TE. (2011) Effects of fibre geometry and volume fraction on the flexural behaviour of steel-fibre reinforced concrete. *Strain*, 47e535–e541.
- [18] Gao D, Li W, Pang Y, Huang Y. (2021) Behavior analysis and strength prediction of steel fiber reinforced recycled aggregate concrete column under axial compression. *Construction and Building Materials*, 290123278. doi: <https://doi.org/10.1016/j.conbuildmat.2021.123278>.
- [19] Atea RS. (2019) A Case Study On Concrete Column Strength Improvement with Different steel fibers and polypropylene fibers. *Journal of Materials Research and Technology*, 8(6): 6106-6114. doi: <https://doi.org/10.1016/j.jmrt.2019.10.005>.
- [20] BS EN 197-1. (2011) Cement, Composition, Specifications and Conformity Criteria for Common Cements. London, England: British, British Standards Institution-BSI and CEN European Committee for Standardization.
- [21] Iraqi Standard No.45. (1984) Aggregate from Natural Sources for Concrete and Building Construction. Central Organization for Standardization and Quality Control, Baghdad, Iraq.
- [22] ASTM C494/C494M, ASTM 494/C 494M. (2013) Standard Specification for Chemical Admixtures for Concrete. ASTM International, West Conshohocken, PA.
- [23] ASTM A615. (2009) Standard specification for deformed and plain carbon-steel bars for concrete reinforcement. ASTM International, West Conshohocken, PA.
- [24] ACI 363R. (2010) Report on High-Strength Concrete.
- [25] BS 1881: Part 116. (2003) Method for determination of compressive strength of concrete cubes. British Standards Institution, UK.
- [26] ASTM C496. (2011) Standard Test Method for Splitting Tensile Strength of Cylindrical Concrete Specimens. ASTM International, West Conshohocken, PA.
- [27] ASTM C78. (2015) Standard test method for flexural strength of concrete (using simple beam with third-point loading). ASTM International, West Conshohocken, PA.
- [28] Abbass W, Khan MI, Mourad S. (2018) Evaluation of mechanical properties of steel fiber reinforced concrete with different strengths of concrete. *Construction and building materials*, 168556-569.
- [29] Mohammad SA, Krishna TNC, Saketh T, Ganesh CY, Sathyan D. (2022) Fresh and hardened state properties of waste tire fiber and steel fiber reinforced concrete. *Materials Today: Proceedings*, 80: 443–448.

- [30] Dawood ET, Ramli M. (2011) High strength characteristics of cement mortar reinforced with hybrid fibres. *Construction and building materials*, 25(5): 2240-2247.
- [31] Khabaz A. (2016) Monitoring of impact of hooked ends on mechanical behavior of steel fiber in concrete. *Construction and Building Materials*, 113857-863.
- [32] Ramkumar KB, PR KR. (2022) Impact of hybrid steel fibres on fresh and mechanical properties of Self-compacting concrete. *Case Studies in Construction Materials*, 17e01274.
- [33] Sengul O. (2018) Mechanical properties of slurry infiltrated fiber concrete produced with waste steel fibers. *Construction and Building Materials*, 1861082-1091.
- [34] Bhargava P, Sharma UK, Kaushik SK. (2006) Compressive stress-strain behavior of small scale steel fibre reinforced high strength concrete cylinders. *Journal of advanced concrete technology*, 4(1): 109–121.
- [35] Tokgoz S, Dundar C. (2010) Experimental study on steel tubular columns in-filled with plain and steel fiber reinforced concrete. *Thin-Walled Structures*, 48(6): 414-422.  
doi: <https://doi.org/10.1016/j.tws.2010.01.009>.
- [36] Dhanapal J, Jeyaprakash S. (2020) Mechanical properties of mixed steel fiber reinforced concrete with the combination of micro and macro steel fibers. *Structural Concrete*, 21(1): 458-467.
- [37] Naser MH, Naser FH, Dhahir MK. (2020) Tensile behavior of fiber reinforced cement mortar using wastes of electrical connections wires and galvanized binding wires. *Construction and Building Materials*, 264120244.

# KEY SUCCESS FACTORS IN ROAD MAINTENANCE MANAGEMENT PROJECTS (A CASE STUDY OF MAYSAN PROVINCE, IRAQ)

MILAD GHANBARI<sup>1\*</sup> AND ZAID KHALID HASANI<sup>2</sup>

<sup>1</sup>Department of Civil Engineering, East Tehran Branch,  
Islamic Azad University, Tehran, Iran

<sup>2</sup>Department of Project Management and Construction,  
South Tehran Branch, Islamic Azad University, Tehran, Iran

\*Corresponding author: [Milad.ghanbari@srbiau.ac.ir](mailto:Milad.ghanbari@srbiau.ac.ir)

(Received: 17 May 2023; Accepted: 2 September 2023; Published on-line: 1 January 2024)

**ABSTRACT:** Developing roads is a crucial and essential activity, but maintaining them regularly is equally important to improve their performance. A well-maintained road network facilitates economic, industrial, cultural, and social growth. Once the construction phase of a road is complete, its operating phase commences, which is subject to wear and tear due to various factors like traffic and weather conditions. Hence, regular and continuous road maintenance activities are essential to increase the useful life of roads and manage national resources effectively. However, road maintenance management in Iraq, particularly in the province of Maysan, is suffering from poor performance due to the absence of an effective maintenance management system. Therefore, this research aims to identify the critical success factors of road maintenance projects, with a focus on the Maysan province as a case study of Iraq. The study identified and analyzed 27 key success factors in road maintenance projects, which were classified into three groups: management, technical, and resources. Based on the analysis of the literature review and field study in Maysan province, the top five key success factors were determined to be: 1. Adequate funds; 2. Timely payment to contractor and employees; 3. Quality of materials; 4. Use of advanced technology to detect or evaluate road defects; and 5. Communication and coordination among parties.

**ABSTRAK:** Pembangunan jalan adalah sangat penting bagi aktiviti harian, tetapi penyelenggara secara berkala adalah sama penting bagi menambah baik prestasi jalan. Jaringan jalan yang terpelihara membantu dalam ekonomi, industri, budaya, dan perkembangan sosial. Sebaik fasa pembangunan jalan siap, fasa operasi bermula, bergantung pada tahap jalan disebabkan pelbagai faktor seperti trafik dan kondisi jalan. Oleh itu, penyelenggaraan jalan berkala dan berterusan sangat penting kepada jangka hayat jalan dan ianya dapat menyumbang kepada pengurusan sumber negara dengan efektif. Walau bagaimanapun, penyelenggaraan jalan di Iraq, khususnya di daerah Maysan, memiliki kekurangan dalam penyelenggaraan jalan disebabkan oleh ketiadaan sistem pengurusan jalan yang efektif. Oleh itu, kajian ini menumpukan tentang mencari faktor kejayaan penting sesebuah projek penyelenggaraan jalan, sebagai fokus kes kajian ini dipilih di daerah Maysan, di Iraq. Kajian ini merincikan dan menilai 27 kunci kejayaan dalam projek penyelenggaraan jalan di bawah 3 kumpulan: pengurusan, teknikal dan sumber. Berdasarkan analisis dapatan kajian terdahulu dan bidang kajian di daerah Maysan, lima kunci faktor kejayaan didapati dari: 1. Sumber yang mencukupi; 2. Pembayaran tepat kepada kontraktor dan pekerja; 3. Material kualiti; 4. Penggunaan teknologi moden bagi mengesan dan menganalisa kerosakan jalan; dan 5. Komunikasi dan koordinasi antara semua yang terlibat.

**KEYWORDS:** *success factors; project success; road maintenance; project management; performance assessment*

## 1. INTRODUCTION

Developing a country's road network is an essential requirement for societal growth and development [1,2]. By enhancing accessibility and reducing poverty, well-maintained roads can contribute to economic and social development [3].

Although the construction of new roads is expensive, it is vital to maintain them properly to prevent quick deterioration. Poor management of road maintenance will lead to the need for replacement or significant repairs in just a few years [4]. However, with proper planning and prioritization, even small maintenance budgets can make a significant improvement in service quality of road transportation. Road maintenance costs that are neglected will eventually be cost the users and the community rather than the country's budget [5].

Constructing roads with a specific quality and standard requires a significant amount of resources, which are typically provided or managed by the government [6]. However, roads, like other infrastructure assets, are subject to depreciation. The extent of the road deterioration process depends on various factors, including traffic volume, weather conditions, and the maintenance activities implemented for that road. For example, areas with high traffic volumes and severe weather conditions require more frequent and focused maintenance activities [7]. Establishing a road management system leads to planning, monitoring, and effective management of roads [8]. Obtaining information about the technical and financial status of road network maintenance is crucial since it impacts the overall economy of the province or country [3].

The neglect of road maintenance in Iraq has resulted in severe deterioration of the existing road network and has transformed low maintenance costs into significant expenses for renovation and reconstruction. Iraq, as a whole, lacks an efficient road management system and a comprehensive database detailing the maintenance measures undertaken on its roads. Sustaining the service level of infrastructure assets, including roads, and preventing their deterioration necessitates ongoing analysis and planning [9]. The regular and consistent execution of road maintenance activities contributes to prolonging the lifespan of roads and effectively managing national resources, indicating the success of the road maintenance program [10,11]. It is evident that enhancing the quality of existing roads must be carried out within the constraints of financial and technological resources [8].

Determining the success of a project and ensuring that it stays on track in terms of quality, cost, and meeting goals is a crucial aspect of project management. It is important to have knowledge of key factors and tools that can be used to measure, monitor progress and to take appropriate action if a project deviates from the expected path [12].

Due to the significant expenses associated with road construction and its key role in a country's development, coupled with the high maintenance costs, it is crucial to identify and investigate the critical success factors for road maintenance projects. Hence, the primary objective of present research is to study the critical success factors in road maintenance projects, with a focus on the Maysan province as a case study in Iraq.

## 2. LITERATURE REVIEW

The purpose of this section is to identify the elements that play a role in the success of road maintenance projects in Iraq. This entails examining research from different countries,

encompassing both developing and developed nations, along with studies related to various construction project types.

Road maintenance involves a series of regular and periodic activities and techniques that ensure road components (such as pavement, shoulders, slopes, drainage systems, and other technical road facilities) are kept in the in-service condition [4,13].

Kog et al. [14] conducted research on the influence of critical success factors on the budget, schedule, and quality of construction projects. They identified key factors such as senior management support, contractor team competence, and project manager commitment and involvement. Toor and Ogunlana [15] emphasized the importance of studying critical success factors for large-scale projects, which is particularly relevant for road and road maintenance projects as they fall under this category.

Ataei Jafari and Ahmadvand [16] conducted research on the critical success factors of intelligent transportation system (ITS) projects. According to their findings, outsourcing large ITS projects require careful consideration of critical success factors that fall under four categories: organizational, management, environmental, and individual factors. Organizational factors include elements such as organizational trust, adequate resource allocation, supervision, organizational culture, and quality of communications. Management factors include supplier identification and selection, information technology standards, establishing a steering committee, competent project management, human resource management, cost management, and senior management support. Environmental factors encompass laws and regulations, activities of competitors, and government policies. Lastly, individual factors involve technical expertise, flexibility, and user involvement. The successful implementation of ITS requires proper organizational support, efficient project management, and effective communication, which could also be essential for successful road maintenance projects.

According to the research of Li et al. [17] effective communication and cooperation among project participants is a key success factor. Banihashemi et al. [18] emphasized the importance of clear definition of responsibilities, emphasis on high quality work, and the experience and competence of the project manager as crucial success factors for integrating sustainability into projects.

Ghanbari and Mojtahedzadeh Asl [19] state that creating a maintenance checklist can enhance the effectiveness of planning, implementation, and monitoring of maintenance activities. Similarly, according to Chen et al. [20], identifying critical success factors and understanding their interrelationships can assist project managers in focusing on key factors and allocating appropriate resources. Additionally, Williams [21] examined the multidimensionality of success and demonstrated how success factors interact with one another through causal loops.

Osei-Kyei et al. [22] suggest that studying critical success factors is highly beneficial for projects involving public sector participation. Tabish and Jha [23] found that awareness and adherence to laws and regulations are the most important success factors in government projects. Meanwhile, Obeng and Tuffour [24] have researched alternative financing sources for road network maintenance in developing countries. They argue that traditional financing options have become increasingly challenging, and alternative arrangements are necessary since governments are unable to meet their planned expenditure commitments.

Yarmukhamedov et al. [7] examined the effectiveness of competitive bidding and cost efficiency in road maintenance services in Sweden, utilizing econometric methods. The study revealed that the government provider incurred higher costs (8-20%) compared to private

companies. The findings showed that significant savings could be achieved by outsourcing road maintenance services to the private sector through market competition.

A study conducted by McPherson and Bennett [8] explored the critical factors required for the effective implementation of a computerized road management system (RMS). This type of system relies on three fundamental components - processes, people, and technology, which must be supported by adequate funding. The study findings suggested that the absence of any of these components could lead to system failure. The primary objective of an RMS is to assist the road organization in planning and prioritizing road investments.

In a study analyzing urban road maintenance plans in Palestine, Issa and Abu-Eisheh [25] found that 95% of maintenance work was done through foreign contracts, indicating a need for support and equipment for municipalities to carry out basic road maintenance works. Safety is also a crucial success criterion in construction project management, as emphasized in the research of Dann and Fry [26] and Aksorn and Hadikusumo [27]. Additionally, stakeholder management [28] and improving team integrity [29] are also important considerations for project success. Clear definition of responsibilities is also cited as a critical success factor for partnering in construction projects, according to Chan et al. [30].

The utilization of optimization methods enables the identification of the most suitable approach for managing road and pavement maintenance [31,32]. Mahmood et al. [33] introduced a multi-objective particle swarm algorithm for pavement maintenance design. The algorithm can improve maintenance solutions' quality and efficiently analyze large road networks.

Osman and Kimutai [34] conducted a study on the critical success factors in road construction projects in Kenya. They emphasize the importance of officials not only ensuring the availability of guidelines for the contractor selection process but also adhering to them and taking measures to prevent corruption and political influences in contract agreements. The research suggests the establishment of a comprehensive system that maintains and integrates the details and records of road contractors who have previously worked with the government. This system aims to facilitate easy tracking of contractors' performance to minimize the selection of inefficient contractors.

The topic of road management includes the study of performance-based road maintenance contracting (PBRMC) [5,6,35,36]. PBRMC is an effective way to shift the responsibility of road maintenance activities to the private sector. The structure of performance indicators, as well as the penalties and incentives included in the contract, has a significant impact on the overall cost and level of service provided to the public [36]. PBRMCs that are well-designed maintain roads in predefined good conditions at relatively low costs [6].

Shrestha and Shrestha [4] conducted research on change orders in road maintenance contracts in the United States. The study found that there are several reasons for change orders in maintenance projects, such as an incorrect scope of work, errors in estimation, changes in the initial design, changes in material specifications, and failure to confirm the work site conditions before signing the contract.

### **3. ROAD MAINTENANCE STATUS IN MAYSAN**

Maysan province is situated in Iraq and has a network of exit roads in all directions, covering a length of approximately 700 km. The province's road and bridge infrastructure is in critical and difficult conditions due to insufficient budget allocation and financial capacity. The roads are suffering from issues like rutting and creeping in the asphalt layers, which is caused

by several factors such as the lack of control over truckloads and the use of a weak asphalt mixture. To address this issue, axial weighing stations were installed at the entrance of the governorate to regulate the loads and polymer asphalt used. These corrective measures led to a reduction in maintenance work and costs compared to previous periods.

Several successes and failures have been observed in road maintenance and repair projects in Iraq, which provide valuable experiences. To achieve more success in road maintenance projects, it is necessary to conduct a scientific analysis of the key success factors in Maysan's road maintenance projects. The results of this analysis can be beneficial to Iraq's road infrastructure.

## 4. RESEARCH METHOD

### 4.1 Research Conceptual Model

This research is practical in terms of its purpose and descriptive in terms of its research method. Data collection was done through a questionnaire. The study collected 27 key success factors for Iraqi maintenance projects. Section 5 of this article presents the statistical analysis of the model. Figure 1 shows the conceptual model of this research, which identifies the relationship between the key success factors and the success of Iraqi maintenance projects.

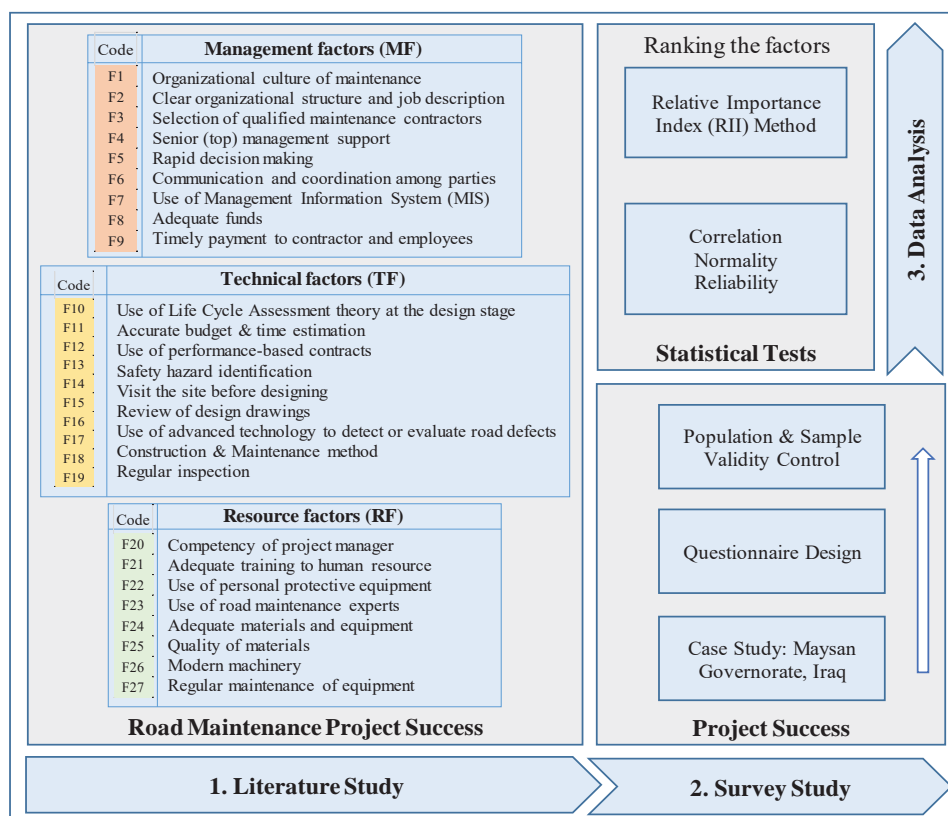


Fig. 1: Conceptual model of the research.

The conceptual model presented in Fig. 1 shows that the classification of key success factors of road maintenance projects is based on three indicators: management factors, technical factors, and resource factors, all of which are independent variables. The dependent variable in this model is the success of road maintenance projects. Then, a questionnaire was created and sent to the road maintenance engineers of Maysan, who were the statistical

population of the research. The questionnaire was developed based on a 5-point Likert scale and 27 factors (which are classified into three groups of managerial, technical, and resource factors). To ensure content validity, the questionnaire was reviewed by two civil engineering university professors, who provided their opinions for the questionnaire.

The data collected from the surveys were analyzed using SPSS 20 software, and then the key success factors were ranked using the Relative Importance Index (RII) method. The sample size of the research is 45, of which 43 road maintenance engineers answered all the questions in the questionnaire, which resulted in a 95% efficiency rate. The demographic characteristics of the respondents are presented in Table 1.

Table 1: Demographic description of respondents

Characteristics	Category	Frequency	Percentage
Age (years)	> 40	12	27.91%
	30-40	27	62.79%
	< 30	4	9.30%
Specialty	Civil engineering	27	62.79%
	Architecture	5	11.63%
	Electricity	4	9.30%
	Mechanics	5	11.63%
	Other	2	4.65%
Experience	> 25	2	4.65%
	15-25	14	32.56%
	10-14	13	30.23%
	6-9	12	27.91%
	3-5	2	4.65%
Education level	PhD	2	4.65%
	Master	12	27.91%
	Bachelor	29	67.44%
Affiliation	Client	28	65.12%
	Consultant	11	25.58%
	Contractor	4	9.30%

## 4.2 Relative Importance Index Method

Previous studies have provided a formula to calculate the RII based on expert questionnaire data, and this formula has been used in this study as well [4,37,38]. The RII formula, shown in Eq. (1), calculates the weight of each factor based on the expert responses:

$$RII = \frac{\sum_{i=1}^I W_i}{A \times N} \quad (1)$$

Table 2: The weighted importance scale of the responses

Option	Not important	Slightly important	Moderately important	Important	Very important
Likert value	1	2	3	4	5
RII value	0 - 0.2	0.2 - 0.4	0.4 - 0.6	0.6 - 0.8	0.8 - 1

The RII values were calculated for each response using Table 2 and Eq. (1). According to Table 2, if the RII value of a factor is greater than 0.6, it is considered a key success factor.

## 5. RESULTS AND DISCUSSION

### 5.1 Statistical Data Screening

The reliability of the questionnaire used in this research was evaluated by computing Cronbach's alpha in SPSS software, which yielded a value of 0.86. As this value is greater than 0.7, it indicates that the measurement tool used in this research is reliable. The normality of the research data was evaluated using the Kolmogorov-Smirnov and Shapiro-Wilk nonparametric tests in SPSS software, and the results showed that the research variables follow a normal distribution, as the deviation from normal distribution was found to be greater than 0.05. Subsequently, Pearson's test was conducted to examine the correlation between variables using SPSS software (see Table 3). A significant correlation was found between the research variables and the success of road maintenance projects, indicating that each group of managerial, technical, and resource factors significantly affects the success of road maintenance projects in Maysan.

Table 3: The result of Pearson's correlation test

		Management	Technical	Resource
<b>Management</b>	Correlation Coefficient	1	0.677	0.605
	Sig. (2-tailed)	.	0	0
	N	43	43	43
<b>Technical</b>	Correlation Coefficient	0.677	1	0.533
	Sig. (2-tailed)	0	.	0
	N	43	43	43
<b>Resource</b>	Correlation Coefficient	0.605	0.533	1
	Sig. (2-tailed)	0	0	.
	N	43	43	43

### 5.2 Factors Ranking

This study examined 27 essential factors for the success of road maintenance projects in Maysan province, and based on the statistical tests and their RII score, all of the factors were identified as crucial factors for success.

#### 5.2.1 Ranking of the Management Factors

According to the survey responses of 43 road maintenance engineers, the top 5 management factors contributing to the success of road maintenance projects are as follows:

- Adequate funds
- Timely payment to contractor and employees
- Communication and coordination among parties
- Selection of qualified maintenance contractors
- Senior (top) management support

The study identified and ranked 9 management factors that were found to be effective in road maintenance project success. Table 4 displays the prioritized list of these factors. The

analysis indicated that the organizational culture of maintenance was ranked the least effective among these factors.

Table 4: Ranking of management factors affecting the success of road maintenance projects

Code	Key Success Factor	RII	Rank
F8	Adequate funds	0.874	1
F9	Timely payment to contractor and employees	0.871	2
F6	Communication and coordination among parties	0.856	3
F3	Selection of qualified maintenance contractors	0.847	4
F4	Senior (top) management support	0.833	5
F5	Rapid decision making	0.791	6
F7	Use of Management Information System (MIS)	0.767	7
F2	Clear organizational structure and job description	0.749	8
F1	Organizational culture of maintenance	0.740	9

### 5.2.2 Ranking of the Technical Factors

Based on the collected responses of 43 road maintenance engineers, the top 5 technical factors in the success of road maintenance projects are:

- Use of advanced technology to detect or evaluate road defects
- Accurate budget & time estimation
- Construction & Maintenance method
- Regular inspection
- Visit the site before designing

Table 5 shows a summary of the ranking of technical factors based on the RII score. The Life Cycle Assessment theory used during the design phase was found to have the least priority in the technical group.

Table 5: Ranking of technical factors affecting the success of road maintenance projects

Code	Key Success Factor	RII	Rank
F16	Use of advanced technology to detect or evaluate road defects	0.865	1
F11	Accurate budget & time estimation	0.851	2
F17	Construction & Maintenance method	0.819	3
F18	Regular inspection	0.819	4
F14	Visit the site before designing	0.800	5
F15	Review of design drawings	0.753	6
F19	Flexibility in different weather conditions	0.749	7
F12	Use of performance-based contracts	0.735	8
F13	Safety hazard identification	0.735	9
F10	Use of Life Cycle Assessment theory at the design stage	0.730	10

### 5.2.3 Ranking of the Resource Factors

According to the analysis of 43 questionnaires, the top five resource factors that contribute to the success of road maintenance projects are as follows:

- Quality of materials
- Modern machinery
- Adequate materials and equipment
- Use of road maintenance experts
- Regular maintenance of equipment

Table 6 presents the prioritized ranking of resource factors based on the RII score obtained from the data analysis of 43 questionnaires. It was found that the use of personal protective equipment was ranked lowest among the resource factors.

Table 6: Ranking of resource factors affecting the success of road maintenance projects

Code	Key Success Factor	RII	Rank
F25	Quality of materials	0.870	1
F26	Modern machinery	0.846	2
F24	Adequate materials and equipment	0.837	3
F23	Use of road maintenance experts	0.833	4
F27	Regular maintenance of equipment	0.823	5
F20	Competency of project manager	0.800	6
F21	Adequate training to human resource	0.753	7
F22	Use of personal protective equipment	0.721	8

### 5.2.4 Top Ten Success Factors

The top 10 key factors that influence the success of road maintenance projects are presented in Table 7. The ranking chart of these factors based on their RII scores is illustrated in Fig. 2. According to the findings of the research, incorporating these 10 factors can lead to more successful road maintenance and repair projects.

Table 7: Ranking of resource factors affecting the success of road maintenance projects

Code	Key Success Factor	Category	RII	Rank
F8	Adequate funds	Management factors (MF)	0.874	1
F9	Timely payment to contractor and employees	Management factors (MF)	0.871	2
F25	Quality of materials	Resource factors (RF)	0.870	3
F16	Use of advanced technology to detect or evaluate road defects	Technical factors (TF)	0.865	4
F6	Communication and coordination among parties	Management factors (MF)	0.856	5
F11	Accurate budget & time estimation	Technical factors (TF)	0.851	6
F3	Selection of qualified maintenance contractors	Management factors (MF)	0.847	7
F26	Modern machinery	Resource factors (RF)	0.846	8
F24	Adequate materials and equipment	Resource factors (RF)	0.837	9
F4	Senior (top) management support	Management factors (MF)	0.833	10

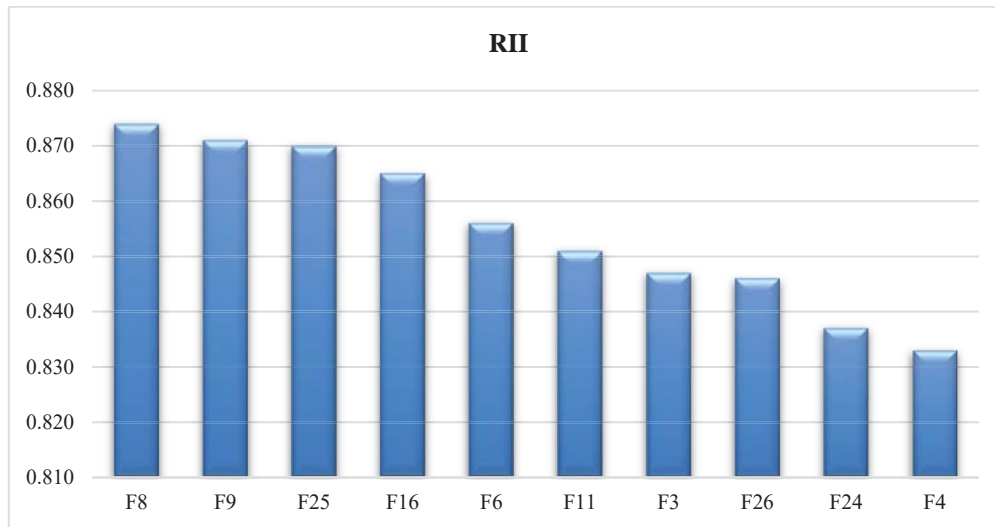


Fig. 2: Bar chart of RII score of top ten key success factors in road maintenance projects in Maysan province.

This research suggests several key factors for successful road maintenance projects, based on the results obtained. The first important factor is the systematic allocation of maintenance budget and timely payment of invoices to contractors and workforce. Negligence in budgeting can cause delays in completing maintenance plans. The second key factor is the quality of equipment and materials used, which requires continuous improvement planning and efforts. The third factor is the use of advanced technologies to accurately detect road defects in a timely manner. The fourth factor is effective communication and coordination among project organizations. The fifth factor is accurate budget estimation for the project to avoid time and cost overruns. The sixth factor is the selection of efficient road maintenance contractors with strict implementation of qualification assessment. The seventh factor is the use of modern and well-maintained machines to increase project productivity. Lastly, continuous monitoring of road maintenance sites is essential to ensure safety and quality improvement.

## 6. CONCLUSION

The significance of maintenance in systems with components that undergo wear and tear during operation is undeniable. Every year, a significant portion of Iraq's budget is allocated to the construction of new roads, while the maintenance of existing roads is neglected. Apart from the very low maintenance budget, the lack of an efficient road maintenance program has caused the failure of maintenance projects. Achieving success in road maintenance projects necessitates thorough planning. Considering the deterioration of Iraq's road infrastructure and the ineffective utilization of resources in maintenance projects, there is an immediate need to explore the critical factors that contribute to the successful execution of these projects.

The aim of this study is to recognize and prioritize the critical factors that lead to the success of road maintenance projects in Maysan province. To achieve this goal, the researchers initially identified 27 key success factors of road maintenance projects that were classified into three groups: management, technical, and resources, based on previous research. Following this, a questionnaire was developed, consisting of 27 questions, and was circulated among road maintenance engineers in Maysan. The data gathered from the questionnaires underwent statistical tests to assess normality, reliability, and correlation to ensure the precision and accuracy of the data. Finally, the relative importance index (RII) method was employed to

analyze the data, and the results indicated that all 27 key success factors had a significant impact on the success of road maintenance projects in Maysan.

Based on the study, the top 10 critical factors for the success of road maintenance projects are: 1) adequate funds, 2) timely payment to contractors and employees, 3) quality of materials, 4) use of advanced technology to detect or evaluate road defects, 5) communication and coordination among the involved parties, 6) accurate budget and time estimation, 7) selection of qualified maintenance contractors, 8) use of modern machinery, 9) adequate materials and equipment, and 10) senior management support.

To further research road maintenance, it is suggested to explore the dynamic management of road network maintenance through the system dynamics method. Additionally, studying the use of artificial intelligence in road maintenance management, particularly for detecting and evaluating road defects, is also recommended.

## ACKNOWLEDGEMENT

The authors would like to acknowledge the respondents of the questionnaires.

## REFERENCES

- [1] Villalba-Romero F, Liyanage C. (2016) Evaluating success in PPP road projects in Europe: a comparison of performance measurement approaches. *Transportation Research Procedia*, 14: 372-381.
- [2] Ghanbari M, Mehr AG, Nehzat H. (2015) Introducing an intelligent transportation system decision support model for the highways in Iran based on fuzzy logic. *International Journal of Soft Computing and Engineering*, 5(5): 101-104.
- [3] Sewell SJ, Desai SA, Mutsaa E, Lottering RT. (2019) A comparative study of community perceptions regarding the role of roads as a poverty alleviation strategy in rural areas. *Journal of Rural Studies*, 71: 73-84.
- [4] Shrestha KK, Shrestha PP. (2019) Change orders on road maintenance contracts: Causes and preventive measures. *Journal of Legal Affairs and Dispute Resolution in Engineering and Construction*, 11(3): 04519009.
- [5] Anastasopoulos PC, McCullouch BG, Gkritza K, Mannering FL, Sinha KC. (2010) Cost savings analysis of performance-based contracts for highway maintenance operations. *Journal of Infrastructure Systems*, 16(4): 251-263.
- [6] Mehany MSHM, Guggemos AA. (2016) Risk-Managed Lifecycle Costing for Asphalt Road Construction and Maintenance Projects Under Performance-Based Contracts. *ASCE-ASME Journal of Risk and Uncertainty in Engineering Systems, Part A: Civil Engineering*, 2(4): 05016001.
- [7] Yarmukhamedov S, Smith AS, Thiebaud JC. (2020) Competitive tendering, ownership and cost efficiency in road maintenance services in Sweden: A panel data analysis. *Transportation Research Part A: Policy and Practice*, 136: 194-204.
- [8] McPherson K, Bennett CR. (2006) Success Factors for Road Management Systems. *Transport Notes Series; No. TRN 29*. © World Bank, Washington, DC. <http://hdl.handle.net/10986/11777> License: CC BY 3.0 IGO.
- [9] Shrestha PP, Shrestha KK, Kandie TK. (2017) Effects of change orders on the cost and schedule of rural road maintenance projects. *Journal of Legal Affairs and Dispute Resolution in Engineering and Construction*, 9(3): 04517010.
- [10] Abdurrahman MA, Samang L, Adisasmitha SA, Ramli MI. (2015) Modeling and determining urban road priority rank for maintenance program based on multi-criteria decision making in Makassar City, Indonesia. *Traffic*, 1, B3.
- [11] Nautiyal A, Sharma S. (2021) Condition Based Maintenance Planning of low volume rural roads using GIS. *Journal of Cleaner Production*, 312: 127649.

- 
- [12] Hauashdh A, Jailani J, Rahman IA. (2021) Structural equation model for assessing factors affecting building maintenance success. *Journal of Building Engineering*, 44: 102680.
- [13] Ouma YO, Opudo J, Nyambenya S. (2015) Comparison of fuzzy AHP and fuzzy TOPSIS for road pavement maintenance prioritization: methodological exposition and case study. *Advances in Civil Engineering*, vol. 2015, 12-28. <https://doi.org/10.1155/2015/140189>
- [14] Kog YC, Loh PK. (2012) Critical success factors for different components of construction projects. *Journal of Construction Engineering and Management*, 138(4): 520-528.
- [15] Toor SUR, Ogunlana SO. (2009) Construction professionals' perception of critical success factors for large-scale construction projects. *Construction Innovation*, 9(2): 149-167.
- [16] Ataei Jafari AM, Ahmadvand AM. (2018) Identification of Pattern used in Determination of Critical Success Factors in ITS Projects, Case Study: Road Maintenance and Transportation Organization. *International Journal of Transportation Engineering*, 5(4): 319-330.
- [17] Li Y, Song H, Sang P, Chen PH, Liu X. (2019) Review of Critical Success Factors (CSFs) for green building projects. *Building and Environment*, 158: 182-191.
- [18] Banihashemi S, Hosseini MR, Golizadeh H, Sankaran S. (2017) Critical success factors (CSFs) for integration of sustainability into construction project management practices in developing countries. *International Journal of Project Management*, 35(6): 1103-1119.
- [19] Ghanbari M, Mojtahedzadeh Asl M. (2021) Proposing a Building Maintenance Management Framework to Increase the Useful Life of the Building. *International Journal of Industrial Engineering and Management Science*, 8(1): 52-61.
- [20] Chen YQ, Zhang YB, Liu JY, Mo P. (2012) Interrelationships among critical success factors of construction projects based on the structural equation model. *Journal of Management in Engineering*, 28(3): 243-251.
- [21] Williams T. (2016). Identifying success factors in construction projects: A case study. *Project Management Journal*, 47(1): 97-112.
- [22] Osei-Kyei R, Chan AP. (2017) Implementing public-private partnership (PPP) policy for public construction projects in Ghana: critical success factors and policy implications. *International Journal of Construction Management*, 17(2): 113-123.
- [23] Tabish SZS, Jha KN. (2011) Identification and evaluation of success factors for public construction projects. *Construction Management and Economics*, 29(8): 809-823.
- [24] Obeng DA, Tuffour YA. (2020) Prospects of alternative funding sourcing for maintenance of road networks in developing countries. *Transportation Research Interdisciplinary Perspectives*, 8: 100225.
- [25] Issa A, Abu-Eisheh S. (2017) Evaluation of implementation of municipal roads' maintenance plans in Palestine: A pilot case study. *International Journal of Pavement Research and Technology*, 10(5): 454-463.
- [26] Dann S, Fry ML. (2009) Benchmarking road safety success: Issues to consider. *Australasian marketing journal*, 17(4): 226-231.
- [27] Aksorn T, Hadikusumo BH. (2008) Critical success factors influencing safety program performance in Thai construction projects. *Safety Science*, 46(4): 709-727.
- [28] Yang J, Shen GQ, Ho M, Drew DS, Chan AP. (2009) Exploring critical success factors for stakeholder management in construction projects. *Journal of Civil Engineering and Management*, 15(4): 337-348.
- [29] Nawi MNM, Lee A, Kamar KAM, Hamid ZA. (2012) Critical success factors for improving team integration in Industrialised Building System (IBS) construction projects: The Malaysian case. *Malaysian Construction Research Journal*, 10(1): 45-63.
- [30] Chan AP, Chan DW, Chiang YH, Tang BS, Chan EH, Ho KS. (2004) Exploring critical success factors for partnering in construction projects. *Journal of Construction Engineering and Management*, 130(2): 188-198.
- [31] Jesus M, Akyildiz S, Bish DR, Krueger DA. (2011) Network-level optimization of pavement maintenance renewal strategies. *Advanced Engineering Informatics*, 25(4): 699-712.
- [32] Jorge D, Ferreira A. (2012) Road network pavement maintenance optimisation using the HDM-4 pavement performance prediction models. *International Journal of Pavement Engineering*, 13(1): 39-51.
-

- [33] Mahmood M, Mathavan S, Rahman M. (2018) A parameter-free discrete particle swarm algorithm and its application to multi-objective pavement maintenance schemes. *Swarm and Evolutionary Computation*, 43: 69-87.
- [34] Osman MA, Kimutai G. (2019) Critical success factors in the implementation of road projects in Wajir County, Kenya. *International Academic Journal of Information Sciences and Project Management*, 3(3): 73-104.
- [35] Sultana M, Rahman A, Chowdhury S. (2013) A review of performance based maintenance of road infrastructure by contracting. *International Journal of Productivity and Performance Management*, 62(3): 276-292.
- [36] Abu Samra S, Osman H, Hosny O. (2017) Optimal maintenance and rehabilitation policies for performance-based road maintenance contracts. *Journal of Performance of Constructed Facilities*, 31(1): 04016075.
- [37] Shahsavand P, Marefat A, Parchamijalal M. (2018) Causes of delays in construction industry and comparative delay analysis techniques with SCL protocol. *Engineering, Construction and Architectural Management*, 25(4): 497-533.
- [38] Zidane YJT, Andersen B. (2018) The top 10 universal delay factors in construction projects. *International Journal of Managing Projects in Business*, 11(3): 650-672.

## EFFECTS OF SOIL ERODIBILITY ON RIVERBANK EROSION AND FAILURES

NUR AQILAH MOHD ROSLI<sup>1</sup>, SAERAHANY LEGORI IBRAHIM<sup>1\*</sup>  
AND SITI HAJAR YUSOFF<sup>2</sup>

<sup>1</sup>Department of Civil Engineering, Kulliyah of Engineering,  
International Islamic University Malaysia, Kuala Lumpur, Malaysia

<sup>2</sup>Department of Electrical and Computer Engineering, Kulliyah of Engineering,  
International Islamic University Malaysia, Kuala Lumpur, Malaysia.

\*Corresponding author: [saerahany@iium.edu.my](mailto:saerahany@iium.edu.my)

(Received: 11 August 2023; Accepted: 4 November 2023; Published on-line: 1 January 2024)

**ABSTRACT:** Riverbank erosion is a natural process of removal of earthen materials from the bank surface. The process of riverbank erosion that is induced naturally results in the formation of landforms such as valleys, canyons, and productive floodplains. However, riverbank erosion can also be considered a hazard when the process occurs at an alarming rate causing loss of land. The extent of erosion depends on many factors. One of the main factors responsible for riverbank erosion is the soil erodibility which is the resistance of soil to erosion. The aim of this study is to quantify the riverbank erosion rates and the potential magnitude of riverbank erosion in order to generate an empirical predictive model to estimate riverbank erosion from physical and geomorphic variables for rivers susceptible to riverbank erosion. Several models were trained using the Regression Learner application in MATLAB software. Models that include soil erodibility parameters perform better than the models without the soil erodibility parameters. The model with the highest accuracy was found to be Model 2, with Root Mean Square Error (RMSE) of 3.70E-08 and coefficient of determination,  $R^2$  of 0.55. The model produced in this study will be helpful to analyze and predict the effects of riverbank erosion and assist in the development of bank stabilization solution.

**ABSTRAK:** Hakisan tebing sungai adalah proses semula jadi terhadap penyingkiran bahan tanah dari permukaan tebing. Proses hakisan tebing sungai yang terjadi secara semula jadi ini mengakibatkan pembentukan bentuk muka bumi seperti lembah, ngarai dan dataran banjir yang produktif. Bagaimanapun, hakisan tebing sungai juga boleh dianggap sebagai ancaman apabila proses berlaku pada kadar membimbangkan sehingga menyebabkan kehilangan tanah. Tahap hakisan bergantung pada banyak faktor. Salah satu faktor utama yang menyebabkan hakisan tebing sungai adalah kebolehhakisan tanah iaitu ketahanan tanah terhadap hakisan. Kajian ini bertujuan untuk mengukur kadar hakisan tebing sungai, mengkaji potensi magnitud hakisan tebing sungai dan menghasilkan model ramalan empirik bagi menganggarkan hakisan tebing sungai daripada pembolehubah fizikal dan geomorfik bagi sungai yang terdedah kepada hakisan tebing sungai. Beberapa model telah dilatih menggunakan aplikasi *Regression Learner* dalam perisian MATLAB. Dapatan menunjukkan model yang mengandungi parameter kebolehhakisan tanah adalah lebih baik berbanding model tanpa parameter kebolehhakisan tanah. Model 2 didapati mempunyai ketepatan tertinggi dengan ralat punca min kuasa dua (RMSE) sebanyak 3.70E-08 dan pekali penentuan,  $R^2$  sebanyak 0.55. Model dalam kajian ini dapat membantu dalam analisa berkaitan kesan hakisan tebing sungai dan penyelesaian kepada pembangunan kestabilan tebing.

**KEYWORDS:** *riverbank erosion; soil erodibility; erosion pin; Sungai Pusu*

## 1. INTRODUCTION

Riverbank erosion is a complex phenomenon which has garnered the attention of people all over the world. Riverbank erosion as defined by [1] is the removal of earth materials from the bank of a river. It is a geological process in which earthen materials from the bank of a river get detached and enter the receiving water body. Riverbank erosion can be a slow-paced process and can also occur at an alarming rate which leads to severe loss of bank material. It is an unpredictable hazard which has severe impacts on the land and people nearby.

Riverbank erosion studies are crucial to determine the rate of erosion due to fluvial entrainment and bank instability. In Malaysia, research conducted on riverbank erosion are limited due to the complexity of the fieldwork investigations which consist of measurement of riverbank erosion, soil properties and flow condition. Prediction of the magnitude of erosion using existing equations obtained from previous research that deals with rivers outside Malaysia may produce unfavorable results due to the difference in soil properties and river characteristics. Besides, most of the research conducted mostly focused on the surface erosion which utilizes the Universal Soil Loss Equation (USLE) method to determine the soil erodibility [2-4]. However, this method is not best suited for riverbank erosion investigation. In recent years, research conducted on riverbank erosion mostly utilizes remote sensing data to predict the riverbank erosion rate [5-7]. By using only remote sensing data, not all factors governing riverbank erosion will be included in the model development. Field riverbank measurements need to be conducted to properly investigate all the variables affecting riverbank erosion including flow parameters, riverbank geometry, and soil properties and characteristics to incorporate them into the riverbank erosion rate prediction.

The degree of riverbank erosion is dependent on various factors. Soil erodibility is one of the factors that plays a significant role in determining the rate of riverbank erosion. Soil erodibility is the soil's resistance to erosion based on the physical characteristics of each soil [8]. It is one of the major factors that govern the rate of riverbank erosion. The physical properties of soil that influence erodibility are aggregate size, particle size distribution, bulk density, water content, and temperature [9]. The erodibility of soil also varies with soil structure, stability, shear strength, aggregates, soil depth, soil organic matter, bulk density and chemical constituents [10]. In general, soil with high erodibility factor may be eroded much more easily compared to soil with low erodibility factor. Low erodibility soil has higher resistance to both detachment and transport process.

The aim of this study is to quantify the rates of riverbank erosion and generate a model to estimate riverbank erosion from physical and geomorphic variables for rivers susceptible to riverbank erosion. In this study, ascertaining the effects of soil erodibility to riverbank erosion and failures by comparing the riverbank erosion prediction model, which incorporates soil erodibility parameters, with models that exclude the soil erodibility parameters is attempted.

## 2. STUDY AREA AND METHODOLOGY

The study area is Sungai Pusu which has a total length of approximately 4.1 kilometers and flows through the International Islamic University Malaysia (Gombak campus) before it joins Sungai Gombak. Sungai Pusu is currently classified as a Class IV River, which is regarded as the worst river water quality condition according to Malaysian water quality standards [11]. Riverbank erosion is also prominent at several sections of the river. Figure 1 shows the flow path of Sungai Pusu and the selected fieldwork sites. A total of four sections of the riverbank were selected where it is deemed suitable and accessible for field measurements and data

collection. Table 1 shows the geographical coordinates of all the selected bank sections of Sungai Pusu.

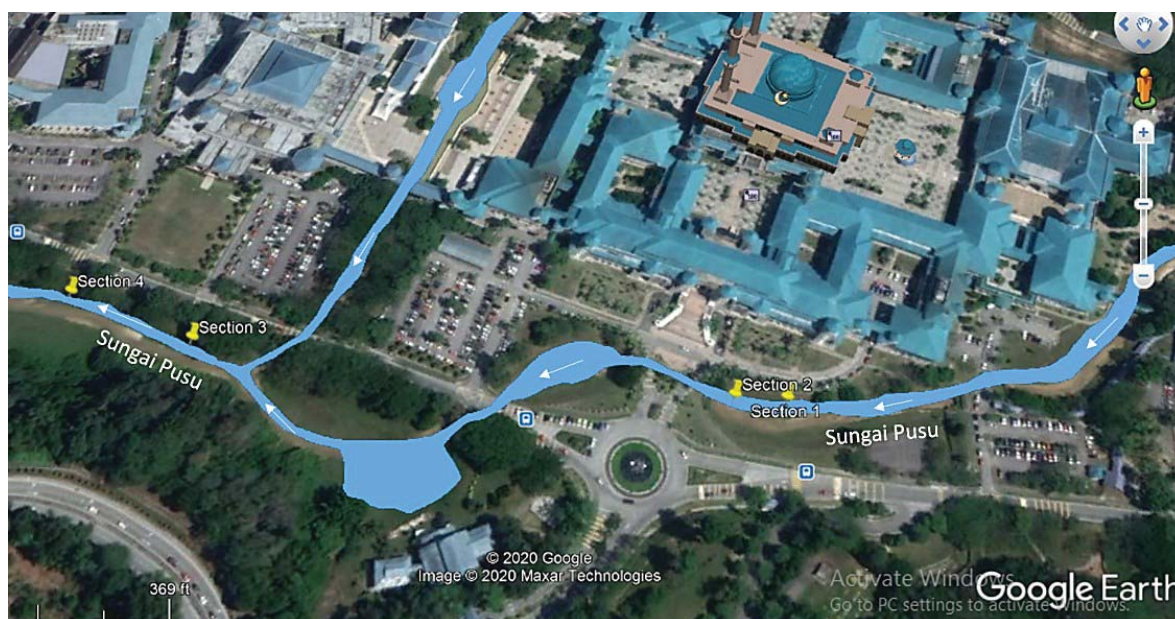


Fig. 1: Sungai Pusu flowing through the International Islamic University Malaysia, Gombak campus.

Table 1: Coordinate of sections

Section no.	Coordinate
1	3°15'01"N 101°43'52"E
2	3°15'00"N 101°43'55"E
3	3°14'59"N 101°44'05"E
4	3°14'59"N 101°44'07"E

Figure 2 shows the riverbank of the selected sections of Sungai Pusu. Riverbank erosion features were observed at a few stretches of the river. Distinct signs of sedimentation were also discovered along the riverbank. The length of each section is approximately 10 to 15 meters.

A significant amount of erosion can be seen at the riverbank from the figure above. Based on field observation, it is evident that several parts of the river have considerable amount of erosion which could eventually lead to problems in the future. Additionally, distinct signs of sedimentation were observed along the river network. High concentration of sediments in the river have also caused floods, the worst of which was recorded specifically in 2014 at the International Islamic University Malaysia, Gombak campus [12].

## 2.1 Field Measurement

Field measurements were carried out to obtain the data needed to investigate riverbank erosion. The process included measurement of the erosion rate, soil erodibility, riverbank cross-section and bank geometry, river flow velocity and collection of soil samples. The cross-section and riverbank geometry were established through measurement and surveys. The data that were measured in the field includes river width, depth, riverbank angle, and riverbank height. Flow velocities were measured using a current meter each time the measurement of erosion pins was taken.

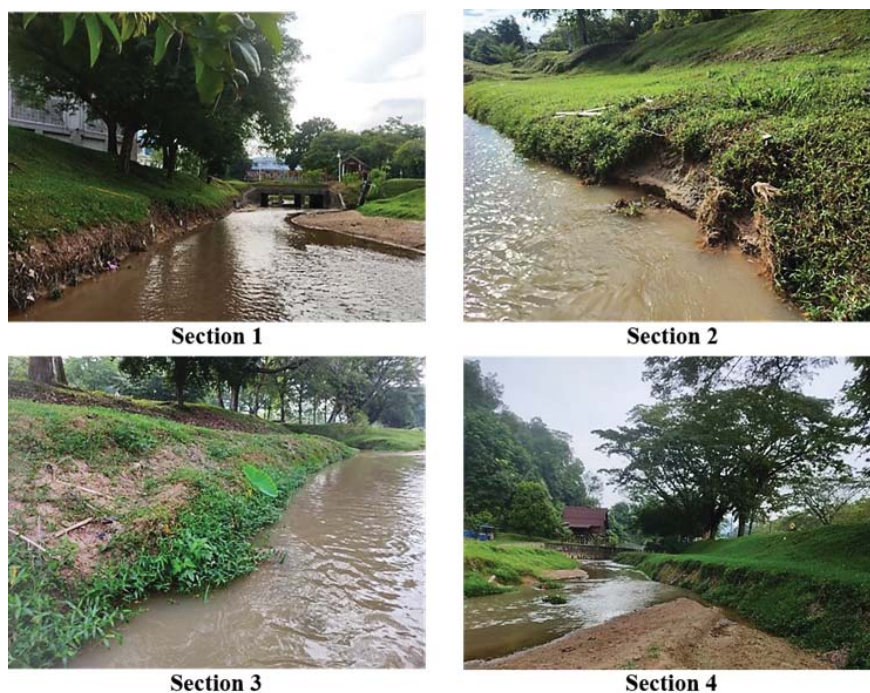


Fig. 2: Selected sections of Sungai Pusu.

## 2.2 Erosion Pins Method

The method that was used for measurement of the riverbank erosion rate was the erosion pin method. Numerous publications have emphasized the advantages of employing erosion pins. Erosion pins are an economical way to quantify erosion and deposition rates of soil [13]. This method can easily be employed without having to use any special equipment and the erosion pins themselves are relatively low cost. Erosion pins have high sensitivity where small changes in bank retreat can be measured using erosion pins. Figure 3 shows the erosion pins installed at the riverbank of Sungai Pusu.



Fig. 3: Erosion pins installed at the site.

Erosion pins were installed at the left and right bank for all the selected sections of the river. The ideal length of the pin is between 0.30 to 0.50 meters [14]. Erosion pins with a length of 60 cm were used in a recent study that was conducted to estimate rates of riverbank erosion for Sungai Bernam [15]. In this study, mild steel rods that were 60 cm long and 6 mm in diameter were utilized. The pin diameter in this study was selected to be as small as possible to avoid material disturbance and minimize public visibility. Selection of the pin length depends on the expected rate of erosion, the frequency of site visits, and pin resetting. The pins

were inserted horizontally into the bank leaving out only 10 cm from the total length of the pin. The end of the pins were labeled with numbers to ease the pin measurement process. A total of 140 pins were installed at the site. Figure 4 shows the schematic diagram of the erosion pins arrangement.

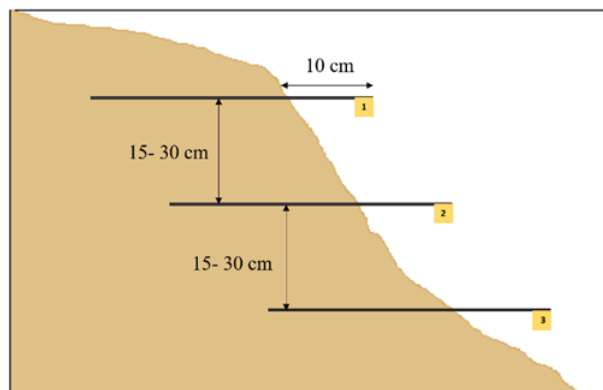


Fig. 4: Schematic diagram of the erosion pins arrangement.

The pins were arranged in a grid pattern along the river sections, spaced evenly at one-meter intervals and vertically at intervals of between 15 and 30 cm, depending on the height of the bank. Each site consisted of 10 to 15 plots with 3 pins installed at each plot. As erosion proceeds, more and more of rod will be exposed.

### 2.3 Soil Sampling

A total of 10 soil samples were collected from the selected bank sections of Sungai Pusu using a hand auger. The number of soil samples to be collected depends on the variation of soil at the site. Based on previous study, a total of 10 to 13 samples is considered sufficient to study the soil properties of the river [16-19]. The soil samples collected were sent to the laboratory to conduct soil testing. In this study, sieve analysis, a hydrometer test, an Atterberg limits test, and a bulk density test were conducted to determine mean particle diameter,  $d_{50}$ , the percentage of silt, sand, and clay in the soil composition, plasticity index, bulk density, and soil porosity.

### 2.4 Soil Erodibility Coefficient Determination

The soil erodibility coefficients were computed using the equation by [20]. The equation shows the correlation between critical shear stress and clay-silt fraction.

$$\tau_c = 0.1 + 0.1779 (SC\%) + 0.0028 (SC\%)^2 - 2.343 \times 10^{-5} (SC\%)^3 \quad (1)$$

Where  $\tau_c$  is the critical shear stress and SC% is the combined percentage of clay and silt. After calculating the critical shear stress, the soil erodibility coefficient was determined using the empirical correlation found by [21].

$$k_d = 0.2 \tau_c^{-0.5} \quad (2)$$

Where  $k_d$  is the soil erodibility coefficient ( $\text{cm}^3/\text{N-s}$ ).

### 2.5 Dimensional Analysis

Dimensional analysis was performed to determine the relationship between variables that influence riverbank erosion rate and reduce the number of variables for subsequent analysis. The variables involved in quantifying the riverbank erosion were grouped into five categories namely bank geometry, hydraulic characteristic, soil characteristics and properties and others. Table 2 shows the selected variables used in the dimensional analysis and the categories.

Table 2: Selected variables for dimensional analysis

Categories	Variables	Symbol	Units	Fundamental quantities
Riverbank erosion rate	Erosion rates	$\xi$	m/s	LT <sup>-1</sup>
Hydraulic characteristics	Near bank velocity	$u_b$	m/s	LT <sup>-1</sup>
	Fall velocity	$\omega$	m/s	LT <sup>-1</sup>
	Water depth	D	m	L
Bank geometry	Bank height	$h_b$	m	L
	Bank angle	$\beta$	-	-
	Bankfull width	B	m	L
Soil characteristics and properties	Mean particle density	$d_{50}$	m	L
	Porosity	P	-	-
	Plasticity index	PI	-	-
	Critical shear stress	$\tau_c$	N/m <sup>2</sup>	ML <sup>-1</sup> T <sup>-2</sup>
	Erodibility coefficient	$k_d$	m <sup>3</sup> /N-s	
Others	Particle density	$\rho_s$	kg/m <sup>3</sup>	ML <sup>-3</sup>
	Water density	$\rho_w$	kg/m <sup>3</sup>	ML <sup>-3</sup>

Functional relationships addressing riverbank erosion rates were established using Buckingham's Pi Theorem. There were fourteen (14) variables and three fundamental dimensions selected in the relationship. As the number of variables, n is 14, and the number of fundamental dimensions, m is 3, the number of dimensionless groups will be 11. The selection of repeating variables to be used in the dimensional analysis was based on the guidelines from previous study [22] which are as follows; (1) The repeating variables must not be able to form a dimensionless group by themselves; (2) The repeating variables must represent all the fundamental quantities in the study which are M, L and T; (3) The repeating variables should not have the same dimensions or dimensions that differ by only an exponent ; (4) Whenever possible, simple variables should be selected over complex variables. Table 3 shows the different sets of repeating variables selected in this study.

Table 3: Repeating variables

No	Repeating variables
1	$u_b, \rho_w, h_b$
2	$u_b, \rho_w, d_{50}$
3	$u_b, \rho_w, D$

There is a total of three sets of repeating variables which yield three sets of functional relationship between the parameters. In order to form the dimensionless groups or also called as  $\pi$ -term, each non-repeating variable is multiplied to repeating variables that are raised to an exponent. Typically, it takes the form of  $x_i x_1^a x_2^b x_3^c$ , where a, b, and c are determined through calculations to make the combination dimensionless. The example of calculation for the  $\pi$ -term is as follows;

For repeating variables:  $u_b, d_{50}, \rho_w$

$$\begin{aligned} \pi_1 &= \xi u_b^a \rho_w^b d_{50}^c \\ &= M^0 L^0 T^0 \end{aligned}$$

Substitute the dimensions,

$$M^0 L^0 T^0 = (LT^{-1})^{a^1} (ML^{-3})^{b^1} (L)^{c^1}$$

$$a^1 = -1$$

$$b^1 = 0$$

$$c^1 = 0$$

$$\pi_1 = \frac{\xi}{u_b}$$

The calculations were then repeated for the other  $\pi$ -terms. The functional relationship derived from the dimensional analysis were presented in the result and discussion section.

## 2.6 Regression Learner

Different models were trained using the Regression Learner app in the MATLAB software to develop a model to estimate rates of riverbank erosion. Regression Learner is an app that can interactively train and validate regression models to predict data. There are many model type options such as linear regression, regression tree, Gaussian process regression, support vector machines, ensembles of regression tree and neural network regression models. Using the parallel pool, these multiple models can be trained at a time and be compared side to side to validate the errors. The best model with the lowest Root Mean Square Error (RMSE) and the highest R-squared value were selected.

## 3. RESULTS AND DISCUSSION

Dimensional analysis was utilized to identify significant dimensionless numbers for the riverbank erosion process. The potential variables governing the riverbank erosion process were grouped into five categories: riverbank erosion rate, bank geometry, hydraulic characteristics and soil characteristics and properties. The parameters for hydraulic characteristic include near-bank velocity,  $u_b$ , fall velocity,  $\omega$ , and water depth,  $D$ . The parameters for bank geometry consist of bank height,  $h_b$ , bank angle,  $\beta$ , and bankfull width,  $B$ . The parameters for soil characteristics and properties include mean particle diameter,  $d_{50}$ , particle specific gravity, porosity,  $p$ , plasticity index,  $PI$ , critical shear stress,  $\tau_c$  and erodibility coefficient,  $k_d$ . The Buckingham  $\pi$  theorem is applied to obtain all sets of dimensionless parameters from the selected variables. The riverbank erosion rate,  $\xi$  serves as the dependent variable. The dimensional analysis performed in this study yields several functional relationships using different sets of repeating variables.

Table 4 shows the sets of repeating variables and the respective functional relationships for the dimensional analysis performed using all 14 variables from all parameter categories. Table 5 shows the established functional relationship by performing dimensional analysis using the variables from the hydraulic characteristic and bank geometry categories only. Two sets of repeating variables were selected which results in two sets of functional relationship. This step was conducted in order to determine the significance of soil parameters in the riverbank erosion prediction. In order to do so, the training result for models which include soil parameters and models that exclude soil parameters will be compared.

Different regression models were trained using the Regression Learner application available in MATLAB software. A total of 220 data from field observations were used in the model development. The data were split into training and testing data by a ratio of 70:30. After running the data through several different models, models that showed best fit were extracted

and compared. The process was then repeated for the other equations. The model’s accuracy was measured using the R-squared ( $R^2$ ) and Root Mean Squared Error (RMSE) value. RMSE is the standard deviation of residuals or prediction error. It is used to measure the average magnitude of error in the predicted value. The RMSE value is measured in the same unit as the independent variables or the predictor. Generally, the lower the value of RMSE, the better is the model performance. Meanwhile,  $R^2$ , also known as coefficient of determination, gives an indication of the model fits. High  $R^2$  value indicates that the model has good fits for the dataset. Table 6 shows the training results for the trained regression models for Eqs. 3 - 5.

Table 4: Repeating variables and its functional relationship (Eqs. 3 - 5)

Equation No.	Repeating Variables	Functional Relationship
3	$u_b, \rho_w, h_b$	$\frac{\xi}{u_b} = f\left(\frac{B}{h_b}, \frac{D}{h_b}, \frac{d_{50}}{h_b}, \beta, \frac{\tau_c}{\rho_w u_b^2}, p, PI, \frac{\omega}{u_b}, \frac{\rho_s}{\rho_w}, \frac{gh_b}{u_b^2}, u_b \rho_w k_d\right)$
4	$u_b, \rho_w, d_{50}$	$\frac{\xi}{u_b} = f\left(\frac{B}{d_{50}}, \frac{D}{d_{50}}, \frac{h_b}{d_{50}}, \beta, \frac{\tau_c}{\rho_w u_b^2}, p, PI, \frac{\omega}{u_b}, \frac{\rho_s}{\rho_w}, \frac{gd_{50}}{u_b^2}, u_b \rho_w k_d\right)$
5	$u_b, \rho_w, D$	$\frac{\xi}{u_b} = f\left(\frac{B}{D}, \frac{d_{50}}{D}, \frac{h_b}{D}, \beta, \frac{\tau_c}{\rho_w u_b^2}, p, PI, \frac{\omega}{u_b}, \frac{\rho_s}{\rho_w}, \frac{gD}{u_b^2}, u_b \rho_w k_d\right)$

Table 5: Repeating variables and its functional relationship (Eqs. 6 and 7)

Equation No.	Repeating Variables	Functional Relationship
6	$u_b, \rho_w, h_b$	$\frac{\xi}{u_b} = f\left(\frac{B}{h_b}, \frac{D}{h_b}, \beta, \frac{\rho_s}{\rho_w}, \frac{gh_b}{u_b^2}\right)$
7	$u_b, \rho_w, D$	$\frac{\xi}{u_b} = f\left(\frac{B}{D}, \frac{h_b}{D}, \beta, \frac{\rho_s}{\rho_w}, \frac{gD}{u_b^2}\right)$

Table 6: Training results for Eqs. 3 - 5

Functional Relationship	Model No.	Model Type	Equation Type	RMSE	R-squared
Functional Relationship 1 (3)	1	Stepwise Linear Regression	Stepwise Linear	4.27E-08	0.43
	2	Ensemble	Boosted tree	3.70E-08	0.55
	3	Ensemble	Bagged tree	4.13E-08	0.47
Functional Relationship 2 (4)	4	Linear Regression	Linear	4.71E-08	0.31
	5	Stepwise Linear Regression	Stepwise linear	4.21E-08	0.45
	6	Ensemble	Boosted tree	4.60E-08	0.34
Functional Relationship 3 (5)	7	Linear Regression	Linear	4.83E-08	0.28
	8	Stepwise Linear Regression	Stepwise Linear	4.66E-08	0.33
	9	Ensemble	Boosted tree	4.87E-08	0.28

Among the models trained, Model 2 which showed the lowest RMSE value and highest R-squared value were selected as the best model. The RMSE and R-squared values are respectively 3.70E-08 and 0.55.

Table 7 shows the training results for the trained model using equation 6 and equation 7. Model 15 was selected as the best models among the other six models as it has the lowest RMSE value and the highest R<sup>2</sup> value. The RMSE and R<sup>2</sup> value are 4.63E-08 and 0.33 respectively.

Table 8 shows the comparison of training results for the selected models for the functional relationship that includes parameters from the soil characteristics and the equation that exclude the variables from that particular category. Both models have the same model type which is the Ensemble boosting model. Ensemble Boosting is a well-known ensemble learning approach used to improve the performance and accuracy of machine learning systems. The fundamental idea behind the boosting technique is the sequential addition of additional models to the ensemble. Weak learners are efficiently boosted to strong learners in this ensemble [23]. Most of the weak models do not perform well on their own mostly because they contain high bias. The final strong model is created by combining all of the weak learners by weighted majority voting [24,25].

Table 7: Training results for Eqs. 6 and 7

Functional Relationship	Model No.	Model Type	Equation Type	RMSE	R-squared
Functional Relationship 1 (6)	10	Linear Regression	Linear	5.16E-08	0.16
	11	Ensemble	Bagged tree	4.88E-08	0.25
	12	Ensemble	Boosted tree	4.86E-08	0.26
Functional Relationship 2 (7)	13	Linear Regression	Linear	5.11E-08	0.18
	14	Ensemble	Bagged tree	4.89E-08	0.25
	15	Ensemble	Boosted tree	4.63E-08	0.33

Table 8: Comparison of training results for Model 2 and Model 15

Model	Functional Relationship	Model Type	Equation Type	RMSE	R-squared
2	$\frac{\xi}{u_b} = f\left(\frac{B}{h_b}, \frac{D}{h_b}, \frac{d_{50}}{h_b}, \beta, \frac{\tau_c}{\rho_w u_b^2}, p, PI, \frac{\omega}{u_b}, \frac{\rho_s}{\rho_w}, \frac{gh_b}{u_b^2}, u_b \rho_w k_d\right)$	Ensemble	Boosted tree	3.70E-08	0.55
15	$\frac{\xi}{u_b} = f\left(\frac{B}{D}, \frac{h_b}{D}, \beta, \frac{\rho_s}{\rho_w}, \frac{gD}{u_b^2}\right)$	Ensemble	Boosted tree	4.63E-08	0.33

It can be seen from the result that models which include soil characteristic and properties perform better compared to the models which include only hydraulic characteristic and bank geometry parameters. The R-squared value for Model 2 was significantly higher compared to Model 15. The RMSE value of Model 2 is also lower compared to Model 15 which signifies that the error in predicted value is also smaller.

The performance of the selected trained model was assessed using the predicted vs actual response plot, residual plot and the performance of test set. The predicted vs actual response plot is a visual representation of the actual and predicted values. Fig. 5 shows the predicted vs true graph for Model 2.

The model that performed well should have the predicted values scattered near the diagonal line. To obtain a perfect regression model, all the points must be on the line. The error of the prediction is equal to the vertical distance from the line to any given point. The vertical distance from the line to any point is the error of the prediction for that point. The residual plots are presented in Fig. 6 which shows the error functions of the model.

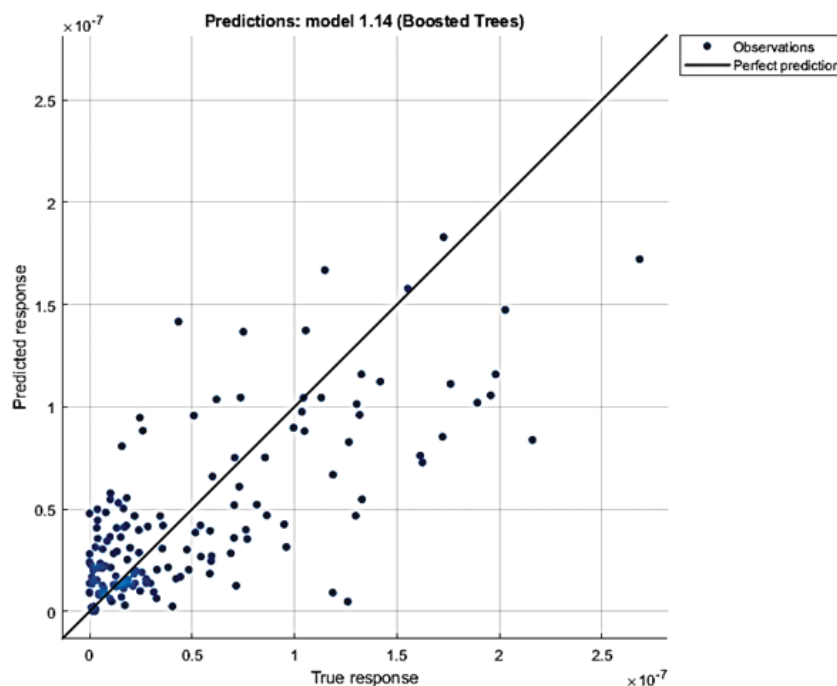


Fig. 5: Predicted vs True Graph for Model 2.

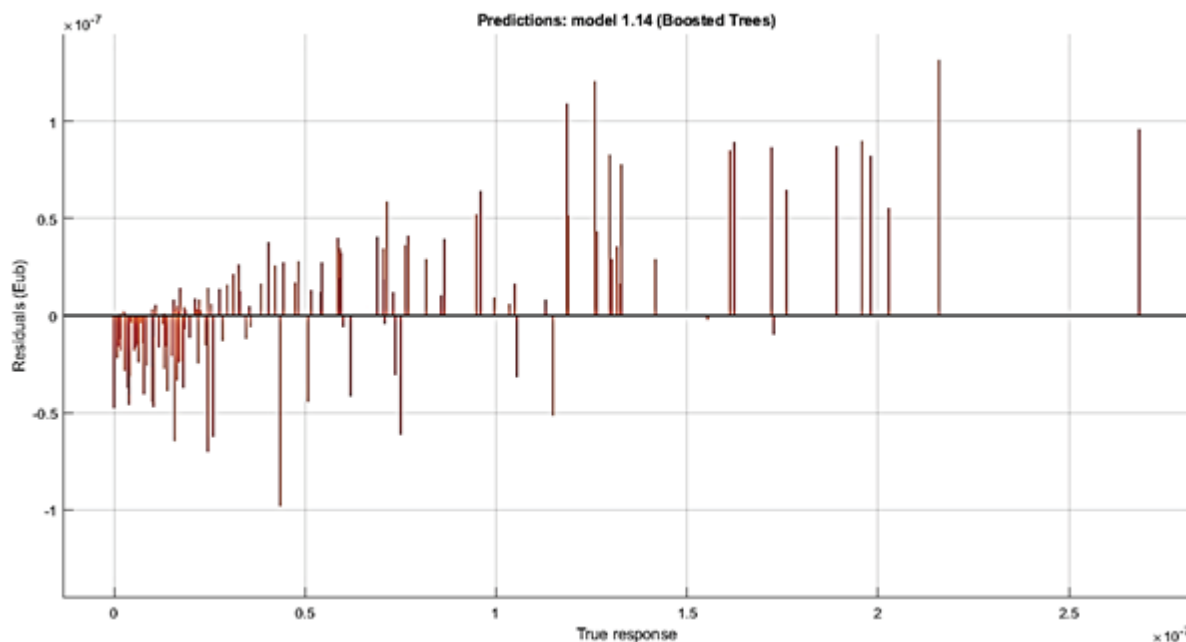


Fig. 6: Residual Plots of Model 2.

The graph explains how far away the predicted values are compared to the true values. The horizontal line at the position  $y=0$  represents the True values scales. The further the points from

the line, the less accurate the predicted values. Based on Fig. 5 and Fig. 6, it can be seen that the model gives better prediction for lower values of riverbank erosion. One of the possible reasons is that the higher value of erosion rate is the bank erosion that is caused by bank failures which occurs only when there is a storm event. In order to improve the models, it might be better to separate the data for grain by grain erosion and bank failure and train the models separately. However, in this study, there is not enough data for the model to be trained separately and thus all the riverbank erosion rates are combined and trained in a single model.

The model was also validated using test set to assess the performance. A total number of 66 data were used for model verification. The comparison between the training and testing results is shown in Table 9.

Table 9: Comparison of training and testing result

	Root Mean Square Error (RMSE)	Coefficient of Determination, R <sup>2</sup>
Training data	3.70E-08	0.55
Testing data	3.88E-08	0.51

There should be a good agreement between the training and testing results. It is normal for the training accuracy to be slightly higher than testing accuracy. From the table, it can be seen that the R<sup>2</sup> value for training and testing model does not differ greatly. Table 10 shows the model performance of published studies on riverbank erosion prediction for rivers in Malaysia.

Table 10: Model performance of published studies on riverbank erosion prediction for rivers in Malaysia

Source	Method of Data Collections	Model Type	Model Performance
Saadon et al. [26]	Field measurement and erosion pins	Non-linear Multiple Regression	Coefficient of determination, R <sup>2</sup> = 0.422
Saadon et al. [27]	Field measurement and erosion pins	NARX-QR Factorization Model	Coefficient of determination, R <sup>2</sup> = 0.740

The result from this research was compared with results with published studies with similar methods of data collections and variables selected for model training. The table suggests that the model performance obtained from this study falls within the range of R<sup>2</sup> value obtained by previous study which uses similar methodology in terms of data collections. It is quite challenging to produce a riverbank erosion rate predictive model with high accuracy using the field measurement method as there are some limitations to it such as loss of erosion pins that could lead to missing data. Models that are generated using remote sensing data usually yield higher accuracy. However, field measurement is better suited for small rivers such as Sungai Pusu as the data from remote sensing will not be as accurate due to geometric distortion. This kind of error greatly affects the results obtained for small rivers.

#### 4. CONCLUSION

In conclusion, the aims of the study have been achieved. This research was carried out to quantify the riverbank erosion rates at Sungai Pusu, through field measurement and to generate a model that incorporates soil erodibility parameters to estimate riverbank erosion for a river that is susceptible to erosion.

It can be seen from the result that Model 2, which incorporates parameters from the soil characteristics and properties category performed better compared to the Model 15 which excluded the soil characteristics and properties variables. Model 2 has a significantly higher  $R^2$  value and lower RMSE value. Model 2 was selected as the best model with RMSE of 3.70E-08 and  $R^2$  value of 0.55. The model produced will be helpful to predict the riverbank erosion for river susceptible to bank erosion.

Future improvement of this research can be made to further refine the results obtain from the research. This study mostly focused on soil physical properties such as mean particle diameter, soil composition, porosity, plasticity index, specific gravity, critical shear stress, and soil erodibility coefficient. Other soil parameters such as soil organic matter, infiltration capacity, stability and chemical constituents can be studied further to develop a more accurate predictive model to estimate bank erosion rate using soil properties.

## ACKNOWLEDGEMENT

This research was financially supported by Fundamental Research Grant Scheme for Research Acculturation of Early Career Researches (FRGS-RACER), Research Project no. (RACER/1/2019/TK01/UIAM//2) entitled “Formulation of Empirical Equation for Quick Riverbank Erosion Prediction”.

## REFERENCES

- [1] Chatterjee S, Mistri B. (2013) Impact of riverbank erosion on human life: A Case Study in Shantipur Block, Nadia District, West Bengal. *International Journal of Humanities and Social Science Invention*, 2(8): 108-111.
- [2] Chadli K. (2016) Estimation of soil loss using RUSLE model for Sebou watershed (Morocco). *Modeling Earth Systems and Environment*, 2: 1-10.
- [3] Karas E, Oguz I. (2015) A new approach to determine land use planning and soil conservation measures based on soil erosion classification. *Carpathian Journal of Earth and Environmental Sciences*, 10(2): 145-158.
- [4] Lastoria B, Miserochi F, Lanciani A, Monacelli G. (2008) An estimated erosion map for the Aterno-Pescara river basin. *European Water*, 21(22): 29-39.
- [5] Mohamad NB. (2017). Riverbank erosion assessment using GIS approach at Kilim Geoforest Park, Langkawi.
- [6] Suhaimi HM, Jamal MH, Ahmad A. (2018) Assessment of riverbank erosion at Kilim River, Langkawi using geospatial technique. In *IOP Conference Series: Earth and Environmental Science*: June 2018. IOP Publishing; pp 012012.
- [7] Mohamad N. (2019) Evaluation of riverbank erosion based on mangrove boundary changes identification using multi-temporal satellite imagery. Master Thesis. Universiti Teknologi Malaysia, Faculty of Built Environment & Surveying.
- [8] Andoh HF, Antwi BO, Wakatsuiki T, Eric TA. (2012) Estimation of soil erodibility and rainfall erosivity patterns in the agroecological zones of Ghana. *Journal of Soil Science and Environmental Management*, 3(11): 275-279.
- [9] Ibrahim SL, Ariffin J, Abdullah J, Muhamad NS. (2016) Jet Erosion Device (JED) – Measurement of soil erodibility coefficients. *Jurnal Teknologi (Sciences & Engineering)*, 5(5): 63-67.
- [10] Musa JJ, Anijofor SC, Obasa P, Avwevuruvwe JJ. (2017) Effects of soil physical properties on erodibility and infiltration parameters of selected areas in Gidan Kwano.
- [11] Nuruzzaman M, Al-Mamun A, Salleh MNB. (2017) Challenges in the rehabilitation of the Pusu River. *International Journal of Conservation Science*, 8(1): 121-130.

- 
- [12] Al Mamun A, Salleh MN, Nuruzzaman M, Dom NM, Amin MZM, Eusuf MA, Chowdhury AJK. (2016) Impact of improper land use changes on flash flood and river system—a case of Sg Pusu. *ARPN J. Eng. Appl. Sci*, 11: 5372-5379.
- [13] Kearney SP, Fonte SJ, García ED, Smukler SM. (2017) Improving the utility of erosion pins: absolute value of pin height change as indicator of relative erosion. *Catena*.
- [14] Lawler DM. (1993) The measurement of riverbank erosion and lateral channel change: A Review. *Earth Surface Processes and Landforms*, 18: 777-821.
- [15] Saadon A, Abdullah J, Muhammad NS, Ariffin J, Julien PY. (2021) Predictive models for the estimation of riverbank erosion rates. *Catena*, 196: 104917.
- [16] Islam MS, Hoque F. (2014) Riverbank erosion of the Surma River due to slope failure. *Int J Res Innov Earth Sci*, 1(2): 54-58.
- [17] Kimiaghalam N, Clark SP, Ahmari H. (2016) An experimental study on the effects of physical, mechanical, and electrochemical properties of natural cohesive soils on critical shear stress and erosion rate. *International Journal of Sediment Research*, 31(1): 1-15.
- [18] Hasan M, Quamruzzaman C, Rahim A, Hasan I, Methela NJ, Imran SA. (2018) Determination of river bank erosion probability: Vulnerability and risk in southern shoreline of Bangladesh. *International Journal of Energy and Sustainable Development*, 3(3): 44-51.
- [19] Bhowmik M, Das N, Das C, Ahmed I. (2018) Bank material characteristics and its impact on river bank erosion, West Tripura district, Tripura, North- East India, 115(8): 1571-1576.
- [20] Julian JP, Torres R. (2006) Hydraulic erosion of cohesive riverbanks. *Geomorphology*, 76: 193-206.
- [21] Hanson GJ, Simon A. (2001) Erodibility of cohesive streambeds in the loess area of the midwestern USA. *Hydrological Processes*, 15: 23-38.
- [22] Yunus AC, John MC. (2006) *Fluid mechanic and fundamentals and applications*. McGraw-Hill, New York. ISBN 978-007-125640.
- [23] Zounemat-Kermani M, Batelaan O, Fadaee M, Hinkelmann R. (2021) Ensemble machine learning paradigms in hydrology: A review. *Journal of Hydrology*, 598:126266.
- [24] Schapire RE. (2003) The boosting approach to machine learning: An overview. *Nonlinear estimation and classification*, 149-171.
- [25] Alfaro E, Gamez M, Garcia N. (2013) adabag: An R package for classification with boosting and bagging. *Journal of Statistical Software*, 54: 1-35.
- [26] Saadon A, Ariffin J, Abdullah J, Daud NM. (2016) Dimensional analysis relationships of streambank erosion rates. *Jurnal Teknologi*, 78(5).
- [27] Saadon A, Abdullah J, Muhammad NS, Ariffin J. (2020) Development of riverbank erosion rate predictor for natural channels using NARX-QR Factorization model: a case study of Sg. Bernam, Selangor, Malaysia. *Neural Computing and Applications*, 32: 14839-14849.

## COMPARISON OF THE MECHANICAL PERFORMANCE OF DENSE GRADING AND POROUS GRADING MIXTURE UTILIZED WITH CRUMB RUBBER MODIFIED BINDER

NOOR YUSRIAH ESA, WAN NUR AIFA WAN AZAHAR\*,  
NORHIDAYU KASIM, NUR KHAIRIYAH BASRI

*Department of Civil Engineering, Kulliyah of Engineering,  
International Islamic University Malaysia, Kuala Lumpur, Malaysia*

*\*Corresponding author: aifa@iium.edu.my*

*(Received: 21 August 2023; Accepted: 25 October 2023; Published on-line: 1 January 2024)*

**ABSTRACT:** Pavement and road networks play a very huge role in everyone's daily lives to connect from one point to another point. With globalization, growth in the economy, and development, the number of vehicles traveling each day on the road increases rapidly over the years. Thus, the constant application of heavy loads together with Malaysia's climatic factors lead the pavement to be susceptible to deterioration such as potholes and cracking. The service life and resistance of the pavement to deterioration can be improved with the incorporation of crumb rubber modified binder (CRMB) for asphaltic pavement. Hence, the objective of this research is to do a comparative evaluation of the mechanical performance of the CRMB that is utilized in dense grading and porous grading mixtures with varying percentage of crumb rubber replacement. The experimental portion of the research was done by substituting the crumb rubber at the replacement percentages of 12%, 14%, 16% and 18% (from the weight of asphalt binder) in preparing the modified binder that was further evaluated by conducting physical testing (penetration and softening point test). Then, the mechanical evaluation of dense and porous grading asphalt mixtures incorporating the crumb rubber was performed with Marshall stability and flow prior to comparing the strength performance for both asphalt mixtures. Based on the result obtained, it was found that the highest percentage of crumb rubber replacement, which is 18%, would give the highest level of stiffness and softening point on the binder. Furthermore, from the Marshall test, it was established that 16% of crumb rubber replacement on asphaltic binder is the most optimum for a porous mixture, given that the CRMB is 5% of the total mix. Nonetheless, at the same 16% of crumb rubber replacement, the value for Marshall test on the dense mixture shows an adverse result when compared to the control. Hence, it was concluded that the mechanical performance of CRMB utilized with porous mixtures shows more impressive results compared CRMB utilized with dense mixtures.

**ABSTRAK:** Turapan dan rangkaian jalan raya memainkan peranan besar dalam kehidupan harian setiap orang dalam berhubung dari tempat ke tempat lain. Melalui globalisasi dan pertumbuhan ekonomi dan pembangunan, bilangan kenderaan bergerak setiap hari di atas jalan raya telah meningkat mendadak beberapa tahun kebelakangan ini. Oleh itu, beban berat berterusan bersama-sama faktor iklim Malaysia menyebabkan turapan jalan terdedah kepada kerosakan seperti jalan berlubang dan keretakan. Jangka hayat perkhidmatan dan rintangan turapan terhadap kerosakan jalan boleh diperbaiki melalui turapan asfaltik yang diubah suai dengan pengikat serbuk getah (CRMB). Justeru, kajian ini bertujuan bagi membanding prestasi mekanikal CRMB yang digunakan dalam campuran penggedan padat dan campuran berliang dengan peratusan penggantian serbuk getah berbeza. Kajian dijalankan dengan menggantikan serbuk getah pada peratusan penggantian pada 12%, 14%, 16% dan 18%

(daripada berat pengikat asphalt) dalam menyediakan bahan pengikat yang diubah suai dan seterusnya dinilai melalui ujian fizikal (ujian takat penembusan dan takat lembut). Kemudian, penilaian mekanikal dijalankan ke atas campuran serbuk getah bersama asphalt bergred padat dan berliang. Kajian dijalankan mengguna pakai ujian kestabilan dan aliran Marshall sebelum membandingkan prestasi kekuatan bagi kedua-dua campuran asphalt. Keputusan menunjukkan dapatan peratusan pada 18% memberikan tahap kekakuan dan takat lembut tertinggi pada bahan penggantian pengikat serbuk getah. Tambahan, ujian Marshall menunjukkan 16% daripada penggantian serbuk getah pada pengikat asphaltik adalah paling optimum pada campuran berliang, di mana 5% daripada jumlah campuran merupakan CRMB. Namun, ujian Marshall pada campuran padat dengan penggantian serbuk getah 16% yang sama, menunjukkan dapatan nilai buruk berbanding pada kawalan. Oleh itu, prestasi mekanikal CRMB yang digunakan bersama campuran berliang menunjukkan dapatan lebih mengagumkan berbanding CRMB yang digunakan melalui campuran padat.

---

**KEYWORDS:** *crumb rubber modified binder (CRMB); dense grading; porous grading mixture*

## 1. INTRODUCTION

In line with the rapid growth of Malaysia's population and economy, pavement or roadways serve for 24 hours per day and 7 days per week as a medium for the road users to perform daily responsibilities or duties. As the massive loads from vehicles are constantly applied onto the pavement together with Malaysia's tropical climate factor and copious rainfall, this has consequently caused the pavement to be very much susceptible to deterioration and degradation over the years throughout its in-service life. Examples of the common deteriorations that can be seen in Malaysia's pavement are potholes and cracking. Although some maintenance and restoration to the pavement can be done, this will require great expense to the government if constant rehabilitation work needs to be done. Thus, a modification on the binder at this point would be worth its expense to increase the strength and the resistance of pavement to rutting and cracking. Polymer is one of the examples of binder modifier that could enhance the properties of the asphalt binder and pavement. Nonetheless, some types of polymers can be quite expensive and not cost effective to cater to this issue. Hence, modification of asphaltic binder by using recycled tire rubber is introduced to tackle the deterioration issue without compromising on the enhancement effect to the pavement [1].

According to the author of [2], the incorporation of crumb rubber with asphalt binder extends the service life of roads and intensifies the adhesion of aggregates, ultimately leading to better strength and stability, and reducing the risk of stripping. Moreover, the Arizona Department of Transportation (ADOT), which conducted an observation on asphalt rubber pavement for 30 years, stated that asphalt rubber pavement expands resistance to deformation, diminishes the chance of reflective cracking, contributes to the desired rutting and smoothness which is below 0.25 inches and below 93 inches per mile respectively, as well as improves on noise reduction properties. These conclusions are supported with the findings from [3], who reported that the combination of crumb rubber and asphalt binder would produce a modified binder with higher fatigue and rutting resistance based on the higher value of the complex shear modulus,  $G^*$  achieved. This leads to the enhancement of  $G^*/\sin \delta$  and  $G^* \times \sin \delta$  which respectively represent rutting resistance and fatigue resistance. Furthermore, as established by [4], the modification of asphalt binder through replacement with crumb rubber also could contribute to the noise reduction that occurs due to tire and pavement interaction. Noise is reported to be reduced by 2.5 dB for vehicles that are driven at 50 mph on the pavement with CRMB. The noise reduction arises due to the "cushion" effect provided by the swelling of the

crumb rubber, thus leading to the reduction of noise of around 3-5 dB [5]. In terms of physical properties, superior results are recorded for the enhancement of stiffness and softening points with the increased content of crumb rubber, thus validating the credibility of crumb rubber as a binder modifier.

In order to incorporate crumb rubber with asphalt binder, there are two methods that can be adopted namely, the dry method and wet method. These two processes are known to produce different end products of asphalt rubber pavement in terms of the performance and properties [1]. The dry method is achieved by adding the shredded tire rubber to replace the fine aggregate, where the crumb rubber is introduced to the aggregate before the asphalt binder is added to the mixture. As for the wet method, the crumb rubber particles are first incorporated and blended together with the asphalt binder at 175-200 °C for 45 to 60 minutes before aggregate is introduced to the mixture.

However, it was reported by the author of [6] that the CRMB may have exceptional field performance, but its effects may be diminished due to the poor design, varying properties of CRMB, and poor construction practices. Furthermore, the research findings claimed that the performance of the CRMB may be dependent on the crumb rubber size, surface area, percentage of replacement, time, and temperature for the mixing process, as well as the aggregate gradation used. Previous findings only focused on the conventional mixture, which is dense graded, without considering porous grading which is usually applied to reduce water runoff on the pavement surface. Porous graded mixtures should be emphasized since they comprise different aggregate gradings that might exhibit diverse interaction effects with crumb rubber and eventually affect the mixture performance.

Thus, this research paper intends to determine the performance of modified asphalt binder containing crumb rubber while comparing the effect of mechanical performance for different types of gradation utilized with crumb rubber in modified binder. The investigation on the mechanical performance of modified binder with crumb rubber in different gradations of dense and porous mixture is significant since functional effect of the crumb rubber as a modifier will differ in dense and porous asphalt mixture gradations, since they comprise different properties inside the bituminous mixture.

## 2. METHODOLOGY

As the main focus of this research is to assess the performance of modified binder rather than modified aggregate, thus the wet method is implemented to introduce the crumb rubber into the asphaltic mixture. The crumb rubber that is first obtained from end-of-life tires (ELTs) is ground to form crumb rubber powder and sieved through a 300 µm mesh to obtain a specific size that passes through the sieve. This ensures the usage of only fine crumb rubber size. This is vital, as finer crumb rubber size would lead to better storage stability and prevent the segregation of crumb rubber. Furthermore, smaller crumb rubber size also would lead to a higher rate of interaction between the crumb rubber and asphalt binder [1,7,8]. In this laboratory work, asphalt binder with a penetration grade of PEN 60/70 was used as a control sample. Binder source was supplied from Eksklusif Alfa Enterprise Company located in Shah Alam, Selangor, Malaysia. Basic physical and rheological properties of the binder were tested to meet all standard requirements. Upon preparing CRMB stock with a percentage of crumb rubber replacement of 12%, 14%, 16% and 18% (from the weight of asphalt binder), the physical properties for each of the modified binders with CRMB were tested via the penetration and softening point test and the results were then compared with the control binder. The small scale of replacement percentage of crumb rubber was selected since this modifier is categorised

under the polymer group, even small content would contribute to superior strength that could improve the rutting resistance in the mixture. It is predicted that large amount replacement of crumb rubber gives adverse impact of strength which leads to cracking deterioration thus reducing the mechanical performance of the asphalt mixture.

Before incorporating the asphaltic binder with aggregate, some tests and checks must be executed to evaluate the performance and liability of the aggregates by performing aggregate properties testing. In order to check on the aggregates' resistance towards abrasion and crushing, Los Angeles Abrasion test and Aggregate Crushing value test were conducted. Both tests were conducted according to ASTM C131-96 and ASTM D5821, respectively.

Next, 5% of CRMB stocks was then mixed with the aggregate to form modified asphaltic mixes incorporating crumb rubber, in which, each of the CRMB percentages would have two samples where one sample is for dense mixture while the other sample is for porous mixture. For the dense mixture, gradation size AC 14 is utilized while for the porous mixture, Grading B is used. For the mixing of the asphaltic binder and aggregate, the aggregates were first heated at 110 °C. Then, the asphaltic binder and aggregate were mixed homogeneously at 160 °C for both the dense mixture and the porous mixture. After ensuring the aggregates were well coated, the sample was transferred into the mould and tamped manually for 15 blows per layer using steel rod. The samples were then compacted using a manual compactor for 75 blows per face for dense mixture and 50 times blow per face for porous mixture. The compacted sample was left for 24 hours at room temperature and then extracted from the moulds. Later, the samples were tested for the mechanical performance through the Marshall stability and flow test.

## **2.1 Penetration Test**

The penetration test was carried out according to ASTM D5-97. A penetration test is a physical property test conducted to analyse the consistency of the asphaltic binder. Asphaltic binders are known to have a viscous property; hence the test is conducted to check on whether the binder has a high level of viscosity and stiffness or low level of viscosity with high fluidity. The test was done by firstly heating the bitumen until it liquidized and became sufficiently fluid to be poured into a sample container. Any air bubbles that formed in the asphalt were eliminated by stirring it. The samples were then kept at ambient temperature for a day before transferring them into a transfer dish and submerging them in a water bath. Then, the sample was removed from the water bath, and was ready to be tested with the penetrometer machine. After placing the sample right on the penetrometer, the needle was carefully adjusted and brought in contact with the surface of the sample. The penetrometer reading was adjusted to zero and the needle was released for exactly 5 seconds. Lastly, the readings were then recorded in tenths of millimeters and the test was repeated thrice to obtain the average penetration value and improve the accuracy of the penetration result.

## **2.2 Softening Point Test**

The softening point test was conducted in accordance with ASTM D36-95, as shown in Fig. 1. The softening point test was conducted to attain the specific temperature at which the asphaltic binder would achieve a specific degree of softening. During the sample preparation, the metal rings and the glass surface were coated with glycerin to prevent the asphalt binder from adhering to it. As the asphalt binder liquidized, the sample was then poured into a ring that was placed on top of a glass surface. After waiting for the asphalt binder to cool down and stiffen at the ambient room temperature for 30 minutes, the excess asphalt was removed using a heated spatula. The ring and ball apparatus were assembled, and the beaker was filled with distilled water beyond the upper surface of the rings. To reach a starting temperature of 5 °C, the beaker was filled with ice and the steel balls were immersed into the water as well for them

to have the same starting temperature. As the water was maintained at the desired starting temperature for 15 minutes, the balls were then placed at the center of the ring. The beaker containing the samples was then heated while ensuring uniform heat distribution in the beaker. Lastly, the temperature at which the asphalt binder melts and reaches the bottom plate was recorded and the data was graphically presented for proper result analysis.



Fig. 1: Softening point equipment testing.

### 2.3 Los Angeles Abrasion Value Test

The Los Angeles abrasion test, was performed based on ASTM C131-96 in order to evaluate on the resistance of the aggregate to abrasion, crushing, and degradation. This test was performed using a rotating steel drum to simulate the way aggregate was going to be impacted in real life situations during the mixing and compaction or during the in-service time when loads are applied on it. For the test procedure, the aggregate samples and the steel spheres (charge) were placed into the rotating drum and the machine was rotated at a speed of 30 to 33 r/min for 500 revolutions. Then, the aggregate was removed from the drum, and it was sieved through sieve no. 12. The weight of aggregate retained on the sieve was recorded to find the difference between the retained weight and the original weight of the aggregates in terms of percentage for the LA abrasion loss value.

### 2.4 Aggregate Crushing Value Test

Similar to the Los Angeles abrasion test, the aggregate crushing test was conducted to determine its resistance to crushing. However, for this test, different equipment was utilized, where compressive load was applied to the aggregate. The procedure was done according to ASTM D 5821. Prior to the aggregate test, the aggregates were filtered through sieves with size openings of 12.5 mm and 10 mm. For this test, only aggregates that passed the 12.5 mm sieve but retained on the 10 mm sieve were utilized. A steel cylinder was filled with aggregates until they met 1/3 of its height and the cylinder was slowly compacted with a tamping rod for 25 blows per layer. More layers of aggregate were added until the cylinder are fully filled with aggregates, the samples were then weighed. Next, the plunger was inserted into the steel cylinder and positioned so that it would rest horizontally on top of the aggregate. By using the compression machine, a compressive load of around 393 kN for 10 minutes was applied to the sample. Upon finishing, the aggregates were removed from the steel cylinder, and it was sieved through a sieve with openings of 2.36 mm. Lastly, the weight of the aggregate that retained on the sieve was recorded.

## 2.5 Marshall Test

Marshall stability and flow test, as depicted in Fig. 2, was performed by first letting the asphaltic mixture cure at ambient room temperature after the compaction process. During the curing, the asphaltic binder had to be placed on a smooth flat surface to ensure consistent thickness throughout the mold. The checking of the bulk specific gravity and the specimen thickness had to be made 24 hours after the compaction using the ASTM D2726 and ASTM D3549, respectively. The cured asphaltic mixture was then soaked in a water bath for 30 to 40 minutes at 60 °C. The sample was then removed from the water bath and placed on the lower segment of the testing head and the assembly of the overall machine completed. The flowmeter was placed over the guide rods, adjusted to zero, the flowmeter sleeve was released, and the micrometer dial reading was recorded.



Fig. 2: Marshall testing.

Upon receiving the results of Marshall stability and Marshall flow for each of the samples, the results for Marshall stiffness were computed based on the formula below.

$$\text{Marshall stiffness} = \frac{\text{Marshall stability (kN)}}{\text{Marshall flow (mm)}}$$

All of the results were then tabulated into graphs to have proper analysis on the result. Additionally, by preparing graphs, the pattern or the relationship between the percentage of crumb rubber replacement and Marshall stability, flow, and stiffness also could be assessed by the value of the coefficient of correlation, R. Thus, the strength of the relationship could be concluded, and it was easier to examine the percentage of crumb rubber replacement that would contribute to the most superlative stability and flow performance to the asphalt mixture sample.

## 3. RESULTS AND DISCUSSION

### 3.1 Penetration

Figure 3 shows the relationship between the percentage of crumb rubber and the depth of the penetration needle. The readings of the penetration depth were taken from the average of three readings. Based on the graph, it can be seen that before the modification of binder with crumb rubber, the value of penetration is as according to the supposed value for asphalt binder PEN 60/70 which is 6 cm. However, with the 12% replacement of crumb rubber, the penetration depth reduced by 19.5% to 4.82 cm. With further replacement to 14% and 16%, the depth reduced more significantly to 4.44 cm and 4.18 cm respectively. Lastly, at the highest percentage of replacement of 18%, the depth reduced to the lowest value of 3.94 cm. From the pattern, it can be observed that control binder gives the highest penetration depth while the

highest percentage of replacement, 18% gives the lowest value for penetration. Thus, it is apparent that, as the percentage of crumb rubber increases, the penetration depth decreases progressively. This represents a strong enhancement of the asphalt binder in terms of viscosity and stiffness as the percentage of crumb rubber increases. Not to mention, from the graph, the coefficient of correlation obtained was,

$$R = \sqrt{0.8672} = 0.93$$

Since the coefficient of correlation, R is closer to 1, it is proven that the percentage of crumb rubber signifies an influential impact on the stiffness and viscosity of the asphaltic binder. Nonetheless, stiffer binder does not necessarily prove an enhancement of the pavement during later use. The authors of [9] established that the higher stiffness of the asphaltic binder that occurred due to the swelling of the crumb rubber is advantageous for pavement that is in use in hot climate regions due to its higher flow resistance, which leads to improvement in the pavement's flexibility. However, if it is constructed at a cold climate region with low temperatures, the asphaltic mixture may have issue on the ductility, thus leading to higher risk of thermal cracking. This is supported by [10], in which bitumen underwent high brittleness rate and was prone to experience cracking failure at low temperature exposure.

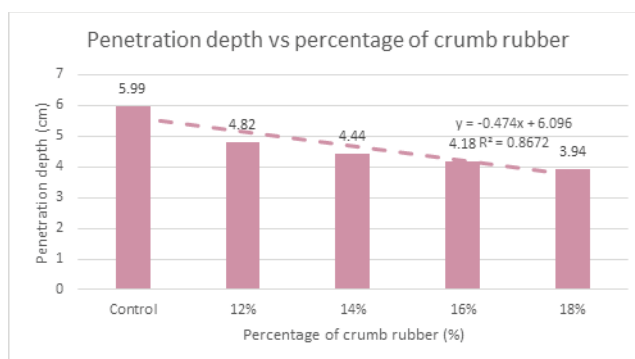


Fig. 3: Penetration depth of asphalt binder with percentage of crumb rubber varying from 0% to 18%.

### 3.2 Softening Point

Figure 4 proves how the higher percentage of crumb rubber replacement would result in the softening point increasing continuously. At 0% of crumb rubber replacement, the softening point achieved is the lowest, which is at 49.5 °C. However, the value is still valid for asphalt binder PEN 60/70 as it is still within the range of 49 to 56 °C. As the crumb rubber replacement increases to 12%, the softening point of the asphaltic binder raises up to 50.5 °C, validating the improvement of the binder to lower temperature susceptibility. Next, with further replacement of the binder with 14% and 16% crumb rubber, the softening point continues to climb to 51.5 and 54 °C respectively. At the maximum percentage of crumb rubber replacement, which is 18%, the binder eventually met its maximum softening point value at 56.5 °C. Hence, a conclusion can be made in which the higher the percentage of crumb rubber used for replacement, the higher the softening point of the asphaltic binder. Relating this with the stiffness of the asphaltic binder results from the penetration test, since the stiffness increases with higher crumb rubber replacement, a higher temperature would be required for the asphaltic binder to change its physical property from solid to liquid form.

Therefore, this signifies that as the content of crumb rubber replacement increases, the lower the temperature susceptibility of the asphaltic binders, since higher temperatures are required for the asphaltic binder to change its form. Hence, the pavement that is incorporated

with crumb rubber will be less likely to go through any deterioration due to hot climatic weather such as rutting. This conclusion can also be supported by the authors of [6], as the authors mentioned on the research paper that the results of inclining softening point value with increment of percentage of crumb rubber indicate that pavements that is constructed using CRMB would be less susceptible to traffic deformation distress at high temperatures compared to conventional asphalt pavements. According to [11], high softening point was desirable for hot and warm climates application. In order to prove the strength of the influence of crumb rubber towards the softening point, the coefficient of correlation was computed, as shown below.

$$R = \sqrt{0.9486} = 0.97$$

The calculation above shows how close the value of the coefficient of correlation is to 1. Therefore, this signifies that the softening point of the asphaltic binder is highly influenced by the incorporation of crumb rubber.

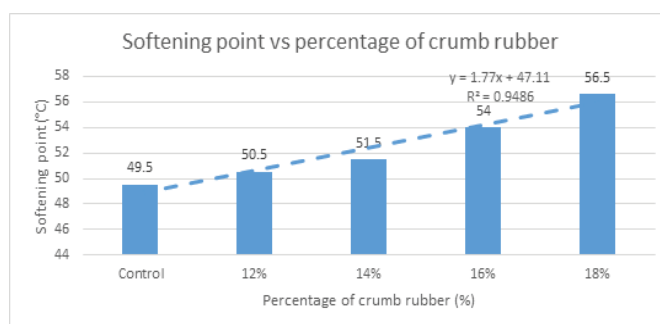


Fig. 4: Softening point of asphalt binder with percentage of crumb rubber varying from 0% to 18%.

### 3.3 Los Angeles Abrasion Value

According to the result, for the first test, the weight of aggregate retained on sieve no. 4 was 2.5 kg while the weight of retained aggregate on sieve no.12 was 0.82 kg. Hence, the computed value of the LAAV based on those two weights was 32.8% whereas for the second test, the weight of aggregate retained on sieve no. 4 was 2.5 kg while the weight of retained aggregate on sieve no.12 was 0.76 kg. Therefore, the value of LAAV obtained was 30.4%. The mean was determined from these two values, which is 31.6%.

According to ASTM C131, the Los Angeles Abrasion Value must be not more than 40%. As a result, the aggregates employed in this research are appropriate and fulfil the standard criterion. Based on the results, it is possible to infer that the aggregates utilised have a high hardness value and are appropriate for usage. According to [12], the strength of the aggregate is very important as it does impact the overall strength of the pavement. Aggregates with high resistance towards abrasion are less likely to wear down or be broken apart under the friction and grinding forces from vehicle loads. It is quite vital for the aggregates to resist breaking apart as this could contribute to more even load distribution on the pavement. Thus, this remarkably could enhance the longevity of the pavement as well.

#### First Test:

Weight of retained aggregate on no. 4 ASTM sieve (kg) = 2.5 kg

Weight of retained aggregate on no.12 ASTM sieve (kg) = 0.82 kg

$$\text{Los Angeles abrasion value (\%)} = \frac{0.82}{2.5} \times 100\% = 32.8\%$$

### Second Test (Repetition):

$$\text{Weight of retained aggregate on no.4 ASTM sieve (kg)} = 2.5 \text{ kg}$$

$$\text{Weight of retained aggregate on no.12 ASTM sieve (kg)} = 0.76 \text{ kg}$$

$$\text{Los Angeles abrasion value (\%)} = \frac{0.76}{2.5} \times 100\% = 30.4\%$$

### Taking Average Based on Both Test:

$$\text{Los Angeles abrasion value (\%)} = \frac{32.8+30.4}{2} = 31.6\%$$

### 3.4 Aggregate Crushing Value

The calculation to determine the aggregate crushing value is as shown below. Prior to the crushing of the aggregate via the compression machine, the total initial weight of the aggregates was 2.65 kg. After the aggregates were crushed and filtered through sieve with an opening of 2.36 mm, the weight of aggregate passing through the sieve was 0.65 kg. Therefore, proving that only 24.53% of the total aggregates underperformed and were not impervious against the gradually applied compressive load.

Based on the result obtained, the aggregate crushing value of the aggregates is within the acceptable range. This is because, the aggregate crushing value for wearing course should not exceed 30% according to BS 812-110:1990. In another interpretation, the aggregate is suitable for use in wearing course layer construction as it has high resistance to impact. According to [13], aggregates are highly responsible in determining the load carrying capacity of the pavement, thus, it is paramount to choose aggregates that are sufficiently strong and durable towards the applied load. Not to mention, aggregates are constantly exposed to crushing and impact not only during the pavement in-service, but also throughout the process of constructing the pavement, such as during the stockpiling of the aggregate and during the compaction of the pavement. Therefore, if the aggregates are too substandard and have low impact resistance, the aggregates would be most likely to break apart or be broken down right before the pavement was even in-service. Hence, ensuring the aggregates are highly durable and tough is very beneficial to avoid early defects on the pavement surface.

$$\text{Aggregate crushing value (\%)} = \frac{\text{Weight of aggregate passing (kg)}}{\text{weight of aggregate (kg)}} \times 100\%$$

$$\text{Weight of aggregate (kg)} = 2.65$$

$$\text{Weight of aggregate passing sieve (kg)} = 0.65$$

$$\text{Aggregate crushing value (\%)} = \frac{0.65}{2.65} \times 100\% = 24.53\%$$

### 3.5 Marshall Stability, Flow and Stiffness

Based on the Figs. 5-7, it is noticeable how the same percentage of crumb rubber would give different impact and end-result to the stability, flow, and stiffness of the asphaltic mixture with different grading. From Fig. 5, it can be seen that within dense mixture, with the introduction of 12% crumb rubber, the stability suddenly decreased from 17.8 kN (control mixture) to 12.03 kN for dense mixture. The stability steadily decreased until the percentage of crumb rubber replacement was 18%. At 18% the value struck back to 15 kN, in which the value was still lower than the control mixture but was the highest within all the modified CRMB

mixtures. As for the porous graded mixture, it is recorded that with the introduction of crumb rubber of 12%, the stability increased slightly from 5.04 to 5.37 kN. With further replacement to 14% and 16%, the value kept on rising to 9.33 kN and 12.88 kN, respectively. However, at 18% of crumb rubber replacement, the result started to turn counterproductive as the value dropped back to 11.8 kN. This is because at larger content percentage of crumb rubber, high stiffness tendency was exhibited by the asphalt mixture, thereby reducing the stability performance when subjected to the load due to the loss of one-to-one contact points of the aggregate particles in the bituminous mixture.

As for the correlation between the percentage of crumb rubber and Marshall stability result for both dense mixture and porous mixtures, it can be computed as below:

$$R_{\text{dense}} = \sqrt{0.1346} = 0.367$$

while for porous mixture,

$$R_{\text{porous}} = \sqrt{0.8539} = 0.924$$

Based on the coefficient of correlation calculated above, it certainly can be concluded that the CRMB contributes to more significant impact on the porous mixture than dense mixture as the coefficient of correlation for porous mixture is closer to 1. This may be happening due to the porous mixture grading containing fewer fine particles compared to dense mixture grading. Hence, porous mixture would be comprised of bigger air voids in between the coarse particles. As the crumb rubber swelled during the mixing process, it then could eventually fill up the space, thus increasing the overall stability of the mixture. From the result of the Marshall stability on the porous mixture as well, it can be established that the optimum percentage of crumb rubber replacement is 16% as the mixture achieved the highest value of stability, where the stability rises up by 85.1%. This proves that the incorporation of crumb rubber in porous mixture would influence the overall strength and resistance towards applied loads.

In terms of the Marshall flow for dense mixtures as shown in Fig. 6, with a replacement of crumb rubber of 12%, the value of flow decreases from 3.05 mm to 2.96 mm, but the value rises back to 3.16 and 3.88 mm with a replacement of 14% and 16%. Nonetheless, at 18%, the value of flow drops back to 2.8 mm which is the lowest value from the overall. As for the porous mixture, in contrary with the stability result, the percentage of 16% of crumb rubber replacement also seems to produce the utmost flow value, where the value obtained is the lowest within the CRMB mixed with porous grading with a value of 4 mm. Marshall flow is one of the paramount mechanical properties of the pavement that needs to be checked. Marshall flow is signifying on the deformation rate potential that is undergone by the pavement at the highest value of load applied. High flow indicated that the high tendency in pavement mixture easily exposed the deformation. Thus, having the lowest value of Marshall flow is preferred since it would lead to the higher resistance towards deformation such as rutting. The strength of the relationship between the percentage of crumb rubber and the Marshall flow are as shown below:

$$R_{\text{dense}} = \sqrt{0.0252} = 0.159$$

while for porous mixture,

$$R_{\text{porous}} = \sqrt{0.7651} = 0.875$$

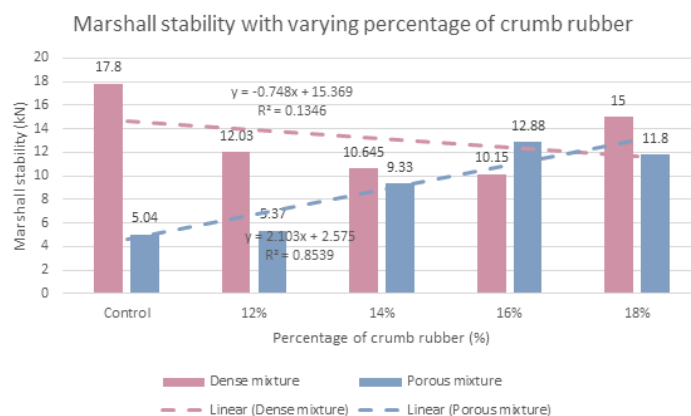


Fig. 5: Marshall stability for asphaltic binder utilizes to both dense mixture and porous mixture with percentage of crumb rubber varying from 0% to 18%.

Similar to the Marshall stability, the porous mixture seems to exhibit a stronger relationship for the Marshall flow with increasing percentage of crumb rubber replacement as the value for  $R_{porous}$  is closer to 1 compared with the value for  $R_{dense}$ . This ultimately signifies that the introduction of crumb rubber in the porous mixture could help influence and increase the resistance of the pavement towards permanent deformation or instability.

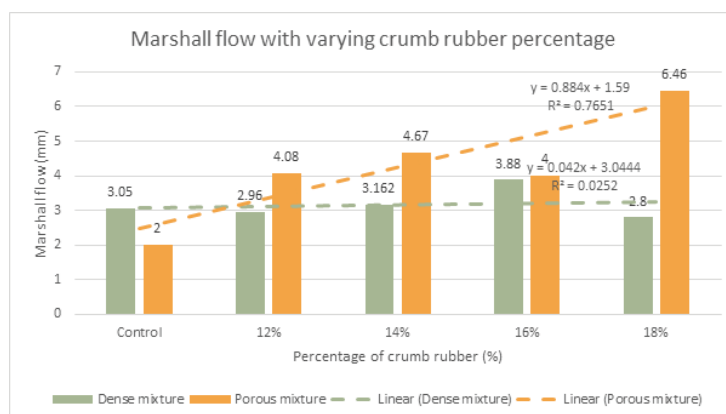


Fig. 6: Marshall flow for asphaltic binder utilizes to both dense mixture and porous mixture with percentage of crumb rubber varying from 0% to 18%.

Upon computing the values for stiffness using the equation in section 2.5 of this paper, the results were tabulated into the graph shown in Fig. 7. From the figure, it can be concluded that 18% of crumb rubber replacement gives the overall highest value of stiffness. Therefore, 18% is chosen as the most optimum percentage for dense graded mixtures. For porous mixtures, 16% of crumb rubber is the most ideal for porous grading aggregate as at this percentage, the stiffness value is the highest among all other crumb rubber replacement percentages with a value of 3.22 kN/mm. Established by the authors of [14], it is paramount for the value of the stiffness to be high as it signifies the higher ability of the pavement layer to spread the applied load and resistance relatively. In order to establish and compare the influence of the crumb rubber on both dense mixture and porous mixture, the coefficient of correlation for both dense mixture and porous mixture were computed as shows below.

$$R_{dense} = \sqrt{0.0801} = 0.283$$

while for porous mixture,

$$R_{\text{porous}} = \sqrt{0.0127} = 0.113$$

Nonetheless, as for the dense mixture, it is fair to say the crumb rubber does not signify any improvement on it, as the value of Marshall stability and Marshall stiffness for control mixture is higher compared to any dense mixture that is incorporated with CRMB. However, when comparing the result within the mixture with CRMB itself, 18% or the highest percentage of CR replacement, is shown to produce asphalt mixtures with the highest Marshall stability and stiffness of 15 kN and 5.36 kN/mm respectively and lowest Marshall flow value of 2.8 mm. Therefore, proving that the optimum percentage of CR replacement for dense mixture is 18%. According to the previous research executed by the authors of [2] and [15], the value of the Marshall stability and stiffness should be enhanced as the percentage of crumb rubber replacement increases, however the result of this research shows a different outcome especially for the dense mixture. Nonetheless, the authors of [6] stated in the findings that the reduction in the value of Marshall stability and stiffness after the introduction of crumb rubber to the mixture may happen due to lack of adhesion between the aggregates. This may occur as with higher crumb rubber percentage, the binder would become more viscous and less workable. This can be proven based on the result of the penetration test shown in section 3.1. Thus, due to this, it is harder to coat all the aggregates properly and fully, which eventually leads to the occurrence of stripping and reduction of the overall strength of the sample. In observing the structure of the dense mixture itself, the typical structure arrangement inside the mixture is close and compact. As the crumb rubber was added in dense mixture, it contributed to the excessive stiffness that led to the high potential of cracking, thereby reducing the stability performance of dense mixture.

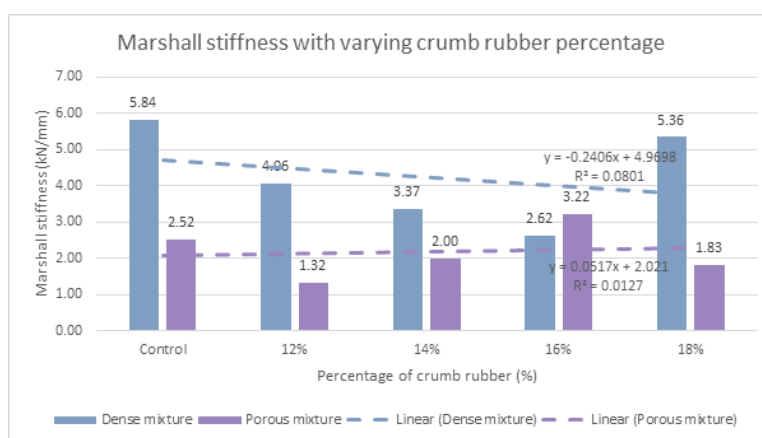


Fig. 7: Marshall stiffness for asphaltic binder utilizes to both dense mixture and porous mixture with percentage of crumb rubber varying from 0% to 18%.

#### 4. CONCLUSION

The following conclusions were drawn to summarise the result obtained during the research work:

- For higher percentage of crumb rubber replacement, the binder would be stiffer as the value of penetration depth reduced progressively when the percentage increases. Other than that, from the result of softening point, it was also proven that the modification of asphalt binder with crumb rubber would cause the binder to be less susceptible towards temperature changes and the relationship between percentage of CR and softening point value shows a positive linear relationship, in which as the percentage of CR increases, the softening point rises as well.

- Marshall stability and Marshall flow test on the asphaltic mixture are conducted in identifying optimum percentage of crumb rubber replacement in the modified binder for dense asphalt mixture and porous asphalt mixture. From the analysis, it was acquired that for dense asphalt mixture, the optimum percentage of CR is 18% whereas for porous asphalt mixture, 16% gives the most optimum result.
- Based on the analysis executed, it was established that the utilization of CRMB for porous mixtures shows a more significant improvement compared to the utilization of CRMB for dense mixtures. This is proven as the coefficient of correlation obtained for Marshall stability in porous mixtures is higher than the coefficient of correlation obtained for Marshall stability in dense mixture, in which 0.924 is bigger than 0.367. Since the value of coefficient of correlation obtained for Marshall stability at porous mixtures is closer to 1, it shows that the relationship between the percentage of CR and Marshall stability for the porous mixture is very strongly significant.

## ACKNOWLEDGEMENT

This study fully conducted in Geotechnical and Transportation Laboratory and special thankful to the Department of Civil Engineering, Kulliyyah of Engineering, International Islamic University Malaysia. The support provided by Fundamental Research Grant Scheme (FRGS) from Malaysian Ministry of Higher Education (MOHE) in the form of a research grant number FRGS/1/2023/TK02/UIAM/02/3 (Project ID: FRGS23-319-0928) for this study is highly appreciated.

## REFERENCES

- [1] Milad A, Ahmeda AGF, Taib AM, Rahmad S, Solla M, Yusoff NIM. (2020) A review of the feasibility of using crumb rubber derived from end-of-life tire as asphalt binder modifier. *Journal of Rubber Research*, 23: 203-216. <https://doi.org/10.1007/s42464-020-00050-y>
- [2] Soleimani SM, Faheiman A, Mowaze Z. (2020) The Effects of Using Crumb Rubber Modified Binder in an Asphalt Pavement. *American Journal of Engineering and Applied Sciences*, 13(2): 237-253. <https://doi.org/10.3844/ajeassp.2020.237.253>
- [3] Rodríguez-Alloza AM, Gallego J. (2017) Mechanical performance of asphalt rubber mixtures with warm mix asphalt additives. *Materials and Structures*, 50: 147. <https://doi.org/10.1617/s11527-017-1020-z>
- [4] Ghabchi R, Arshadi A, Zaman M, March F. (2021) Technical challenges of utilizing ground tire rubber in asphalt pavements in the United States. *Materials*, 14(16): 4482. <https://doi.org/10.3390/ma14164482>
- [5] Yu HY, Deng GS, Wang DY, Zhang ZY, Oeser M. (2020) Warm asphalt rubber: A sustainable way for waste tire rubber recycling. *Journal of Central South University*, 27(11): 3477-3498. <https://doi.org/10.1007/s11771-020-4467-y>
- [6] Osman SA, Adam AAM. (2013) Evaluation of crumb tire rubber-modified hot mix asphalt concrete in Sudan. *Sustainable Construction Materials 2012 - Proceedings of the 2nd International Conference on Sustainable Construction Materials - Design, Performance, and Application*. <https://doi.org/10.1061/9780784412671.0021>
- [7] Bayagoob AAS, Füleki P. (2022) A brief overview of utilizing crumb rubber as asphalt binder modifier. *International Journal of Recent Technology and Engineering (IJRTE)*, 11(1): 83-90. <https://doi.org/10.35940/ijrte>
- [8] Ahmed AZ, Maniruzzaman AAM, Anuar KK, Baffa JH. (2016) A short review on using crumb rubber as modification of bitumen binder. *Jurnal Teknologi (Science & Engineering)*, 78 (7-3): 29-36. <https://doi.org/10.11113/jt.v78.9479>

- [9] Ren S, Liu X, Xu J, Lin P. (2021) Investigating the role of swelling-degradation degree of crumb rubber on CR/SBS modified porous asphalt binder and mixture. *Construction and Building Materials*, 300: 124048. <https://doi.org/10.1016/j.conbuildmat.2021.124048>
- [10] Tia M. (2003) *Bituminous Materials and Mixtures*. Civil Engineering Handbook. Boca Raton, Florida: CRC press Inc, pp. 436-451.
- [11] Sun Z, Yi J, Huang Y, Feng D, Guo C. (2016) Properties of Asphalt Binder Modified by Bio-Oil Derived from Waste Cooking Oil. *Construction and Building Materials*, 102: 496-504.
- [12] Golalipour A, Jamshidi E, Niazi Y, Afsharikia Z, Khadem M. (2012) Effect of Aggregate Gradation on Rutting of Asphalt Pavements. *Procedia - Social and Behavioral Sciences*, 53: 440-449. <https://doi.org/10.1016/j.sbspro.2012.09.895>
- [13] Mang T. (2003) *Lecture Notes on Bituminous Materials and Mixtures*, University of Florida. Retrieved from <http://nersp.nerdc.ufl.edu/~tia/BituminousMaterials.pdf>
- [14] Rosli IJ, Sarif AS. (2021) Performance Review of Crumb Rubber as A Modifier in Asphalt Pavement. *Progress in Engineering Application and Technology*, 2(1): 174-182. <https://doi.org/10.30880/peat.2021.02.01.017>
- [15] Sana ASAL, Hussin AMY, Ismael AAS. (2018) Rubber asphalt technique (a new concept for asphalt pavements in Oman. 8<sup>th</sup> National Symposium on Engineering Final Year Projects. <https://www.researchgate.net/publication/328772440>

## MIXING SEQUENCE EFFECT OF CEMENT COMPOSITES WITH CARBON FIBRES

ELIZER NEVALL ANTHONY, AHMAD NURFAIDHI RIZALMAN\*, ANAND RYAN  
THURAIRAJAH, S.M. IQBAL S. ZAINAL AND MUHD FAUZY SULAIMAN

*Civil Engineering Programme, Faculty of Engineering, Universiti Malaysia Sabah,  
Jalan UMS, 88400, Kota Kinabalu, Sabah, Malaysia*

\*Corresponding author: [ahmadnurfaidhi@ums.edu.my](mailto:ahmadnurfaidhi@ums.edu.my)

*(Received: 31 August 2023; Accepted: 16 November 2023; Published on-line: 1 January 2024)*

**ABSTRACT:** Carbon fibres are widely recognised as reinforcement materials that effectively control cracks in concrete structures. Nonetheless, these fibres do not disperse uniformly inside the cement matrix, disrupting the mixture homogeneity. To address this concern, this study investigated two distinct mixing sequences of cement composites with carbon fibres. Two mixing sequences were investigated including the addition of fibres after cement (AC-CF) and the addition of fibres before cement (BC-CF). The surface topography of carbon fibres and the engineering properties of the cement paste were also examined. Consequently, carbon fibres in cement composite produced lower flowability due to the surface roughness. The AC-CF specimen demonstrated the highest hardened density at 28 days with 2679.22 kg/m<sup>3</sup> followed by BC-CF and the control specimen with 2386.08 kg/m<sup>3</sup> and 2278.36 kg/m<sup>3</sup>, respectively. The AC-CF specimen also had the highest compressive strength at 28 days with 69.91 MPa, followed by BC-CF and the control specimen with 65.92 MPa and 63.20 MPa, respectively. Further, the flexural strength of the AC-CF specimen exhibited the highest strength with 10.86 MPa, followed by BC-CF and the control specimen with 9.35 MPa and 9.17, respectively. The fibre dispersion in AC-CF was also superior to BC-CF. Therefore, it can be concluded that the best mixing sequence is the addition of fibre after cement (AC-CF) because it had better fibre dispersion and engineering properties compared to the addition of fibre before cement (BC-CF).

**ABSTRAK:** Gentian karbon lebih dikenali sebagai bahan bantuan yang berkesan dalam mengawal keretakan pada struktur konkrit. Walau bagaimanapun, gentian ini tidak tersebar secara seragam di dalam matrik simen dan akan mengganggu kehomogenan campuran. Bagi mengatasi masalah ini, kajian ini mengkaji tentang dua susunan campuran berbeza simen komposit dengan gentian karbon. Dua susunan campuran ini adalah melalui penambahan gentian selepas simen (AC-CF) dan penambahan gentian sebelum simen (BC-CF). Permukaan topografi gentian karbon dan sifat kejuruteraan pes simen turut diperiksa. Kajian mendapati bahawa gentian karbon dalam komposit simen mengurangkan kebolehaliran pes simen disebabkan oleh kekasaran pada permukaan gentian. Spesimen AC-CF menunjukkan ketumpatan pengerasan tertinggi pada hari ke-28 dengan 2679.22 kg/m<sup>3</sup> diikuti spesimen BC-CF dan spesimen kawalan sebanyak 2386.08 kg/m<sup>3</sup> dan 2278.36 kg/m<sup>3</sup>, masing-masing. Spesimen AC-CF juga mempunyai kekuatan mampatan tertinggi pada hari ke-28 dengan 69.91 MPa, diikuti oleh spesimen BC-CF dan spesimen kawalan sebanyak 65.92 MPa dan 63.20 MPa, masing-masing. Seterusnya, kekuatan lenturan spesimen AC-CF menunjukkan kekuatan tertinggi dengan 10.86 MPa, diikuti spesimen BC-CF and spesimen kawalan dengan 9.35 MPa dan 9.17 MPa, masing-masing. Penyebaran gentian dalam AC-CF juga lebih baik daripada BC-CF. Oleh itu, kajian ini merumuskan bahawa susunan campuran terbaik adalah dengan penambahan gentian selepas simen (AC-CF) kerana ia mempunyai kekuatan lenturan

gentian terbaik dan sifat kejuruteraan berbanding penambahan gentian sebelum simen (BC-CF).

---

**KEYWORDS:** *mixing sequence; cement composite; carbon fibre; engineering properties*

## 1. INTRODUCTION

Fibres are a fibrous material type commonly employed to improve the properties of concrete. Moreover, fibres mitigate cracks from plastic with drying shrinkage and restrict the permeability of concrete [1]. Fibres have been widely used in several applications, including pavements, bridge decks, offshore structures, and machine foundations. Generally, these fibres are categorised into three distinct types: steel, glass, and synthetic [2]. Carbon fibres are widely recognised for their favourable elastic modulus, tensile strength, and thermal and electrical conductivities [3]. When fibres are added to concrete, several mechanical properties are enhanced [4]. These properties include compressive strength, flexural strength, tensile strength, durability, and cracking resistance. Nevertheless, multiple parameters, including fibre percentage, diameter, and length, can affect these characteristics.

Numerous studies demonstrated that gradually adding carbon fibre into concrete reduced workability [5-8]. This outcome occurred due to the fresh concrete movement obstruction from the fibre interaction with other concrete constituents [9]. Previous studies also demonstrated a positive correlation between the higher fibre percentage and fibre length in improving the compressive and flexural strength of concrete [6-12]. These improved concrete properties were attributed to the fibres, serving as a bridge to maintain the proximity of concrete particles [13]. Nonetheless, lower concrete strength was presented when the fibre percentage was 1.0% due to fibre agglomerations [10,12].

One of the primary concerns associated with fibres is their tendency to aggregate, leading to non-uniform dispersion within the cement matrix and lower strength. Conversely, the fibre mixing sequence can impact their dispersion inside the matrix. According to the American Concrete Institute (ACI) 6.44-3R, fibres should be incorporated into a fluid mixture in the final mixing stage or added to the mixer with aggregates [14]. Several studies have supported this reasoning, recording enhanced fibre dispersion within the matrix when the fibres are introduced into a fluid mix [15-18]. To the authors' knowledge, the correlation between the fibre dispersion inside the hardened cement matrix and their engineering properties has not been explored. Thus, this study focused on the investigation of synthetic carbon fibres.

This study evaluated the surface topography of carbon fibres. A carbon fibre blending sequence assessment was conducted inside a cement paste based on several engineering properties, including flowability, hardened density, compressive strength, and flexural strength. This study investigated two different mixing sequences: fibres added after cement (AC-CF) and fibres added before cement (BC-CF). The surface topographies of the specimens were used to compare the fibre dispersions in the hardened AC-CF and BC-CF. Finally, the optimal mixing sequence of a cement composite with carbon fibres was identified.

## 2. MATERIALS AND METHODS

### 2.1 Materials

The cement composite utilised in this study consisted of Ordinary Portland Cement (OPC), water, and carbon fibres (see Fig. 1). Three specimens were assessed in this study: cement paste without fibres (control), AC-CF, and BC-CF. The AC-CF denotes fibres added after cement,

while BC-CF was defined as fibres added before cement. Table 1 tabulates the mixture proportions of the specimens. For example, 1014 g of AC-CF contained 778 g of cement, 233 g of water, and 3 g of carbon fibres.

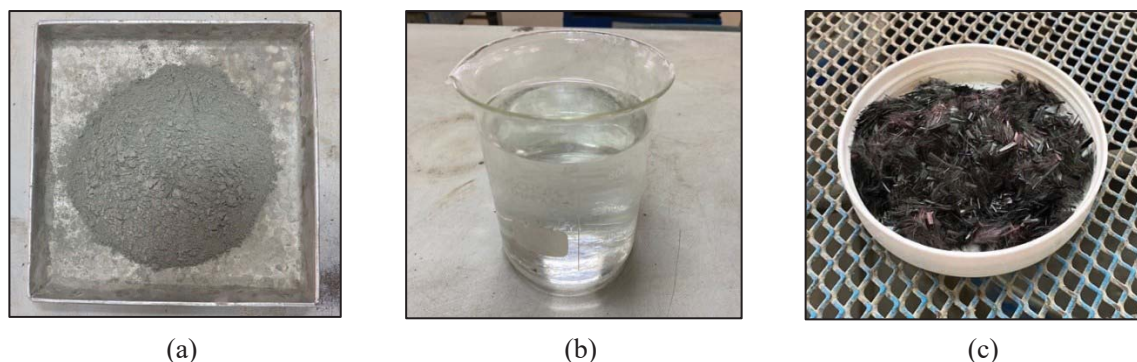


Fig. 1: The (a) OPC, (b) water, (c) carbon fibre components used in this study.

Table 1: Summary of specimen designations and mixture proportions

Specimen	Water/Cement Ratio	Cement (g)	Water (g)	Fibre Content (g)
Control	0.30	778	233	0
AC-CF	0.30	778	233	3
BC-CF	0.30	778	233	3

The methodology employed for the control specimen adhered to the American Society for Testing and Material (ASTM) C305 guidelines [14]. Meanwhile, the specimen preparation containing carbon fibres was conducted following the method described by Gao et al. [15]. Figure 2 depicts the mixing sequences and duration methodologies for all specimens.

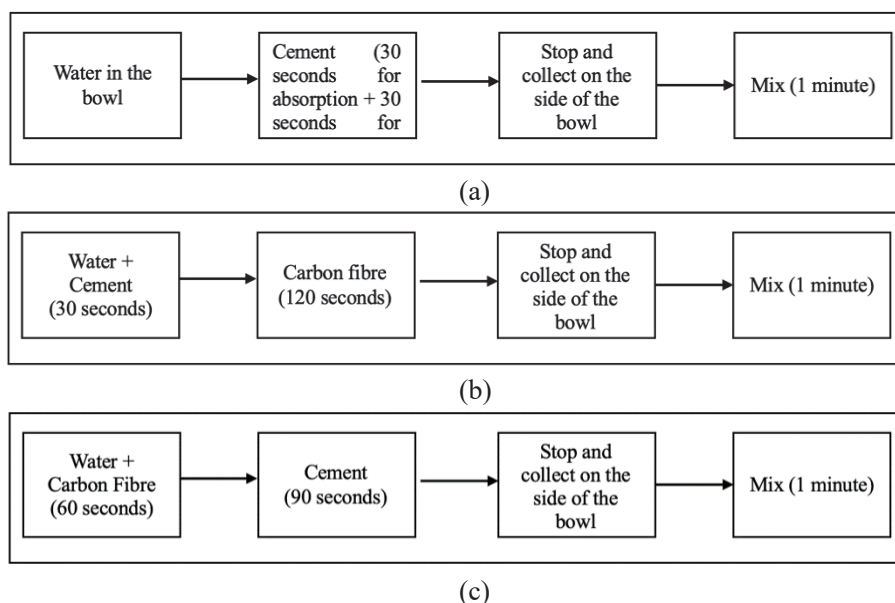


Fig. 2: Schematic flow chart indicating the mixing methods for (a) control, (b) AC-CF, and (c) BC-CF specimens.

## 2.2 Methodology

This study involved the surface topography acquisition of carbon fibres using Atomic Force Microscopy (AFM) and Field Emission Scanning Electron Microscopy (FESEM). Both experiments were conducted at the Centre for Instrumentation and Science Services, Universiti Malaysia Sabah (UMS). The carbon fibre dispersion in hardened cement composite was also achieved using Scanning Electron Microscopy (SEM). These characterisations were performed at the Biotechnology Research Institute, UMS. Figure 3 illustrates the instruments employed in this study.

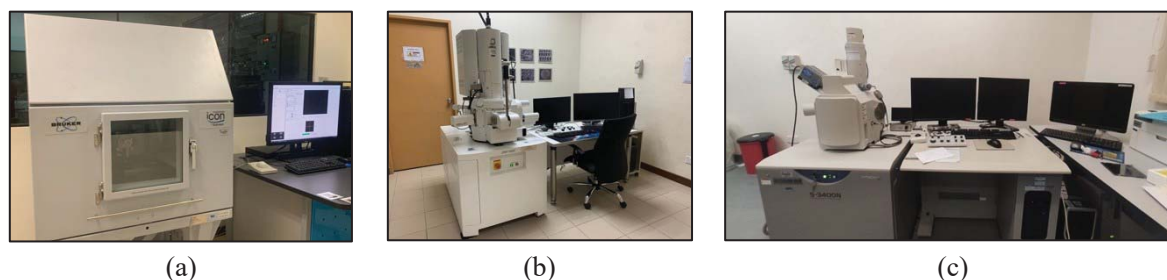


Fig. 3: The (a) AFM, (b) FESEM, and (c) SEM instruments used to examine the carbon fibre properties.

Approximately 54 cement-paste specimens were fabricated, of which 36 specimens (50 mm × 50 mm × 50 mm) were utilised for hardened density and compression strength tests. An additional 18 specimens (40 mm × 40 mm × 160 mm) were applied for flexural strength tests. The mixing procedure was initially performed using a mechanical mixer, following the guidelines outlined in ASTM C305 [19]. The cement paste was then carefully introduced into the cube and the prism moulds and allowed to cure for one day. Subsequently, the specimens were demoulded and cured through water tank immersion for 7, 28, and 56 days. The flowability, hardened density, compressive strength, and flexural strength of the cement composite were evaluated using standardised test methods, including ASTM C1437, BS EN 1015-10, ASTM C109, and ASTM C348, respectively [20-23]. Alternatively, the flowability, hardened density, and compressive strength tests were conducted in the Concrete Lab and Material, UMS. The flexural strength test was also performed at the Faculty of Tropical Forestry, UMS. Figure 4 portrays the instrumentation employed in the study.

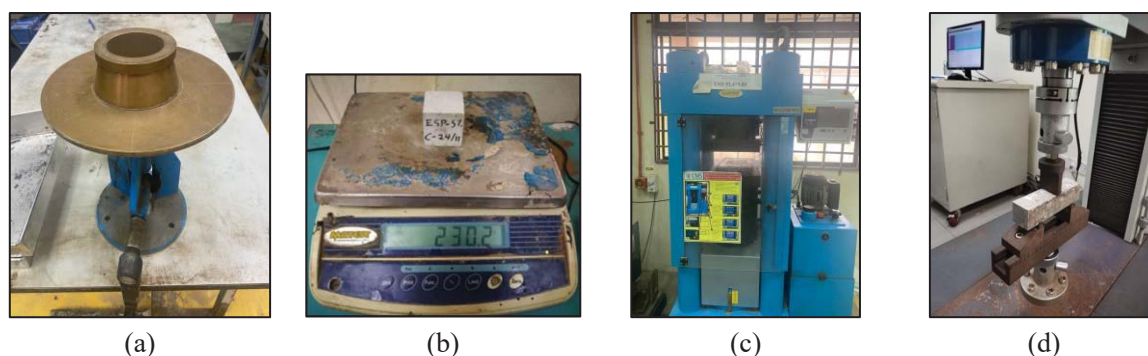


Fig. 4: The (a) flowability, (b) hardened density, (c) compressive strength, and (d) flexural strength test instruments used to test the engineering properties of the cement composites.

### 3. RESULTS AND DISCUSSION

#### 3.1 Surface Topographies of the Carbon Fibres

Figure 5(a) and 5(b) present the surface topographies of carbon fibres using FESEM at low and high magnifications, respectively. The diameters varied from 36  $\mu\text{m}$  to 40  $\mu\text{m}$ , while extrusion lines along the longitudinal axis of the carbon fibre (red circle) indicated a smooth surface.

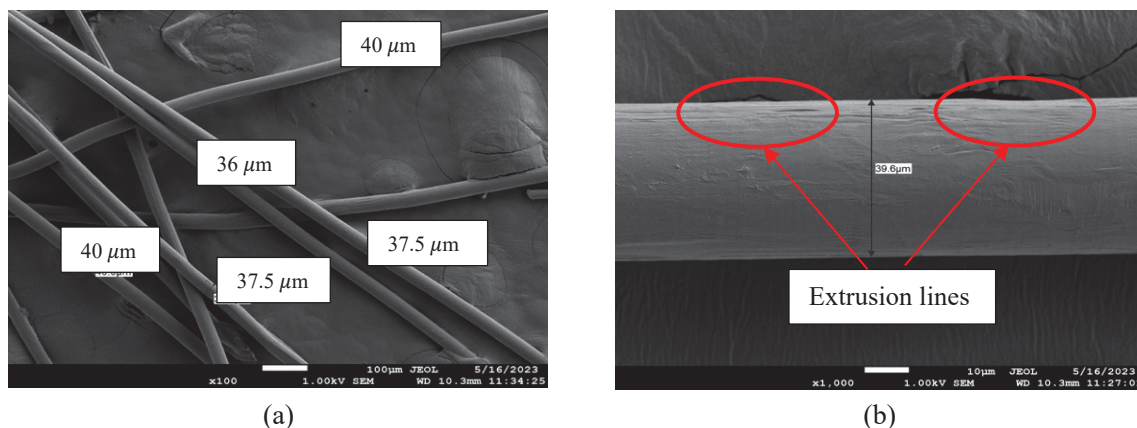


Fig. 5: The FESEM topographies of carbon fibres at (a) low and (b) high magnifications.

The FESEM images were compared with the AFM images (see Fig. 6). A distinct presence of extrusion lines on the fibre surface was observed, suggesting the low fibre roughness. Moreover, a discernible hairy structure in the fibres was demonstrated. A study by He and Yang proposed that this characteristic could improve the interfacial binding strength between the fibre surface and the surrounding cement-paste matrix by introducing additional Van der Waals forces [24].

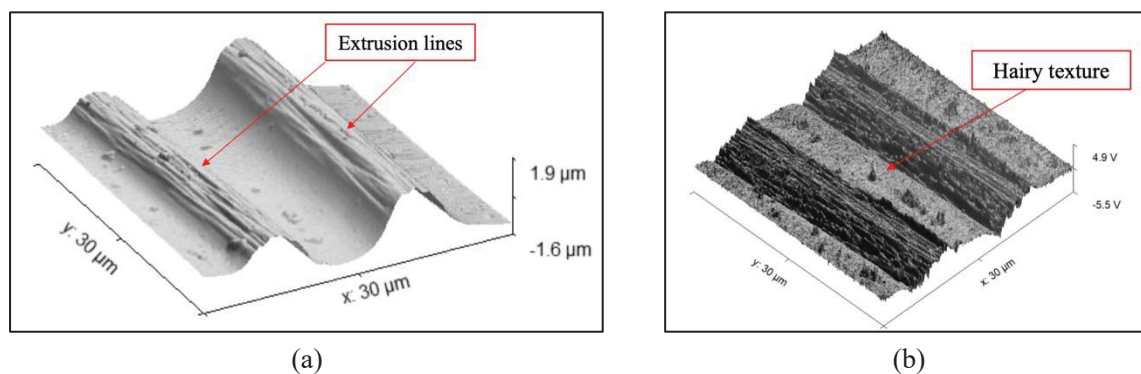


Fig. 6: The AFM topography of the carbon fibres indicating the (a) extrusion lines on the surface and (b) the hairy texture.

#### 3.2 Flowability Values of the Cement Composites

Table 2 lists the flow diameters of the control and cement composites. The results indicated that the control specimen exhibited the largest flow diameter, followed by the AC-CF and BC-CF specimens. These measurements were 205 mm, 204 mm, and 202 mm, respectively. According to the ASTM standard [20], all diameters fell within the permitted range from 205 mm to 215 mm (105% to 115%). The AC-CF and BC-CF produced lower diameters due to the carbon fibre roughness, which was proven by the FESEM and AFM images. These features

were widely recognised to significantly impact the fibre dispersion within the cement matrix [25]. Therefore, the flowability of the matrix was restricted.

Table 2: Summary of the flow diameters for the specimens

Specimen	Control	AC-CF	BC-CF
Flow diameter (mm)	205	204	202

### 3.3 Hardened Densities of the Cement Composites

A higher hardened density in cement composites is vital for proper fibre dispersion. If the fibres are not adequately dispersed, their ability to occupy the vacant spaces is compromised. This process develops a lower hardened material density [26]. Consequently, the hardened densities of all samples presented an upward trend with increased curing duration (7, 28, and 56-day periods) (see Fig. 7). The results also demonstrated that the hardened density of the AC-CF specimen was higher than the BC-CF and control specimens at all curing durations. For example, the measured hardened densities of the AC-CF, BC-CF, and control specimens on day 56 were 2679.22 kg/m<sup>3</sup>, 2386.08 kg/m<sup>3</sup>, and 2278.37 kg/m<sup>3</sup>, respectively.

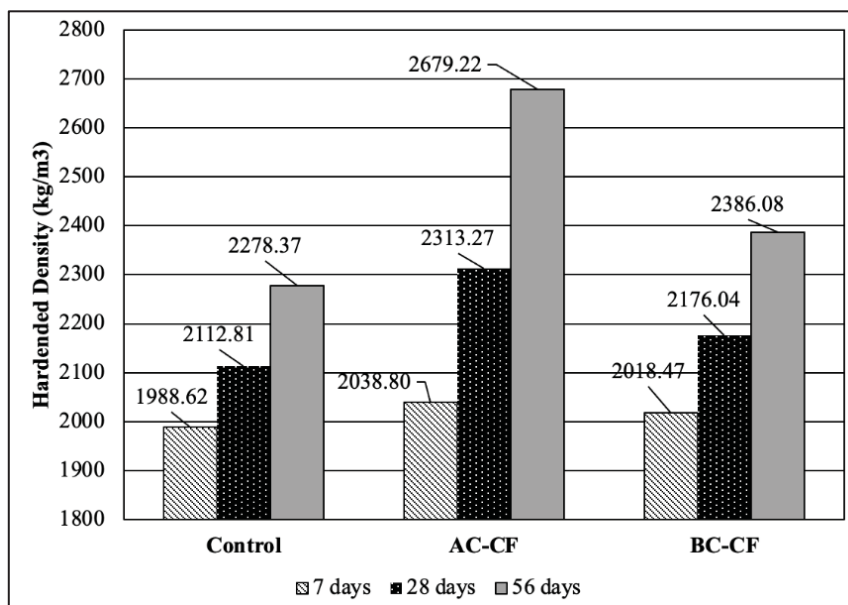


Fig. 7: The hardened densities of various specimens.

### 3.4 Compressive Strengths of the Cement Composites

Figure 8 presents the compressive strengths of the control, AC-CF, and BC-CF specimens. The results indicated a positive correlation between the curing duration and the compressive strengths of the specimens across the 7, 28, and 56-day periods. Additionally, the AC-CF specimen exhibited the highest compressive strength, followed by the BC-CF and the control specimens. Considering that the experimental conditions for AC-CF and BC-CF were fixed at 3 g, these findings aligned with previous studies that demonstrated improved compressive strength of cement composites when the fibre percentage was below 0.75% [6,7,9]. Denser cement composites typically develop smaller void amounts, leading to higher compressive strength [27].

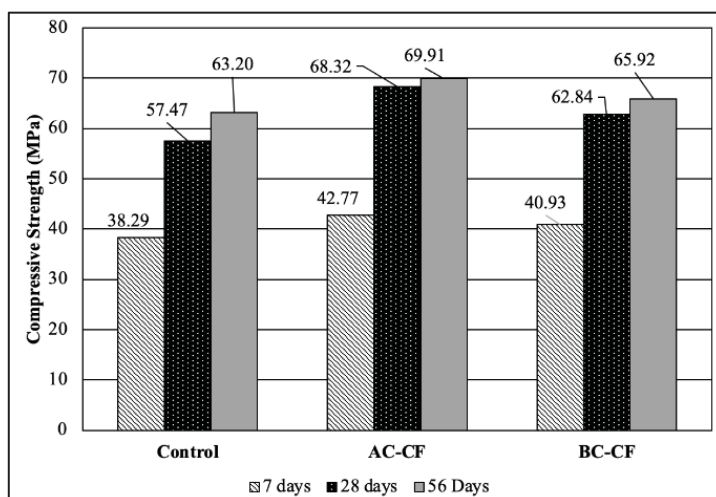


Fig. 8: The compressive strengths of the specimens.

Figure 9 reveals the correlation between the hardened density and compressive strength of the specimens at days 28 and 56. The analysis presented that the coefficient of determination ( $R^2$ ) exceeded 0.90, suggesting a strong, positive, and linear relationship between the two variables [28].

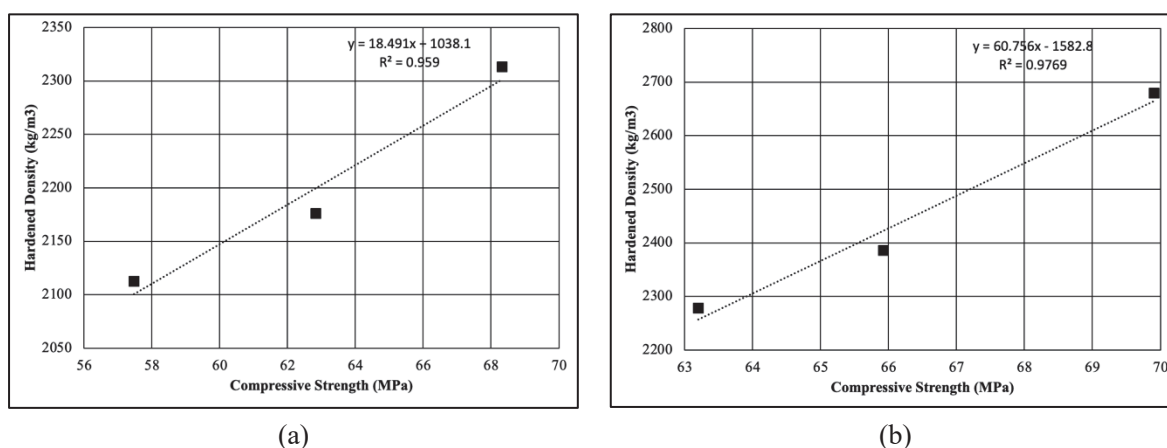


Fig. 9: The correlation between hardened density and compressive strength at the (a) 28<sup>th</sup> and (b) 56<sup>th</sup> day periods.

### 3.5 Flexural Strengths of the Cement Composites

Figure 10 depicts the flexural strengths of the control, AC-CF, and BC-CF specimens. Similar to the compressive strength, the flexural strength of all specimens exhibited an upward trend with increasing curing days (7, 28, and 56-day periods). Furthermore, the AC-CF specimen acquired the highest flexural strength, followed by the BC-CF and the control specimens.

A study by Paul et al. discovered that the fibres in cement composites formed bridges that effectively inhibited crack opening, which improved the flexural strength of the cement composites [13]. Figure 11 portrays the conditions of the specimens after failure. After failure, the control specimen was split into two sections, while a small crack was observed in the AC-CF specimen. Thus, the fibres present in the specimen contributed to its flexural residual strength, which prevented the crack expansion.

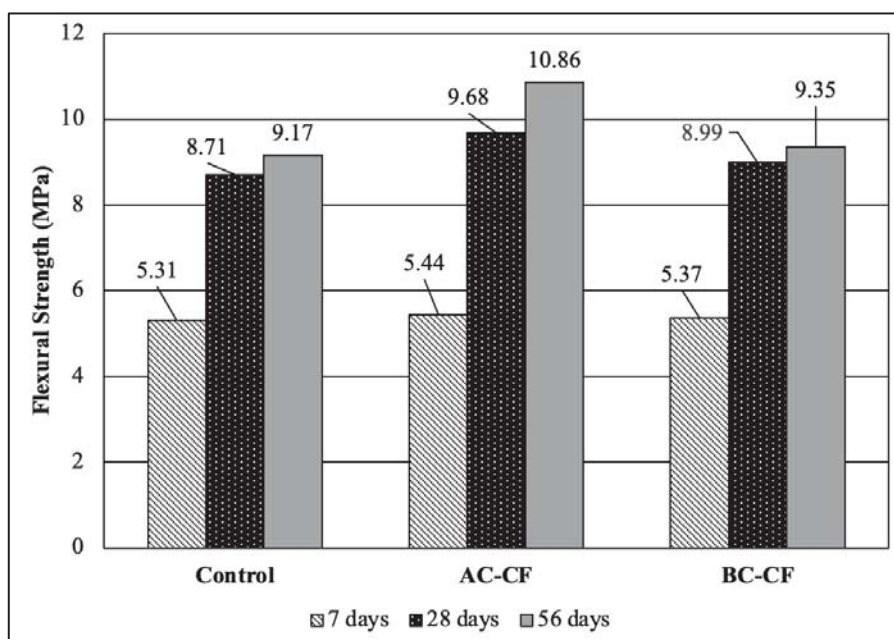


Fig. 10: The compressive strengths of the specimens.



Fig. 11: The conditions of the (a) control and (b) AC-CF specimens after failure.

### 3.6 Carbon Fibre Dispersions in the Cement Composites

The engineering properties of cement-based composites are significantly influenced by fibre dispersion. This property can be improved by using a more uniform fibre dispersion. Figure 12 presents the carbon fibre dispersions in AC-CF and BC-CF specimens using SEM images, respectively. The carbon fibres were scattered in the AC-CF specimen, suggesting a homogeneous distribution. Entangled fibres were observed in the BC-CF specimen, indicating inadequate dispersion. These findings demonstrated that the AC-CF was superior and acquired a more uniform fibre dispersion than BC-CF. This discovery was also consistent with earlier research that reported well-dispersed fibres could successfully contribute to higher cement-based composite strengths [29,30]. Therefore, fibre additions in the fluid cement mixture were concluded to facilitate the uniform fibre dispersion process.

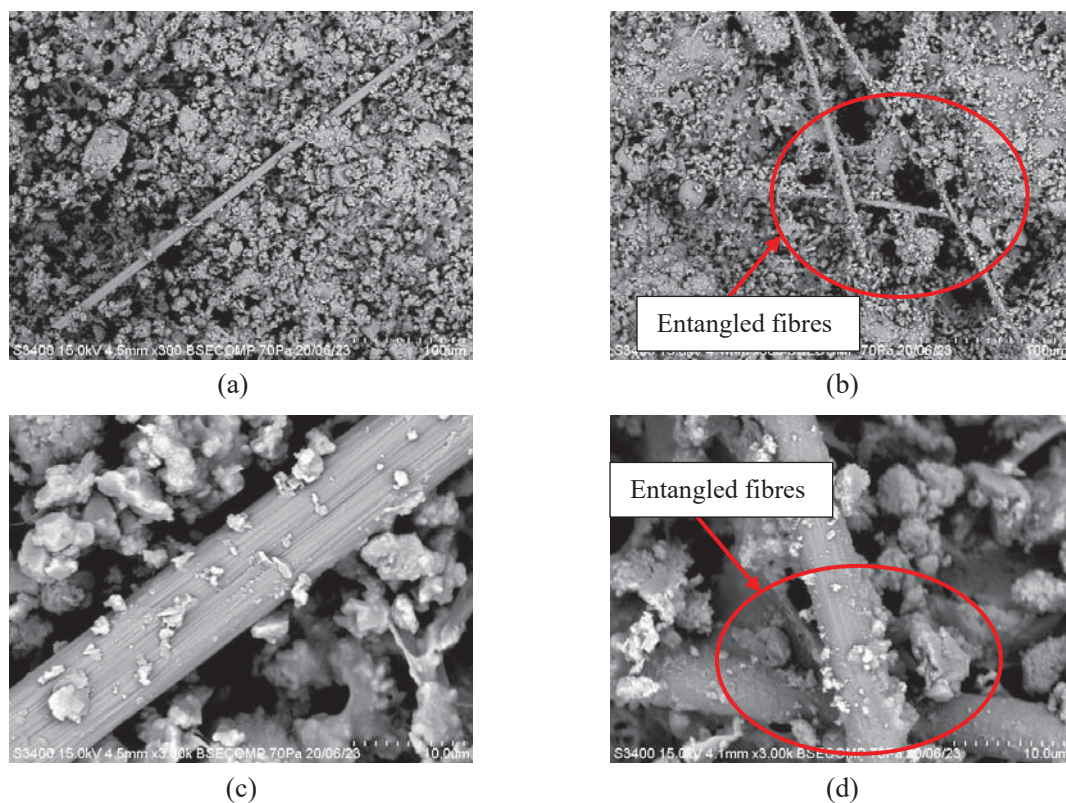


Fig. 12: The low and high magnification of SEM images for (a, b) AC-CF and (c, d) BC-CF specimens.

#### 4. CONCLUSION

This study successfully evaluated two distinct mixing sequences (AC-CF and BC-CF) by investigating the engineering properties of the cement composites and carbon fibre dispersions. Based on the findings and analysis presented in this study, the conclusions are as follow:

- a) The flowability values of AC-CF and BC-CF were lower than the control, attributed to surface roughness on the carbon fibre.
- b) Carbon fibres improved the hardened density, compressive strength, and flexural strength values of the cement composites.
- c) The AC-CF fibre dispersion was superior to the BC-CF specimen. This outcome increased the hardened density, compressive strength, and flexural strength of the cement composite.
- d) The AC-CF specimen demonstrated the optimal mixing sequence for a cement composite containing carbon fibres.

#### ACKNOWLEDGEMENT

This study was supported by the Dana Kluster Penyelidikan (DKP0087), Universiti Malaysia Sabah, under "Dispersion and Mixing Method of Synthetic Fibre Reinforced Cementitious Mortar."

## REFERENCES

- [1] Ragavendra S, Reddy IP, Dongre DA. (2017) Fibre reinforced concrete – a case study. Proceedings of the Architectural Engineering Aspect for Sustainable Building Envelopes, Khairatabd, Hydreabad, India, 10-11.
- [2] ASTM (2007). ASTM C 1116/C 1116M Part 6 – Standard Specification for Fibre-Reinforced Concrete. ASTM International. West Conshohocken.
- [3] Abdel-Rahman AG, Mirza FAM, Salah, AA. (2019) An overview of fibre reinforced concrete, FRC and fibres properties and current applications. International Journal of Science and Research (IJSR), 8(10): 504-515.
- [4] Thakur P, Singh K. (2018) A review: effect of carbon fibre on different mixes of concrete. International Research Journal of Engineering and Technology (IRJET), 5(3): 3996-3999.
- [5] Wang Z, Ma G, Ma Z, Zhang Y. (2021) Flexural behavior of carbon fibre reinforced concrete (RC) beams under impact loading. Cement and Concrete Composites, 118: 103910. doi: <https://doi.org/10.1016/j.cemconcomp.2020.103910>
- [6] Abbas N, Saad M, Habib M. (2022) Impact of carbon fibres on mechanical and durability properties of self-compacting concrete. Engineering Proceedings, 22(1): 9. doi: <https://doi.org/10.3390/engproc2022022009>
- [7] Aljalawi NMF, Al-Jelawy HM. (2018) Possibility of using concrete reinforced by carbon fibre in construction. International Journal of Engineering and Technology, 7(4.20): 449-452.
- [8] Salama AHES, Edris WF. (2021) Performance of carbon fibre filament reinforcing cement mortar. Civil Engineering Journal, 7(10): 1693-1701. doi: <https://doi.org/10.28991/cej-2021-03091753>.
- [9] Mello E, Ribellato C, Mohamedelhassan E. (2014) Improving concrete properties with fibres addition. International Journal of Civil and Environmental Engineering, 8(3): 249-254. doi: <https://doi.org/10.5281/zenodo.1091168>
- [10] Li YF, Yang TH, Kuo CY, Tsai YK. (2019) A study on improving the mechanical performance of carbon-fibre-reinforced cement. Materials, 12(17): 2715. doi: <https://doi.org/10.3390/ma12172715>
- [11] Deepesh P, Jayant K. (2016) Study of mechanical and durability properties of SIFCON by partial replacement of cement with fly ash as defined by an experimental based approach. International Journal for Innovative Research in Science & Technology, 5(5): 8568-8574.
- [12] Deore SM, Bodke JS, Aware RV, Ahire CV, Kamble PM, Pendhari AR. (2017) Addition of carbon fibre in concrete with partial replacement of sand by waste foundry sand. International Research Journal of Engineering and Technology (IRJET), 4(4): 2017-2079.
- [13] Paul SC, Zijl GPAGv, Savija B. (2020) Effect of fibres on durability of concrete: A practical review. Materials, 13(20): 4562. doi: <https://doi.org/10.3390/ma13204562>.
- [14] ACI Committee 6.44. (1982). State-of-the-art report on fibre reinforced concrete. ACI 6.44 IR, ACI, Detroit.
- [15] Gao J, Wang Z, Zhang T, Zhou L. (2017) Dispersion of carbon fibres in cement-based composites with different mixing methods. Construction and Building Materials, 134: 220-227. doi: <https://doi.org/10.1016/j.conbuildmat.2016.12.047>
- [16] Gyawali TR. (2019) Investigation on mixing process for the development of high ductile mortar containing thin and short fibres. Investigation Journal of Materials Engineering, 9(1): 8-15.
- [17] De Franca MS, Cardoso FA, Pileggi RG. (2016) Influence of the addition sequence of PVA-fibres and water on mixing and rheological behavior of mortars. Ibracon Structures and Materials Journal, 9(2): 226-243. doi: <https://doi.org/10.1590/S1983-41952016000200005>
- [18] Zhou J, Qian S, Ye G, Copuroglu O, Breugel KV, Li VC. (2012) Improved fibre distribution and mechanical properties of engineered cementitious composites by adjusting the mixing sequence. Cement & Concrete Composites, 34(3): 342-348. doi: <https://doi.org/10.1016/j.cemconcomp.2011.11.019>
- [19] ASTM. (1999). ASTM C305-94 – Standard Practice for Mechanical Mixing of Hydraulic Cement Pastes and Mortars of Plastic Consistency. ASTM International. West Conshohocken.

- 
- [20] ASTM. (2007). ASTM C1437-20 – Standard Test Method for Flow of Hydraulic Cement Mortar. ASTM International. West Conshohocken.
- [21] BSI. (1999). BS EN 1015-10 – Methods of Test for Mortar for Masonry – Part 10: Determination of Dry Bulk Density of Hardened Mortar. British Standard. BSI Standards Limited.
- [22] ASTM. (1999). ASTM C 109/C109M-02 – Standard Test Method for Compressive Strength of Hydraulic Cement Mortars (Using 2-in. or [50 mm] Cube Specimens). ASTM International. West Conshohocken.
- [23] ASTM. (2002). ASTM C 348-02 – Standard Test Method for Flexural Strength of Hydraulic-Cement Mortars. ASTM International. West Conshohocken.
- [24] He S, Yang EH. (2021) Strategic strengthening of the interfacial transition zone (ITZ) between microfibre and cement paste matrix with carbon nanofibres (CNFs). *Cement and Concrete Composite*, 119: 104019. doi: <https://doi.org/10.1016/j.cemconcomp.2021.104019>
- [25] Kao GJ, Gowripalan N, Bandyopadhyay S. (2000) Preliminary studies of carbon fibre reinforced cementitious composites by AFM and FESEM. International Composites Conference (ACUN-2), Sydney, New South Wales, Australia.
- [26] Li M, Li VC. (2013) Rheology, fibre dispersion, and robust properties of engineered cementitious composites. *Materials and Structures*, 46: 405-420.
- [27] Othman R, Jaya RP, Muthusamy K, Sulaiman M, Duraisamy Y, Abdullah MMAB, Przybl A, Sochacki W, Skrzypczak T, Vizureanu P, Sandu AV. (2021) Relation between density and compressive strength of foamed concrete. *Materials*, 14(11): 2967. doi: <https://doi.org/10.3390/ma14112967>
- [28] Zaid O, Ahmad J, Siddique MS, Aslam F, Alabduljabbar H, Khedher KM. (2021) A step towards sustainable glass fibre reinforced concrete utilising silica fume and waste coconut shell aggregate. *Scientific Reports*, 11: 12822. <https://doi.org/10.1038/s41598-021-92228-6>.
- [29] Zhu H, Zhou H, Gou H. (2021) Evaluation of carbon fiber dispersion in cement-based materials using mechanical properties, conductivity, mass variation coefficient, and microstructure. *Construction and Building Materials*, 266(A): 120891. doi: <https://doi.org/10.1016/j.conbuildmat.2020.120891>
- [30] Wang C, Li KZ, Li HJ, Jiao GS, Lu J, Hou DS. (2008) Effect of carbon fiber dispersion on the mechanical properties of carbon fiber-reinforced cement-based composites. *Materials Science and Engineering: A*, 487(1-2): 52-57. doi: <https://doi.org/10.1016/j.msea.2007.09.073>.

## STRATEGIES TO REDUCE THE NUMBER OF SEVERELY INJURED VICTIMS IN ADOLESCENT MOTORCYCLE RIDERS

PADA LUMBA<sup>1\*</sup>, ANTON ARIYANTO<sup>1</sup> AND AHMAD FATHONI<sup>2</sup>

<sup>1</sup>Civil Engineering Study Program, Faculty of Engineering,  
Universitas Pasir Pengaraian, Pasir Pengaraian, 28457, Indonesia

<sup>2</sup>Mechanical Engineering Study Program, Faculty of Engineering,  
Universitas Pasir Pengaraian, Pasir Pengaraian, 28457, Indonesia

\*Corresponding author: [padalumba@gmail.com](mailto:padalumba@gmail.com)

(Received: 8 September 2023; Accepted: 25 October 2023; Published on-line: 1 January 2024)

**ABSTRACT:** Statistical data in 2021 in Indonesia shows that the number of accident victims reached 103,645 cases. Around 25% of these accident victims were underage drivers. For this reason, efforts must be made to minimize the number of accident victims, especially avoiding severe injuries. The criteria for respondents are motorcycle riders aged 12 - 25 years who are still categorized as adolescent riders. The data collection was carried out by interviewing respondents for approximately 10 minutes. For data analysis, the number of respondents used was 308 respondents. The location for data collection was Riau Province, Indonesia. The data was analyzed by Bayesian network. To get a good model, the basic model was validated. The number of respondents used to validate this model was 107 respondents. The results of the analysis show that the probability of an adolescent driver to experience severe injury is 27% and mild injury is 73%. Scenario 1 shows that poor driving performance will increase the probability of severe injury by 3%. Scenario 2 shows that driver fatigue will increase the probability of severe injury by 3%. Scenario 3 shows that drivers who conduct traffic violations will increase the probability of severe injury by 5%. Scenario 4 shows that drivers who perform long trips (more than 1 hour) increase their fatigue from 28% to 60%, which also increases the probability of severe injury by 1%. Scenario 5 shows that late night driving (between 24:00 – 06:00) not only increases the probability of fatigue but also increases the probability of severe injury by 1%. Strategic steps to reduce severe injury among adolescent motorcyclists include driving with good performance, avoiding fatigue-inducing conditions, abiding by all traffic rules, and avoiding driving between the hours of 24:00-06:00.

**ABSTRAK:** Data statistik pada tahun 2021 di Indonesia menunjukkan jumlah mangsa kemalangan mencapai 103,645 kes. Kira-kira 25% mangsa kemalangan ini adalah pemandu bawah umur. Oleh itu, usaha perlu dilaksanakan bagi meminimumkan mangsa kemalangan, terutama dalam mengelakkan kecederaan parah. Kriteria responden adalah penunggang motosikal berumur 12 - 25 tahun yang masih dikategori sebagai penunggang remaja. Pengumpulan data dijalankan dengan menemu bual responden selama lebih kurang 10 minit. Analisis data ini melibatkan 308 orang responden. Lokasi pengumpulan data adalah di Riau, Indonesia. Data dianalisis dengan rangkaian Bayesian. Bagi mendapatkan model terbaik, model asas telah disahkan. Bilangan responden yang terlibat dalam mengesahkan model ini adalah seramai 107 orang responden. Dapatan kajian menunjukkan kebarangkalian pemandu remaja yang mengalami kecederaan parah adalah 27% dan cedera ringan sebanyak 73%. Senario 1 menunjukkan pemanduan tidak berhemah akan meningkatkan kebarangkalian cedera parah sebanyak 3%. Senario 2 menunjukkan bahawa memandu dalam keadaan letih akan meningkatkan kebarangkalian cedera parah sebanyak

3%. Senario 3 menunjukkan bahawa pemandu yang melanggar peraturan lalu lintas akan meningkatkan kebarangkalian cedera parah sebanyak 5%. Senario 4 menunjukkan pemandu yang melakukan perjalanan melebihi 1 jam akan meningkatkan keletihan dari 28% kepada 60%, juga menyumbang kepada peningkatan kebarangkalian cedera parah sebanyak 1%. Senario 5 menunjukkan bahawa pemanduan lewat malam (antara 24.00 – 06.00) bukan sahaja meningkatkan kebarangkalian keletihan tetapi juga meningkatkan kebarangkalian cedera parah sebanyak 1%. Langkah strategik bagi mengurangkan kecederaan parah di kalangan penunggang motosikal remaja termasuk: memandu dengan berhemah, tidak memandu dalam keadaan letih, mematuhi segala undang-undang jalan raya dan mengelak dari memandu pada jam 24.00 hingga 06.00.

---

**KEYWORDS:** *road traffic accident; Bayesian network; mildly injured; motorcycle rider; severely injured*

## 1. INTRODUCTION

The biggest contributing cause to traffic accidents is the human error factor. The age of the driver influences the driver's behavior when driving [1] and also influences the risk of accident [2]. Motorcycles have high mobility thus they are very popular with young riders. This vehicle is less stable and lacks protection for the driver while driving, resulting in greater risk of accident severity. In general, young drivers have very little experience in driving compared to adult drivers [3] which results in young drivers tending to commit more traffic violations due to mistakes or ignorance of traffic rules [4]. This certainly results in young drivers having the potential to experience accidents [5] compared to experienced drivers who tend to drive more effectively [6]. Unfortunately, the tendency for young drivers to commit traffic violations is well documented [7-12]. Additionally, stress factors caused by work can also influence risky behavior when driving [13,14]. Other researchers state that personality and attitude factors also influence risky behavior when driving [15]. In general, young drivers are less stable mentally and emotionally, increasing their risk of accidents [16,17]. The accident rate at a young age is quite high compared to adult drivers, however this accident rate rises again for drivers aged 60-69 years [18]. In general, young drivers' risks are influenced by road type, visibility conditions, gender [19], and speed [20].

Generally, young riders have better stamina than other age groups, which allows young riders to accept travel routes that quite far and long. Driving too far and for a long time can result in fatigue in the driver during the trip [21]. Moreover, if the driver lacks sleep and then travels far, this will increase fatigue [22] and drowsiness that will affect the driver's performance [23,24]. This can increase the risk of an accident [25] as well as and increase the level of severity when experiencing an accident [26,27]. Besides that, driving time can also affect the level of driver fatigue, thereby increasing the risk of accidents [28] and their severity [29-31]. Fatigue can reduce the driver's abilities and can even increase the risk of an accident [25,32,33] and the severity of said accident [34]. Apart from the age factor that influences accidents, another factor is the gender of the driver. There is a tendency for male drivers to be more involved in accidents than female drivers, however female drivers are more likely to be injured during accidents than male drivers [35,36]. Leading research in this area is as shown in Fig. 1.

Accident cases in Indonesia from 2020 to 2021 are likely to increase, as shown in Fig. 2 [37]. In addition, about 25% of accident victims are underage drivers. Ninety two percent of adolescent drivers often experience distractions while driving [38]. Accident statistics in Indonesia show that every 20 minutes, one life is lost on the highway. Other data shows the number of accident victims for drivers aged 10-19 years amounted to 26,906 and drivers aged

20-29 years amounted to 29,281 [39]. The use of motorcycles is quite high among adolescents, resulting in high accident rates for this age group. In 2021, the number of motorcycles in Indonesia reached 124,042,298 units [37], as shown in Fig. 3.

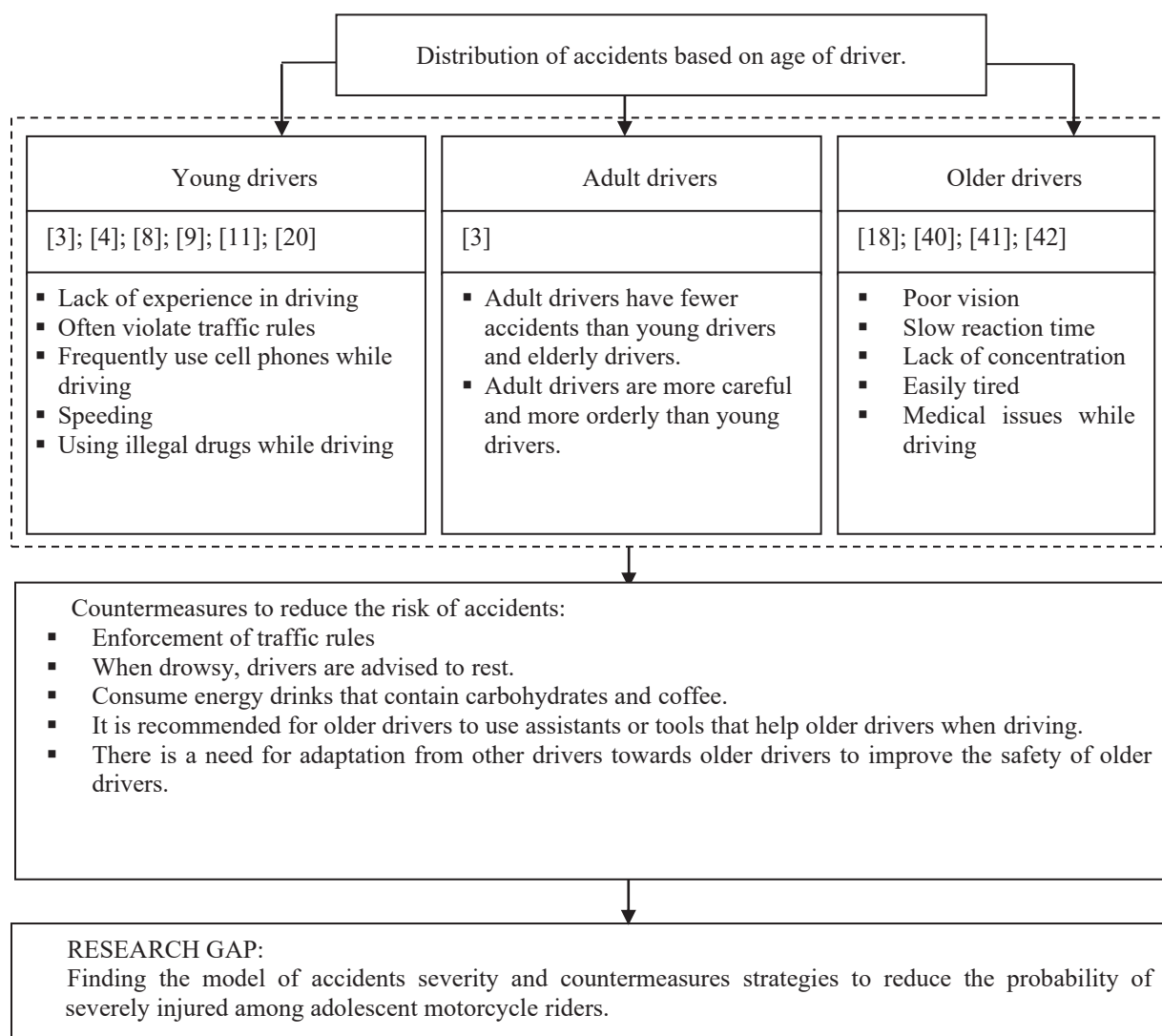


Fig. 1: Category of drivers' and previous of road accidents in the world.

Thus, it is necessary to conduct the research to reduce the number of severely injured victims in Indonesia, namely by finding the dominant variable that affects the severity of accidents in adolescent motorcycle riders and finding the model and strategies to reduce the risk of severe injury. The research parameters of this study are: 1) respondents are adolescent motorcycle riders aged 12 until 25 years and have had accidents; 2) the data was analyzed by Bayesian Network; 3) the probability of accident severity in terms of human factor, road and environmental factor and vehicle factor.

## 2. METHODS

The research was carried out in Riau Province. A total of 415 respondents were used, of which 308 respondents were used for modeling and 107 respondents were used for model validation. The number of samples was calculated by using the equation:

$$n = \frac{N}{1 + Ne^2} \tag{1}$$

Information: n=number of samples, N=population, e=margin of error, The number of accident victims in Riau Province = 2750 people, e value = 5%.

$$349.21 = \frac{2750}{1 + 2750 \times 0.05^2}$$

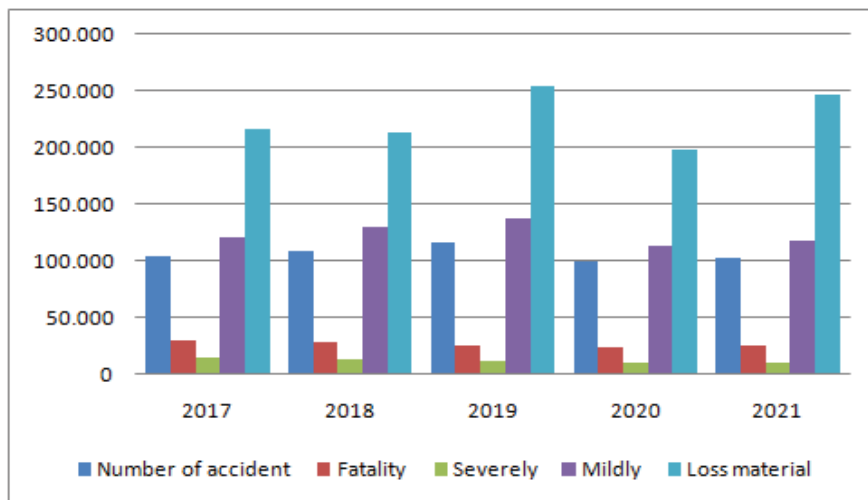


Fig.2: Number of accidents and number of victims of accidents severity in Indonesia [37].

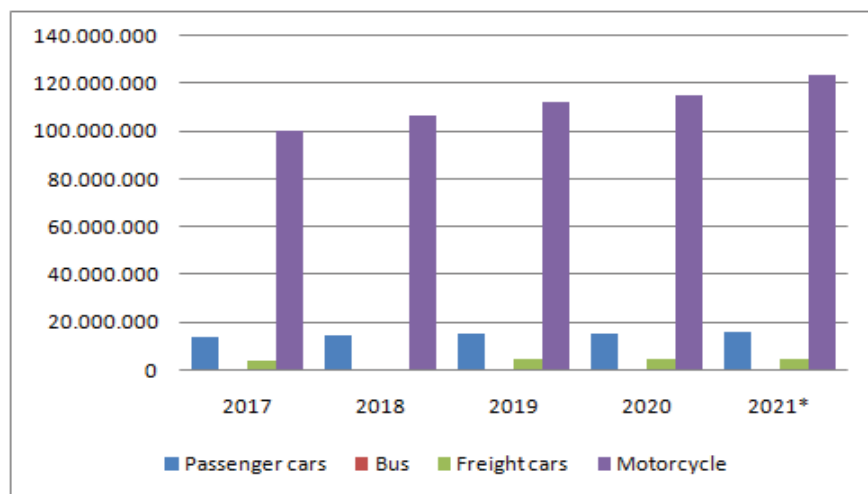


Fig.3: Number of motorcycle vehicles in Indonesia [37].

The number of samples that were used to analyze data and validate the model was 415 respondents.

The criteria for respondents in this study were adolescent motorcycle riders (12 years to 25 years) who had experienced an accident by either hitting another vehicle, being hit by another vehicle, or without the involvement of another vehicle. The data was collected by interviewing adolescent motorcycle riders who had experienced accidents.

Variables that affect the model included driving behavior, driving fatigue, driving performance, time of accident, driving time before the accident, gender, engine capacity, driving license ownership, monotony while driving, roadside variability at the accident site, and road geometry at the accident scene. Details of variables and questions asked to the respondents are given in Table 1.

Table 1: Variables and statistics

Variable	Value	Percentage
Gender	Male	61
	Female	39
Possession of a Driver's License	Have	15
	Do Not have	85
Rider performance	Good	74
	Not good	26
Risky behavior	Violating	21
	Not violating	79
Fatigue	Yes	28
	No	72
Duration of driving	≤ 30 minutes	67
	30 < DURATION ≤ 60	21
	> 60 minutes	12
Time of the accident occurred	06.00 – 12.00	28
	12.00 – 18.00	49
	18.00 – 24.00	21
	24.00 – 06.00	2
Road geometry	Flat and straight	72
	Curve	28
Roadside variability	Varied	52
	Not varied	48
Road condition	Monotonous	47
	Not monotonous	53
Engine capacity	≤ 125 cc	74
	> 125 cc	26

Data was analyzed with Bayesian network using GeNIe 2.0 software [43]. Bayesian networks originate from Bayes theory, which is an approach used to analyze probabilistic data or data that is uncertain. Bayesian theory is more suitable for predicting accident severity than regression models [44]. The Bayesian network shows the relationship between the probability of event A occurring provided that event B has occurred  $P(A|B)$ , with the following formula:

$$P(A|B) = \frac{P(B|A)P(A)}{P(B|A)P(A)+P(B|-A)P(-A)} \quad (2)$$

After the data was analyzed, a probability model for accident severity among adolescent motorcycle riders was obtained. The model was validated to know its accuracy. Validation was conducted by calculating the MAD (Mean Absolute Deviation) value with the formula:

$$MAD = 1/2 \sum |Actual - Forecast| \quad (3)$$

The model was considered accurate if the results of the model and the results in the field were not significantly different. If the model was accurate enough, then several scenarios

were carried out in the next step to find strategies to reduce the number of cases of severe injury to motorcyclists. The research flow chart is shown in Fig. 4.

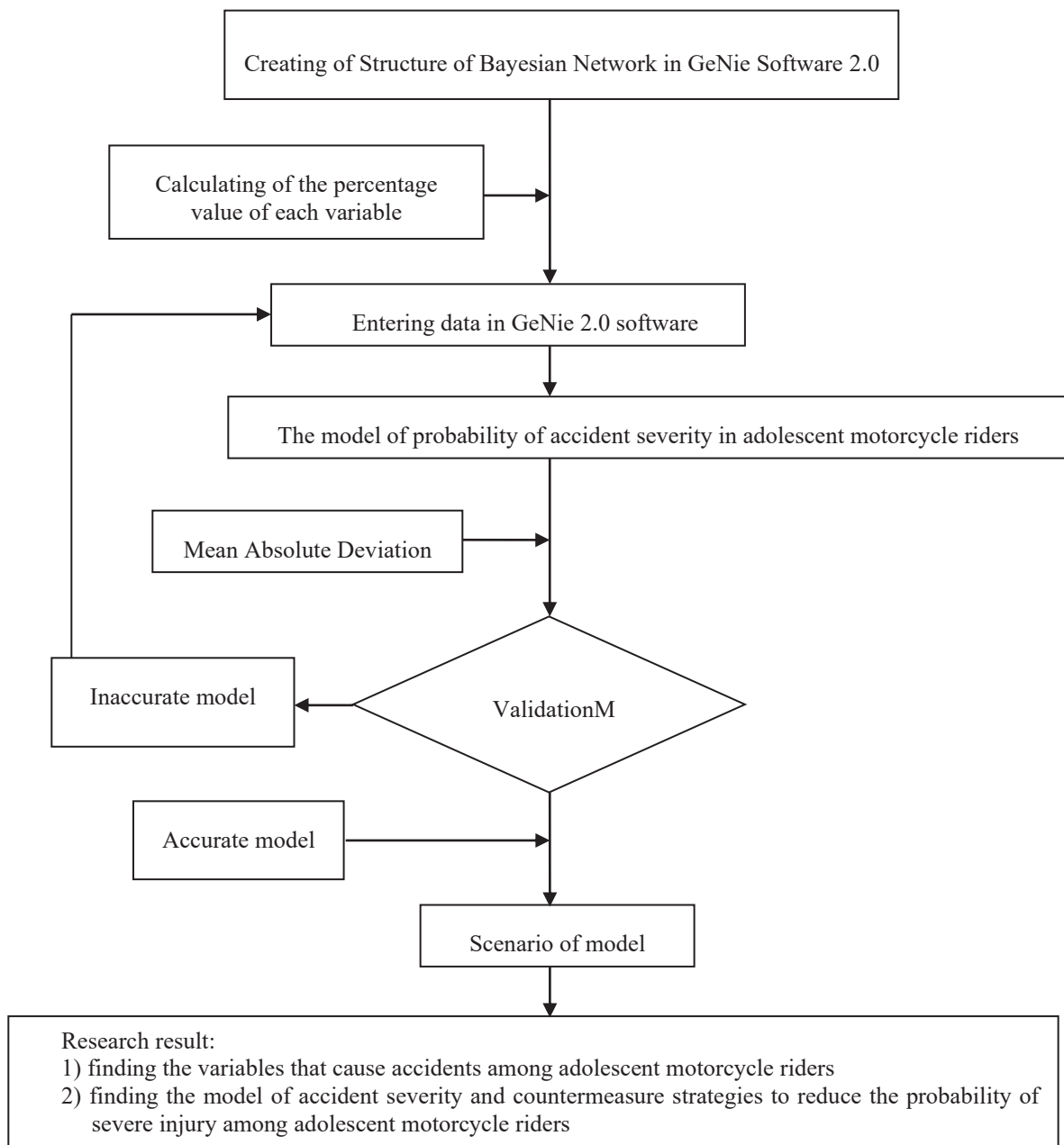


Fig. 4: Flow chart of research.

### 3. RESULTS AND DISCUSSION

Variables and accident statistics at the study sites are shown in Table 1. Meanwhile, the resulting structure of the Bayesian network model shows that the probability of adolescent drivers who experience severe injury is 27% and mild injury is 73%, as shown in Fig. 5. The root causes of probability of serious injury were quite high among adolescent motorcycle riders namely, risky driving behavior such as speeding, using cell phones while driving, and violating traffic rules. The model equations that were obtained from the structure of Bayesian network above can be seen in Table 2.

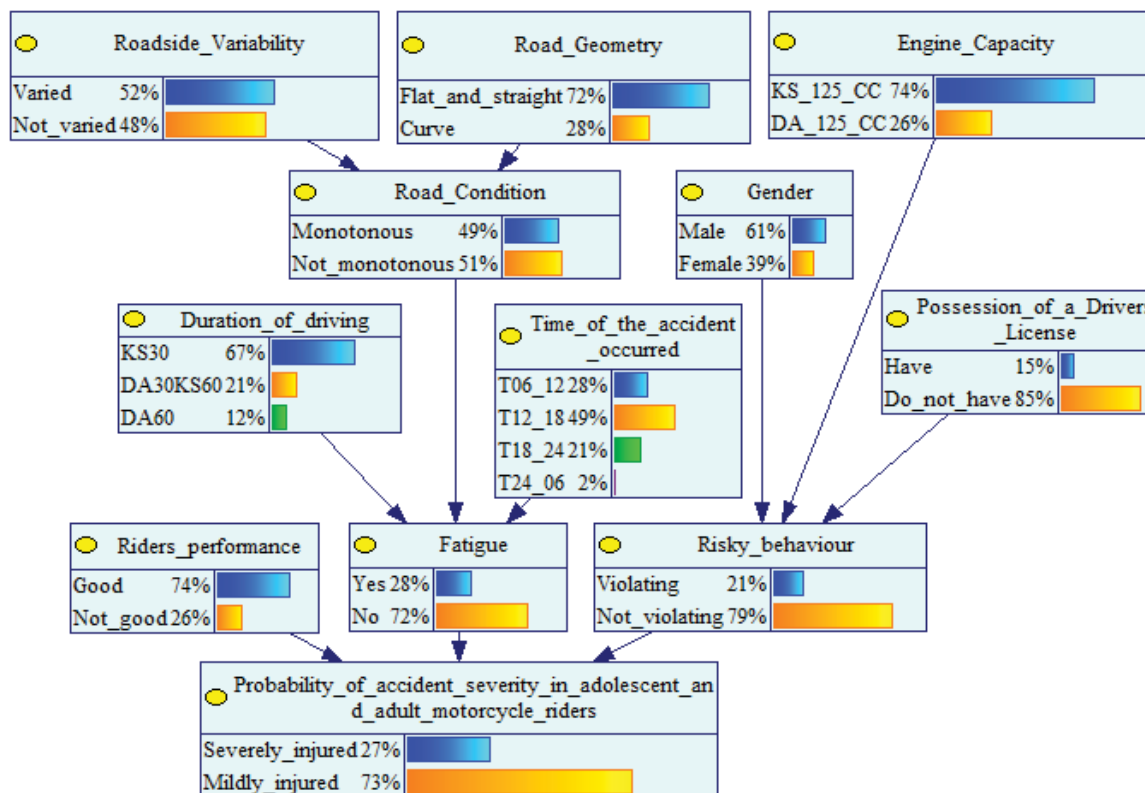


Fig.5: Model of the probability of accidents severity in adolescent riders.

Table 2: Equality model of probabilities of accident severity in adolescent motorcycle riders

P(BS)	P(TS)	P(FS)	P(ACS)
BS1	TS1	FS1	$P(ACS)1 = P(ACS BS1, TS1, FS1, LDS, TMS, LS, MS, GS, RSS, RGS, CS)$ $P(BS1 LS, GS, CS) P(TS1 LDS, MS, TMS) P(MS RSS, RGS)$
BS1	TS1	FS2	$P(ACS)2 = P(ACS BS1, TS1, FS2, LDS, TMS, LS, MS, GS, RSS, RGS, CS)$ $P(BS1 LS, GS, CS) P(TS1 LDS, MS, TMS) P(MS RSS, RGS)$
BS1	TS2	FS1	$P(ACS)3 = P(ACS BS1, TS2, FS1, LDS, TMS, LS, MS, GS, RSS, RGS, CS)$ $P(BS1 LS, GS, CS) P(TS2 LDS, MS, TMS) P(MS RSS, RGS)$
BS1	TS2	FS2	$P(ACS)4 = P(ACS BS1, TS2, FS2, LDS, TMS, LS, MS, GS, RSS, RGS, CS)$ $P(BS1 LS, GS, CS) P(TS2 LDS, MS, TMS) P(MS RSS, RGS)$
BS2	TS1	FS1	$P(ACS)5 = P(ACS BS2, TS1, FS1, LDS, TMS, LS, MS, GS, RSS, RGS, CS)$ $P(BS2 LS, GS, CS) P(TS1 LDS, MS, TMS) P(MS RSS, RGS)$
BS2	TS1	FS2	$P(ACS)6 = P(ACS BS2, TS1, FS2, LDS, TMS, LS, MS, GS, RSS, RGS, CS)$ $P(BS2 LS, GS, CS) P(TS1 LDS, MS, TMS) P(MS RSS, RGS)$
BS2	TS2	FS1	$P(ACS)7 = P(ACS BS2, TS2, FS1, LDS, TMS, LS, MS, GS, RSS, RGS, CS)$ $P(BS2 LS, GS, CS) P(TS2 LDS, MS, TMS) P(MS RSS, RGS)$
BS2	TS2	F2	$P(ACS)8 = P(ACS BS2, TS2, FS2, LDS, TMS, LS, MS, GS, RSS, RGS, CS)$ $P(BS2 LS, GS, CS) P(TS2 LDS, MS, TMS) P(MS RSS, RGS)$
			$\Sigma P(ACS)$

P=Probability, ACS=Accident Severity, BS=Risky Behavior, BS1=Violating, BS2=Not Violating, TS=Fatigue, TS1=Yes, TS2=No, FS=Rider performance, FS1=Good, FS2=Not good, ACS=Accident, LDS=Long duration of driving, TMS=Time of the accident occurred, LS=Possession of a Driver's License, MS=Road Condition, GS=Gender, RSS=Roadside variability, RGS=Road Geometry, CS=Engine Capacity

The model needed to be validated to be able to move on to the next stage. After validation, the difference between the model results and the actual results (MAD) was 22.93%, as shown in Table 3. This shows that the accuracy of the model is 77.07%.

Furthermore, several scenarios were carried out to obtain strategic treatment to reduce serious injuries. Because rider performance variables, fatigue variables, and risky behavior variables have a direct influence on the severity level when an accident occurs, several scenarios were carried out to see the influence of these three variables on the accident severity. Meanwhile, to see the influence of long driving duration variables and driving time variables on the possibility of increasing fatigue and increasing the accident severity, several scenarios were carried out to determine the magnitude of the influence of these variables on the level of driver fatigue and accident severity.

Table 3: The calculation of mean absolute deviation (MAD)

Risky Behavior	Fatigue	Rider Performance	Probability of Accident Severity in Adolescents		Deviation
			Actual	Model	
BS1	TS1	FS1	25.00	44	19.00
BS1	TS1	FS2	66.67	17	49.67
BS2	TS1	FS1	33.33	23	10.33
BS2	TS2	FS2	14.29	27	12.71
					<b>22.93</b>

Scenario 1 shows the influence of driver performance on accident severity. The results of the analysis show that drivers who drive when their performance is not good will increase the probability of severe injury from 27% to 30%, as shown in Fig.6. Even though the rate of probability increase of serious injury to riders was only 3%, this certainly cannot be ignored because it is closely related to the level of accident severity. This research is in line with research conducted by [26,27]. Meanwhile, scenario 2 shows the effect of driver fatigue on the accident severity. The results of the analysis identified that when a driver is in a fatigued condition, the probability of severe injury will increase from 27% to 30%, as shown in Fig. 7. When the rider feels tired, the ability to drive well will decrease, the driver's level of alertness will also decrease, resulting in a very high risk of accidents and high accident severity. This research is in line with research conducted by [26,27]. Scenario 3 shows the effect of traffic violations on the accident severity. The results of the analysis show that drivers who commit traffic violations will be at risk of increasing the probability of severe injury from 27% to 32%, as shown in Fig. 8. This means that the effect of violating traffic rules will increase the probability of severe injury by 5%. This research is in line with research conducted by [4,7-12]. Scenario 4 shows the effect of driving duration on the level of fatigue and the accident severity. The results of the analysis show that driving for only 1 hour increases the probability of fatigue but does not increase the probability of severe injury. However, for trips longer than 1 hour, apart from increasing the probability of fatigue, it also increases the possibility of severe injury from 27% to 28%, as shown in Fig. 9. This means that adolescent motorcycle riders who drive for more than 1 hour are more likely to suffer severe injury than riders who drive for less than 1 hour.

Scenario 5 shows the effect of driving time on the accident severity. Driving in the time periods of 06:00-12:00, 12.00-18.00, 18.00-24.00 only affects the increase in driver fatigue, but driving in the time period of 24.00 - 06.00 not only increases the probability of fatigue but also increases the probability of being severely injured from 27% to 28%, as shown in Fig. 10. This shows that driving in the time period of 24.00 - 06.00 is very risky, the possibility of the riders experiencing fatigue and driving at this time also increases the probability of severe injury. This research is in line with research conducted by [29-31].

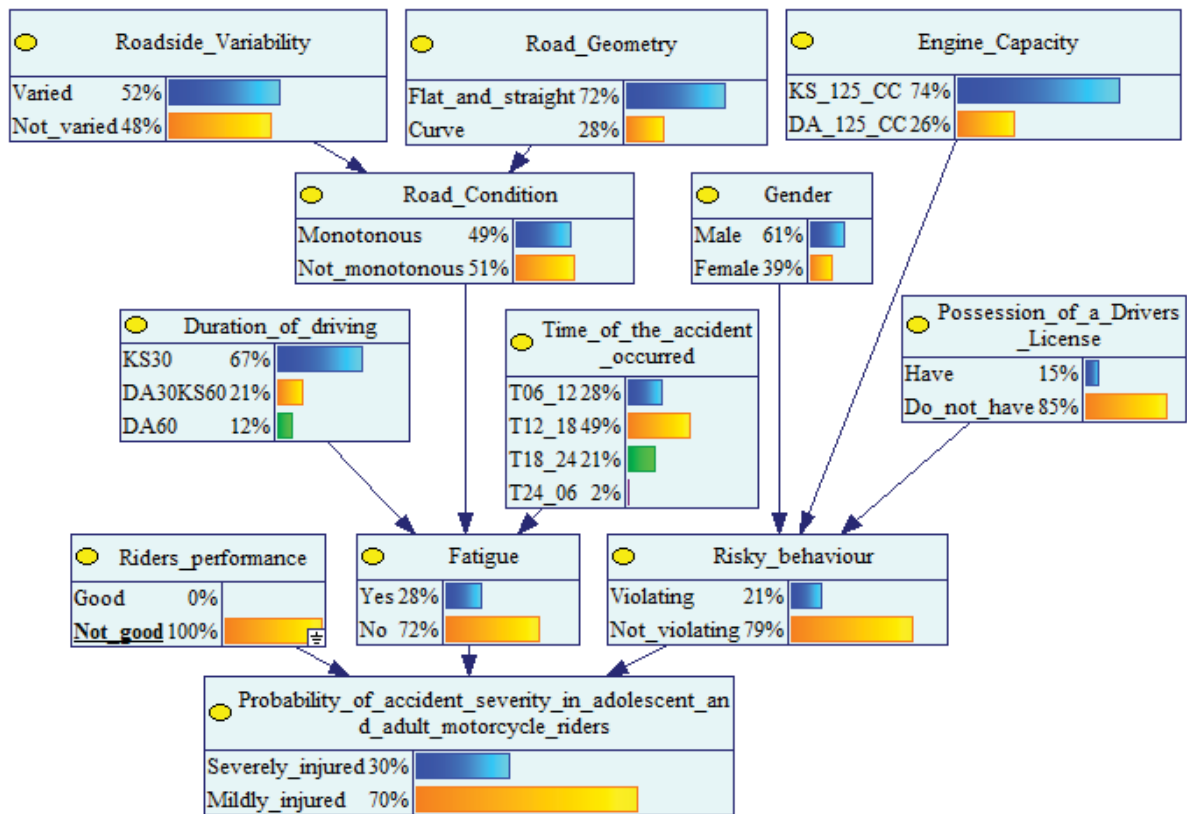


Fig.6: Scenario 1- Influence of driver performance on accident severity.

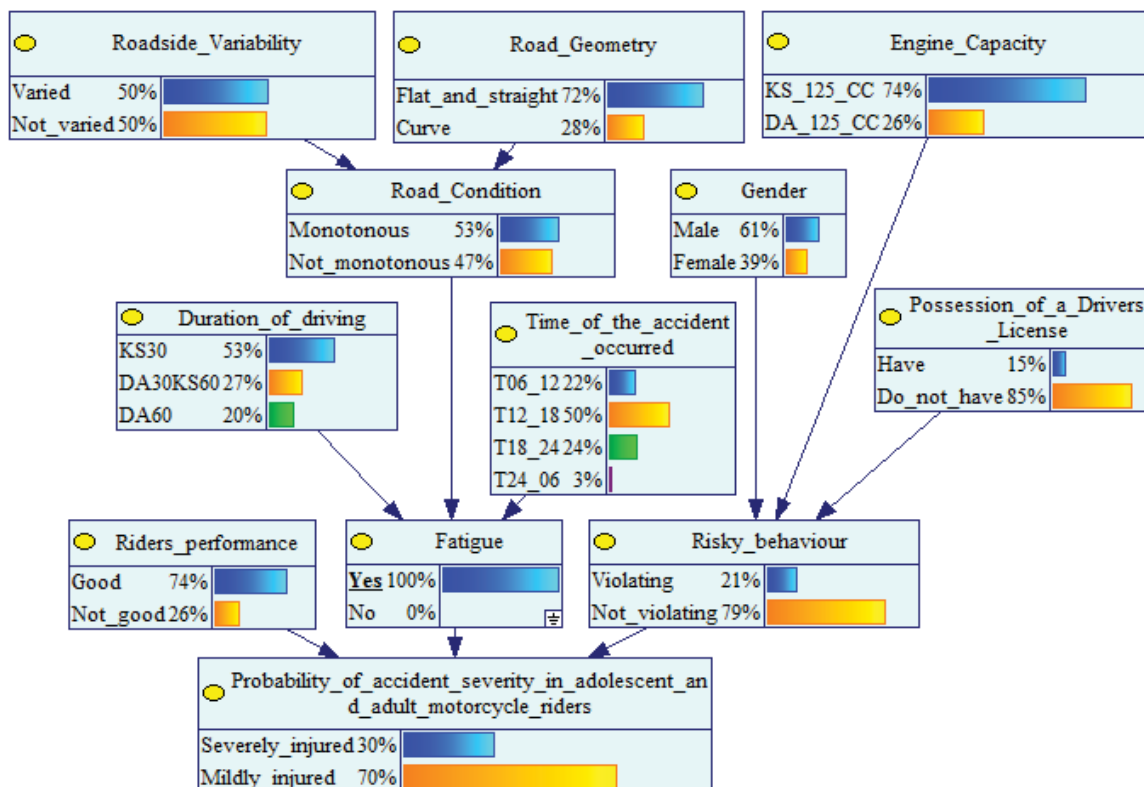


Fig.7: Scenario 2 - Effect of driver fatigue on accident severity.

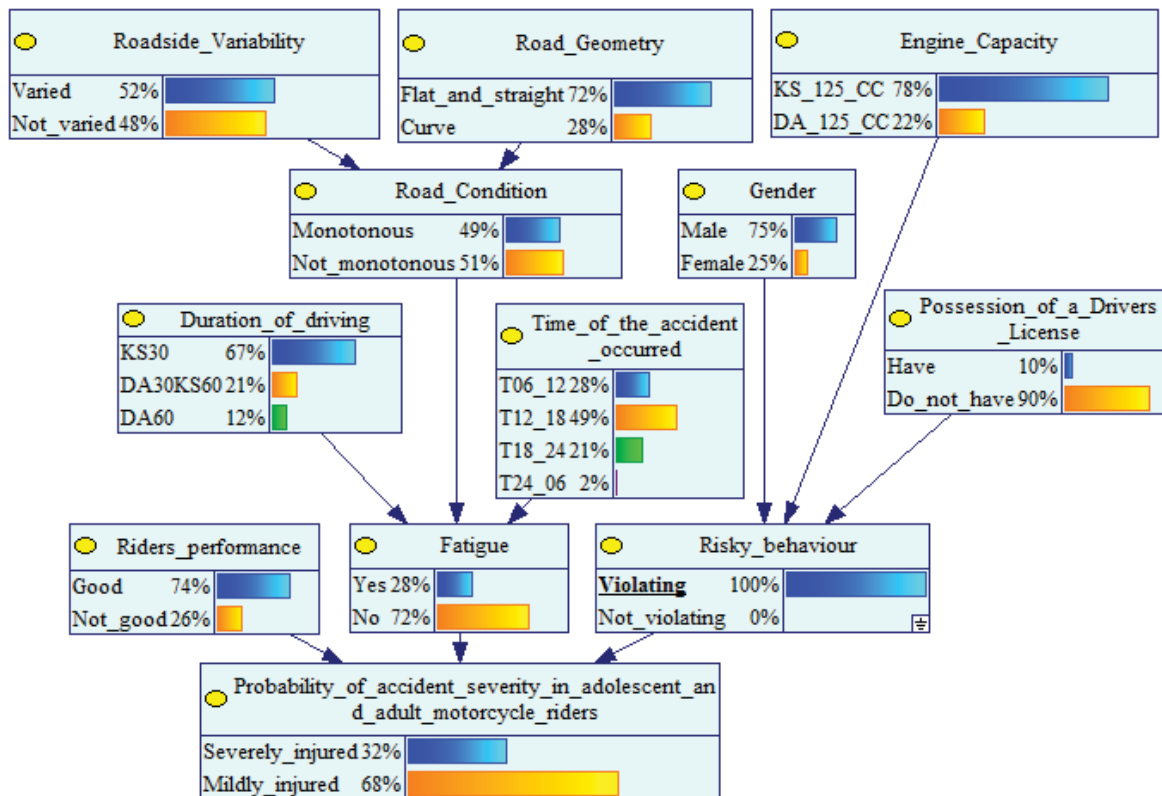


Fig.8: Scenario 3 - Effect of traffic violations on accident severity.

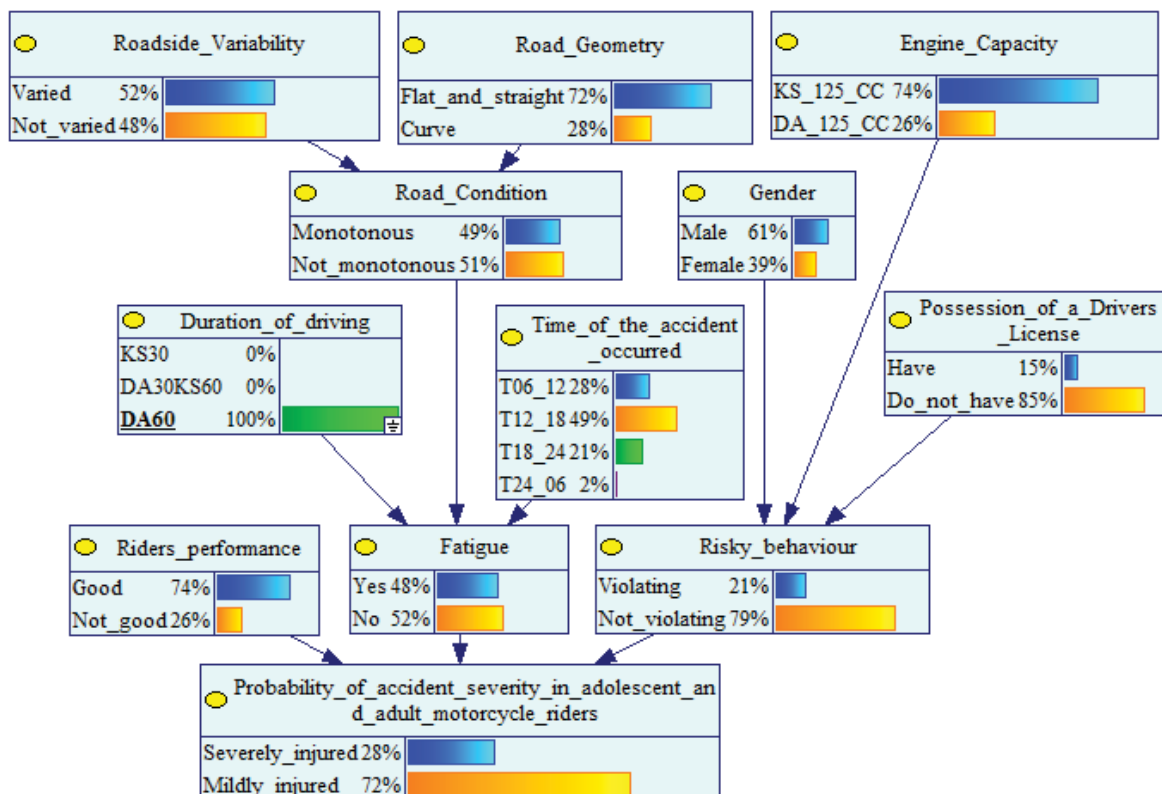


Fig. 9: Scenario 4 - Effect of driving time on fatigue level and accident severity.

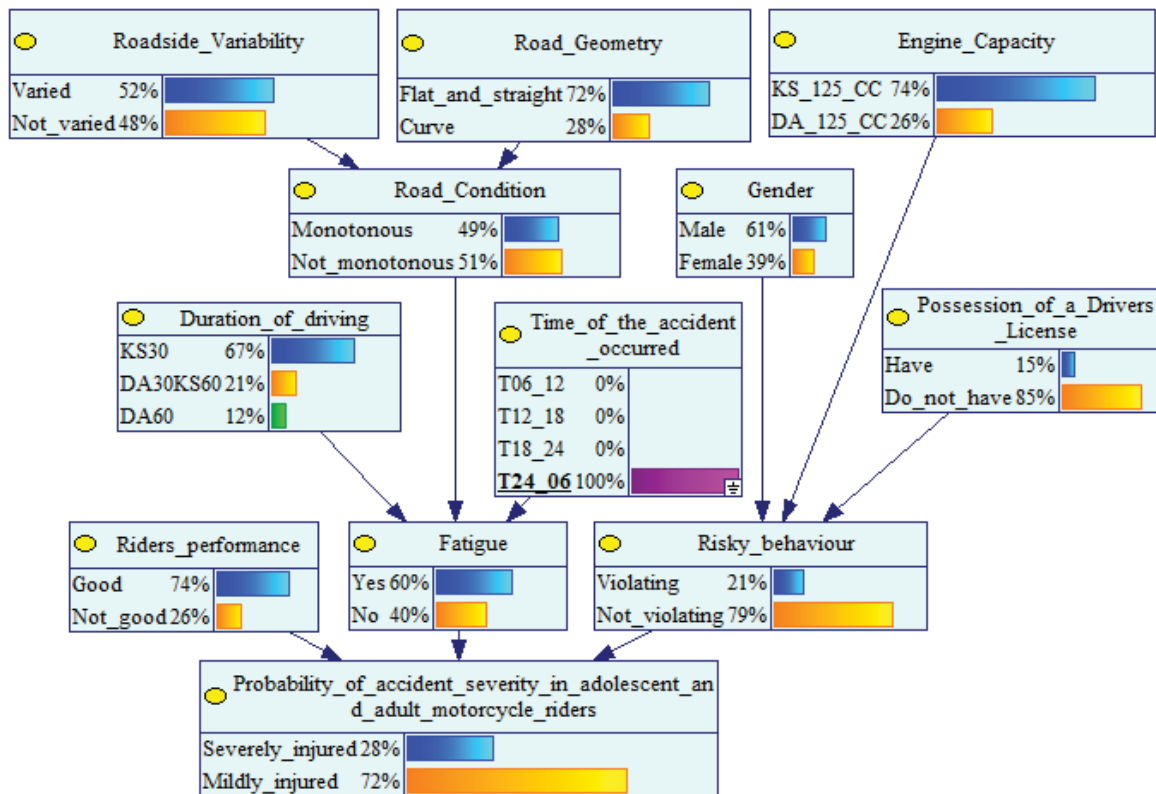


Fig. 10: Scenario 5 - Effect of driving time on accident severity.

Several strategic steps that can be taken to reduce the number of severe injuries include:

1. Adolescent drivers drive in good performance conditions because in this condition the probability of being severely injured decreases from 27% to 26%.
2. Adolescent drivers drive when they are not tired because this condition can reduce the probability of being severely injured from 27% to 26%.
3. The drivers do not violate traffic rules, because this condition can reduce the probability of serious injury from 27% to 26%.
4. Motorcycle riders do not drive during the time period 24.00-06.00, because during this time period the probability of fatigue increases from 28% to 60% and trips made during this period can increase the probability of severe injury by 1%.

## 5. CONCLUSION

The results of analysis using a Bayesian network show that the probability of adolescent drivers experiencing severe injury is 27% and mild injury is 73%. Scenario 1 shows that driving with poor performance will result in an increase in the probability of severe injury by 3%. Scenario 2 shows that when a driver experiences fatigue, the probability of severe injury will increase by 3%. Scenario 3 shows that traffic violations will increase the probability of severe injury by 5%. Scenario 4 shows that driving for only 1 hour increases the probability of fatigue but it does not increase the probability of severe injury. However, for trips longer than 1 hour, apart from increasing the probability of fatigue, it also increases the possibility of severe injury by 1%. Scenario 5 shows that the time periods of 06:00-12:00, 12:00-18:00, 18:00-24:00 only increase the driver's fatigue factor, but driving in the time period of 24:00-

06:00 not only increases the probability of fatigue but also increases the probability of severely injured by 1%. Several strategic steps that can be taken to reduce severe injury to victims include maintaining good driving performance, driving without being fatigued, not violating traffic rules, and not driving during the 24:00-06:00 time period.

## ACKNOWLEDGMENT

We would like to express our gratitude to the Directorate General of Higher Education (DIKTI), Indonesia for funding this research, and we also extend our thanks to the LPPM University of Pasir Pengaraian for their support in bringing this publication to completion.

## REFERENCES

- [1] Bucsuházy K, Matuchová E, Zůvala R, Moravcová P, Kostíková M, Mikulec R. (2020) Human factors contributing to the road traffic accident occurrence. *Transportation Research Procedia*, 45: 555-561. <https://doi.org/10.1016/j.trpro.2020.03.057>
- [2] Chouhan SS, Kathuria A, Sekhar CR. (2023) The motorcycle rider behaviour questionnaire as a predictor of crashes: A systematic review and meta-analysis. *IATSS Research*, 47: 61-72.
- [3] Kerruish L, Cheng ASK, Ting K-H, Liu KPY. (2022) Exploring the sustained and divided attention of novice versus experienced drivers. *Transportation Research Interdisciplinary Perspectives*, 16: 100702. <https://doi.org/10.1016/j.trip.2022.100702>
- [4] Rahman MA, Hossain MdM, Mitran E, Sun X. (2021) Understanding the contributing factors to young driver crashes: A comparison of crash profiles of three age groups. *Transportation Engineering*, 5: 100076. <https://doi.org/10.1016/j.treng.2021.100076>
- [5] Moller H, Ivers R, Cullen P, Rogers K, Boufous S, Patton G, Senserrick T. (2021) Risky youth to risky adults: Sustained increased risk of crash in the DRIVE study 13 years on. *Preventive Medicine*, 153: 106786. <https://doi.org/10.1016/j.ypmed.2021.106786>
- [6] Tselentis DI, Folla K, Agathangelou V, Yannis G. (2019) Investigating the correlation between driver's characteristics and safety performance. *World Conference on Transport Research – WCTR 2019, Mumbai, 26-30 May 2019*. *Transportation Research Procedia*, 48: 1254-1262. <https://doi.org/10.1016/j.trpro.2020.08.147>
- [7] Muley D, Dias C, Umlai A-H, AlArdah H, Shah M, Murtaza M, Firas AS. (2022) Assessment of turn signal use at two-lane roundabouts in Doha city. *Procedia Computer Science*, 201: 79-86. <http://dx.doi.org/10.1016/j.procs.2022.03.013>
- [8] Lyon C, Mayhew D, Granié M-A, Robertson R, Vanlaar W, Woods-Fry H, Thevenet C, Furian G, Soteropoulos A. (2020) Age and road safety performance: Focusing on elderly and young drivers. *IATSS Research*, 44: 212–219. <https://doi.org/10.1016/j.iatssr.2020.08.005>
- [9] Ali Y, Haque MdM. (2023) Modelling braking behaviour of distracted young drivers in car-following interactions: A grouped random parameters duration model with heterogeneity-in-means. *Accident Analysis and Prevention* 185: 107015. <https://doi.org/10.1016/j.aap.2023.107015>
- [10] Katrakazas C, Michelaraki E, Sekadakis M, Yannis G. (2020) A descriptive analysis of the effect of the COVID-19 pandemic on driving behavior and road safety. *Transportation Research Interdisciplinary Perspectives*, 7: 100186
- [11] Jannusch T, Shannon D, Völler M, Murphy F, Mullins M. (2021) Smartphone use while driving: An investigation of young novice driver (YND) behaviour. *Transportation Research Part F*, 77: 209–220. <https://doi.org/10.1016/j.trf.2020.12.013>
- [12] Brands D, Klingen J, Ostermeijer F. (2022) Hands on the wheel, eyes on the phone: The effect of smartphone usage fees on road safety. *European Economic Review* 146: 104130. <https://doi.org/10.1016/j.eurocorev.2022.104130>
- [13] Chen C-F (2023) Investigating the effects of job stress on the distraction and risky driving behaviors of food delivery motorcycle riders. *Safety and Health at Work*, 14: 207-214.

- [14] Papakostopoulos V, Nathanael D. (2021) The complex interrelationship of work-related factors underlying risky driving behavior of food delivery riders in Athens, Greece. *Safety and Health at Work* 12: 147-153.
- [15] Tanglai W, Chen C-F, Rattanapan C, Laosee, O (2020). The effects of personality and attitude on risky driving behavior among public van drivers: Hierarchical modeling. *Safety and Health at Work*, 13: 187-191.
- [16] Megias-Robles A, Sanchez-Lopez MT, Fernandez-Berrocal P. (2022) The relationship between self-reported ability emotional intelligence and risky driving behaviour: Consequences for accident and traffic ticket rate. *Accident Analysis and Prevention* 174: 106760. <https://doi.org/10.1016/j.aap.2022.106760>
- [17] Maghelal PK, Lara JCF, Goonetilleke RS, Luximon A. (2023) Determinants of self-efficacy of driving behavior among young adults in the UAE: Impact of gender, culture, and varying environmental conditions in a simulated environment. *Heliyon*, 9(3): e13993. <https://doi.org/10.1016/j.heliyon.2023.e13993>
- [18] Zhu Y, Jiang M, Yamamoto T. (2022) Analysis on the driving behavior of old drivers by driving recorder GPS trajectory data. *Asian Transport Studies*, 8: 100063. <https://doi.org/10.1016/j.eastsj.2022.100063>
- [19] Etika A, Merat N, Carsten O. (2021) Identifying salient beliefs underlying speeding behaviour: An elicitation study of Nigerian drivers. *Transportation Research Interdisciplinary Perspectives*, 9: 100279. <https://doi.org/10.1016/j.trip.2020.100279>
- [20] Babic D, Cavka M, Babic D, Hrabac P. (2022) Young drivers' perception of speed: VR and video footage comparison study. *Transportation Research Procedia*, 64: 205-214. <https://doi.org/10.1016/j.trpro.2022.09.025>
- [21] Elvik R. (2023). Driver mileage and accident involvement: A synthesis of evidence. *Accident Analysis and Prevention* 179: 106899. <https://doi.org/10.1016/j.aap.2022.106899>
- [22] Lumba P, Edison B, Fahmi K, Sibarani AS, Ariyanto A, Hidayat A, Rahmi A, Rismalinda. (2022) Effects of Sleep Deprivation on Probability of Traffic Violations in Motorcyclists: Analysis Using Bayesian Network Science and Technology Asia, 27(2): 115-125. doi: 10.14456/scitechasia.2022.29.
- [23] Wijayanto T, Marcillia SR, Lufityanto G, Wisnugraha BB, Alma TG, Abdianto RU. (2021) The effect of situation awareness on driving performance in young sleep-deprived drivers. *IATSS Research*, 45: 218-225. <https://doi.org/10.1016/j.iatssr.2020.10.002>
- [24] Takeyama E, Tomooka K, Wada H, Sato S, Sakiyama N, Shirahama R, Tanigawa T. (2023) Association between daytime sleepiness and motor vehicle accidents among Japanese male taxi drivers. *IATSS Research*, 47: 299-304. <https://doi.org/10.1016/j.iatssr.2023.05.002>
- [25] Lumba P. (2022) Fatigue Factor on Motorcyclists' Accident: Analysis Using Bayesian Network. *Suranaree J. Sci. Technol.*, 29(6): 010169(1-9). <https://ird.sut.ac.th/e-journal/Journal/pdf/220104831.pdf>
- [26] Lumba P. (2022) The impact of fatigue and behaviour of driver on probability of accidents severity in motorcyclists. *ASM Sc. J*, 17: <https://doi.org/10.32802/asmscj>,
- [27] Bille J, Udholm S. (2022) Obstructive sleep apnea and road traffic accidents: a Danish nationwide cohort study. *Sleep Medicine*, 96: 64-69.
- [28] Vipin N, Rahul T. (2021) Road traffic accident mortality analysis based on time of occurrence: Evidence from Kerala, India. *Clinical Epidemiology and Global Health*, 11: 100745. <https://doi.org/10.1016/j.cegh.2021.100745>
- [29] Zhao L, Wang C, Yang H, Wu X, Zhu T, Wang J. (2023) Exploring injury severity of non-motor vehicle riders involving in traffic accidents using the generalized ordered logit model. *Ain Shams Engineering Journal*, 14: 101962. <https://doi.org/10.1016/j.asej.2022.101962>
- [30] Li K, Xu H, Liu X. (2022) Analysis and visualization of accidents severity based on Light GBM-TPE. *Chaos, Solitons and Fractals*, 157: 111987
- [31] Barman S, Bandyopadhyaya R. (2023) Modelling crash severity outcomes for low speed urban roads using back propagation – Artificial neural network (BP – ANN) – A case study in Indian context. *IATSS Research*, 47: 382-400.

- [32] Madvari RF, Sefidkar R, Halvani GH, Alizadeh HM. (2023) Quantitative indicators of street lighting with mood, fatigue, mental workload and sleepiness in car drivers: Using generalized structural equation modeling. *Heliyon*, 9: e12904. <https://doi.org/10.1016/j.heliyon.2023.e12904>
- [33] Abdubrani R, Mustafa M, Zahari ZI. (2023) A robust framework for driver fatigue detection from EEG signals using enhancement of modified z-score and multiple machine learning architectures. *IIUM Engineering Journal*, 24(2):354-372. <https://doi.org/10.31436/iiumej.v24i2.2799>
- [34] Davidovic J, Pešić D, Lipovac K, Antic B. (2019) The significance of the development of road safety performance indicators related to driver fatigue. *AIIT 2nd International Congress on Transport Infrastructure and Systems in a changing world (TIS ROMA 2019)*, 23rd-24th September 2019, Rome, Italy. *Transportation Research Procedia*, 45: 333-342. <https://doi.org/10.1016/j.trpro.2020.03.024>
- [35] Cullen P, Moller H, Woodward M, Senserrick T, Boufous S, Rogers K, Brown J, Ivers R. (2021) Are there sex differences in crash and crash-related injury between men and women? A 13-year cohort study of young drivers in Australia. *SSM - Population Health*, 14: 100816. <https://doi.org/10.1016/j.ssmph.2021.100816>
- [36] Gazder U, Khaled J, Assi KJ. (2022) Determining driver perceptions about distractions and modeling their effects on driving behavior at different age groups. *Journal of Traffic and Transportation Engineering (English edition)*, 9(1): 33-43. <https://doi.org/10.1016/j.jtte.2020.12.005>
- [37] Statistik Transportasi Darat; 2021. Available: <https://www.bps.go.id/publication/download.html?nrbvfeve=YTJhZTZiMmFhOGM1NjUxMDYzZjQ1ZGZj&xzmn=aHR0cHM6Ly93d3cuYnBzLmdvLmlkL3B1YmtpY2F0aW9uLzIwMjIvMTEvMjgvYTJhZTZiMmFhOGM1NjUxMDYzZjQ1ZGZjL3N0YXRpc3Rpay10cmFuc3BvcnRhc2ktZGFyYXQtMjAyMS5odGls&twoadfnofearauf=MjAyMy0wNC0wNyAyMDoxODo0OQ%3D%3D>
- [38] Carter M, Raymond Bingham C, Zakrajsek JS, Shope JT, Sayer TB. (2014). Social norms and risk perception: predictors of distracted driving behavior among novice adolescent drivers. *Journal of Adolescent Health*, 54: S32-S41
- [39] Kementerian Perhubungan; 2020. Available: <https://dephub.go.id/post/read/korban-kecelakaan-lalin-didominasi-usia-produktif,-menhubajak-para-pelajar-selalu-disiplin-berlalu-lintas-dan-utamakan-aspek-keselamatan>
- [40] Regev S, Rolison JJ, Moutari S. (2018) Crash risk by driver age, gender, and time of day using a new exposure methodology, *Journal of Safety Research*, 66: 131-140. <https://doi.org/10.1016/j.jsr.2018.07.002>
- [41] Chu, H-C. (2020) Risky behaviors of older taxi drivers and suggested requirements for renewing their professional driver's licenses. *Transportation Research Interdisciplinary Perspectives*, 8: 100272. <https://doi.org/10.1016/j.trip.2020.100272>
- [42] Skyving M, Forsman A, Willstrand TD, Laflamme L, Moller J. (2021) Medical impairment and road traffic crashes among older drivers in Sweden – A national, population-based, case-control study. *Accident Analysis and Prevention*, 163: 106434. <https://doi.org/10.1016/j.aap.2021.106434>
- [43] Software GeNie. (2023) <https://download.bayesfusion.com/files.html?category=Academia>
- [44] Zong F, Xu H, Zhang H. (2013) Prediction for traffic accident severity: Comparing the Bayesian network and regression models. *Mathematical Problems in Engineering*, 2013: 475194. <https://doi.org/10.1155/2013/475194>

# OPTIMAL CLUSTERING OF WIRELESS MULTIPATHS BY UNIFORM MANIFOLD APPROXIMATION AND PROJECTION-ASSISTED DBSCAN

EMMANUEL TRINIDAD\*<sup>1</sup> AND LAWRENCE MATERUM<sup>2,3</sup>

<sup>1</sup>*Electronics Engineering Department, Don Honorio Ventura State University,  
Bacolor, Philippines*

<sup>2</sup>*De La Salle University, Philippines*

<sup>3</sup>*Tokyo City University, Japan*

\*Corresponding author: [ettrinidad@dhvsu.edu.ph](mailto:ettrinidad@dhvsu.edu.ph)

(Received: 7 January 2023; Accepted: 21 October 2023; Published on-line: 1 January 2024)

**ABSTRACT:** Uniform Manifold Approximation and Projection (UMAP) is applied to reduce the multipath dataset into 2-dimensions (2D) for visualization and clustering. Density-based spatial clustering of applications with noise (DBSCAN) is used as the clustering approach and the performance of different search radius epsilon  $\epsilon$ . The proposed approach was used to cluster semi-urban scenarios of the COST2100 channel model (C2CM), which has many multipath components (MPCs). The approach is validated by comparing the clustering results to the ground truth and computing the Adjusted Rand Index (ARI) and the cluster-wise Jaccard index  $\eta$ . The results suggest that lowering the search radius up to 0.3 achieved a median below 0.6 in the multiple-links scenarios due to the overlapping nature of clusters. Nevertheless, the median values above 0.7 and 0.8 for the ARI and Jaccard index  $\eta$ , respectively for the single-link scenarios indicate the robustness of the approach.

**ABSTRAK:** Anggaran Manifold Seragam dan Unjuran (UMAP) 2-dimensi (2D) digunakan sebagai penggambaran dan pengelasan bagi mengurangkan set data pelbagai laluan. Aplikasi pengelasan ruang bersama bunyi berdasarkan ketumpatan (DBSCAN) ini mengguna pakai pendekatan pengelasan dan prestasi pelbagai radius carian epsilon  $\epsilon$ . Pendekatan yang dicadangkan ini digunakan bagi pengelasan senario separa-bandar model saluran COST2100 (C2CM), di mana komponen ini mempunyai banyak laluan (MPCs). Pendekatan ini disahkan dengan membandingkan dapatan pengelasan kepada kesahihan lapangan, pengiraan Indeks Rawak Terlaras (ARI) dan indeks Jaccard pengelasan  $\eta$ . Dapatan menunjukkan pengurangan radius carian sehingga 0.3 dicapai pada median di bawah 0.6 dalam senario pelbagai pautan disebabkan oleh sifat pertindihan pengelasan. Walau bagaimanapun, nilai median di atas 0.7 dan 0.8 untuk ARI dan indeks Jaccard  $\eta$ , masing-masing menunjukkan kaedah ini berkesan bagi senario pautan-tunggal.

**KEYWORDS:** *multipath clustering; dimensionality reduction; channel modeling*

## 1. INTRODUCTION

The development of wireless communications relies on characterizing the physical wireless channel. Utilizing Multiple-Input Multiple-Output (MIMO) antennas at both the transmitter and receiver enables the wireless systems to achieve fourth-generation (4G) and fifth-generation (5G) mobile communication standards. Channel models have been used to test algorithms and approaches before developing the actual system, using the characteristics of the complicated propagation environment; thus, channel modeling plays a vital role in wireless system design. Recently, the use of geometry-based stochastic channel models (GBSCM) has

gained popularity and developed the double-directional channel models [1]. The GBSCM also uses cluster concepts, attributing clusters to scatterers in the propagation environment. The presence of multipath clusters and their exploitation opens up the benefits of spatial multiplexing, diversity, and beamforming. The scatterers produce multipath components (MPCs), which diffuse and scatter the signal propagated, causing delays and different paths called multipaths. Generating a channel model for different scenarios and accurately clustering the MPCs in the angular and time domain can simplify obtaining the channel impulse response (CIR). Accurately modeling the propagation space can produce better channel models for different scenarios that technically advance the wireless system's design and present achievable reliability, data rates, and latency. Hence, finding optimal ways to cluster MPCs is crucial in channel modeling.

Recently, the use of automatic algorithms gained attraction in clustering the MPCs. Different methods have been proposed to cluster MPCs in different scenarios. The first framework for applying an automatic algorithm was reported by [2], [3], where the  $K$ -means algorithm was utilized, and the Multipath Component Distance (MCD) was used. The  $K$ -means algorithm was also used in an urban scenario reported by [4]. A spectral-based power-weighted algorithm was proposed by [5] and applied to measured data in a hall environment. The automatic and manual approach combined to produce a middle-ground technique is reported in [6], in an urban macrocell where it was stated that human interaction in clustering should not be ignored.

Furthermore, the  $K$ -means is extended to include the power, also known as the  $K$ -power means (KPM) algorithm, and tracking the multipaths was reported in [7]. The Variational Gaussian Mixture Model (GMM) was proposed to cluster the outdoor-to-indoor propagation scenario [8]. Additionally, a comparative study of different algorithms and their performance is presented in [9]. The use of Simultaneous Clustering and Model Selection (SCAMS) is proposed in [10,11] to cluster the C2CM generated datasets. Finally, a visualization tool using 3D point cloud data to locate small interacting objects in a microcell was proposed to include the visualization process in the wireless channel characterization [12]. Different approaches are presented in clustering the MPCs due to the difference in propagation environment, frequency band, and scenario being studied and modeled.

Big data analysis gained research interest due to the massive data available today. Visualization techniques have been one of the focuses of research in exploratory data analysis. Data's high dimensional nature gave birth to techniques to reduce the dimensionality of data to address the "curse of dimensionality." Dimensionality reduction (DR) has benefitted other fields of science, especially for data with many features that need to be reduced, visualized, and clustered. DR techniques can preserve the global or local structure of the data while reducing the features that can be used to visualize in lower dimensions. The mutation dataset of the SARS-CoV-2 was visualized using t-distributed Stochastic Neighbor Embedding (t-SNE) and UMAP, followed by the  $K$ -means algorithm for clustering [13]. DR has gained popularity, especially in genome sequencing. In [14], DBSCAN is used after applying t-SNE and UMAP to find repeating patterns in the biological signaling of single-cell calcium spiking.

Furthermore, DR techniques have been used to improve the performance of different machine learning algorithms for intrusion detection systems [15]. Furthermore, DR techniques before automatic clustering have not been fully utilized in clustering the MPCs. The main contribution of this paper is to obtain accurate number of clusters and their membership using UMAP to reduce the dimension into 2 (for visualization) and cluster the latent space using DBSCAN.

This paper applies the DR technique to the C2CM data to visualize the MPCs using Principal Component Analysis (PCA) and UMAP, followed by DBSCAN to cluster the reduced data. The rest of the paper is structured as follows: Section 2 discusses the methods utilized in this paper, the dataset, DR techniques, and the validation metrics. Section 3 presents the clustering results and the performance for each scenario, and Section 4 concludes this work.

## 2. METHODS

The methodology and techniques in this study are discussed. Figure 1 illustrates the procedures implemented from the dataset used, the PCA and UMAP techniques, and the MCD distance metric. The dataset is prepared and read using MATLAB software. Each scenario has 30 snapshots that are read per sheet in an Excel file imported to the MATLAB interface. The PCA is applied to rotate the data, capturing the maximum variance without reducing the dimension. The UMAP is modified using the MCD metric to suit the angular nature of data to capture the actual distance and avoid the circular nature of data. The computation of MCD is done using a developed script in MATLAB. The UMAP then computes a low-dimensional representation in 2D that can be visualized and utilized for clustering.

Additionally, the default DBSCAN implementation in MATLAB was used, and the  $\epsilon$  was varied to improve the groupings of the UMAP output. Finally, the ARI and Jaccard index are computed to validate the approach in the number of clusters and their membership. This section discusses each of the methods used in this paper.

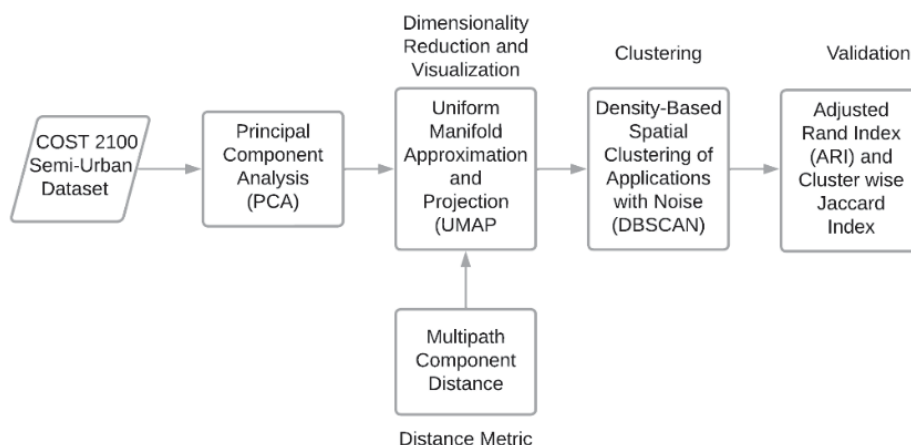


Fig. 1: Methodology of the study.

### 2.1 COST 2100 Dataset

The European Cooperation in Science and Technology (COST) 2100 channel model is based on the cluster of MPCs which has similar delays and angular parameters [16]. The C2CM generates the double-directional channel containing the large-scale and small-scale parameters. The dataset used in this work is found in the Institute of Electrical and Electronics Engineers (IEEE) DataPort [17], which has eight scenarios. Only the semi-urban scenarios were used in this work since the DBSCAN performance relies on the density of points and the neighbors. The settings are as follows:

1. Band 1 Semi-urban NLOS Single Link
2. Band 1 Semi-urban LOS Single Link

3. Band 1 Semi-urban LOS Multiple Links
4. Band 2 Semi-urban NLOS Single Link
5. Band 2 Semi-urban LOS Single Link
6. Band 2 Semi-urban LOS Multiple Links

Band 1 refers to the narrowband, while Band 2 is for the wideband. Additionally, the LOS refers to line-of-sight and NLOS refers to non-line-of-sight. A vector represents the MPCs  $\mathbf{x}_\ell = [\theta_{\ell, \text{AOA}}, \phi_{\ell, \text{AOA}}, \theta_{\ell, \text{AOD}}, \phi_{\ell, \text{AOD}}, \tau_\ell, \alpha_\ell]$  where  $x_l$  represents the  $\ell^{\text{th}}$  MPC which has the delay parameter  $\tau$ , the Angle of Arrival (AOA), Angle of Departure (AOD),  $\phi$  is the azimuth angle,  $\theta$  as the elevation angle, and the power represented by  $\alpha$ . The MPCs are clustered based on the similarity of these parameters, excluding the power. Each dataset contains 30 snapshots, where one snapshot is represented by a data matrix  $\mathbf{X}$  that contains  $\ell$  number of MPCs.

The C2CM is part of the COST action project and the COST family of channel models. A 200 MHz bandwidth is supported by this model for frequencies below 6 GHz. The model assumes that there is only one terminal fixed for the BS, which limits the dual mobility conditions. Dynamic modeling, multi-link, spherical, and spatial consistency are the advantages of the C2CM as compared to other channel models.

## 2.2 Dimensionality Reduction

PCA is considered a DR technique that aims to direct the components to maximum variance using orthogonal axes. PCA produces uncorrelated variables, which can then be reduced to a number of principal components. The first principal component explains most of the variance in the data, followed by the second principal component. PCA can be achieved using the singular value decomposition (SVD) or the covariance matrix and its eigenvectors. In this work, all the components are retained; thus, PCA is used for the decorrelation of the variables, which are then fed to the UMAP algorithm.

UMAP is a relatively new technique for embedding high-dimensional data in low dimensions based on topological data analysis and graph theory [18]. The algorithm begins by constructing a  $K$ -neighbor graph  $G$  using a specific distance metric  $d$  which computes the distance in high dimension. The  $G$ 's low dimensional graph is constructed using Laplacian eigenmaps. The cross-entropy between the two graphs is minimized, producing an optimized layout in the low dimension [19]. UMAP has hyperparameter  $n$ -neighbors, which in this work is set to the square root of  $N$ , where  $N$  is the number of paths in each snapshot. The reason for the square root is to deflate the varying number of MPC in each snapshot, and selecting  $\sqrt{N}$  is widely accepted when using  $k$ -nn [20]. The MATLAB implementation of UMAP [21] is used in this work. The UMAP preserves both local and global structure of data. Another manifold learning technique that uses the same principle of optimizing the low dimensional embeddings is the t-SNE. In contrast, UMAP utilizes graph theory, while t-SNE is based on the student-t distribution in finding the neighboring points. As mentioned earlier, the PCA is a DR technique as well, but falls under the category of linear techniques and is employed alongside t-SNE or UMAP.

The parameters of the MPCs are in terms of angle and time domain. In clustering and neighborhood embedding, the similarity of the distance is the Euclidean distance which is the default distance metric of UMAP and other dimensionality reduction algorithms. It measures the distance between points in a linear manner. A more generalized distance metric is the Minkowski distance where  $p$  represents the norm where  $p = 2$  for the Euclidean, and  $p = 1$  for the Manhattan distance. However, because of the angular nature of the multipath

components, the Euclidean distance should be modified to address the angular ambiguity and separation between the MPCs. Considering also the fact that the delay feature  $\tau$  is a dimension of time, the Euclidean distance cannot measure the spatio-temporal difference of MPCs. The MCD is a measure to quantify the separations between multipaths  $i, j$  introduced in [22] given by Eq. 1:

$$\text{MCD}_{ij} = \sqrt{\|\text{MCD}_{\text{AoA},ij}\|^2 + \|\text{MCD}_{\text{AoD},ij}\|^2 + \text{MCD}_{\tau,ij}^2} \quad (1)$$

$$\text{MCD}_{\text{AoA}/\text{AoD},ij} = \frac{1}{2} \left| \begin{pmatrix} \sin(\theta_i)\cos(\phi_i) \\ \sin(\theta_i)\sin(\phi_i) \\ \cos(\theta_i) \end{pmatrix} - \begin{pmatrix} \sin(\theta_j)\cos(\phi_j) \\ \sin(\theta_j)\sin(\phi_j) \\ \cos(\theta_j) \end{pmatrix} \right| \quad (2)$$

where  $\text{MCD}_{\text{AoA}/\text{AoD},ij}$  computes the distance of the angle of arrival or departure; Equation 2 is used to compute the angular distance between the  $i^{\text{th}}$  and  $j^{\text{th}}$  multipath. Equation 3 quantifies the separation between delays given by  $\text{MCD}_{\tau,ij}$ , where  $\zeta$  is the scaling factor and the standard deviation of the delays denoted by  $\tau_{\text{std}}$ .

$$\text{MCD}_{\tau,ij} = \zeta \cdot \frac{|\tau_i - \tau_j|}{\Delta\tau_{\text{max}}} \cdot \frac{\tau_{\text{std}}}{\Delta\tau_{\text{max}}} \quad (3)$$

The MCD provides a metric integrated into the UMAP algorithm to measure the probability of neighboring points in the high-dimensional space. Using PCA and UMAP, where MCD is the distance metric, each snapshot is projected into 2D space for visualization, and the 2D data is clustered using the DBSCAN algorithm.

### 2.3 Density-Based Spatial Clustering of Applications with Noise

The DBSCAN algorithm relies on three parameters, the core points, boundary points, and noise points [14]. The core points can be determined by the radius of the search represented by epsilon  $\epsilon$  and the minimum number of neighbors (minPts). Furthermore, core points are defined as the reference of the data points in the center of the group with the least minPts connected within the distance  $\epsilon$ . The number of core points can also be treated as the number of clusters since it defines how DBSCAN can find many core points. The DBSCAN treats the neighbors to be connected to a core point, and the non-core points are treated as noise. One advantage of DBSCAN from  $K$ -means is that DBSCAN does not require the number of clusters  $K$  in advance but produces clusters based on the density of points around the core point that the radius  $\epsilon$  and the minPts specifies. In this paper,  $\epsilon$  was varied from 1, 0.8, 0.5, and 0.3, while the minPts was set to the default value of 5. The reason for varying the  $\epsilon$  in decreasing order is to separate highly dense points from the projection of UMAP. The abstract algorithm of DBSCAN is first to identify the core points, followed by assigning core points, and for non-core points, the border points are assigned, adding the neighboring points to a core point and finally assigning the noise points. The original DBSCAN paper was proposed in [23] and was recently criticized due to the misuse of distance metrics. However, the suitable use of its parameters  $\epsilon$  and the distance metric are discussed and highlighted in [24] and still encourages its usage.

### 2.4 Validation Metrics

The availability of the true cluster number and cluster membership from the C2CM data, external clustering validity indices are used. The Adjusted Rand Index (ARI), which compares

the cluster members to the reference cluster membership, and the Jaccard index to assess the accuracy in identifying the number of clusters. The ARI is given in equation 4 [25].

$$ARI = \frac{M_{11} + M_{00}}{M_{00} + M_{01} + M_{10} + M_{11}} = \frac{M_{11} + M_{00}}{\binom{M}{2}} \in [0,1] \quad (4)$$

The value of the ARI ranges from 1 if the clustering matches perfectly. In equation 4,  $M_{11}$  pertains to the number of pairs that exist in the same cluster while  $M_{00}$  are the instances that exist in a different cluster. The number of pairs that exist in the reference cluster but not in the clustering output is denoted by  $M_{01}$  while  $M_{10}$  is for the opposite.

On the other hand, the number of clusters is evaluated using the Jaccard index, which ranges from 0 to 1, where 0 indicates void similarity and 1 for a perfect match. The cluster-wise Jaccard index is computed using equation 5, where  $|\cdot|$  denotes the cardinality,  $C_{ref}$  is the reference multipath cluster, and  $C_{cal}$  indicates the calculated clusters.

$$\eta_{Jac} = \frac{|C_{ref} \cap C_{cal}|}{|C_{ref} \cup C_{cal}|} \in [0,1] \quad (5)$$

The results of cluster labels can sometimes change depending on the clustering discovery of DBSCAN. Consequently, the use of ARI to measure the similarity of cluster membership as compared to the Adjusted Mutual Index (AMI) is due to the balanced nature of clusters generated by C2CM. Since the dataset generated has equal number of MPC per cluster, the dataset is said to be balanced and the ARI is used toward a balanced clustering solution.

### 3. RESULTS AND DISCUSSION

The results of using PCA+UMAP and MCD are first projected with their reference clusters to validate the embedding quality. The DBSCAN is then used on the projected data to visualize and assess the performance by computing the ARI. Figure 2 illustrates the ground truth projection and the DBSCAN clustering on the UMAP results. The projected data is from one snapshot of the B1 NLOS scene with 911 MPCs. Varying the  $\epsilon$  value shows a difference in the clusters in the middle being separated as the value of the search radius decreases.

Consequently, when the value of  $\epsilon$  is small, the clusters are separated from the core points and are treated as noise, as illustrated in the last plot of Fig. 2, where the  $\epsilon = 0.1$  achieves an ARI of only 0.0814. The search radius  $\epsilon$  was lowered to the value of 0.3; further lowering this value, the ARI and Jaccard index decreased. With these trials, the PCA+UMAP and MCD are applied to reduce the parameters into new variables UMAP1 and UMAP2 and are projected in 2D space for visualization and clustering. This process was applied to thirty snapshots for each semi-urban channel scenario.

Table 1 shows the mean ARI for each semi-urban scenario corresponding to the search radius values of 1, 0.8, 0.5, and 0.3. The number of clusters was evaluated using the Jaccard index  $\eta_{Jac}$ . Furthermore, the mean computational durations using the proposed approach were recorded. The simulations were carried out using MATLAB 2020b on a desktop with AMD Ryzen 5 3600 6-Core Processor with 16 GB of installed RAM, and the duration was computed using the timer functions of MATLAB.

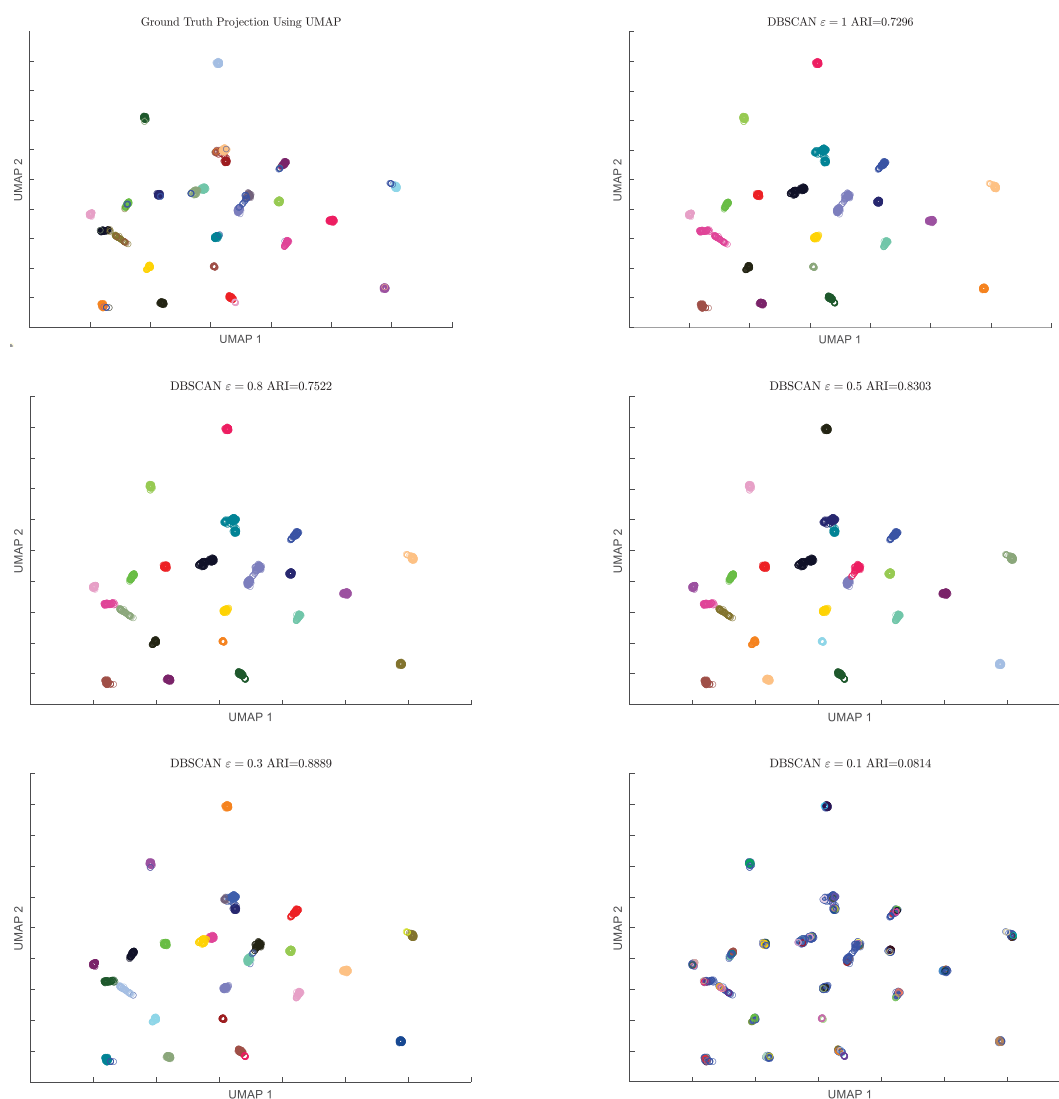


Fig. 2: UMAP of Ground-truth and DBSCAN results with varying  $\epsilon$ .

The applied approach had an excellent performance in the scenario B1 semi-urban LOS single link with the highest ARI and  $\eta_{Jac}$  of 0.7359 and 0.8726, respectively. The same scenario follows this result in the B2 with 0.7116 and 0.8390. On the other hand, the lowest scores are in the multiple links scenarios; this is due to the overlapping clusters in one dense point, and the UMAP cannot separate the clusters clearly, mainly due to the number of links that has the same parameters which only achieves only half of the number of clusters. This limitation also affects the memberships of the clusters resulting in lower ARI. Furthermore, in the multiple link scenarios, the highest mean computational duration of approximately 7 seconds can be attributed to the high number of paths. Finally, the overall scores show that at  $\epsilon = 3$  achieves the highest ARI and  $\eta_{Jac}$  as opposed to using  $\epsilon = 1$  where a significant difference in the scores is observed.

Table 1: Mean ARI, Jaccard index, and Computational Duration of UMAP and DBSCAN

Scenario	ARI				$\eta_{Jac}$				Computational Duration (seconds)
	$\varepsilon = 1$	$\varepsilon = 0.8$	$\varepsilon = 0.5$	$\varepsilon = 0.3$	$\varepsilon = 1$	$\varepsilon = 0.8$	$\varepsilon = 0.5$	$\varepsilon = 0.3$	
B1 Semi-urban NLOS Single Link	0.5453	0.5741	0.6342	0.7299	0.6685	0.7046	0.7655	0.8736	5.0469
B1 Semi-urban LOS Single Link	0.4980	0.5307	0.6139	0.7359	0.5874	0.6257	0.7126	0.8726	1.9335
B1 Semi-urban LOS Multiple Links	0.3128	0.3245	0.3780	0.4612	0.3562	0.3704	0.4377	0.5637	6.8409
B2 Semi-urban NLOS Single Link	0.5362	0.5659	0.6277	0.7166	0.6150	0.6435	0.7301	0.8617	5.4050
B2 Semi-urban LOS Single Link	0.5097	0.5340	0.6114	0.7116	0.5739	0.6054	0.6850	0.8390	2.1443
B2 Semi-urban LOS Multiple Links	0.3536	0.3733	0.4305	0.4983	0.3726	0.3893	0.4579	0.5724	6.6561

Figure 3a illustrates the Empirical Cumulative Distribution Function (ECDF) of ARI for all 180 snapshots of channel scenarios and their corresponding ARI. The figure shows a significant difference and improved scores at  $\varepsilon = 0.3$ . The 10<sup>th</sup> percentile, median, and 90<sup>th</sup> percentile of  $\varepsilon = 0.3$  are graphed in Figure 3a. The percentiles indicate that at less than 10% of the data, the performance is 0.4486; at less than 50%, an ARI of 0.6763; and at less than 90% of the ARI is 0.8018. The graph summarizes the performance in terms of the ARI.

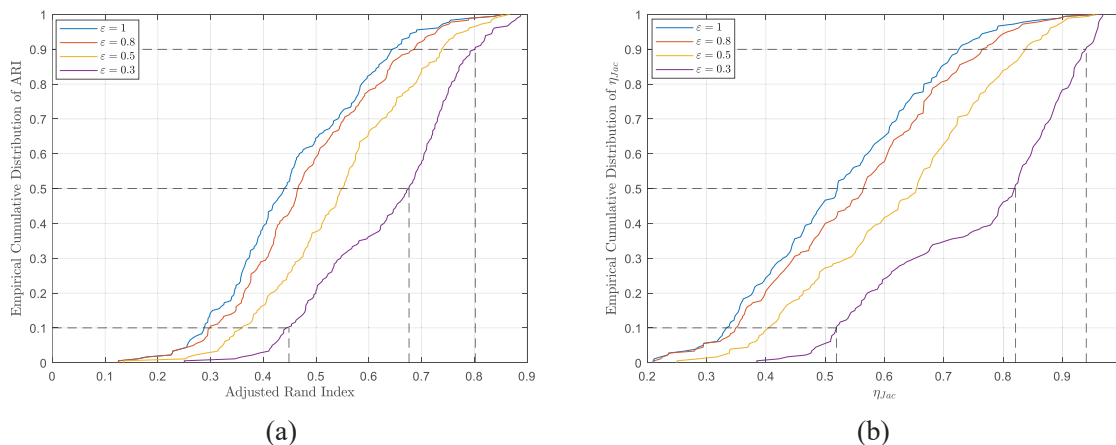
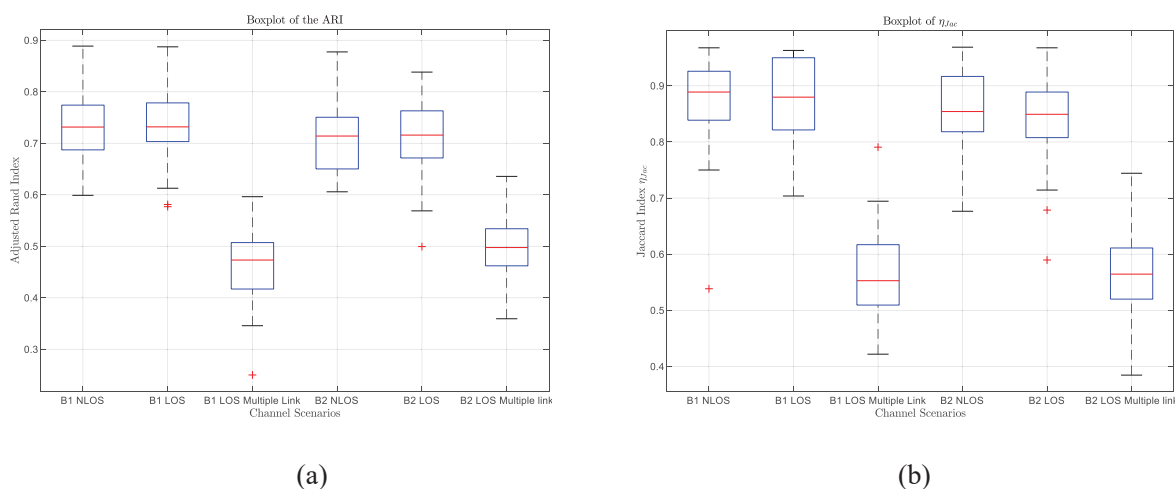


Fig. 3: ECDF of ARI and  $\eta_{Jac}$  for all channel scenarios.

Furthermore, Fig. 3b provides the ECDF of the cluster-wise Jaccard index for all scenarios. The ECDF shows a steeper curve in the ECDF of  $\varepsilon = 0.3$  where at the median, less than 50% of the Jaccard indices are less than 0.8214, indicating a good approximation of the actual number of clusters. Consequently, the lower percentile indicates that at less than 10%, the Jaccard index of the number of clusters is 0.5193, which can be associated with the approach's performance in the multiple-links scenarios.

In Fig. 4, the summary statistic of the ARI and Jaccard index for the six channel scenarios with the highest performing parameter  $\varepsilon$  is shown using box plots. The boxplot shows the

median using the red mark and the 25<sup>th</sup> and 75<sup>th</sup> percentiles using the bottom and top of the box, respectively. Additionally, some outliers in the data are present, denoted by the red + mark. Figure 4a shows the ARI performance where the single-link performance of above 0.7 ARI in the median values, while the performance of the approach on the multiple link scenario, the median ranges at only half of the cluster membership. The ARI performance also affects the Jaccard number of clusters; the median is above 0.8 for the single-link scenarios indicating a close approximation to the number of clusters. The same performance is shown by the boxplot of the Jaccard index in Fig. 4b, where the number of clusters in the multi-link has achieved less than 0.5 value. A total of four outliers in the box plots indicates that the approach's performance is robust and applicable for most of the 180 datasets.



(a) (b)  
 Fig. 4: Boxplot of ARI and  $\eta_{Jac}$  for all channel scenarios.

The approach has been proven effective on the C2CM datasets and has been verified using the Jaccard index and ARI. The use of the approach to different channel models such as IMT-2020, WINNER II, and QuaDRiGa are considered for future work.

## 4. CONCLUSION

This paper presents the performance results of applying UMAP to MPC for visualization prior to clustering. The UMAP reveals the clustering tendencies in the data utilizing PCA and the distance metric MCD. Visualizing the data can aid the clustering process, especially for the increasing number of paths. In addition, the clustering performance of DBSCAN to the membership and number of clusters, along with the varying values of the search radius  $\epsilon$  are evaluated. The selection of the  $\epsilon$  at 0.3 shows promising results in clustering the projected 2D transformed data of the MPCs. A median of 0.6763 and 0.8214 of the ECDF for the ARI and Jaccard index, respectively, suggests the accuracy of the approach. Incorporating DR techniques to visualize and cluster the MPCs proves to be optimal and can be used as an alternative to cluster the MPC of the C2CM semi-urban scenarios.

## ACKNOWLEDGEMENT

The Research Management Office of Don Honorio Ventura State University and De La Salle University is acknowledged for supporting this work.

## REFERENCES

- [1] Bonek E. (2013) MIMO propagation channel modeling. 7th European Conference on Antennas and Propagation (EuCAP), pp. 2488-2492.
- [2] Czink N, Cera P, Salo J, Bonek E, Nuutinen J, Ylitalo J. (2006) A framework for automatic clustering of parametric mimo channel data including path powers. In Proceedings IEEE Vehicular Technology Conference, pp. 1-5. <https://doi.org/10.1109/VTCF.2006.35>.
- [3] Czink N, Cera P, Salo J, Bonek E, Nuutinen J, Ylitalo J. (2006) Improving clustering performance using multipath component distance. Electronics Letters. 42(1): 33-45. <https://doi.org/10.1049/el:20063917>.
- [4] Moayyed MT, Antonescu B, Basagni S. (2019) Clustering algorithms and validation indices for mmwave radio multipath propagation. In Proceedings Wireless Telecommunications Symposium (WTS), pp. 1-7. <https://doi.org/10.1109/WTS.2019.8715540>.
- [5] Hu M, Ye Y, He R, Ai B, Huang C, Zhong Z. (2020) A novel power weighted multipath component clustering algorithm based on spectral clustering. In Proceedings IEEE 91st Vehicular Technology Conference (VTC2020-Spring), pp. 1-5. <https://doi.org/10.1109/VTC2020-Spring48590.2020.9129206>.
- [6] Materum M, Takada J, Ida I, Oishi Y. (2009) Mobile station spatio-temporal multipath clustering of an estimated wideband MIMO double-directional channel of a small urban 4.5 GHz macrocell. EURASIP Journal on Wireless Communications and Networking, 2009: 1-16. <https://doi.org/10.1155/2009/804021>
- [7] Hanpinitsak P, Saito K, Takada J, Kim M, Materum L. (2017) Multipath clustering and cluster tracking for geometry-based stochastic channel modeling. IEEE Transactions on Antennas and Propagation, 65(11): 6015-6028. <https://doi.org/10.1109/TAP.2017.2754417>.
- [8] Li Y, Zhang J, Ma Z, Zhang Y. (2020) Clustering analysis in the wireless propagation channel with a variational gaussian mixture model. IEEE Transactions on Big Data. 6(2): 223-232. <https://doi.org/10.1109/TBDATA.2018.2840696>.
- [9] Teologo A, Materum L, Blanza J, Hirano T. (2020) Comparative study of k-power means, ant colony optimization, kernel power density-based estimation, and gaussian mixture model for wireless propagation multipath clustering. International Journal of Emerging Trends in Engineering Research. 8(7). <https://doi.org/10.30534/ijeter/2020/164872020>
- [10] Blanza J, Materum L. (2019) Joint identification of the clustering and cardinality of wireless propagation multipaths. International Journal of Emerging Trends in Engineering Research, 7: 763-767. <https://doi.org/10.30534/ijeter/2019/057122019>.
- [11] Blanza J, Materum L. (2019) Grouping of COST 2100 indoor multipaths using simultaneous clustering and model selection. International Journal of Emerging Trends in Engineering Research 7(8): 197. <https://doi.org/10.30534/ijeter/2019/15782019>
- [12] Diallo DM, Takada J, Saito K. (2021) .Visualization tool of the urban microcell radio propagation paths. IEICE Communications Express, 10(11): 834-839. <https://doi.org/10.1587/comex.2021XBL0128>.
- [13] Hozumi Y, Wang R, Yin C, Wei G-W. (2021) UMAP-assisted K-means clustering of large-scale SARS-CoV-2 mutation datasets. Computers in Biology and Medicine, 131: 104264. <https://doi.org/10.1016/j.combiomed.2021.104264>
- [14] Gare S, Chel S, Kuruba M, Jana S, Giri L. (2021) Dimension reduction and clustering of single cell calcium spiking: comparison of t-SNE and UMAP. In Proceedings 2021 National Conference on Communications (NCC), pp. 1-6. <https://doi.org/10.1109/NCC52529.2021.9530128>.
- [15] Varunram TN, Shivaprasad MB, Aishwarya KH, Balraj A, Savish SV, Ullas S. (2021) Analysis of different dimensionality reduction techniques and machine learning algorithms for an intrusion detection system. IEEE 6th International Conference on Computing, Communication and Automation (ICCCA), pp. 237-242. <https://doi.org/10.1109/ICCCA52192.2021.9666265>.
- [16] Liu L, Oestges C, Poutanen J, Haneda K, Vainikainen P, Quitin F, Tufvesson F, Doncker D P. (2012) The COST 2100 MIMO channel model. IEEE Wireless Communications. 19(6): 92-99. <https://doi.org/10.1109/MWC.2012.6393523>.

- 
- [17] Blanza J, Teologo A, Materum L. (2019) Datasets for multipath clustering at 285 MHz and 5.3 GHz bands based on COST 2100 MIMO channel model. 2019 International Symposium on Multimedia and Communication Technology (ISMAC), pp. 1-5. <https://doi.org/10.1109/ISMAC.2019.8836143>.
- [18] McInnes L, Healy J, Melville J. (2018). UMAP: uniform manifold approximation and projection for dimension reduction. ArXiv e-prints. <https://doi.org/10.48550/arXiv.1802.03426>
- [19] Pealat C, Bouleux G, Cheutet V. (2020) Improved time-series clustering with UMAP dimension reduction method. 2020 25th International Conference on Pattern Recognition (ICPR), pp. 5658-5665. <https://doi.org/10.1109/ICPR48806.2021.9412261>.
- [20] A Detailed Introduction to K-Nearest Neighbor (KNN) Algorithm [<https://saravananthirumuruganathan.wordpress.com/2010/05/17/a-detailed-introduction-to-k-nearest-neighbor-knn-algorithm/>]
- [21] Meehan C, Ebrahimian J, Moore W, Meehan S. (2022) Uniform manifold approximation and projection (UMAP). [<http://www.mathworks.com/matlabcentral/fileexchange/71902>]
- [22] Steinbauer M, Ozcelik H, Hofstetter H, Mecklenbrauker C F, Bonek E. (2002) How to quantify multipath separation. IEICE Transactions on Electronics, 85(3): 552-557.
- [23] Ester M, Kriegel H -P, Sander J, Xu X. (1996) A density-based algorithm for discovering clusters in large spatial databases with noise. In Proceedings of the Second International Conference on Knowledge Discovery and Data Mining, pp. 226-231.
- [24] Schubert E, Sander J, Ester M, Kriegel HP, Xu X. (2017) DbSCAN revisited, revisited: why and how you should (still) use dbSCAN. ACM Trans Database Syst (TODS), 42(3): 1-21. <https://doi.org/10.1145/3068335>.
- [25] Fahad A, Alshatri N, Tari Z, Alamri A, Khalil I, Zomaya AY, Foufou S, Bouras A. (2014) A survey of clustering algorithms for big data: Taxonomy and empirical analysis. IEEE Transactions on Emerging Topics in Computing, 2(3): 267-279. <https://doi.org/10.1109/TETC.2014.2330519>.

## MOBILE GAS SENSING FOR LABORATORY INFRASTRUCTURE

RADUAN SARIF<sup>1</sup>, MOHAMMED FAEIK RUZAIJ AL-OKBY<sup>2,3\*</sup>,  
THOMAS RODDELKOPF<sup>1</sup> AND KERSTIN THUROW<sup>3</sup>

<sup>1</sup>*Institute of Automation, University of Rostock, 18119 Rostock, Germany*

<sup>2</sup>*Technical Institute of Babylon, Al-Furat Al-Awsat Technical University (ATU), Kufa 54003, Iraq*

<sup>3</sup>*Center for Life Science Automation (Celisca), University of Rostock, 18119 Rostock, Germany*

\*Corresponding author: [mohammed.al\\_okby@atu.edu.iq](mailto:mohammed.al_okby@atu.edu.iq)

(Received: 31 January 2023; Accepted: 30 November 2023; Published on-line: 1 January 2024)

**ABSTRACT:** Indoor air quality has become a growing concern in modern society due to prolonged indoor working hours that lead to the frequent exposure to numerous toxic gases from various sources. These pollutants, including volatile organic compounds (VOCs), pose severe health risks such as asthma and lung cancer. To address this critical issue, this project focuses on developing and evaluating an advanced gas detection system that explicitly targets VOCs by integrating two novel metal oxide semiconductor (MOX)-based gas sensors, ENS 160 and TED110. Different sensor parameters, such as the air quality index (AQI) and volatile organic compounds (VOCs), were evaluated using 12 volatile organic chemicals. The findings revealed that the ENS 160 sensor performs excellently, detecting 60 gas samples out of 72, with an average detection rate of approximately 83%. In contrast, the TED110 sensor demonstrated considerably lower performance and response in 24 out of 72 gas samples, with a detection rate of about 33%. The results contribute insights into the gas sensor's characteristics, providing essential information to enhance indoor air quality monitoring technology, particularly in laboratory environments.

**ABSTRAK:** Kualiti udara dalam bangunan semakin mendapat perhatian di kalangan masyarakat moden kerana waktu bekerja yang panjang di dalam bangunan dan ini berpotensi terdedah kepada gas toksik dari pelbagai sumber. Pencemaran ini, adalah termasuk kepada sebatian organik mudah meruap (VOCs), yang menimbulkan resiko kesihatan yang teruk, seperti asma dan kanser paru-paru. Bagi menangani isu kritikal ini, projek ini memfokuskan tentang sistem pembangunan dan penilaian secara eksplisit mensasarkan VOCs dengan mengintegrasikan dua pengesan gas berasaskan semikonduktor logam oksida (MOX), ENS 160 dan TED110 yang baru. Parameter berbeza pada pengesan, seperti indeks kualiti udara (AQI) dan sebatian organik mudah meruap (VOCs), dinilai menggunakan 12 bahan kimia organik mudah meruap. Dapatan menunjukkan pengesan ENS 160 berjaya mengesan 60 jenis gas daripada 72 jenis, dengan purata kadar identifikasi sebanyak 83%. Secara perbandingan pengesan TED110 hanya mengesan 24 daripada 72 sampel gas, dengan kadar pengesanan sebanyak 33%. Dapatan ini menyumbang kepada pemahaman tentang ciri-ciri pengesan gas, penyumbang kepada pengetahuan penting tentang teknologi pemantauan kualiti udara iaitu secara khususnya dalam persekitaran makmal.

**KEY WORDS:** *Mobile gas sensing, hazardous gas detection, volatile organic compounds, environmental gases, gas sensors, toxic gases.*

## 1. INTRODUCTION

In laboratory infrastructure, employees should be familiar with the chemicals they may come across, potentially reactive or explosive liquids and gases that can be highly hazardous. Accidental or uncontrolled chemical reactions are significant causes of severe personal injury and property damage. Dangerous gases are sufficiently toxic or reactive substances that vigorously or violently give off heat and energy, and become poisonous in contact with air, water, or some other common material. They can be classified in various ways, including acutely toxic, corrosive, flammable, dangerously reactive, and oxidizing compounds [1–7]. Toxic compounds include hydrogen chloride, benzene or toluene, dioxin, and volatile organic compounds (VOCs, such as hydrocarbons, fluorocarbons, chlorofluorocarbons.), or elements such as cadmium, mercury, and chromium. Different VOCs in indoor air are produced from building materials, for instance, wood, cement, stones, asbestos used during construction, and utility items placed inside the building, such as carpets. These are sources of hazardous/toxic gases that can be inorganic, organic, biological, or even radioactive.

In the laboratory infrastructure for learning and experimentation purposes, the laboratory staff must handle a variety of dangerous, poisonous, and reactive chemicals or gases. A particular quantity of hazardous/toxic gases pollutes the atmosphere and can significantly influence human health, creating severe illnesses and threatening worker safety. This expanding number of dangerous gases is sometimes the cause of catastrophic incidents, ruining assets and the causing the deaths of many people [4], [8–10]. Therefore, toxic gases may be acidic, explosive, and extremely dangerous, depending on the concentration and surroundings. A hazardous gas may harm living tissues, affect the central nervous system, cause severe disease, or, in the worst situations, result in death when consumed, breathed, or absorbed by the skin or eyes, according to specialists in gas detection. Furthermore, the employee may regularly be in contact with various hazardous gases in the chemical research laboratory [11], [12]. For instance, long-time exposure to the following gases, CO<sub>2</sub>, carbon monoxide, and nitrogen oxide (NO<sub>2</sub>), can cause headaches, dizziness, restlessness, tingling, or pins or needles feeling, difficulty breathing, sweating, tiredness, increased heart rate, elevated blood pressure, coma, asphyxia, and convulsions [13–15]. The effects of different VOCs on human health, such as carbonyl and aromatic compounds, like HCHO, CH<sub>3</sub>CHO, C<sub>6</sub>H<sub>6</sub>, C<sub>6</sub>H<sub>5</sub>CH<sub>3</sub>, and C<sub>8</sub>H<sub>10</sub>, severely impact human health and are causes of cancer. Besides, inhaling these compounds can lead to lung cancer [13–17], so experimenting with the effect of these compounds on human health is worthwhile for researchers. Numerous commercial gas detection sensors are available, such as MOX, electrochemical, catalytic, and optical infrared, detect hazardous gases including volatile organic compounds (VOCs). These sensors can be portable or fixed devices and provide alarms when gas concentrations exceed specified thresholds. Several criteria should be considered to evaluate the performance of gas sensors, such as sensitivity, selectivity, stability, response time, reversibility, energy consumption, adsorptive capacity, and fabrication cost. These factors play a crucial role in determining the effectiveness and reliability of gas detection systems in different applications [18] [19].

Neubert et al. [20] discussed a modular Internet of Things (IoT)-based sensor node for hazardous gas detection and monitoring. This experiment used two MOX gas sensors which are BME688 (Bosch Sensortec, Reutlingen, Germany) and SGP30 (Sensirion AG, Stafa, Switzerland). Moreover, a WROOM WiFi module (Espressif Systems, Shanghai, China) transfers the collected data to an IoT cloud for data monitoring and storage. The processing unit for this project was an NXP MKL27Z128VLH4 (NXP Semiconductors N.V., Eindhoven, Netherlands) ARM microcontroller. Furthermore, the experiments were done with various VOCs as a standalone unit and hosted by a stationary and mobile robot.

Two metal oxide (MOX) gas sensors were tested with Al-Okby et al., namely SPG30 and SPG40 (Sensirion AG, Stäfa, Switzerland), to measure the indoor air quality parameters IAQ index and the total volatile organic compound TVOC [7]. The WeMos D1 Mini is a WiFi-based Microcontroller for IoT applications that has been used in the following project with the chip ESP8266 (Espressif Systems, Shanghai, China). The sensors have been tested on various VOC compounds in two different test conditions. Several sensor placements, including a moving robot, were utilized to assess the effectiveness of the two sensors based on the recorded characteristics (IAQ-index and TVOC) [19–21].

Demonstrating a gas sensor system for domestic air quality monitoring, K. Gupta et al. [24] applied Tin Dioxide (SnO<sub>2</sub>) based MOX gas sensors MQ-135, MQ-6, and MQ-4 ( Winsen Electronics Technology, Zhengzhou, China.). They detected ammonia (NH<sub>3</sub>), nitrous gases (NO<sub>x</sub>), nicotine, benzene, carbon dioxide (CO<sub>2</sub>), butanes, LPG, propane, and LNG, and natural gases (methane, CH<sub>4</sub>) with an Arduino UNO microcontroller and ESP8266 (Espressif Systems, Shanghai, China) for the WiFi communication interface. Data was shown on the LCD screen and stored on the server. This system can be used as a wireless sensor network for environmental monitoring. Similar technology is utilized for multiple purposes in [23–26].

W. Wojnowski et al. employed electrochemical sensors in E-noses [29]. The sensors included DGS-CO 968-034, DGS-Ethanol 968-035, DGS-H<sub>2</sub>S 968-036, DGS-NO<sub>2</sub> 968-037, DGS-SO<sub>2</sub> 968-038, DGS-RESPIRR 968-041, 2E 50, 3E 100 SE (SPEC Sensors LLC, Newark, CA, USA). They were used for the measurement of carbon monoxide (C.O.), ethanol, hydrogen sulfide (H<sub>2</sub>S), nitrogen dioxide (NO<sub>2</sub>), sulfur dioxide (SO<sub>2</sub>), VOC, and ammonia (NH<sub>3</sub>). The communication interface used a USB driver with an LTC2433 ADC (Linear Technology, Milpitas, California, United States) to transfer the data to a PC-class computer.

A. Somov et al. presented a wireless sensor-actuator system for methane detection using a catalytic sensor (NTC-IGD, Stockport, Russia) [30]. Using the Micro Controller Unit (MCU) ADuC836 (One Technology Way, Norwood, USA), the node was connected to the WSN via the ETRX3 module; the communication interface was UART. The calibration notices were recorded in EEPROM M95640, connected to MCU using SPI. Apart from the calibration information, the memory chip stored information on the occurring events, e.g., emergencies.

S. Esfahani et al. developed an electrical nose for VOC, carbon dioxide (CO<sub>2</sub>), and methane (CH<sub>4</sub>) using optical and infrared sensors such as LFP3144C-337, LFP-3850C-337, LFP-8850-337, and 90 V LFP- 8850-337 (InfraTec GmbH, Dresden, Germany) [31]. This work used a Teensy 3.6 (PJRC, Portland, USA) microcontroller with a UART communication interface. A laptop with a USB serial port was connected for storing and displaying data. This portable optical e-nose can be applied to a robot for environment monitoring.

A fumigant gas trace detection system (FGTDS) based on a photoionization detector (PID) was designed for the inspection and quarantine port to monitor the gas leakage within the dosing room of the fumigant warehouse [32]. It used PID-A1 (Alphasense, Braintree, U.K.) with MCU STC12LE5A60S2 (Shenzhen LCSC Electronics Technology, Shenzhen, China) and ADS8325 A/D (Texas Instruments, Texas, United States) converter, which was applied for MCU controls.

This research focused on developing and evaluating an advanced volatile organic compounds (VOCs) detection system using novel metal oxide semiconductor (MOX)-based gas sensors. Besides, the study investigated the sensor performance, such as sensitivity, selectivity, and detectable gas limit, focusing on distinct sensor parameters, including the air quality index (AQI) and total volatile organic compounds (VOCs). Overall contribution was to develop an advanced gas detection system specifically for VOCs using two novel MOX-based

gas sensors, ENS160 (Sciosense B.V., Eindhoven, Netherlands) and TED110 (Wise Control Inc, Seoul, Korea). In addition, it evaluated distinct sensor parameters, such as AQI and TVOCs, in a typical chemical hood environment with 12 distinct VOCs. It also analyzed the sensors' different characteristics, such as sensitivity, accuracy, response, and recovery time. The comparison of the system's stability, accuracy, and effectiveness with existing design from the University of Rostock, including sensors BME688 (Bosch Sensortec, Reutlingen, Germany), SGP 40, and SGP 30 (Sensirion AG, Stäfa, Switzerland), offers valuable benchmarks and validates the system's performance. In a nutshell, the findings from this research enhance the understanding of gas detection technology and provide essential insights for improving indoor air quality monitoring systems and safety, particularly in laboratory environments [7], [20].

## 2. MATERIALS AND METHODS

### 2.1. Sensor Selection

One of the significant challenges of a gas detection system is determining the appropriate gas sensor type. Different gas sensor technologies have limitations; none can be used for all gas types or applications. The primary goal of this project is the detection of indoor TVOC with a specific focus on a quick response for the safety laboratory employees. The initially chosen MOX gas sensor ENS160 (Sciosense B.V., Eindhoven, Netherlands; see Fig. 1) can measure three separate parameters, AQI (100 to 500), TVOC (0-65,000 PPB-Parts per billion), and eCO<sub>2</sub> (0-65,000 PPM-Parts per Million). The TED110 (WISE Control Inc, Seoul, Republic of Korea), shown in Fig. 2, was chosen as a second gas sensor for the detection of a wide range of gases in concentrations between 1 and 1,000 ppm, including VOCs, carbon monoxide, ethanol, methane, nitrogen dioxide, toluene, and hydrogen sulfide. Detailed descriptions of both sensor specifications are provided in Table 1:



Fig. 1: ENS 160 Gas Sensor, Sciosense B.V., Eindhoven, Netherlands [33]



Fig. 2: TED110 sensor, Wise control inc., Seoul, Republic of Korea [34].

Table 1: Selected Sensor Specifications

Sensor Specifications	ENS 160	TED 110
Structure	Metal Oxide (MOX)	MOX type Micro-Electro-Mechanical System (MEMS)
Measure Gases	AQI (100-500), TVOC (0 – 65,000 PPB), (400 – 65,000 PPM)	TVOC (VOCs, CO, EtOH, CH <sub>4</sub> , NO <sub>2</sub> , Toluene, H <sub>2</sub> S et) (1-1000 PPM)
Humidity and temperature	Yes	Yes
Response time	1s	10s
Warm-up	< 3 min	< 50 seconds
Communication Interface	I2C and SPI	I2C
Positive supply	1.8V(VDD) & 3.6V(VDDIO)	3.3 V
Lifetime	10 years	5 years
Package dimension	3.0 × 3.0 × 0.9 mm <sup>3</sup>	3 × 3 × 1 mm <sup>3</sup>
Cost	\$6.06 \$12.50	
Manufacturers	Sciosense B.V., Eindhoven, Netherlands	Wise control inc., Seoul, Republic of Korea.

## 2.2. Microcontroller Selection

Microcontrollers are used to analyze and process the measured data, in decision-making, and in sending the proper action signals to the output ports. The Kinetics KL27 Microcontroller, illustrated in Fig. 3, was chosen for this experiment, which uses an MKL27Z128VLH4 processor (NXP Semiconductors, Eindhoven, Netherlands). The project selected this Microcontroller [18], which was tested before with two gas sensors (BME 688 and SGP 30). It is optimized for cost-sensitive and battery-powered applications requiring low-power USB connectivity. The specification of the MCU is shown in Table 2.

Table 2: Specification of the Microcontroller

Specifications	Values
Core Type	Arm Cortex-M0+
Operating Frequency (MHz)	48
Number of bits	32bit
Temperature range (°C)	-40° to 105 °C
Flash (kB)	128
SRAM (kB)	32
Serial Communication	2 × I <sup>2</sup> C, 2 × SPI, 3 × UART
Supply Voltage (V)	1.71 V to 3.6 V
Power supply and data Transfer	USB-C

## 2.3. Experimental Setup

This project is the extension of an existing developed system called CELISCA at the University of Rostock, Germany [20], which consists of two sensors in the sensing layers, such as BME688 (Robert Bosch GmbH, Stuttgart, Germany) and SGP40 (Sensirion AG, Stäfa, Switzerland), as shown in Figure 5(a). The sensor layer was tested with the processing layer

NXP MKL27Z128LH4 MCU (NXP Semiconductors N.V., Eindhoven, Netherlands) board. Since gas sensors are heat sensitive, these sensor layers were designed in two fingers to keep a particular air gap. The heat generated by the sensors may interfere with the degradation of their function. The main objective of the current project was the extension of a novel sensor layer and the design of a relevant system. For the extension, two novel gas sensors, ENS160 (Sciosense B.V., Eindhoven, Netherlands), TED110 (Wise Control Inc, Seoul, Korea), and the processing layer MKL27Z128LH4 MCU board (NXP Semiconductors, Eindhoven, Netherlands) were added. Developing the design idea from the previous project, the first selected sensor, ENS160, was placed in the middle of the previous two sensors, shown in Fig. 5 (b). Finally, by adding the TED110, the overall sensor board then has four fingers - TED110, BME688, ENS160, and SGP40 as seen in Fig. 5(c). All selected sensors and necessary electronics were designed on a printed circuit board (PCB) by Autodesk Eagle software (Autodesk, San Rafael, California, USA). After manufacturing the PCB, sensors and relevant electronics were mounted on the board.

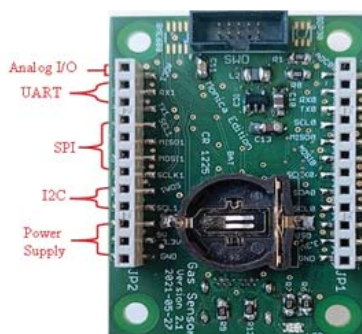


Fig. 3: MKL27Z128VLH4 MCU board

This project consists of two main layers, as shown in Fig. 4. The first layer is the sensing layer, which detects various gas parameters. The second layer is the processing layer (MCU) with the power supply, which receives the measured data from the sensing layer and processes it. The MCU acts as a master, communicating with the sensors (working as slaves) using the I2C communication protocol. The MCU sends a register address to initiate the sensor's I2C clock, baud rate, and data length; after receiving the initiate acknowledgment command from the sensor, the MCU requests the sensor data. Then the MCU writes register addresses on the sensors for individual parameters, reads them as gas data, and converts all the data into appropriate units. The MCU's programming was performed using MCUXpresso IDE (NXP Semiconductors N.V., Eindhoven, Netherlands) and debugged using J-Link EDU (SEGGER Microcontroller GmbH, Monheim am Rhein, Germany). The detection results were displayed in Tera Term (open-source software under the BSD License) serial monitor connected via USB-C and saved in a CSV file.

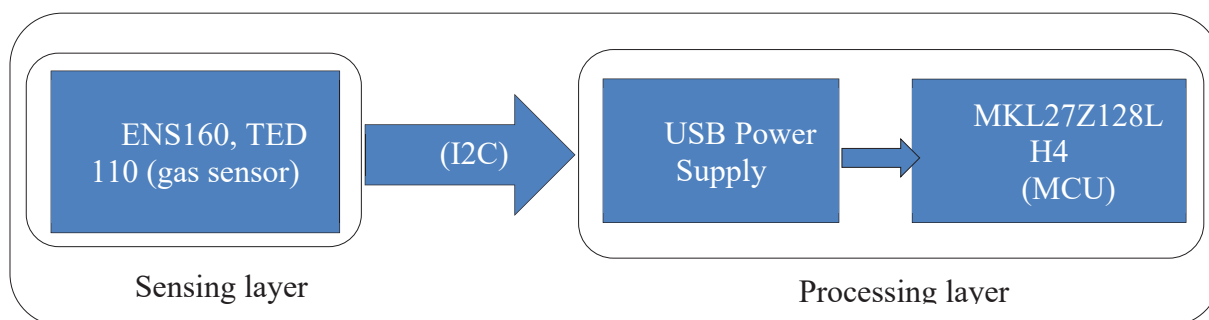


Fig. 4: Overall project structure

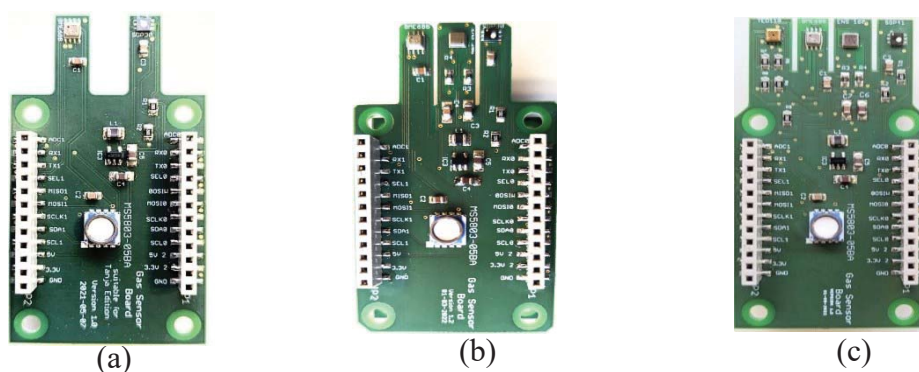


Fig. 5: (a) Sensor board with BME688 and SGP40; (b) BME688 and SGP40 and ENS160; (c) TED110, BME688, ENS160 and SGP40

## 2.4. Experimental Procedure

To evaluate the sensor characteristics, 12 different low volatile organic compounds were selected, which are commonly used in the laboratory [7], [12], [35]. Among the 12 VOCs, benzene, toluene, and formic acid are exceptionally toxic and carcinogenic, posing significant risks of long-term health effects, including leukemia and cancer, even at low exposure levels [36]. Additionally, acetone, acetonitrile, dichloromethane, diethyl ether, ethanol, heptane, hexane, and iso-propanol are harmful to human health as they can cause respiratory irritation, dizziness, and in severe cases, damage to organs such as the liver and nervous system when exposed to elevated concentrations [2], [37]. So, detecting all these gases is crucial for ensuring safety in the laboratory and assisting in developing better gas detection technologies. Table 3 displays the selected 12 gases with their molecular formulas and the boiling point [7]. The entire experiment was done in a classical chemical hood (Waldner Holding GmbH and Co. KG, Wangen im Allgäu, Germany); Fig. 6 illustrates a hood design for a laboratory for chemical and analytical purposes. Eppendorf pipettes were used to inject the testing samples within a Petri dish (Eppendorf AG, Hamburg, Germany). In addition, the sensor node was mounted on a movable stand with a manually adjustable height. The experiment was performed for 5 minutes, during which data was taken for 300 s. The amount of the gas samples were 5 $\mu$ L, 10 $\mu$ L, and 50 $\mu$ L; all experiments were done from 40 cm and 100 cm sensor node distance from the testing vapors. For the ENS160, the target parameter is the air quality index AQI (100 to 500), total volatile organic compounds concentration TVOC (0 – 65,000 ppb), and CO<sub>2</sub> (400 – 65,000 ppm). The target parameter for the TED 110 gas sensor is the Gas Density (0 – 1,000 ppm). Every second of data was stored in a CSV file for further graphical visualization. Table 4 displays the various levels of gases for ENS160.

Table 3: Selected 12 gases with the molecular formula and the boiling point [7]

Name	Molecular Formula	Boiling point in °C
Acetone	C <sub>3</sub> H <sub>6</sub> O	56
Acetonitrile	C <sub>2</sub> H <sub>3</sub> N	82
Benzene	C <sub>6</sub> H <sub>6</sub>	80.1
Dichloromethane	CH <sub>2</sub> Cl <sub>2</sub>	39.6
Diethyl ether	C <sub>4</sub> H <sub>10</sub> O	34.6
Ethanol	C <sub>2</sub> H <sub>6</sub> O	78.37
Formic Acid	CH <sub>2</sub> O <sub>2</sub>	100.8
Heptane	C <sub>7</sub> H <sub>16</sub>	98.42
Hexane	C <sub>6</sub> H <sub>14</sub>	69
Iso propanol	C <sub>3</sub> H <sub>8</sub> O	82.5
Methanol	CH <sub>3</sub> OH	64.7
Toluene	C <sub>7</sub> H <sub>8</sub>	110.6

**Table 4:** ENS160 concern for different gas concentrations [33]

Level	AQI	TVOC (ppb)	CO <sub>2</sub> (Without baseline 400) (ppm)
Unhealthy	500	>2,200	>1500(1100)
Poor	400	660-2,200	1000-1500(600-1100)
Moderate	300	220-660	800-1000(400-600)
Good	200	65-220	600-800(200-400)
Excellent	100	0-65	400-600(0-200)

To avoid any influence from air ventilation, the ventilation system of the hood was shut off during system testing. The chemical hood is shown in Fig. 6.



Fig. 6: Experiment in a traditional chemical hood

### 3. RESULTS AND DISCUSSION

The goal of the tests in all scenarios and positions was to determine the smallest quantity of VOC detected by the two utilized sensors from the testing distance (e.g., the length between the VOC leakage source and the sensors). The sensor responses were analyzed by presenting all the experimented data in a graph. The result can be defined for ENS 160 from Table 4 as low response (all parameters are in excellent level), moderate response (all parameters are good & moderate level), and excellent response (all parameters are poor & unhealthy level). Additionally, TED110 has low performance in this experiment, so in this research, just its response was tested.

The ENS 160 gas sensor demonstrates high effectiveness and performance for acetone (C<sub>3</sub>H<sub>6</sub>O) detection, showing excellent response to sample amounts >5 $\mu$ L and all desired parameters, including AQI, TVOC, and CO<sub>2</sub>. Its reliable performance at lower sample concentrations showcases its sensitivity and ability to detect acetone accurately. On the other hand, the TED110 sensor's low response to acetone, except at >50 $\mu$ L and 100 cm distance, indicates a low gas detectable limit, assuming a reason of cross-sensitivity or environmental interference. The principle of the MOX gas sensor is that its surface is adsorbed by oxygen, changing the sensor's response quickly [38], so that the ENS160 gas sensor strongly reacts to oxygen containing compounds, but TED 110 needs intensive investigation to improve performance and expanding detection limit. Both sensor responses for acetone are presented in Fig. 7.

Acetonitrile ( $C_2H_3N$ ) has an excellent response with ENS160's required parameters with a volume  $>5\mu L$ , illustrated in Figure 8, showing a good sensitivity and detection level. The AQI, TVOC, and  $CO_2$  exhibit an excellent response for  $>10\mu L$ . TED110 gas sensor (gas density) has no response for any amounts of acetonitrile 40 cm and 100 cm. ENS 160 has good performance without oxygen-containing compounds, but TED110 failed in this context; further improvement is necessary.

Detecting low benzene concentrations ( $C_6H_6$ ) is essential because inhaling it for a long time can cause cancer. ENS160 has an excellent response with the benzene samples concentration of  $>10\mu L$  for all required parameters, such as AQI, TVOC, and  $CO_2$ , presented in Fig. 9. Although it has no oxygen compounds, ENS 160 is responding, but the TED110 gas sensor has no response for benzene. ENS160's ability to detect benzene at concentrations  $>10\mu L$  demonstrate that it has a low detection limit (has no oxygen compounds); further calibration is necessary to enhance its gas detectable limit and broaden its application range for benzene detection.

Dichloromethane ( $CH_2Cl_2$ ) increases the risk for several specific cancers, including brain, liver, and biliary tract cancer. Unfortunately, as seen in Fig. 10, ENS 160 has a low response to this vapor, and the TED110 gas sensor has no response for all the required parameters. The low response of both sensors creates concern about the sensor's traceability, testing methods, sensitivity, and selectivity, probably following the MOX sensor principle. In short, to improve accuracy and eliminate external factor contamination, a more extensive experimental procedure must be developed or choosing gas sensors with appropriate sensitivity and selectivity.

ENS160 has an excellent response to diethyl ether ( $C_4H_{10}O$ ) from the sample amount of  $>5\mu L$  for all the necessary parameters, indicating its significant effectiveness and detection capability, illustrated in Fig. 11. The AQI, TVOC, and  $CO_2$  showed excellent responses for the sensor node distances, such as 40 cm and 100 cm. ENS 160 has an excellent response; although no oxygen compound, the TED110 gas sensor (Gas Density) declines to respond to diethyl ether.

Ethanol ( $C_2H_6O$ ) has an excellent response of  $>5\mu L$  for all the desired parameters in ENS160. Similarly, the TED110 gas sensor (gas density) has a reaction for ethanol in all gas sample concentrations. Fig. 12 exhibits both sensor responses for ethanol. Overall, based on the MOX gas sensor principle, both sensors possess appropriate gas detectable limits and sensitivity, which makes them suitable for ethanol detection.

Formic Acid ( $CH_2O_2$ ) has a low response in the ENS 160 gas sensor for all the expected parameters (AQI, TVOC, and  $CO_2$ ). On the other hand, the TED110 gas sensor (gas density) has a response to formic acid, showing the highest reaction for sample size at  $>5\mu L$  at 40 cm. Similarly, for the 100 cm distance, the TED110 gas sensor (Gas Density) has a response from  $>10\mu L$  gas samples. Both sensors' response to formic acid are shown in Fig. 13. Based on oxygen compounds, ENS160 should have had a reaction but failed; TED110 has a response but low detection level, so both sensors require more calibration and intensive investigation to improve sensitivity, effectiveness, and performance to the formic acid.

As shown in Fig. 14, heptane ( $C_7H_{16}$ ) has a low response for all the desired parameters at the ENS160 gas sensor. Similarly, the TED110 gas sensor (Gas Density) has no response. As no oxygen compounds, both sensors declined to respond. As a result, testing methods for the current sensors or the adoption of a heptane-specific sensor, need to improve.

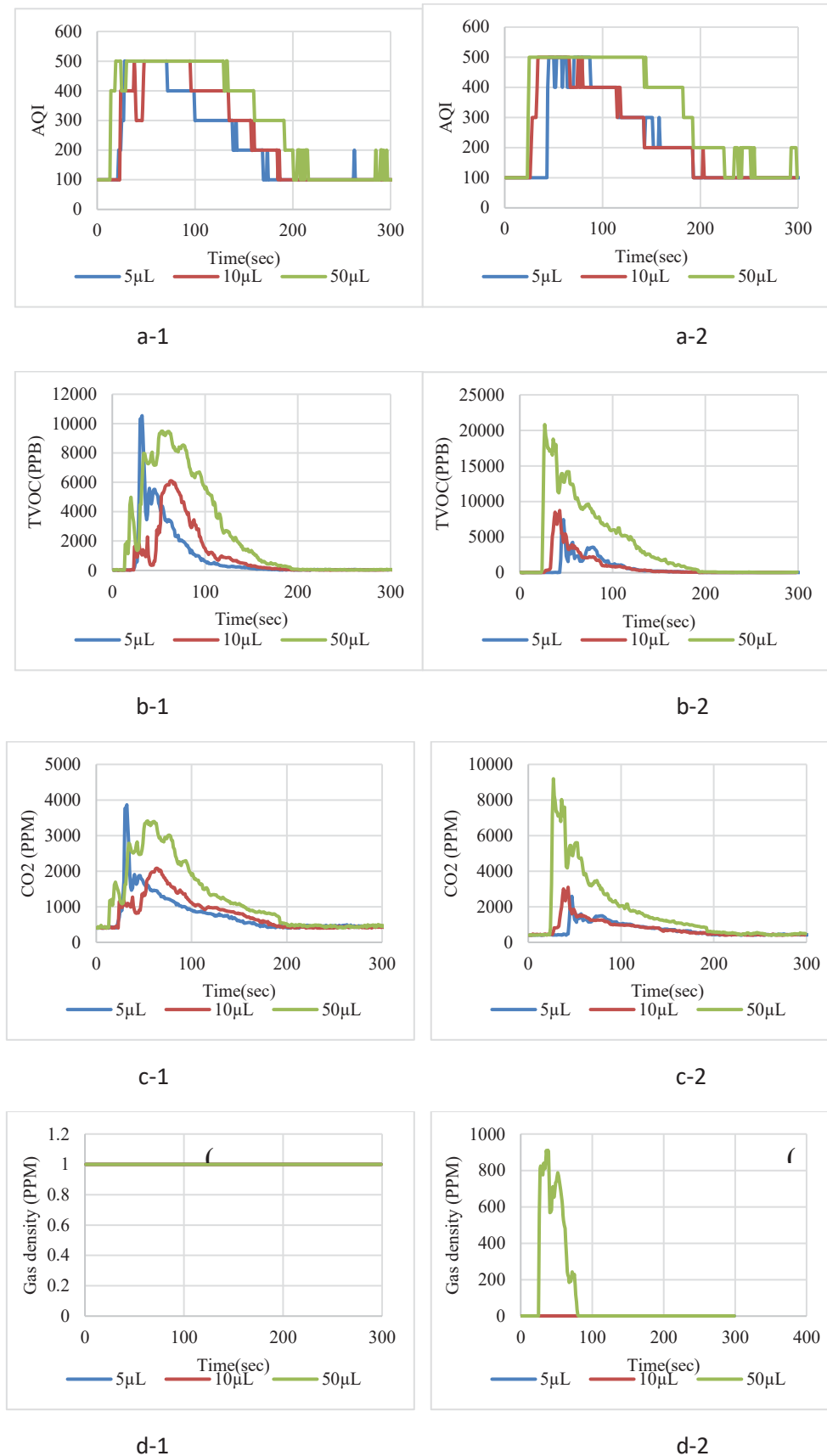


Fig. 7: Acetone ( $C_3H_6O$ ) response for ENS160 (a, b, c) and TED110 (d) at 40 cm (1) and 100 cm (2)

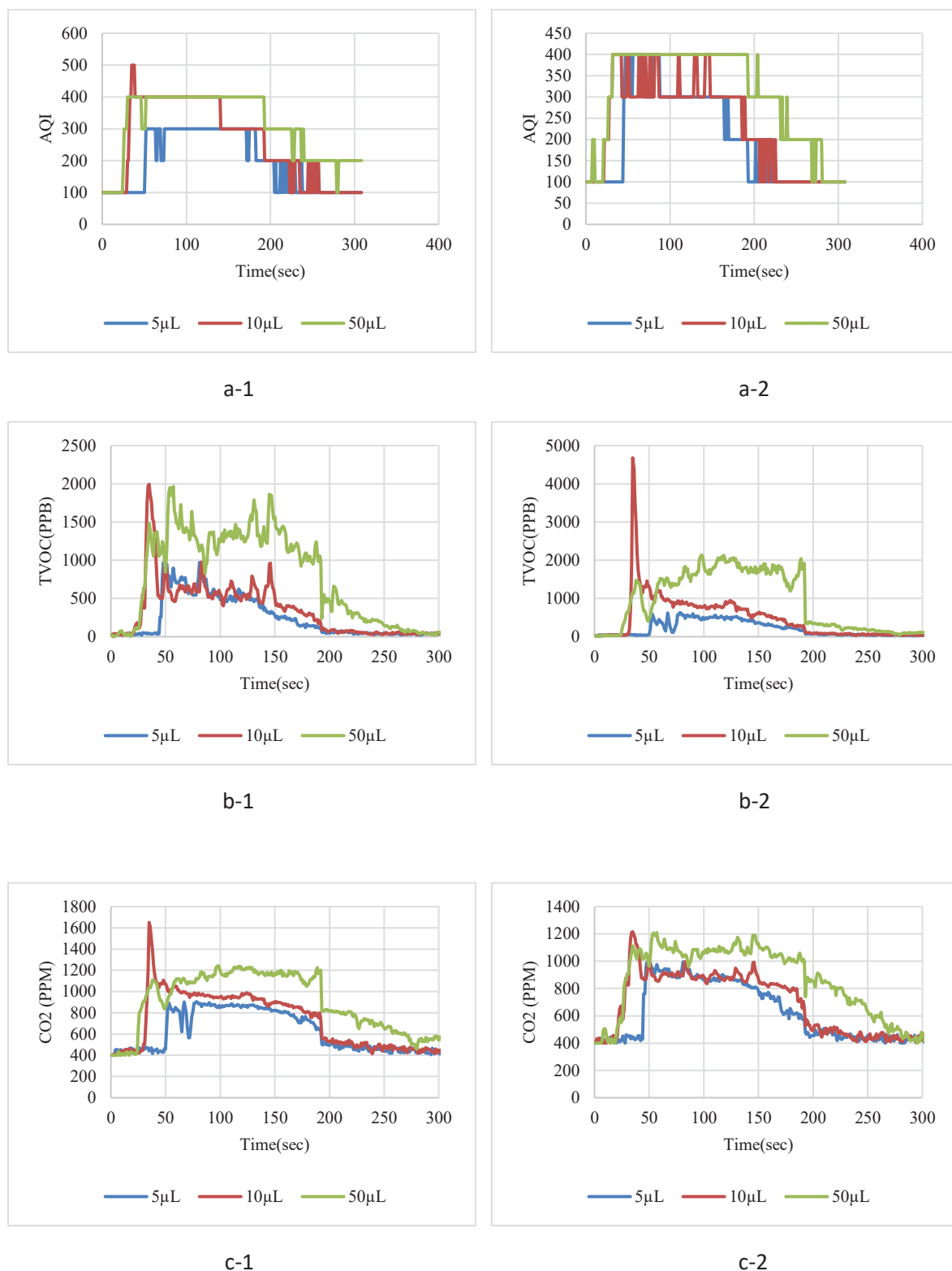


Fig. 8: Acetonitrile ( $C_2H_3N$ ) response for ENS160 (a, b, c) at 40 cm (1) and 100 cm (2).

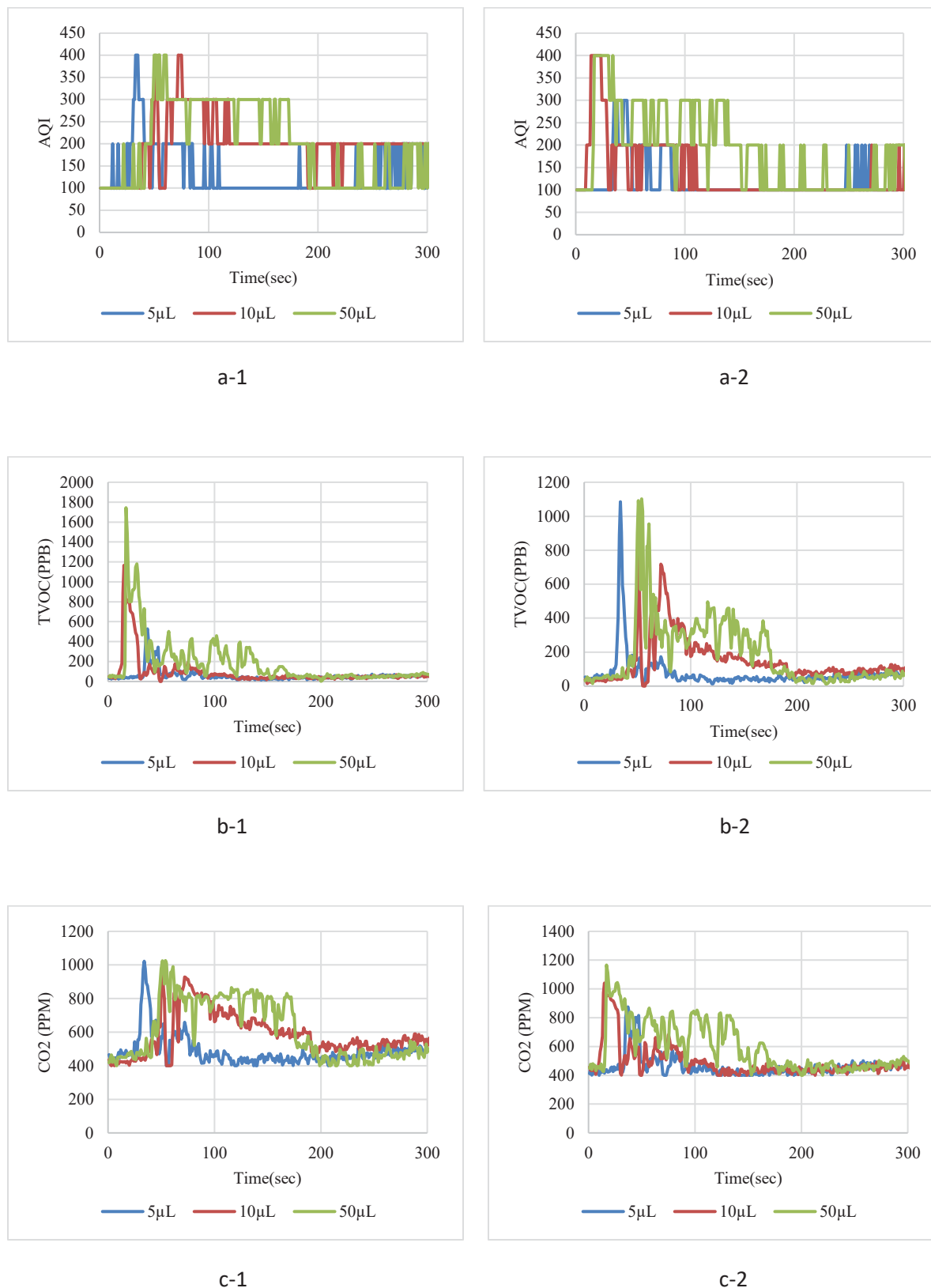


Fig. 9: Benzene (C<sub>6</sub>H<sub>6</sub>) response for ENS160 at 40 cm (1) and 100 cm (2)

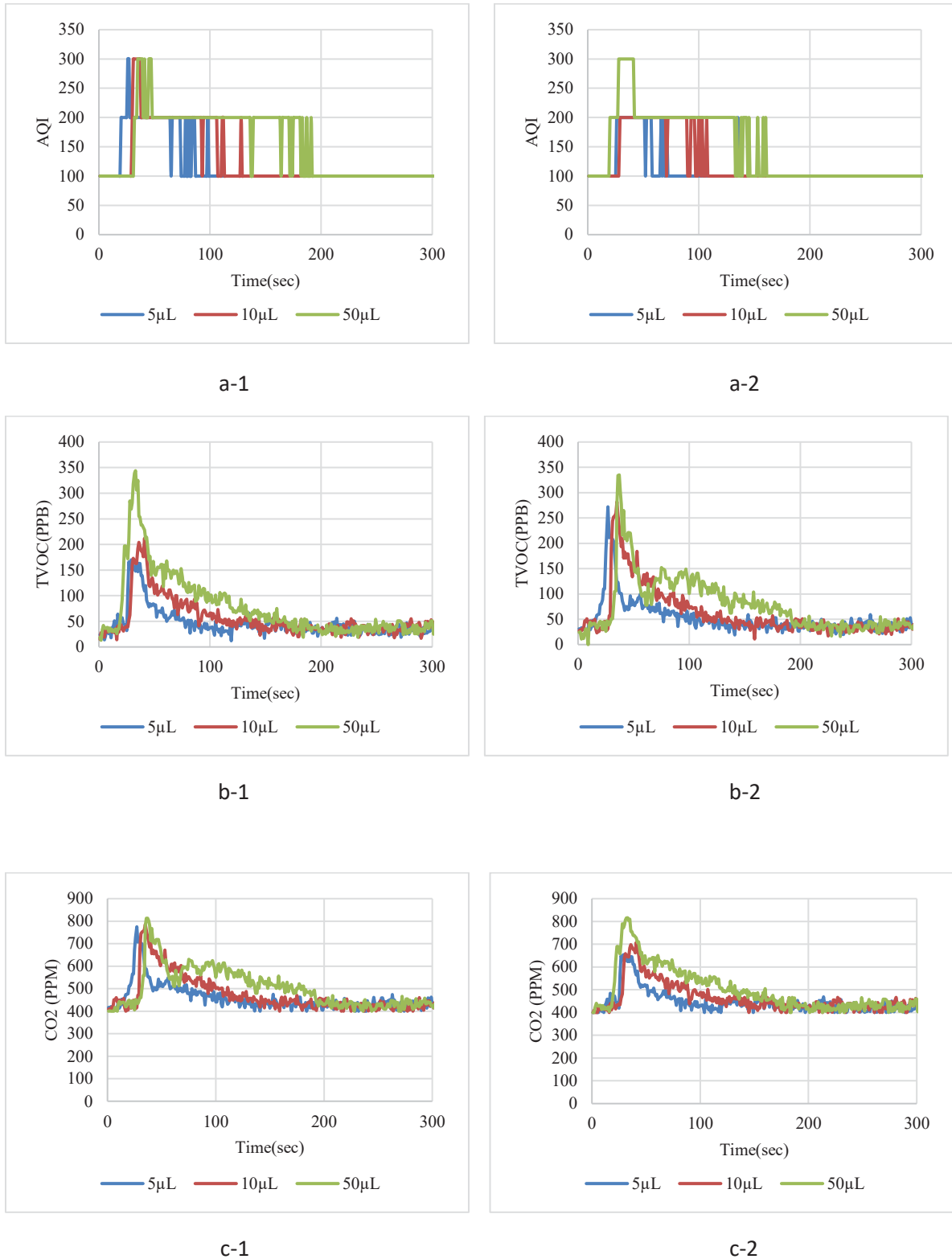


Fig. 10: Dichloromethane ( $\text{CH}_2\text{Cl}_2$ ) response for ENS160 (a, b, c) at 40 cm (1) and 100 cm (2)

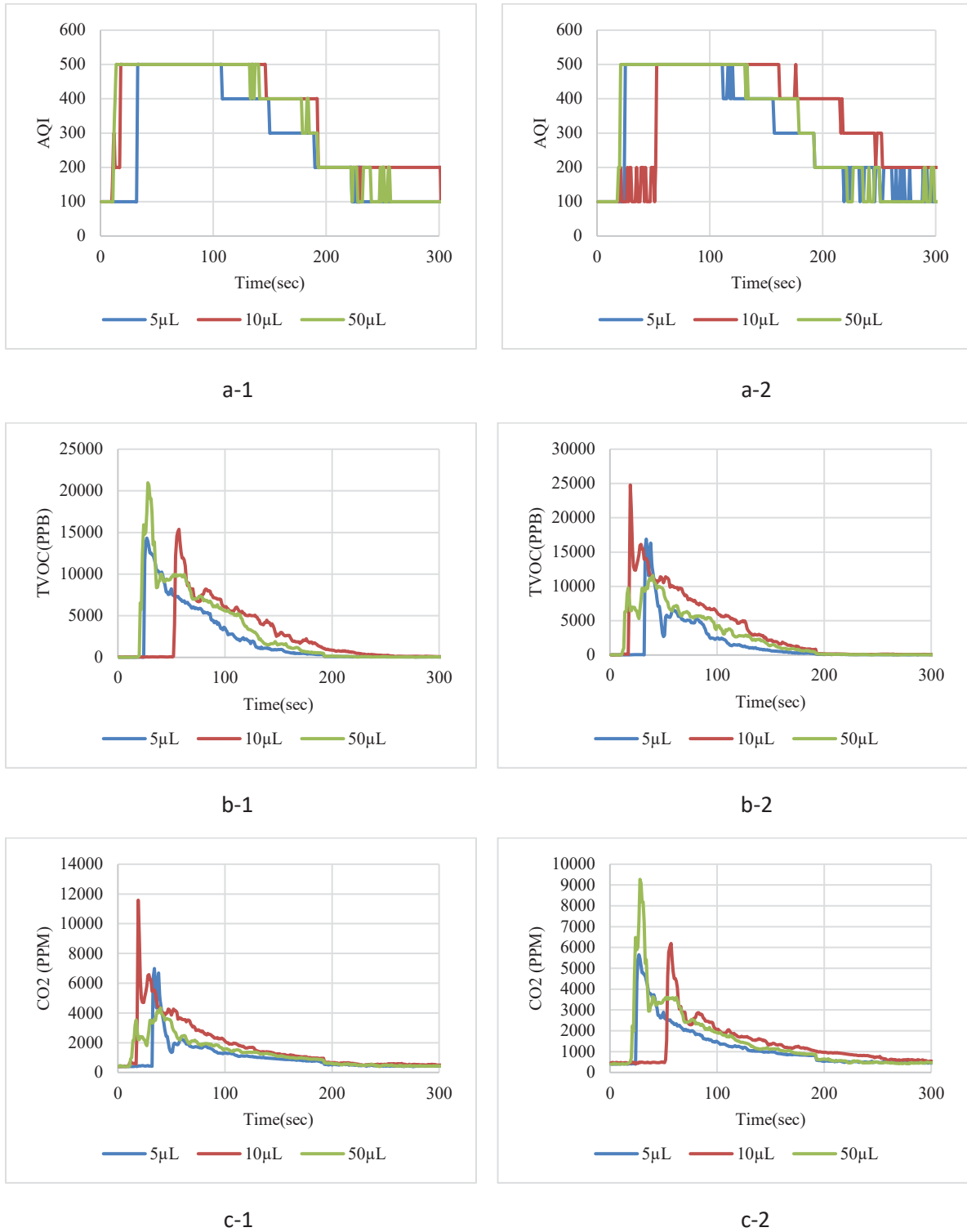


Fig. 11: Diethyl Ether ( $C_4H_{10}O$ ) response for ENS160 (a, b, c) at 40 cm (a) and 100 cm (b),

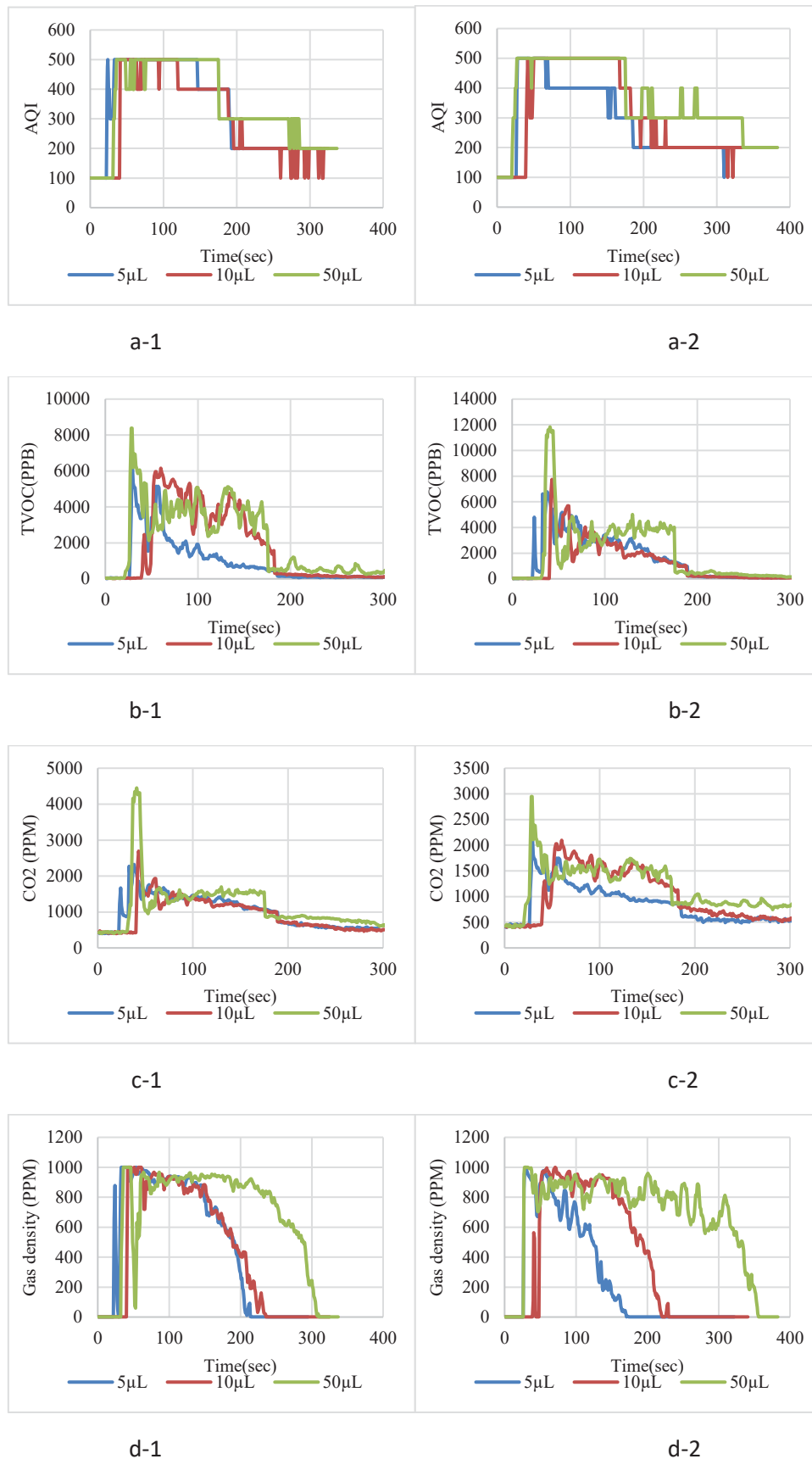


Fig. 12: Ethanol ( $C_2H_6O$ ) response for ENS160 (a, b, c) and TED110 (d) at 40 cm (1) and 100 cm (2)

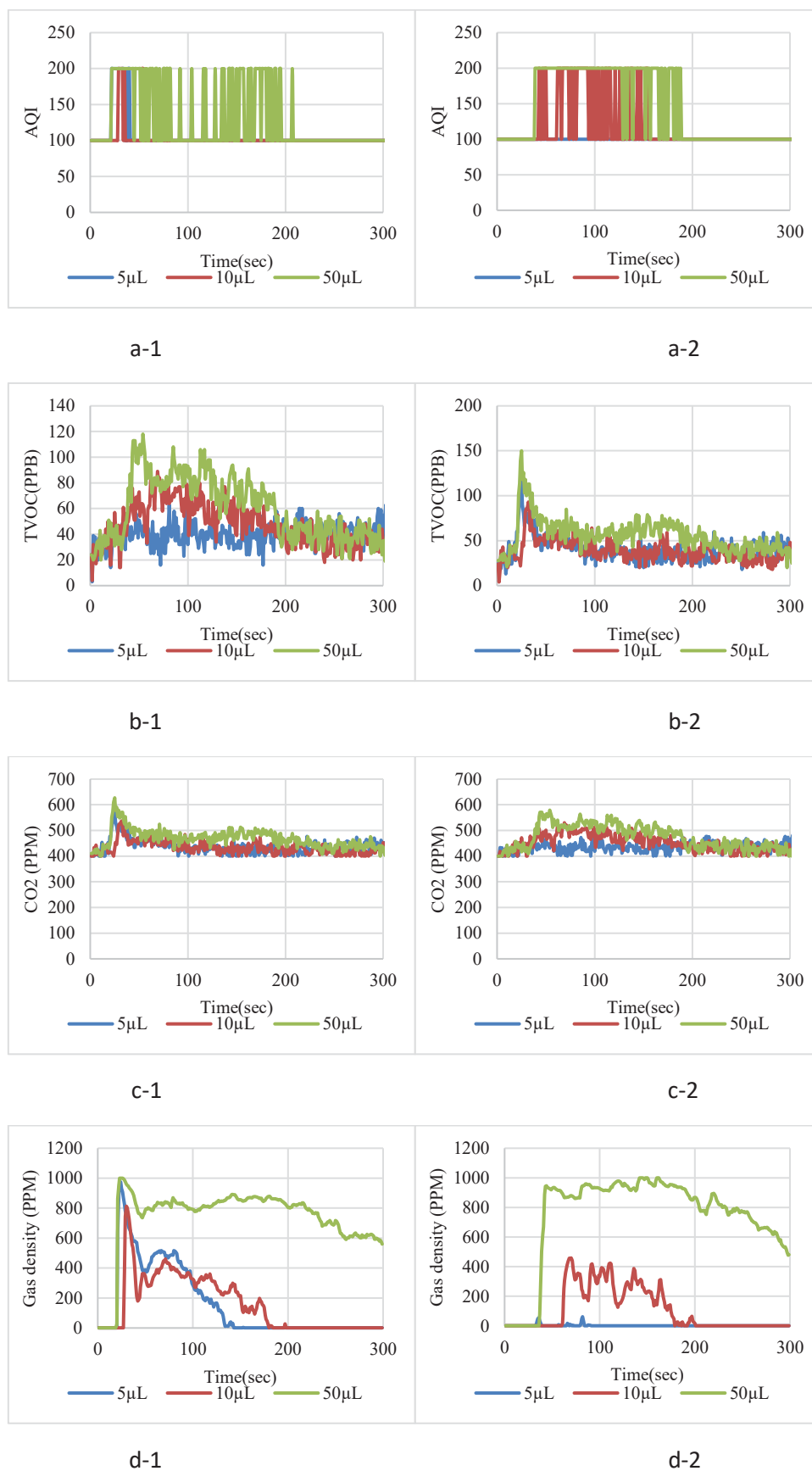


Fig. 13: Formic Acid ( $\text{CH}_2\text{O}_2$ ) response for ENS160 (a, b, c) and TED110 (d) at 40 cm (1) and 100 cm (2)

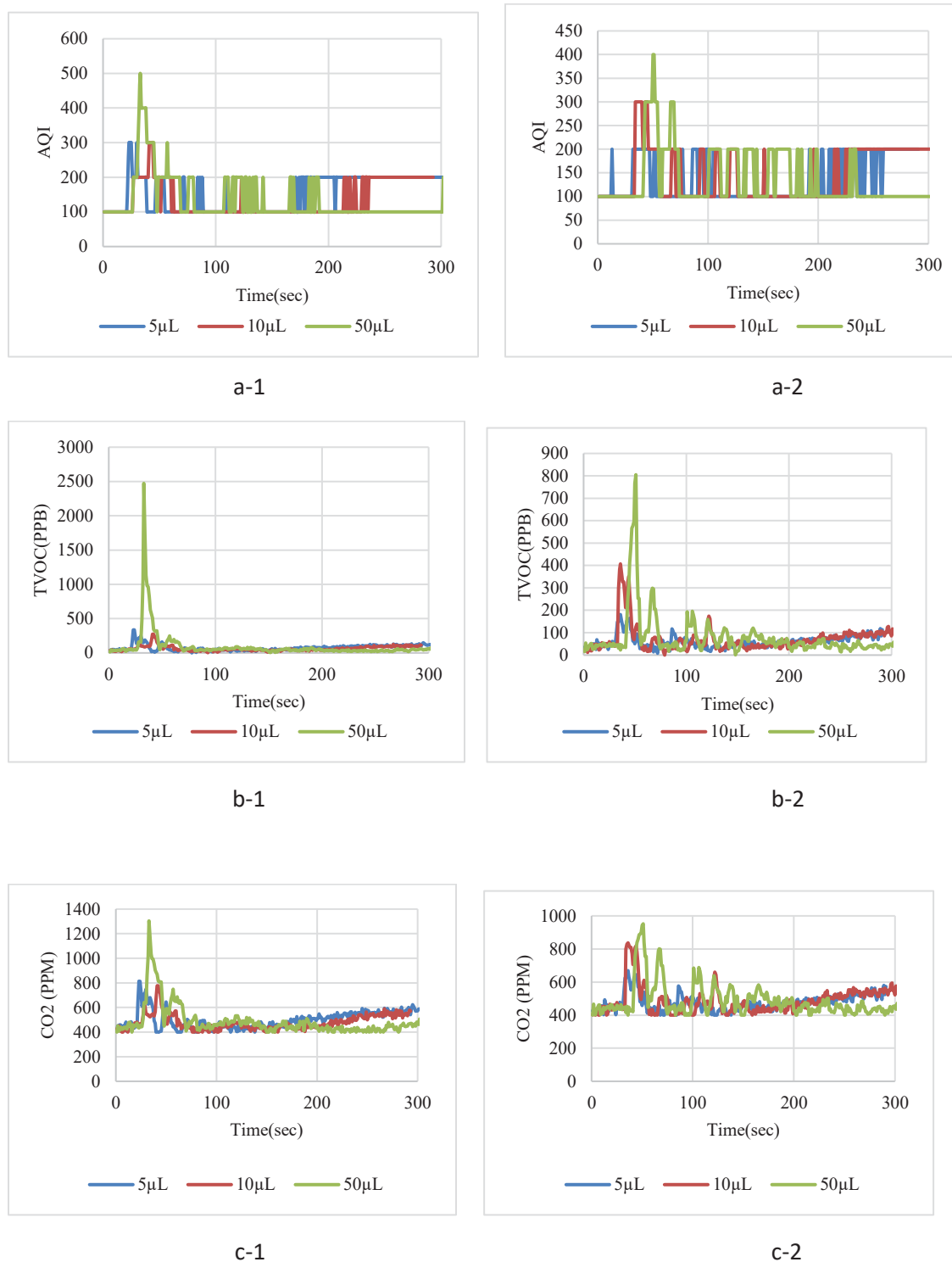


Fig. 14: Heptane ( $C_7H_{16}$ ) response for ENS160 (a, b, c) at 40 cm (1) and 100 cm (2)

ENS160 hexane ( $C_6H_{14}$ ) has an excellent response from  $>50\mu L$  for 40 cm for all the required parameters. The AQI, TVOC, and  $CO_2$  responded well with  $>50\mu L$  at 40 cm with a low response at 100 cm. In contrast to the MOX sensor principle, ENS160 can detect hexane but shows low sensitivity, effectiveness, and detection level. Fig. 15 depicts the hexane responses for ENS160. The TED110 gas sensor (gas density) hexane has not responded in any amount.

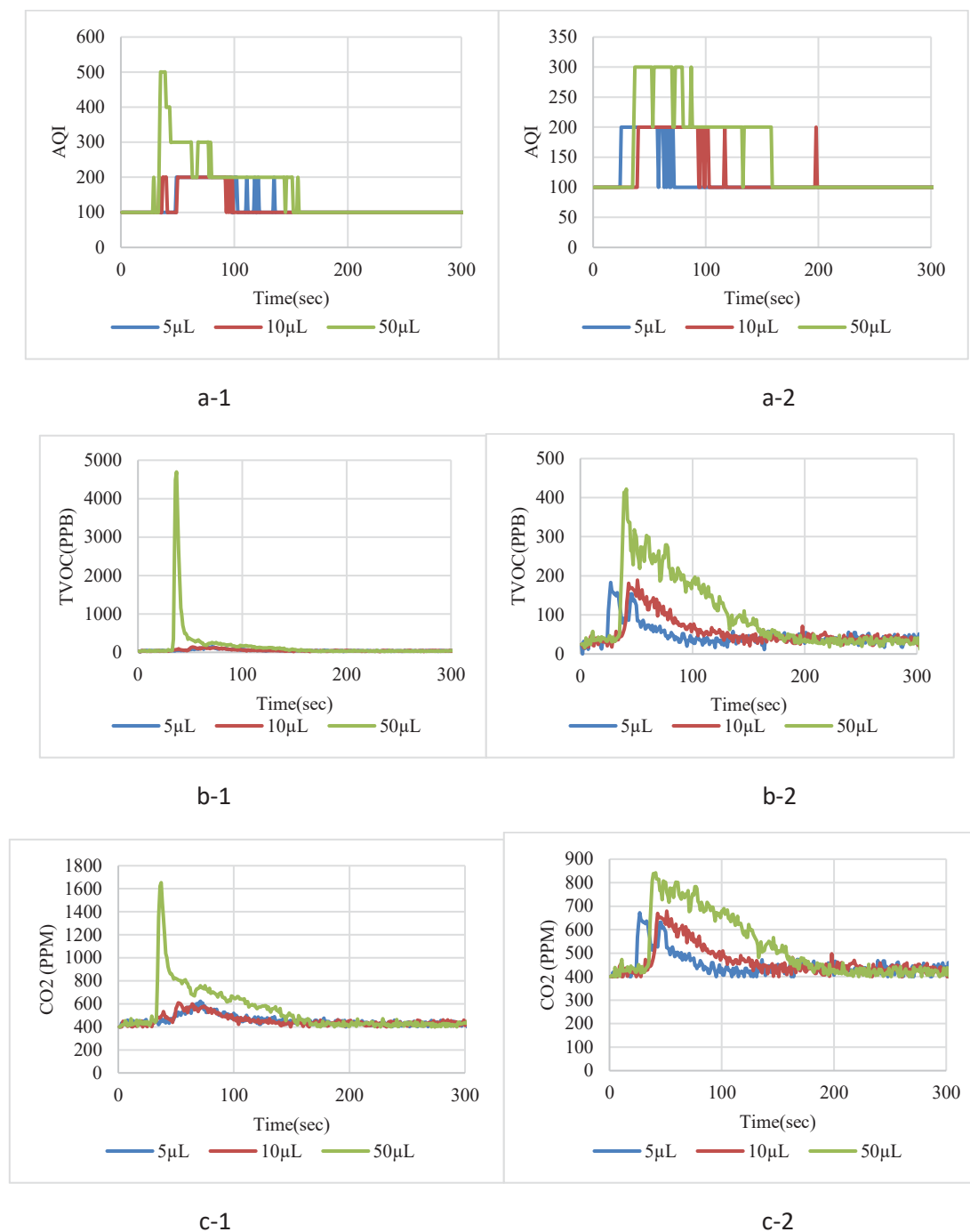


Fig. 15: Hexane ( $C_6H_{14}$ ) response for ENS160 (a, b, c) at 40 cm (1) & 100 cm (2).

For all the required parameters, isopropanol ( $C_3H_8O$ ) shows an excellent response with the ENS 160 gas sensor from the sample amounts at  $>5\mu L$ . The TED110 gas sensor (gas density) at a 40 cm distance has an excellent response with isopropanol from  $>10\mu L$ . Based on the MOX gas sensor concepts, the ENS160 and TED110 gas sensors effectively detect isopropanol under varying sample amounts and distances. Further investigations specifically for TED110 are essential to optimize sensor performance and understand the extent of their accuracy and reliability in real-world environments. Fig. 16 displays the isopropanol sensor responses for both sensors.

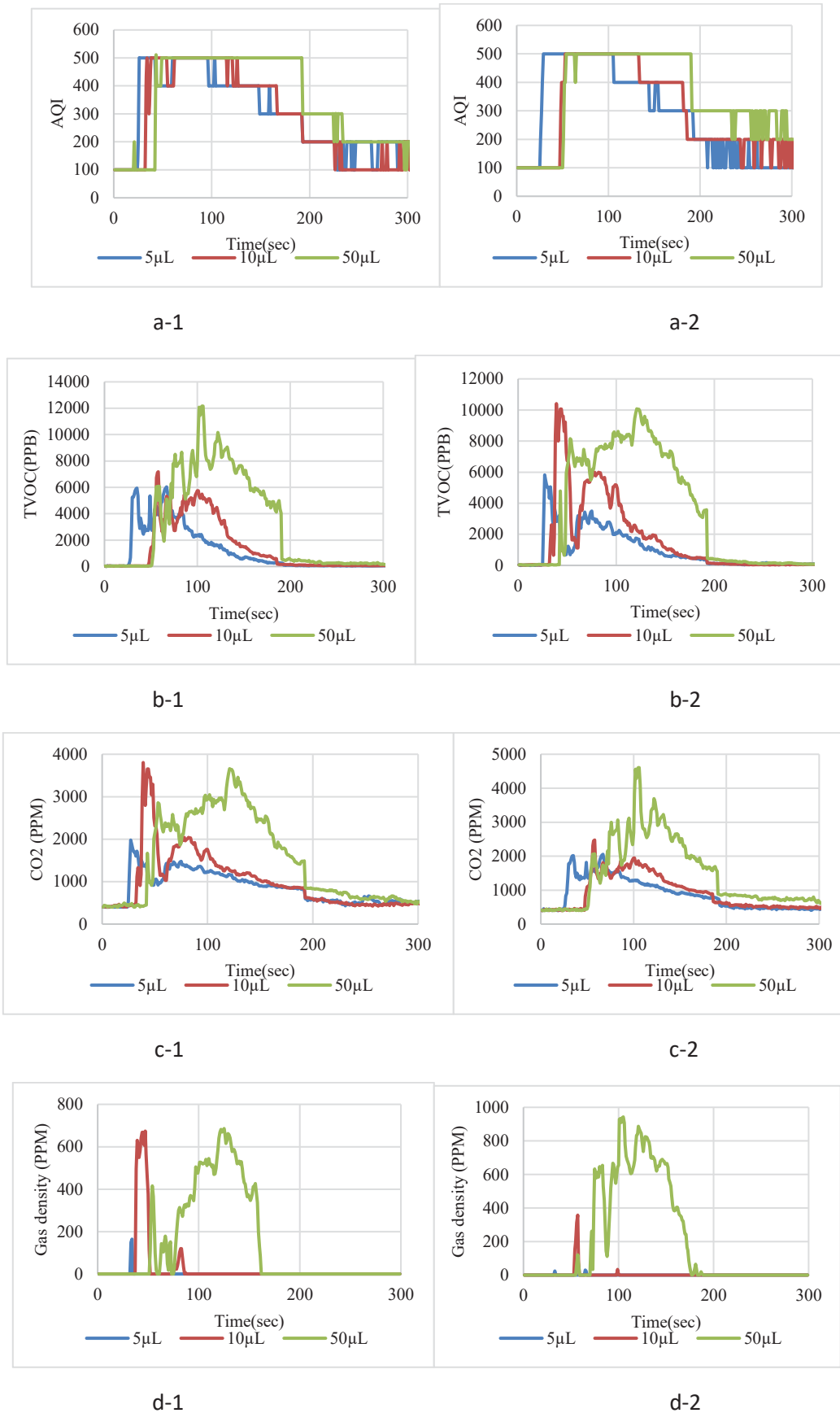


Fig. 16: Isopropanol ( $C_3H_8O$ ) for ENS160 (a, b, c) and TED110 (Gas density) (d) at 40 cm (1) and 100 cm (2)

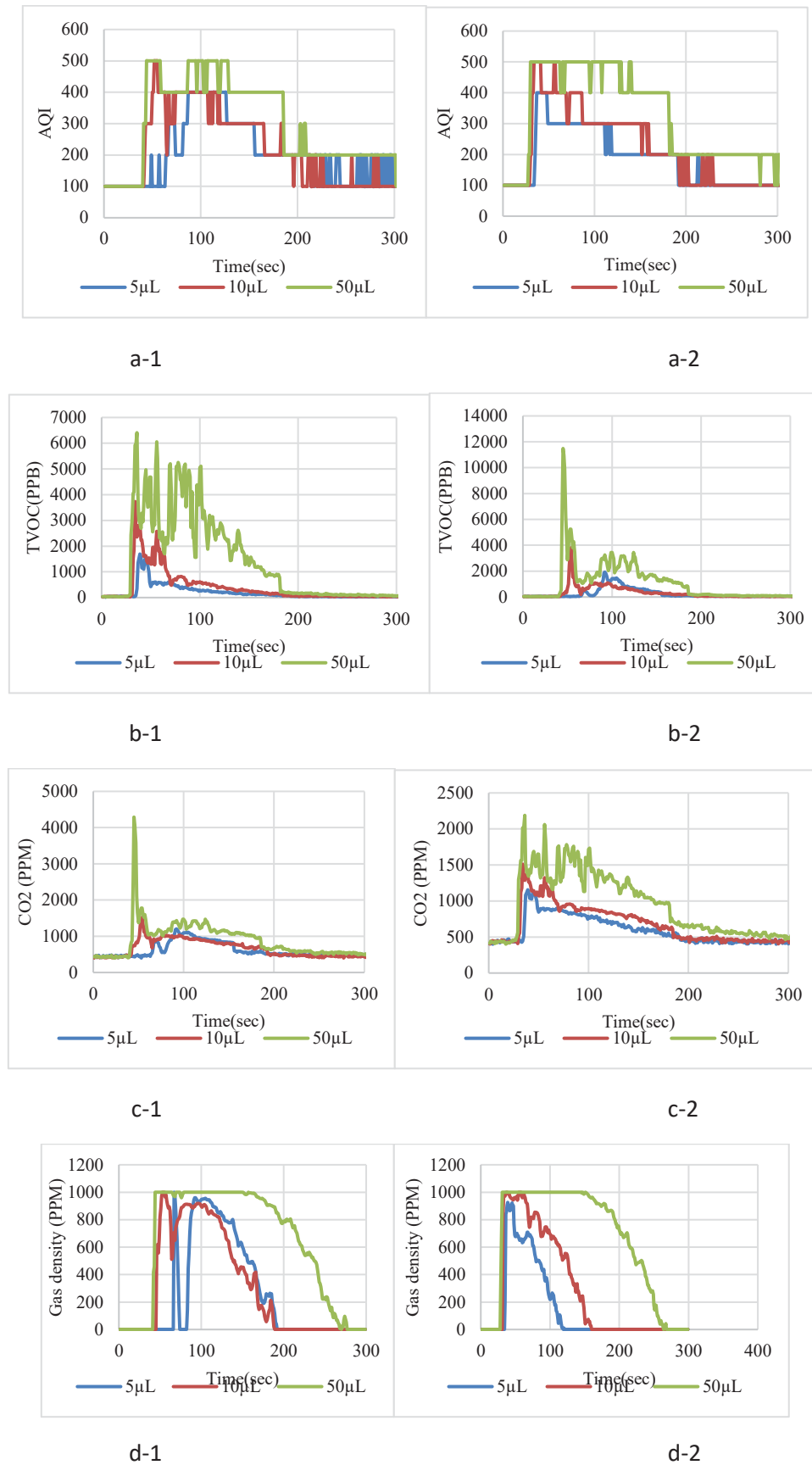


Fig. 17: Methanol (CH<sub>3</sub>OH) response for ENS160 (a, b, c) and TED110 (d) at 40 cm (1) & 100 cm (2)



Fig. 18: Toluene ( $C_7H_8$ ) response for ENS160 (a, b, c) at 40 cm (1) & 100 cm (2)

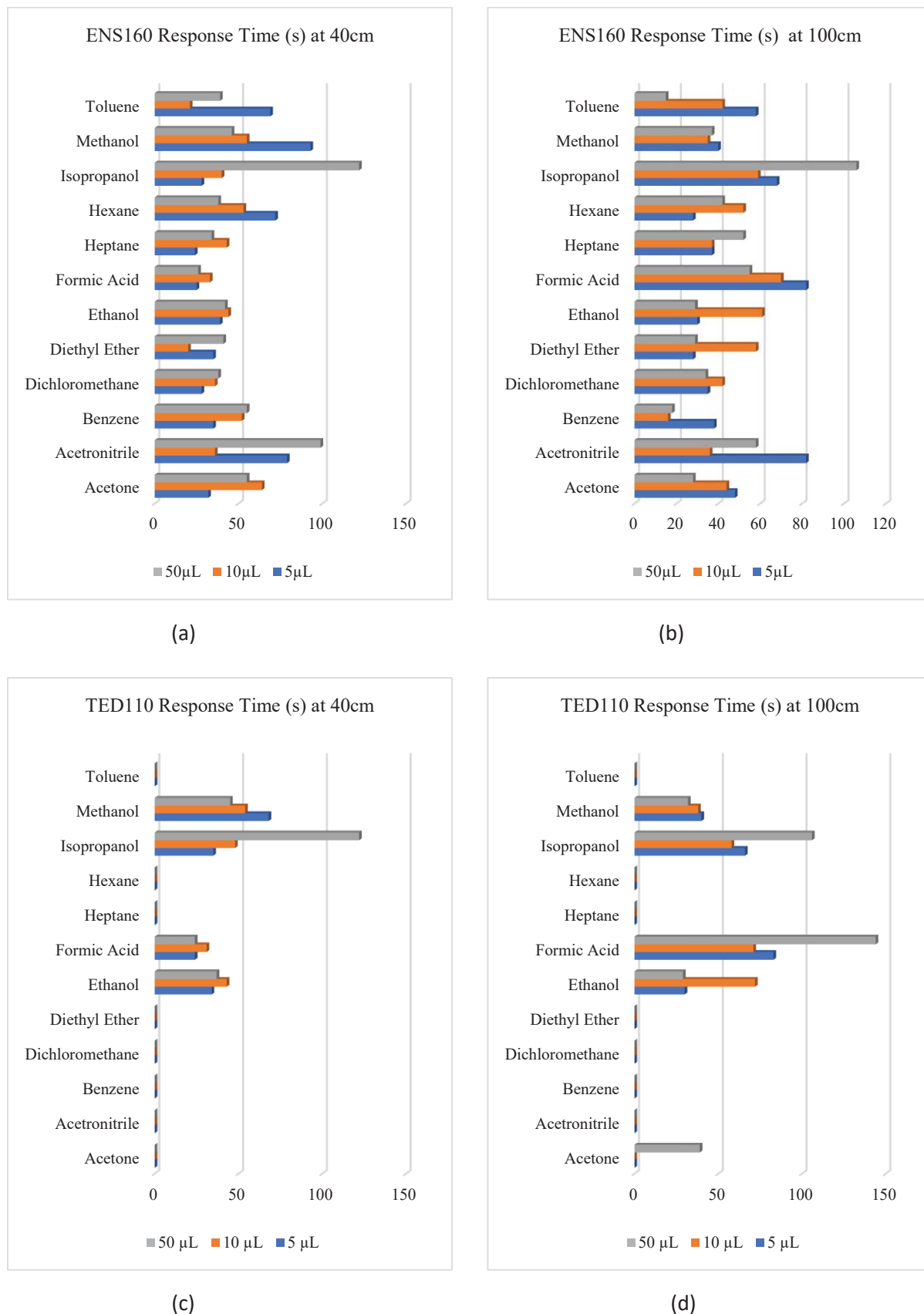


Fig. 19: ENS160 maximum Response time (s) at 40 cm (a) and 100 cm (b), TED110 maximum Gas Density Response Time(s) at 40 cm (c) and 100 cm (d).

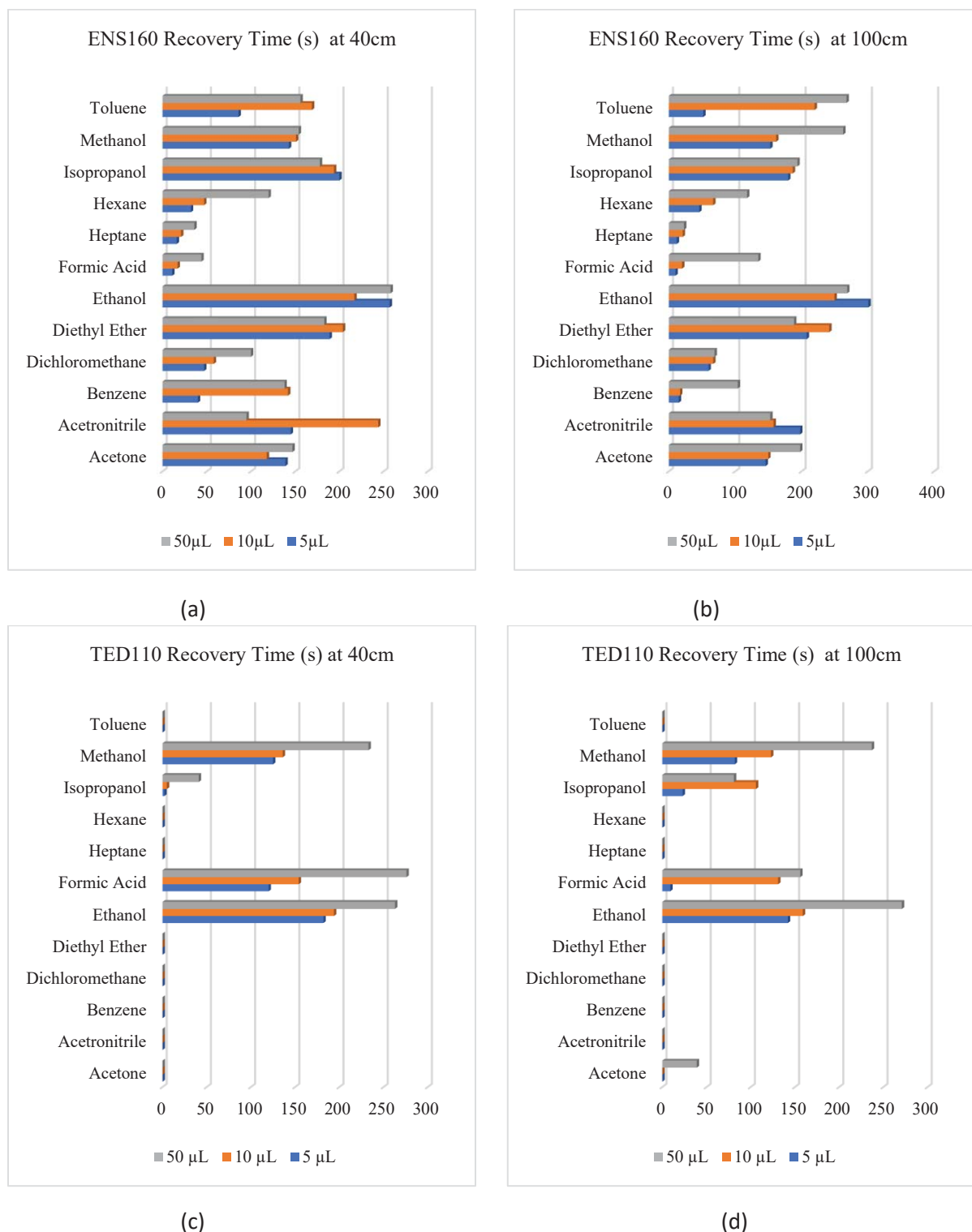


Fig. 20: ENS160 maximum Recovery time (s) at 40 cm (a) and 100 cm (b); TED110 maximum Gas Density Recovery Time(s) at 40 cm (c) and 100 cm (d).

The ENS160 shows an excellent response for methanol ( $\text{CH}_3\text{OH}$ ) with gas samples amounting to  $>5\mu\text{L}$ . All sample compounds, such as AQI, TVOC, and  $\text{CO}_2$ , show the highest response in the desired parameters. The TED110 gas sensor (gas density) for ethanol ( $\text{C}_2\text{H}_6\text{O}$ ) at 40 cm and 100 cm for amounts at  $>5\mu\text{L}$  has a response. Both sensors' excellent response to methanol based on the MOX sensor concept and significant performance among all sample

compounds make them valuable for gas detection applications. Fig. 17 depicts both sensor responses for methanol.

Toluene ( $C_7H_8$ ) exhibits an excellent response with a sample amount of  $10\mu L$  for all necessary parameters for ENS160, as illustrated in Fig. 18. With a quantity of  $>10\mu L$ , the AQI shows an excellent response at 40 cm sensor node distances. The reaction rate of TVOC and  $CO_2$  increases the high volumes of gases. Above all, ENS160 has a low detection level for toluene due to no oxygen compounds, which need further investigation to improve the accuracy. The TED110 gas sensor (Gas density) does not react to amounts of toluene at 40 cm and 100 cm.

The response time (s) is the time it takes for the sensor output signal to reach 90% of its highest measured value from its initial settled condition; some strong gas with more sensitivity has quick response time, e.g., ethanol, methanol. Both sensors require a long response time (s) for isopropanol to reach its maximum point compared to other samples' response times (s); ethanol shows a rapid response (it requires less time to get its maximum response point). This indicates ENS160 has high sensitivity and efficiency in detecting most vapors; has a quick response for most of the strong gases. Improving response times can enhance gas sensors' effectiveness and accuracy to provide real-time and accurate measurements in environments. Fig. 19 presents both sensor's response times (s) for the different distances and specific amounts of the samples.

Correspondingly, the recovery time (s) is when the sensor response signal returns to its initial condition from its maximum measured value. Compared to other experimental gas samples' recovery time (s), the ENS160 gas sensing of ethanol needs longer to recover to its initial state. In contrast, methanol causes the longest recovery for the TED110 sensor. Gas sensors can exhibit varying response and recovery times based on the sensitivity to the gases. Some gases have rapid responses and longer recovery times based on their characteristics. By improving recovery times, gas sensors can become more responsive and reliable, making them better suited for safety monitoring in laboratory infrastructure. Fig. 20 displays both sensor's recovery times (s) for the different distances and specific amounts of the samples.

The data overview for all tested materials that was acquired from the two sensors and their response graphical presentation is listed below-

- ENS 160 successfully detects the AQI, TVOCs, and  $CO_2$  60 test out of 72 Tests.
- ENS 160 AQI, TVOCs, and  $CO_2$  detection rate is around 83%.
- TED110 successfully detects the Gas Density 24 test out of 72 Tests.
- TED110 overall detection rate is 33%.

The concentration of the exposed analytes directly relates to the change in sensor resistance. On the surface of MOX, oxygen is adsorbed at high temperatures. The charge carrier concentration changes due to the adsorbed oxygen capturing electrons from the conduction band, which impacts the resistance of the MOX sensing Sensor layer. So, the ENS160 gas sensor strongly reacts to oxygen containing compounds such as acetone ( $C_3H_6O$ ), diethyl ether ( $C_4H_{10}O$ ), isopropanol ( $C_3H_8O$ ), methanol ( $CH_3OH$ ), and ethanol ( $C_2H_6O$ ): Only formic acid ( $CH_2O_2$ ) has no response. Its response is excellent in specific amounts and sensor node distances; it maintains a good sensitivity, selectivity, and detection limit. The ENS 160 reaction

for the other compounds depends on the specific amounts of gas samples and sensor node distances. The reaction changes as the sample concentration or sensor node distances vary; a higher sample rate and a lower sensor node distance achieve a good response. The TED110 responds with the strongest gases, such as isopropanol (C<sub>3</sub>H<sub>8</sub>O), methanol (CH<sub>3</sub>OH), ethanol (C<sub>2</sub>H<sub>6</sub>O), and formic acid (CH<sub>2</sub>O<sub>2</sub>), where all the gases contain oxygen. According to the datasheet [34], the TED110 can detect methene and toluene. However, these gases don't contain oxygen. However, in this experiment, the sensor failed to detect these gases. The reason for this lack of detection was likely sensor contamination during the electronics assembly or incorrect sensor purchase, e.g., some aging effect.

Table 5: Comparison of BME88, SGP 40, SGP 30, ENS 160, TED 110

Samples	BME88	SGP 40	SGP 30	ENS 160	TED 110
Acetone	—	Good response ≥ 10μL	Good response ≥ 10μL	Strong response ≥ 5μL	No response
Diethyl ether	—	Good response ≥ 50μL	Weak response < 100μL	Strong response ≥ 5μL	No response
Isopropanol	—	Good response ≥ 10μL	Weak response < 100μL	Strong response ≥ 5μL	Strong response ≥ 5μL
Methanol	—	Good response ≥ 2μL	Good response ≥ 100μL	Strong response ≥ 5μL	Strong response ≥ 5μL
Toluene	—	Good response ≥ 100μL	Good response ≥ 100μL	Strong response ≥ 50μL	No response
Ethanol	Strong response ≥ 10μL	Good response ≥ 2μL	Good response ≥ 5μL	Strong response ≥ 5μL	Strong response ≥ 5μL
Hexane	Weak response	Weak response < 100μL	Weak response < 100μL	Strong response ≥ 10μL	No response
Acetonitrile	Weak response	Weak response < 100μL	Good response ≥ 10μL	Good response ≥ 5μL	No response
Benzene	-	Good response ≥ 100μL	Good response ≥ 100μL	Good response > 5μL	No response
Dichloromethane	Weak response	Good response ≥ 100μL	Good response ≥ 100μL	Weak response < 50μL	No response
Formic Acid	Strong response ≥ 10μL	Good response ≥ 2μL	Good response ≥ 2μL	Weak response < 50μL	Strong response ≥ 5μL
Heptane	-	Good response ≥ 5μL	Weak response < 100μL	Weak response < 50μL	No response

In [20], Neubert et al. used the BME 688 and SPG30 gas sensors in their project. Those sensors were tested with various TVOCs (ethanol, formic acid, acetonitrile, dichloromethane, and hexane). The studies employed two distinct heights, 25 and 40 cm, and four different

quantities of each component. Dichloromethane, acetonitrile, and hexane were chosen in quantities of 1, 5, 10, and 20mL, respectively, while ethanol and formic acid were selected in quantities of 10, 100, 500, and 1000 $\mu$ L. Both sensors produced excellent results with ethanol and formic acid but had insufficient responses to acetonitrile, dichloromethane, and hexane.

Furthermore, in [7], Al-Okby et al. tested SPG40 and SPG30 with 12 samples of VOC. This experiment tested VOC in two locations, one directly 1 m below the sensor. The sensor node was moved one meter horizontally from the bottom for the second position. The volume was raised according to the sensor's reaction. The quantities used were 2 $\mu$ L, 5 $\mu$ L, 10 $\mu$ L, 50 $\mu$ L, and 100 $\mu$ L. The test volume was not increased once the lowest detectable volume for a particular position and distance was determined to avoid sensory overload. The evolution of the sensor based on TVOC (ppm) and AQI is the SPG30 that has an inadequate response for diethyl ether, isopropanol, hexane, and heptane. All other VOCs have a good reaction with the SPG30 gas sensor. Besides, the SPG 40 has a weak hexane and acetonitrile response among the 12 VOC samples. This project used the ENS 160 sensor, showing a weak response signal in dichloromethane and formic acid. All other gas samples with this sensor have good responses. Finally, the TED110 had an excellent reaction for isopropanol, ethanol, methanol, and formic acid. Almost all other eight gas samples did not respond. The gas sensor comparison table from the previous project and the current experiment are shown in Table 5.

The comparison results with other sensors (BME688, SGP 40, and SGP 30) show that the ENS 160 has an excellent response, making it suitable for laboratory gas detection. On the other hand, the TED110 shows inadequate response compared to all other gas sensors, possibly due to contamination or incorrect sensor selection. Without additional testing and improvement, this sensor may not be appropriate for the project's extension. Since this experiment was conducted in a real laboratory, measures were taken to avoid destructive factors such as traditional chemical hood air drafts, air conditioning, opening doors, and human presence, which can impact measurements due to cosmetics and human body exudation. Above all, for further accuracy improvement and avoiding external factors, different calibration methods can be utilized, for instance, reference measurements, and dynamic calibration, to adapt to changing conditions and minimize the impact of external factors like air drafts and human presence. Additionally, implementing signal processing techniques, such as noise filtering and pattern recognition algorithms, can improve the system's performance by accurately isolating gas-specific signals from background noise. Regular maintenance and sensor calibration is crucial to maintaining optimal performance and sensitivity. Lastly, incorporating machine learning algorithms and sensor fusion techniques can enhance the system's effectiveness and gas detectable limit by intelligently analyzing and combining data from multiple sensors to improve accuracy and reliability.

#### 4. CONCLUSION

This project aims to implement a mobile gas sensing system to detect hazardous and toxic gases/chemical vapors. We investigated the performance of two novel gas sensors, ENS160 and TED110, using multiple parameters (AQI, TVOC, CO<sub>2</sub>, and Gas Density). In the future, the plan is to extend this project into gas detection with alarming systems; for that reason, it also helps to find efficient parameters among all parameters (AQI, TVOC, CO<sub>2</sub>, and Gas Density). Overall, from the data visualization and the data analysis, both sensors have shown that they are generally suitable for detecting VOC leakages in laboratories. The ENS 160 sensor

has a low sensing rate for dichloromethane and formic acid. All other experimented samples responded very well; it has a detection rate of 60 out of 72 samples; in the three parameters, such as AQI, TVOCs, and CO<sub>2</sub>, it has an 83% response rate. In contrast, the TED110 has an excellent reaction for isopropanol, ethanol, methanol, and formic acid (the other eight experimental samples have no response), responded to 24 out of 72 tests, and the detection rate was 33%. Therefore, both sensors must do more tests with higher sample amounts. This system can be adapted to a flexible IoT platform; the required modules, such as IoT wireless communication modules and portable power supplies, can be connected and used independently by connecting to a computer. The drawback of this developed system is that the sensor node is comparably bigger than the divided processing units, resulting in the system consuming more energy. In terms of measured parameters and functional qualities, this mobile gas sensing system can be adapted to various application scenarios, for example, moving objects such as robots and trolleys. The TED110 gas sensor requires more investigation to improve its accuracy, sensor data calibration, and more accurate data conversion. Furthermore, machine learning applications can distinguish different VOCs to precisely identify the natural hazard and sensor calibration, as well as real-time data analysis and visualization. This mobile sensing can be used in laboratory robots or moveable equipment so that in the future, the indoor localization sensor can be implemented to record the position of detection of the robots or movable objects, for example, roller carriages with laboratory equipment, which need to be monitored for gases and location.

## ACKNOWLEDGEMENT

This research was supported by the Synergy Project ADAM (Autonomous Discovery of Advanced Materials) funded by the European Research Council (grant number 856405).

## REFERENCES

- [1] O. US EPA. (2016). Technical Air Pollution Resources. Retrieved from <https://www.epa.gov/technical-air-pollution-resources> (Accessed: October 23, 2021).
- [2] Pandey, P., & Yadav, R. (2018). A Review on Volatile Organic Compounds (VOCs) as Environmental Pollutants: Fate and Distribution. *Int. J. Plant Environ.*, 4. doi: 10.18811/ijpen.v4i02.2.
- [3] Ghorani-Azam, A., Riahi-Zanjani, B., & Balali-Mood, M. (2016). Effects of air pollution on human health and practical measures for prevention in Iran. *J. Res. Med. Sci. Off. J. Isfahan Univ. Med. Sci.*, 21, 65. doi: 10.4103/1735-1995.189646.
- [4] Hou, L., Li, Y., Qian, X., Shu, C.-M., Yuan, M., & Duanmu, W. (2021). Large-scale experimental investigation of the effects of gas explosions in underdrains. *J. Saf. Sci. Resil.*, 2(2), 90–99. doi: 10.1016/j.jnlssr.2021.03.001.
- [5] Al-Okby, M. F. R., Neubert, S., Roddelkopf, T., & Thurow, K. (2021). Mobile Detection and Alarming Systems for Hazardous Gases and Volatile Chemicals in Laboratories and Industrial Locations. *Sensors*, 21(23). doi: 10.3390/s21238128.
- [6] Al-Okby, M. F. R., Roddelkopf, T., Fleischer, H., & Thurow, K. (2022). Evaluating a Novel Gas Sensor for Ambient Monitoring in Automated Life Science Laboratories. *Sensors*, 22(21). doi: 10.3390/s22218161.
- [7] Al-Okby, M. F. R., Neubert, S., Roddelkopf, T., Fleischer, H., & Thurow, K. (2022). Evaluating of IAQ-Index and TVOC Parameter-Based Sensors for Hazardous Gases Detection and Alarming Systems. *Sensors*, 22(4). doi: 10.3390/s22041473.

- [8] Ten health issues WHO will tackle this year. <https://www.who.int/news-room/spotlight/ten-threats-to-global-health-in-2019> (Accessed: October 23, 2021).
- [9] Hunter, G. W., et al. (2020). Editors' Choice - Critical Review - A Critical Review of Solid State Gas Sensors. *J. Electrochem. Soc.*, 167(3). doi: 10.1149/1945-7111/ab729c.
- [10] Liu, X., Cheng, S., Liu, H., Hu, S., Zhang, D., & Ning, H. (2012). A Survey on Gas Sensing Technology. *Sensors*, 12(7), 9635–9665. doi: 10.3390/s120709635.
- [11] Xu, L., et al. (2022, July). Hybrid Gas Sensor Array to Identify and Quantify Low-Concentration VOCs Mixtures Commonly Found in Chemical Industrial Parks. *IEEE Sens. J.*, 22(13), 13434–13441. doi: 10.1109/JSEN.2022.3176049.
- [12] Examples of Common Laboratory Chemicals and their Hazard Class. <https://orf.od.nih.gov/EnvironmentalProtection/WasteDisposal/Pages/Examples+of+Common+Laboratory+Chemicals+and+their+Hazard+Class.aspx> (Accessed: July 09, 2022).
- [13] Wyatt, P. (2021). Long-Term Effects of Severe Carbon Monoxide Poisoning. Wyatt Law Firm, PLLC. <https://www.wyattlawfirm.com/long-term-effects-of-severe-carbon-monoxide-poisoning/> (Accessed: July 06, 2022).
- [14] Chrisodgen. (2019). CO2 affects human health at lower levels than previously thought. *AirQualityNews*. <https://airqualitynews.com/2019/07/10/co2-affects-human-health-at-lower-levels-than-previously-thought/> (Accessed: July 06, 2022).
- [15] Shiwen Huang and Haomin Li and Mingrui Wang and Yaoyao Qian and Kyle Steenland and William Michael Caudle and Yang Liu and Jeremy Sarnat and Stefania Papatheodorou and Liuhua Shi (2021). Long-term exposure to nitrogen dioxide and mortality: A systematic review and meta-analysis. *Sci. Total Environ.*, 776, 145968. doi: 10.1016/j.scitotenv.2021.145968.
- [16] Cheng, Shumin and Chang-Chien, Guo-Ping and Huang, Qianli and Zhang, Yu-Bo and Yan, Ping and Zhang, Jiale and Wang, Yujing and Zhang, Daqing and Teng, Guopeng (2019). Global Research Trends in Health Effects of Volatile Organic Compounds during the Last 16 Years: A Bibliometric Analysis. *Aerosol Air Qual. Res.*, 19(8), 1834–1843. doi: 10.4209/aaqr.2019.06.0327.
- [17] Clifton, J. (2017, November 03). What are the Uses of Acetone? | The Chemistry Blog. ReAgent Chemicals. <https://www.chemicals.co.uk/blog/what-are-the-uses-of-acetone> (Accessed: July 06, 2022).
- [18] Liu, X., Cheng, S., Liu, H., Hu, S., Zhang, D., & Ning, H. (2012). A Survey on Gas Sensing Technology. *Sensors*, 12(7). doi: 10.3390/s120709635.
- [19] Dhall, S., Mehta, B. R., Tyagi, A. K., & Sood, K. (2021). A review on environmental gas sensors: Materials and technologies. *Sens. Int.*, 2, 100116. doi: 10.1016/j.sintl.2021.100116.
- [20] Neubert, S., Roddelkopf, T., Al-Okby, M. F. R., Junginger, S., & Thurow, K. (2021). Flexible IoT Gas Sensor Node for Automated Life Science Environments Using Stationary and Mobile Robots. *Sensors*, 21(21). doi: 10.3390/s21217347.
- [21] Al-Okby, M. F. R., Neubert, S., Roddelkopf, T., & Thurow, K. (2021). Integration and Testing of Novel MOX Gas Sensors for IoT-based Indoor Air Quality Monitoring. In 2021 IEEE 21st International Symposium on Computational Intelligence and Informatics (CINTI), pp. 000173–000180. doi: 10.1109/CINTI53070.2021.9668462.
- [22] Al-Okby, M. F. R., Roddelkopf, T., Fleischer, H., & Thurow, K. (2022). Robot-based Environmental Monitoring in Automated Life Science Laboratories. In 2022 IEEE 10th Jubilee International Conference on Computational Cybernetics and Cyber-Medical Systems (ICCC), pp. 000395–000400. doi: 10.1109/ICCC202255925.2022.9922865.

- [23] Al-Okby, M. F. R., & Al-Barrak, S. S. (2020). New Approach for Fall Detection System Using Embedded Technology. In 2020 IEEE 24th International Conference on Intelligent Engineering Systems (INES), pp. 209–214. doi: 10.1109/INES49302.2020.9147170.
- [24] Gupta, K., Krishna, G. G., & Anjali, T. (2020). An IoT based System for Domestic Air Quality Monitoring and Cooking Gas Leak Detection for a Safer Home. In 2020 International Conference on Communication and Signal Processing (ICCSP), pp. 0705–0709. doi: 10.1109/ICCSP48568.2020.9182051.
- [25] Das, T., Sut, D. J., Gupta, V., Gohain, L., Kakoty, P., & Kakoty, N. M. (2020). A Mobile Robot for Hazardous Gas Sensing. In 2020 International Conference on Computational Performance Evaluation (ComPE), pp. 062–066. doi: 10.1109/ComPE49325.2020.9200082.
- [26] Joshna, V., Kashyap, M., Ananya, V., & Manitha, P. V. (2019). Fully Autonomous Robot to Detect and Degasify Hazardous Gas after Flood Disaster. In 2019 2nd International Conference on Power and Embedded Drive Control (ICPEDC), pp. 134–139. doi: 10.1109/ICPEDC47771.2019.9036703.
- [27] Amin, A. B., Patel, H. P., Vaghela, S. P., & Patel, R. R. (2019). IOT Based Vehicle Anti-Collision And Pollution Control System. In 2019 3rd International conference on Electronics, Communication and Aerospace Technology (ICECA), pp. 108–110. doi: 10.1109/ICECA.2019.8822059.
- [28] Waworundeng, J. M. S., Kalalo, M. A. T., & Lokollo, D. P. Y. (2020). A Prototype of Indoor Hazard Detection System using Sensors and IoT. In 2020 2nd International Conference on Cybernetics and Intelligent System (ICORIS), pp. 1–6. doi: 10.1109/ICORIS50180.2020.9320809.
- [29] Wojnowski, W., Majchrzak, T., Dymerski, T., Gębicki, J., & Namieśnik, J. (2017). Portable Electronic Nose Based on Electrochemical Sensors for Food Quality Assessment. *Sensors*, 17(12), 2715. doi: 10.3390/s17122715.
- [30] Somov, A., Baranov, A., & Spirjakin, D. (2014). A wireless sensor–actuator system for hazardous gases detection and control. *Sens. Actuators Phys.*, 210, 157–164. doi: 10.1016/j.sna.2014.02.025.
- [31] Esfahani, S., Tiele, A., Agbroko, S. O., & Covington, J. A. (2020, December). Development of a Tuneable NDIR Optical Electronic Nose. *Sensors*, 20(23), 6875. doi: 10.3390/s20236875.
- [32] Gong, S., et al. (2014, October). Design and Experiment of Fumigant Gas Trace Detection System Based on Photoionization. *Adv. Mater. Res.*, 1037, 129–133. doi: 10.4028/www.scientific.net/AMR.1037.129.
- [33] SC-001224-DS-7-ENS160-Datasheet.pdf. <https://www.sciosense.com/wp-content/uploads/documents/SC-001224-DS-7-ENS160-Datasheet.pdf> (Accessed: October 15, 2022).
- [34] TED1X-MEMS-Gas-Sensor-data-1909.pdf. <https://www.eoc-inc.com/wp-content/uploads/TED1X-MEMS-Gas-Sensor-data-1909.pdf> (Accessed: July 17, 2023).
- [35] EPAs List of Volatile Organic Compounds in order of toxicity. (2020, May 18). Define Instruments. <https://defineinstruments.com/blog/epas-list-of-volatile-organic-compounds-in-order-of-toxicity/> (Accessed: July 15, 2023).
- [36] 6 Hidden Toxins Around Your Home That Can Cause Cancer. (2018). <https://learn.kaiterra.com/en/air-academy/6-hidden-toxins-that-can-cause-cancer> (Accessed: July 15, 2023).
- [37] O. US EPA. (2014). Volatile Organic Compounds’ Impact on Indoor Air Quality. <https://www.epa.gov/indoor-air-quality-iaq/volatile-organic-compounds-impact-indoor-air-quality> (Accessed: July 15, 2023).

- [38] Spinelle, L., Gerboles, M., Kok, G., Persijn, S., & Sauerwald, T. (2017). Review of Portable and Low-Cost Sensors for the Ambient Air Monitoring of Benzene and Other Volatile Organic Compounds. *Sensors*, 17(7). doi: 10.3390/s17071520.

Table 6: Table of nomenclature

<b>Symbol/Abbreviation</b>	<b>Description</b>
MOX	metal oxide semiconductor
VOC	volatile organic compounds
TVOC	total volatile organic compounds
AQI	air quality index
PPM	Parts per Million
PPB	Parts per billion
MEMS	Micro-Electro-Mechanical System
MCU	Microcontroller unit
PCB	Printed circuit board.
I2C	Inter-Integrated Circuit
IDE	Integrated Development Environment

## SPECTROSCOPY DATA CALIBRATION USING STACKED ENSEMBLE MACHINE LEARNING

MAHMUD IWAN SOLIHIN<sup>1\*</sup>, CHAN JIN YUAN<sup>1</sup>, WAN SIU HONG<sup>1</sup>,  
LIEW PHING PUT<sup>2</sup>, CHUN KIT ANG<sup>1</sup>, Wafa HOSSAIN<sup>1</sup> AND AFFIANI MACHMUDAH<sup>3</sup>

<sup>1</sup>Faculty of Engineering, Technology and Built Environment, UCSI University, Malaysia

<sup>2</sup>Faculty of Applied Sciences, UCSI University, Malaysia

<sup>3</sup>Research Centre for Hydrodynamics Technology, National Research and Innovation Agency (BRIN), Surabaya, Indonesia

\*Corresponding author: mahmudis@ucsiuniversity.edu.my

(Received: 20 March 2022; Accepted: 4 June 2023; Published on-line: 1 January 2024)

**ABSTRACT:** Near infrared spectroscopy (NIRS) is a widely used analytical technique for non-destructive analysis of various materials including food fraud detection. However, the accurate calibration of NIRS data can be challenging due to the complexity of the underlying relationships between the spectral data and the target variables of interest. Ensemble learning, which combines multiple models to make predictions, has been shown to improve the accuracy and robustness of predictive models in various domains. This paper proposes stacking ensemble machine learning (SEML) for calibration of NIRS data with two levels of learning involved. Eight (8) spectroscopy datasets from public repository and previously published works by the authors are used as the case study. The model well generalized the data in the respective regression tasks with  $R^2$  of at least  $\approx 0.8$  in the test samples and in the respective classification tasks with classification accuracy (CA) of at least  $\approx 0.8$  also. In addition, the proposed SEML can improve, or at least reach par with, the accuracy of individual base learners in both train and test samples for all cases of regression and classification datasets. It shows superior performance in test samples for both regression and classification datasets with respectively  $R^2$  ranging from 0.86 to nearly 1 and CA ranging from 0.89 to 1.

**ABSTRAK:** Spektroskopi inframerah dekat (NIRS) adalah teknik analitikal yang banyak digunakan bagi analisa pelbagai bahan tanpa merosakkan bahan termasuk ketika mengesan penipuan makanan. Walau bagaimanapun, kalibrasi yang tepat bagi data NIRS adalah sangat mencabar kerana hubungan antara data spektral dan pemboleh ubah sasaran yang ingin dikaji bersifat kompleks. Gabungan pembelajaran (*Ensemble learning*), iaitu gabungan pelbagai model bagi membuat prediksi, telah terbukti dapat meningkatkan ketepatan dan kecekapan model prediksi dalam pelbagai bentuk. Kajian ini mencadangkan Turutan Gabungan Pembelajaran Mesin (*Stacking Ensemble Machine Learning*) (SEML), bagi teknik penentu ukuran data NIRS melibatkan dua tahap pembelajaran. Lapan (8) set data spektroskopi dari repositori awam dan kajian terdahulu oleh pengarang telah digunakan sebagai kes kajian. Model ini menggeneralisasi data dalam tugas regresi  $R^2$  masing-masing sebanyak 0.8 bagi sampel ujian dan pengelasan tugas masing-masing dengan ketepatan klasifikasi (CA) sekurang-kurangnya 0.8. Tambahan, SEML yang dicadangkan ini dapat membantu, atau sekurang-kurangnya setanding dengan ketepatan individu dalam pembelajaran berkumpulan dalam kedua-dua sampel latihan dan ujian bagi semua kes set data regresi dan klasifikasi. Ia menunjukkan prestasi terbaik dalam sampel ujian bagi kedua-dua kumpulan set data regresi dan klasifikasi dengan masing-masing  $R^2$  antara 0.86 hingga hampir 1 dan antara julat 0.89 hingga 1 bagi CA.

**KEYWORDS:** *chemometrics calibration; stacking ensemble machine learning; near infrared spectroscopy; food fraud detection; food safety and security*

## 1. INTRODUCTION

Near infrared spectroscopy (NIRS) is a sort of high-energy vibrational spectroscopy that operates in the wavelength range of 750 to 2500 nm ( $13333$  to  $4000\text{ cm}^{-1}$ ). By probing a sample with electromagnetic radiation in that wavelength range, NIRS obtains spectral information that can aid in the development of appropriate qualitative and/or quantitative analytical procedures. NIRS has gained wide acceptance of industrial applications and research as a secondary non-destructive material fingerprinting. The applications can include medical-pharmaceutical fields [1-3], food/agricultural analysis [4-7], forensic [8], etc. NIRS is described as the hallmark for one of the most rapidly advancing analytical techniques over the last few decades [9].

The calibration of NIR spectra into meaningful quantitative or qualitative information is normally performed using advanced statistical learning, or chemometrics, analysis. Chemometrics methods are used for analyzing molecular spectroscopy data such as near infrared (NIR), Fourier transform infrared (FTIR), ultraviolet–visible (UV-vis), induced breakdown spectroscopy (LIBS), Raman spectroscopy and nuclear magnetic resonance (NMR) spectroscopy [10]. This problem is essentially multivariable data analysis or calibration to reveal meaningful chemical information from the samples being scanned by the respective spectrometers.

Due to advancement of computational methods, recently machine learning (ML) and deep learning are also used in NIRS chemometrics analysis. Generally, their applications enhance the calibration accuracy performed using common conventional statistical learning such as partial least square (PLS) regression and linear discriminant analysis (LDA). For example, the study in [11] has used deep and ensemble learning for milk adulteration detection using Fourier transformed infrared spectroscopy (FTIR). The proposed neural network architecture can outperform the composition recognition made by commonly used methods. In another study [4], support vector machine (SVM) was used to perform regression on NIR spectra data of mango fruits brix level (sugar content). The SVM performance outperforms PLS algorithm. SVM was also used for food powder classification based on handheld NIR spectrometer data and the results were excellent [12]. Another study [13] also using SVM as a classifier to estimate the sample quality of *Andrographis paniculate* obtained from different sources. The NIR reflectance spectroscopy instrument was used here.

Furthermore, Chen et al. [14] proposed the Least Squares Support Vector Machine (LSSVM) algorithm to establish NIR calibration models for the quantitative determination of chemical oxygen demand, which is a critical indicator of water pollution level. Michel et al. [15] used k-nearest neighbors (KNN) in addition to SVM, combined with principal component analysis (PCA) for identifying type of both consumer plastics and marine plastic debris based on different spectroscopy data namely Fourier transform infrared spectroscopy (ATR–FTIR), NIR reflectance spectroscopy, laser-induced breakdown spectroscopy (LIBS), and X-ray fluorescence (XRF) spectroscopy. Success rates indicate that ATR–FTIR, NIR reflectance spectroscopy, and LIBS coupled with ML classifiers can be used to identify both consumer and environmental plastic samples. Perez et al. [16] showed good results for the classification of chicken meat parts, where the portable NIR spectrophotometer together with chemometrics and ML algorithms allowed to discriminate the different parts of chicken by LDA, random forest (RF), and SVM. Wang et al. [17] investigated three conventional ML methods, namely

ordinary least square estimation (OLSE), RF, and extreme learning machine (ELM), while for the deep learning methods, three different structures of convolutional neural network (CNN) incorporated Inception module were constructed and investigated. The study conducted chemometrics calibration for total soil nitrogen using Visible-near-infrared spectrum (Vis-NIR) spectroscopy. The results indicate that the baseline-corrected and smoothed ELM model reached practical precision (coefficient of determination,  $R^2=0.89$ ) and the best result of CNN was obtained with  $R^2=0.93$ .

ML is basically a data-driven modelling that can be applied for multivariable calibration like in NIR spectroscopy, i.e. chemometrics calibration. As it has been discussed, there are various ML algorithms applied for multivariable calibration methods. Ensemble ML emerges as an effort for improving prediction accuracy of individual ML models by combining multiple ML models into a final prediction output. RF is one of the best ensemble ML that performs well in many applications [18]. RF is basically a multiple model of decision tree. Another approach of ensemble ML is called stacking ensemble. In the stacking ensemble ML, some base ML algorithms will be used as first level (base) learners and logistic regression (LR) will be used as the second level learner to aggregate the outputs of first level learners and come up with the final prediction output [19].

However, the applications ensemble ML for NIR spectroscopy calibration still needs to be further explored. Particularly, to our knowledge, stacking ensemble ML applied for multiple NIRS datasets is not found in the literature. Most of research works applied the method for an individual NIRS data such in [20]. Our main contribution in this research is the implementation of stacking ensemble machine learning (SEML) for chemometrics calibration where multiple NIR spectroscopy datasets will be used as the case study involving classification (qualitative) and regression (quantitative). This is proposed to improve the accuracy of the calibration model using conventional calibration methods. The performance of the proposed stacking ensemble ML will be compared to the base ML algorithm and conventional statistical learning in chemometrics.

## 2. SPECTROSCOPY DATASETS

There are two types of NIR spectroscopy multivariable calibrations from the perspective of supervised ML, namely classification (class label/qualitative prediction) and regression (quantitative prediction). Here, four datasets are used from each type thus making a total of 8 NIR spectroscopy datasets. For the regressions problem, the four datasets are adulteration of honey (AH) [18], active substance in a pharmaceutical tablet (AST) [21], dry matter content within mango fruit (DMM) [22] and moisture content of grain protein (MGP) [23]. The four datasets used for the classification task are adulteration of rice dataset (RA) [6], coffee type (CF) dataset [24], strawberry fruit (SB) [25] and starch powder classification (SP) [12]. The summary of the datasets and their attributes are shown in Table 1 (Regression and Classification).

### 2.1 Regression Datasets

The following are the details of the four regression datasets. The first regression dataset is the AH dataset, which deals with the regression of the level of adulteration of Kelulut honey (Malaysia) with syrup. The adulteration levels are given from 0%, 10%, etc., up to 100%. The level of 0% adulteration means pure honey sample and vice versa. NIR spectra data were collected using a micro NIR handheld instrument with a wavelength range of 900-1700 nm. The data are described in more detail in the study in [18]. Note that the original wavelength points are from 900 nm to 1700 nm, but the data is cut at the longer wavelengths due to the

presence of noise, resulting in data at wavelengths of 900 nm to 1650 nm. In this study [18], the calibration was performed in classification mode where k-nearest neighbour (KNN) and random forest were used, achieving accuracy of 90%. In this paper, we will extend this study and convert the problem into regression mode which has not been done before.

The second regression dataset deals with the chemometrics quantitation of the active substance in a pharmaceutical tablet (% per tablet), i.e. AST dataset. Four different dosage values of this pharmaceutical drug (5, 10, 15, and 20 mg per tablet) were used. In total, 31 batches were used, and from each batch 10 tablets were individually weighed and analyzed: making up 310 NIR spectra data. The data are described in more detail in the study in [21]. NIR transmittance and Raman spectroscopy chemometric calibrations of the active substance content of a pharmaceutical tablet were developed using partial least-squares regression (PLS) and no machine learning calibration were involved. The results gave relative prediction errors (RMSECV/ynom) of 2.6–3.7%. The latest study that employs this dataset was in 2021 [26] where KNN, SVM, RF and deep learning were used. However, the AST data was used in classification mode and not regression. We will use the AST dataset for the regression problem.

The third regression dataset deals with the dry matter content (%) regression of mango fruit. Let us call it the DMM dataset. Originally, the data for intact mango fruit was collected with short wave near infrared spectra using an interactance geometry, with total data set collected across three seasons ( $n = 10243$ ) and that of a fourth season ( $n = 1,448$ ) consisting of 306 wavelength points [22]. The dataset was reduced after pre-processing to have a number of samples ( $n=11362$ ) with 103 wavelength points (features) as published in [27]. In the paper [22], PLS regression and ANN were used as regression models and they achieve similar performance with Root Mean Square Error of Prediction (RMSEP) of around 1%.

The fourth regression dataset deals with regression of the moisture (wt%) of grain protein from NIR instrument with 231 samples created by Tormod Naes and Tomas Isaakson, as described on the website [23]. We call it the MGP dataset. The NIR spectrum have 117 wavelength points, ranging from 1104 to 2495 nm. The latest publication that used this dataset was found in [28]. The reported calibration result was obtained with  $R^2 = 0.93$ . This still can be improved and there was no involvement of ML algorithms during calibration.

Table 1: Summary of the eight (8) spectroscopy datasets used in this study

Calibration types	Dataset	Target variable	Wavelength range	Number of samples	Instrument
Regression (quantitative)	AH	Adulteration level (%) – kelulut honey	900-1700 nm	1846	Micro handheld NIR
	AST	Active substance (% per tablet) – tablet	7400-10500 $\text{cm}^{-1}$ (~950 nm to 1350 nm)	309	NIR FT-Raman
	DMM	Dry matter content (% weight) – mango fruit	684-990 nm	11362	F750 handheld NIR
	MGP	Moisture (% weight) – grain protein	1100-2500 nm	231	NIR reflectance
Classification (qualitative)	RA	Authentic and adulterated rice	900-1700 nm	123	Micro handheld NIR
	CF	Two categories of coffee	810-1910 nm	56	FTIR spectroscopy
	SB	Strawberry and non-strawberry	900-1800 nm	983	FTIR spectroscopy
	SP	Five categories of flour	900-1700 nm	75	Micro handheld NIR

## 2.2 Classification Datasets

Next, the four classification datasets are explained as follows. The first classification dataset is rice adulteration (RA dataset) where a total of 123 NIR spectra data were collected from 31 unadulterated rice samples and ten adulterated rice samples in 3 different illumination conditions. Rice samples were bought from Tesco Hypermarket and NSK Trade City, Kuala Lumpur, Malaysia. The rice samples were all milled rice in which the rice husk was removed. The total of 31 rice samples included 14 brands of local white rice, 10 brands of Thailand fragrance rice, 3 brands of Thailand white rice, and four other types of rice. Rice replica was bought from Titoonic Enterprise (Malaysia) and chosen as the adulterant [6]. For the chemometric calibration, Principal Component Analysis (PCA) and Logistic Regression (LR) were used simulataneously to perform qualitative analysis whether the rice sample was adulterated on unadulterated, achieving 97.2% accuracy. This accuracy was only achieved with inclusion of PCA as feature reduction. We will extend the study using different machine learning algorithms and no PCA will be used to simplify the process.

The second classification dataset is the CF dataset which is to discriminate the samples according to two coffee species, robusta and arabica. A total of 56 spectra samples were acquired using DRIFT (diffuse reflection infrared Fourier transform) and ATR (attenuated total reflection) sampling techniques in FTIR spectroscopy. The dataset is publicly accessible from the website [24]. The most recent publication using this dataset was in [29] where deep learning convolutional neural networks (CNN) was used in the calibration resulting in 100% accuracy. From the computation perspective, deep learning is more complex than ML.

The third classification dataset is the SB dataset which deals with strawberry adulteration discrimination [24]. A total of 983 FTIR spectra data were collected representing two sample types, i.e., strawberry and non-strawberry puree. The adulterated strawberry puree samples were obtained by mixing with certain adulterants as discussed in the study. Recent publication using this dataset was found in [30]. The results of classification accuracy using FM (frequency modulation) synthesis as the sound synthesiser and PCA as the dimensionality reduction method yields a mean classification accuracy of 88.57%. The result can be improved, and a more advanced ML algorithm can be used, as will be done in this paper.

The fourth classification dataset is the SP dataset, which is used to differentiate between various types of starch powder, including organic wheat flour, non-organic wheat flour, rice flour, tapioca starch, and corn starch [12]. The NIR spectra data was collected using micro NIR spectroscopic instrument with wavelength range from 900-1700 nm. A total of 75 NIR spectra samples were collected for five different food powder types, i.e., 15 samples for each type. Here, SVM was used as ML algorithm for chemometric calibration producing 100% test accuracy. However, as SVM involve extensive kernel tuning, we will apply different ML algorithms to study the feasibility.

## 3. MACHINE LEARNING FOR CHEMOMETRICS CALIBRATION

The qualitative or quantitative information from infrared spectra data is only obtained after the calibration process using chemometrics and this process naturally involves multivariate statistical analysis. Machine learning (ML) as a subset of AI (artificial intelligence), in addition to conventional multivariate statistical tools, seems to get more popularity for chemometrics calibration in spectroscopy nowadays due to its well-known capability to perform complex classification and regression tasks based on the data provided, i.e. data-driven method [33].

Regardless of their suitability of application for regression or classification, some famous ML algorithms are artificial neural networks (ANN), support vector machine (SVM), k-Nearest Neighbor (KNN), Naïve Bayes (NB), Gradient Boosting (GB), Random Forest (RF), etc. In this study, we focus on applying the ANN, SVM, GB and RF algorithms in the ensemble ML scheme. Among the considerations for choosing these ML algorithms are ease of interpretation and visualization, requiring less effort on data pre-processing, i.e., not requiring scaling and normalization, and not largely influenced by outliers or missing values.

Further improvement of standard ML model is called ensemble ML. The idea of ensemble ML is basically creating multiple ML models and aggregating the final prediction using a certain method to improve the accuracy of each individual base model performance. There are fundamentally three methods of ensemble namely bagging (bootstrap aggregating), boosting, and stacking.

Bagging typically involves using a single machine learning algorithm, almost always an unpruned decision tree (DT), and training each model on a different sample of the same training dataset. The predictions made by the ensemble members are then combined using simple statistics, such as voting or averaging [32]. A popular example of bagging ensemble method is random forest (RF) which is basically the bagging ensemble of DT.

Boosting on the other hand, refers to a family of algorithms that can convert weak learners to strong learners. Intuitively, a weak learner is just slightly better than random guess, while a strong learner is very close to perfect performance [19]. It involves the use of very simple decision trees that only make a single or a few decisions, referred to as ‘weak learners’. The predictions of the weak learners are combined using simple voting or averaging, although the contributions are weighed proportional to their performance or capability. The objective of Gradient Boosting (GB) is to develop a so-called ‘strong learner’ from many ‘weak learners’. Adaptive Boosting (Adaboost) and eXtreme Gradient Boosting (XGB) are among the popular methods in boosting ensemble [34]. The general boosting procedure is described in Fig. 1 [19].

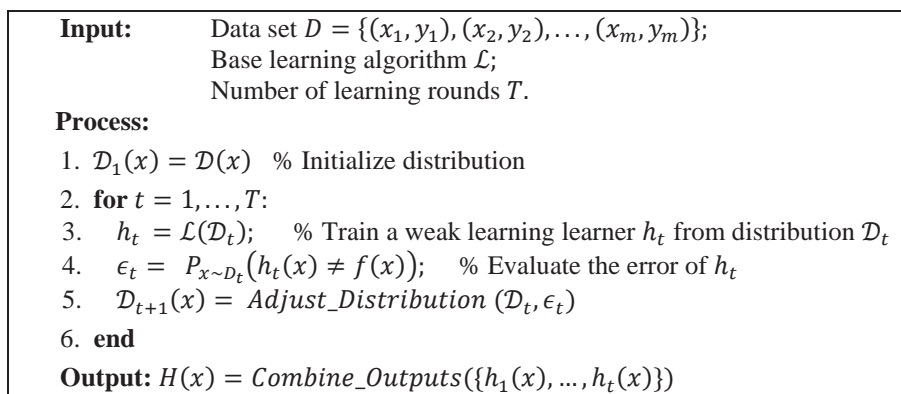


Fig. 1: General procedure of boosting algorithm.

#### 4. STACKING ENSEMBLE PROCEDURE

Stacking ensemble ML (SEML) is proposed for spectroscopy data calibration in this paper. In stacking ensemble, two levels of learning are used where 1<sup>st</sup> level (base) learners can be different ML algorithms and a 2<sup>nd</sup> level learner is used to combine the predictions (normally a logistic regression for classification). In this study, the proposed stacking ensemble ML algorithm uses four ML algorithms as base learners (1<sup>st</sup> level learners) namely Gradient Boosting (GB), Random Forest (RF), Support Vector Machine (SVM) and Artificial Neural

Network (ANN). The 2<sup>nd</sup> level learner uses Logistic Regression (LogReg) for the case of classification and uses Linear Regression (LinReg) for the case of regression to aggregate the final output.

Thus, suppose that  $\hat{y}_{reg}$  and  $\hat{y}_{class}$  are the final prediction output for regression and classification respectively, they can be expressed as:

$$\hat{y}_{reg} = LinReg(\hat{y}_{GB}, \hat{y}_{RF}, \hat{y}_{SVM}, \hat{y}_{ANN}) \quad (1)$$

$$\hat{y}_{class} = LogReg(\hat{y}_{GB}, \hat{y}_{RF}, \hat{y}_{SVM}, \hat{y}_{ANN}) \quad (2)$$

Accordingly, the diagram of the proposed stacking ensemble, ML, is shown in Fig. 2. Here, the algorithm takes the process as illustrated in Fig. 3. The stacking ensemble learns a high-level classifier/regressor on top of the base learner. It can be regarded as a meta learning approach in which the base learners are called first-level learners and a second-level models have learnt to combine the first-level learners.

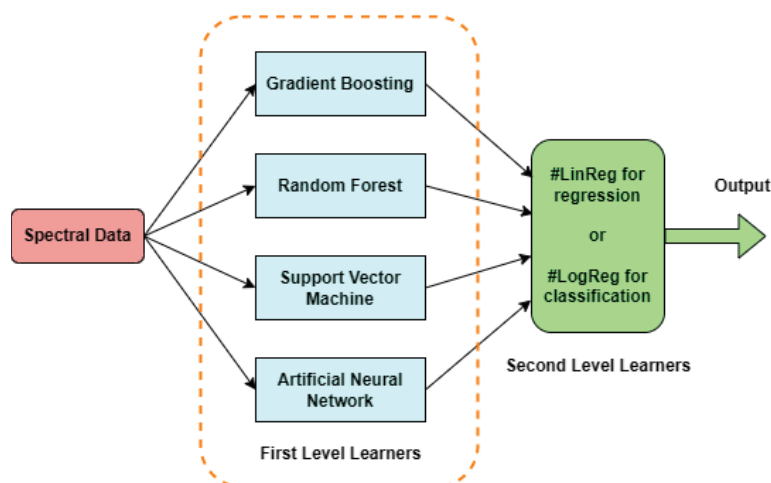


Fig. 2: Diagram of the stacking ensemble ML for regression and classification.

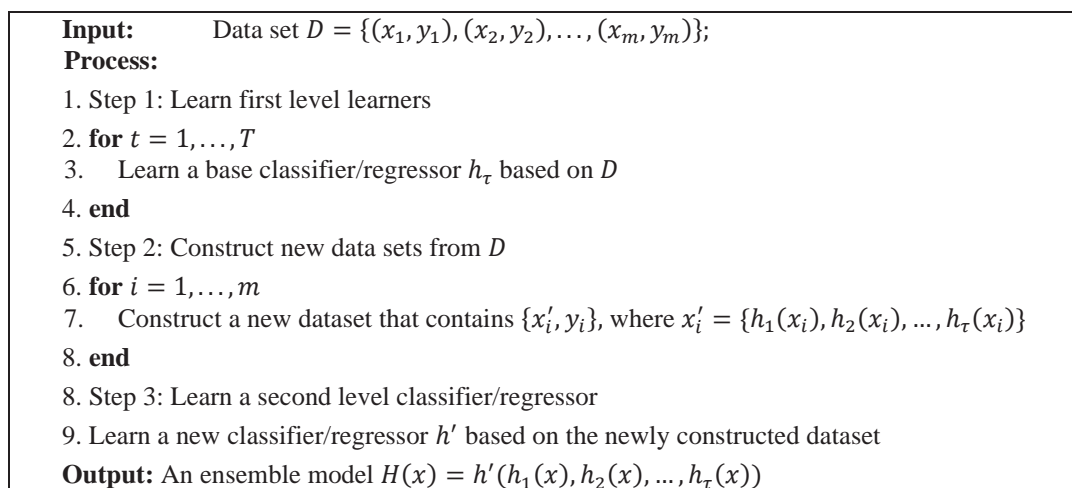


Fig. 3: General procedure of stacking ensemble.

Based on Fig. 3, the general procedure of stacking ensemble has the following three major steps:

- Step 1: Learn first-level learners (GB, RF, SVM, ANN) based on the original training data set.
- Step 2: Construct a new data set based on the output of base learners. Here, the output predicted labels/values of the first-level learners are regarded as new features, and the original labels/values are kept as the labels/values in the new data set.
- Step 3: Learn a second-level learner based on the newly constructed data set. LinReg and or LogReg are applied as second-level learners for regression and classification tasks respectively.

## 5. CALIBRATION MODEL DEVELOPMENT AND EVALUATION

As the general procedure in ML model development, the ML is trained using a training dataset. Once the training is completed, the model is tested using the test dataset to evaluate the prediction accuracy. Here, 70% - 30% ratio is used to assign the size of the training and testing datasets, respectively. In the random assignment into the classification datasets, stratified sampling is applied to make sure a balanced class is achieved in the training and testing datasets. Spectra data preprocessing is also applied according to the common sense of spectra data processing experience. Simple preprocessing, such as edge cutting, Gaussian smoothing, and Savitsky-Golay (SG) derivative filter, is executed in this study to show that the proposed ML model is robust to preprocessing methods.

Table 2 shows the spectra pre-processing used and the ML hyperparameters setup of the individual base learners and the stacking ensemble ML. The implementation of the ML training and evaluation is performed in the Python programming environment. For the spectra preprocessing, edge cutting is necessary as the micro handheld NIR spectrometer (used in AH, BG, BM, SP, RA datasets) produced noise on both edges of the 900-1700 nm wavelength window. Here, edge cutting means to cut and keep the wavelengths at 950-1650 nm for these four datasets. For all datasets, gaussian smoothing is applied to reduce signal noise. For all classification datasets, SG derivative order 1 is applied to remove effects of shifting baselines and sloping or curving due to scattering [35]. For the regression datasets, SG derivative order 2 is applied on the AH dataset whilst SG derivative order 1 is applied to the AST, DMM, and MGP datasets.

Once the ML model is successfully calibrated with 70% of the samples, the performance evaluation is carried out by testing with the remaining 30% of the samples in the respective dataset. The evaluation aims to assess the model accuracy in the sense of regression or classification problems. For regression, the ML model is evaluated using the coefficient of determination ( $R^2$ ) and mean absolute error (MAE) expressed as:

$$R^2 = 1 - \frac{\sum_{i=1}^n (\hat{y}_k - y_k)^2}{\sum_{i=1}^n (y_k - \bar{y}_k)^2} \quad (3)$$

$$MAE = \frac{1}{n} \sum_{i=1}^n |\hat{y}_k - y_k| \quad (4)$$

In Eqns. (3)-(4),  $\hat{y}_k$  indicates the predicted output at sample  $k$ ,  $y_k$  represents the observed value, and  $\bar{y}_k$  is the mean of the observed values.

For classification, the evaluation is performed by looking at the classification accuracy (CA) and area under curve (AUC) values of the receiver operating characteristic curves. CA is defined as ratio of correctly predicted class label to the total number of the samples, i.e.:

$$CA = \frac{\text{number of correct prediction}}{\text{total number of samples}} \quad (5)$$

Table 2: The spectra preprocessing and the ML hyperparameters setup.

Data-set	Type	Spectra Pre-processing	ML Hyperparameters Setting				
			XGB	RF	SVM	ANN	SEML
AH	Regression	Edge cutting, gaussian smoothing & SG derivative order 2	Number of estimators = 500 Learning rate = 0.25	Number of estimators = 800 Max depth = 85	C = 1000 Gamma = 0.01	Alpha = 0.01 Learning rate = 0.0001	
AST		Gaussian smoothing & SG derivative order 1	Number of estimators = 300 Learning rate = 0.25	Number of estimators = 800 Max depth = 85	C = 1 Gamma = 1	Alpha = 0.01 Learning rate = 0.0001	Linear regression with elastic net regularization L1:L2=0.5:0.5
DMM		Gaussian smoothing & SG derivative order 1	Number of estimators = 500 Learning rate = 0.25	Number of estimators = 800 Max depth = 85	C = 1000 Gamma = 0.01	Alpha = 0.01 Learning rate = 0.01	
MGP		Gaussian smoothing & SG derivative order 1	Number of estimators = 300 Learning rate = 0.25	Number of estimators = 500 Max depth = 60	C = 1000 Gamma = 0.01	Alpha = 0.01 Learning rate = 0.0001	
RA	Classification	Edge cutting, gaussian smoothing & SG derivative order 1	Trees: 50 Depth: 10	C: 10	Lr: 0.1 Trees: 50	Lr: 0.0001 Neurons: 50	
CF		Gaussian smoothing & SG derivative order 1	Trees: 50 Depth: 10	C: 10	Lr: 0.01 Trees: 50	Lr: 0.0001 Neurons: 50	Logistic regression with Ridge (L2) regularization
SB		Gaussian smoothing & SG derivative order 1	Trees: 50 Depth: 10	C: 10	Lr: 0.1 Trees: 200	Lr: 0.01 Neurons: 200	
SP		Edge cutting, gaussian smoothing & SG derivative order 1	Trees: 50 Depth: 30	C: 100	Lr: 0.01 Trees: 100	Lr: 0.0001 Neurons: 50	

This CA metric can be obtained directly from the confusion matrix of classification datasets. Furthermore, the metrics in Eqns. (3) – (5) will be computed for the training (calibration) and testing data samples in each dataset. In addition, AUC can be generally defined as the measure of the ability of a classifier to distinguish between classes. The AUC=1 is for a perfect classifier while AUC=0.5 is for the worst classifier, as it only gives a random guess.

## 6. RESULTS AND ANALYSIS

This section discusses the results and analysis on the ML model performance to predict outputs for calibration and test samples in each dataset. The performance of the proposed SEML is compared to the individual ML model for each dataset.

Table 3 shows the performance metrics of the calibration model for the regression datasets as discussed in the previous section. Generally, all the ML algorithms used for calibration on the five regression datasets perform excellently in the training samples. Bold marks in the table indicate the highest performance in terms of  $R^2$  value on each dataset. If two ML models proclude the same value, then both will be marked with bold.

Table 3: Evaluation results of the calibration model (regression datasets)

Dataset	ML model	Calibration		Test	
		$R^2$	MAE	$R^2$	MAE
AH	GB	$\approx 1$	0.134	0.877	8.919
	RF	0.999	0.596	0.820	11.007
	SVM	0.945	5.359	0.936	6.117
	ANN	0.939	5.954	0.933	6.397
	SEML	0.938	5.944	<b>0.940</b>	<b>6.076</b>
AST	GB	$\approx 1$	$\approx 0$	0.955	0.211
	RF	0.999	0.018	<b>0.963</b>	<b>0.200</b>
	SVM	0.951	0.206	0.961	0.207
	ANN	0.941	0.234	0.950	0.243
	SEML	0.959	0.184	<b>0.963</b>	<b>0.199</b>
DMM	GB	0.959	0.382	0.841	0.752
	RF	0.999	0.046	0.855	0.657
	SVM	0.863	0.678	0.864	0.687
	ANN	0.669	1.110	0.662	1.145
	SEML	0.889	0.608	<b>0.896</b>	<b>0.601</b>
MGP	GB	$\approx 1$	0.002	0.994	0.263
	RF	$\approx 1$	$\approx 0$	0.995	0.245
	SVM	0.999	0.102	<b>0.998</b>	<b>0.139</b>
	ANN	0.999	0.118	<b>0.998</b>	<b>0.162</b>
	SEML	0.999	0.115	<b>0.998</b>	<b>0.141</b>

They also well generalize the data in the respective regression tasks where  $R^2$  of at least 0.662 is achieved in the test samples. The fact that only simple spectra pre-processing steps are applied as shown in Table 2 can be appreciated. For instance, most of the datasets only required gaussian smoothing and SG derivative order 1. In addition, the proposed SEML can improve, or at least perform on par with, the accuracy of individual base ML especially in the test samples.

Figure 6 shows the regression graph of observed values vs predicted values performed by SEML for test samples. This graph is displayed based on the results shown in Table 3. The model performs best for the DMM dataset and worst for the AH dataset as compared relative

to other datasets. Since the DMM dataset has a bigger size (11362 samples) as compared to the MGP dataset (231 samples), the ML models should be able to learn sufficiently from the DMM data. However, the spectra pre-processing plays an important role contributing to the accuracy. This can be improved by implementing different pre-processing techniques, but this aspect is not the main focus of this paper and will not be explored further. Instead, a simple and relatively uniform preprocessing technique has been applied for all datasets.

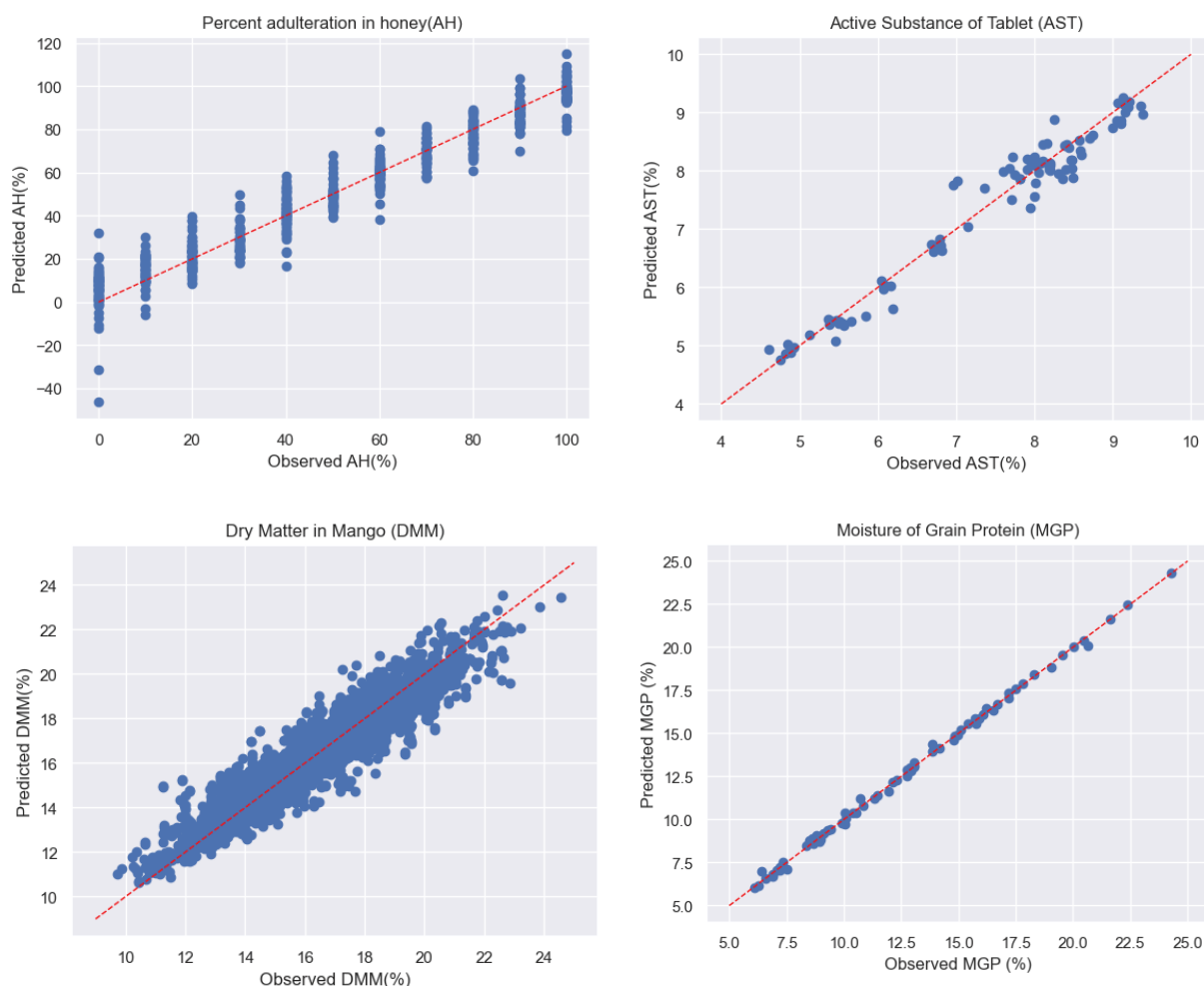


Fig. 6: Observed vs predicted values by SEML in test samples for regression datasets.

Table 4 shows the performance metrics of the calibration model for the classification datasets, as discussed in the previous section. Bold marks in the table indicate the highest performance in terms of CA value on each dataset. If two or more ML models procure the same value, then they will be marked with bold.

Generally, all the ML algorithms used for calibration on the selected four classification datasets perform excellently in the training samples that most of the predictions result in CA=1. They also well generalize the data in the respective classification tasks where CA of at least approximately 0.8 is achieved with most of the resulting CA being approximately 0.95 up to 1. The proposed SEML can achieve CA=1 for both training and testing samples in two datasets used, for example, CF and SP. In the classification datasets, the pre-processing only uses gaussian smoothing and an SG derivative of order 1. Edge cutting is only used for the spectra data collected by micro NIR spectrometer due to noises at around edges around 900-950 nm

and 1650 nm – 1700 nm. In addition, the proposed SEML can slightly improve, or at least in par with, the accuracy of individual base ML in both training and testing samples. All four general models such as RF, SVM, GB and ANN can be considered as very competitive methods for some specific dataset to SEML. For example, SEML in RA dataset have similar CA with ANN and RF, while CF dataset SEML’s CA have a similar result with ANN and SVM, etc.

Table 4: Evaluation results of the calibration model (classification datasets)

Dataset	ML model	Calibration		Test	
		CA	AUC	CA	AUC
RA	GB	1	1	0.946	0.925
	RF	1	1	<b>0.973</b>	<b>0.966</b>
	SVM	0.872	0.997	0.865	0.991
	ANN	1	1	<b>0.973</b>	<b>1</b>
	SEML	1	1	<b>0.973</b>	<b>0.978</b>
CF	GB	1	1	0.941	0.993
	RF	1	1	0.941	1
	SVM	1	1	<b>1</b>	<b>1</b>
	ANN	1	1	<b>1</b>	<b>1</b>
	SEML	1	1	<b>1</b>	<b>1</b>
SB	GB	1	1	0.976	0.993
	RF	1	1	0.966	0.993
	SVM	0.932	0.973	0.946	0.975
	ANN	0.968	0.993	0.969	0.993
	SEML	0.999	1	<b>0.980</b>	<b>0.994</b>
SP	GB	1	1	0.870	0.935
	RF	1	1	0.826	0.903
	SVM	1	1	<b>1</b>	<b>1</b>
	ANN	1	1	0.957	0.969
	SEML	1	1	<b>1</b>	<b>1</b>

Figure 7 shows the confusion matrices of the SEML for classification test samples. There is an interesting point here that the RA dataset is an imbalanced classification case. Despite the imbalanced data, all the ML models are still able to generalize the data very well especially for GB, RF, ANN and SEML. Furthermore, they also perform well for the CF and SP datasets despite their small number of samples.

## 7. DISCUSSION

Based on calibration results for both regression and classification tasks, in most cases, the Stacked Ensemble Machine Learning (SEML) approach performs better or at least comparably to the base learners. The observation is more evident in the regression case. It is important to focus on the robustness of SEML's generalization capability. The effectiveness of stacked ensemble models stems from the fact that different base learners tend to make different types of errors. Some base learners excel in capturing specific patterns or relationships in the data, while others perform better on different subsets or under varying circumstances. By combining the predictions of multiple base learners, the ensemble model achieves improved generalization and robustness. For instance, in regression case, in the AST and MGP datasets, Gradient Boosting (GB) performs exceptionally well on the training data but exhibits the worst performance on the test data compared to SEML, indicating a tendency of GB to overfit the data.

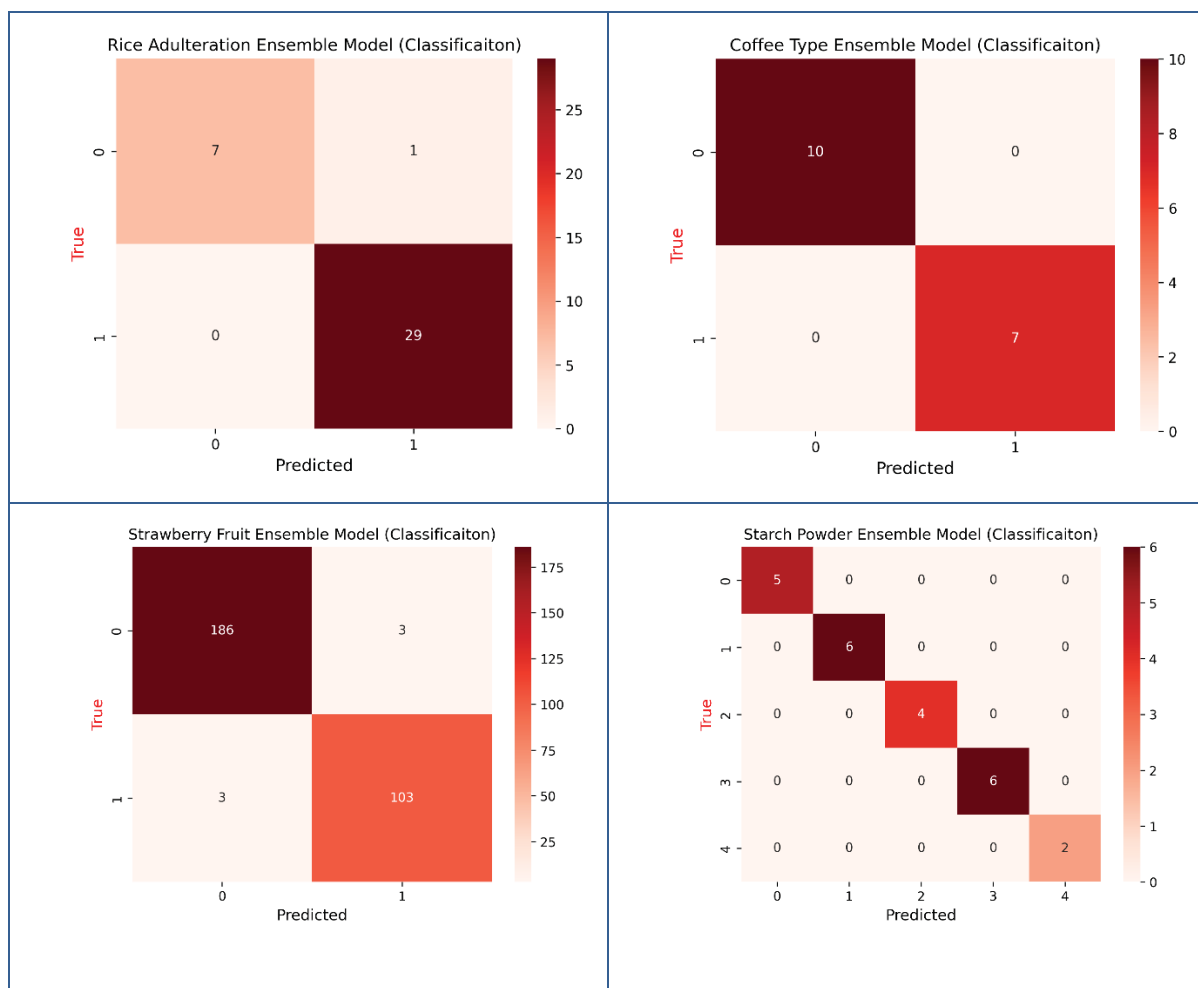


Fig. 7: Confusion matrix of SEML prediction in test samples for classification datasets.

In the classification scenario, the superiority of SEML becomes less evident, especially when considering the CF and SP datasets. This can be attributed to the fact that the base learner, Support Vector Machine (SVM), exhibits exceptional performance, accomplishing the task perfectly. Since SVM, and also ANN in the CF dataset, are already proficient in capturing the intricacies of these particular datasets, the additional benefits of utilizing SEML might be limited or negligible. Nonetheless, it is important to note that the potential advantages of SEML can still manifest in other datasets or when faced with more complex classification challenges where the base learner alone might not suffice.

## 8. DISCUSSION

Based on calibration results for both regression and classification tasks, in most cases, the Stacked Ensemble Machine Learning (SEML) approach performs better or at least comparably to the base learners. The observation is more evident in the regression case. It is important to focus on the robustness of SEML's generalization capability. The effectiveness of stacked ensemble models stems from the fact that different base learners tend to make different types of errors. Some base learners excel in capturing specific patterns or relationships in the data, while others perform better on different subsets or under varying circumstances. By combining the predictions of multiple base learners, the ensemble model achieves improved generalization and robustness. For instance, in regression case, in the AST and MGP datasets, Gradient

Boosting (GB) performs exceptionally well on the training data but exhibits the worst performance on the test data compared to SEML, indicating a tendency of GB to overfit the data.

In the classification scenario, the superiority of SEML becomes less evident, especially when considering the CF and SP datasets. This can be attributed to the fact that the base learner, Support Vector Machine (SVM), exhibits exceptional performance, accomplishing the task perfectly. Since SVM, and also ANN in the CF dataset, are already proficient in capturing the intricacies of these particular datasets, the additional benefits of utilizing SEML might be limited or negligible. Nonetheless, it is important to note that the potential advantages of SEML can still manifest in other datasets or when faced with more complex classification challenges where the base learner alone might not suffice.

We will now present the average performance of each algorithm along with the corresponding metrics for both regression and classification tasks. The results can be found in Table 5. Bold marks in the table represent the highest performance in terms of the respective metrics. It is evident that SEML calibration yields better generalization capability, i.e. always produces higher metrics on test data. In addition, it is worth to note that the closest performance with SEML are provided by GB and RF. This makes sense as GB and RF are a type of ensemble learning via boosting and bagging mechanism respectively, as discussed earlier.

Table 5: Average performance of each algorithm over regression datasets

ML model	Calibration		Test	
	$R^2$	MAE	$R^2$	MAE
GB	0.99	0.13	0.92	2.54
RF	<b>1.00</b>	<b>0.17</b>	0.91	3.03
SVM	0.94	1.59	0.94	1.79
ANN	0.89	1.85	0.89	1.99
SEML	0.95	1.71	<b>0.95</b>	<b>1.75</b>

Table 6: Average performance of each algorithm over classification datasets

ML model	Calibration		Test	
	CA	AUC	CA	AUC
GB	<b>1.00</b>	<b>1.00</b>	0.93	0.96
RF	<b>1.00</b>	<b>1.00</b>	0.93	0.97
SVM	0.95	0.99	0.95	0.99
ANN	0.99	1.00	0.97	0.99
SEML	<b>1.00</b>	<b>1.00</b>	<b>0.99</b>	<b>0.99</b>

## 9. CONCLUSION REMARKS

The results of chemometrics calibration for NIR spectroscopy data using stacked ensemble machine learning (SEML) have been presented. The prediction performance of the machine learning-based calibration model was evaluated and verified using eight (8) spectroscopy datasets representing both regression and classification cases. Despite employing a simple procedure for spectra data pre-processing, the machine learning methods, particularly GB, RF, SVM, and ANN as base learners, accurately predict both training and testing samples. Importantly, the proposed SEML, by combining the output of base learners, generally improves the accuracy of these individual base learners and provides better overall generalization, as confirmed through evaluation with test data.

The future direction of this research is to explore the potential applications of the proposed SEML to other datasets. The aim is to develop a robust calibration method that includes the

exploration of deep learning models, which could simplify the pre-processing of spectra. Deep learning holds potential for breakthroughs in this area due to its automatic feature extraction process, which is lacking in traditional machine learning approaches.

## ACKNOWLEDGEMENT

This project is supported by the Ministry of Higher Education Malaysia under the Fundamental Research Grant Scheme, with code: FRGS/1/2020/TK0/UCSI/02/4.

## REFERENCES

- [1] Solihin MI, Shameem Y, Htut T, Ang CK, Hidayab M. (2019) Non-Invasive Blood Glucose Estimation using Handheld Near Infrared Device. *Int. J. Recent Technol. Eng.*, 3: 16-19. doi: 10.35940/ijrte.C1004.1083S19.
- [2] Chen CJ, Akowuah GA. (2023) Comparison of HPLC and ATR-FTIR Methods for the Determination of Rosmarinic Acid in Aqueous Leaf Extract of *Orthosiphon stamineus*. *Nat. Prod. J.*, 13(1): 40-46. doi: 10.2174/2210315512666220429114935.
- [3] B. A. Sabbagh, P. V. Kumar, Y. L. Chew, J. H. Chin, and G. A. Akowuah. (2022) Determination of metformin in fixed-dose combination tablets by ATR-FTIR spectroscopy. *Chem. Data Collect.*, 13: 100868. doi: 10.1016/J.CDC.2022.100868.
- [4] D. G. Abdullah Al-Sanabani, M. I. Solihin, L. P. Pui, W. Astuti, C. K. Ang, and L. W. Hong. (2019) Development of non-destructive mango assessment using Handheld Spectroscopy and Machine Learning Regression. *Journal of Physics: Conference Series*, 1367(1): 012030. doi: 10.1088/1742-6596/1367/1/012030.
- [5] S. H. Tan, L. P. Pui, M. I. Solihin, K. S. Keat, W. H. Lim, and C. K. Ang. (2021) Physicochemical analysis and adulteration detection in Malaysia stingless bee honey using a handheld near-infrared spectrometer," *J. Food Process. Preserv.*, 45(7): e15576. doi: 10.1111/JFPP.15576.
- [6] K. T. Liew, L. P. Pui, and M. I. Solihin. (2020) Feasibility of fraud detection in rice using a handheld near-infrared spectroscopy. *AIP Conference Proceedings*, 2306(1): 020018. doi: 10.1063/5.0032679.
- [7] P. S. Sampaio, A. Soares, A. Castanho, A. S. Almeida, J. Oliveira, and C. Brites. (2018) Optimization of rice amylose determination by NIR-spectroscopy using PLS chemometrics algorithms. *Food Chem.*, 242: 196–204. doi: 10.1016/j.foodchem.2017.09.058.
- [8] R. F. Kranenburg et al. (2020) Rapid and robust on-scene detection of cocaine in street samples using a handheld near-infrared spectrometer and machine learning algorithms. *Drug Test. Anal.*, 12(10): 1404–1418. doi: 10.1002/DTA.2895.
- [9] K. B. Beć and C. W. Huck. (2019) Breakthrough potential in near-infrared spectroscopy: Spectra simulation. A review of recent developments. *Frontiers in Chemistry*, 7(FEB). doi: 10.3389/fchem.2019.00048.
- [10] H. P. Wang et al. (2022) Recent advances of chemometric calibration methods in modern spectroscopy: Algorithms, strategy, and related issues. *TrAC Trends Anal. Chem.*, 153: 116648. doi: 10.1016/J.TRAC.2022.116648.
- [11] H. A. Neto, W. L. F. Tavares, D. C. S. Z. Ribeiro, R. C. O. Alves, L. M. Fonseca, and S. V. A. Campos. (2019) On the utilization of deep and ensemble learning to detect milk adulteration. *BioData Min.*, 12(1): 1–13. doi: 10.1186/s13040-019-0200-5.
- [12] M. Y. Mohamed, M. I. Solihin, W. Astuti, C. K. Ang, and W. Zailah. (2019) Food powders classification using handheld Near-Infrared Spectroscopy and Support Vector Machine. *J. Phys. Conf. Ser.*, 1367: 012029. doi:10.1088/1742-6596/1367/1/012029.
- [13] D. Sing et al., (2021) Estimation of Andrographolides and Gradation of Andrographis paniculata Leaves Using Near Infrared Spectroscopy Together With Support Vector Machine. *Front. Pharmacol.*, 12(May): 1–8. doi:10.3389/fphar.2021.629833.
- [14] H. Chen, L. Xu, W. Ai, B. Lin, Q. Feng, and K. Cai. (2020) Kernel functions embedded in

- support vector machine learning models for rapid water pollution assessment via near-infrared spectroscopy. *Science of the Total Environment*, 714: 136765. doi: 10.1016/j.scitotenv.2020.136765.
- [15] A. P. M. Michel, A. E. Morrison, V. L. Preston, C. T. Marx, B. C. Colson, and H. K. White. (2020) Rapid Identification of Marine Plastic Debris via Spectroscopic Techniques and Machine Learning Classifiers. *Environ. Sci. Technol.*, 54(17): 10630–10637. doi: 10.1021/acs.est.0c02099.
- [16] I. M. Nolasco Perez, A. T. Badaró, S. Barbon, A. P. A. Barbon, M. A. R. Pollonio, and D. F. Barbin. (2018) Classification of Chicken Parts Using a Portable Near-Infrared (NIR) Spectrophotometer and Machine Learning. *Appl. Spectrosc.*, 72(12): 1774–1780. doi: 10.1177/0003702818788878.
- [17] Y. Wang, M. Li, R. Ji, M. Wang, and L. Zheng. (2020) Comparison of soil total nitrogen content prediction models based on Vis-NIR spectroscopy. *Sensors (Switzerland)*, 20(24): 1–20. doi: 10.3390/s20247078.
- [18] V. Woeng, L. Y. Lim, L. Abdul Kalam Saleena, M. I. Solihin, and L. P. Pui. (2022) Physicochemical properties and detection of glucose syrup adulterated Kelulut (*Heterotrigna itama*) honey using Near-Infrared spectroscopy. *J. Food Process. Preserv.*, 46(7): e16686. doi: 10.1111/JFPP.16686.
- [19] K. Nordhausen. (2022) Ensemble Methods: Foundations and Algorithms by Zhi-Hua Zhou. *Int. Stat. Rev.*, 81(3): 470–470. doi: 10.1111/INSR.12042\_10.
- [20] H. Cao et al. (2022) Application of stacking ensemble learning model in quantitative analysis of biomaterial activity. *Microchem. J.*, 183: 108075. doi: 10.1016/J.MICROC.2022.108075.
- [21] M. Dyrby, S. B. Engelsen, L. Nørgaard, M. Bruhn, and L. Lundsberg-Nielsen. (2022) Chemometric Quantitation of the Active Substance (Containing C=N) in a Pharmaceutical Tablet Using Near-Infrared (NIR) Transmittance and NIR FT-Raman Spectra. *Applied Spectroscopy*, 56(5): 579–585. <https://doi.org/10.1366/0003702021955358>
- [22] N. T. Anderson, K. B. Walsh, J. R. Flynn, and J. P. Walsh. (2021) Achieving robustness across season, location and cultivar for a NIRS model for intact mango fruit dry matter content. II. Local PLS and nonlinear models. *Postharvest Biol. Technol.* 171: 111358. doi: 10.1016/J.POSTHARVBIO.2020.111358.
- [23] “Data Sets - Eigenvector.” [Online]. Available: <https://eigenvector.com/resources/data-sets/>. [Accessed: 28-Oct-2021].
- [24] “Core Science Resources at QI.” [Online]. Available: <https://csr.quadram.ac.uk/>. [Accessed: 29-Oct-2021].
- [25] Holland. JK, Kemsley. EK, and Wilson. RH. (1998) Use of Fourier transform infrared spectroscopy and partial least squares regression for the detection of adulteration of strawberry purees. *J. Sci. Food Agric.*, 76(2): 263–269. doi: 10.1002/(SICI)1097-0010(199802)76:2.
- [26] U. Blazhko, V. Shapaval, V. Kovalev, and A. Kohler. (2021) Comparison of augmentation and pre-processing for deep learning and chemometric classification of infrared spectra. *Chemom. Intell. Lab. Syst.*, 215: 104367. doi: 10.1016/j.chemolab.2021.104367.
- [27] D. Passos and P. Mishra. (2022) A tutorial on automatic hyperparameter tuning of deep spectral modelling for regression and classification tasks. *Chemom. Intell. Lab. Syst.*, 223: 104520 . doi: 10.1016/j.chemolab.2022.104520.
- [28] D. S. Long, R. E. Engel, and M. C. Siemens. (2008) Measuring Grain Protein Concentration with In-line Near Infrared Reflectance Spectroscopy. *Agron. J.*, 100(2): 247–252. doi: 10.2134/AGRONJ2007.0052.
- [29] J. Acquarelli, T. van Laarhoven, J. Gerretzen, T. N. Tran, L. M. C. Buydens, and E. Marchiori. (2017) Convolutional neural networks for vibrational spectroscopic data analysis. *Anal. Chim. Acta*, 954: 22–31. doi: 10.1016/J.ACA.2016.12.010.
- [30] H. Kew. (2021) A model for spectroscopic food sample analysis using data sonification. *Int. J. Speech Technol.*, 24(4): 865–881. doi: 10.1007/s10772-020-09794-9.
- [31] M. I. Solihin, Z. Zekui, C. K. Ang, F. Heltha, and M. Rizon. (2021) Machine Learning Calibration for Near Infrared Spectroscopy Data: A Visual Programming Approach. *Lecture Notes in Electrical Engineering*, 666: 577–590. doi: 10.1007/978-981-15-5281-6\_40/COVER

- [32] M. I. Solihin, Yanto, G. Hayder, and H. A. Q. Maarif. (2023) Landslide Susceptibility Mapping with Stacking Ensemble Machine Learning. *Adv. Sci. Technol. Innov.*, 1: 35–40. doi: 10.1007/978-3-031-26580-8\_7/COVER.
- [33] T. Chen and C. Guestrin. (2016) XGBoost: A Scalable Tree Boosting System. *Proceedings of the 22nd ACM SIGKDD International Conference on Knowledge Discovery and Data Mining*, 1: 785–794. doi: 10.1145/2939672.2939785.
- [34] Z. Cheng, Y. Yang, and H. Zhang. (2022) Interpretable ensemble machine-learning models for strength activity index prediction of iron ore tailings. *Case Stud. Constr. Mater.*, 17: e01239. doi: 10.1016/J.CSCM.2022.E01239.
- [35] K. P. Chan, M. I. Solihin, C. K. Ang, and L. P. Pui. (2022) Experimentation on Spectra Data Regression Using Dense Multilayer Neural Networks with Common Pre-processing. *Lect. Notes Electr. Eng.*, 900: 97–112. doi: 10.1007/978-981-19-2095-0\_10/COVER.

# COMPACT CPW 4X4 MIMO ANTENNA FOR WI-FI 6 (IEEE802.11.AX) AND 5G(NR77/NR78/NR79) COMMUNICATIONS

NOORA SALIM<sup>1\*</sup>, MANDEEP J. SINGH<sup>2</sup> AND AMER T. ABED<sup>3</sup>

<sup>1,2</sup>Department of Electrical and Electronics Engineering,  
Faculty of Engineering & Built Environment (FKAB)

Universiti Kebangsaan Malaysia, 43600 UKM Bangi, Selangor, Malaysia

<sup>1</sup>Faculty of Engineering, Al-Qasim Green University, Babylon, Iraq

<sup>2</sup>Space Science Center (ANGKASA), Institute of Climate Change,

Universiti Kebangsaan Malaysia, 43600 UKM Bangi, Selangor, Malaysia

<sup>3</sup>Department of Medical Instrumentation Techniques Engineering, Dijlah University  
College, Baghdad, Iraq

\*Corresponding author: p110366@siswa.ukm.edu.my

(Received: 14 June 2023; Accepted: 12 July 2023; Published on-line: 1 January 2024)

**ABSTRACT:** This research proposes a compact 4x4 MIMO coplanar waveguide antenna for 5G NR and Wi-Fi 6 applications. The antenna has a size of 34x32x1.6 mm and operates in the 4.2-7 GHz band. By cutting slots on the ground and radiator, the mutual coupling is reduced to less than -15 dB between adjacent and opposite elements and less than -25 dB between diagonal elements. The antenna achieves good measured gains (3-6 dBi) and efficiency (60%-80%). The proposed antenna is suitable for high-performance wireless communication systems that require a small and low-cost MIMO antenna.

**ABSTRAK:** Kajian ini mencadangkan antena pandu gelombang yang kompak 4x4 MIMO koplanar bagi aplikasi 5G NR dan Wi-Fi6. Antena ini mempunyai saiz 34x32x1.6 mm dan beroperasi dalam kelompok gelombang 4.2-7 GHz. Dengan memotong slot pada tanah dan radiator, *mutual coupling* dikurangkan sebanyak -15 dB antara adjasen dan elemen bertentangan dan kurang daripada -25 dB antara elemen diagonal. Antena ini mencapai ukuran terbaik pada *gain* (3-6 dBi) dan kecekapan (60%-80%). Antena yang dicadangkan ini sesuai bagi sistem komunikasi tanpa wayar berprestasi tinggi yang memerlukan antena kecil dan murah seperti antena MIMO.

**KEYWORDS:** slot; CPW; MIMO; Wi-Fi6; 5G

## 1. INTRODUCTION

As new uses for the Internet of Things (IoT), smart cities, driverless vehicles, etc. have emerged, there has been a rise in the demand for fast wireless connections. Wi-Fi 6 (IEEE802.11ax) and 5G (nr77/nr78/nr79) are two examples of newly created standards that aim to address this need by delivering faster data speeds, lower latency, and more reliability. The requirements for wide bandwidth, high efficiency, high gain, and low mutual coupling that these standards impose provide new obstacles for antenna design. Furthermore, these standards operate at various frequency bands, making it challenging to create a universal antenna.

The literature reports a number of works on MIMO antenna design for 5G and Wi-Fi 6. However, most of these works suffer from some sort of restriction or flaw that prevents them from functioning at peak efficiency. Here, we evaluate several of these publications and discuss their merits and shortcomings.

In [1], one of the early works on MIMO antenna design for Wi-Fi 6 and 5G communications, a four-element CPW-fed MIMO antenna with a large impedance spectrum from 3 GHz to 11 GHz was proposed. To accomplish polarization diversity and great isolation, the design made use of four jug-shaped radiating devices with orthogonal polarization. The design's low gain, however, was consistent across the entire operating frequency range at -2 dB or less. The MIMO antenna studied in [2] was quite large and missed many critical frequencies, but its planar spiral line structure increased the diversity coefficient between dual radiating elements. In addition, [3] demonstrated a broad-bandwidth four-element CPW-fed MIMO antenna operating between 3 and 9 GHz, making it suitable for use in Wi-Fi 6 and 5G communications. To better isolate the two antenna parts, a rectangular slit was incorporated into the design, and a T-shaped stub was placed on the ground. The patch was designed with a U-shaped slot that produced a band notch at 5.5 GHz. Across the usable spectrum, this design's gain was just 0.5–2 dB, though.

For Wi-Fi 6 and 5G communications, an alternative MIMO antenna design was published in [3,4] which suggested a four-element MIMO antenna operating in three frequency bands: 0.5-1 GHz, 2.8-3.5 GHz, and 4.3-7.3 GHz. To achieve UWB performance, a rectangular patch was employed in conjunction with two inverted L-shaped slots and a rectangular slot. Band notches were also incorporated into the design by using two C-shaped slots at Wi-Fi and WLAN frequencies. However, this layout suffered from low efficiency at lower band and low gain at lower band in addition to its enormous 90x90x0.5 mm<sup>3</sup> size.

In addition to the aforementioned works, others [5-9, 13-16] have reported on MIMO antenna design for Wi-Fi 6 and 5G communications. However, there are also downsides to these works that need to be considered. These include the works' bulkiness, bandwidth restriction, isolation coefficient, efficiency, gain, and missing frequencies. Table 2 provides a comparison of these previous works to the new design proposal.

Based on the reviewed literature, it is clear that a MIMO antenna design is needed that can operate over the frequency ranges needed for Wi-Fi 6 and 5G communications while still providing satisfactory results in terms of bandwidth, mutual coupling, efficiency, gain, and size. In this study, we present such a scheme and show how it improves upon prior proposals.

Using multiple-input multiple-output (MIMO) antennas, which improve wireless communication performance by spatial diversity and multiplexing, is one approach to this issue. MIMO antennas feature numerous radiating elements that may both send and receive data at the same time. However, creating MIMO antennas for Wi-Fi 6 and 5G communications is no easy task due to the need to strike a balance between multiple different aspects of their performance. For example: increasing the number of radiating elements can boost diversity gain and channel capacity, but it can also increase mutual coupling and lower efficiency. The antenna's bandwidth and gain can be compromised when its size is decreased to make it more portable.

Since Wi-Fi 6 and 5G communications both necessitate use of different frequency bands, this paper's primary objective is to offer a novel MIMO antenna design that can cover those spectrums while still providing respectable performance in terms of bandwidth, mutual coupling, efficiency, gain, and size. In order to increase isolation at high frequencies, the suggested design makes use of a coplanar waveguide (CPW) approach that employs four

radiating components with orthogonal polarization and a floating parasitic element. The proposed design additionally employs a notch in the patch based on a split ring resonator (SRR) to block Wi-Fi and WLAN frequencies.

## 2. ANTENNA DESIGN AND ANALYSIS

### 2.1 Single Element Design

A CPW antenna was shown in Fig. 1a, where the ground and radiator were located on the same substrate face. On the ground plate, an elliptical slot E1 is cut with a major radius of mm and a minor radius of mm to form the antenna. The radiator fits into the elliptical slot E and has the following dimensions:  $W \times L$ . The feeding strip line F with width (FW) and length (FI) feeds the radiator. The feeding strip line F then becomes (f) with width (fw) and length (FI) (fl). On the radiators S1 and S2, dual slots have been carved in order to produce greater resonant frequencies. Antenna dimensions  $L_g \times W_g$  were etched with  $\tan \delta = 0.027$ ,  $r = 4.3$ , and thickness = 1.6 mm on the FR-4 substrate. Table 2 shows all the planned antenna's dimensions as a single piece.

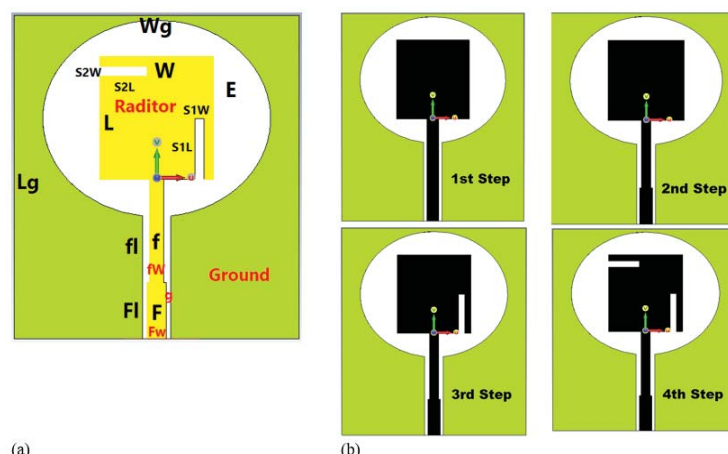


Fig. 1: Proposed antenna as a single element. (a) Single element, (b) Progress of antenna design.

It is clear that four procedures were necessary to create the recommended antenna as a single unit, as depicted in Fig. 1b. While the advancement of the impedance across the four design phases is shown in Fig. 2. The proposed antenna's working range at the first stage is shown by the dotted curve in Fig. 2 as being between 5 and 6.1 GHz. The width of the feeding line was altered at the second step to configure step impedance feeding the radiator, which resulted in the creation of more resonant frequencies that combined to produce a wide operating window of 4-5, 5 GHz, as shown in Fig. 2 (the dashed curve).

More resonant frequencies are produced when the radiator is divided by slot S1 r at the third stage of antenna construction. Thus, the dashed-dotted curve in Fig. 2 shows a large operating band of 4.1–6.1 GHz. As illustrated in the solid curve in Fig. 2, slot S2 added more frequencies to the antenna's impedance bandwidth, resulting in a wide band of 4.1–7 GHz that can handle a variety of wireless communications, including 5G (n78/n79) and Wi-Fi 6.

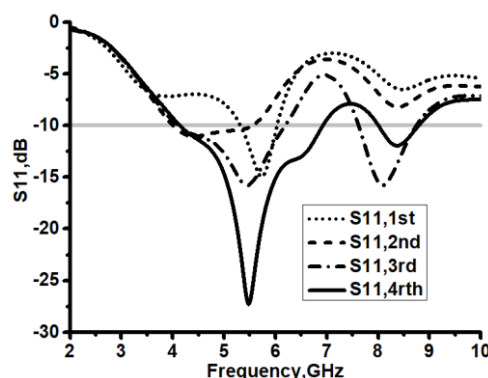


Fig. 2: The progress of the impedance of the antenna.

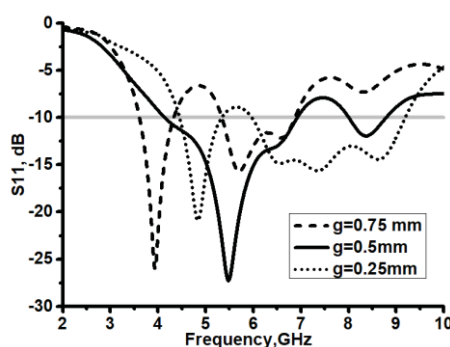


Fig. 3: The reflection coefficient with different gap.

The impact of altering the size of the gap  $g$  between the ground and the feeding line  $F$  on the antenna's impedance is depicted in Fig. 3. The antenna missed a crucial band for Wi-Fi 6 and 5G when  $g=0.75$  mm when twin operational bands were observed (3.5-4.3 GHz and 5.4-6.2 GHz). The values of  $S_{11}$  were indicated by the dotted curve in Fig. 3. It is obvious that the antenna missed the most crucial region of 5-6 GHz when  $g=0.25$  mm. Thus, as seen by the solid curve in Fig. 4, the gap's ideal size is 0.5 mm. The dimensions of the intended antenna as a whole are shown in Table 1.

Table 1: All dimensions of Spanner shaped antenna

Element	mm	Element	mm	Element	mm
$f_1$	5.25	$S_{1w}$	0.5	$L_g$	16
$F_1$	3	$S_{2w}$	0.5	$W_g$	15
$f_w$	0.75	$S_{11}$	2.8	$W$	6
$F_w$	1	$S_{21}$	2.5	$L$	6.5

## 2.2 MIMO Antenna Design

Figure 4 shows the structure of a MIMO antenna with four elements, the four elements etched on the FR-4 substrate with  $W_w=34$  mm,  $L_1=32$  mm and thickness of 1.6 mm. Despite the suggested 4x4 MIMO antenna's small size, the mutual coupling values between all radiating elements were so low that they indicated a significant degree of variety, as seen in Fig. 5. Antennas 1 and 2 and antennas 3 and 4 had mutual coupling values that ranged from -35 dB to -15 dB (see the dotted curve). According to the dashed curve in Fig. 5, the mutual coupling values between the adjacent antennas (antennas 1-3 and antennas 2-4) were less than -20 dB.

The mutual coupling between the crossed antennas (antennas 1-4 and antennas 2-3) was shown as a dashed-dotted curve, and it was discovered to be less than -30 dB during the operating range of 4.1 to 7 GHz.

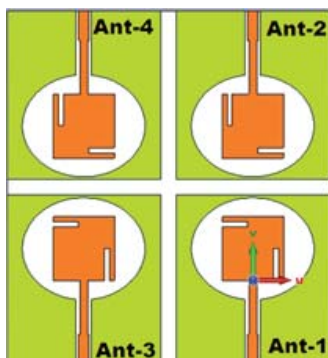


Fig. 4: 4x4 MIMO proposed antenna.

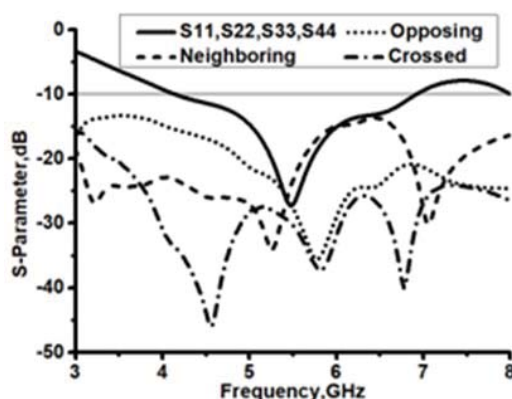


Fig. 5: Simulated mutual coupling between the radiating antennas.

### 3.3 Diversity Performance

The ECC can be calculated by either using three-dimensional (3D) radiation pattern values as in Eq. (1) or by using scattering parameter values as in Eq. (3) [8].

$$ECC_{ij} = \frac{\int_0^{2\pi} \int_0^\pi A_{ij}(\theta, \Phi) \sin \theta d\theta d\Phi}{\sqrt{\int_0^{2\pi} \int_0^\pi A_{ii}(\theta, \Phi) \sin \theta d\theta d\Phi \int_0^{2\pi} \int_0^\pi A_{jj}(\theta, \Phi) \sin \theta d\theta d\Phi}} \quad (1)$$

$$A_{ij} = XPR \cdot E_{\theta,i}(\theta, \Phi) E_{\theta,j}^*(\theta, \Phi) P_\theta(\theta, \Phi) + E_{\phi,i}(\theta, \Phi) E_{\phi,j}^*(\theta, \Phi) P_\phi(\theta, \Phi) \quad (2)$$

$$ECC_{ij} = \frac{|s_{ii}^* s_{ij} + s_{ji}^* s_{jj}|^2}{(1 - |s_{ii}|^2)(1 - |s_{jj}|^2) - |s_{ji}|^2 - |s_{ij}|^2} \quad (3)$$

XPR means the cross-polarization ratio,  $P_\theta(\theta, \Phi)$   $P_\phi(\theta, \Phi)$  represent the incident power spectrum. **In the MIMO system**  $E_{\theta,i}(\theta, \Phi) E_{\theta,j}^*(\theta, \Phi)$  and  $E_{\phi,i}(\theta, \Phi) E_{\phi,j}^*(\theta, \Phi)$  represent the vertical ( $\theta$ ) and horizontal ( $\phi$ ) polarized radiation patterns of the antennas i and j,

respectively. the vertical ( $\Theta$ ) and horizontal ( $\Phi$ ) polarized radiation patterns of the antennas  $i$  and  $j$ , respectively.

The envelope correlation coefficient (ECC) values between the opposite antennas (antennas 1- 2 and antennas 3 - 4) within the operating band of 4.1-7 GHz are less than 0.025 except in the working band of 4.1-7 GHz. The envelope correlation coefficient (ECC) values between the opposing antennas (antennas 1-2 and antennas 3-4) are less than 0.025, with the exception of the range of 4.1–4.2GHz, which reached 0.05 as indicated in the dotted curve in Fig. 6. Every ECC value between the adjacent antennas (antennas 1-3 and antennas 2-4) is less than 0.025 (the dashed black curve). The red dashed-dotted curve in Fig. 6 depicts ECC values that are less than 0.01 for all operational bands for crossed antennas (antennas 1-4 and antennas 2-3). As a result, by positioning the radiating components so that they matched the mutual coupling values shown in Fig. 5, the diversity between all radiating elements of the proposed MIMO antenna is increased.

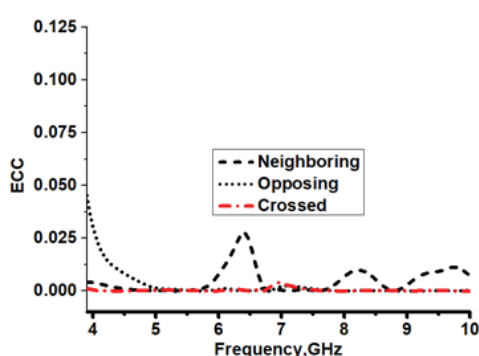


Fig. 6: Simulated ECC between opposite, neighboring, and crossed antennas.

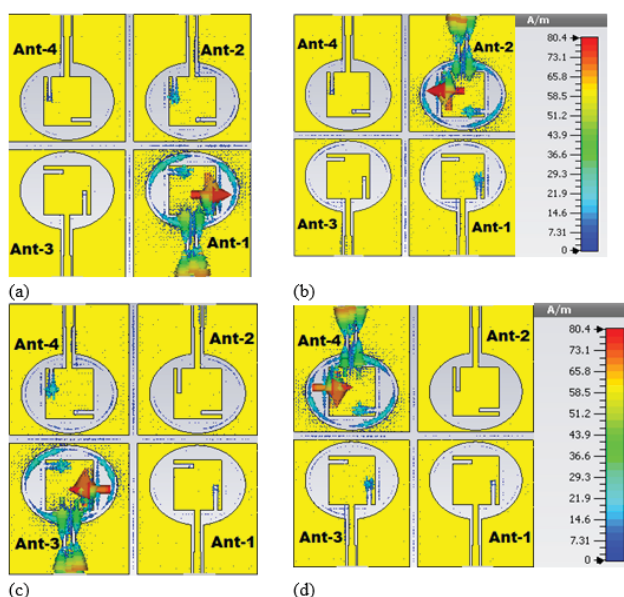


Fig. 7: The surface current distribution at resonant frequency 5.5 GHz for all elements.

## 2.4 Surface Current Distribution

For the surface current distribution at 5.5 GHz, the resonant frequency, is shown in Fig. 7. The current distribution is clearly seen to be largely dispersed along the feeding lines  $F, f$ , and the along the right side of the square radiator when antenna -1 is excited, as shown in Fig. 7a. For the resonant frequency of 5.5 GHz, the length of the surface current route is 22 mm, or

almost half of a wavelength, which accounts for the low reflection coefficient S11 (-28 dB) result. Also, when antenna 1 is turned on, antenna 2 and 3 next to it show very little current distribution and little mutual coupling between the radiating elements, respectively. This suggests that the surface current is low. When antennas 2, 3, and 4 were activated, the same effect was observed (Fig. 7b, 7c and 7d). The analysis of the surface current distribution improved both the ECC values in Fig. 6 and the low mutual coupling value in Fig. 5.

### 3. MEASUREMENTS AND RESULTS

According to the prototype images in Fig. 8, the MIMO antenna's overall dimensions are 34 x 30 x 1.6 mm. Figure 9 shows values for the simulated (solid curves) and measured (dashed-dotted curve) reflection coefficients of the MIMO antenna used in this study. The measured and simulated S-Parameters showed good agreement.

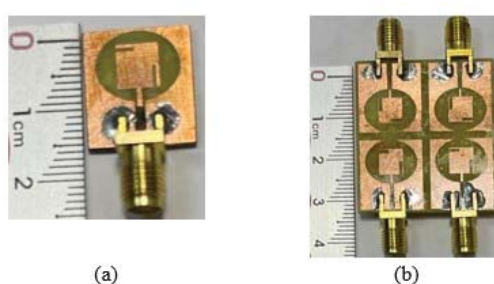


Fig. 8: Prototype photographs. (a) the single element, (b) the MIMO antenna.

For various wireless communications, including 5G (n77/n78/n790, Wi-Fi 6, and (Industrial, Scientific, and medical ISM), this operating band is advantageous. The measured impedance of the antenna (the black dashed-dotted curve) became 4.2-7 GHz. Within the working band, the mutual coupling values between the opposing antennas (antennas 1-2 and antennas 3-4) ranged from -15 dB to -25 dB (the red dashed-dotted curve). The mutual coupling values between the adjacent antennas (antennas 1-3 and antennas 2-4) ranged between -15 dB and -35 dB, according to the blue dashed-dotted curve in Fig. 9, while the mutual coupling values between the crossed antennas (antenna 1-4 and antennas 2-3) oscillated between -25 dB and -60 dB.

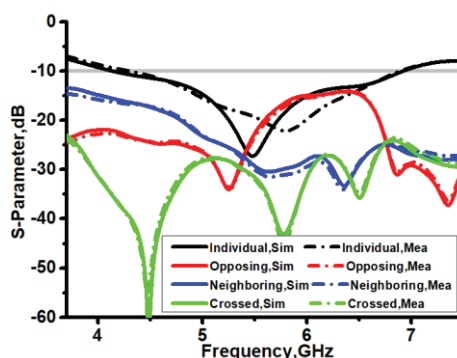


Fig. 9: The measured and simulated values of S-parameters.

By contrasting the SIR with and without the diversity scheme, the diversity gain can be determined. The diversity gain is defined as  $G = 10 \log_{10} (\text{SIR}_d / \text{SIR}_0)$  (dB), where  $\text{SIR}_d$  is the SIR with diversity and  $\text{SIR}_0$  is the SIR without it [20],

or

$$G \text{ (power factor)} = \text{SIR} (d/0) \quad (4)$$

Using numerous antennas at both ends of a MIMO communication link allows for a diversity strategy to be implemented. The channel matrix  $H$ , which represents the coefficients associated with each path between a send antenna and a receive antenna, is critical to the SIR with diversity. Without diversity, the SIR is a function of both the transmit antenna count ( $N_t$ ) and the receive antenna count ( $N_r$ ).

Using the channel matrix  $H$ 's eigenvalues is one technique to get an approximation of the SIR while using diversity. Each spatial subchannel's effective gains in a MIMO system are represented by an eigenvalue. SNR is the signal-to-noise ratio,  $\min(N_t, N_r)$  is the number of spatial subchannels, and  $\min$  is the minimal eigenvalue of  $H$ , hence  $\text{SIR} d$  is a good approximation for the SIR with diversity.

Without diversity, you can use the average power of the channel matrix  $H$  to make an approximation of the SIR. The sum of all pathways' gains in a MIMO system is reflected in the average power.  $\text{SIR} 0 \text{ SNR} \|H\|_F^2 / N_t$  where  $\|H\|_F^2$  is the Frobenius norm of  $H$ , equal to the sum of squares of all elements of  $H$ , and  $N_t$  is the number of samples [20].

The formula for MIMO diversity gain can be derived using these approximations as follows:

The formula for generating  $G$  is as follows:  $G = 10 \log_{10} (\text{SIR} d / \text{SIR} 0) = 10 \log_{10} (\text{SNR} \min(N_t, N_r) \min / \text{SNR} 10 \log_{10} (\min(N_t, N_r) \min N_t / \|H\|_F^2) = 10 \log_{10} (\min(N_t, N_r)) + 10 \log_{10} (\min) + 10 \log_{10} (N_t) - 10 \log_{10} (\|H\|_F^2)$

Power gain from spatial multiplexing is represented by the first term, and it grows as the number of spatial subchannels does. The second term, which represents the power boost from geographical variety, grows larger as the minimum eigenvalue of  $H$  decreases. As more transmit antennas are used, more power is lost, as represented by the third term, which is the result of transmit power split. The average power of  $H$  is shown in the fourth term, which indicates power loss due to channel fading.

We may use some statistical aspects of  $H$  to simplify this calculation if we assume that  $H$  contains independent and identically distributed (i.i.d.) entries with zero mean and unit variance. As an illustration, let's say that:

We can write  $E[\|H\|_F^2] = N_t N_r$  and  $E[\min] = (1 - \gamma) / N_r$ , where  $\gamma$  is Euler's constant.

Based on these assumptions, the typical MIMO diversity gain can be calculated as follows:

The formula for  $E[G]$  is as follows:  $-20 \log_{10} (e) + -20 \log_{10} ((1 - \gamma) / e) + -20 \log_{10} (\min(N_t, N_r) / N_r) = -8.69 + 3.64 + 20 \log_{10}$  The ratio between the minimum and maximum values of  $N_t$  and  $N_r$  is 10.

The average MIMO diversity gain is calculated using this formula and is shown to depend exclusively on the ratio of  $\min(N_t, N_r)$ . Assuming that  $N_t = N_r = N$  leads to the following:

$$E[G] \approx -5.05 \text{ dB} \quad (5)$$

The average diversity gain from using MIMO is less than 1, indicating that this type of system does not always improve diversity. This conclusion, however, relies on an average channel matrix  $H$  that may not accurately portray the channel state. The actual MIMO diversity gain could change depending on how  $H$  is realized and the signal-to-noise ratio (SNR) [20].

Figure 10 displays the proposed MIMO antenna's measured gain (the black circle dots) and efficiency (the blue square points). Gain for the proposed MIMO antenna varies between

3dBi at 4 GHz and 6.dBi at 8 GHz. While the efficiency ratings ranged from 60% to 80%. Thus, during the working spectrum of 4.2-7 GHz, the recommended MIMO antenna had acceptable values of gain and efficiency.

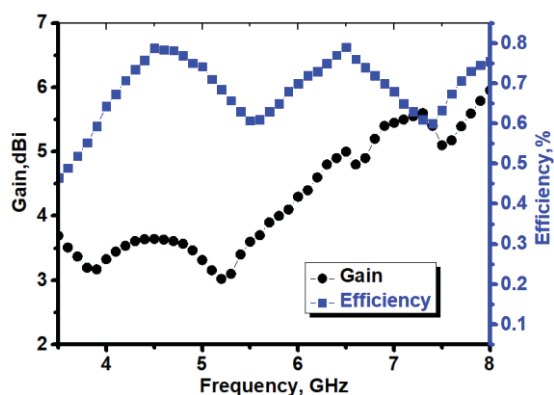


Fig. 10: Measured and simulated values of gain and efficiency for single and MIMO antenna.

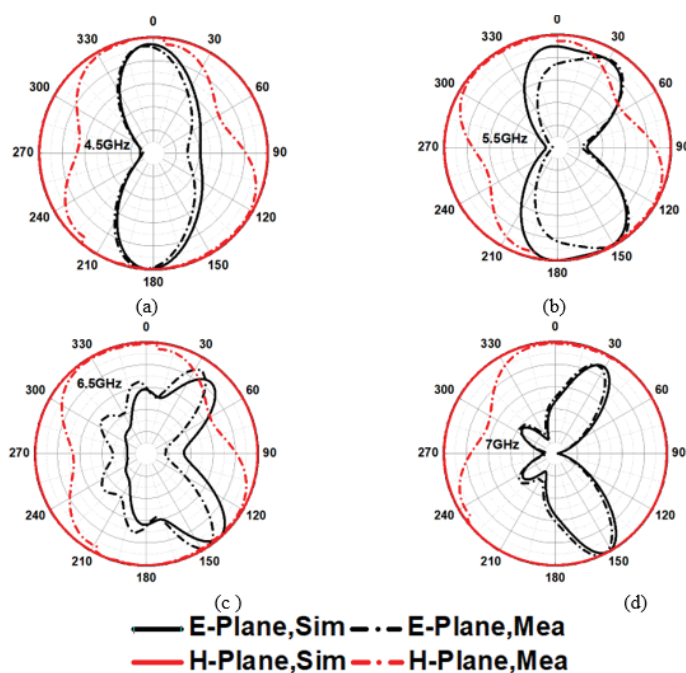


Fig. 11: Simulated and measured radiation patterns.

Displayed in Fig. 11 are the normalized radiation patterns at 4.5, 5.5, 6.5, and 7 GHz. There was a good degree of agreement between the measured patterns and the predicted patterns (the solid curves) (the dashed-dotted curves). All radiation patterns in the H-plane (4.5, 5.5, 6.5, and 7 GHz) are nearly omnidirectional. Figure 11a's black dashed-dotted curve, for example, lobes were identified at angles of 30° and 150° in the E-plane at 5.5 GHz, where the radiation pattern in that region became more directed (the black dashed-dotted curve, Fig. 11b). At the resonance frequency of 6.5 GHz, the black dashed-dotted curve in Fig. 11c displays twin major lobes at angles of 35° and 145° in the E-Plane as well as newly formed side lobes at angles of 350°, 300°, 235°, and 190°. The black dashed-dotted curve in Fig. 11d, at a frequency of 7 GHz, shows dual major lobes at angles of 30° and 150° and dual minor lobes at angles of 240° and 300°.

Table 2 compares the proposed MIMO with other methods evaluated at [7,9, 11-16, 20-22, and 25]. All of the prior works listed in Table 3 were larger than this one, with the exception of [7,9,12, and 14]. The antennas used in the [12] experiment, however, only had a low isolation coefficient (9 dB), which does not support all necessary spectrum. Low isolation coefficients between radiating elements, low-efficiency values, missing the bands 5 GHz and 6 GHz for Wi-Fi 6, and missing the bands n78 and n79 for 5G all characterize the antenna described in [14]. Although having eight elements, the antennas reported in [22 and 25] had low efficiency and gain, especially at lower operating bands, and they failed to receive many of the necessary frequencies for Wi-Fi 6 and 5G.

Consequently, it is simple to state that the MIMO suggested in this study had a low profile, was compact, had minimal mutual coupling between radiation elements, acceptable values for gain, and covered the entire frequency range needed for Wi-Fi 6 and 5G communications.

Table 2: Comparison between proposed MIMO antenna and other related previous works

Ref.	No. El	B.W (GHz)	M. couple.	Effie. %	Gain (dB)	Size (mm <sup>3</sup> )	Weakness
[1]	4	(1.95-2.5) (3.1-3.85) (4.95-6.6)	< -15	60-80	-1 to 2	40×40×1.6	Low values of gain
[2]	4	(3-9)	< -10	60-85	0.5-2	40×40×0.8	Low values of gain
[3]	4	(0.5-1) (2.8-3.5) (4.3-7.3)	< -10	10-90	-0.05-6.9	90×90×0.5	Large size, low efficiency at the lower band, low gain at the lower band
[4]	4	(3.26-3.88)	< -9	60-80	2-3.5	90×35×0.7	Large size, low isolation coefficient, does not support all required spectra
[5]	4	(4.23-4.82)	< -24	55-85	5-6	98×60×3	Large size, did not support 5G (n78, n79) and Wi-Fi 6
[6]	4	(3.4-4.3)	< -9	40-60	–	46×42×1.2	Did not cover all required band, no gain values reported, low efficiency, low isolation coefficient
[7]	4	(1.8-2.5)	< -10	51-73	-2.6 to 2.4	120×60×0.7	Large size, missed many required frequencies, low gain & efficiency at the lower band
[8]	4	(2.15-2.33)	< -11	75-85	–	100×60×0.8	Large size, narrow BW, there are no reports about values of gain and efficiency
[9]	4	(3.5 - 6)	< -10	40-80	–	150×57×7	Large size, missed many required frequencies, gain values not reported
[10]	4	(4.23-4.82)	< -24	55-85	5-6	98×60×3	Large size did not support 5G (n78,n79) and Wi-Fi 6
[11]	8	(3.3 - 5)	< -10	40-70	–	145×70×6	Large size, did not support 5G (n78/n79) and Wi-Fi 6, values of gain are not reported
[12]	8	(4.4 - 5)	< -22	20-55	-2.5 - 5	150×72×1	Large size did not support all required bands, low efficiency, low gain at the lower band
<b>Proposed Design</b>	4	(4.2 - 7)	< -15	60-80	3-6	34×32×1.6	

## 4. CONCLUSIONS

In this paper, we propose a novel MIMO antenna design that achieves high performance in terms of bandwidth, mutual coupling, efficiency, gain, and size while covering the frequency bands necessary for Wi-Fi 6 and 5G communications. In order to increase isolation at high frequencies, the proposed design makes use of a coplanar waveguide (CPW) technique that employs four radiating elements with orthogonal polarization and a floating parasitic element. To further avoid interfering with Wi-Fi and WLAN frequencies, the proposed design incorporates a notch in the patch that is based on a split ring resonator (SRR). The simulation and experimental results show that the proposed antenna has a wide bandwidth and good impedance matching in the frequency range of 4.2 GHz to 7 GHz. In addition to its high efficiency (from 60% to 80%) and high gain (from 3 dB to 6 dB) across the operating band, the proposed antenna also features high isolation (more than -15 dB) between its four radiating elements. In addition, the proposed antenna is smaller than most existing designs, coming in at just  $34 \times 32 \times 1.6 \text{ mm}^3$ . As a result, the proposed antenna is a viable option for both Wi-Fi 6 and 5G networks.

The proposed antenna's performance can be further enhanced by optimizing its design parameters in a future study. We also intend to put the proposed antenna through its paces in real-world scenarios, where its capabilities, diversity gain, and bit error rate will be put to the test. We intend to develop the proposed architecture further to incorporate support for additional wireless communication standards like LTE and WiMAX.

## REFERENCES

- [1] M. A. a. et.al. (2019) Mutual Coupling Suppression Between Two Closely Placed Microstrip Patches Using EM-Bandgap Metamaterial Fractal Loading. *IEEE Access*, 7: 23606 - 23614.
- [2] O. A. S. Amjad Iqbal and A. B. a. A. B. (2018) Metamaterial-Based Highly Isolated MIMO Antenna for Portable Wireless Applications. *MDPI*, 7: 1-8.
- [3] Y. C. Yan Pan, Chang Long Qi, RongLin Li. (2017) Evaluation of dual-polarised triple-band multibeam MIMO antennas for WLAN/WiMAX applications. *IET Microwaves, Antennas & Propagation*, 11: 1469-1475.
- [4] J.-H. Xun, L.-F. S. , W.-R. L. , G.-X. L. , and S. C. (2017) Compact Dual-band Decoupling Structure for Improving Mutual Coupling of Closely Placed PIFAs. *IEEE Antennas and Wireless Propagation Letters*. 16: 1985 - 1989.
- [5] Kumud Ranjan. et.al. (2021) 4-Port MIMO Antenna Using Common Radiator on a Flexible Substrate for Sub-1GHz, Sub-6GHz 5G NR, and Wi-Fi 6 Applications. *IEEE Open Journal of Antennas and Propagation*. 2: 689-701.
- [6] Syed S. Jehangir and Mohammad S. Sharawi. (2020) A Compact Single Layer Four-Port Orthogonally Polarized Yagi-Like MIMO Antenna System. *IEEE Transactions on Antennas and Propagation*, 68: 1985 – 1989.
- [7] Kin-Lu Wong et.al. (2020) Three Wideband Monopolar Patch Antennas in a Y-Shape Structure for 5G Multi-Input- Multi-Output Access Points. *IEEE Antennas and Wireless Propagation Letters*, 19: 393 - 397.
- [8] Yu-Xuan Zhang. et.al. (2020) Low-Profile Wideband Conjoined Open-Slot Antennas Fed by Grounded Coplanar Waveguides for  $4 \times 4$  5G MIMO Operation. *IEEE Transactions on Antennas and Propagation*, 68: 2646 - 2657.
- [9] Hussain R, Sharawi MS. (2017) Annular slot-based miniaturized frequency-agile MIMO antenna system. *IEEE Antennas and Wireless Propagation Letters*, 16: 2489-2492.
- [10] A. T. Abed. (2019) Fractal and Slot Antenna for Portable Communication Devices. Germany. LAP LAMBERT Academic Publication.
- [11] A. T. Abed, et.al. (2021) Challenges and limits of fractal and slot antennas for WLAN, LTE, ISM, and 5G communication: a review paper. *Annals of Telecommunications*, 76(2): 547–557.

- 
- [12] Abed AT. (2020) A Novel Coplanar Antenna Butterfly Structure for Portable Communication Devices: A compact antenna with multioperating bands. *IEEE Antennas and Propagation Magazine*, 62(3): 83-89.
- [13] A. T. Abed. (2019) Compact size MIMO amer fractal slot antenna for 3G, LTE (4G), WLAN, WiMAX, ISM and 5G communications. *IEEE Access*, 7: 125542-125551.
- [14] A. T. Abed. (2020) Novel sunflower MIMO fractal antenna with low mutual coupling and dual wide operating bands. *International Journal of Microwave and Wireless Technologies*, 12(4): 323 – 331.
- [15] Abed AT. (2018) Highly compact size serpentine-shaped multiple-input–multiple-output fractal antenna with CP diversity. *Microwave, Antenna & Propagation*, 12: 636-640.
- [16] Ghalib A, Sharawi MS. (2017) TCM analysis of defected ground structures for MIMO antenna designs in mobile terminals. *IEEE Access* 5: 19680-19692.
- [17] Park S-J, Myung-Hun J, Kyung-Bin B, Dong-Chan K, Laxmikant M. (2017) Performance comparison of  $2 \times 2$  MIMO antenna arrays with different configurations and polarizations in reverberation chamber at millimetre-waveband *Transactions on Antennas and Propagation* 65: 6669-6678.
- [18] Rajkumar S, Narayanaswamy VS, Sharada M and Krishnasamy TS. (2017) Heptaband swastik arm antenna for MIMO applications. *IET Microwaves, Antennas & Propagation* 11: 1255-1261.
- [19] Saeed Khan M, Antonio DC, Adnan I, Raed MS and Dimitris EA. (2017) Ultra-compact dual-polarised UWB MIMO antenna with meandered feeding lines. *IET Microwaves, Antennas and Propagation* 11: 997-1002.
- [20] Jin, Yuzhe. (2007) Capacity, Diversity and Multiplexing Gain for MIMO Channels. *Microwaves* 53: 667-676.

# PHOTOVOLTAIC MODULE TEMPERATURE ESTIMATION MODEL FOR THE ONE-TIME-POINT DAILY ESTIMATION METHOD

KINFATT WONG<sup>1</sup>, ROBIAH AHMAD<sup>1\*</sup>, KUSHSAIRY ABDUL KADIR<sup>2</sup>,  
NORULHUSNA AHMAD<sup>1</sup>

<sup>1</sup>Razak Faculty of Technology and Informatics, University Technology Malaysia, Jalan Sultan Yahya  
Petra, 54100 Kuala Lumpur, Malaysia

<sup>2</sup>British Malaysian Institute, University Kuala Lumpur, Batu 8,  
Jalan Sungai Pusu, 53100 Selangor, Malaysia

\*Corresponding author: robiahahmad@utm.my

(Received: 27 June 2023; Accepted: 3 October 2023; Published on-line: 1 January 2024)

**ABSTRACT:** Based on the hourly solar radiation and ambient temperature, the hourly power estimation work is carried out using the conventional photovoltaic output power (PVOP) estimation model which is used in conjunction with the conventional photovoltaic module temperature (PVMT) estimation model. These hourly data must be processed further before they can be applied to the daily power estimation work. This estimation work is carried out using conventional estimation methods, which are the multiple estimation processes that are complex, time-consuming, and error prone. Therefore, to avoid these shortcomings, one estimation process is designed and used for daily power estimation work. However, this process produces an incorrect daily output power value due to an invalid module temperature value. Thus, a new PVMT estimation model is developed to solve the problem of the invalid value based on a simple linear regression analysis. The performance of the new model has been validated, giving a Normalized Root Mean Squared Error (NRMSE) value of 0.0215 and a Coefficient of Determination (R<sup>2</sup>) value of 0.9862. The correct daily output power value is produced with a valid module temperature value, giving a NRMSE value of 0.0034 and a R<sup>2</sup> value of 0.9999. These results demonstrate the new model's applicability and makes the one estimation process accurate, easy, user-friendly, instantaneous, and direct in daily power estimation work.

**ABSTRAK:** Berdasarkan sinaran matahari dan suhu persekitaran per jam, kerja-kerja anggaran kuasa setiap jam dijalankan menggunakan model anggaran kuasa dari dapatan fotovolt konvensional (PVOP) yang digunakan bersempena dengan model anggaran suhu modul fotovolt konvensional (PVMT). Data per jam ini perlu diproses dengan lebih lanjut sebelum ia boleh digunakan pada kerja anggaran kuasa harian. Kerja-kerja penganggaran ini dijalankan menggunakan kaedah penganggaran konvensional, iaitu proses penganggaran berganda yang kompleks, memakan masa dan mudah ralat. Oleh itu, bagi mengelakkan kekurangan ini, satu proses anggaran direka bentuk dan diguna bagi kerja anggaran kuasa harian. Namun, proses ini menghasilkan nilai dapatan kuasa harian yang salah disebabkan oleh nilai suhu modul tidak sah. Oleh itu, model anggaran PVMT baharu telah dibina bagi menyelesaikan masalah nilai tidak sah berdasarkan analisis mudah regresi linear. Prestasi model baharu telah disahkan, memberi nilai Ralat Punca Min Kuasa Dua Ternormal (NRMSE) sebanyak 0.0215 dan nilai Pekali Penentuan (R<sup>2</sup>) sebanyak 0.9862. Nilai dapatan kuasa harian yang betul dihasilkan dengan nilai suhu modul yang sah, iaitu nilai NRMSE 0.0034 dan R<sup>2</sup> 0.9999. Dapatan ini menunjukkan bahawa kebolegunaan model baharu menjadikan proses anggaran lebih tepat, mudah, mesra pengguna, serta-merta dan terus dalam kerja anggaran kuasa harian.

**KEYWORDS:** *Daily module temperature, daily output power, hour-based climatic data, day-based climatic data, estimation method*

## 1. INTRODUCTION

The conventional PVOP estimation model is used in conjunction with the conventional PVMT estimation model for estimating the possible output power based on the climatic variables of solar radiation and ambient temperature. These conventional PV estimation models are derived based on the PV module performance test under Standard Test Conditions (STC) and Nominal Operating Module Temperature (NOCT). All the relevant data parameters of the models are available from the product specification, as shown in Appendix A [1], except the climatic variable data of solar radiation and ambient temperature. These data can be acquired in hourly, daily, monthly, and yearly data formats from the satellite-based or ground-based climatic measurement centre.

For the conventional PV estimation models, Chang and Zhang [2] stated that it is more suitable to use the hourly climatic data for estimating the hourly output power. In other words, the conventional PV estimation models can be regarded as the hour-based estimation models which estimate the hourly output power using the conventional one-time-point hourly (OTP-H) estimation method. This hourly output power is further used as the primary data to form the daily, monthly, and yearly output power. For instance, Murat Ates and Singh [3] proposed a spreadsheet-based analytical model to simulate the performance of a one-year large-scale rooftop solar PV system based on the daily, monthly, and yearly output power, which are estimated through the sum of the hourly output powers within a day, a month, and a year. Razmjoo *et al.* [4] proposed a techno-economic evaluation of PV-wind-diesel hybrid renewable energies which considered the sum of the PV hourly output powers within a year to estimate the PV yearly output power. As a result, the daily, monthly, and yearly output power estimation method can be considered as the conventional multiple-time-point sum-hourly (MTP-SH) estimation method.

Besides the hourly climatic data, the average hourly climatic data within the sunshine hours of a day, namely the daily hour-average-based climatic data within the sunshine-hours (HAB-SH), is also suitable for the conventional PV estimation models as stated in [5]. Furthermore, Skoplaki and Palyvos [6] provided an overview description of the PV module operating temperature which indicated that the daily HAB-SH climatic data is applicable for the conventional PVMT estimation model to aid in the daily output power estimation. This demonstrates that the daily HAB-SH climatic data has the same function as the hourly data, and hence both can be taken as hour-based climatic data. Since the daily HAB-SH climatic data is exclusively used in the PVMT estimation model, it can be considered as the main hour-based estimation model. Moreover, the estimation method for estimating the daily output power in [6] can be regarded as the conventional multiple-time-point average-hourly (MTP-AH) estimation method, since it deals with the daily HAB-SH climatic data.

According to Chang and Zhang [2], the day-based climatic data is unsuitable for use in the conventional PV estimation models for performing the daily power estimation work. To make the day-based climatic data applicable for the daily power estimation work, a new hour-based estimation model, namely a new PVMT estimation model is proposed. This new model is developed by referring to the references of multiple linear regression analyses which describes the relationship between one dependent variable of PVMT and multiple independent climatic variables. For instance, Tamizhmani *et al.* [7] proposed a prediction model to predict the PVMT based on multiple linear regression analysis, which explores the relationship between the

measured PVMT and the climatic conditions of ambient temperature, wind speed, wind direction, solar radiation, and relative humidity. The model's efficiency depends on the climatic conditions of the site location and the PV technology type. Kamuyu *et al.* [8] proposed a prediction model of PVMT for a floating PV system based on multiple linear regression analyses, which explores the relationship between the measured PVMT and the effect of ambient temperature, solar radiation, wind speed, and water temperature. By the comparison between the predicted and measured values, it gave the corresponding model error range of between 2% and 4%.

Aside from that, new model development is also referred to the references of simple linear regression analysis which describes the relationship between one dependent climatic variable and one independent climatic variable. For instance, Ibrahim *et al.* [9] proposed a prediction model based on simple linear regression analysis, which explores the relationship between solar radiation and ambient temperature. The results elaborated that their relationship is linear and gave an R<sup>2</sup> value of 0.5593. Furthermore, this simple linear regression analysis serves as the foundation for performance validation, which is used to explore the relationship between the same variable that is recorded in two different ways. For instance, Alam *et al.* [10] proposed a dynamic model for a standalone PV distributed power generation system to predict the system's maximum power. The performance of the proposed model is relevant to a simple linear regression analysis, which is used to explore the relationship between the experimental and predicted output power. Li *et al.* [11] proposed a new attenuation hourly solar radiation model based on seasonal and stochastic features. The performance of the proposed model is related to the regression analysis, which explores the relationship between the measured and estimated hourly solar radiation. Cetina-Quiñones *et al.* [12] proposed a machine learning surrogate model of an indirect solar dryer with thermal energy storage. The performance validation was related to the exploration of the relationship between the experimental and predicted temperature.

The new regression coefficients that were used for the new PVMT estimation model are developed based on the climatic variables of solar radiation and ambient temperature. Each of the climatic variables can be recorded in various ways. For instance, Almaktar *et al.* [13] stated that the ambient temperature in their research is recorded as an average of hourly data in 24 hours and within sunshine hours of a day. While the solar radiation is recorded as a sum and average of the hourly data within the sunshine hours of a day. Essentially, this averages of the solar radiation and ambient temperature within the sunshine hours of a day are the uncommon daily climatic variables in the database of NASA [14]. However, Mellit and Pavan [15] specifically mentioned the use of these uncommon daily climatic variables in their research. As a result, these uncommon daily climatic variables, namely daily HAB-SH climatic data, are used as the key climatic variables in this study for developing the new PVMT estimation model, and they are basically the manual-processing hour-based climatic data.

The aim of this study is to develop a new PVMT estimation model based on simple linear regression analysis, which explores the relationship between the hour-based and day-based climatic data to allow the daily power estimation work to be performed with one estimation process, namely the one-time-point daily (OTP-D) estimation method. The following objectives best describe the main contribution of this study:

- To study and analyse the conventional PV estimation models and methods, as well as the ways of recording the climatic variables.
- To develop a new regression coefficient for the new PVMT estimation model to carry out the OTP-D estimation method.

- To validate the new PVMT estimation model with the ground-based climatic dataset using standard statistical indicators, NRMSE and R2.

NRMSE is calculated for the predicted model's degree distributions based on the original, and R2 is used to assess the quality of fit in a linear regression model.

Hence, this new PVMT estimation model is expected to be accurate, easy, user-friendly, instantaneous, and direct for daily power estimation work in the pre-installation phase. The remaining sections of this study are structured as follows: Section 2 discusses the relevant climatic data format. The conventional PV estimation models and methods are presented in section 3. Section 4 describes the research methodology for developing the new PVMT estimation model. The results and discussion for developing the new model are given in Section 5. Section 6 provides the conclusion and recommendations for future development.

## 2. THE RELEVANT CLIMATIC DATA FORMAT

### 2.1. Satellite-based Climatic Data

National Aeronautics and Space Administration (NASA) is a well-known satellite-based climatic measurement centre that provides free climatic datasets of hourly, daily, monthly, and yearly data of solar radiation and ambient temperature [13]. These free datasets are used to analyse the conventional PV estimation methods and develop the new PV estimation model in this study. Moreover, the hourly climatic data is used as the primary data to form the daily, monthly, and yearly climatic data as shown in Table 1 [14]. Solar radiation refers to all-sky surface shortwave downward irradiance in NASA, and the total hourly data within the sunshine hours of a day is daily hour-total-based (HTB-SH) data. The average daily HTB-SH data of a month is monthly day-average-based (DAB-SH) data. The average monthly DAB-SH data for a year is yearly month-average-based (MAB-SH) data. Then, the ambient temperature refers to the temperature at 2 meters in NASA, and the average hourly data in 24 hours of a day is daily hour-average-based (HAB-24) data. The average daily HAB-24 data of a month is monthly day-average-based (DAB-24) data. The average monthly DAB-24 data of a year is yearly month-average-based (MAB-24) data.

Table 1: Example of NASA climatic data

Variable	Data Format	Description
Ambient Temperature	Daily HAB-24	Average hourly data in 24 hours of a day
	Monthly DAB-24	Average daily HAB-24 data of a month
	Yearly MAB-24	Average monthly DAB-24 data of a year
Solar Radiation	Daily HTB-SH	Total hourly data within the sunshine hours of a day
	Monthly DAB-SH	Average daily HTB-SH data of a month
	Yearly MAB-SH	Average monthly DAB-SH data for a year

### 2.2. Ground-based Climatic Data

Ground-based climatic measurement centres are exceedingly expensive to establish; there are not many of them worldwide [13]. Although ground-based data have the same climatic data formats as NASA satellite-based data, they have different measured values. Therefore, the ground-based climatic datasets will be used as the testing datasets in this study for a new estimation model validation. These datasets are measured according to the standard of Typical Meteorological Year Three (TMY3) Dataset [16] at Tasik Banding, Malaysia in 2005, with a Latitude of 5.554 and a Longitude of 101.337 as shown in Fig. 1.



Fig. 1. Map of Tasik Banding, Malaysia

### 2.3. Hour-based and Day-based Climatic Data

According to NASA [14], the daily HAB-24 ambient temperature data and daily HTB-SH solar radiation data are the day-based data, and the hourly data of ambient temperature and solar radiation are the hour-based data as shown in Table 2. On the other hand, the uncommon daily HAB-SH ambient temperature and solar radiation data for NASA are the manual-processing data. According to the principle presented in [5] and [6], the manual-processing daily HAB-SH climatic data have the same function as the hourly climatic data and are considered as hour-based climatic data that can be applied into the hour-based estimation model, namely the PVMT estimation model as stated in [2].

Table 2: Hour-based and day-based climatic data

Climatic Variable	Hour-based Data		Day-based Data
	NASA	Manual-processing	NASA
Ambient Temperature	Hourly	Daily HAB-SH	Daily HAB-24
Solar Radiation	Hourly	Daily HAB-SH	Daily HTB-SH

The difference between the manual-processing daily HAB-SH ambient temperature and the NASA daily HAB-24 ambient temperature is that the former does not include the data records during the night-time. While for the manual-processing daily HAB-SH solar radiation and the NASA daily HTB-SH solar radiation, the former does not sum up all the hourly data within the sunshine hours of a day.

## 3. PV ESTIMATION MODELS AND METHODS

### 3.1. Conventional PV Estimation Models

One of the conventional PVOP estimation models is given as [4][17]

$$P_{pv} = P_{max}(G/G_{STC})[1 + \beta_p(T_m - T_{m\_STC})] \quad (1)$$

where  $G$  is the solar radiation ( $W/m^2$ ) and the PVMT estimation model,  $T_m$  is defined as [17]

$$T_m = T_a + (T_{NOCT} - T_{a\_NOCT}) G/G_{NOCT} \quad (2)$$

where  $T_a$  is the ambient temperature ( $^{\circ}C$ ). These conventional estimation models are used in a variety of estimation methods to produce a variety of estimation results for further analysis.

### 3.2. Conventional PV Estimation Methods

#### 3.2.1. OTP-H Estimation Method

For the conventional OTP-H estimation method, the hourly climatic data of solar radiation,  $G_h$  and ambient temperature,  $T_{a\_h}$ , which are extracted directly from NASA, will be applied into Eq. (2) for estimating the hourly module temperature [18],  $T_{m\_h\_1H}$

$$T_{m\_h\_1H} = T_{a\_h} + (T_{NOCT} - T_{a\_NOCT}) G_h / G_{NOCT} \quad (3)$$

$G_h$  will be further applied into Eq. (1) for estimating the hourly output power [17],  $P_{pv\_h\_1H}$

$$P_{pv\_h\_1H} = P_{max}(G_h / G_{STC}) [1 + \beta_p (T_{m\_h\_1H} - T_{m\_STC})] \quad (4)$$

### 3.2.2. Multiple-time-points Daily (MTP-D) Estimation Method

The conventional MTP-D estimation method is referring to the MTP-SH and MTP-AH estimation methods. These estimation methods perform the daily power estimation work based on the hour-based climatic data as shown in Table 3. Moreover, they are the estimation method that involved multiple processes in estimating the daily output power.

Table 3: Conventional MTP-D estimation methods

Estimation Method	Description	Input	Output	Reference
MTP-SH Estimation Method	Sum of hourly output powers	$G_h, T_{a\_h}, H_s$	$P_{pv\_d\_sum}$	[3, 4]
MTP-AH Estimation Method	Average of hourly climatic data	$G_{d\_HAB\_SH}, H_s$ $T_{a\_d\_HAB\_SH}$	$T_{m\_h\_avg}$ $P_{pv\_d\_avg}$	[5, 6]

The MTP-SH estimation method sums up each  $P_{pv\_h\_1H}$  within the sunshine hours of a day,  $H_s$  to produce the daily output power, which is given as [3]

$$P_{pv\_d\_sum} = \sum_{i=1}^{H_s} P_{pv\_h\_1H} \quad (5)$$

$H_s$  is a manual-processing climatic variable as well. It will be used in conjunction with the manual-processing data of daily HAB-SH solar radiation,  $G_{d\_HAB\_SH}$  and daily HAB-SH ambient temperature,  $T_{a\_d\_HAB\_SH}$  for performing the daily power estimation work with the MTP-AH estimation method. This method is first using  $G_{d\_HAB\_SH}$  and  $T_{a\_d\_HAB\_SH}$  to produce the daily HAB-SH module temperature,  $T_{m\_h\_avg}$ , which is defined as [6]

$$T_{m\_h\_avg} = T_{a\_d\_HAB\_SH} + (T_{NOCT} - T_{a\_NOCT}) G_{d\_HAB\_SH} / G_{NOCT} \quad (6)$$

$T_{m\_h\_avg}$  is an hour-based module temperature since it deals with the hour-based climatic data, namely daily HAB-SH climatic data. Then, it will be applied in conjunction with  $G_{d\_HAB\_SH}$  into Eq. (1) to produce the daily HAB-SH output power,  $P_{pv\_h\_avg}$

$$P_{pv\_h\_avg} = P_{max}(G_{d\_HAB\_SH} / G_{STC}) [1 + \beta_p (T_{m\_h\_avg} - T_{c\_STC})] \quad (7)$$

$P_{pv\_h\_avg}$  is also an hour-based output power which is then multiplied by  $H_s$  to produce the daily output power,  $P_{pv\_d\_avg}$

$$P_{pv\_d\_avg} = P_{pv\_h\_avg} \times H_s \quad (8)$$

The concept of  $P_{pv\_d\_avg}$  adheres to the multiplier principle of Peak Sun Hour (PSH) [13].

### 3.3. Linear Regression Model

The number of independent variables in a simple and multiple linear regression analysis will differ. More than one independent variable will be included in the multiple linear regression analysis. For instance, the regression model includes five independent climatic variables in the proposed model, which is given as [7]

$$T_{m\_MLR\_1} = a_1 G + a_2 T_a + a_3 v_w + a_4 v_{dir} + a_5 RH + a_6 \quad (9)$$

where  $a_1, a_2, a_3, a_4, a_5$  and  $a_6$  are the regression coefficients,  $v_w$  is the wind speed (m/s),  $v_{dir}$  is the wind direction ( $^\circ$ ), and  $RH$  is the relative humidity (%). Besides, Kamuyu *et al.* propose the regression model with four independent climatic variables, which is defined as [8]

$$T_{m\_MLR\_2} = a_1G + a_2T_a + a_3v_w + a_4T_w + a_5 \quad (10)$$

where  $T_w$  is the water temperature ( $^\circ\text{C}$ ).

On the other hand, the simple linear regression analysis will include only one independent variable. For instance, Ibrahim *et al.* proposed a model that explores the relationship between two different climatic variables, the model is given as [9]

$$G = mT_a + c \quad (11)$$

where  $m$  and  $c$  are the regression coefficients of the slope and intercept. Moreover, Alam *et al.* proposed a model that explores the relationship between the same power variables, but recorded per different methods, the model is defined as [10]

$$P_{pv\_measured} = mP_{pv\_estimated} + c \quad (12)$$

where  $P_{pv\_measured}$  is the measured output power (W) and  $P_{pv\_estimated}$  is the estimated output power (W).

#### 4. RESEARCH METHODOLOGY

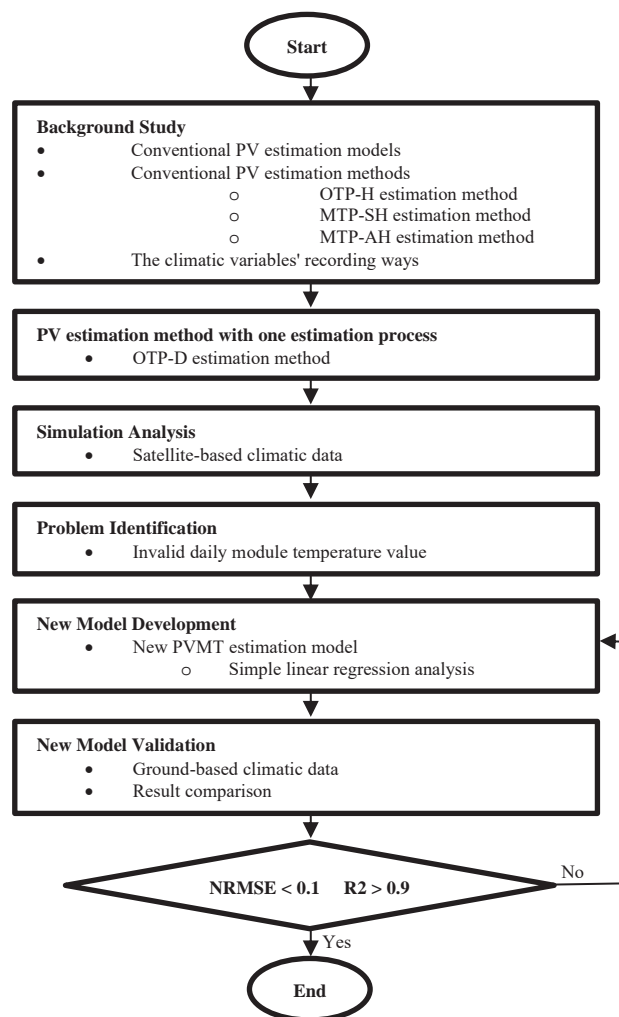


Fig. 2. Research methodology

The flow chart of the research methodology of this study is shown in Fig. 2. The background study focuses on the basic principles of the conventional PV estimation models and methods as well as the ways for recording the climatic variables. According to these studies, the conventional daily power estimation works involve multiple estimation processes in estimating the daily output power. Since the multiple estimation processes is complex, time-consuming, and error-prone, a one estimation process, namely the OTP-D estimation method, is designed and used. This method uses the day-based climatic data directly to perform the daily power estimation work. It is then analysed further in a simulation experiment using satellite-based climatic datasets. However, the experiment results reveal that the problem of the invalid daily module temperature value in the OTP-D estimation method. This is because the day-based climatic data is not suitable to use in the hour-based estimation model, namely the PVMT estimation model. Thus, a new PVMT estimation model is developed based on the simple linear regression analysis to solve the problem of the invalid daily module temperature value. This new model is validated using the same simulation experiment but based on the ground-based climatic datasets. It compares the estimation results that were produced by the MTP-AH estimation method and the OTP-D estimation method with the new PVMT estimation model. The result comparison demonstrates the new model's applicability in the OTP-D estimation method because it gives the NRMSE value less than 0.1 and the R2 value more than 0.9. In other words, the OTP-D estimation method with the new PVMT estimation model is compatible with the conventional MTP-AH estimation method.

#### 4.1. OTP-D Estimation Method

For the OTP-D estimation method, the day-based climatic data, daily HAB-24 ambient temperature data,  $T_{a\_d\_HAB\_24}$  and daily HTB-SH solar radiation data,  $G_{d\_HTB\_SH}$  which extracted directly from NASA will be applied into Eq. (2) for estimating the daily module temperature,  $T_{m\_d\_1D}$

$$T_{m\_d\_1D} = T_{a\_d\_HAB\_24} + (T_{NOCT} - T_{a\_NOCT}) G_{d\_HTB\_SH} / G_{NOCT} \quad (13)$$

$G_{d\_HTB\_SH}$  will be further applied into Eq. (1) for estimating the daily output power,  $P_{pv\_d\_1D}$

$$P_{pv\_d\_1D} = P_{max} (G_{d\_HTB\_SH} / G_{STC}) [1 + \beta_p (T_{m\_d\_1D} - T_{m\_STC})] \quad (14)$$

However,  $T_{a\_d\_HAB\_24}$  and  $G_{d\_HTB\_SH}$  in  $T_{m\_d\_1D}$  produce an invalid daily module temperature value, resulting in an incorrect daily output power value. This invalid value refers to the value that exceeded the operational module temperature's maximum stated value in the data specification sheet [1], and it differs greatly from the module temperature value estimated by the conventional MTP-AH estimation method.

#### 4.2. New Model Development

The problem of the invalid daily module temperature value is solved by developing a new PVMT estimation model for the OTP-D estimation method. This new model is derived from the simple linear regression analysis, which explores the relationship between the hour-based and day-based climatic data, namely the suitable and unsuitable climatic data. The hour-based climatic data refers to the uncommon and manual-processing climatic data,  $T_{a\_d\_HAB\_SH}$  and  $G_{d\_HAB\_SH}$  as presented in Eq. (6) which are used in the conventional MTP-AH estimation method. While the day-based climatic data refer to the NASA satellite-based climatic data,  $T_{a\_d\_HAB\_24}$  and  $G_{d\_HTB\_SH}$  as presented in Eq. (13) which are used in the OTP-D estimation method.

Based on the principle as presented in [10–12], the new regression coefficient for ambient temperature is derived based on the exploration of the relationship between  $T_{a,d\_HAB\_SH}$  and  $T_{a,d\_HAB\_24}$

$$T_{a,d\_HAB\_SH} = m_T T_{a,d\_HAB\_24} + c_T \quad (15)$$

where  $m_T$  and  $c_T$  are the regression coefficients of slope and intercept for ambient temperature. While the new regression coefficient for solar radiation is derived based on the exploration of the relationship between  $G_{d\_HAB\_DH}$  and  $G_{d\_HTB\_DH}$

$$G_{d\_HAB\_SH} = m_G G_{d\_HTB\_SH} + c_G \quad (16)$$

where  $m_G$  and  $c_G$  are the regression coefficients of slope and intercept for solar radiation. Because of these regression coefficients, the day-based climatic data has same function as the hour-based climatic data and is suitable for the PVMT estimation model. Then, the new PVMT estimation model,  $T_{m,d\_1D\_new}$  is proposed as

$$T_{m,d\_1D\_new} = (m_T T_{a,d\_HAB\_24} + c_T) + (T_{NOCT} - T_{a\_NOCT}) (m_G G_{d\_HTB\_SH} + c_G) / G_{NOCT} \quad (17)$$

to aid in the daily output power estimation.

#### 4.2.1. Simple Linear Regression Analysis

The new regression coefficients,  $m_T$  and  $c_T$ ,  $m_G$  and  $c_G$  are not derived from the simple linear regression analysis rather than the multiple linear regression analysis. This is due to the problem of invalid values, which is caused solely by the unsuitable climatic data format. So, the simple linear regression analysis explores the relationship between the same climatic variable but recorded in two different ways, referring to the suitable and unsuitable climatic variables. This analysis is carried out in accordance with the principle stated in [10–12]. These regression coefficients can lead to the main structure of the PVMT estimation model to remain constant, with no significant impact on future development. Therefore, the new PVMT estimation model is a combination model to some extent, where the conventional PVMT estimation model and regression model are combined.

#### 4.2.2. Regression Coefficient

For the OTP-D estimation method, the PVMT estimation model, as presented in Eq. (13), needs the regression coefficients for  $T_{a,d\_HAB\_24}$  and  $G_{d\_HTB\_SH}$  to avoid the problem of the invalid daily module temperature value. However,  $G_{d\_HTB\_SH}$  in the PVOP estimation model, as presented in Eq. (14), is not required. This is because  $G_{d\_HTB\_SH}$  adheres to the multiplier principle of Peak Sun Hour (PSH), which makes Eq. (14) the same as Eq. (7), the principle is given as [13]

$$G_{d\_HTB\_SH} = G_{d\_HAB\_SH} \times H_s \quad (18)$$

In other words, multiplying  $H_s$  in Eq. (8) by  $G_{d\_HAB\_SH}$  in Eq. (7) will make Eq. (7) become Eq. (14). Furthermore, when both are given the same daily module temperature value, they will produce the same daily output power value.

### 4.3. Model validation

In this study, the one-year NASA satellite-based climatic datasets are used for analysing the conventional PV estimation methods. Moreover, they are also used as the training dataset for developing the new PVMT estimation model for the OTP-D estimation method. While the one-year ground-based climatic datasets are used as the testing datasets for the validation of the new PVMT estimation model. Although the ground-based and satellite-based climatic data

have the same data format, they have different measured values. Furthermore, the length of one year dataset in this study is set according to the standard data length of a long-term experiment [19], which is acceptable for PV performance planning, managing, and monitoring. Based on the ground-based climatic datasets, the performance of the new PVMT estimation model, as presented in Eq. (17), for the OTP-D estimation method is validated by the standard statistical indicators as follows.

The Root Mean Squared Error (RMSE) is the typically used standard deviation of the estimation errors, which is defined as [2]

$$RMSE = \sqrt{\sum_{i=1}^N (OTP_i - MTP_i)^2 / N} \quad (19)$$

where  $OTP_i$  is the estimated value which produced based on the OTP-D estimation method with the new PVMT estimation model,  $MTP_i$  is the estimated value which produced based on the conventional MTP-AH estimation method,  $N$  is the total number of days per year. It can be further interpreted as NRMSE, in which it will provide the normalized value from zero to one, which is given as [11]

$$NRMSE = RMSE / MTP_{mean} \quad (20)$$

where  $MTP_{mean}$  is the mean value of  $MTP_i$ . When the proposed model is with better performance, the NRMSE value is closer to zero but not more than 0.1 [20]. R2 is used to measure the relationship between two datasets which also provides the value from zero to one, which is expressed as [20]

$$R^2 = 1 - \sum_{i=1}^N (MTP_i - OTP_i)^2 / \sum_{i=1}^N (MTP_i - MTP_{mean})^2 \quad (21)$$

When the proposed model is more efficient, the R2 value is closer to one [20].

## 5. Result and Discussion

Based on the NASA hour-based climatic data, the conventional MTP-SH and MTP-AH estimation methods produce the daily output power,  $P_{pv\_d\_sum}$  and  $P_{pv\_d\_avg}$  which are approximately equal, as shown in Fig. 3. Since all the values differ between  $P_{pv\_d\_sum}$  and  $P_{pv\_d\_avg}$  their range is from 0.3135% to 3.6379%.

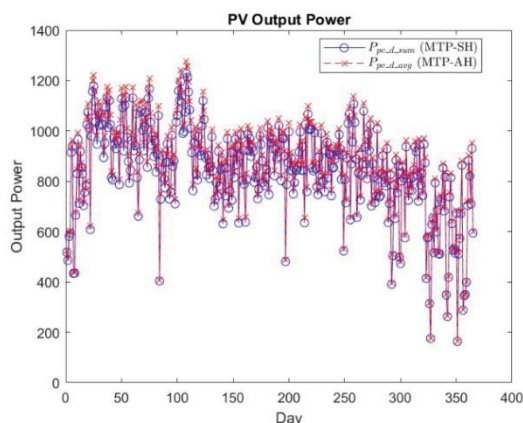


Fig. 3. Daily output power in 2005: MTP-SH and MTP-AH estimation methods

However, when  $P_{pv\_d\_sum}$  and  $P_{pv\_d\_avg}$  are compared to the daily output power,  $P_{pv\_d\_1D}$ , produced using the NASA day-based climatic data and OTP-D estimation method, all  $P_{pv\_d\_1D}$  in a year are given a lower output power value as shown in Fig. 4. According to the values

comparison, all the values of  $P_{pv\_d\_1D}$  range from 9.4809% to 89.329% lower than  $P_{pv\_d\_sum}$  and range from 9.814% to 89.7172% lower than  $P_{pv\_d\_avg}$ . This is due to the PVMT estimation model for the OTP-D estimation method produces an extremely high value of the daily module temperature,  $T_{m\_d\_1D}$ , which can far exceed the maximum stated value of the operational module temperature, 85 °C and has a different module temperature value than the conventional MTP-AH estimation method,  $T_{m\_h\_avg}$  as shown in Fig. 5. Based on the values comparison, all the values of  $T_{m\_d\_1D}$  range from 48.3953% to 82.4163% higher than  $T_{m\_h\_avg}$ . In other words,  $T_{m\_d\_1D}$  value is clearly an invalid daily module temperature value resulting in an incorrect  $P_{pv\_d\_1D}$  value.

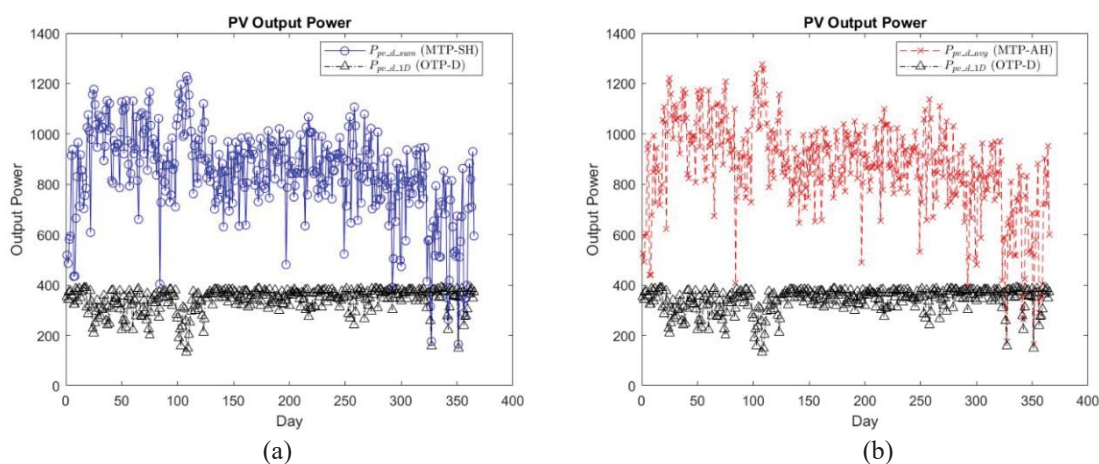


Fig. 4. Daily output power in 2005: (a) MTP-SH and OTP-D estimation methods. (b) MTP-AH and OTP-D estimation methods.

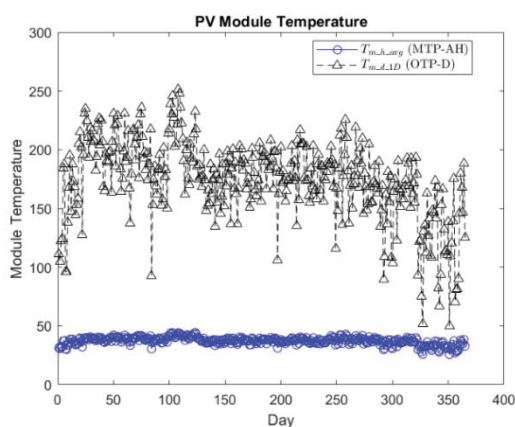


Fig. 5. Daily module temperature in 2005: MTP-AH and OTP-D estimation methods

The problem of the invalid  $T_{m\_d\_1D}$  value for the OTP-D estimation method is solved by developing a new PVMT estimation model based on the simple linear regression analysis. This analysis explores the relationship between the climatic variables of the solar radiation,  $G_{d\_HAB\_DH}$  and  $G_{d\_HTB\_DH}$ , as well as between the ambient temperature variables,  $T_{a\_d\_HAB\_SH}$  and  $T_{a\_d\_HAB\_24}$  as shown in Fig. 6. The developed regression coefficients are derived based on the training datasets from NASA. These datasets are the satellite-based climatic datasets with different measured values from the ground-based climatic datasets, as shown in Fig. 7. In terms of solar radiation and ambient temperature data, the ground-based climatic data mostly have higher measured values than the NASA satellite-based climatic data. Thus, the ground-based

datasets can be used as the testing datasets for new model validation. Since all the values difference between  $G_{d\_HAB\_DH}$  and  $G_{d\_HTB\_DH}$  range from 0.0453% to 88.2497%, while for  $T_{a\_d\_HAB\_SH}$  and  $T_{a\_d\_HAB\_24}$  range from 0.0364% to 26.5204%.

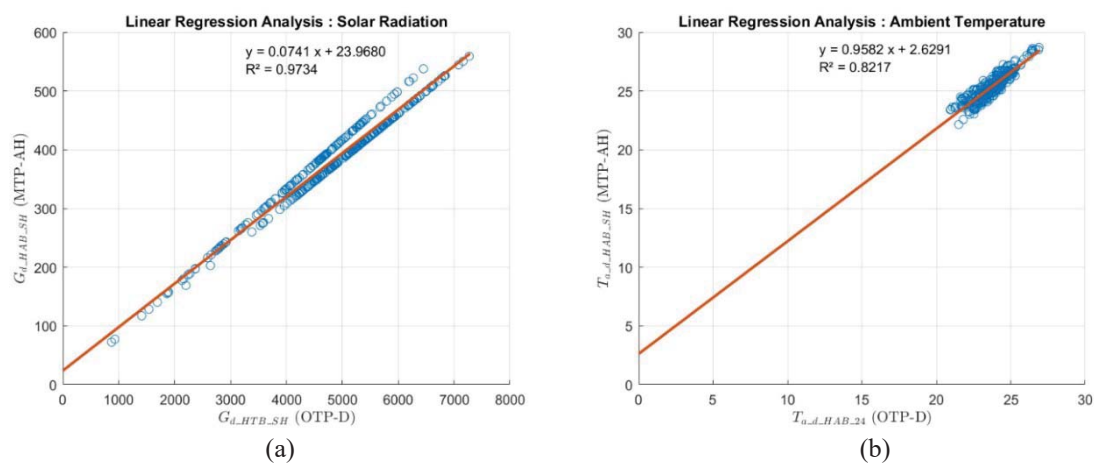


Fig. 6. Linear regression Analysis: (a) Solar radiation. (b) Ambient temperature.

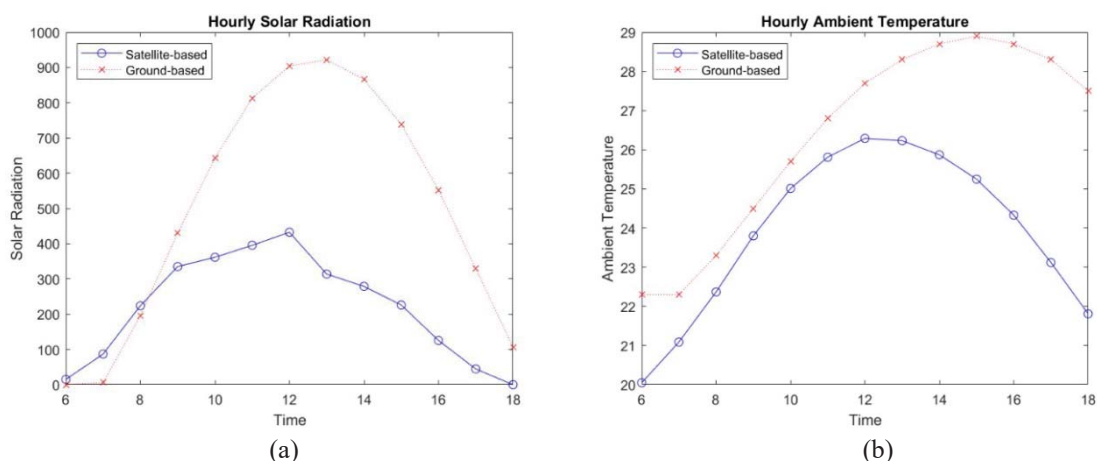


Fig. 7. Example of satellite-based and ground-based climatic data on 1/1/2005: (a) Solar radiation. (b) Ambient temperature.

Based on the ground-based data of solar radiation and ambient temperature, the day-based data are used in the OTP-D estimation method with the new PVMT estimation model, while the hour-based data are used in the conventional MTP-AH estimation method for further results comparison. According to the results comparison, all the value differences between  $T_{m\_d\_1D\_new}$  and  $T_{m\_h\_avg}$  range from 0.0024% to 4.6061%, as shown in Fig. 8. The NRMSE value is 0.0215 and R2 value is 0.9862 as shown in Table 4. When  $T_{m\_d\_1D\_new}$  returns the valid daily module temperature value,  $P_{pv\_d\_1D}$  returns the correct daily output power value. Consequently, all the values difference between  $P_{pv\_d\_1D}$  and  $P_{pv\_d\_avg}$  range from 0.0002% to 0.8057% as shown in Fig. 9. The NRMSE value is 0.0034 and R2 value is 0.9999.

Aside from that, when the results of the OTP-D estimation method which with the new PVMT estimation model are compared to the MTP-SH estimation method, all the value differences between  $P_{pv\_d\_1D}$  and  $P_{pv\_d\_sum}$  range from 0.0914% to 4.0206%, as shown in Fig. 10. The NRMSE value is 0.0318 and R2 value is 0.9997. Due to development of the new PVMT

estimation model, the OTP-D estimation method can produce the daily module temperature value that are approximately equal to the MTP-AH and MTP-SH estimation methods.

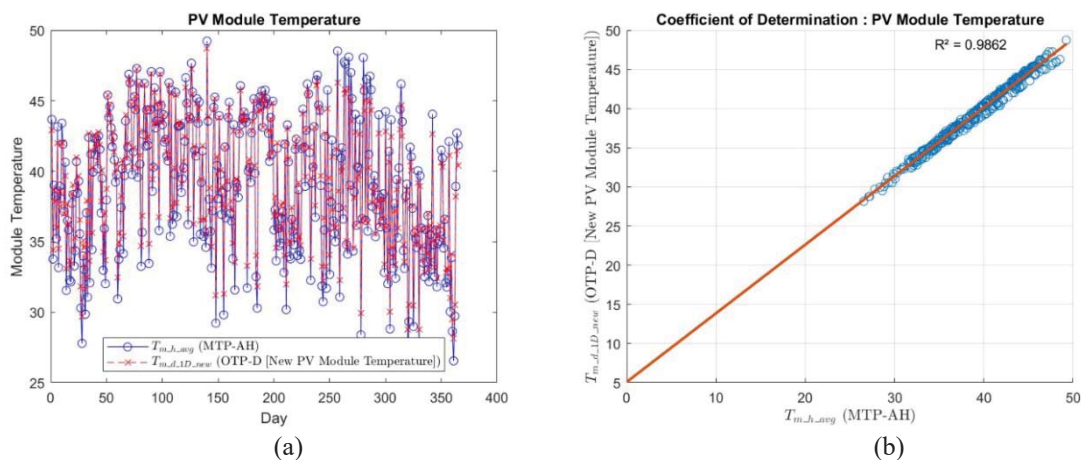


Fig. 8. PVMT comparison of MTP-AH and OTP-D (with the new PVMT estimation model): (a) Linear plot graph. (b) Scatter plot graph.

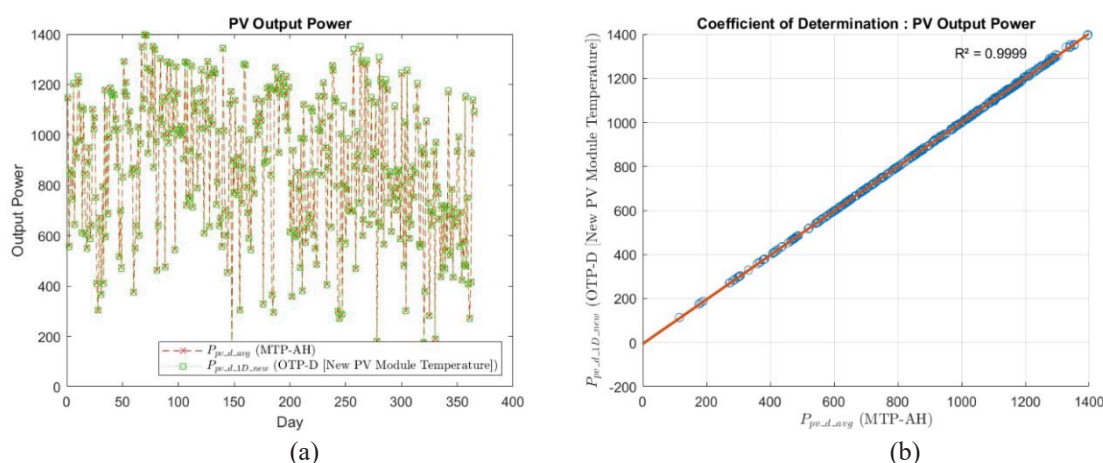


Fig. 9. PVOP comparison of MTP-AH and OTP-D (with the new PVMT estimation model): (a) Linear plot graph. (b) Scatter plot graph.

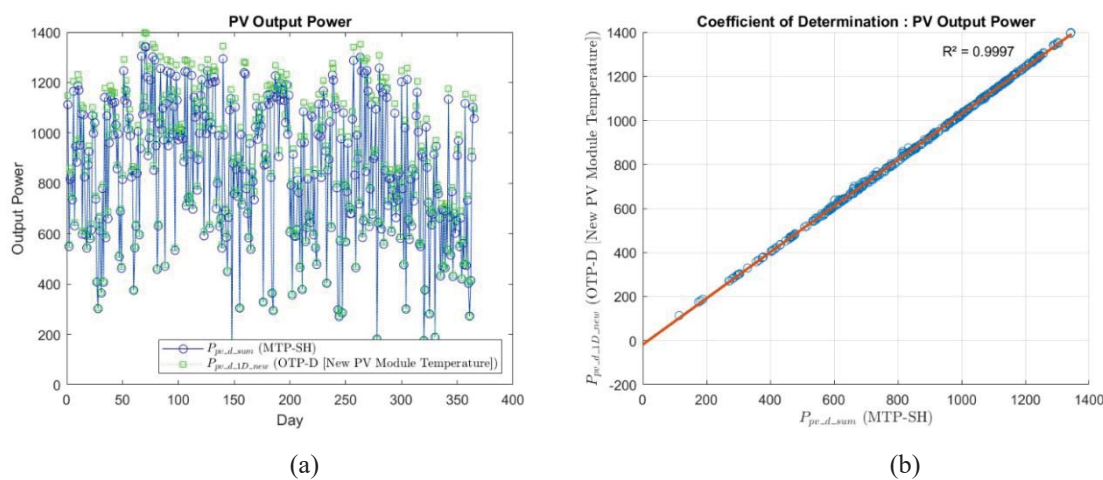


Fig. 10. PVOP comparison of the MTP-SH and OTP-D (with the new PVMT estimation model): (a) Linear plot graph. (b) Scatter plot graph.

Table 4: New model validation

Standard Indicator	PVMT (MTP-AH)	PVOP (MTP-AH)	PVOP (MTP-SH)
RMSE	0.8389	2.9834	27.134
NRMSE	0.0215	0.0034	0.0318
R2	0.9862	0.9999	0.9997

## 6. CONCLUSION AND RECOMMENDATION

The conventional PVOP estimation model and PVMT estimation model are the hour-based estimation models derived from the PV module performance test under STC and NOCT. In the OTP-H estimation method, the PVOP estimation model is used in conjunction with the PVMT estimation model to estimate the hourly output power based on the hourly solar radiation and hourly ambient temperature. The hourly output power is then used to estimate the daily output power using the conventional MTP-SH estimation method. While the hourly solar radiation and hourly ambient temperature are processed before being used in the conventional MTP-AH estimation method to estimate the daily output power. Since both MTP-SH and MTP-AH estimation methods involve multiple estimation processes in the hourly data, producing the daily output power becomes complex, time-consuming, and error-prone. Therefore, to avoid these shortcomings, a one estimation process is designed and used to reduce the process of estimating the daily output power. This process directly uses the day-based climatic data to perform the daily power estimation work, but it resulted in an incorrect daily output power value due to an invalid module temperature value. Thus, a new PVMT estimation model for the OTP-D estimation method is developed to solve the problem of invalid values. This new model is derived from the simple linear regression, which explores the relationship between the hour-based and day-based climatic data to develop a new regression coefficient for daily solar radiation and daily ambient temperature. The performance of the new model in the OTP-D estimation method is validated using the one-year ground-based climatic data, which has higher measured values than the NASA satellite-based climatic data. When the new and conventional PVMT estimation models' results are compared, the NRMSE value is 0.0215 and the R2 value is 0.9862. With the valid module temperature, the daily output powers produced by the OTP-D estimation method are compared to the MTP-AH estimation method, and the NRMSE value of 0.0034 and the R2 value of 0.9999 are obtained. The comparison of the results shows that the new model's applicability makes the OTP-D estimation method accurate, easy, user-friendly, instantaneous, and direct in daily power estimation work. The next step is to develop a new regression coefficient for the month-based and year-based climatic data to perform the monthly and yearly power estimation work.

## ACKNOWLEDGEMENT

The author would like to acknowledge the Government of Malaysia under Fundamental Research Grant Scheme (FRGS) Vote FRGS/1/2019/TK10/UTM/02/16 by the Ministry of High Education (MOHE) and Trans-Disciplinary Research (TDR) grant Vote Q.K130000.3556.05G82 by University Technology Malaysia (UTM) for financial support of this research. The authors would also like to acknowledge British Malaysian Institute, University Kuala Lumpur, (BMI, UniKL) for the technical support throughout the research.

## REFERENCES

- [1] (2013). Solar System Panel Specifications (TSM-190 DC/DA01A) by Trina Solar. [chrome-extension://efaidnbmnnnibpcajpcggleflefndmkaj/https://static.trinasolar.com/sites/default/files/Comax\\_DC01A\\_Datasheet\\_Feb13\\_EN.pdf](chrome-extension://efaidnbmnnnibpcajpcggleflefndmkaj/https://static.trinasolar.com/sites/default/files/Comax_DC01A_Datasheet_Feb13_EN.pdf). Accessed 3 Jan 2023
- [2] Chang K, and Zhang Q (2020). Development of a solar radiation model considering the hourly sunshine duration for all-sky conditions – A case study for Beijing, China. *Atmos Environ*, 234(February):117617. <https://doi.org/10.1016/j.atmosenv.2020.117617>
- [3] Murat Ates A, and Singh H (2021). Rooftop solar Photovoltaic (PV) plant – One year measured performance and simulations. *J King Saud Univ - Sci*, 33(3):101361. <https://doi.org/10.1016/j.jksus.2021.101361>
- [4] Razmjoo A, Shirmohammadi R, Davarpanah A, and Pourfayaz F (2019). Stand-alone hybrid energy systems for remote area power generation. *Energy Reports*, 5231–241. <https://doi.org/10.1016/j.egy.2019.01.010>
- [5] (2013). Grid-Connected Solar PV Systems: Design Guidelines for Accredited Installers by Clean Energy Council
- [6] Skoplaki E, and Palyvos JA (2009). Operating temperature of photovoltaic modules: A survey of pertinent correlations. *Renew Energy*, 34(1):23–29. <https://doi.org/10.1016/j.renene.2008.04.009>
- [7] Tamizhmani G, Ji L, Tang Y, Petacci L, and Osterwald C (2003). Photovoltaic Module Thermal/Wind Performance : Long-Term Monitoring and Model Development For Energy Rating. *NCPV Sol Progr Rev Meet*, 936–939
- [8] Kamuyu WCL, Lim JR, Won CS, and Ahn HK (2018). Prediction model of photovoltaic module temperature for power performance of floating PVs. *Energies*, 11(2):. <https://doi.org/10.3390/en11020447>
- [9] Ibrahim S, Daut I, Irwan YM, Irwanto M, Gomesh N, and Razliana ARN (2012). An estimation of solar radiation using robust linear regression method. *Energy Procedia*, 181413–1420. <https://doi.org/10.1016/j.egypro.2012.05.157>
- [10] Alam MS, Alouani AT, and Azeem MF (2015). Efficient prediction of maximum PV module output power through dynamic modeling. *Sustain Energy Technol Assessments*, 1127–35. <https://doi.org/10.1016/j.seta.2015.06.001>
- [11] Li Y, Wang Y, Qian H, Gao W, Fukuda H, and Zhou W (2023). Hourly global solar radiation prediction based on seasonal and stochastic feature. *Heliyon*, 9(9):e19823. <https://doi.org/10.1016/j.heliyon.2023.e19823>
- [12] Cetina-Quiñones AJ, Santamaria-Bonfil G, Medina-Esquivel RA, and Bassam A (2023). Techno-economic analysis of an indirect solar dryer with thermal energy storage: An approach with machine learning algorithms for decision making. *Therm Sci Eng Prog*, 45(August):102131. <https://doi.org/10.1016/j.tsep.2023.102131>
- [13] Almaktar MA, Mahmoud HY, Daoud EY, and Hasan ZR (2017). Meteorological Parameters in Malaysia: An Investigation Between Real Measurements and NASA Database Drive train of wind turbine View project. *AEEESJ-Advanced Electr Electron Eng Sci J Copyr AEEESJ-@*, (1):1
- [14] (2021). NASA POWER: Data Processing. In: Version 1.0, Last Modif. 23 Nov. <https://power.larc.nasa.gov/docs/methodology/data/processing/>. Accessed 3 Jan 2023
- [15] Mellit A, and Pavan AM (2010). A 24-h forecast of solar irradiance using artificial neural network: Application for performance prediction of a grid-connected PV plant at Trieste, Italy. *Sol Energy*, 84(5):807–821. <https://doi.org/10.1016/j.solener.2010.02.006>
- [16] S. Wilcox and W. Marion (2008). Users Manual for TMY3 Data Sets
- [17] Zhao P, Xu W, Zhang S, Wang J, and Dai Y (2020). Technical feasibility assessment of a standalone photovoltaic/wind/adiabatic compressed air energy storage based hybrid energy supply system for rural mobile base station. *Energy Convers Manag*, 206(July 2019):112486. <https://doi.org/10.1016/j.enconman.2020.112486>

- [18] Alshawaf M, Poudineh R, and Alhajeri NS (2020). Solar PV in Kuwait: The effect of ambient temperature and sandstorms on output variability and uncertainty. *Renew Sustain Energy Rev*, 134(August):110346. <https://doi.org/10.1016/j.rser.2020.110346>
- [19] Mayer MJ, and Gróf G (2021). Extensive comparison of physical models for photovoltaic power forecasting. *Appl Energy*, 283(October 2020): <https://doi.org/10.1016/j.apenergy.2020.116239>
- [20] Al-Dahidi S, Al-Nazer S, Ayadi O, Shawish S, and Omran N (2020). Analysis of the effects of cell temperature on the predictability of the solar photovoltaic power production. *Int J Energy Econ Policy*, 10(5):208–219. <https://doi.org/10.32479/ijeep.9533>

## APPENDIX

### Appendix A: Example of product specification [1]

Data Type	Parameter	Value
Electrical Data	Peak Power, $P_{max}$	190 W
	Module Efficiency, $\eta_{pv}$	14.9 %
Temperature Ratings	Nominal Operating Module Temperature, $T_{NOCT}$	45 °C
	Temperature Coefficient of Power, $\beta_p$	-0.4 %/°C
Mechanical Data	Module Dimensions	1581 × 809 × 35 mm
Maximum Ratings	Operational Module Temperature	-40 ~ 85 °C
Standard Test Conditions (STC)	Reference Solar Radiation, $G_{STC}$	1000 W/m <sup>2</sup>
	Reference Module Temperature, $T_{m\_STC}$	25 °C
	Reference Air Mass, $AM_{STC}$	1.5
Nominal Operating Module Temperature (NOCT)	Reference Solar Radiation, $G_{NOCT}$	800 W/m <sup>2</sup>
	Reference Ambient Temperature, $T_{a\_NOCT}$	20 °C
	Reference Wind Speed, $v_{NOCT}$	1 m/s

## ADVANCING SYSTEM INTEGRATION: VERILOG-BASED HARDWARE IMPLEMENTATION OF AN ASIC INTERFACE FOR THREE AMBA PROCESSORS

S.M.A. MOTAKABBER<sup>1\*</sup>, MOHAMMAD IQBAL RAHMAN ROKON<sup>1</sup>,  
AHM ZAHIRUL ALAM<sup>1</sup>, GAZI ZAHIRUL ISLAM<sup>1</sup>,  
MOHAMMAD ABDULMATIN<sup>2</sup> AND MD. MAHMUD<sup>3</sup>

<sup>1</sup>*Department of Electrical and Computer Engineering,  
International Islamic University Malaysia, 53100 Kuala Lumpur, Malaysia*

<sup>2</sup>*Department of Electrical and Computer Engineering, North South University,  
Dhaka, Bangladesh*

<sup>3</sup>*Department of Electrical and Computer Engineering, College of Engineering,  
Lamar University, Beaumont-77710, Texas, USA*

\*Corresponding author: [amotakabber@iium.edu.my](mailto:amotakabber@iium.edu.my)

(Received: 13 June 2023; Accepted: 12 November 2023; Published on-line: 1 January 2024)

**ABSTRACT:** This paper presents the development of a multi-AMBA system processor interface employing multiple AMBA processors. The primary goal of this interface is to establish connections between various AMBA AHB interfaces and external memory units such as RAM and REGISTER, leveraging the high-performance capabilities of AMBA AHB. The research delves into the utilization of ASICs to integrate processors and functional blocks into a System-On-Chip (SoC) configuration, enabling the execution of intricate applications. Within the ASIC environment, the research explores how processors communicate with their designated targets through an interface that standardizes the communication protocol for all targets. It underscores the challenges posed by data throughput and inter-processor/RTL communication in contemporary processors and suggests the concurrent use of multiple AMBA processors for accessing their respective targets. Additionally, the paper introduces an arbitration system for managing multiprocessor access and investigates the optimization of bulk data access while prioritizing crucial ASIC design constraints, including speed, low power consumption, and efficient area utilization. The proposed system was rigorously validated through simulation using Verilog HDL, yielding positive and promising results.

**ABSTRAK:** Kajian ini adalah mengenai pembangunan antara muka, sistem pemproses berbilang AMBA yang mengandungi berbilang pemproses AMBA. Tujuan antara muka ini adalah bagi mewujudkan hubungan pelbagai antara muka AMBA AHB dengan unit memori luaran seperti RAM dan REGISTER, ini sekaligus memanfaatkan keupayaan tinggi AMBA AHB. Kajian ini mengguna pakai ASIC bagi menyatukan pemproses dan blok berfungsi pada konfigurasi Sistem-Atas-Cip (SoC), membolehkan pelaksanaan aplikasi rumit. Pada persekitaran ASIC, kajian ini meneroka cara pemproses berkomunikasi dengan sasaran yang ditetapkan melalui perantaraan antara muka yang menyeragam protokol komunikasi bagi semua sasaran. Ia menggariskan cabaran yang ditimbulkan oleh pemprosesan data dan komunikasi antara pemproses/RTL dalam pemproses kontemporari dan mencadangkan penggunaan secara serentak pemproses berbilang AMBA bagi mengakses sasaran masing-masing. Selain itu, kertas kerja ini memperkenalkan sistem timbang tara bagi mengurus akses berbilang pemproses dan mengkaji akses data pukal yang optimum sambil mengutamakan kekangan reka bentuk ASIC, seperti kelajuan, penggunaan kuasa rendah dan penggunaan

kawasan secara cekap. Sistem ini telah disahkan dengan teliti melalui simulasi menggunakan Verilog HDL, memberikan dapatan positif dan harapan baik.

---

**KEYWORDS:** *AMBA protocol; AMBA processor interface; multiprocessor arbitration; FPGA; Verilog HDL*

## 1. INTRODUCTION

In the modern era, digital control is pervasive, extending from simple toys to sophisticated high-tech devices, all orchestrated by VLSI chips [1]. These chips have not only become increasingly complex to accommodate advanced functions but have also grown significantly in size. Devices like the AMBA processor can operate at extremely high clock speeds. To harness the full potential of these processors and synchronize the remaining hardware with their speed, an efficient interface is imperative for any ASIC. Furthermore, if this interface can support multiprocessor access instead of a single processor, it would enable concurrent execution of tasks. This research aims to address these critical challenges and propose an interface capable of concurrent multiprocessor access with reduced flop-to-flop delay, minimized area requirements, and lower power consumption. The interface is constructed using multiple AMBA AHB-side components for controlling read and write operations on memory storage elements from the AHB side. All of these components are interconnected using Hardware Description Language (HDL), ensuring a seamless connection between the AHB Bridge, RAM, and registers. Using the efficient hardware interface, AMBA AHB bus ensures the efficient connection of processors, on-chip memory and off-chip external memory interfaces with targeted areas such as be registers, RAMs, FIFO, UART, PCI Interface or Network link. It also ensures ease of use in an efficient design flow using synthesis and simulation techniques using EDA hardware simulator [1].

When it comes to AMBA-based microcontrollers, the standard configuration includes a sturdy system backbone that can efficiently manage external memory bandwidth. This backbone serves as the central hub connecting the CPU, on-chip memory, and various Direct Memory Access (DMA) devices. More specifically, the AMBA AHB bus functions as this high-performance system backbone. The hardware architecture of multiprocessors access to the slave devices [2-4] is shown in Fig. 1. It is finely tuned for use in high-frequency system modules, forming the core of the high-performance system architecture. This core ensures smooth connectivity between processors, on-chip memories, and off-chip external memory interfaces, all while accommodating low-power peripheral microcell functions. Moreover, it facilitates the efficient connection of processors, on-chip memory, and off-chip external memory interfaces to support low-power peripheral macro cell functions. Its specifications are carefully crafted to guarantee ease of use within an efficient design process, incorporating synthesis and automated testing techniques.

## 2. METHODOLOGY

This research followed the Top-Down Hierarchical Technique to partition the design. Processor interfaces provide bridge connection between processor and rest of the hardware. Processors operate as per its bus protocols: it can be processor specific or standard protocol. Interface needs to understand those protocols and provide access into the targets like registrar, memory, FIFO, network link or other PCI interfaces as per their own access control. This research will focus on developing an interface that can support multiple AMBA AHB processor access concurrently with higher speed, lower power and area. As designing multi processors are complex both in hardware and software, so in our research we need to focus on managing

---

complexity using hierarchical methodology and we need to be further concern if one processor fails then it will not affect in the speed. It should perform in low power and should take low area. After design specification is complete, interface will be modeled using Verilog HDL. Below is the Verilog HDL based ASIC design flow.

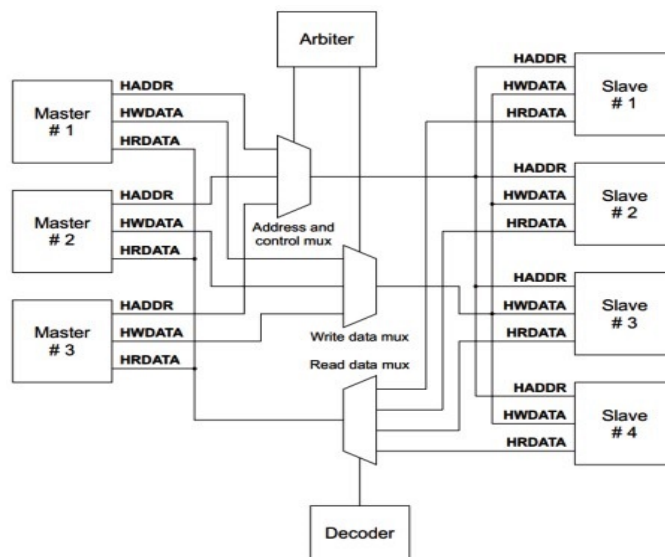


Fig. 1: Multiplexer interconnections for multiple AHB masters [2-4].

## 2.1 AHB Signals and Transfers Involving AMBA Masters

### 2.1.1 HADDR [31:0]

During write operations, the write data bus plays a critical role in conveying data from the master to the bus slaves. It is highly recommended to maintain a minimum data bus width of 32 bits. Nonetheless, it can be effortlessly expanded to facilitate higher bandwidth [3,4].

### 2.1.2 HWDATA [31:0]

The write data bus is driven by the bus master during write transfers. If the transfer is extended then the bus master must hold the data valid until the transfer complete, as indicated by HREADY HIGH.

### 2.1.3 HRDATA [31:0]

During read operations, the relevant slave device takes control of the read data bus. If this slave prolongs the read process by keeping the signal HREADY in a LOW state, it is only required to furnish valid data at the conclusion of the final cycle of the transfer. This point is signified by the transition of HREADY to a HIGH state, as documented in reference [3].

## 3. RTL HARDWARE DESIGN SPECIFICATION

Design specification enables designers to implement their ideas systematically on paper. This specification appears in text/document format and represent what designers expect their chip to do. At this point of the design process, designers demonstrate very little concern about hardware consideration such as area, speed or power consumed by the chip. Design specification contains multiple identical processors (AMBA processor in our case). It is capable of interpreting processor BUS protocols in order to read/write operations on target devices.

Both Fixed and Round-Robin arbitration systems would be available to deal with situations requiring multiple processors to access a particular generic device concurrently [5].

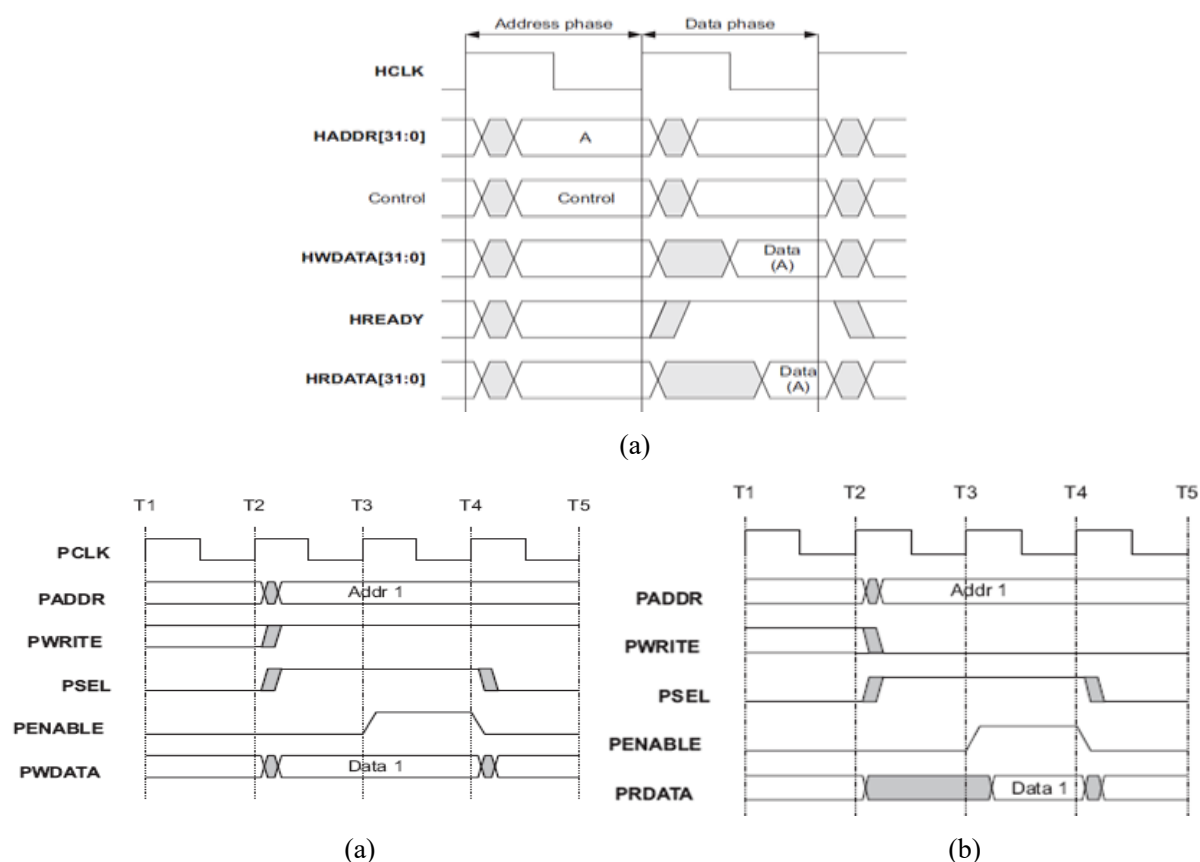


Fig. 2: AMBA transfer (a) simple with no wait states, (b) write and (c) read.

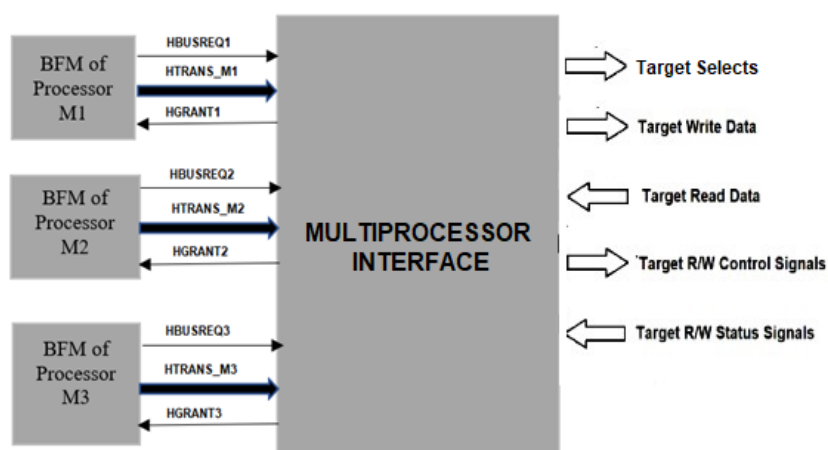


Fig. 3: Proposed simulation test environment.

Control flow and simulation test environment for the proposed AMBA multiprocessor interface is shown in Fig. 3.

In this design specification we are using four AMBA Master AHB bus and three input signals which are HADDR, HWDATA and HRDATA. These signals will go to the slaves which can be RAM, REGISTER, and FIFO etc. These three master signals cannot reach the

slaves altogether at a time. So, for this arbiter will select which signal will reach the slaves first. There are address and control mux, write data mux, read data mux and decoder. This design specification is implemented for 32-bit, 64 bit and 128 bits. The address signal HADDR will address the signal. If the arbiter selects 00 then it will select HADDR1, for 01 it is HADDR2, for 10 it is HADDR3 and for 11 it is HADDR4 like this [6]. Same thing will be applicable for other signals [7].

### 3.1 Top Level Block Diagram of Multiprocessor Access

Interface allows three AMBA AHB processors to access the target areas according memory mapping of each processor address bus value. Target areas can be Control and Status Registers, Memory, FIFO, UART, PCI Interface and Network Link. Figure 4 shows the block diagram of interface in multiprocessor access [2,6].

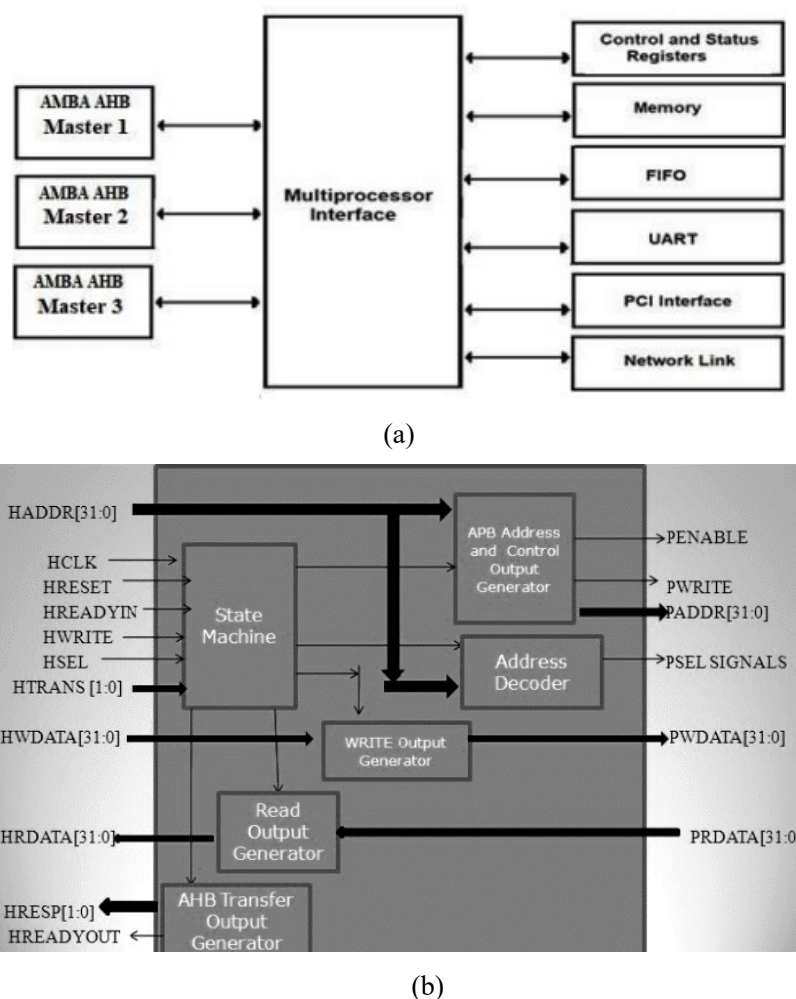


Fig. 4: (a) Top level block diagram in AMBA multiprocessor access, and (b) major blocks inside the interface [2,6].

### 3.2 State Machine

This is a very vital block for the interface. It determines when different output signals will come in effect. Two most significant signal of this block is next state and current state both of which are 3 bit signals. To generate next state some other signals are needed like HWRITE, registered version of HWRITE (Reg. write), accept and current state as well. Next state and current state will be used as internal input signals in other blocks [7].

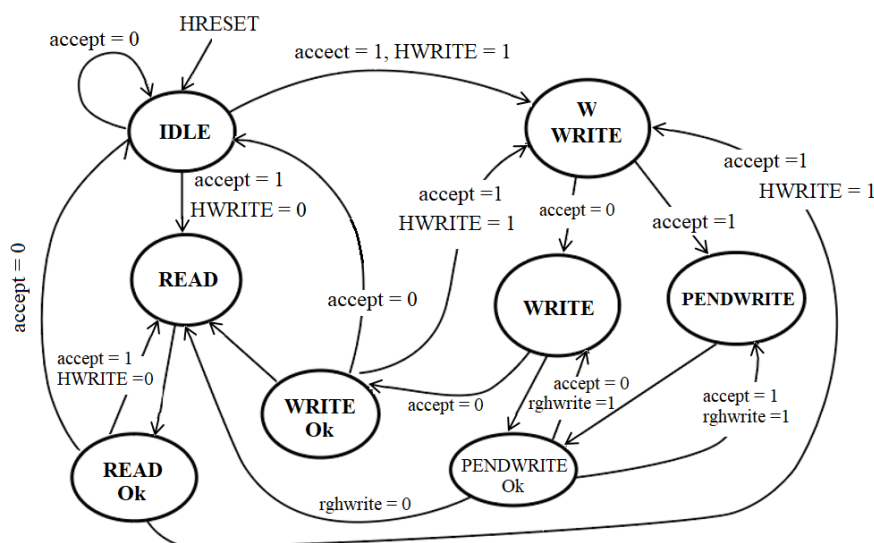


Fig. 5: Processor access control state machine.

### 3.2.1 Write Output Generator

This sub-block is implemented by a DFF. Here input will be taken as HCLK, HRESET and HWDATA then output will be driven to PWDATA. Here reset is asynchronous.

### 3.2.2 Read Output Generator

To implement this one more DFF is used. Here input will be taken as HCLK, HRESET and PRDATA. The output will then drive to HRDATA. Asynchronous reset is used.

### 3.2.3 AHB Transfer Output Generator

Here transfer generation is used as output HREADYOUT and HRESP as response signals. State machine and AHB inputs generates HREADYOUT. To show the complete of transfer 00 is always set to HRESP.

## 3.3 AHB Arbiter

The bus arbiter guarantees that only one bus master can initiate data transfers at any given time. Despite having a fixed arbitration protocol, various arbitration algorithms, such as highest priority or fair access, can be implemented based on the specific requirements of the application. An AHB system typically incorporates only one arbiter, although this is a straightforward setup in single bus master systems. The AHB decoder is responsible for decoding the address of each data transfer and generating a select signal for the slave involved in the transfer. In all AHB implementations, a single centralized decoder is necessary [4].

### 3.3.1 Arbitration System

The arbitration mechanism's primary purpose is to uphold the principle of allowing only one master to utilize the bus at a time. This function is executed by the arbiter, which assesses multiple requests from potential bus users and identifies the current highest-priority master seeking bus access. Furthermore, the arbiter handles requests from slaves wishing to execute SPLIT transfers. For slaves not engaged in SPLIT transfers, the intricacies of the arbitration process may not be relevant, but it's essential for them to acknowledge that a series of transfers could remain incomplete if the bus's ownership status changes [8].

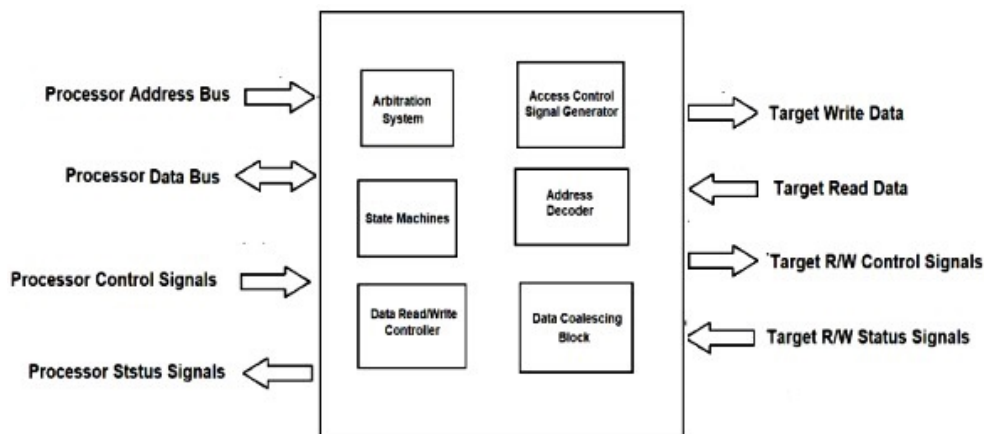


Fig. 6: Arbitration system inside the interface [9].

### 3.3.2 Arbitration Control State Machine

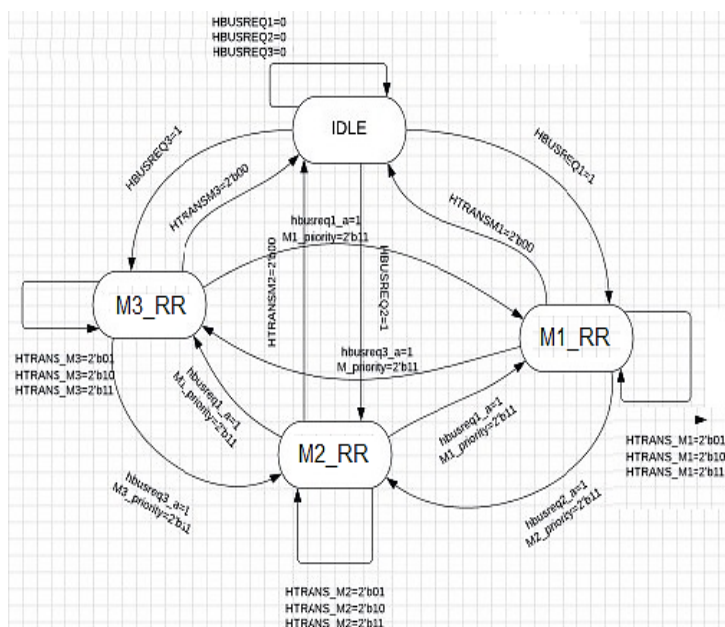


Fig. 7: State transitions of dual mode arbitration under Round Robin.

## 4. RESULTS AND DISCUSSION

The proposed system has implemented the interface by design using four master AMBA AHB buses and each contains three input signals HADDR, HWDATA and HRDATA. We tested the input signals in Verilog HDL. In our result we got some signals of high impedance which were not expected. But the other outputs of the timing diagram were according to our desired output. This work is extended to simulation part. And further work will cover the simulation of the designed part. After implementing design improvements, simulation results will be studied and timing diagram will be analyzed and compared with results. Efficient usage of logic synthesis tools will limit area requirements and power consumption of transistors inside chip as per requirements of the design. The wave form of simulation of the design is shown in Fig. 8.

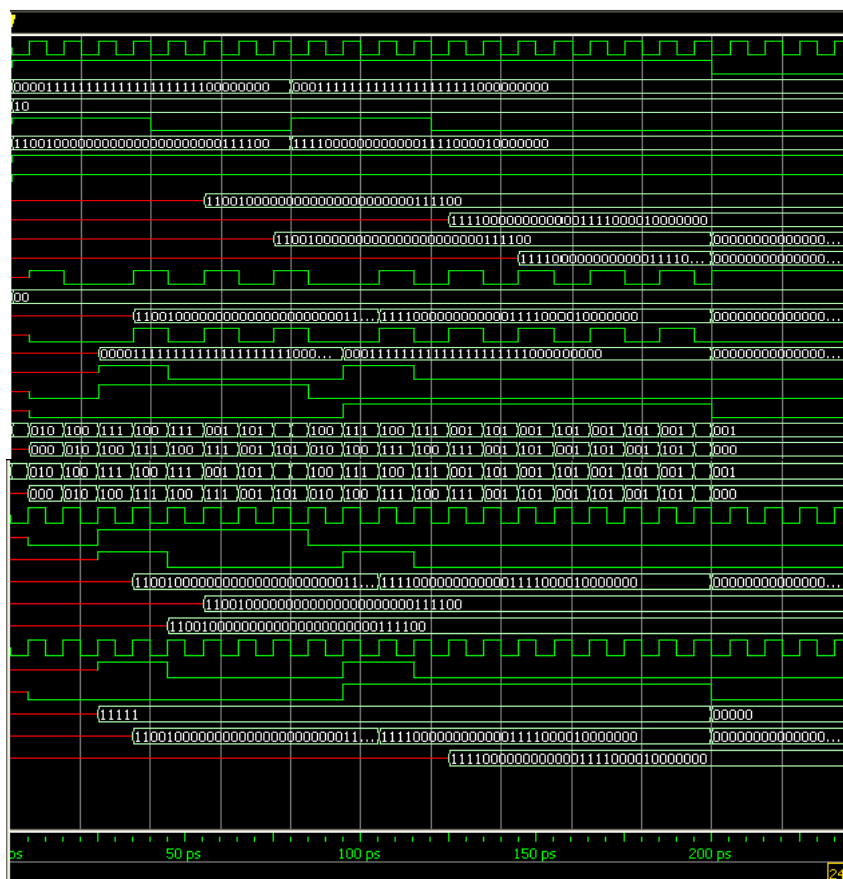


Fig. 8: The Verilog functional simulation results of the proposed system.

The Verilog HDL RTL code has been synthesized using Xilinx XST targeting its FPGA device. Figures show the synthesized blocks and logics.

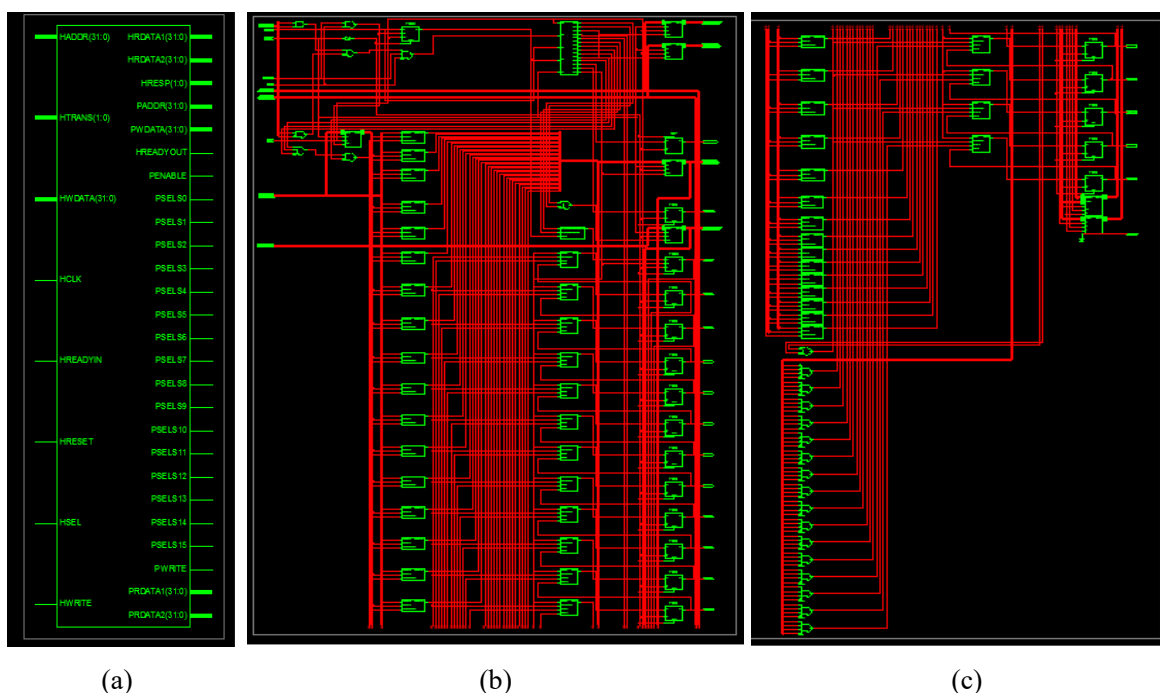


Fig. 9: Synthesized top block design (a), Synthesized Internal logic of the Interface part-1 (b) and Synthesized Internal logic of the Interface part-2 (c).

The synthesis reports are shown in Table 1. Analyzing FSM < FSM\_0 > for best encoding. Optimizing FSM < FSM\_0 > on signal < currentstate [1:3] > with gray encoding.

Table 1: Logic state, and list of components and their numbers

State	Encoding	Macro Statistics	Macro Structure	No. of blocks
000	000			
010	001	Registers : 1	Registers : 60	
001	011	Flip-Flops : 1	1-bit register : 20	
101	010	Multiplexers : 303	32-bit register : 40	
100	110	32-to-1 multiplexer : 1303	Multiplexers : 1	
011	111		32-to-1 multiplexer : 1	
111	101			
110	100			

While previous research has explored multiprocessor system interfaces, our work takes a unique approach by focusing on multi AMBA AHB system processors, which has not been extensively addressed before [5]. Unlike prior studies that concentrated on a single signal, we have developed our interface design to accommodate four AMBA AHB bus protocols, effectively serving as masters for these protocols. These protocols utilize three crucial input signals: HADDR, HWDATA, and HRDATA.

Furthermore, considering the ever-evolving landscape of technology, we have future-proofed our design to support not only the current 32-bit standard but also 64-bit and even 128-bit configurations [9]. Our upcoming plans involve delving into system coalescence to enable efficient bulk data access. We aim to implement two distinct arbitration systems, namely Fixed and Round-Robin, which will come into play when multiple processors simultaneously require access to the same location. This forward-looking approach positions our research to make a meaningful contribution to the future of processor technology.

## 5. CONCLUSION

This study aims to develop a cutting-edge System-On-Chip (SoC) with a high-speed processor by introducing an efficient integrated interface. The primary goal of this research is to create an interface that supports multiple AMBA AHB system processors. The project involves the design of multiple AHB Masters within a multi-AMBA system using Verilog HDL. Building upon the concepts presented in the references, this work delves into the intricacies of multiprocessor concurrent access, including the implementation of advanced arbitration mechanisms and coalescing techniques. The anticipated result of this research is the potential to contribute to the development of future high-tech chips with intricate functionalities operating at top speeds.

## REFERENCES

- [1] Giridhar P, Choudhury P. (2019) Design and Verification of AMBA AHB. 1st International Conference on Advanced Technologies in Intelligent Control, Environment, Computing & Communication Engineering (ICATIECE), 19-20th Mar 2019, India.
- [2] Iqbalur Rahman Rokon TRAA. (2011) Hardware Implementation of AMBA Processor, in International Conference on Electrical, Electronics and Civil Engineering (ICEECE'2011), Pattaya, Dec 17-18, 2011.
- [3] Deekhsa L, Shivakumar BR. (2019) Effective Design and Implementation of AMBA AHB Bus Protocol using Verilog. International Conference on Intelligent Sustainable Systems (ICISS), 21-22nd Feb 2019, Palladam, India.

- [4] AMBA: The Standard for On-Chip Communication, [Online]. Available: <https://www.arm.com/products/siliconip-system/embedded-system-design/amba-specifications>.
- [5] Dobberpuhl DW. (1997) Circuits and technology for Digital's StrongARM and ALPHA microprocessors [CMOS technology]. In Proceedings Seventeenth Conference on Advanced Research in VLSI, 2-11. doi: 10.1109/ARVLSI.1997.634842.
- [6] Saluja H, Grover N. (2020) Multiple Master Communication in AHB IP using Arbiter. *International Journal of Engineering and Manufacturing (IJEM)*, 10(1): 29-40.
- [7] Iqbalur R. and Reasat C. (2011) Hardware Implementation of StrongARM Processor Interface Using Verilog & FPGA. *International Conference on Electrical, Electronics and Civil Engineering (ICEECE'2011)*. Pattaya, Thailand, Dec 17-18, 2011.
- [8] Tu J, Ou C. (2017) A practice of 2-to-2 fixed priority arbiter used to multi-core processors. *International Conference on Applied System Innovation (ICASI 2017)*, 13-17th May 2017, Sapporo, Japan.
- [9] Mishra A. (2020) Design of a Round Robin Bus Arbiter using System Verilog. *International Research Journal of Engineering and Technology (IRJET)*, 7(1): 29-40.

## EXTENDABLE HIGH-GAIN DC-DC CONVERTER FOR STORAGE BATTERY AND PHOTOVOLTAIC CELL

S.M.A. MOTAKABBER, KHADIZA AKTER\*, AHM ZAHIRUL ALAM  
AND SITI HAJAR YUSOFF

*Department of Electrical and Computer Engineering, Kulliyyah of Engineering,  
International Islamic University Malaysia, Kuala Lumpur, Malaysia*

*\*Corresponding author: khadiza@iubat.edu*

*(Received: 12 October 2023; Accepted: 20 November 2023; Published on-line: 1 January 2024)*

**ABSTRACT:** DC-DC converters with significant gain, ripple-free input current, and shared ground are required to elevate the output voltages of batteries, fuel cells, and Photovoltaic sources. The proposed topology utilizes a solitary switch to control the circuit and it has additional inculcation of a voltage doubler cell at the load side, a switch capacitor cell in the middle, and a quadratic cell at the output side. These cascaded configurations lead to significant voltage gains at moderate duty cycle rates. Additionally, the voltage stress over the power components is negligible, coming in under one-third of the resultant voltage. Moreover, the number of cells at the input and output side can be extended to obtain high voltage according to the requirements of the load. The gain in voltage, efficiency, and normalized voltage stress of the semiconductor elements in the circuit are examined concerning other solutions found in the literature. Eventually, photovoltaic and battery sources were included to analyze the proposed topology to confirm the circuit's multifaceted functionality. The circuit was developed for 270 W, 440 V output from 36 V input, and a 40 kHz switching pulse was used to drive the switch. The theoretical and simulation analysis states that incorporating photovoltaic and other sources did not deteriorate the transformation efficiency. Simulink and PSIM analysis found that the circuit successfully transferred 95% power from source to load.

**ABSTRAK:** Penukar DC-DC yang mempunyai gandaan ketara, input arus bebas riak dan pembumi berkongsi penting bagi meningkatkan voltan keluar bateri, sel bahan api dan sumber fotovolt. Topologi yang dicadangkan ini menggunakan suis tersendiri bagi mengawal litar dan ia mengandungi sel pendua voltan tambahan bagi menghentikan arus di bahagian beban, sel suis kapasitor di tengah dan sel kuadratik di bahagian voltan keluar. Konfigurasi berturutan ini membawa kepada gandaan voltan ketara pada kadar kitar tugas sederhana. Tambahan, tekanan voltan ke atas komponen kuasa boleh diabaikan, iaitu satu pertiga daripada voltan terhasil. Selain itu, bilangan sel di bahagian kemasukan dan keluaran arus boleh dilanjutkan bagi mendapatkan voltan tinggi mengikut keperluan beban. Gandaan voltan, kecekapan dan tekanan voltan ternormal pada bahan dalam litar semikonduktor diperiksa dengan menyamai penyelesaian lain yang ditemui dalam kajian terdahulu. Akhirnya, sumber fotovolt dan bateri dimasukkan bagi menganalisis topologi yang dicadangkan bagi mengesahkan fungsi pelbagai rupa litar. Litar yang dibangunkan ini digunakan pada kuasa 270 W, pada aras voltan 440 V dengan kemasukan voltan 36 V dan suis operasi berfrekuensi 40 kHz. Analisis teori dan simulasi menyatakan bahawa gabungan fotovolt dan sumber lain tidak mengurangkan kecekapan transformasi. Analisis Simulink dan PSIM mendapati litar ini berjaya memindahkan 95% kuasa dari sumber kepada beban.

**KEYWORDS:** *PV system; MPPT; DC-DC converter; voltage stress on semiconductor; CCM; DCM*

## 1. INTRODUCTION

High voltage gain power electronic converters are crucial to the renewable energy system field because of their linking capability between RES and electrical power systems. They are widely used in electrical systems, including electric trains, satellites, electric vehicles, street lighting, battery charging, tracking a PV array's MPP, and high-voltage DC transmission [1]. The voltage output from a solar PV array or a fuel cell is rather low and contingent upon external conditions [2]. PV systems are designed in a series-parallel arrangement to obtain high output voltage. However, this configuration lowers efficiency and increases system size [3]. Hence, a high-boosting factor configured converter is used for these voltage-boosting applications because it can alter the converter's duty cycle to raise the voltage at the output to significantly higher levels relative to its input.

Figure 1 depicts the overall design of a DC grid-tied diagram using an HVG DC-DC step-up converter. As a result, various configurations of these kinds of topology have been put out in the literature to achieve the required voltage output [4].

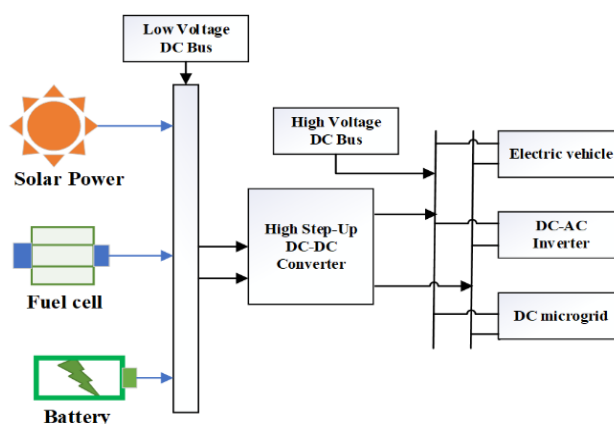


Fig. 1: Basic structure of the proposed converter applications.

These types of topologies can be classified as current-fed or voltage-fed, isolated or non-isolated, unidirectional or bidirectional, and soft-switched or hard-switched type. The transformer is used in an isolated converter topology to increase voltage at the input side by modifying its turn ratio [5]. On the other hand, these converters have a strong secondary side voltage overload and an excessive input current ripple content [6]. Furthermore, the two main disadvantages of isolated converters are leakage energy, heavy transformers, and multiple stages of the power conversion procedure [7]. As a result, non-isolated configurations such as Boost, Buck-Boost, CUK, and SEPIC converters are being utilized to adjust the system's performance [8,9]. They are commonly used because these converters are easy to use, affordable, effective, and have a wide variety of useful applications.

Many methods, such as the employment of a voltage multiplier, switched inductor, switched capacitor, etc., are employed to improve the functionality of high-gain converters. High-efficiency, step-up DC-DC converters have been presented in [10]. Active clamps have been used in these converters to recuperate leakage energy and lessen the problem with the diode's reverse recovery. The suggested converter in [11] obtained a considerable step-up voltage gain by combining a switching capacitor and two linked inductors. Furthermore, the reduced resistance had reduced conduction losses, thereby raising efficiency and lowering the diodes' reverse recovery.

A highly effective method using dual-coupled inductors and an efficient step-up DC-DC converter for grid-tied solar systems has been demonstrated in [12]. Using a few extra auxiliary parts, a modified SEPIC circuit with a marginally greater gain than a boost converter has been described in [13]. Quadratic gain structures are introduced to boost the gain in [14] further, and when the duty ratio exceeds 70%, the quadratic converter produces higher gains. Consequently, inductor core saturation is a serious issue in these kinds of high-frequency operating converters. The voltage transformation can now be enhanced using quasi-z-source and z-source networks in conjunction with SC, SI, or other voltage-amplifying topologies. The converters described in [15] have higher element voltage stress and less gain in voltage. However, the converter's power density drops when more inductors are used. Additional boosting circuits and a dual switch-based flipping capacitor are employed to raise the gain. The topologies developed in [16] can attain high voltage gain (HVG) with higher efficiency. Nevertheless, the incorporation of a PV source deteriorates the input current smoothness and lessens the output voltage level. Moreover, most topologies are not compatible with tracking optimum power in the shortest time. Some topologies can track maximum power, but they offer high steady-state oscillation.

This brief proposes a single switched SC-employed non-isolated improved voltage gain DC-DC converter to address the shortcomings. Common ground, constant input current with little ripple content, HVG at varying duty ratios, and decreased voltage stress on components are all aspects of the suggested topology. With considerable efficiency, it can generate 440 V from 36 V of input even at a low-duty cycle. The steady-state investigation in DCM and CCM mode, the PV source implementation, MPP tracking analysis, performance comparison, and assessment are covered in the remaining sections of the study.

## 2. DESCRIPTION OF PROPOSED CIRCUIT

The suggested converter is being introduced to increase voltage gain using fewer components and reducing the stress caused by the voltage across the output semiconductor. The PV output is connected to the MOSFET switching circuit through an electric charge pump network. Finally, the output of the circuit uses a voltage doubler network and is connected to the load, as shown in Fig. 2. The circuit has two functioning modes since the MOSFET switch has two modes of operation: ON and OFF.

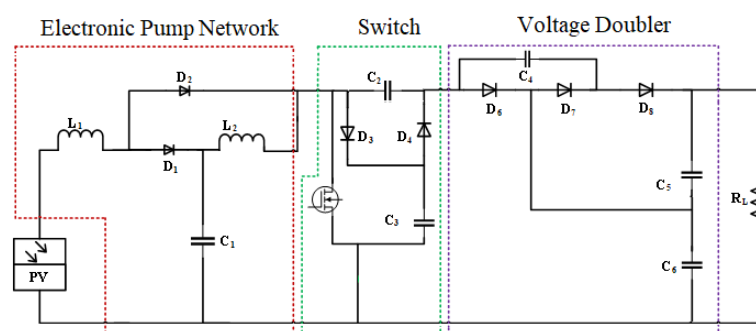


Fig. 2: Proposed design.

### 2.1 CCM Analysis of the Proposed Converter

When the converter operates in Continuous Conduction Mode (CCM), the current passing through the inductor never zeroes out throughout the switching cycle. It indicates that the inductor continuously receives current and is not completely discharged during the switching

cycle's off-time. Designing DC-DC converters that are dependable and efficient requires the use of CCM analysis, particularly in situations where a steady and tightly monitored output voltage is required.

### 2.1.1 When Switch is ON ( $0 \leq t \leq DT$ )

When the MOSFET switch  $S$  is turned ON, the diodes  $D_2, D_4, D_6$ , and  $D_8$  are forward-biased, and diodes  $D_1, D_3$ , and  $D_5$  are reverse-biased, the flow direction in this situation is shown in Fig. 3. The PV energy is pumped to store in the  $L_1$ , simultaneously the storage energy of  $C_1$  is pumped to store in the  $L_2$ . The output diode-capacitor doubler circuit is in action and increases the voltage across the load.

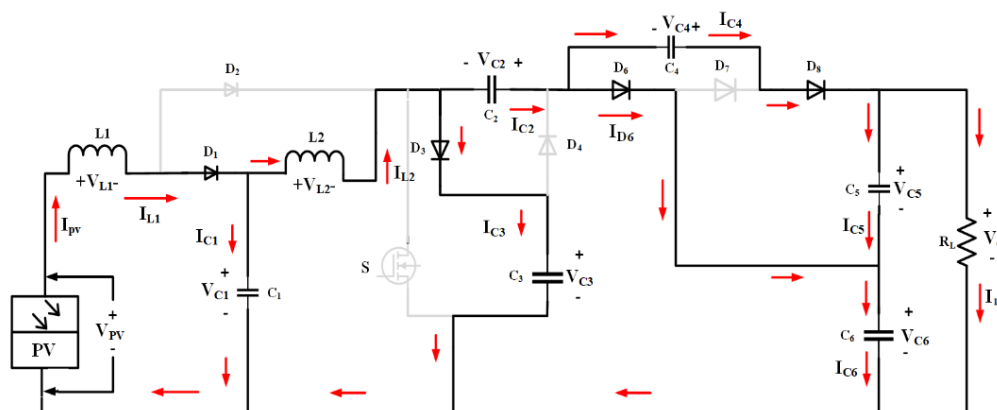


Fig. 3: Current flow direction when the MOSFET Switch is ON.

### 2.1.2 When Switch is OFF ( $0 \leq t \leq DT$ )

When the MOSFET switch is turned OFF, the diodes  $D_1, D_3, D_5, D_6$  and  $D_7$  are forward-biased, and the diodes  $D_2, D_4$  and  $D_8$  are reversed bias. Capacitors  $C_4$  and  $C_5$  are connected in parallel; thus, voltage drops across them are equal. Capacitor  $C_1$  discharge through  $L_2$  and stored the electrical energy for the next half cycle simultaneously. The capacitor  $C_4$  discharge through the load, the current flow direction is shown in Fig. 4.

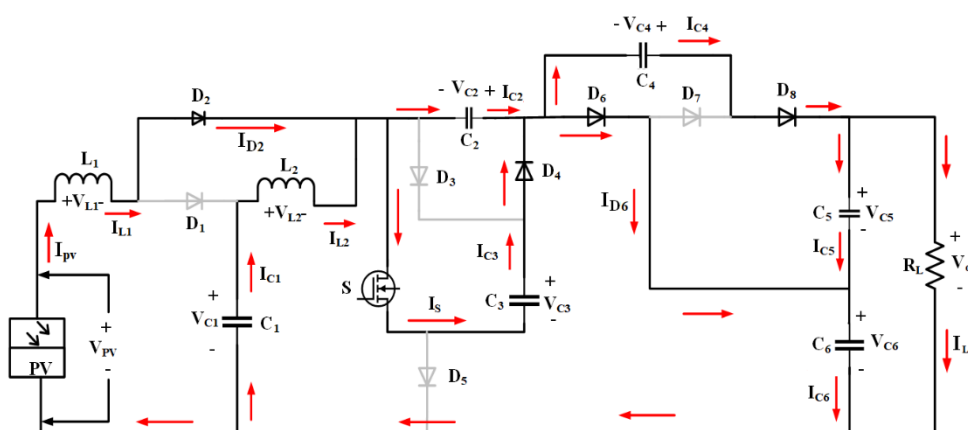


Fig. 4: Switch OFF operating principle.

### 2.1.3 Voltage Gain

The volt/sec change approach is implemented on the inductor to calculate the voltage gain.

$$\int_0^{DT_s} V_{PV} dt + \int_{DT_s}^{T_s} (V_{PV} - V_{C1}) dt = 0 \quad (1)$$

After solving the Eq. (1), the voltage across the capacitor  $C_1$  can be calculated as,

$$V_{C1} = \frac{V_{PV}}{(1-D)} \quad (2)$$

Similarly, the voltage across the capacitor  $C_2$  can be calculated as,

$$\int_0^{DT_s} V_{C1} dt + \int_{DT_s}^{T_s} (V_{C1} - V_{C2}) dt = 0 \quad (3)$$

$$V_{C2} = \frac{V_{PV}}{(1-D)^2} \quad (4)$$

The output voltage across the load can be calculated as,

$$\therefore V_o = \frac{3V_{in}}{(1-D)^2} \quad (5)$$

where  $D$  is the duty cycle of the switching frequency.

## 2.2 DCM Analysis of the Proposed Converter $0 \leq t \leq (1 - D - Dx)T_s$

In discontinuous conduction mode (DCM), the current flowing through the inductor becomes zero. Hence, there will be no voltage drop across the inductor. As a result, no power is pulled from the source or the inductor. Both output capacitors  $C_5$  and  $C_6$  deliver current to the load. Figure 5 shows the operating diagram of DCM.

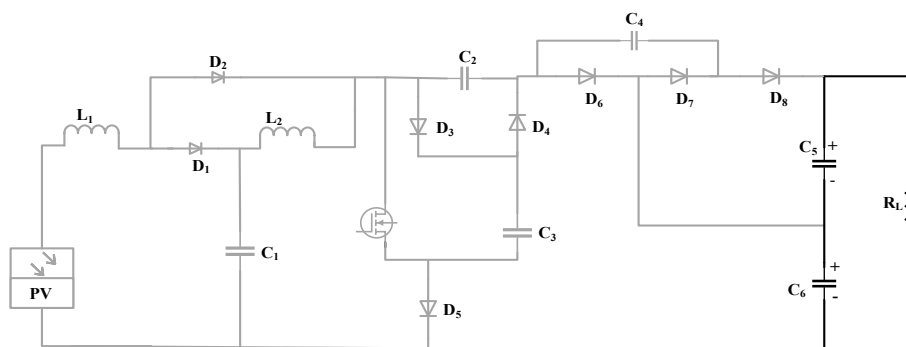


Fig. 5: DCM diagram of the circuit.

## 2.3 Ripple Current Computation

For a lossless circuit as an assumption, the equation of input and output power can be written as,

$$\begin{aligned} P_{PV} &= P_{out} \\ V_{PV} I_{PV} &= V_o I_o \end{aligned} \quad (6)$$

Considering the current through the  $L_1$  inductor is equal to the input current  $I_{pv}$

$$\Delta I_L = \frac{DV_{PV}}{L(1-D)}(1-DT_S) \quad (7)$$

## 2.4 Assessment of Voltage Stresses on Semiconductor Device

The voltage stress across semiconductor devices appears during their reverse-biased state. For the first operating mode, the following voltage equation can be written as,

$$V_{D1} = V_{L2} \quad (8)$$

$$V_{L2} = V_{C1} \quad (9)$$

$$V_{C1} = \frac{V_{PV}}{(1-D)} \quad (10)$$

$$V_{D1} = \frac{V_{PV}}{(1-D)} \quad (11)$$

Similarly, the voltage stress across the other diodes is summarised in Table 1.

Table 1: Voltage stress across semiconductor components

Parameters	Voltage Stress	Parameters	Voltage Stress
$V_{D1}$	$\frac{V_{PV}}{(1-D)}$	$V_{D5}$	$\frac{V_o}{3}$
$V_{D2}$	$\frac{V_{PV}}{(1-D)}$	$V_{D6}$	$\frac{V_o}{3}$
$V_{D3}$	$\frac{V_{PV}}{(1-D)^2}$	$V_{D7}$	$\frac{V_o}{3}$
$V_{D4}$	$\frac{V_{PV}}{(1-D)^2}$	$V_S$	$\frac{V_{PV}}{(1-D)^2}$

## 3. PERFORMANCE OF THE CONVERTER WITH BATTERY SOURCE

MATLAB/Simulink and PSIM software simulated the recommended converters and validated the theoretical formulation. The parameters taken into account for the simulation are  $V_{in} = 36 \text{ V}$ ,  $V_o = 440 \text{ V}$ ,  $D = 0.5$ ,  $C_1 = 250 \mu\text{F}$ ,  $C_2 = C_3 = 40 \mu\text{F}$ ,  $C_4 = C_5 = C_6 = 100 \mu\text{F}$ ,  $L_1 = L_2 = 2.5 \text{ mH}$  and  $R_L = 750 \Omega$ . The switching frequency of the MOSFET switch is  $40 \text{ kHz}$ . Fig.7 displays the input-output voltage and current profile. The resultant  $440\text{V}$  output voltage with  $0.58 \text{ A}$  current appeared across a  $750 \Omega$  load. The inductor current is  $6.9\text{A}$ , while the ripple current is  $0.17 \text{ A}$ , which is  $2.4\%$  of the average current. The average value of the voltage across  $C_1$  is  $72 \text{ V}$  when the voltage over the rest of the capacitors is around  $146\text{V}$ , the voltage between capacitors  $C_5$  is increased to  $150 \text{ V}$  and becomes  $292 \text{ V}$ . Figure 6(a) and 6(b) show the proposed circuit's input voltage and current signal. Figure 6(c) and 6(d) demonstrate the output voltage and current.

The peak-to-peak output voltage difference is less than  $0.25$ , which is a promising example of low fluctuation. The proposed topology has been incorporated with a  $36 \text{ V}$  battery source during simulation. The waveform characteristics of the proposed topology have been verified for voltage across each circuit element and semiconductor components. The simulation output of each component in terms of voltage and current flowing through them complies with the theoretically obtained output, as displayed in Fig. 6.

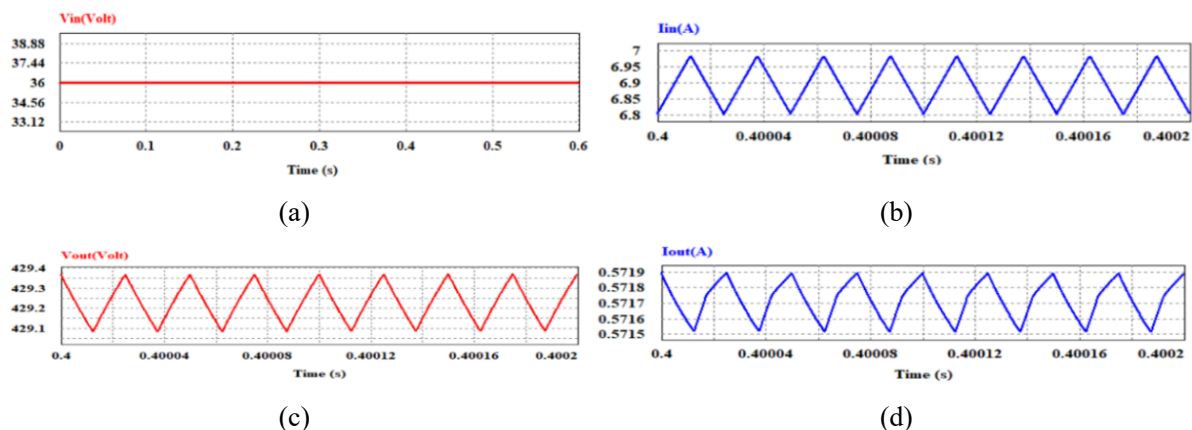


Fig. 6: Input voltage (a), Input current (b), output voltage (c) and output current waveform of proposed design.

#### 4. PERFORMANCE OF THE CONVERTER WITH PV SOURCE

PV systems generally have intermittent characteristics, poor stability, and lower energy efficiency during conversion. The MPPT algorithm is required to guarantee that the solar energy system can produce the most electricity possible. The proposed design has been incorporated with the PV source to ensure the optimum power obtained from the PV source. Two parallel strings are used for simulation, each containing three modules. The maximum power of the PV panel is 1050.55 watts, shown in the PV curve of Fig. 7. The Perturb and Observe (P&O) algorithm has been utilized to ensure the tracking of optimum power [17].

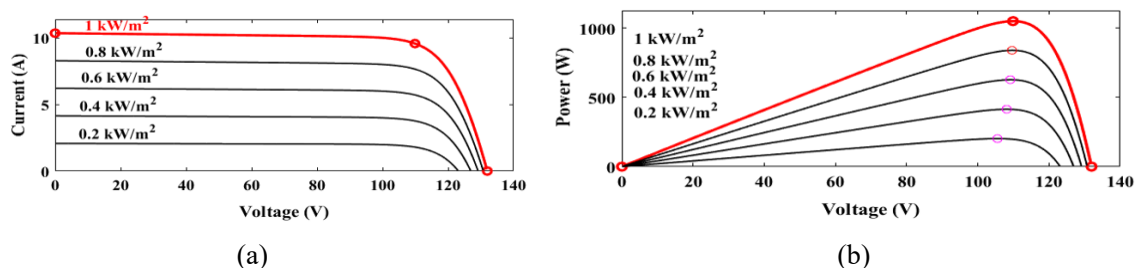


Fig. 7: Characteristics of the implemented solar module (a) I-V and (b) P-V.

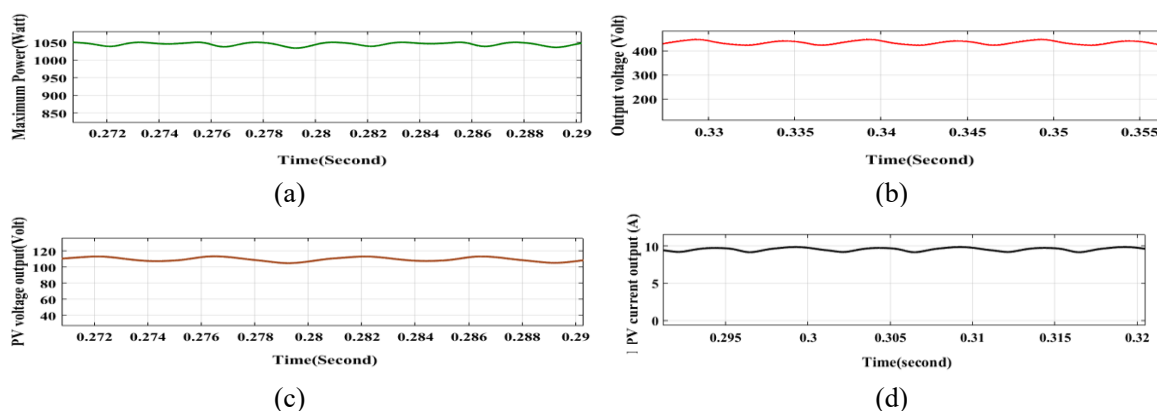


Fig. 8: Graphical representation of the proposed system (a) MPP module, (b) converter output voltage, (c) PV output voltage and (d) PV output current.

Figure 8(a) shows the proposed converter tracking efficiency capability with less tracking time and less steady-state oscillation. Incorporating the MPPT controller did not affect the boosting factor of the circuit. Figure 8(b) shows the converter output voltage, which complies with the battery output voltage. The PV current and voltage waveform are demonstrated in Fig. 8(c) and (d), which show the resemblance of the I-V curve in Fig. 7(a).

## 5. COMPARATIVE ANALYSIS

The suggested converter was contrasted with its more recent counterpart to verify the viability of the recommended converters successfully. Eight recently developed step-up converter circuits were compared. A detailed comparison is made between the various features of these converters concerning voltage across semiconductors, efficiency, and boost factor. Figures 9, 10, 11 graphically represent the performance of different circuit topologies, including the proposed design. In the figure, the x-axis number within the square bracket represents the reference number of the article to home compared to the proposed design.

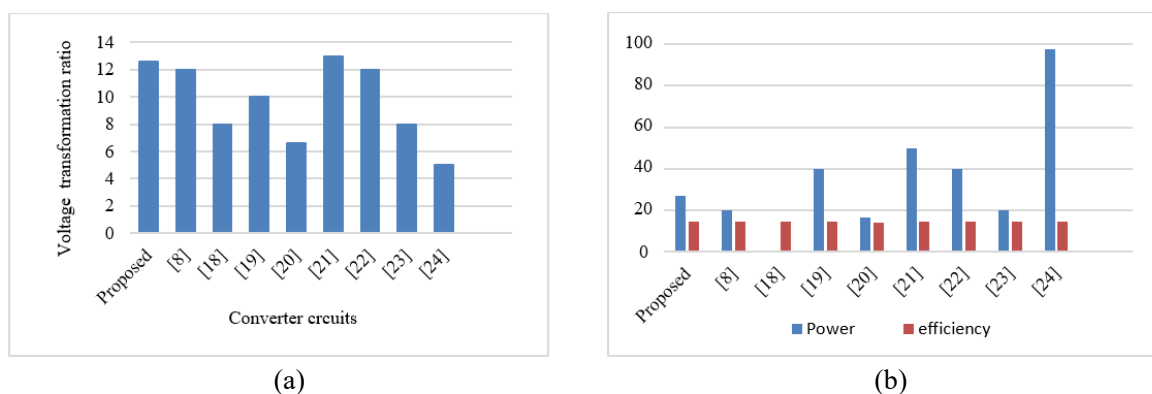


Fig. 9: Performance of various topologies (a) voltage boosting and (b) efficiency concerning power comparison.

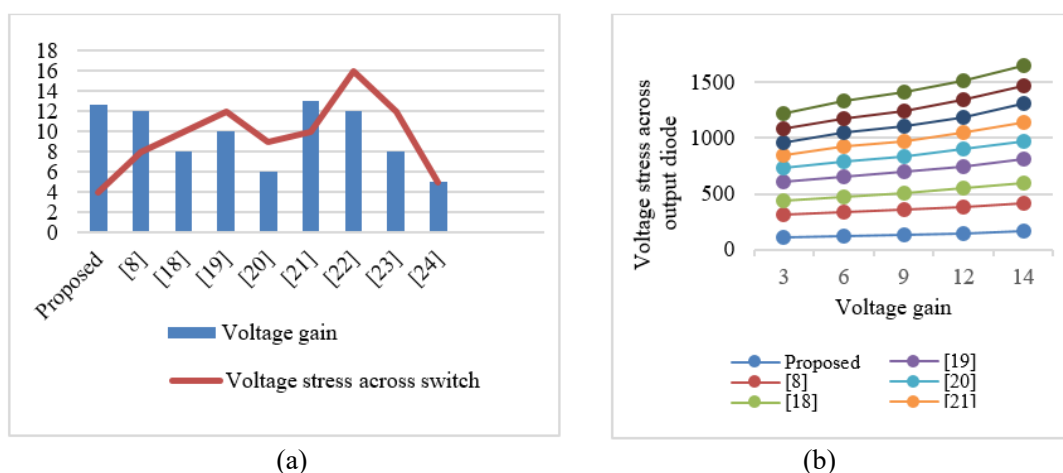


Fig. 10: Represents (a) voltage gain concerning voltage stress and (b) voltage stress comparison of various topologies.

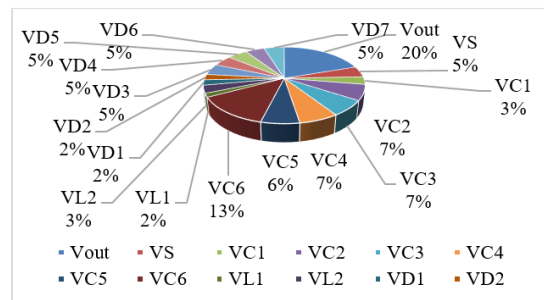


Fig. 11: Percentage voltage drops across each element of the proposed topology.

## 6. CONCLUSION

This paper proposes a unique design of non-isolated boost topology with a large conversion efficiency. A thorough discussion of the theoretical analysis and operating principles is provided in detail here. With neither an excessive duty cycle nor a high turns ratio, the suggested converter has been effectively built to obtain an extremely high step-up voltage gain. The suggested converter's construction might be expanded by increasing the QC and VDC cell to attain a greater step-up voltage boosting range. A significant reduction in the voltage stress on semiconductors was observed concerning gain. The primary side's quadratic structure contributed to a notable reduction in the input current fluctuation. Having low distortion in input current the proposed topology could efficiently track the optimum power of the PV panel without deteriorating circuit transformation efficiency. The circuit transformation efficiency was found to be 95%, whereas 98% transformation efficiency was observed for MPPT. A comparison between the suggested converter and other recently developed topologies is provided for better justification. The result analysis section complies with the similarity between analytical and simulation output. Considering all these merits, the suggested converter is ideally suited for integrating RES and battery sources, which requires high effectiveness and voltage enhancement.

## ACKNOWLEDGEMENT

This research has been supported by the Engineering Merit Scholarship Scheme 2021 and Research Management Centre, International Islamic University Malaysia.

## REFERENCES

- [1] Forouzesh M, Siwakoti YP, Gorji SA, Blaabjerg F, Lehman B. (2017) Step-Up DC-DC converters: A comprehensive review of voltage-boosting techniques, topologies, and applications. *IEEE Trans. Power Electron.*, 32(12): 9143-9178. doi: 10.1109/TPEL.2017.2652318
- [2] Kolli A, Gaillard A, De Bernardinis A, Bethoux O, Hissel D, Khatir Z. (2015) A review on DC/DC converter architectures for power fuel cell applications. *Energy Convers. Manag.*, 105: 716-730. doi: 10.1016/j.enconman.2015.07.060.
- [3] Esram T, Chapman PL. (2007) Comparison of photovoltaic array maximum power point tracking techniques. *IEEE Trans. Energy Convers.*, 22(2): 439-449. doi: 10.1109/TEC.2006.874230
- [4] Gopinathan S, Rao VS, Sundaramoorthy K. (2022) Family of nonisolated quadratic high gain DC-DC converters based on extended capacitor-diode network for renewable energy source integration. *IEEE J. Emerg. Sel. Top. Power Electron.*, 10(5): 6218-6230. doi: 10.1109/JESTPE.2022.3167283

- [5] Kasper M, Ritz M, Bortis D, Kolar JW. (2013) PV panel-integrated high step-up high efficiency isolated GaN DC-DC boost converter. INTELEC, Int. Telecommun. Energy Conf., pp. 602-608.
- [6] Hasanpour S, Forouzesh M, Siwakoti Y, Blaabjerg F. (2021) A new high-gain, high-efficiency SEPIC-based energy applications. *IEEE Journal of Emerging and Selected Topics in Industrial Electronics*, 2(4): 567-578. doi: 10.1109/JESTIE.2021.3074864
- [7] Nguyen MK, Duong TD, Lim YC. (2018) Switched-capacitor-based dual-switch high-boost DC-DC converter," *IEEE Trans. Power Electron.*, 33(5): 4181-4189. doi: 10.1109/TPEL.2017.2719040.
- [8] Hasanpour S, Nouri T, Blaabjerg F, Siwakoti YP. (2023) High step-up SEPIC-based trans-inverse DC-DC converter with quasi-resonance operation for renewable energy applications. *IEEE Trans. Ind. Electron.*, 70(1): 485-497. doi: 10.1109/TIE.2022.3150103.
- [9] Sarikhani A, Allahverdinejad B, Hamzeh M. (2021) A nonisolated buck-boost DC-DC converter with continuous input current for photovoltaic applications. *IEEE J. Emerg. Sel. Top. Power Electron.*, 9(1): 804-811. doi: 10.1109/JESTPE.2020.2985844
- [10] Rajabi A, Rajaei A, Tehrani VM, Dehghanian P, Guerrero JM, Khan B. (2022) A nonisolated high step-up DC-DC converter using voltage lift technique: Analysis, design, and implementation. *IEEE Access*, 10: 6338-6347. doi: 10.1109/ACCESS.2022.3141088
- [11] Alghaythi ML, O'Connell RM, Islam NE, Khan MMS, Guerrero JM. (2020) A high step-up interleaved DC-DC converter with voltage multiplier and coupled inductors for renewable energy systems. *IEEE Access*, 8: 123165-123174. doi: 10.1109/ACCESS.2020.3007137
- [11] Forouzesh M, Shen Y, Yari K, Siwakoti YP, Blaabjerg F. (2017) High-efficiency high step-up DC-DC converter with dual coupled inductors for grid-connected photovoltaic systems. *IEEE Trans. Power Electron.*, 33(7): 5967-5982. doi: 10.1109/TPEL.2017.2746750
- [12] Ansari SA, Moghani JS. (2019) A novel high voltage gain noncoupled inductor SEPIC converter. *IEEE Trans. Ind. Electron.*, 66(9): 7099-7108. doi: 10.1109/TIE.2018.2878127
- [13] Jalilzadeh T, Rostami N, Babaei E, Maalandish M. (2023) Nonisolated topology for high step-up DC-DC converters. *IEEE J. Emerg. Sel. Top. Power Electron.*, 11(1): 1154-1168. doi: 10.1109/JESTPE.2018.2849096
- [14] Haji-Esmaili MM, Babaei E, Sabahi M. (2018) High step-up quasi-Z source DC-DC converter. *IEEE Trans. Power Electron.*, 33(12): 10563-10571. doi: 10.1109/TPEL.2018.2810884
- [15] Jiya IN, Van Khang H, Kishor N, Ciric RM. (2022) Novel family of high-gain nonisolated multiport converters with bipolar symmetric outputs for DC microgrids. *IEEE Trans. Power Electron.*, 37(10): 12151-12166. doi: 10.1109/TPEL.2022.3176688
- [16] Gopinathan S, Rao VS, Kumaravel S. (2023) Enhanced voltage gain boost DC-DC converter with reduced voltage stress and core saturation. *IEEE Trans. Circuits Syst. II Express Briefs*, 70(8): 3019-3023. doi: 10.1109/TCSII.2023.3252721
- [17] Verma D, Nema S, Agrawal R, Sawle Y, Kumar A. (2022) A different approach for maximum power point tracking (MPPT) using impedance matching through nonisolated DC-DC converters in solar photovoltaic systems. *Electron.*, 11(7): 1053. doi: 10.3390/electronics11071053.
- [18] Shahrukh K, Mohammad Z, Arshad M, Abbas S. N, Javed A, Mamdouh L. A, Basem A, Mohd T, Adil S and Chang-Hua L. (2021) A new transformerless ultra high gain DC-DC converter for DC microgrid application. *IEEE Access*, 9: 124560-124582. doi: 10.1109/ACCESS.2021.3110668.
- [19] Gopinathan S, Rao VS, KS. (2023) Enhanced voltage gain boost DC-DC converter with reduced voltage stress and core saturation. *IEEE Trans. Circuits Syst. II Express Briefs*, 70(8), 3019-3023, doi: 10.1109/TCSII.2023.3252721.
- [20] Subhani N, May Z, Alam MK, Khan I, Hossain MA, Mamun S. (2023) An improved nonisolated quadratic DC-DC boost converter with ultra high gain ability. *IEEE Access*, 11: 11350-11363. doi: 10.1109/ACCESS.2023.3241863

- [21] Li H, Du H, Zeng Y, Qiu Z, Jiang X, Chen Z. (2022) A modified interleaved capacitor clamped DC-DC converter with non-resonant soft switching. *IEEE Trans. Power Electron.*, 37(10): 12221-12236. doi: 10.1109/TPEL.2022.3163010.
- [22] Sadaf S, Al-Emadi N, Maroti PK, Iqbal A. (2021) A new high gain active switched network-based boost converter for DC microgrid application. *IEEE Access*, 9: 68253-68265. doi: 10.1109/ACCESS.2021.3077055
- [23] Nouri T, Hosseini SH, Babaei E. (2014) Analysis of voltage and current stresses of a generalized step-up DC-DC converter. *IET Power Electron.*, 7(6): 1347-1361. doi: 10.1049/iet-pel.2013.0496
- [24] Bao D, Kumar A, Pan X, Xiong X, Beig AR, Singh SK. (2021) Switched inductor double switch high gain DC-DC converter for renewable applications. *IEEE Access*, 9: 14259-14270. doi: 10.1109/ACCESS.2021.3051472.

## THIOL FUNCTIONALIZED GOLD NANOBIPYRAMIDS-BASED PLASMONIC SENSOR FOR GLUCOSE DETECTION

NATASYA SALSABIILA<sup>1,2,3</sup>, MARLIA MORSIN<sup>1,2\*</sup>, MUHAMMAD HANIF<sup>1</sup>,  
SURATUN NAFISAH<sup>1,2,3</sup>, NUR LIYANA RAZALI<sup>1,2</sup> AND IWANTONO<sup>4</sup>

<sup>1</sup>Faculty of Electrical & Electronic Engineering, Universiti Tun Hussein Onn Malaysia,  
86400 Parit Raja, Batu Pahat, Johor, Malaysia

<sup>2</sup>Microelectronics & Nanotechnology - Shamsuddin Research Centre (MiNT-SRC), Institute of Integrated  
Engineering, Universiti Tun Hussein Onn Malaysia, 86400 Parit Raja, Batu Pahat Johor, Malaysia

<sup>3</sup>Department of Electrical Engineering, Faculty of Industrial and Production Technology,  
Institut Teknologi Sumatera (ITERA), Lampung Selatan, 35365 Indonesia

<sup>4</sup>Department of Physics, Faculty of Mathematics and Natural Sciences, Universitas Riau,  
Pekanbaru, 28293, Indonesia

\*Corresponding author: marlia@uthm.edu.my

(Received: 30 March 2023; Accepted: 13 June 2023; Published on-line: 1 January 2024)

**ABSTRACT:** Gold nanobipyramids (GNBPs) have high selectivity in detecting changes in their surrounding medium because of their electric field enhancements and larger surface areas. In this study, we functionalized GNBPs using a thiol group that acts as a ligand to improve the detection performance of the analytes. The investigation is carried out by varying the functionalization periods from 12 to 72 hours. The optimum thiol-functionalized GNBPs (t-GNBPs) are obtained in 60 hours, with a length of  $36.84 \pm 2.05$  nm, a width of  $24.02 \pm 0.74$  nm, and an aspect ratio of  $1.54 \pm 0.11$ . Then, the optimum t-GNBPs are used as a sensing material in a plasmonic sensor to detect glucose. The limit of detection (LoD) of glucose is  $1 \mu\text{M}$  for this sensor. The plasmonic sensor has been successfully built with reliable performance in detecting glucose with excellent linearity, sensitivity and  $R^2 = 1$ ; good selectivity compared to four similar chemical structure analytes; high stability with a low error value, i.e.,  $\pm 0.02$  a.u.; and almost consistent repeatability values in each cycle with low percent variance of 0.000025% for the t-SPR area and 0.000032% for the l-SPR area. Therefore, a plasmonic sensor based on t-GNBPs is an alternative method of detecting glucose with high sensitivity, selectivity and repeatability.

**ABSTRAK:** Nanobipiramid Emas (GNBPs) memiliki selektiviti yang tinggi dalam mengesan perubahan medium sekitar kerana memiliki peningkatan medan elektrik dan luas permukaan yang besar. Kajian ini merupakan fungsionalisasi terhadap GNBPs dengan menggunakan kumpulan thiol sebagai ligan bagi meningkatkan prestasi pengesanan analit. Kajian ini dilakukan dengan mempelbagaikan tempoh masa fungsionalisasi dalam julat waktu 12 hingga 72 jam. GNBPs optimum yang difungsionalisasi oleh thiol (t-GNBPs) diperolehi pada 60 jam, dengan panjang  $36.84 \pm 2.05$  nm, lebar  $24.02 \pm 0.74$  nm, dan nisbah aspek  $1.54 \pm 0.11$ . Kemudian, t-GNBPs optimum digunakan sebagai bahan penerima pada sensor plasmonik bagi mengesan glukosa. Limit pengesanan glukosa (LoD) bagi sensor ini adalah sebanyak  $10^0 \mu\text{M}$ . Sensor plasmonik telah berhasil dibangunkan dengan kecekapan boleh percaya dalam mengesan glukosa dengan lineariti dan sensitiviti sebanyak  $R^2 = 1$ . Pemilihan yang baik dibandingkan dengan 4 analit yang sama dari segi struktur kimia. Kestabilan yang tinggi dengan nilai ralat rendah iaitu  $\pm 0.02$  a.u, dan memiliki nilai keberulangan yang hampir konsisten pada setiap kitar dengan peratusan varian rendah iaitu sebanyak 0.000025% bagi bahagian t-SPR dan 0.000032% bagi l-SPR. Oleh itu, pengesanan plasmonik berdasarkan t-GNBPs ini adalah kaedah alternatif bagi mengesan glukosa dengan sensitiviti, selektiviti, dan kebolehulangan yang tinggi.

**KEYWORDS:** gold nanobipyramids; glucose; plasmonic sensor; thiol

## 1. INTRODUCTION

Gold is a metal nanoparticle commonly used as a sensing material due to its unique surface plasmon resonance (SPR) property that makes it sensitive to the surrounding medium. In addition, this metal has high biocompatibility and reactivity, low cost, and is non-toxic and environmentally friendly [1]. The SPR properties of gold nanomaterials depend on their shape and size, with nanospherical being the most synthesized nanoparticles. Other than that, several forms of non-spherical gold nanoparticles have been successfully synthesized, such as nanorod, nanorice, nanoplate, and nanoarray, each of which can be used to detect mercury (II) and  $\text{Hg}^{2+}$  ions [2], boric acid [3], as well as sepsis [4]. Moreover, a form of non-spherical gold nanomaterial with high figures of merit is gold nanobipyramids (GNBPs), which has higher sensitivity and the potential to be applied as a sensing material in sensor systems [5]. The GNBPs have local field enhancements, a wider surface area than other forms, and a spectral surface that can be modified. The applications of GNBPs as sensing material include detecting glyphosate [5], aflatoxin B1 [6], and dopamine [7], using various detection methods. In this study, GNBPs have been synthesized and act as a sensing material for SPR-based sensors, called plasmonic sensors. The plasmonic sensor is chosen because it can detect analytes quickly and accurately.

The plasmonic sensor was built to detect glucose as a pre-indicator of diabetes. Diabetes is a type of disease in which the body is unable to produce insulin hormone properly, resulting in the body's inability to process carbohydrates into a source of energy, which is characterized by fluctuations in blood sugar from its normal range and can increase the prevalence of complications compared to other types of disease. According to the World Health Organization (WHO), diabetes is predicted to be the 7<sup>th</sup> most significant cause of death in 2030 [8]. According to a study conducted by Pouya et al., using the logistic regression method, it is predicted that people with diabetes worldwide will reach 578 million in 2030 and 700 million in 2045 [9]. Meanwhile, Malaysia was ranked 4<sup>th</sup> on the list of countries with the most diabetics in Southeast Asia in 2016. Then, Malaysia was also ranked as the 1<sup>st</sup> country with the highest number of people with diabetes in the West Pacific in 2018, with a prevalence reaching 16.8% and affecting 3.6 million people from the total adult population. Also, the annual costs incurred by Malaysia reached US\$ 600 million [10]. Thus, it is crucial to have the glucose detection system to improve diabetes care and the plasmonic sensor is an alternative method to solve this problem.

Functionalization was performed on the GNBPs surface to produce additional ligands that bind with the targeted analyte. Thiol, as one of the functionalization agents, is commonly used for detecting glucose due to its ability to conjugate with strong affinity on the nanoparticle surface. Therefore, it can bind with carbohydrate molecules such as glucose and increase the sensor's selectivity, characterized by long emission waves [11]. Thus far, several researchers have reported that thiol can be used in gold nanoparticles to detect glucose. A study by Samanta *et al.* performed glucose detection based on gold nanospheres [12]. Then, a study by Asim *et al.* used thiol to functionalize thin gold film as a sensing material [13]. Another structure is cubes functionalized with thiol, used in the study by Zhenyu et al. with an electrochemical detection method [14]. Meanwhile, GNBPs have shown a promising and greater potential structure to be functionalized with thiol and used to detect glucose as well due to their several advantages, i.e., the higher figure of merit value compared to other structures. Hence, this study proposes thiol-functionalized GNBPs (t-GNBPs) as a sensing material for detecting glucose based on plasmonic resonance.

## 2. MATERIALS AND METHOD

### 2.1 Materials

The materials used in this study were gold (III) chloride trihydrate ( $\text{HAuCl}_4 \cdot 3\text{H}_2\text{O}$ ), chloroplatinic acid hydrate ( $\text{H}_2\text{PtCl}_4 \cdot \text{H}_2\text{O}$ ), cetylmethylammonium bromide ( $\text{C}_{19}\text{H}_{42}\text{BrN}$ ), sodium borohydride ( $\text{NaBH}_4$ ), ascorbic acid ( $\text{C}_6\text{H}_8\text{O}_6$ ), and (3-mercaptopropyl) trimethoxysilane which were purchased from Sigma Aldrich, USA. Silver nitrate ( $\text{AgNO}_3$ ) and hydrochloric acid ( $\text{HCl}$ ) were purchased from RCI Labscan.

### 2.2 Preparation of Gold Nanobipyramids

#### 2.2.1 Synthesis

The synthesis method used was the bottom-up seed-mediated growth method (SMGM) which is divided into two processes, i.e., seeding and growth, as mentioned in the previous studies [5]. The materials needed to produce bipyramid nanoseeds solution include  $\text{HAuCl}_4 \cdot 3\text{H}_2\text{O}$  (0.15, 0.01 M),  $\text{H}_2\text{PtCl}_4 \cdot \text{H}_2\text{O}$  (0.1 mL, 0.01 M),  $\text{C}_{19}\text{H}_{42}\text{BrN}$  (9.75 mL, 0.1 M), and cold  $\text{NaBH}_4$  (0.9 mL, 0.01 M), which were mixed and then left undisturbed for 2 hours at 27 °C. After 2 hours, the nanoseeds were used for the growth process. The materials needed to produce growth solutions include  $\text{HAuCl}_4 \cdot 3\text{H}_2\text{O}$  (0.875 mL, 0.01 M),  $\text{H}_2\text{PtCl}_4 \cdot \text{H}_2\text{O}$  (0.0025 mL, 0.01 M),  $\text{C}_{19}\text{H}_{42}\text{BrN}$  (20 mL, 0.1 M),  $\text{AgNO}_3$  (0.2 mL, 0.01 M),  $\text{HCl}$  (0.4 mL, 1 M),  $\text{C}_6\text{H}_8\text{O}_6$  (0.16 mL, 0.1 M), and 0.05 mL of nanoseeds. The materials were mixed and left undisturbed for 2 hours at 27 °C. After 2 hours, the growth solution was functionalized with thiol groups.

#### 2.2.2 Functionalization

The thiol group (3-mercaptopropyl) trimethoxysilane was diluted in 20 mL ethanol (10 mM) for the functionalization solution. Then, 2 mL of functionalization solution was added to the growth solution and stirred at 500 rpm with several time variations. The time variations in the stirring process included 12 hours, 24 hours, 48 hours, 60 hours, and 72 hours. Meanwhile, the temperature during the stirring process was kept constant at 27 °C.

#### 2.2.3 Characterization

In this work, the characterization was carried out using ultraviolet - visible (UV - Vis), X-Ray Diffraction (XRD), and Field Emission Scanning Electron Microscopy (FESEM). Each technique was used to observe the optical, structural, and morphological properties of t-GNBPs. For UV-Vis characterization, the UV-1800 Shimadzu Spectrophotometer (Japan) instrument was used with a wavelength range of 400 nm – 1000 nm. The XRD characterization uses the Bruker D8 Advance X-Ray Diffractometer (Germany) device with an angle range of 20° - 60°. Meanwhile, the FESEM characterization uses the Joel JSM-7600 Field Emission Scanning Electron Microscopy (USA) instrument. The characterization samples were centrifuged for 30 minutes at 5000 rpm and then dispersed in a deionized water (DIW) solution. This process was repeated three times. After that, the residue was mixed with 25  $\mu\text{L}$  DIW and deposited on glass and ITO substrates for XRD and FESEM characterization, respectively. Finally, the sample substrate was dried in an oven for 30 minutes at 50 °C.

### 2.3 Preparation of Analytes

The glucose target analyte (20 mL) was prepared with various concentrations, including  $10^0$   $\mu\text{M}$ ,  $10^1$   $\mu\text{M}$ ,  $10^2$   $\mu\text{M}$ ,  $10^3$   $\mu\text{M}$ ,  $10^4$   $\mu\text{M}$ ,  $10^5$   $\mu\text{M}$ , and  $10^6$   $\mu\text{M}$ . This variation was selected to improve the range of glucose levels in an automatic insulin delivery system with adjustable glucose in a previous study, i.e., 110 mg/dL – 150 mg/dL (6111.1  $\mu\text{M}$  – 8333.3  $\mu\text{M}$ ) [15]. For

the selectivity study, lactose, natrium, vitamin C, and calcium were used as analytes, each was prepared in 20 mL with a concentration of  $10^1 \mu\text{M}$ .

## 2.4 Plasmonic Sensor Setup

The plasmonic sensor comprises six components: a light source, simplex fiber optic, chamber, material sensing, and a computer equipped with Ocean View Software to analyze the absorbance spectrum data. The component setup used is shown in Fig. 1. This component setup refers to previous research on herbicide detection using gold nanorods [16]. In contrast, for detecting formaldehyde, boric acid, and glyphosate, the duplex fiber optic type was used to have a different setup [5].

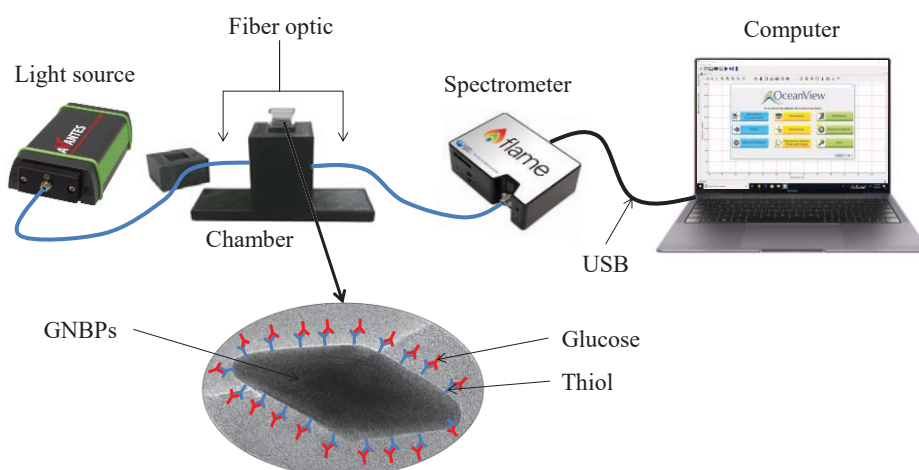


Fig. 1: The setup of the plasmonic sensor for glucose detection.

## 3. RESULTS AND DISCUSSION

### 3.1 Synthesis of GNBP

GNBPs were successfully synthesized using the SMGM method. The initial observation was made by analyzing the color change in the solution during the synthesis process. After successful seeding, the nanoseeds solution turned brown, as shown in Fig. 2(a). This color is consistent with previous research [17], which said that a color change indicates a nanoseeds size of 4 nm. Meanwhile, the solution changed color to purple for the growth process, as shown in Fig. 2(b), which appeared during the first 30 minutes of reaction time. In this process,  $\text{C}_{19}\text{H}_{42}\text{BrN}$  functions as a capping agent which controls the elongation of gold particles. Then, adding  $\text{AgNO}_3$  affects the formation of GNBP during the growth process.

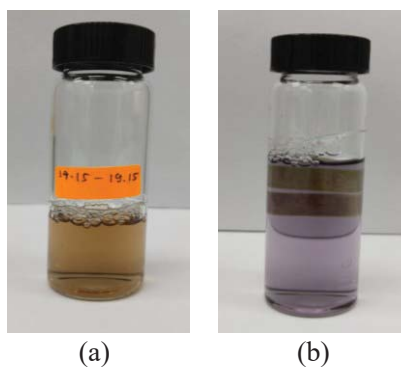


Fig. 2: Color visualization of (a) nanoseeds solution and (b) growth solution.

### 3.2 Effect of Thiol Functionalization on GNBP

Functionalization of GNBP using thiol was successfully carried out after the growth solution was produced. The solution was prepared using 12- to 72-hour time variations to determine the optimum and specific functionalization time. After the stirring process with a magnetic stirrer, the resulting t-GNBP solution is shown in Fig. 3. The solution's color changed from dark purple to light purple as the functionalization time increased. Thus, it can be confirmed that t-GNBP were successfully formed. As a comparison, an unfunctionalized solution was also observed and denoted as 0 hours.

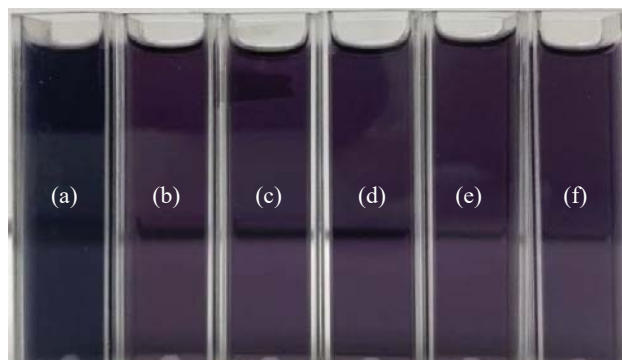


Fig. 3: Final color solution after functionalization with (a) 0 hours, (b) 12 hours, (c) 24 hours, (d) 48 hours, (e) 60 hours, and (f) 72 hours.

Optical characterization was carried out using UV-Vis. The resulting absorbance spectrum is shown in Fig. 4. The figure shows the spectral region in the range of 400 – 1000 nm and has two peaks, namely Transverse Surface Plasmon Resonance (t-SPR) in the area of 500 nm – 600 nm and Longitudinal Surface Plasmon Resonance (l-SPR) in the range of 700 nm – 900 nm. The intensity and peak positions of the absorbance spectrum are formulated in Table 1. Based on the data in Fig. 4 and Table 2, it was found that the absorbance spectrum underwent a hyperchromic shift in the range of 0 hours – 60 hours. In contrast, the hypochromic change occurred in the range of 60 hours – 72 hours. Thus, t-GNBP with a functionalization time of 60 hours are the optimum sample, also used as a sensing material in a plasmonic sensor.

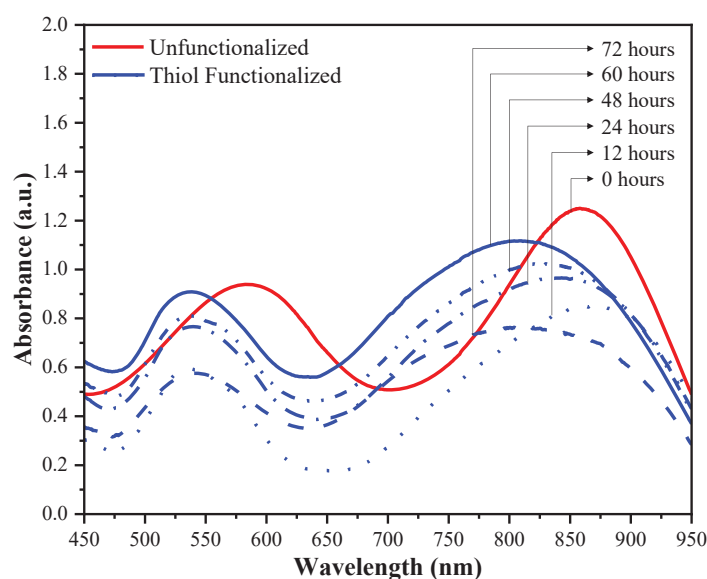


Fig. 4: The UV-Vis Spectrum of t-GNBP.

Table 1: Position of the peak wavelength and absorbance of t-GNBPs in the t-SPR and l-SPR areas

Sample (hours)	t-SPR		l-SPR	
	$\lambda$ (nm)	I (a.u.)	$\lambda$ (nm)	I (a.u.)
0	586	0.942	855	1.249
12	536	0.606	874	0.851
24	540	0.735	843	0.966
48	542	0.791	830	1.024
60	544	0.881	810	1.117
72	559	0.551	804	0.764

XRD was used for structural characterization to determine the chemical and crystal structure composition of the t-GNBPs, as shown in Fig. 5. The figure shows six samples and their detailed diffraction peak positions are detailed in Table 2. Each sample shows two diffraction peaks in the range of  $20^\circ$  -  $60^\circ$ . The positions of the two peaks follow the standard Inorganic Crystal Structure Database (ICSD) file No. 98-061-1625, with the resulting gold particles having a face-centered cubic (FCC) crystal structure. The crystal size of t-GNBPs was calculated using the Debye-Scherrer equation. The highest peak was obtained in the (111) plane at  $38.105^\circ$  –  $38.369^\circ$ , indicating that the dominant preferred orientation of the crystal is parallel to the surface of the substrate. Another FCC gold nanocrystal was found in the (200) plane at  $44.458^\circ$  –  $44.555^\circ$ . In general, the functionalization process slowly increased the intensity of the (111) and (200) planes compared to pure GNBPs.

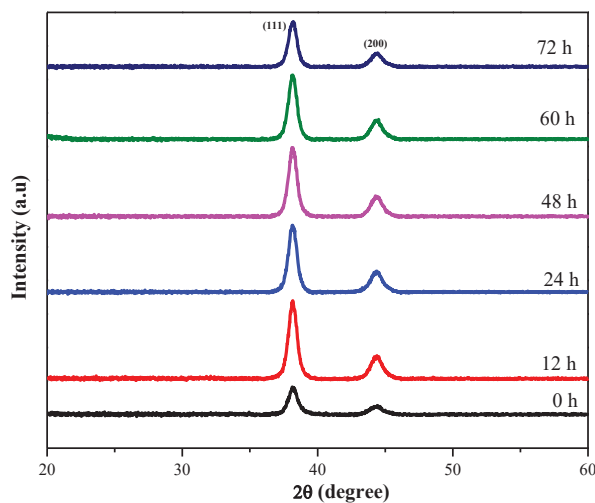


Fig. 5: XRD pattern of t-GNBPs.

Table 2: Detailed of t-GNBPs XRD parameters

Sample (hours)	Plane (111)		Plane (200)		FWHM	Crystallite Size (nm)
	$2\theta$ ( $^\circ$ )	I (a.u.)	$2\theta$ ( $^\circ$ )	I (a.u.)		
0	38.152	770.58	44.554	218.26	0.354	23.731
12	38.369	1843.39	44.555	598.25	0.197	42.739
24	38.212	1949.62	44.458	567.93	0.433	19.416
48	38.294	1856.23	44.313	583.42	0.240	35.038
60	38.108	1878.87	44.302	556.83	0.624	13.468
72	38.239	1299.21	44.398	378.29	0.720	11.678

Subsequently, morphological characterization was performed using FESEM, as shown in Fig. 6, to confirm the shape. Then, the aspect ratio and surface density analysis were performed. The aspect ratio is the ratio between the length and width of the nanomaterial. Meanwhile, the surface density is the ratio between the area covered by t-GNBPs and the entire area [16]. The analysis and calculations were done using ImageJ Software, as shown in Table 3. Based on the data in Table 3, it was found that an increase in functionalization time has caused a decrease in surface density, length, width, and aspect ratio in general. The resulting truncated t-GNBPs (by-products) continued to increase along with the increase in functionalization time because as the functionalization time rose, the gold source decreased, causing some nanoseeds to have insufficient gold sources to grow as perfect GNBPs. The surface density directly correlates with the resulting LSPR phenomenon and sensor sensitivity [18]. Decreases in the length, width, and surface density have caused a reduction in the peak of the absorbance spectrum, a spectral shift towards blue (blue shift), and reduced sensitivity. In addition, increasing functionalization time affected the bipyramidal shape, which became spherical-like. This is because the excess functionalization agents or molecules can etch the nanobipyramids' surfaces and remove material from the sharp tips and edges of the bipyramids, leading to a more rounded shape. Moreover, the Ostwald ripening process can also occur, where smaller nanobipyramids dissolve and transfer material to larger particles, resulting in a more uniform and spherical morphology [19]. Therefore, the functionalization process has allowed a morphological change.

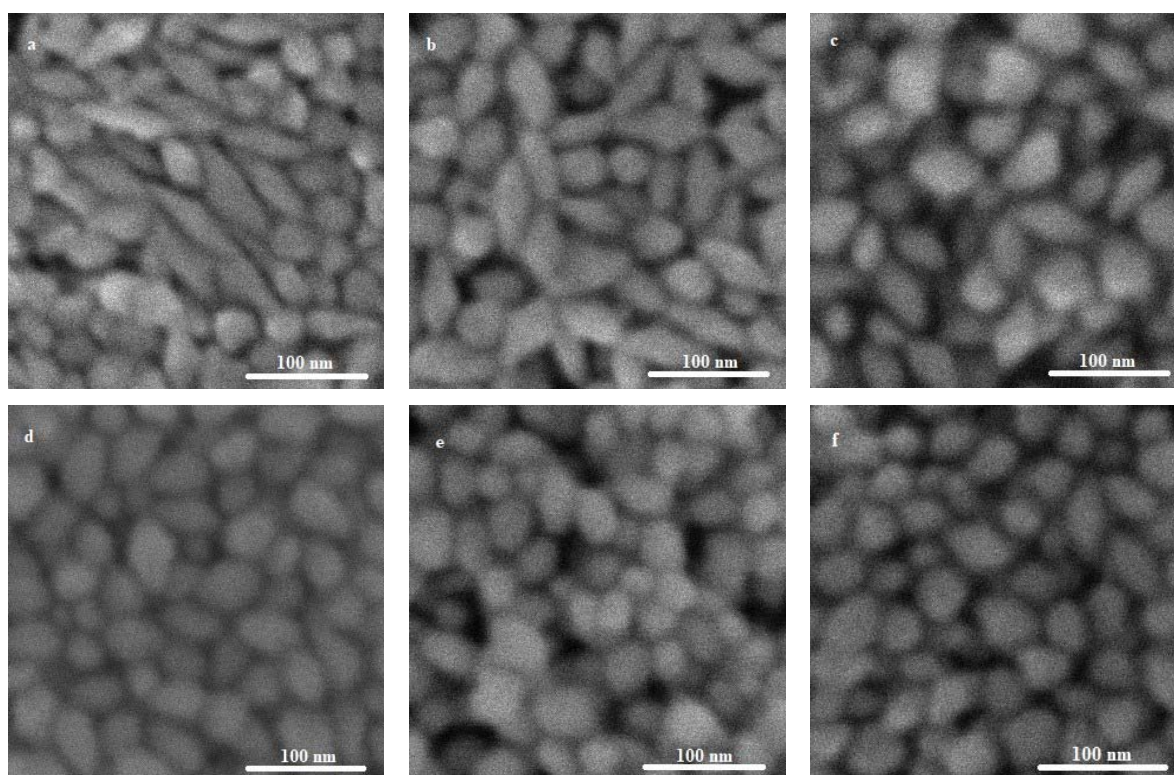


Fig. 6: FESEM image of t-GNBPs synthesized with a variation of time (a) 0 hours, (b) 12 hours, (c) 24 hours, (d) 48 hours, (e) 60 hours, and (f) 72 hours.

Table 3: Length, width, and aspect ratio of sampled t-GNBPs and truncated t-GNBPs

Sample (hours)	Average Size							
	t-GNBPs				Truncated t-GNBPs			
	Surface Density (%)	Width (nm)	Length (nm)	Aspect Ratio	Surface Density (%)	Width (nm)	Length (nm)	Aspect Ratio
0	19.08±6.09	31.31±8.33	59.37±2.97	2.09±0.37	7.08±0.32	27.10±0.34	22.72±0.92	1.04±0.03
12	15.03±1.92	27.85±0.99	53.81±5.85	1.93±0.20	9.40±0.83	33.05±1.71	28.39±1.53	1.17±0.06
24	11.53±1.13	25.86±0.75	44.58±4.15	1.73±0.16	7.88±0.58	27.02±1.04	29.10±1.06	1.08±0.00
48	11.21±0.67	25.57±0.58	43.80±1.84	1.71±0.05	7.19±0.89	27.00±0.98	26.49±2.30	0.98±0.92
60	8.84±5.32	24.02±0.74	36.84±2.05	1.54±0.11	5.17±0.57	23.02±1.08	22.33±1.46	1.03±0.02
72	0.70±0.12	5.47±0.85	13.25±2.25	2.66±0.85	0.50±0.06	7.39±1.44	7.10±0.60	1.09±0.28

### 3.3 t-GNBPs as a Sensing Material for Glucose Detection

#### 3.3.1 Plasmonic Response

A plasmonic response test was performed to ensure that t-GNBPs can detect glucose. The system was observed in two mediums, DIW as a reference and glucose  $10^1 \mu\text{M}$  as the target analyte. The test results are shown in Fig. 7.

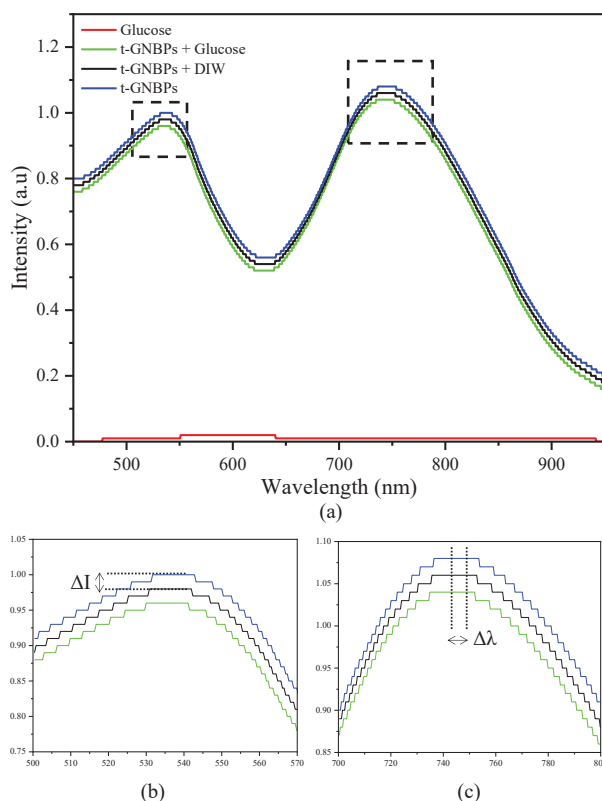


Fig. 7: (a) The plasmonic response of t-GNBPs spectrum. DIW and glucose medium show (b) intensity change and (c) wavelength shift.

Pure  $10^1 \mu\text{M}$  glucose was also recorded by the plasmonic sensor system for comparison. The results show that pure  $10^1 \mu\text{M}$  glucose does not have any peak, proving that the LSPR response generated by the plasmonic sensor is caused by t-GNBPs as material sensing. The positions of the peak intensity and wavelength of the system response are shown in Table 4.

Furthermore, t-GNBPs with various functionalization times were tested in the DIW and  $10^1$   $\mu$ M glucose medium, shown in Fig. 8 and Fig. 9, respectively. The precise peak position for each medium is shown in Table 5 and Table 6. It can be confirmed that 60 hours was an optimum functionalized time through its highest intensity spectrum compared to others in DIW and glucose medium. Then, t-GNBPs with 60 hours of functionalization time were used as sensing material to detect glucose and tested for sensor performances, namely sensitivity, selectivity, stability, and repeatability.

Table 4: Sensor response using t-GNBPs in DIW and glucose

Medium	t-SPR		I-SPR	
	$\lambda$ (nm)	I (a.u)	$\lambda$ (nm)	I (a.u.)
Pure t-GNBPs	537.244	1.00	744.804	1.08
DIW	536.391	0.98	744.010	1.06
Glucose	535.539	0.96	743.215	1.04

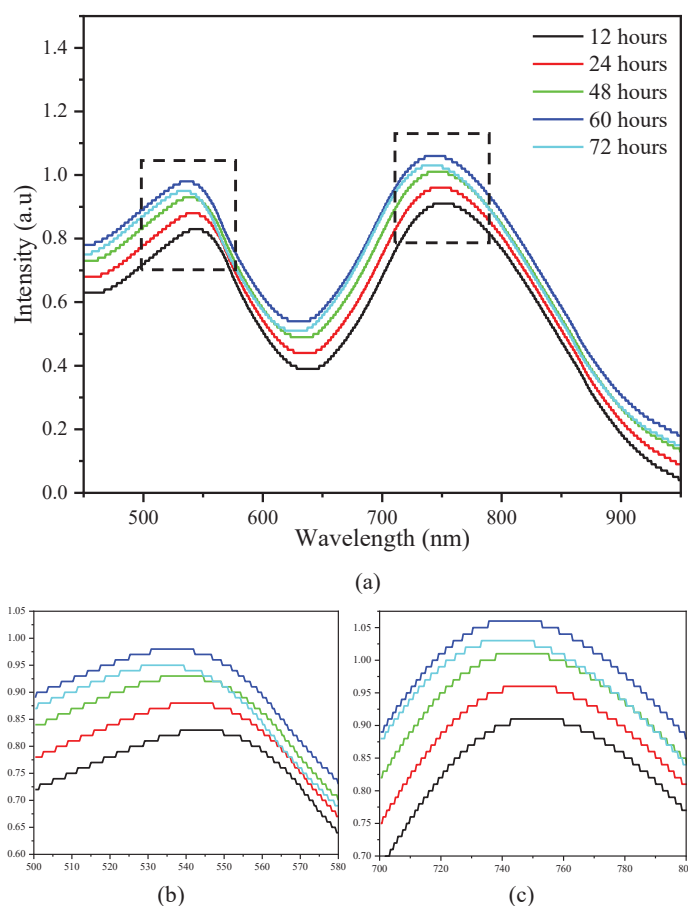


Fig. 8: (a) The plasmonic response of t-GNBPs in DIW medium, with (b) t-SPR area and (c) I-SPR area.

### 3.3.2 Sensitivity Test

The sensitivity test used two test parameters, peak intensity and wavelength changes, referring to previous studies [5]. This test was conducted to determine the effect of t-GNBPs as a sensing material on the resulting sensor response. In this test, the medium used was glucose

with several concentration variations, i.e.,  $10^0 \mu\text{M}$ ,  $10^1 \mu\text{M}$ ,  $10^2 \mu\text{M}$ ,  $10^3 \mu\text{M}$ ,  $10^4 \mu\text{M}$ ,  $10^5 \mu\text{M}$ , and  $10^6 \mu\text{M}$ . The resulting sensor response is shown in Fig. 10. Meanwhile, the peak intensity and wavelength positions are shown in Table 7.

Table 5: The exact peak position of t-GNBPs in DIW medium

Medium	t-SPR		l-SPR	
	$\lambda$ (nm)	I (a.u)	$\lambda$ (nm)	I (a.u.)
12	544.056	0.83	751.150	0.91
24	541.503	0.88	748.770	0.96
48	538.948	0.93	746.390	1.01
60	536.391	0.98	744.010	1.06
72	533.832	0.95	741.625	1.03

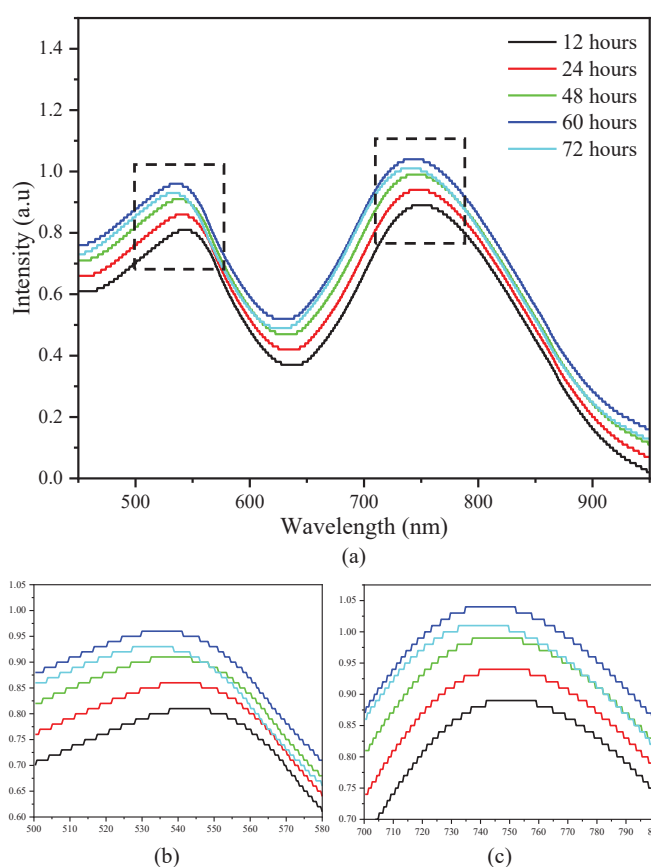


Fig. 9: (a) The plasmonic response of t-GNBPs in glucose medium, with (b) t-SPR area and (c) l-SPR area.

Table 6: The precise peak position of t-GNBPs in glucose medium

Medium	t-SPR		l-SPR	
	$\lambda$ (nm)	I (a.u)	$\lambda$ (nm)	I (a.u.)
12	543.205	0.81	750.360	0.89
24	540.651	0.86	747.980	0.94
48	538.096	0.92	745.599	0.99
60	535.539	0.96	743.215	1.04
72	532.979	0.93	740.829	1.01

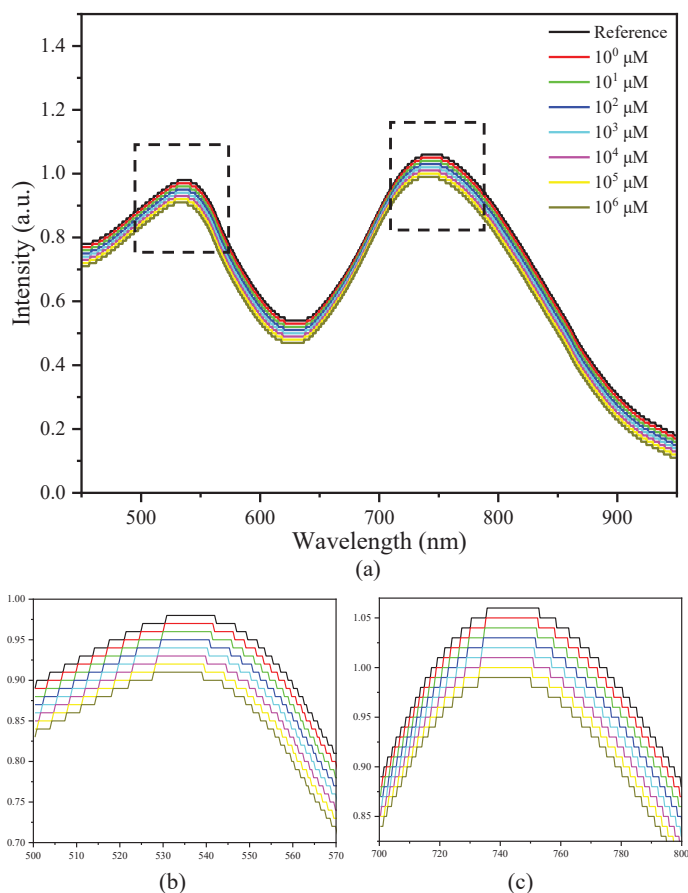


Fig. 10: (a) System response using t-GNBPs. DIW and glucose concentration variations show intensity and wavelength shifts in (b) t-SPR and (c) l-SPR.

Table 7: The detailed peak intensity and wavelength position in system response.

Glucose Concentration ( $\mu\text{M}$ )	t-SPR		l-SPR	
	$\lambda$ (nm)	I (a.u)	$\lambda$ (nm)	I (a.u.)
0	536.391	0.98	744.010	1.06
$10^0$	535.965	0.97	743.613	1.05
$10^1$	535.539	0.96	743.215	1.04
$10^2$	535.112	0.95	742.818	1.03
$10^3$	534.686	0.94	742.420	1.02
$10^4$	534.259	0.93	742.023	1.01
$10^5$	533.832	0.92	741.625	1.00
$10^6$	533.406	0.91	741.227	0.99

Based on Fig. 10 and Table 7, it was found that an increase in glucose concentration caused a constant decrease in peak intensity of 0.01 a.u. In the t-SPR region, the peak intensity decreased from 0.98 a.u. to 0.91 a.u., while in the l-SPR area, it occurred from 1.06 a.u. to 0.99 a.u. The decrease in wavelength and an increase in glucose concentration caused the absorbance spectrum to shift towards the blue region and it occurred constantly. In the t-SPR region, the shift in wavelength started from 536.391 nm to 533.406 nm, while in the l-SPR region, it appeared from 744.010 nm to 741.227 nm. Thus, t-GNBPs can be used as a sensing material to detect glucose in the range of  $10^0$   $\mu\text{M}$ ,  $10^1$   $\mu\text{M}$ ,  $10^2$   $\mu\text{M}$ ,  $10^3$   $\mu\text{M}$ ,  $10^4$   $\mu\text{M}$ ,  $10^5$   $\mu\text{M}$ ,

and  $10^6$   $\mu\text{M}$ , or equal to 0.000198 mg/mL – 198.17 mg/mL. Then, the changes in glucose concentration to changes in peak intensity and wavelength are shown in Fig. 11 and Fig. 12, respectively.

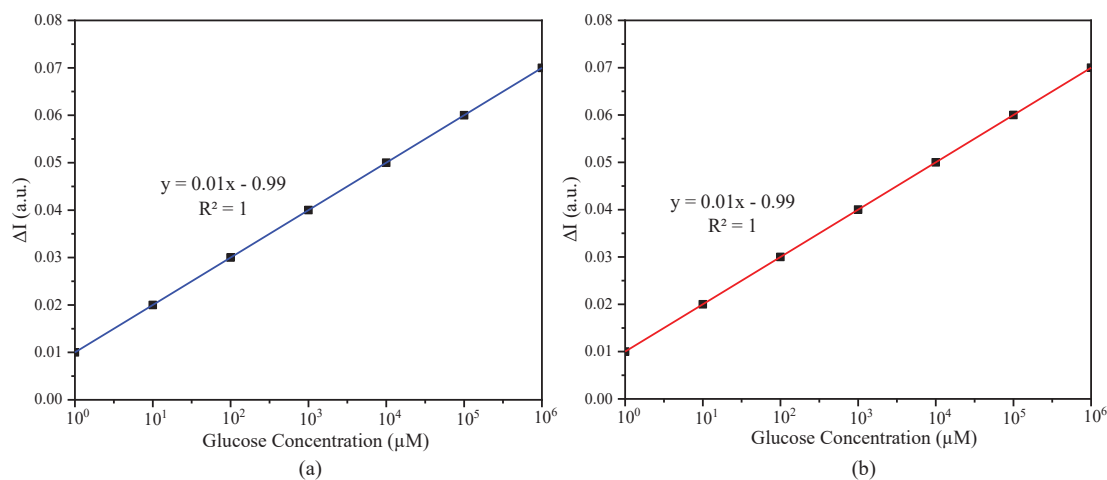


Fig. 11: Linearity between glucose concentration and peak intensity changes in (a) t-SPR and (b) l-SPR region.

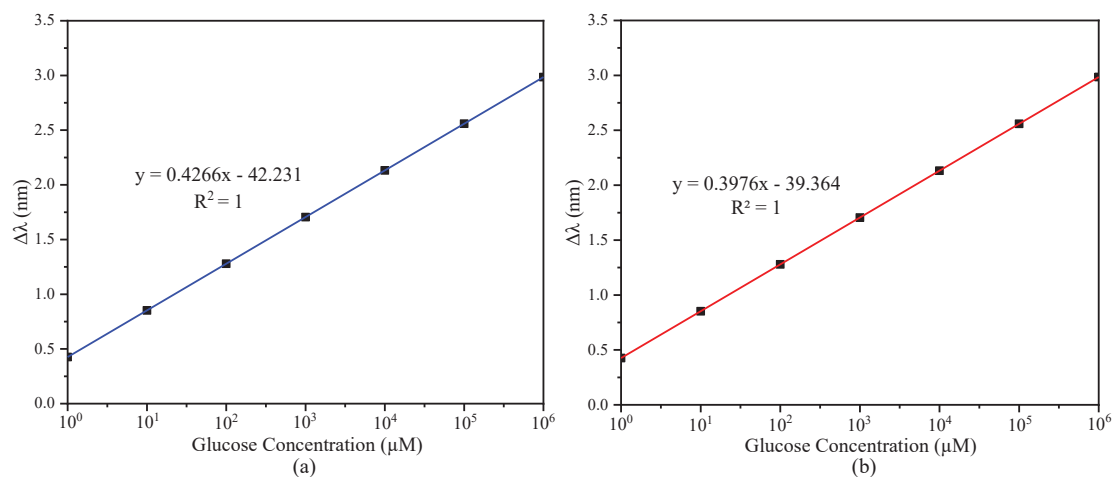


Fig. 12: Linearity between glucose concentration and wavelength shift in (a) t-SPR and (b) l-SPR region.

Figures 11 and 12 show that t-GNBPs have excellent linearity with an  $R^2$  value of 1 at peak intensity and wavelength changes. For changes in peak intensity, the resulting linear regression was  $0.01x - 0.99$  in both the t-SPR and l-SPR regions. As for the shift in wavelength, the resulting linear regression was  $0.4266x - 42.231$  for the t-SPR region and  $0.3976x - 39.364$  for the l-SPR region. This equation can determine unknown glucose concentrations in further research and development. The positions of changes in intensity and wavelength peaks are shown in Table 8. Based on the data, the highest intensity peak changes occurred in  $10^6$   $\mu\text{M}$  glucose medium of 0.07 a.u. Meanwhile, the highest change in wavelength also happened in the same medium of 2.985 nm for the t-SPR region and 2.783 nm for the l-SPR region.

The linearity generated by the t-GNBPs-based plasmonic sensor indicates that the blue shift of the spectral peaks occurred proportionally and constantly with increasing glucose concentration. Good linearity is a prominent indicator of sensor performance and indicates that

the detected glucose concentration is stable. In addition, good linearity is also in line with good sensitivity, as evidenced by the steep slope of the graph. The steeper resulting graph indicates that the change in the value of the sensor output is also increasing in response to small input changes from analytes [20]. Thus, the plasmonic sensor has good performance and can be used to detect glucose properly.

Table 8: The detailed peak intensity and wavelength position in system response.

Glucose Concentration ( $\mu\text{M}$ )	t-SPR		I-SPR	
	$\lambda$ (nm)	I (a.u)	$\lambda$ (nm)	I (a.u.)
$10^0$	0.426	0.01	0.397	0.01
$10^1$	0.852	0.02	0.795	0.02
$10^2$	1.279	0.03	1.192	0.03
$10^3$	1.705	0.04	1.590	0.04
$10^4$	2.132	0.05	1.987	0.05
$10^5$	2.559	0.06	2.385	0.06
$10^6$	2.985	0.07	2.783	0.07

### 3.3.3 Selectivity Test

This test was conducted to assess the ability of the plasmonic sensor to detect sugar analytes such as glucose and lactose and non-sugars such as natrium, vitamin C, and calcium. Each analyte used in the test has a concentration of  $10^1 \mu\text{M}$  to avoid value saturation. Prior to the test, pure GNBP had been compared with GNBP with thiol functionalization and it appears that the functionalized GNBP has higher selectivity. Lactose was chosen because it has a chemical structure similar to glucose, i.e.,  $\text{C}_{12}\text{H}_{22}\text{O}_{11}$  for lactose and  $\text{C}_6\text{H}_{12}\text{O}_6$  for glucose. While the selection of natrium, vitamin C, and calcium was made because both are substances that are often found in the blood and act as indicators of disease, such as natrium as an indicator of hypertension, vitamin C as an indicator of nutritional deficiency disease, and calcium as an indicator of human bone health. The selection of this analyte also refers to previous studies [21]. The resulting sensor response is shown in Fig. 13(b).

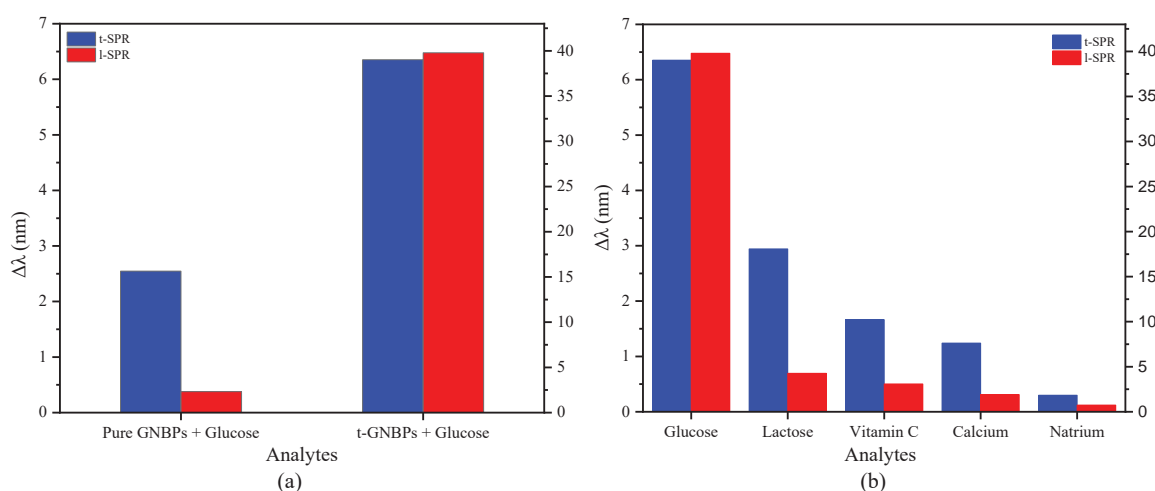


Fig. 13: The selectivity response of the plasmonic sensor in (a) pure GNBP and functionalized GNBP (b) five different analytes.

Figure 13 shows that the plasmonic sensor is selective in detecting glucose, with the parameters used being changes in wavelength referring to previous studies [5]. The l-SPR region has a higher wavelength change value indicating that this region is more sensitive to changes in substituents and analytes. Lactose and vitamin C have high values because they have a chemical structure similar to glucose. Thus, plasmonic sensors based on t-GNBPs can detect glucose and non-glucose even though they have almost the same chemical structure.

### 3.3.4 Stability Test

t-GNBPs were tested in DIW medium and  $10^1 \mu\text{M}$  for 10 minutes without stopping to test the stability of the plasmonic sensor. For sensor testing, the response was located at a wavelength of 536.391 nm for the t-SPR region and 535.539 nm for the l-SPR region. Fig. 14 shows the stability response using t-GNBPs as a sensing material for the t-SPR and l-SPR regions. In the t-SPR area, the average intensity value was  $0.9789 \pm 0.002$  a.u. for DIW and  $0.9600 \pm 0.02$  a.u. for glucose. While in the l-SPR area, the average intensity value was  $1.0609 \pm 0.02$  a.u. for DIW and  $1.0399 \pm 0.02$  a.u. for glucose. The relatively low error values indicate that the plasmonic sensor has high resistance to use for 10 minutes non-stop.

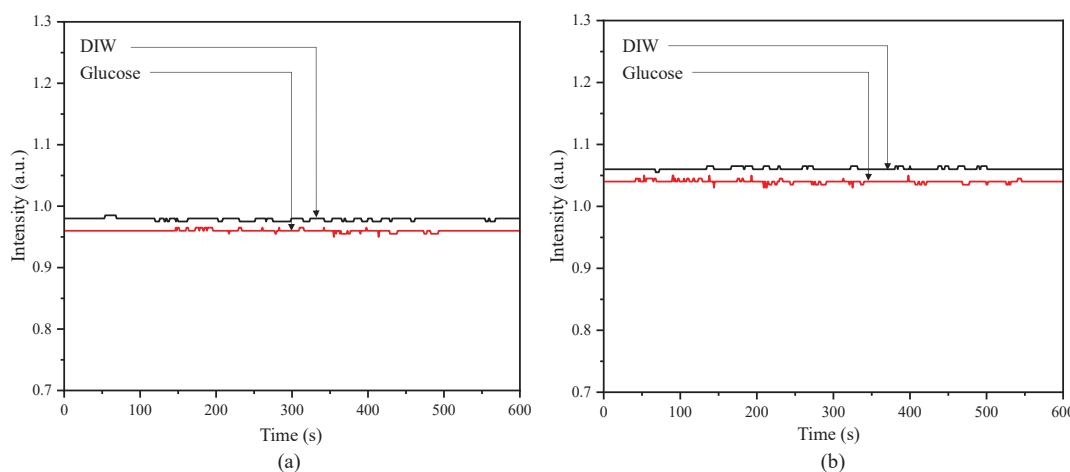


Fig. 14: The stability response of the plasmonic sensor for t-GNBPs in (a) t-SPR and (b) l-SPR peaks.

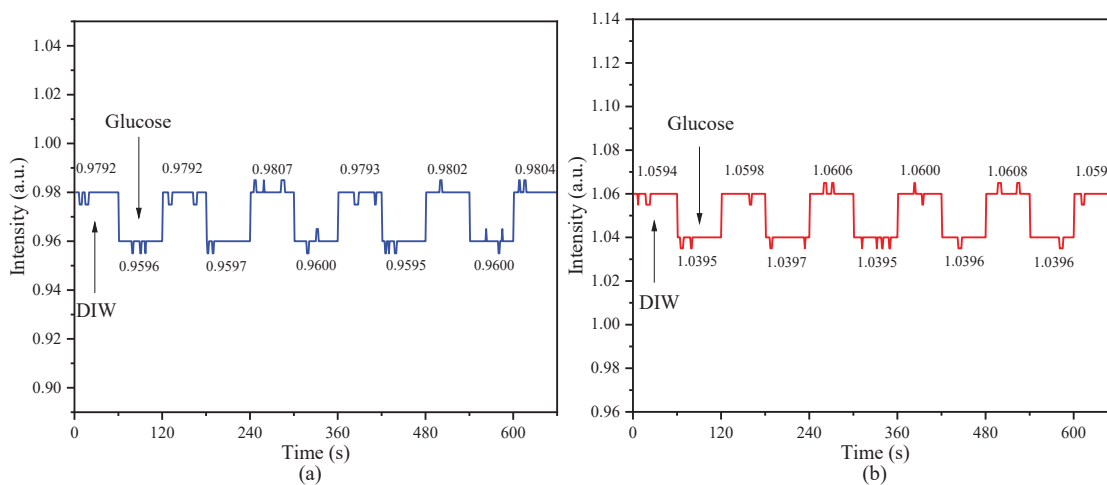


Fig. 15: The stability response of the plasmonic sensor for t-GNBPs in (a) t-SPR and (b) l-SPR region.

### 3.3.5 Repeatability Test

The repeatability test was carried out using DIW medium and glucose  $10^1 \mu\text{M}$  every 60 seconds with five cycles of repetition for each peak, as shown in Fig. 15. Based on this figure, the average intensity of the t-SPR region for DIW and glucose was 0.9797 a.u. and 0.9598 a.u., respectively, with the difference between the two being  $0.0199 \pm 0.0001$ . Then in the l-SPR area, the average intensity for DIW and glucose was 1.0601 a.u. and 1.0396 a.u., with the difference between the two being  $0.0205 \pm 0.0005$ . The percent of variance for 5 iteration cycles was 0.000025% for the t-SPR area and 0.000032% for the l-SPR area. The low value of the iteration variance indicates that the plasmonic sensor based on t-GNBPs has excellent performance in detecting glucose.

## 4. CONCLUSION

GNBPs were successfully synthesized using the SMGM method. The functionalization process using thiol groups was done using several time variations from 12 – 72 hours. The optimum functionalization time was 60 hours, producing t-GNBPs in a length of  $36.84 \pm 2.05$  nm, a width of  $24.02 \pm 0.74$  nm, and an aspect ratio of  $1.54 \pm 0.11$ . In addition, an increase in functionalization time caused a decrease in t-GNBPs and an increase in truncated t-GNBPs. For this reason, it is necessary to continue this study on the functionalization time below 12 hours to determine the appropriate time for the t-GNBPs to grow ideally. The functionalization time also has affected the resulting sensor sensitivity response, which constantly decreased and shifted towards the blue spectrum as the glucose concentration increases. However, this system has excellent linearity and selectivity for glucose and non-glucose analytes. In addition, this system also has high stability with a low error value of  $\pm 0.02$  a.u. for 10 minutes. Besides that, the system has a low percent variance of 0.000025% for the t-SPR area and 0.000032% for the l-SPR area, resulting in a good performance in detecting glucose.

## ACKNOWLEDGEMENT

The authors would like to thank Direktorat Riset, Teknologi, dan Pengabdian kepada Masyarakat (DRTPM) Ministry of Education, Culture, Research, and Technology Indonesia for supporting the project under PDUPT Research Grant (Contract No. 2595/UN19.5.1.3/PT.01.03/2022) and Universiti Tun Hussein Onn Malaysia through International Grant No. W024. Extended gratitude is expressed to Microelectronics & Nanotechnology - Shamsuddin Research Centre (MiNT-SRC) for the laboratory facilities.

## REFERENCES

- [1] Sani A, Cao C, Cui D. (2021) Toxicity of gold nanoparticles (AuNPs): A review. *Biochem. Biophys. Reports*, 26: 100991. doi: 10.1016/j.bbrep.2021.100991
- [2] Zhang W, Liu G, Bi J, Bao K, Wang P. (2023) In-situ and ultrasensitive detection of mercury (II) ions ( $\text{Hg}^{2+}$ ) using the localized surface plasmon resonance (LSPR) nanosensor and the microfluidic chip. *Sensors Actuators A Phys.*, 349: 114074. doi: <https://doi.org/10.1016/j.sna.2022.114074>
- [3] Morsin M, Salleh M. M, Umar A. A, Sahdan M. Z. (2017) Gold nanoplates for a localized surface plasmon resonance-based boric acid sensor. *Sensors (Switzerland)*, 17: 1–9. doi: 10.3390/s17050947
- [4] Sun L. L, Leo Y. S, Zhou X, Ng W, Wong T. I, Deng J. (2020) Localized surface plasmon resonance based point-of-care system for sepsis diagnosis. *Mater. Sci. Energy Technol.*, 3: 274–281. doi: 10.1016/j.mset.2019.10.007

- [5] Nafisah S, Morsin M, Jumadi N. A, Nayan N, Shah N. S. M, Razali N. L, An'Nisa N. Z. (2020) Improved sensitivity and selectivity of direct localized surface plasmon resonance sensor using gold nanobipyramids for glyphosate detection. *IEEE Sens. J.*, 20: 2378–2389. doi: 10.1109/JSEN.2019.2953928
- [6] Bhardwaj H, Sumana G, Marquette C. A. (2021) Gold nanobipyramids integrated ultrasensitive optical and electrochemical biosensor for Aflatoxin B1 detection. *Talanta*, 222: 121578. doi: 10.1016/j.talanta.2020.121578
- [7] Cheng J, Wang X, Nie T, Yin L, Wang S, Zhao Y, Wu H, Mei H. (2020) A novel electrochemical sensing platform for detection of dopamine based on gold nanobipyramid/multi-walled carbon nanotube hybrids. *Anal. Bioanal. Chem.*, 412: 2433–2441. doi: 10.1007/s00216-020-02455-5
- [8] Oo A. M, Al-abed A. A, Lwin O. M, Kanneppady S. S, Sim T. Y, Mukti N. A, Zahariluddin A. S, Jaffar F. (2020) Type 2 diabetes mellitus prediction in Malaysia using modified diabetes risk assessment tool. *Malaysian J. Public Heal. Med.*, 20: 15–21, doi: 10.37268/mjphm/vol.20/no.1/art.442
- [9] Saeedi P, Petersohn I, Salpea P, Malanda B, Karuranga S, Unwin N, Colagiuri S, Guariguata L, Motala A. A, Ogurtsova K. (2019) Global and regional diabetes prevalence estimates for 2019 and projections for 2030 and 2045: Results from the International Diabetes Federation Diabetes Atlas. *Diabetes Res. Clin. Pract.*, 157: 107843. doi: 10.1016/j.diabres.2019.107843
- [10] Ganasegeran K, Hor C. P, Jamil M. F. A, Loh H. C, Noor J. M, Hamid N. A, Suppiah P. D, Manaf M. R. A, Ch'ng A. S. H, Looi I. (2020) A systematic review of the economic burden of type 2 diabetes in Malaysia. *Int. J. Environ. Res. Public Health*, 17: 1–23. doi: 10.3390/ijerph17165723
- [11] Chen J, Yan J, Dou B, Feng Q, Miao X, Wang P. (2021) Aggregatable thiol-functionalized carbon dots-based fluorescence strategy for highly sensitive detection of glucose based on target-initiated catalytic oxidation. *Sensors Actuators B Chem.*, 330: 129325, doi: 10.1016/j.snb.2020.129325
- [12] Samanta A, Dhar B. B, Devi R. N. (2012) Novel porous silica encapsulated Au nanoreactors as peroxidase mimic for one-pot glucose detection. *New J. Chem.*, 36: 2625–2629, doi: 10.1039/c2nj40665a
- [13] Akhtar M. A, Batool R, Hayat A, Han D, Riaz S, Khan S. U, Nasir M, Nawaz M. H, Niu L. (2019) Functionalized graphene oxide bridging between enzyme and au-sputtered screen-printed interface for glucose detection. *ACS Appl. Nano Mater.*, 2: 1589–1596. doi: 10.1021/acsanm.9b00041
- [14] Chu Z, Liu Y, Xu Y, Shi L, Peng J, Jin W. (2015) In-situ fabrication of well-distributed gold nanocubes on thiol graphene as a third-generation biosensor for ultrasensitive glucose detection. *Electrochim. Acta*, 176: 162–171. doi: 10.1016/j.electacta.2015.06.123
- [15] Forlenza G. P, Buckingham B. A, Brown S. A, Bode B. W, Levy C. J, Criego A. B, Wadwa R. P, Cobry E. C, Slover R. J. (2021) First outpatient evaluation of a tubeless automated insulin delivery system with customizable glucose targets in children and adults with type 1 diabetes. *Diabetes Technol. Ther.*, 23: 410–424. doi: 10.1089/dia.2020.0546
- [16] An'Nisa N. Z, Morsin M, Sanudin R, Razali N. L, Nafisah S. (2020) Controlled wet chemical synthesis of gold nanorods for triclopyr butotyl herbicide detection based-plasmonic sensor. *Sens. Bio-Sensing Res.*, 29: 100359. doi: 10.1016/j.sbsr.2020.100359
- [17] Nafisah S, Morsin M, Sanudin R, Nayan N, Yusop M. Z. M, Razali N. L, Shah N. Z. A. M. (2021) Effect of additive acid on seeded growth of gold nanobipyramids. *J. Phys. Chem. Solids*, 148: 109764. doi: 10.1016/j.jpccs.2020.109764
- [18] Shah N. Z. A. M, Morsin M, Sanudin R, Razali N. L, Nafisah S, Soon C. F. (2020) Effects of growth solutions ageing time to the formation of gold nanorods via two-step approach for plasmonic applications. *Plasmonics*, 15: 923–932. doi: 10.1007/s11468-019-01098-2
- [19] Capek I. (2013) Preparation and functionalization of gold nanoparticles. *J. Surf. Sci. Technol*, 29: 1–18.

- [20] Chang Y, Wang L, Li R, Zhang Z, Wang Q, Yang J, Guo C. F, Pan T. (2021) First decade of interfacial iontronic sensing: from droplet sensors to artificial skins. *Adv. Mater.*, 33: 2003464. doi: 10.1002/adma.202003464
- [21] Lin L, Weng S, Zheng Y, Liu X, Ying S, Chen F, You D. (2020) Bimetallic PtAu alloy nanomaterials for nonenzymatic selective glucose sensing at low potential. *J. Electroanal. Chem.*, 865: 114147. doi: 10.1016/j.jelechem.2020.114147

## INVESTIGATION OF THE PROPERTIES OF LITHIUM-CONTAINING CERAMICS BASED ON LOW-PLASTIC CLAY

LUBOV FILIPPOVA<sup>1</sup>, ANASTASIYA AKIMOVA<sup>1</sup>, EVGENIY PIKALOV<sup>2</sup>  
AND OLEG SELIVANOV<sup>3\*</sup>

<sup>1</sup>*Department of Chemistry, Vladimir State University named after A.G.  
and N.G. Stoletovs, Vladimir, Russia*

<sup>2</sup>*Department of Chemical Technologies, Vladimir State University named after A.G.  
and N.G. Stoletovs, Vladimir, Russia*

<sup>3</sup>*Department of Biology and Ecology, Vladimir State University named after A.G.  
and N.G. Stoletovs, Vladimir, Russia*

\*Corresponding author: [selivanov6003@mail.ru](mailto:selivanov6003@mail.ru)

(Received: 12 July 2023; Accepted: 18 October 2023; Published on-line: 1 January 2024)

**ABSTRACT:** Nowadays the production of construction materials and items is a multi-tonnage and actively developing production sphere. The regulatory requirements imposed on construction materials and products provide the assessment of their quality and application efficiency in construction or reconstruction of buildings and structures. The constantly increasing regulatory requirements and the limited availability of high-quality natural reserves demand the rapid development of new raw material resources. This paper presents the results of charge composition development based on low-plasticity clay, which has seen limited application due to the poor performance of items produced from it. However, certain functional additives can be introduced for producing high-quality materials. In this work, alongside lithium carbonate, the following additives have been considered: boric acid used as flux and titanium dioxide as a vitreous phase source. The lithium carbonate effect on total and open porosity, density, thermal conductivity, water absorption, frost resistance, compressive and bending strength has been studied. On the one hand lithium carbonate was found to demonstrate a pore-forming effect due to its decomposition during firing. On the other hand, lithium oxide formed during the additive decomposition facilitated the viscosity reduction of the vitreous phase during firing and its strength increase after cooling. Lithium oxide, similar to boric acid, is a flux, which makes further temperature reduction of liquid-phase sintering possible while preserving the surface self-glazing effect and the formation of the closed-pored internal structure of ceramics. The lithium carbonate pore-forming effect prevails over the flux-hardening and therefore, the amount this additive should be limited to obtain high performance properties and the compliance of resulting ceramics with regulatory requirements. The resulting ceramic material can be used for manufacturing products for buildings' and structures' plinth lining.

**ABSTRAK:** Pada masa kini, pengeluaran bahan dan barangan pembinaan adalah dalam gandaan tan dan aktif dibangunkan terutama dalam bidang pengeluaran. Keperluan pengawalseliaan bahan dan produk pembinaan menyediakan aplikasi penilaian kualiti dan kecekapan pembinaan atau pembinaan semula bangunan dan struktur. Peningkatan berterusan terhadap keperluan pengawalseliaan dan ketersediaan rizab semula jadi berkualiti tinggi yang terhad menuntut kepada pembangunan pesat sumber bahan mentah baru berkembang. Kajian ini memperkenalkan hasil pembangunan komposisi caj berdasarkan tanah liat keplastikan rendah, di mana aplikasi terhad kepada keburukan bahan yang dihasilkan, namun bahan tambahan tertentu boleh diperkenalkan bagi menghasilkan bahan berkualiti tinggi.

Menggunakan litium karbonat bersama bahan tambahan berikut: asid borik digunakan sebagai fluks dan titanium dioksida sebagai sumber fasa vitreus, telah diambil kira dalam kajian ini. Kesan litium karbonat pada keliangan, ketumpatan, kekonduksian terma, penyerapan air, rintangan fros, kekuatan mampatan dan lenturan telah dikaji. Litium karbonat didapati menunjukkan kesan pembentukan liang dalam proses penguraian semasa pembakaran. Sebaliknya, litium oksida dibentuk semasa penguraian aditif dan membantu dalam pengurangan kelikatan fasa vitreus semasa pembakaran dan kekuatannya meningkat selepas penyejukan. Litium oksida, serupa dengan asid borik, adalah fluks, berpotensi menyebabkan suhu sinteran terus berkurang pada fasa cecair sambil mengekalkan kesan kilauan pada permukaan kaca dan menutup pembentukan struktur liang dalaman seramik. Kesan pembentukan liang litium karbonat adalah mengatasi pengerasan fluks. Oleh itu, jumlah bahan tambah ini harus dihadkan bagi mencapai piawaian dan prestasi tinggi seramik yang terhasil. Bahan seramik yang terhasil ini boleh digunakan sebagai lapisan plint bangunan dan struktur dalam pembuatan produk.

---

**KEYWORDS:** *facing ceramics; low-plasticity clay; self-glazing; fluxing agent; vitreous phase*

## 1. INTRODUCTION

Nowadays, construction refers to one of the largest capacity and actively developing industries. Annually, the range of manufactured building materials and products is expanding, and their production is constantly increasing. The quality, application, and effectiveness of construction materials and products are determined by certain basic physical, mechanical, and operational properties, as well as their numerical values. The reasons for the construction industry's ongoing development of an already wide range of building materials and products are large scale construction and reconstruction, a variety of structural types, and operating conditions for buildings and structures.

Construction material and product properties are primarily determined by the characteristics and properties of the raw materials used for their production. In most cases, high-quality materials and products meeting regulatory requirements for the properties cannot be manufactured using only one raw material, therefore, raw material mixtures are used in the production processes, with one component being the basic raw and the others serving as functional additives [1-4].

The increasing requirements for operational properties and limited reserves of high-quality natural raw materials cause the necessity to expand the raw material base, primarily meaning the finding of new additives for producing high-quality finished products [5,6]. The decision to use materials and substances as functional additives is related to their impact on the finished product properties and structure, its cost, prevalence, and complexity of its processing [7-10].

Herewith, it should be considered that each additive introduction into the composition of the raw material mixture causes an increase in some property values and a decrease in other property values [11-14]. Therefore, the comprehensive study of the additives' effect in the raw material mixture composition on the material and product characteristics, for both construction and any other purpose, is extremely urgent [15-17].

The research authors have previously experimented with charge composition development for the production of self-glazing facing ceramics based on low-plasticity clay. One of the experiments resulted in the composition development including 5 wt. % of boric acid as a flux, 10 wt. % titanium dioxide as a vitreous phase source and up to 7.5 wt. % of lithium carbonate as a pore-forming additive and glassy phase modifier. The developed composition was good

for manufacturing products that meet the Russian State Standard GOST 13996-93 requirements for tiles used in facing plinths in buildings and structures [18].

Considering the new, recently additionally stringent, regulatory requirements of Russian State Standard GOST 13996-2019, the composition, regarding water absorption, can be used to manufacture the products of BIIb and BIIa groups, characterized by 100 cycles of frost resistance, and bending strength of min 30 and 22 MPa, respectively. However, for previously developed ceramics, frost resistance does not exceed 66 cycles, and bending strength does not exceed 13.6 MPa. In this respect, some additional studies were required to specify the charge composition and the compliance of the resulting ceramics to the requirements concerning bricks and stones for facing the plinths of buildings and structures.

The research objectives were to study the dependencies of the main physical, mechanical, and operational properties of the lithium carbonate content in the charge composition on the developed self-glazing facing ceramics and to determine the studied additive content for ensuring high quality and good operational properties of the resulting products.

## 2. MATERIALS AND METHODS

The main charge component for producing the studied ceramics was the clay of the Suvorotskoye deposit of the Vladimir region with the following composition (in wt. %):  $\text{SiO}_2 = 67.5$ ;  $\text{Al}_2\text{O}_3 = 10.75$ ;  $\text{Fe}_2\text{O}_3 = 5.85$ ;  $\text{CaO} = 2.8$ ;  $\text{MgO} = 1.7$ ;  $\text{K}_2\text{O} = 2.4$ ;  $\text{Na}_2\text{O} = 0.7$ . This clay plasticity index, determined by the standard method, is 5.2, and, therefore, it is of low-plasticity in accordance with Russian State Standard GOST 9169-75 [18,19].

Boric acid brand B, 2nd grade by Russian State Standard GOST 18704-78 with the basic substance content of min 98.6 wt. % was used as a flux in the charge composition. According to previous experimental results by this research's authors, boric acid application in the amount of 2.5 to 5 wt. % makes it possible to increase the ceramic's strength and reduce its water absorption due to the liquid-phase sintering intensification and its temperature decrease [18-20].

Titanium dioxide of brand R-02 by Russian State Standard GOST 9808-84 containing min 93 wt.% of the basic substance was used as the glassy phase source in the charge composition. As one of the research authors has previously revealed, titanium dioxide in the amount from 5 to 10 wt. % also makes it possible to increase the ceramic's strength and reduce its water absorption due to the glassy phase formation [18,21-23]. Simultaneously, the combined introduction of titanium dioxide and boric acid enhances each additive effect and allows the obtention of a self-glazing effect of the surface, thus additionally reducing water absorption and increasing frost resistance [18,21,22].

Lithium carbonate brand CH by TU 6-09-3728-83, containing min 98 wt.% of the basic substance, was additionally introduced into the charge composition. As one of the research authors has previously found, lithium carbonate introduction along other specified additives allows the production of ceramics with a self-glazing effect of the surface and closed porosity in the depth, which facilitates the decrease in thermal conductivity while maintaining low water absorption and high frost resistance [18]. Lithium carbonate is worth noting to serve as a pore-forming additive because lithium oxide formed during firing is more reactive compared to calcium, magnesium, potassium and sodium oxides, and therefore belongs to stronger fluxes, increasing the effect of boric acid and titanium dioxide. In addition, lithium oxide reduces the vitreous phase viscosity, contributing to its uniform distribution in the material depth and penetration into the small pores and voids, and also increases its strength [18,24,25].

The studied ceramic samples were produced applying semi-dry pressing technology. Prior to the application, the clay was crushed to reach the max particle size fraction of 0.63 mm and dried to a constant mass. Then, the charge components were dry mixed at the specified ratios at the beginning, and then with water addition of 8 wt. % to reach a homogeneous mass, from which ceramic samples were produced at 15 MPa pressing pressure and maximum firing temperature of 1000 °C.

The samples were cube-shaped with 50 mm sides and were made in series of three samples for each charge composition, followed by averaging of the study results for each series. For the determination of bending strength, the samples were made in parallelepiped shape of 10x10x70 mm.

The density  $\rho$  (kg/m<sup>3</sup>) has been determined applying the sample mass ratio in the air-dry state to its volume. Compressive strength  $\sigma_{\text{cmp}}$  (MPa) has been determined by continuous and uniform load impact on the sample until its destruction with maximum load fixation. When determining the bending strength  $\sigma_{\text{bnd}}$  (MPa), the sample was mounted on the supports on both sides at 25 mm from the center. The bending load was applied continuously and evenly through the third support installed in the sample middle. To determine the strength characteristics, a hydraulic press P6326B (JSC "Gidropress", Russia) was used.

Water absorption was determined by increasing the dry sample mass after its saturation with water at the temperature of 20±1 °C at atmospheric pressure for 48 hours. The sample frost resistance was determined after the water absorption test. For this purpose, the water-saturated sample was exposed at temperatures ranging from -15 °C to -20 °C for 4 hours, and then placed in ambient water temperature for 2 hours and examined for cracks. If no cracks were observed, a new freeze-thaw cycle was performed.

To determine the total porosity, the true density  $\rho_{\text{true}}$  (kg/m<sup>3</sup>) was determined by the pycnometric method, and then calculated according to the formula:

$$P_{\text{totl}} = (\rho_{\text{true}} - \rho) \cdot 100 / \rho_{\text{true}}$$

Open porosity was calculated using the formula:

$$P_{\text{opn}} = W \cdot \rho$$

Thermal conductivity  $\lambda$  (W/(m·°C)) was determined using an MIT-1 mobile thermal conductivity meter (NPP Interpribor LLC, Russia). For this purpose, 4 cubic samples with 50 mm sides were taken and placed on top of each other. The samples' touching surfaces were thoroughly polished, and then a hole was drilled through the centers of the samples. A measuring probe was placed into the hole, the expected range of thermal conductivity was set and the device was left for 2 hours to set the heating power and stabilize the heat flow. After that, the device readings were recorded, taking into account that the ambient temperature range should be from 20 to 30 °C.

The developed ceramic material composition was studied using a powder diffractometer D8 ADVANCE (Bruker, Germany), a macrostructure applying microscope MBS-10 (JSC Lytkarinsky Optical Glass Plant, Russia), and a microstructure using scanning electron microscope Quanta 200 3D (Systems for Microscopy and Analysis, LLC, Russia).

### 3. RESULTS AND DISCUSSION

Figure 1 demonstrates the dependences of the ceramic's total and open porosity resulting from experimental studies on lithium carbonate in the charge composition, containing 5 wt. % of boric acid and 10 wt. % of titanium dioxide.

The resulting data proves that the material porosity increases along with an increase in the lithium carbonate amount as during firing, this additive decomposes at temperatures above 730 °C and forms lithium oxide and carbon dioxide [18,26]. Meanwhile carbon dioxide acts as a pore-forming agent, and lithium oxide together with boric acid act as a flux. According to the research data concerning the material macrostructure (see Fig. 2), the flux contribute to the material's liquid-phase sintering and predominantly forms the material's closed-pore structure.

The presented dependencies (see Fig. 1) reveal that the greatest porosity increase is observed at the introduction of up to 5 wt. % of the studied additive, and further increase of lithium carbonate amount only increased the proportion of open pores relative to the total material porosity, which grew less significantly. The research data dealing with the ceramic's microstructure (see Fig. 3) demonstrates that this amount of additive causes the fluxing effect of lithium oxide to compensate for the pore-forming effect of the additive to a greater extent. It is manifested in the vitreous phase increase in the ceramic's depth, filling some of the pores and voids in the material volume and reducing the intensity of the total porosity growth.

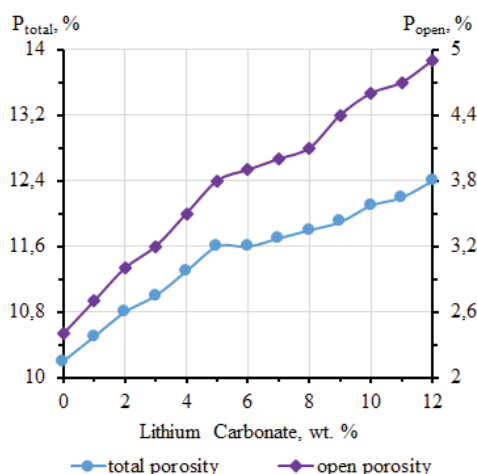


Fig. 1: The effect of lithium carbonate content on the developed ceramic's porosity.

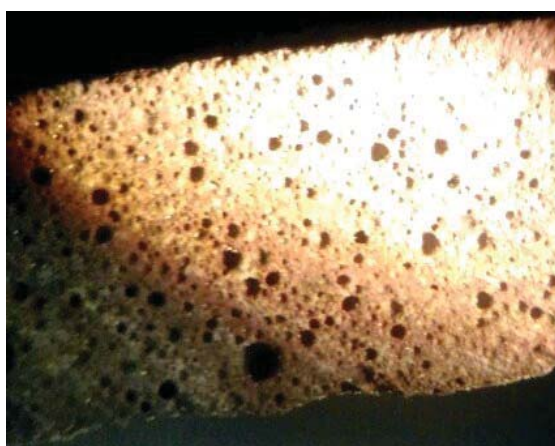


Fig. 2: The developed ceramic's macrostructure with 5 wt. % lithium carbonate introduced into the charge.

Figure 4 presents the dependences of density and thermal conductivity on the quantity of lithium carbonate in the charge composition. The resulting data proved that both considered properties decreased with the increase in the quantity of lithium carbonate. Such dependence

naturally occurs as the pores formed during the lithium carbonate decomposition reduce ceramic density and thermal conductivity. At the same time, the numerical density values decreased from high to medium for construction wall and facing ceramic materials. Thermal conductivity, in turn, decreased from the values typical for clinker products (0.8-1.6 W/(m·°C)) down to the values typical for full-bodied ceramic bricks (0.5-0.65 W/(m·°C)).

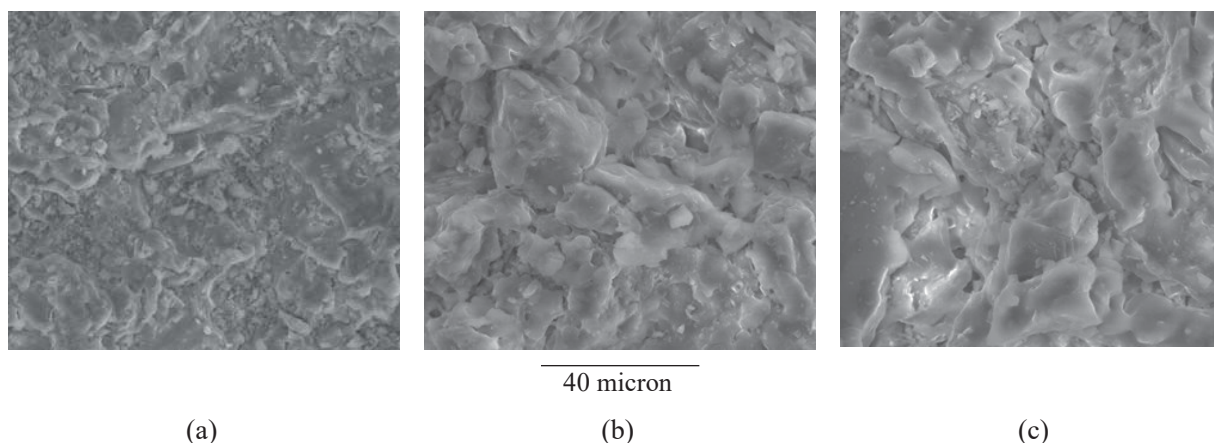


Fig. 3: Microstructure of developed ceramics at different lithium carbonate content in the charge composition: (a) 0 wt. %; (b) 2.5 wt. %; (c) 5 wt. %.

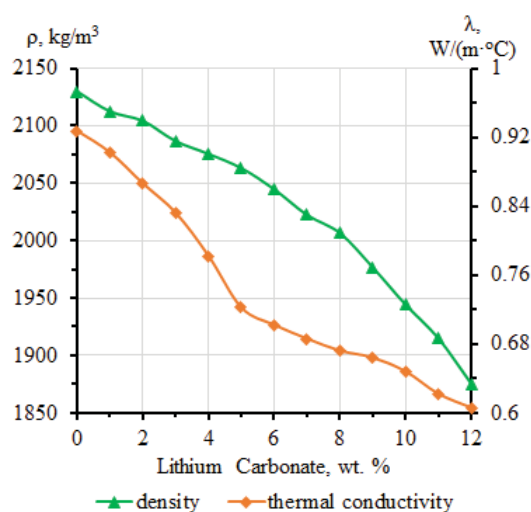


Fig. 4: The effect of lithium carbonate content on the developed ceramic's density and thermal conductivity.

Figure 5 shows the dependences of water absorption and frost resistance of the developed ceramics on lithium carbonate amount in the charge composition. The resulting data demonstrated that the increase in the open porosity share along with the increase in the lithium carbonate amount (see Fig. 1) caused a water absorption increase, which in turn caused frost resistance reduction. The frost resistance reduction depends on the fact that water, penetrating into the open pores, freezes and increases in volume by about 9% when the temperature drops to negative values, causing stress inside the material leading to its destruction during temperature changes.

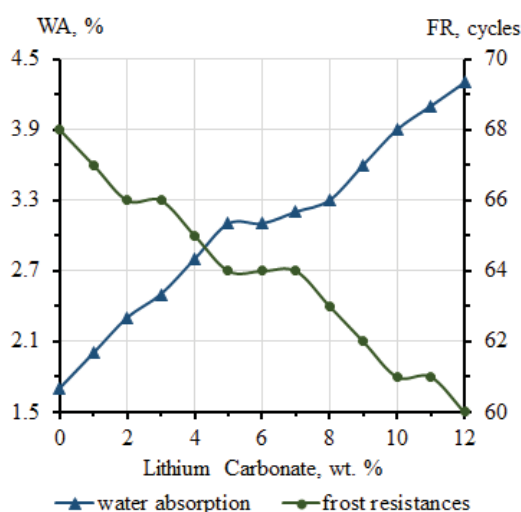


Fig. 5: The effect of lithium carbonate amount on water absorption and frost resistance of the developed ceramics.

The dependence of compressive and bending strength on lithium carbonate amount in the charge is shown in Fig. 6. According to the received data, lithium carbonate significantly reduces the resulting ceramic's strength, which can be explained by the additive pore-forming effect, which, as it was found in previous experiments, was predominant over the fluxing effect of lithium oxide and is associated with a large amount of carbon dioxide formed during the decomposition of lithium carbonate [18].

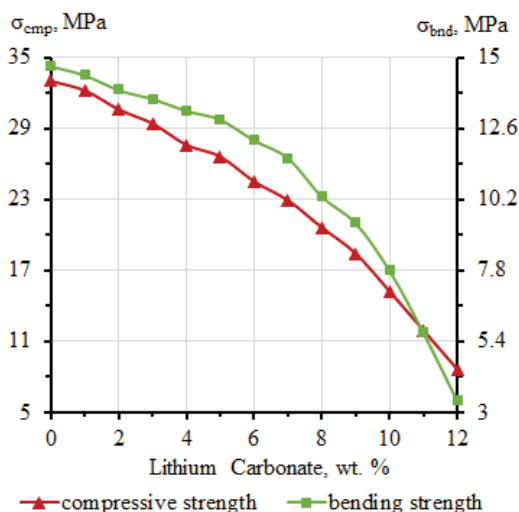
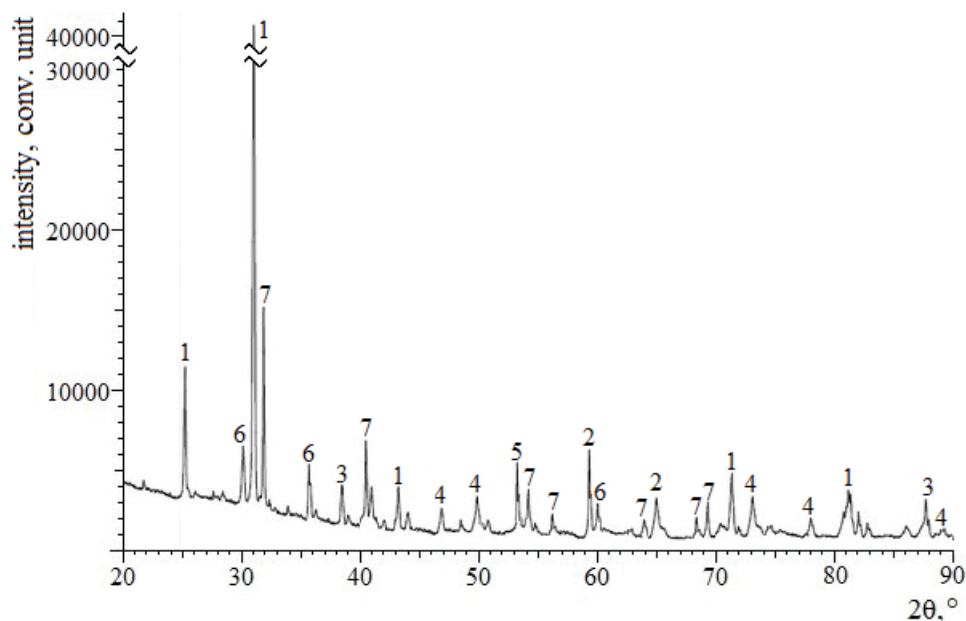
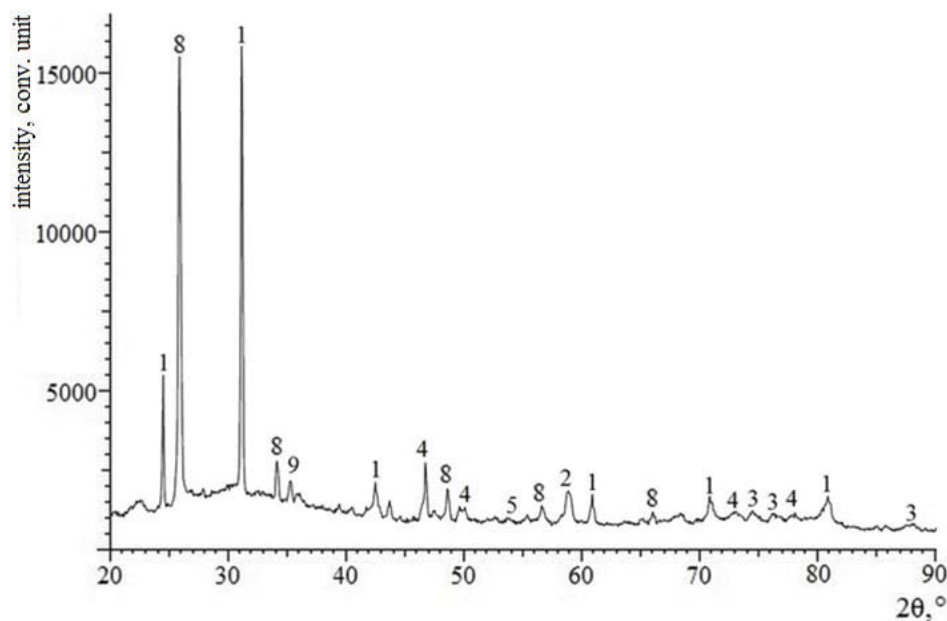


Fig. 6: The effect of the lithium carbonate amount on the developed ceramic's strength.

The resulting dependence was also confirmed by the X-ray phase analysis data (see Fig. 7), which proved that when lithium carbonate was introduced into the charge composition, a considerable reduction in the number of crystalline phases occurred in the developed ceramics. Simultaneously, a significant amount of spodumene appeared, comparable to the silicon oxide amount, as well as a small amount of lithium titanate instead of rutile and iron titanate.



(a)



(b)

Fig. 7: Diffractograms of the developed ceramics based on the charge excluding lithium carbonate (a) and including lithium carbonate (b):

- 1 – quartz  $\text{SiO}_2$ ; 2 – anorthite  $\text{CaO} \cdot \text{Al}_2\text{O}_3 \cdot 2\text{SiO}_2$ ; 3 – hematite  $\text{Fe}_2\text{O}_3$ ; 4 – diopside  $\text{CaO} \cdot \text{MgO} \cdot 2\text{SiO}_2$ ;
- 5 – spinel  $\text{MgO} \cdot \text{Al}_2\text{O}_3$ ; 6 – iron titanate  $\text{FeTiO}_3$ ; 7 – rutile  $\text{TiO}_2$ ; 8 – spodumene  $\text{Li}_2\text{O} \cdot \text{Al}_2\text{O}_3 \cdot 4\text{SiO}_2$ ;
- 9 – lithium titanate  $\text{Li}_2\text{O} \cdot \text{TiO}_2$ .

The decrease in the crystalline phase number, on the one hand, indicates that their aluminosilicate component was involved in the spodumene formation. On the other hand, these phases turn into an amorphous component of the developed ceramics, which in excess can cause increased brittleness and further reduction of the ceramic's strength characteristics, especially bending strength. The phase composition proves that titanium oxide almost completely passed into the composition of phases containing lithium oxide, including lithium

titanate. The significant amount of spodumene, possessing lower mechanical properties than silicon oxide, also contributed to the ceramic's strength decrease.

Since the developed material is planned for the production of bricks and stones, the main properties determining the choice of lithium carbonate amount comprise compressive strength, water absorption, and frost resistance. During the experiments, it was revealed that frost resistance in the entire considered range of changes in lithium carbonate amount in the charge remained constant allowing the application of this material for external cladding (> 50 cycles for face products in compliance with Russian State Standard GOST 530-2012).

The minimum value of water absorption in compliance with this Russian State Standard GOST for facial products is 6%, which exceeds the received values for the developed ceramics. Simultaneously, water absorption for clinker bricks should not exceed 6%, and frost resistance should be min 75 cycles. The compressive strength at 10 wt. of lithium carbonate amounted to 15.2 MPa, thus meeting the requirements for M150 bricks grade, and at 10.8% of lithium carbonate it reached 12.6 MPa, thus meeting the requirements for M125 bricks grade. Facing bricks of these grades are widely used for exterior finishing of buildings and structures having different numbers of stories. The further increase in the amount of the additive causes the decrease in strength, and, consequently, bricks of lower strength grades can be produced, thus limiting the material application scope.

#### 4. CONCLUSIONS

The conducted study's results revealed that the charge composition, based on a low-plasticity clay containing 5 wt. % of boric acid and 10 wt. % of titanium dioxide, can additionally contain up to 10.8 wt. % of lithium carbonate to reduce ceramic thermal conductivity, which increases its energy efficiency maintaining the main operational properties at a level that meets the requirements of Russian State Standard GOST 530-2012 for facing bricks and stones. The resulting products can be considered as an alternative to clinker bricks, although they are somewhat inferior in frost resistance.

Lithium carbonate produces complex effect on the resulting ceramics technology and properties. Firstly, this pore-forming additive allows a reduction in the density and thermal conductivity of the resulting ceramic, which reduces the load on the foundation and supporting structures when using the products and increases their energy efficiency. On the other hand, during lithium carbonate decomposition at firing, lithium oxide was formed, which, alongside boric acid is a flux, and it increased the glassy phase amount during firing and reduced the liquid-phase sintering temperature, which facilitated reduction in the maximum firing temperature from 1050 °C to 1000 °C. Herewith the vitreous phase viscosity decreased, and made it possible to achieve its uniform distribution in the product depth thus increasing its strength.

The pore-forming effect of lithium carbonate prevailed over the fluxing effect of the additive, so its separate introduction reduced the quality of the developed ceramics, based on low-plasticity clay, and the effective application of lithium carbonate was possible only in combination with other functional additives in limited quantities. The combined application of boric acid, titanium dioxide, and lithium carbonate made it possible to produce ceramics with predominantly closed pores and a self-glazing effect of the surface, that is, it reduced density and thermal conductivity while maintaining low water absorption and high frost resistance. At the same time, the material strength met the regulatory requirements for basement facing tiles.

Thus, lithium carbonate in the developed charge composition facilitated the expansion of the raw material base for construction materials through the low-plasticity clay application, which is not in great demand in ceramic production, but is widespread in the manufacture of high-quality products for external cladding of facades and plinths of buildings and structures.

## REFERENCES

- [1] Kusiorowski R, Gerle A, Dudek K, Związek K. (2021) Application of hard coal combustion residuals in the production of ceramic building materials. *Construction and Building Materials*, 304: 124506. doi: 10.1016/j.conbuildmat.2021.124506
- [2] Limame H, Manssouiri I, Cherkaoui K, Khaldoun A. (2021) Mechanical and physicochemical performances of reinforced unfired clay bricks with recycled Typha-fibers waste as a construction material additive. *Cleaner Engineering and Technology*, 2: 100037. doi: 10.1016/j.clet.2020.100037
- [3] Luo Y, Bao S, Zhang Y. (2022) Recycling of granite powder and waste marble produced from stone processing for the preparation of architectural glass–ceramic. *Construction and Building Materials*, 346: 128408. doi: 10.1016/j.conbuildmat.2022.128408
- [4] Simão FV, Chambart H, Vandemeulebroeke L, Cappuyns V. (2021) Incorporation of sulphidic mining waste material in ceramic roof tiles and blocks. *Journal of Geochemical Exploration*, 225: 106741. doi: 10.1016/j.gexplo.2021.106741
- [5] Belfore CM, Amato C, Pezzino A, Viccaro M. (2020) An end of waste alternative for volcanic ash: A resource in the manufacture of ceramic tiles. *Construction and Building Materials*, 263: 120118. doi: 10.1016/j.conbuildmat.2020.120118
- [6] Li Z, Zha, M, Zeng J, Peng C, Wu J. (2017) High-solar-reflectance building ceramic tiles based on titanite (CaTiSiO<sub>5</sub>) glaze. *Solar Energy*, 153: 623-627. doi: 10.1016/j.solener.2017.04.033
- [7] Vakalova TV, Revva IB. (2022) Highly porous building ceramics based on «clay-ash microspheres» and «zeolite-ash microspheres» mixtures. *Construction and Building Materials*, 317: 125922. doi: 10.1016/j.conbuildmat.2021.125922
- [8] Korah LV, Nigay PM, Cutard T, Nzihou A, Thomas S. (2016) The impact of the particle shape of organic additives on the anisotropy of a clay ceramic and its thermal and mechanical properties. *Construction and Building Materials*, 125: 654-660. doi: 10.1016/j.conbuildmat.2016.08.094
- [9] Vakalova TV, Revva IB. (2020) Use of zeolite rocks for ceramic bricks based on brick clays and clay loams with high drying sensitivity. *Construction and Building Materials*, 255: 119324. doi: 10.1016/j.conbuildmat.2020.119324
- [10] Alonso-De la Garza DA, Guzmán AM, Gómez-Rodríguez C, Martínez DI. (2022) Elizondo Influence of Al<sub>2</sub>O<sub>3</sub> and SiO<sub>2</sub> nanoparticles addition on the microstructure and mechano-physical properties of ceramic tiles. *Ceramics International*, 48(9): 12712-12720. doi: 10.1016/j.ceramint.2022.01.140
- [11] Contreras M., Teixeira SR, Santos GTA, Gázquez MJ, Romero M, Bolívar JP. (2018) Influence of the addition of phosphogypsum on some properties of ceramic tiles. *Construction and Building Materials*, 175: 588-600. doi: 10.1016/j.conbuildmat.2018.04.131
- [12] Kizinievič O, Žuraskienė R, Kizinievič V, Žuraskas R. (2013) Utilisation of sludge waste from water treatment for ceramic products. *Construction and Building Materials*, 41: 464-473. doi: 10.1016/j.conbuildmat.2012.12.041
- [13] Kizinievič O, Balkevičius V, Pranckevičienė J, Kizinievič V. (2015) Analysis of the effect of syenite alkali aluminium concentrate (SAAC) on the properties of ceramic products containing the centrifugation waste of a mineral wool melt. *Ceramics International*, 41(9, Part A): 11234-11241. doi: 10.1016/j.ceramint.2015.05.074
- [14] Cremades LV, Cusidó JA, Arteaga F. (2018) Recycling of sludge from drinking water treatment as ceramic material for the manufacture of tiles. *Journal of Cleaner Production*, 201: 1071-1080. doi: 10.1016/j.jclepro.2018.08.094

- [15] Bohn BP, Von Mühlen C, Pedrotti MF, Zimmer A. (2021) A novel method to produce a ceramic paver recycling waste glass. *Cleaner Engineering and Technology*, 2: 100043. doi: 10.1016/j.clet.2021.100043
- [16] Vigneron TQG, Vieira CMF, Delaqua GCG, Júnior FV, Neto ÂC. (2019) Incorporation of mold flux waste in red ceramic. *Journal of Materials Research and Technology*, 8(6): 5707-5715. doi: 10.1016/j.jmrt.2019.09.038
- [17] Hadi EM, Hussein SI. (2019) A sustainable method for Porous refractory ceramic Manufacturing from kaolin by adding of burned and raw wheat straw. *Energy Procedia*, 157: 241-253. doi: 10.1016/j.egypro.2018.11.187
- [18] Shakhova VN, Berezovskaya AV, Pikalov ES, Selivanov OG, Sysoev ÉP. (2019) Development of Self-Glazing Ceramic Facing Material Based on Low-Plasticity Clay. *Glass and Ceramics*, 76(1-2): 11-15. doi: 10.1007/s10717-019-00123-4
- [19] Vitkalova I, Torlova A, Pikalov E, Selivanov O. (2018) Development of environmentally safe acid-resistant ceramics using heavy metals containing waste. *MATEC Web of Conferences*, 193: 03035. doi: 10.1051/mateconf/201819303035
- [20] Kolosova A, Sokolskaya M, Pikalov E, Selivanov O. (2019) Production of facing ceramic material using cullet. *E3S Web of Conferences*, 91: 02003. doi: 10.1051/e3sconf/20199102003
- [21] Pavlycheva EA, Pikalov ES, Selivanov OG. (2021) Recovery of Polymer Waste in the Production of Ceramics Veneer with a Self-glazing Effect. *Ecology and Industry of Russia*, 25(6): 20-25. doi: 10.18412/1816-0395-2021-6-20-25
- [22] Pavlycheva EA, Pikalov ES, Selivanov OG. (2021) Glazing effect for producing environmentally friendly ceramics for cladding applications. *Hemijska Industrija*, 75(3): 167-173. doi: 10.2298/HEMIND210112017P
- [23] Shimanskaya AN, Levitskii IA. (2016) Formation Particularities of titanium-containing glaze coatings for floor tiles. *Glass and Ceramics*, 73(3-4): 94-99. doi: 10.1007/s10717-016-9833-8
- [24] Santos GG, Serbena FC, Fokin VM, Zanotto ED. (2017) Microstructure and mechanical properties of nucleant-free Li<sub>2</sub>O-CaO-SiO<sub>2</sub> glass-ceramics. *Acta Materialia*, 130: 347-360. doi: 10.1016/j.actamat.2017.03.010
- [25] Aliyah LH, Katrina AT, Hasmaliza M. (2019) Preliminary Study on the Development of New Composition Lithium Aluminosilicate Glass Ceramic. *Materials Today: Proceedings*, 17(3): 946-952. doi: 10.1016/j.matpr.2019.06.446
- [26] Surzhikov AP, Lysenko EN, Malyshev AV, Pritulov AM, Kazakovskaya OG. (2012) Influence of mechanical activation of initial reagents on synthesis of lithium ferrite. *Russian Physics Journal*, 55: 672-677. doi: doi.org/10.1007/s11182-012-9865-7

## A WHEELCHAIR SITTING POSTURE DETECTION SYSTEM USING PRESSURE SENSORS

MUHAMMAD ANNUAR ALHADI MOHAMAD YUSOFF,  
NUR LIYANA AZMI\* AND NOR HIDAYATI DIYANA NORDIN

*Department of Mechatronics Engineering, Kulliyah of Engineering,  
International Islamic University Malaysia, Kuala Lumpur, Malaysia*

\*Corresponding author: [liyanazmi@iium.edu.my](mailto:liyanazmi@iium.edu.my)

*(Received: 4 April 2023; Accepted: 1 August 2023; Published on-line: 1 January 2024)*

**ABSTRACT:** The usage of machine learning in the healthcare system, especially in monitoring those who are using a wheelchair for their mobility has also helped to improve their quality of life in preventing any serious life-time risk, such as the development of pressure ulcers due to the prolonged sitting on the wheelchair. To date, the amount of research on the sitting posture detection on wheelchairs is very small. Thus, this study aimed to develop a sitting posture detection system that predominantly focuses on monitoring and detecting the sitting posture of a wheelchair user by using pressure sensors to avoid any possible discomfort and musculoskeletal disease resulting from prolonged sitting on the wheelchair. Five healthy subjects participated in this research. Five typical sitting postures by the wheelchair user, including the posture that applies a force on the backrest plate, were identified and classified. There were four pressure sensors attached to the seat plate of the wheelchair and two pressure sensors attached to the back rest. Three classification algorithms based on the supervised learning of machine learning, such as support vector machine (SVM), random forest (RF), and decision tree (DT) were used to classify the postures which produced an accuracy of 95.44%, 98.72%, and 98.80%, respectively. All the classification algorithms were evaluated by using the k-fold cross validation method. A graphical-user interface (GUI) based application was developed using the algorithm with the highest accuracy, DT classifier, to illustrate the result of the posture classification to the wheelchair user for any posture correction to be made in case of improper sitting posture detected.

**ABSTRAK:** Penggunaan pembelajaran mesin dalam sistem penjagaan kesihatan terutama dalam mengawasi pergerakan pengguna kerusi roda dapat membantu meningkatkan kualiti hidup bagi mengelak sebarang risiko serius seperti ulser disebabkan tekanan duduk terlalu lama di kerusi roda. Sehingga kini, kajian tentang pengesanan postur ketika duduk di kerusi roda adalah sangat kurang. Oleh itu, kajian ini bertujuan bagi membina sistem pengesanan postur khususnya bagi mengawasi dan mengesan postur duduk pengguna kerusi roda dengan menggunakan pengesanan tekanan bagi mengelak sebarang kemungkinan ketidakselesaan dan penyakit otot akibat duduk terlalu lama. Lima pengguna kerusi roda yang sihat telah dijadikan subjek bagi kajian ini. Terdapat lima postur duduk oleh pengguna kerusi roda termasuk postur yang memberikan tekanan pada bahagian belakang telah di kenalpasti dan dikelaskan. Terdapat empat pengesanan tekanan dilekatkan pada bahagian tempat duduk kerusi roda dan dua pengesanan tekanan dilekatkan pada bahagian belakang. Tiga algoritma pengelasan berdasarkan pembelajaran terarah melalui pembelajaran mesin seperti Sokongan Vektor Mesin (SVM), Hutan Rawak (RF) dan Pokok Keputusan (DT) telah digunakan bagi pengelasan postur di mana masing-masing memberikan ketepatan 95.44%, 98.72% dan 98.80%. Semua algoritma pengelasan telah dinilai menggunakan kaedah k-lipatan pengesanan bersilang. Sebuah aplikasi grafik antara muka (GUI) telah dibina menggunakan algoritma dengan ketepatan paling tinggi, iaitu pengelasan DT bagi memaparkan keputusan

---

pengelasan postur untuk pengguna kerusi roda bagi membantu pembetulan postur jika postur salah dikesan.

---

**KEYWORDS:** *posture detection; smart wheelchair; pressure sensor; machine learning; classification*

## 1. INTRODUCTION

A sitting posture detection system (SPDS), also known as sitting posture recognition system (SPRS), is a system used to differentiate between the proper and improper sitting posture possessed by a human on a chair. In the medical field, the system has been widely used to assist medical practitioners in monitoring patients who are confined to a wheelchair due to injuries in the legs, spine, or spinal cord that will limit their body movement as compared to an average person. The main objective of the system is to ensure the wheelchair user leads a better quality of life and prevents them from developing any possible discomforts that may adversely affect their daily activities, such as development of pressure ulcers due to the prolonged sitting on the wheelchair.

Over the years, posture detection systems have been tremendously improved in terms of accuracy, in line with the advancement of technology. Typically, the system consists of three main stages, namely the data acquisition, data processing, and data transmission. Data acquisition is focused on how to acquire data from the user with various types of components, such as pressure sensors, Kinect sensors, force sensors, accelerometers, etc. whereas data processing is involved in classifying the data acquired to differentiate between the proper and improper sitting posture. Most researchers have developed their own systems with the assistance of machine learning techniques in processing their acquired data. Finally, data transmission is the stage where the processed data that has been evaluated is shown to the user for posture correction if necessary.

In defining the improper sitting posture, it is crucial to understand the sitting behavior for every wheelchair user. Research has been conducted on how in-seat movement and weight-shiftings (WSs) (30% - 90% off loading of at least side of the buttocks for at least 15 seconds) behavior of full-time wheelchair users will result in a lifetime risk of developing pressure ulcers [1]. Other than WSs, participants also performed other maneuvers, such as pressure reliefs (PRs) (90% off-loading of the entire buttocks for at least 15 seconds) in order to reduce the pressure, hence increasing the blood flow to the buttock tissues. Based on the analysis performed, it was found that the participants performed WSs much more frequently as compared to PRs. In fact, the WSs were performed nearly two times per hour for many of the subjects' days. At the same time, it is noted that by doing intermediate leans, which are the same as the WSs, may reduce the pressure between 29% and 46% [1].

Nowadays, the development of a sitting posture detection system that mainly focuses on wheelchair users is still rare compared to its development for general purpose sitting posture. Many research papers that are related to the sitting posture detection system are more focused on detecting sitting posture on a chair for a general purpose, such as during work or driving. In Malaysia, 548,186 disabled persons were registered with the Jabatan Kebajikan Masyarakat (Community Welfare Department) and 36.0% of them are physically impaired that mostly are in need to commute using a wheelchair, especially the elderly for easy to commute [2]. To date, the amount of research on sitting posture detection on wheelchairs is limited.

Therefore, this paper aimed to develop a sitting posture detection system that predominantly focused on monitoring and detecting the sitting posture of a wheelchair user

---

by using pressure sensors to avoid any possible discomfort and musculoskeletal disease resulting in prolonged sitting on the wheelchair.

### 1.1 Sensor Selection

The usage of sensors is paramount in ensuring the sitting posture detection system is unobtrusive and will not give any discomfort to the user, especially the wheelchair user. Many of the previous works in this field have opted to use pressure sensors or force sensitive resistors (FSR) in detecting the sitting posture. Ma et al. [3] used a cushion equipped with the pressure sensors. Similarly, Zemp et al. [4] also used a number of pressure sensors (FSR406) in developing the posture recognition system. In recent years, Matuska et al. [5] developed a sitting posture detection system using force sensors that were accessible by mobile applications, which is one of the outcomes of the IoT. The authors used the six single-zone force-sensing resistors FSR402 to obtain the force by measuring the resistance values based on the data acquired from the sensors embedded in the smart wheelchair.

In addition, Fragkiadakis et al. [6] also developed a sitting posture recognition system by using piezoresistive pressure sensors for detecting the distribution of pressure from one sitting posture to another. The reason for choosing the piezoresistive sensor was that this type of sensor has tolerance to temperature changes and a lifespan of three million charging cycles. Additionally, Rosero-Montalvo et al. [7] also developed an identification system for a wheelchair user's posture using pressure sensors. In spite of that, Wan et al. [8] designed their latest posture recognition system by considering the hip position for the sake of posture analysis.

In contrast, recent work on position detection documented the use of a variety of sensors other than pressure or FSR sensors. Another type of sensor used for the sitting posture detection system is the load cell sensor which was developed by Roh et al. [9]. Min et al. [10] developed a scene recognition and semantic analysis in detecting unhealthy sitting posture amongst office workers using Microsoft Kinect Sensor. In addition, Chin et al. [11] also developed a posture recognition system using Kinect Sensor in differentiating between a good and bad sitting posture. Last but not least, Qian et al. [12] had proposed the usage of nanocomposite sensors in identifying human posture.

To sum up, the authors used various types of sensors, and this has been the norm for a long period of time in the posture recognition field. Furthermore, since the release of Kinect Sensor by Microsoft in 2010, it has been famously known to be used in the posture recognition field as it is mainly invented for human sensing purposes. However, in the case of posture recognition for wheelchair users, it is more efficient to use a pressure sensor than a Kinect sensor for its unobtrusiveness for wheelchair users.

### 1.2 Data Classification Technique

One of the biggest data analytic techniques that has been widely used across multiple disciplines is machine learning techniques. In terms of posture detection, the type of machine learning techniques that has been used in most of the developed systems is supervised learning of classification techniques. Most researchers have come out with predetermined postures that might be possessed by the user on the chair or wheelchair and have verified it with the medical experts for distinguishing the proper and improper sitting posture. For instance, Zemp et al. [4] proposed seven different postures that are typical for seated people, while Roh et al. [9] suggested six different postures to be performed by the subjects as the training data. The selection of subjects also played an important role in acquiring classifiers with high accuracy. Ma et al. [3] chose the subjects with the age range of 22 to 36 years old and the BMI range of

16 to 34 in order to avoid any error in recognizing the sitting postures by the users. The summary of the past sensors and classifications used are shown in Table 1.

Table 1: Summary of the Past Sensors and Classification Used

Authors	Types of Chairs	Types of Sensors	Placement of Sensors	Classification Algorithm	Classification Accuracy
Ma et al. [3]	Wheelchair	Pressure Sensor	7 on the seat, 4 on the backrest	J48 Decision Tree (DT)	99.48%
Roh et al. [9]	Office Chair	Load Cell Sensor	4 on the seat plate	SVM using RBF Kernel	97.20%
Min et al. [10]	Office Chair	Kinect Sensor	N/A	Faster R-CNN, Gaussian Mixture	95.60%
Zemp et al. [4]	Office Chair	Pressure Sensor	10 on the seat, 4 on the backrest, 2 on the armrest	Random Forest	90.90%
Matuska et al. [5]	Office Chair	Force Sensor	4 on the seat, 2 on the backrest	Random Forest	97.00%
Rosero-Montalvo et al. [7]	Wheelchair	Pressure Sensor	3 on the seat	k-NN	>75%
Qian et al. [12]	Office Chair	Nanocomposite Sensor	Wearable on the back	ANN	98.76%
Fragkiadakis et al. [6]	Chair	Pressure Sensor	8 on the seat, 5 on the backrest	WG30NN	98.33%
Chin et al. [11]	Office Chair	Pressure Sensor Array	Cushion on the seat	SVM with Linear Kernel	97.10%
Wan et al. [8]	Office Chair	Kinect Sensor	N/A	SVM with Polynomial Kernel	89.60%

Based on the literature review, the objectives of this paper are: (a) to investigate improper sitting postures in a wheelchair, (b) to identify and classify the improper sitting posture in a wheelchair using pressure sensors and machine learning, and (c) to develop a sitting posture detection system in a wheelchair. This paper is organized as follows. Section 2 explains the predefined sitting postures selection, sensor deployment, experimental setup and classification of sitting postures and the graphical user interface (GUI) with machine learning model development. The results of classifying the sitting postures with three classifiers and the developed GUI system are presented in Section 3. Finally, the conclusion of the results obtained, and future work are described in Section 4.

## 2. METHODOLOGY

### 2.1 Predefined Sitting Postures Selection

Usually, the predefined sitting postures are selected based on the targeted user's typical postures. Rosero-Montalvo et al. [7] chose the predefined sitting posture based on the typical sitting postures on a wheelchair and related it to the conventional taxonomy recommended by the physician and physiotherapist experts. The typical postures subsequently were classified into two types, namely recommended proper sitting posture and improper sitting postures.

In this project, the predefined proper sitting postures were selected based on previous papers and recommendation by medical experts [3,5,7,9]. On the other hand, the selection of

predefined improper sitting postures will be based on the possible harmful effects on the backbone of the user. Therefore, in this project, the predefined sitting posture with their possible harmful effects is described in Table 2. Figure 1 shows the illustration of predefined sitting postures that were used in this project.

Table 2: Wheelchair Users Postures of Interest

Types of Sitting Posture	Possible Health Problems
<b>Proper Posture</b>	No harm
<b>Lean Right Posture</b>	Respiratory issues, muscle imbalance stress on liver, stomach, and right kidney
<b>Lean Left Posture</b>	Respiratory issues, muscle imbalance stress on spleen and left kidney
<b>Lean Forward Posture</b>	Knee issues, back pain, and stress on abdomen
<b>Lean Backward Posture</b>	Back pain and weaken abdominal muscle

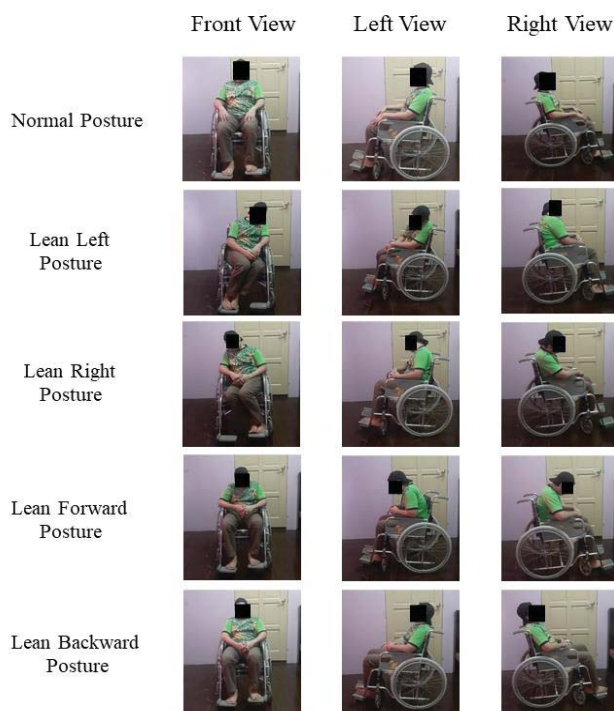


Fig. 1: The predefined sitting postures in this project.

## 2.2 Sensor Deployment

The selection of the sensor position is determined based on the body mass distribution and pressure points on the wheelchair seat. At the same time, the position of the sensor is also determined using the possible pressure points that need to be considered when the predefined sitting postures are possessed by the subject during the experiment. Ma et al. [3] mentioned that sensor deployment on the seat is sufficient to detect sitting posture. However, sensor deployment on the backrest will be supplementary for comprehensively detecting the sitting postures.

Assuming a conventional size for the seat and backrest of a wheelchair is 45 cm x 40 cm, the seat and the backrest are split into 4 square zones that are horizontally and vertically symmetrical with respect to the center point. For the wheelchair seat, one pressure sensor (FSR) was placed at the center of each square zone to represent the body mass distribution regions located on the left and right buttock zone and the front contact zone between thighs and seats. Additionally, one pressure sensor (FSR) was placed at each lower square zone of the backrest. Correspondingly, all the pressure signals were marked as FSR1, FSR2, FSR3, FSR4, FSR5 and FSR6 and the obtained instance vector was  $FPR = [FSR1, FSR2, FSR3, FSR4, FSR5, FSR6]$ . The sensor deployment configuration for this project is shown in Fig. 2.

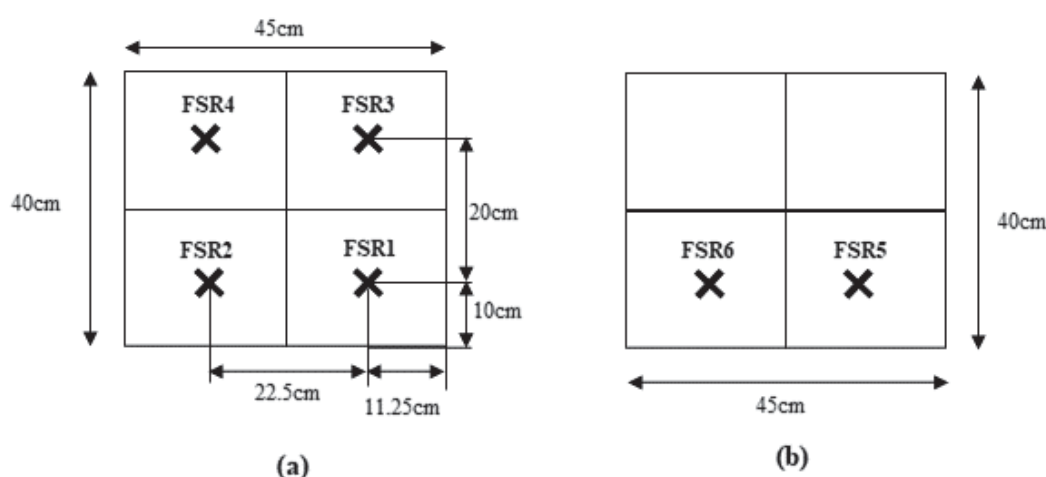


Fig. 2: Schematic diagram for sensor deployment: (a) On the seat plate, (b) On the backrest.

### 2.3 Data Collection

The age and BMI of the subjects had to be in the range of 18 to 40 years old and 16 to 35, respectively. There were 5 subjects (3 males, 2 females;  $22.8 \pm 0.4$  years old;  $BMI = 22.9 \pm 2.6$ ) volunteered in this study. This study was approved by the International Islamic University Malaysia research ethics committee (IREC). Before the data recording session began, all the subjects had the details of the process explained to them. The subjects were also required to read all the information sheets provided prior to starting the experiment. The information included predefined sitting postures that were required to be performed by the subject and the procedure of data recording. Then, the consent form was filled in and signed by the subject to ensure the confidentiality of their data and recording.

### 2.4 Experimental Setup

During the experimental test, the subjects were asked to sit in the wheelchair and perform all the predefined postures that were selected in the previous stage. For each posture, they were required to keep the posture for three minutes for the data to be collected. However, the subjects were allowed to adjust their posture for the first 30 seconds before starting each new data collection. Each subject repeated 3 trials per posture in order to obtain more reliable samples. The FSR sensors, marked as FSR1, FSR2, FSR3, FSR4, FSR5, and FSR6 were sampled with a sampling rate of 1 sample per second as it is sufficient to capture posture transitions. The microcontroller (Arduino Mega 2560) that was used in this project had a low energy consumption property. The deployment of the FSR sensors is displayed in Fig. 3.

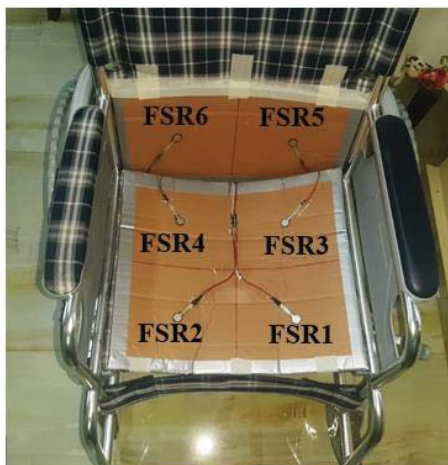


Fig. 3: Sensors deployed on a real wheelchair.

## 2.5 Classification of Sitting Postures

Three classifiers were used to determine the best one for the classification. The selection of the classifiers was based on the accuracy and frequency of use in previous papers on sitting posture recognition, namely support vector machine (SVM), decision tree, and random forest (RF). Furthermore, a cross-validation method was used in order to evaluate the classifiers' performance.

This method is also known as k-fold cross-validation, whereby it is used to estimate a machine learning algorithm performance while generating predictions on data that was not utilized during the model training. The process included only one parameter, k, which specified the number of groups into which a given data sample should be divided. In this particular work, the training and test sets were separated using a 10-fold cross-validation in order to provide a low bias in the estimation of model performance. At the same time, the classifiers were also evaluated by looking into a few more parameters namely, confusion matrix, precision score, recall score, and F-score accuracy. The process flow of the classification work in this project is illustrated in Fig. 4.

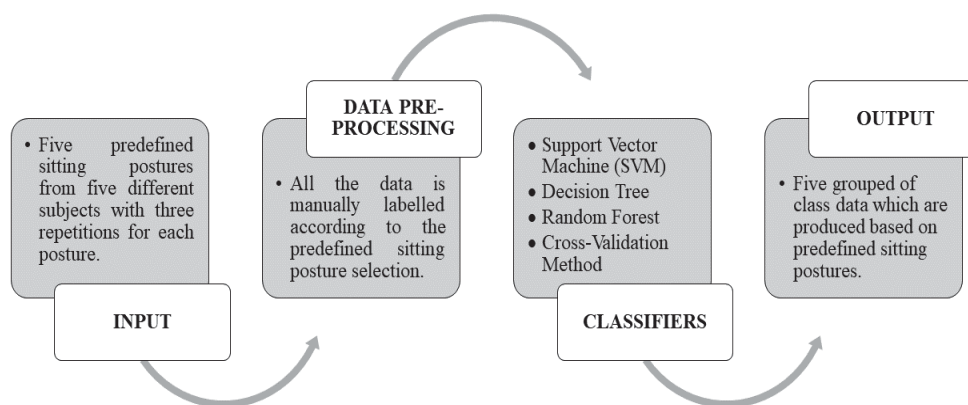


Fig. 4: Process flow of the classification.

On the other hand, the F-measure accuracy (overall accuracy) of the test data was computed to assess recognition performance. F-measure represents the combination of precision and recall, defined, respectively, as follows:

$$precision = \frac{TP}{TP+FP} \tag{1}$$

$$recall = \frac{TP}{TP+FN} \tag{2}$$

$$F - measure = \frac{2(recall)(precision)}{recall+precision} \tag{3}$$

where *TP* is true positive, *TN* is true negative, *FP* is false positive, and *FN* is false negative.

## 2.6 Graphical User Interface (GUI) with Machine Learning Model Development

The final stage of this project is to develop a graphical user interface (GUI) mobile application with embedded machine learning model with the highest value of accuracy. Upon completion of the development of the machine learning model, a smart device mobile application was built using MIT App Inventor. The smart device consists of a mobile application that uses the GUI concept for the user to interact with the electronic device for their well-being while sitting on the wheelchair. In this mobile application, the sensor data will be transferred over the Bluetooth serial connection from the Arduino Microcontroller to the mobile application of the user's smart device. Prior to the data transmission, the sensor data will be analyzed by the trained classifier model that is embedded into the Arduino Microcontroller and subsequently classified the type of posture possessed by the user in real time.

## 3. RESULTS AND ANALYSIS

### 3.1 Experiments

During the experimental test, the number of samples taken for each predefined posture is shown in Table 3. The FSR sensor readings are displayed in Fig. 5 below.

Table 3: Number of samples taken for each predefined sitting postures

Types of Sitting Posture	Description	Number of Samples
<b>Recommended Proper Sitting Posture</b>	User seated correctly on the wheelchair	2,700
<b>Lean Left</b>	User seated leaning to the left	2,700
<b>Lean Right</b>	User seated leaning to the right	2,700
<b>Lean Forward</b>	User seated leaning forward	2,700
<b>Lean Backward</b>	User seated leaning backward	2,700

Based on Fig. 5, the FSR sensor values on both buttocks (FSR3, FSR4) were nearly equivalent illustrating that the body weight on the buttocks was evenly distributed during the posture made. Even though, the FSR sensors value on the knees (FSR1, FSR2) produced a slightly bigger range as compared to the FSR sensors value on the buttocks (FSR3, FSR4). In addition, the FSR sensors value on the backrest which were practically similar supplementing the recorded data for the recommended proper sitting posture.

On the other hand, Fig. 6 depicts the value of FSR3 (located on the left buttock) was higher than FSR4 (located on the right buttock). In addition, the value of FSR sensor on the left knee (FSR1) was significantly higher than the FSR sensor on the right knee (FSR2) and similarly to the value of the FSR sensor on the left part of the backrest (FSR5) which is also leading the value of the FSR sensor on right side of the backrest (FSR6). Therefore, it can be

said that all the values for the FSR sensors located on the left side of the wheelchair were higher in comparison to the values of the FSR sensors which located on the right side of the wheelchair.

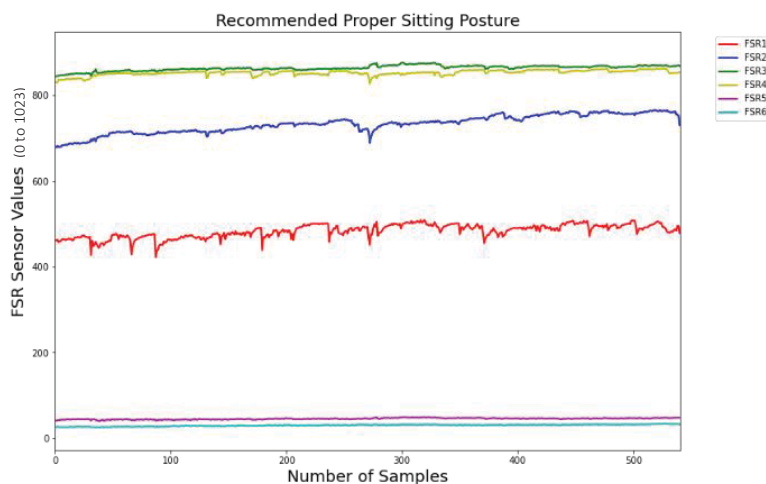


Fig. 5: Pressure sensor data during recommended proper sitting posture.

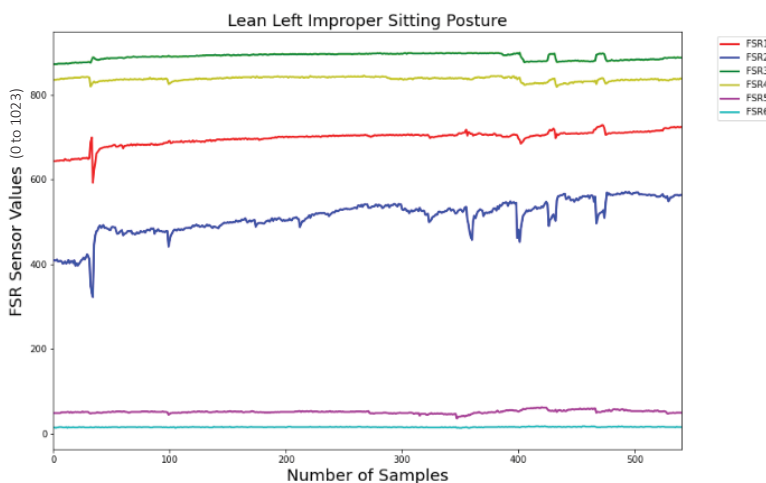


Fig. 6: Pressure sensor data during lean left posture.

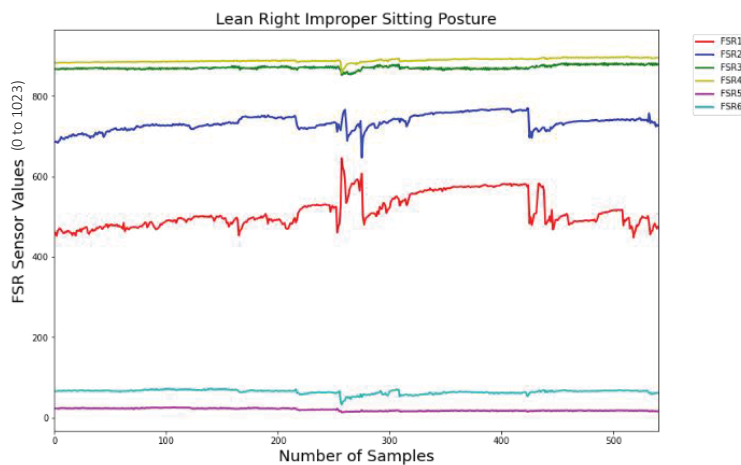


Fig. 7: Pressure sensor data during lean right posture.

In contrast to the previous sitting posture, the readings for FSR sensors on the left side of the wheelchair were greater than the values for FSR sensors on the right side of the wheelchair. It can clearly be seen from the graph that the FSR sensors which located on the right (FSR2, FSR4, FSR6) produced a higher reading in comparison to the FSR sensors which located on the left (FSR1, FSR3, FSR5). This was because the subject was asked to simulate a sitting posture that gave a higher pressure on the right which made the overall body weight of the subject not evenly distributed.

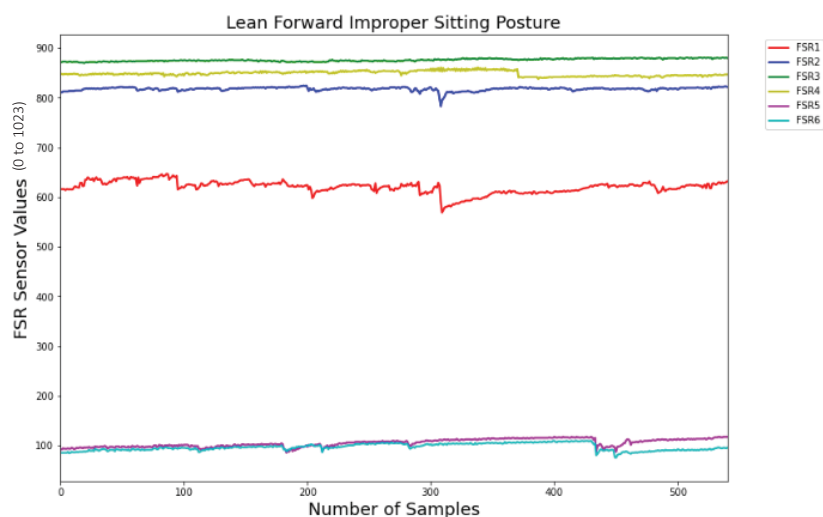


Fig. 8: Pressure sensor data during lean forward posture.

As observed from the plot, the readings of the FSR sensors located on the seat (FSR1, FSR2, FSR3, FSR4) were nearly equivalent for all the sensors. However, the value of FSR1 was slightly lower as compared to the other three FSR sensors.

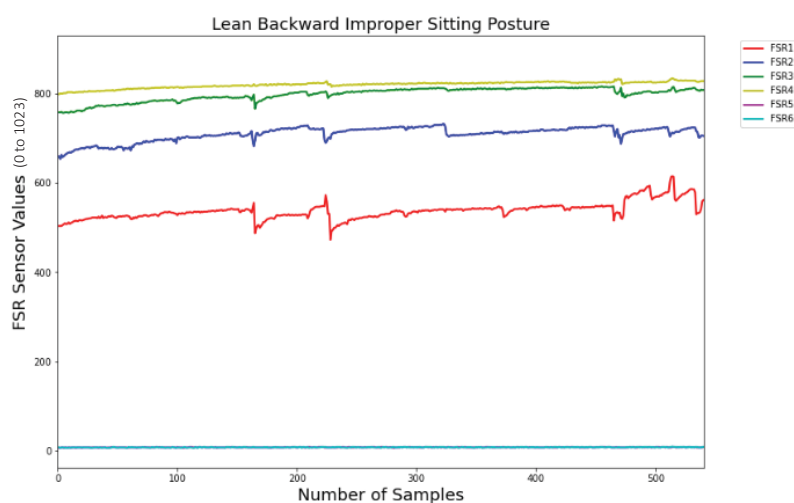


Fig. 9: Pressure sensor data during lean backward posture.

Based on the graph, the reading of the FSR sensors on the seat (FSR1, FSR2, FSR3, FSR4) were approximately comparable to each other, just as they were in the lean forward improper sitting posture. The main difference in this sitting position was that the readings of FSR sensors on the backrest were almost zero, in contrast to the previous sitting posture, in which the reading FSR sensors on the backrest were amongst the highest of all the predefined

sitting postures in this project. This was due to the subject's buttocks creeping forward, resulting in the subject's back barely touching the FSR sensors on the backrest.

### 3.2 Classification of Sitting Postures

In this study, three classification algorithms (support vector machine, random forest, and decision tree) were used to classify each predefined sitting posture. All the datasets were trained, tested, and validated by each of the algorithms prior to deploying as the finalized machine learning model. Since the classification algorithms were so dependent on the nature of the datasets, the number of datasets used to train, test, and validate the classifier was the same for each posture. For each posture, the number of samples were obtained by measuring the data for 3 min for each of the five subjects with three repetitions (180 s x 3 times x 5 subjects) which resulted in 2,700 samples per posture.

The performance of all the classifiers were evaluated by looking into their accuracy, precision score, recall score, and F1-score. These parameters will act as contributing factor in choosing the best classifier for building the machine learning model. At the same time, a confusion matrix was also used to analyze the robustness of the classifier in classifying each of the predefined sitting postures. The confusion matrix is a practical tool in visualizing and summarizing the performance of the classification algorithms.

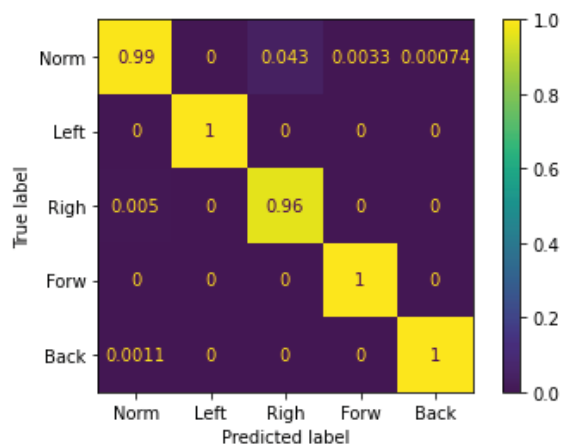


Fig. 10: Confusion matrix for the support vector machine classifier.

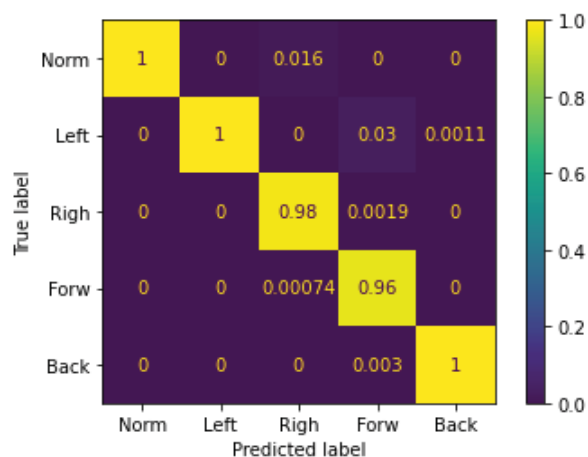


Fig. 11: Confusion matrix for the random forest classifier.

In this work, the predefined sitting postures were classified using the SVM with radial basis function (RBF) as the kernel type. The accuracy obtained from the SVM was 95.44% which was the lowest accuracy obtained in this project. Furthermore, the F1-score of this classifier was 0.9799 which computed with a precision and recall score of 0.9811 and 0.9798, respectively. The confusion matrix of the model showed that the model managed to correctly classify the recommended proper sitting posture with a probability of 0.99. However, the model produced the lowest probability of 0.96 when predicting the lean right improper sitting posture.

Random forest classifiers obtained the second highest value of accuracy which was 98.72% overall. This classifier's precision and recall scores were 0.9887 and 0.9884, respectively, resulting in an F1-score of 0.9884. Since this classifier recall score was higher than the SVM classifier recall score, the F1-score was also higher than the previous classifier. In addition, the confusion matrix of the model showed that the random forest classifier managed to classify all 2,700 samples of the recommended proper sitting posture correctly,

giving a probability of 1. However, the posture that was misclassified the most was “lean forward” in which 0.04 out of 2,700 samples were misclassified.

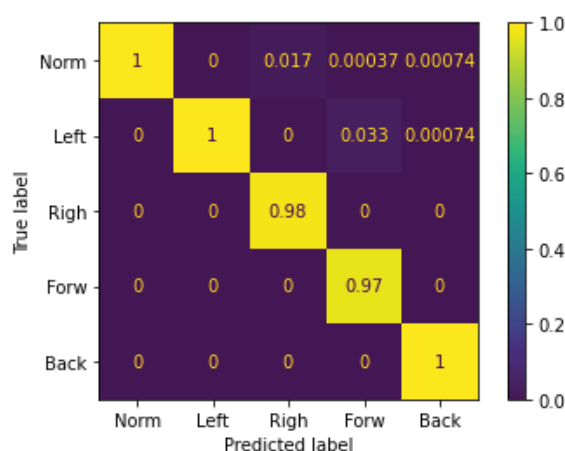


Fig. 12: Confusion matrix for the decision tree classifier.

Apart from that, the decision tree classifier recorded the highest accuracy amongst all the classifiers that were used in this project with an accuracy of 98.8%. In addition, because of the better precision and recall scores of 0.9898 and 0.9896, respectively, this model's F1-score was also the highest of the three, at 0.9896. Like the random forest classifier, the decision tree classifier also managed to successfully classify all the recommended proper sitting posture correctly. However, as compared to the random forest classifier, this classifier was able to improve the probability of correctly recognizing the lean forward improper sitting posture by 0.01.

To summarize, the decision tree classifier was chosen as the top classifier for recognizing the wheelchair user's sitting posture in this project, followed by the random forest classifier with only 0.08% difference in terms of its accuracy. However, there is a significant difference in the accuracy value of the support vector machine classifier in comparison to the other two classifiers. Ma et al. [3] in their previous paper mentioned that the SVM is quite effective for binary classification, but it is considerably more difficult to configure its important parameters for multi classification. As a result, the accuracy of SVM classifiers is significantly lower than that of other classifiers. The summary of the classification report is tabulated in Table 4 below.

Table 4: Summary of the Classifier Performance

Classifiers	Accuracy	Scores		
		Precision	Recall	F1-Score
<b>Support Vector Machine (SVM)</b>	95.44%	0.9811	0.9798	0.9799
<b>Random Forest</b>	98.72%	0.9887	0.9884	0.9884
<b>Decision Tree</b>	98.80%	0.9898	0.9896	0.9896

### 3.3 Graphical User Interface (GUI)

A GUI mobile application was developed in this project as a complementary tool for detecting the sitting posture of the wheelchair user. The mobile application was developed using the open-source application inventor for android, namely MIT App Inventor. In this mobile application, Bluetooth was chosen as the mode of transmission between the Arduino

Microcontroller and user's smart device. Therefore, all the information was sent and received by the mobile application or vice versa via Bluetooth serial connection.

In this platform, the mobile application was built using a web browser where all the works were stored in the App Inventor server. The components that were used to build the mobile application were chosen based on their functionality in the mobile application. Firstly, a ListPicker button was used to display the list of available Bluetooth devices and handle the selection. Next, two buttons were chosen to instruct the Arduino to start and stop the data recording from the sensor. All the data were subsequently processed by the Arduino before the machine learning model, which has been deployed in the Arduino, used to classify the current sitting posture of the user. Figure 13 depicts the build workspace of the mobile application.

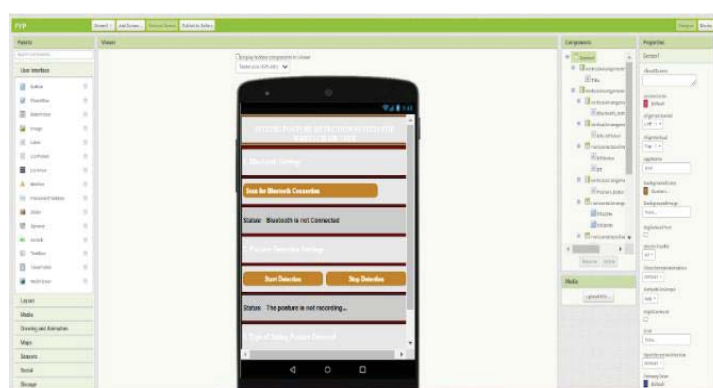
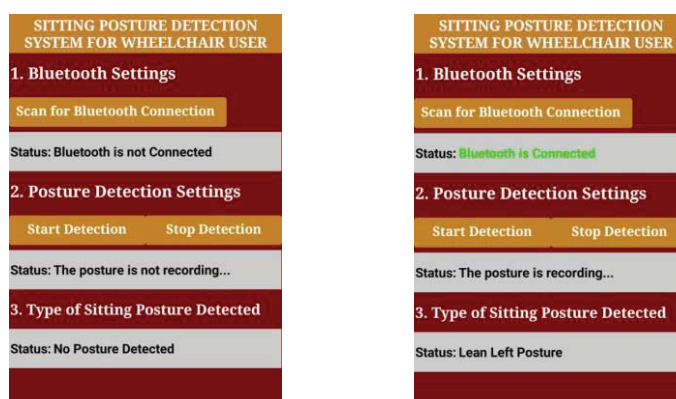


Fig. 13: MIT App Inventor workspace.

On the other hand, all the user interfaces were programmed and controlled using the blocks. The App Inventor technique assembled a sequence of blocks together and formed a group of blocks based on the logic that has been decided by the inventor. Then, all the group blocks were automatically generated into a Java programming code by the software. For instance, in this study, a letter 'n' was sent to the Arduino via Bluetooth serial connection which indicated start of the data recording. Prior to this, the Arduino code was also aligned in defining the receiving data from the mobile application for the start of the FSR sensor recording.



(a)

(b)

Fig. 14: The Default view (a) and Running view (b) of mobile application.

### 3.4 Future Works

This work can still be enhanced by incorporating more predefined sitting postures based on the typical sitting posture possessed by the wheelchair user. The Rapid Upper Limb Assessment (RULA) method can also be used in order to calculate the risk of developing musculoskeletal disease while possessing the chosen predefined sitting posture [13]. Simultaneously, the number of subjects can be raised to collect a wider range of sensor data that could be used in this project and by recruiting real wheelchair users for better simulation of real-life settings. Finally, the GUI mobile application can also be improved with dedicated settings based on the wheelchair user's routine for better sitting posture monitoring.

## 4. CONCLUSION

All related aspects of the concepts, mechanisms and methodologies have been thoroughly discussed in this paper. In addition, a comprehensive literature review on the related topics that highlighted the sitting posture recognition system as well as the sitting posture classification has been done in order to kickstart the project work. Overall, this project managed to achieve all of its objectives. There were 5 sitting postures, including normal posture on the wheelchair that were analyzed. The improper sitting posture in a wheelchair was identified using pressure sensors and classified utilizing machine learning, whereby the decision tree was chosen as the top classifier with the accuracy of 98.8%. Finally, a sitting posture detection system in a wheelchair with DT classifier was developed, whereby the detected posture can be sent as a notification to a mobile phone via Bluetooth.

## ACKNOWLEDGEMENT

This research was supported by the Ministry of Higher Education (MOHE) through Fundamental Research Grant Scheme (FRGS) (FRGS/1/2022/TK07/UIAM/03/6). The authors would like to thank all participants who volunteered for this study.

## REFERENCES

- [1] Sonenblum SE, Sprigle SH, and Martin JS. (2016) Everyday sitting behavior of full-time wheelchair users. *J. Rehabil. Res. Dev.*, 53(5): 585-598.
- [2] Jabatan Kebajikan Masyarakat 2019, Laporan Tahunan 2019 Majlis Kebangsaan Bagi Orang Kurang Upaya Jabatan Pembangunan Orang Kurang Upaya Jabatan Kebajikan Masyarakat, [www.jkm.gov.my](http://www.jkm.gov.my).
- [3] Ma C, Li W, Gravina R, and Fortino G. (2017) Posture detection based on smart cushion for wheelchair users. *Sensors (Switzerland)*, 17(4): 6-18.
- [4] Zemp R, et al. (2016) Application of Machine Learning Approaches for Classifying Sitting Posture Based on Force and Acceleration Sensors. *Biomed Res. Int.*
- [5] Matuska S, Paralic M, Hudec R. (2020) A Smart System for Sitting Posture Detection Based on Force Sensors and Mobile Application. *Mob. Inf. Syst.*, 1-13.
- [6] Fragkiadakis E, Dalakleidi KV, Nikita KS. (2019) Design and Development of a Sitting Posture Recognition System. In *Proc. Annu. Int. Conf. IEEE Eng. Med. Biol. Soc. EMBS*, 3364-3367.
- [7] Rosero-Montalvo PD, Peluffo-Ordonez DH, Lopez Batista VF, Serrano J, and Rosero EA. (2019) Intelligent system for identification of wheelchair user's posture using machine learning techniques. *IEEE Sens. J.*, 19(5): 1936-1942.
- [8] Wan Q, Zhao H, Li J, Xu P. (2021) Hip positioning and sitting posture recognition based on human sitting pressure image. *Sensors (Switzerland)*, 21(2): 1-15.
- [9] Roh J, Park HJ, Lee KJ, Hyeong J, Kim S, Lee B. (2018) Sitting posture monitoring system based on a low-cost load cell using machine learning. *Sensors (Switzerland)*, 18(1): 1-13.

- [10] Min W, Cui H, Han Q, and Zou F. (2018) A scene recognition and semantic analysis approach to unhealthy sitting posture detection during screen-reading. *Sensors (Switzerland)*, 18(9): 3119.
- [11] Chin LCK, Eu KS, Tay TT, Teoh CY, Yap KM. (2019) A Posture Recognition Model Dedicated for Differentiating between Proper and Improper Sitting Posture with Kinect Sensor. In *HAVE 2019 - IEEE Int. Symp. Haptic, Audio-v. Environ. Games, Proc.*, 0–4.
- [12] Qian Z, Bowden AE, Zhang D, Wan J, Liu W, Li X, Baradoy D, Fullwood DT. (2018) Inverse piezoresistive nanocomposite sensors for identifying human sitting posture. *Sensors (Switzerland)*, 18(6): 1-16.
- [13] Erliana K, Kautsar F, Oktaviani D, Yuniawan D, Hariyanto S, Andriono D, Mohamad E, Firdiansyah R (2019) Solving Office Ergonomics Problem Using Rapid Upper Limb Assessment (RULA), 2019 1st International Conference on Engineering and Management in Industrial System (ICOEMIS 2019).

## POWER OF ALIGNMENT: EXPLORING THE EFFECT OF FACE ALIGNMENT ON ASD DIAGNOSIS USING FACIAL IMAGES

MOHAMMAD SHAFTUL ALAM<sup>1,2</sup>, MUHAMMAD MAHBUBUR RASHID<sup>1\*</sup>,  
AHMED RIMAZ FAIZABADI<sup>1</sup> AND HASAN FIRDAUS MOHD ZAKI<sup>1,3</sup>

<sup>1</sup>Department of Mechatronics Engineering, Kulliyah of Engineering  
International Islamic University Malaysia, Kuala Lumpur, Malaysia

<sup>2</sup>Department of Electrical and Electronic Engineering,  
Northern University Bangladesh, Dhaka, Bangladesh

<sup>3</sup>Co-ordinator, Center for Unnamed Technology, Kulliyah of Engineering,  
International Islamic University Malaysia, Kuala Lumpur, Malaysia

\*Corresponding author: mahbub@iium.edu.my

(Received: 15 April 2023; Accepted: 1 August 2023; Published on-line: 1 January 2024)

---

**ABSTRACT:** Autism Spectrum Disorder (ASD) is a developmental disorder that impacts social communication and conduct. ASD lacks standard treatment protocols or medication, thus early identification and proper intervention are the most effective procedures to treat this disorder. Artificial intelligence could be a very effective tool to be used in ASD diagnosis as this is free from human bias. This research examines the effect of face alignment for the early diagnosis of Autism Spectrum Disorder (ASD) using facial images with the possibility that face alignment can improve the prediction accuracy of deep learning algorithms. This work uses the SOTA deep learning-based face alignment algorithm MTCNN to preprocess the raw data. In addition, the impacts of facial alignment on ASD diagnosis using facial images are investigated using state-of-the-art CNN backbones such as ResNet50, Xception, and MobileNet. ResNet50V2 achieves the maximum prediction accuracy of 93.97% and AUC of 96.33% with the alignment of training samples, which is a substantial improvement over previous research. This research paves the way for a data-centric approach that can be applied to medical datasets in order to improve the efficacy of deep neural network algorithms used to develop smart medical devices for the benefit of mankind.

**ABSTRAK:** Gangguan Spektrum Autisme (ASD) adalah gangguan perkembangan yang memberi kesan kepada komunikasi dan tingkah laku sosial. Kelemahan dalam rawatan ASD adalah ianya tidak mempunyai protokol rawatan standard atau ubat. Oleh itu pengenalan awal dan campur tangan betul merupakan prosedur paling berkesan bagi merawat gangguan ini. Kecerdasan buatan boleh menjadi alat berkesan bagi diagnosis ASD kerana bebas campur tangan manusia. Penyelidikan ini mengkaji kesan penjajaran muka bagi diagnosis awal ASD menggunakan imej muka dengan kebarangkalian penjajaran muka dapat meningkatkan ketepatan ramalan algoritma pembelajaran mendalam. Kajian ini menggunakan algoritma penjajaran muka MTCNN berasaskan pembelajaran mendalam SOTA bagi pra-proses data mentah. Selain itu, kesan penjajaran muka pada diagnosis ASD menggunakan imej muka disiasat menggunakan CNN terkini seperti ResNet50, Xception dan MobileNet. ResNet50V2 mencapai ketepatan ramalan maksimum sebanyak 93.97% dan AUC 96.33% dengan sampel penjajaran latihan, yang merupakan peningkatan ketara berbanding penyelidikan terdahulu. Kajian ini membuka jalan bagi pendekatan data berpusat yang boleh digunakan pada set data perubatan bagi meningkatkan keberkesanan algoritma rangkaian saraf mendalam dan membangunkan peranti perubatan pintar bermanfaat untuk manusia.

---

**KEYWORDS:** *autism spectrum disorder; CNN; facial images; alignment; deep learning*

## 1. INTRODUCTION

Autism Spectrum Disorder (ASD) is a complex neurodevelopmental disorder that can significantly affect a person's life by impairing their ability to communicate, engage with others, and control their repetitive behaviors [1]. There is no precise biomarker to identify ASD, and there is no specific medication to treat the condition. Individuals with ASD can benefit from specific therapy and support services catered to their needs, therefore, early identification and intervention are essential for better outcomes [2].

Machine learning techniques have shown potential for assisting in the early diagnosis and detection of ASD [3]. These techniques make use of algorithms to find patterns and links in massive datasets [4], which can assist in pinpointing important characteristics that set ASD sufferers apart from those without the illness. Working with big datasets of medical pictures or behavioral assessments might greatly benefit from machine learning techniques' capacity to process vast amounts of data rapidly and effectively [5]. The capacity of machine learning techniques to recognize subtle patterns that can escape the attention of human observers is another benefit [6]. For instance, facial recognition algorithms can identify tiny variations in facial traits linked to ASD, even in people who do not show more obvious signs of the condition. Traditionally, diagnosis of ASD has relied on behavioral assessments but conventional interview-based methods have human bias, which leads to the unnecessary delay in detection [7]. Rather recent studies have shown that individuals with ASD exhibit distinct facial features that can be identified using computer vision techniques [8]. However, one major challenge in using facial features for diagnosis is the variability in facial expression and pose across individuals [9]. Face alignment is a technique used to normalize facial images and reduce such variability [10]. In this paper, we investigate the effect of face alignment on ASD diagnosis using facial images and demonstrate the power of alignment in improving the accuracy of ASD diagnosis.

## 2. METHOD

Autism Spectrum Disorder (ASD) diagnosis is typically a complex and difficult procedure requiring a combination of behavioral assessments, medical evaluations, and standardized tests. Utilizing facial images and analyzing facial features and expressions to aid in the diagnosis of ASD is a promising area of research [11]. However, the accuracy of such methods may be contingent upon the quality and alignment of the facial images employed. Using advanced image processing techniques and machine learning algorithms, we will specifically investigate the effectiveness of alignment in augmenting the recognition of facial features pertinent to ASD diagnosis.

### 2.1 Dataset

The dataset we are using is the children facial image ASD dataset, which is the only publicly available dataset online containing the facial images of autistic and non-autistic children [12]. This dataset contains a total of 3014 samples of both autistic and non-autistic children of age 2 to 14. The ratio of autistic to non-autistic children is 1:1, while the ratio of male to female children is 3:1. The dataset is divided into three sections: train, test, and validation, with 2654, 280, and 80 samples of ASD and control children, respectively.

Table 1: The formation of ASD dataset

Split	Number	Binary Class
Train set	2654	
Test set	280	0.non-ASD 1.Autistic (ASD)
Valida set	80	

## 2.2 Dataset Pre-processing

The data has been pre-processed in chronological order. MTCNN, a deep CNN for face detection and alignment, was first used to align the test sample as shown in Fig. 1(a). Three levels of Convolutional Neural Networks in the MTCNN can detect faces and landmarks such eyes, noses, and mouths [13]. After detecting left and right eye coordinates, we can calculate the displacement angle and rotate the picture for the final alignment shown in Fig. 1(a). P-Net, the Proposal Network, is the initial phase of the MTCNN and functions as a proposal generator. Its principal function is to generate prospective face-containing bounding boxes. It consists of three convolutional layers and two fully connected layers. The input filter of P-Net takes the images of 12x12 pixels and the filter sizes in the convolutional layers are 3x3. P-Net generates a list of candidate bounding boxes and their corresponding facial landmark positions. The initial objective of these processes is face recognition, where the cross-entropy loss for each sample is calculated as

$$L_i^{det} = -(y_i^{det} \log(p_i) + (1 - y_i^{det})(1 - \log(p_i))) \quad (1)$$

where  $p_i$  is the probability that the sample  $i = \{0,1,\dots,n\}$  contains a face, as determined by the P-Net, and  $y_i^{det}$  is the ground truth level.

The second stage of MTCNN is R-Net, which refines the bounding boxes for different faces, generated by P-Net. There are two fully connected layers followed by three convolutional layers. The input of R-Net is 24x24 pixels, where the filter sizes in convolutional layers are 3x3. R-Net categorizes the candidate boxes as face or non-face and regresses the bounding box coordinates to enhance their precision. For R-Net to construct a bounding box, the four extremities of the box must be located, which is treated as a regression problem, and the Euclidean loss for each sample is computed by multiplying the sample size by the Euclidean loss.

$$L_i^{box} = \|\hat{y}_i^{box} - y_i^{box}\|_2^2 \quad (2)$$

where  $\hat{y}_i^{box}$  is the intended level derived from the neural network and  $y_i^{box}$  is the coordinate of the ground level.

O-Net, the Output Network, is the last stage of MTCNN and is responsible for the most precise face detection and facial feature alignment. It derives detailed facial features, such as facial landmarks (e.g., eyes, nose, mouth), from the refined candidate boxes provided by R-Net. The construction of O-Net is much more complex than the previous P-Net or R-Net, which consists of three convolutional layers followed by three fully connected. O-Net's input dimension is 48x48 pixels. The dimension of the filters in the convolutional layers is 3x3. For accurate face detection, O-Net classifies the candidate boxes, performs facial landmark localization, and refines the bounding box coordinates. For the creation of the bounding box, four coordinates such as top, breadth, and height are necessary, thus  $y_i^{box} \in \mathbb{R}^4$ . In the final phase, the Euclidean loss is again minimised according to the following equation to formulate the face landmark detection task.

$$L_i^{landmark} = \left\| \hat{y}_i^{landmark} - y_i^{landmark} \right\|_2^2 \quad (3)$$

where  $\hat{y}_i^{landmark}$  is the co-ordinates of facial landmarks - Left eye, right eye, nose, left corner of mouth and right corner of mouth and  $y_i^{landmark}$  is the ground truth co-ordinate for the  $i$ th number of images, thus  $y_i^{landmark} \in \mathbb{R}^{10}$ . After the detection of the left and right eye co-ordinates we can get the angle  $\theta$  and the image has to be rotated anti-clockwise at an angle  $\theta$  for Alignment.

Figure 1(b) depicts the subsequent phase of the pre-processing, which is the horizontal flip of the test samples. This action is performed after the alignment procedure and is also used as a separate training set for deep learning models. The horizontal flip improves the training of deep learning models because it increases the quantity of training data and provides the model with more diverse examples from which to learn [14]. A second training set is created by combining the facial image samples with the basic Gaussian salt and pepper noise, as depicted in Fig. 1(c). Previous research predicted that low image quality would negatively impact the training and efficacy of the deep learning model [15]. Adding noise provides the algorithm with a chance to deal with low-quality training samples, which may slightly boost its performance.

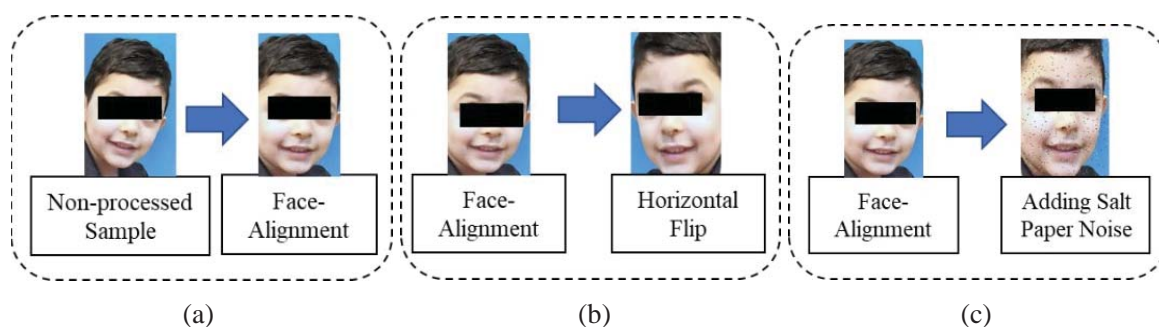


Fig. 1: (a) Face Alignment (b) Horizontal flip and (c) Noise addition pipeline for training samples.

### 2.3 Experimental Setup

The model is trained on Kaggle platform using the Tensorflow library. In this experiment, deep learning models ResNet50V2 [16], Xception [17], and MobileNetV2 [18] are selected based on the high accuracy reported by Alam et al. [19] with transfer learning approach as shown in Fig. 2.

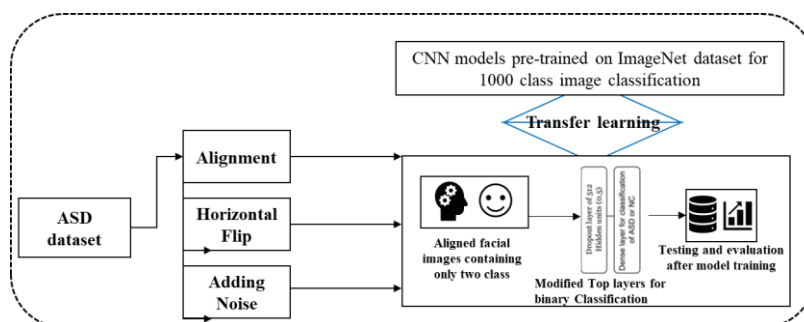


Fig. 2: ASD diagnosis process using facial image and transfer learning approaches.

All these CNN models are pretrained on the large-scale ImageNet database using a supercomputer to determine the initial weights for image classification tasks. The

hyperparameters for model training are held constant in accordance with the best configuration from the same model-centric research. Adagrade is chosen as the optimizer, the batch size is maintained at 32, and the learning rate is set to 0.001. For evaluating performance, Accuracy, AUC, Precision, and Recall were considered as performance metrics to benchmark with existing methods.

### 3. RESULTS AND DISCUSSION

#### 3.1 Performance Evaluation for Different Training Sets

In this section, the results obtained from the distinct training sets were analyzed and presented after face alignment and further processing. Table 2 shows the detection performance of various CNN models with face alignment. The validation and test sets are left unaltered in order to compare the results with recent research. After applying flip and noise addition separately to the aligned training set, the performance evaluation is done again on the test set. Finally, all three sets are combined for training resulting in three times as many training samples as the original training set and later is evaluated with same test set. For face alignment only, ResNet50V2 achieves the highest test accuracy of 93.93% with 96.33% AUC, while the Xception model also performs very closely with 92.14% accuracy and 95.91% AUC. After applying flip and noise to the aligned dataset during training, the test results are not as impressive; rather, the prediction accuracy drops dramatically. The test accuracy is recorded at 88.57% with 93.30% AUC for the ResNet50V2 model applying flip, but the results of other training sets with other models are not good enough to be considered. By combining all three sets while training three distinct deep CNN models, ResNet50V2 achieved the highest performance having 92.86% accuracy and 95.65% AUC which is actually lower than that accuracy of applying face alignment only.

Table 2: The performance of different deep learning models with face alignment

Dataset Processing	Training Dataset size	Algorithm	Accuracy	AUC	Precision	Recall	Loss
Face Alignment	2654	ResNet50V2	<b>93.93</b>	<b>96.33</b>	<b>93.93</b>	<b>93.93</b>	<b>0.373</b>
		Xception	92.14	95.91	92.14	92.14	0.360
		MobileNetV2	84.64	92.20	84.64	84.64	0.451
Face Alignment with Flip	2654	ResNet50V2	88.57	93.30	88.57	88.57	0.576
		Xception	87.50	94.06	87.50	87.50	0.482
		MobileNetV2	82.14	87.23	82.14	82.14	0.742
Face Alignment with Noise Addition	2654	ResNet50V2	72.50	80.66	72.50	72.50	1.017
		Xception	88.21	93.91	88.21	88.21	0.351
		MobileNetV2	63.21	72.33	63.21	63.21	1.247
Face Alignment+ Flip+Noise Addition	7062	ResNet50V2	92.86	95.65	92.86	92.86	0.496
		Xception	92.50	94.75	92.50	92.50	0.473
		MobileNetV2	86.43	91.63	86.43	86.43	0.718

Table 3 displays the training accuracy,  $T_{acc}$ , and validation accuracy,  $V_{acc}$ , for various deep CNN models while training with distinct datasets produced by dataset preprocessing. Face alignment for ResNet50V2 has a  $T_{acc}$  of 99.5%, plainly demonstrating the justification for performing it during training. After employing flip augmentation and merging all processed

datasets for training,  $T_{acc}$  for ResNet50V2 is increased to nearly 99.8%. Using all three training sets (Face Alignment + Flip+ Noise Addition) cumulatively for training, the Xception model also demonstrates a very good training performance with an accuracy of 99.7%. Increase in training accuracy indicates that models are learning more effectively from the training set and are expected to perform well during testing. The 99.8% validation accuracy for face alignment demonstrates the superior learning capability of ResNet50V2, while the models' performances are sufficiently good enough to contribute the value for this research work.

Table 3: The Training ( $T_{acc}$ ) and validation accuracy ( $V_{acc}$ ) after Face alignment and applying augmentations

	Face Alignment		Face Alignment with Flip		Face Alignment with Noise Addition		Face Alignment + Flip+ Noise Addition	
	$T_{acc}$	$V_{acc}$	$T_{acc}$	$V_{acc}$	$T_{acc}$	$V_{acc}$	$T_{acc}$	$V_{acc}$
ResNet50V2	0.995	<b>0.988</b>	<b>0.998</b>	0.950	0.995	0.775	<b>0.998</b>	0.975
Xception	0.988	0.975	0.991	0.950	0.987	0.938	0.997	0.975
MobileNetV2	0.971	0.938	0.970	0.888	0.965	0.688	0.989	0.950

Figure 3 depicts the aforementioned scenario with graphical representations, demonstrating that ResNet50V2 outperforms all other models for aligned facial images of ASD and control children. According to the graph, the performance is lowest for noise addition with aligned training set, which has a testing accuracy of only 62.31%.

Figure 4 shows the training and validation accuracy curve for the best result after face alignment of the training samples. The training is consistent with the validation curve, and no significant overfitting is observed, as the validation accuracy follows the training curve until its convergence. The trend holds true for validation loss as well. Figure 5 depicts the confusion matrix for the identical experimental configuration with face alignment on training samples. The number of missed predictions is indicated by the white boxes, and for the ResNet50V2 model, only one control child was incorrectly classified as autistic, while the number of wrong predicted images for the autistic sample is 16. Thus overall, the number total is 17 while the numbers for missed predictions are 22 and 43 for Xception and MobileNetV2 respectively which makes the ResNet50V2 superior to other models for face alignment on training set.

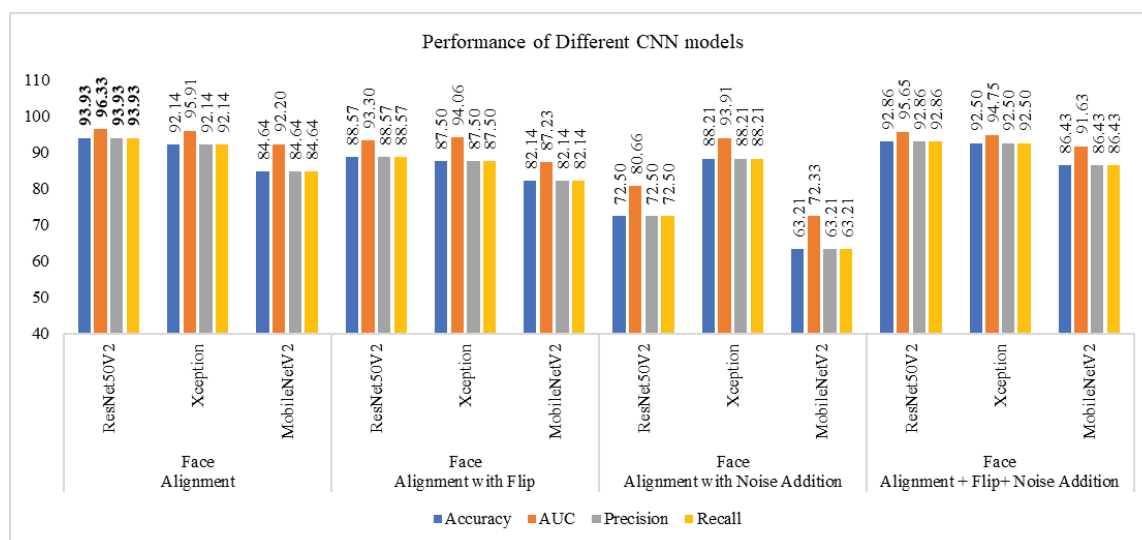


Fig. 3: Performance graph for the different CNN models for a specific training set.

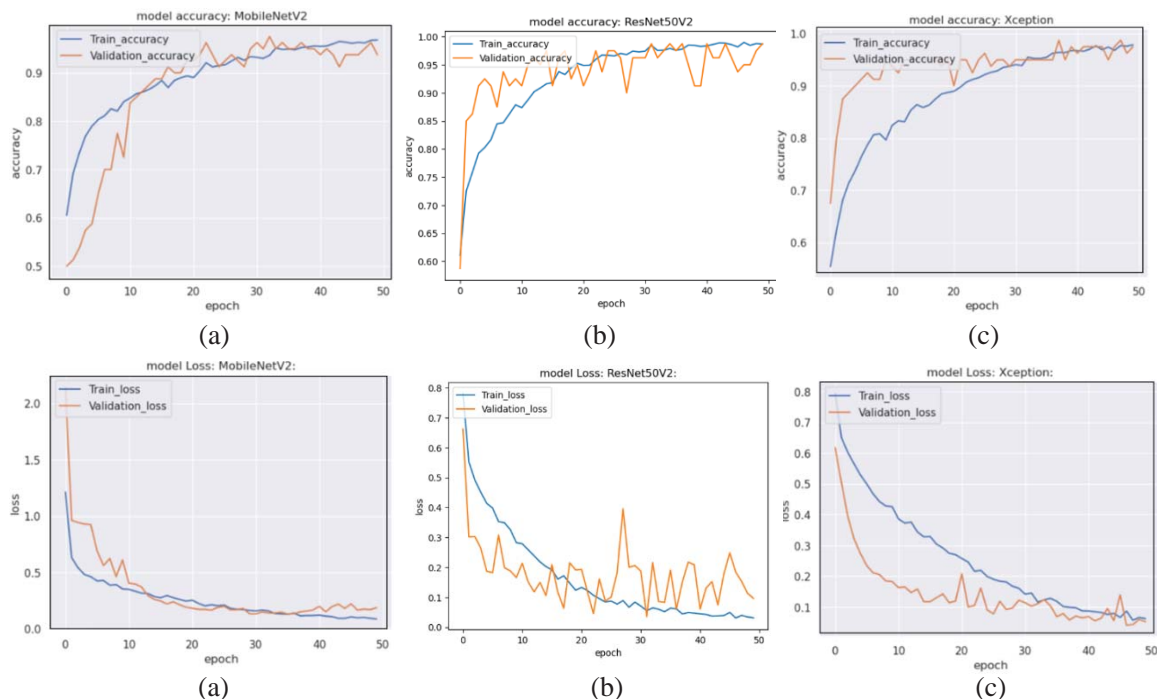


Fig. 4: Graphical representation of training and validation accuracy of (a) ResNet50V2, (b) MobileNetV2 and (c) Xception model and training and validation loss of (a) ResNet50V2, (b) MobileNetV2 and (c) Xception model for face alignment.

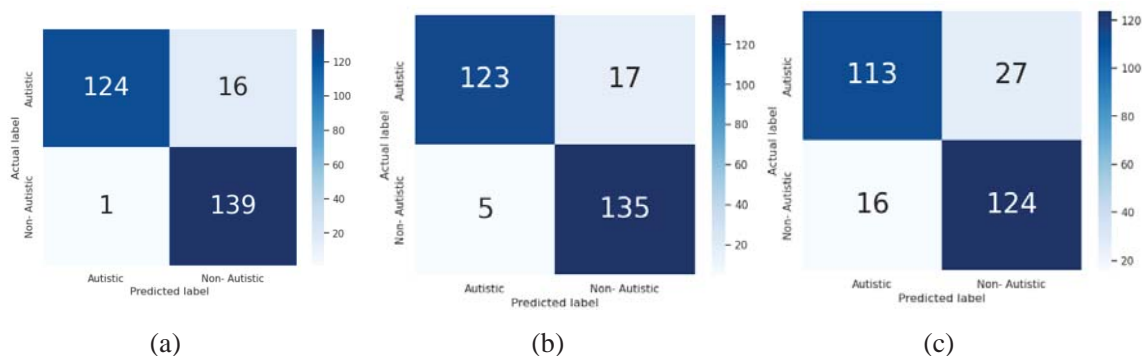


Fig. 5: Confusion matrix of (a) ResNet50V2, (b) Xception and (c) MobileNetV2 model for the face alignment.

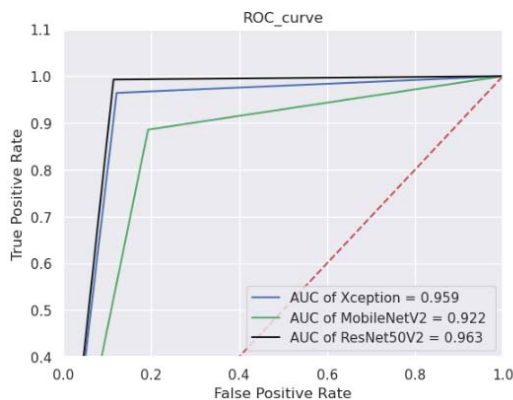


Fig. 6: ROC curve of (a) ResNet50V2, (b) Xception and (c) MobileNetV2 model for the face alignment.

ROC displays the area under the curve, AUC, which provides the region that states the model's coverage; the larger the area, the greater the model's ability to detect the correct class without any error. Figure 6 displays the ROC for three models with values for the best performing experimental setup - alignment of facial images of the training set. Based on the ROC plot, ResNet50V2 has a larger area, indicating a greater likelihood of correctly detecting the sample.

### 3.2 Discussion

In this study the effect of face alignment on the diagnosis of Autism Spectrum Disorder (ASD) is explored using facial images. Here we used ASD dataset containing facial images of children with ASD and typically developing children. The dataset contained facial image samples which were fed through MTCNN for face alignment. It is hypothesized that aligned facial images can improve the accuracy of ASD diagnosis by reducing variations in head position and facial expressions.

The diagnosis of ASD using facial images and a deep learning algorithm is a relatively novel field of research. ASD is a disorder characterized by a deficiency in neurological development and the human face can reveal information about brain function and structure [20]; therefore, the face could be a crucial biomarker for diagnosing ASD. Using deep learning, researchers are attempting to identify facial characteristics that correlate with neurological disorders which are invisible to the human eye. Table 4 shows a very brief comparison of the performance metrics of the contemporary research works. In early 2021, Rabbi et al. [21] accomplished a very good prediction accuracy by training their own CNN using ASD facial image dataset. Later, Arumugam et al. [22], Shaik et al. [23] and Kaur et al. [24] obtained 91%, 84.67% and 70% respectively using VGG16. Akter et al. [25] has performed training using shallow and deep methods and achieved an accuracy of 92.1% using MobileNet-V1. Further, Rahman et al. [15], Alsaade et al. [26] obtained 90~91 percent prediction accuracy using Xception. Recently, Alam et al. [19] performed an ablation study and achieved the highest accuracy (95%) of all.

Table 4: Comparison of performance parameters with the recent research

Ref	CNN Model	Sample size	Accuracy %	Precision	Recall	Data pre-processing
Rabbi et al. [21]	own CNN	2940	92.32	89.72	93.45	None
Arumugam et al. [22]	VGG16	2940	91.00	-	-	None
Shaik et al. [23]	VGG16	2940	84.67	-	-	None
Akter et al. [25]	MobileNet-V1	2940	92.10	92.10	92.10	None
Rahman et al. [15]	Xception	2940	90.00	-	-	None
Alsaade et al. [26]	Xception	2940	91.00	-	-	None
Alam et al. [19]	Xception	3014	95.00	95.00	95.00	Cleaning
Kaur et al. [24]	VGG16	2940	70.00			None
Our Proposed Face Alignment						
Face Alignment	ResNet50V2	3014	<b>93.93</b>	93.93	93.93	Alignment
Face Alignment with Flip	ResNet50V2	3014	88.57	88.57	88.57	Flip
Face Alignment with Noise Addition	ResNet50V2	3014	72.50	72.50	72.50	Noise Addition
Face Alignment + Flip+ Noise Addition	ResNet50V2	8322	92.86	92.86	92.86	All

Dataset pre-processing techniques such as Align, Horizontal flip, or noise addition were not being used by any researchers prior to this work to improve the quality and increase the number of samples of the training data. Image alignment is very necessary to bring symmetry to the dataset by aligning the facial landmarks that result in better outcomes in classification [27]. After aligning the dataset, the highest reported prediction accuracy in this study is 93.93 percent. Despite the fact that employing other augmentations after image alignment improves training accuracy according to Table 2, the evaluation of the test dataset is not remarkable. The training evaluation performance of the synthesized training dataset, comprising all three combinations, is very promising since evaluating with the test dataset results in lower values of accuracy than that of using only face alignment.

Data augmentation introduces high variance in the samples of the training dataset, which can negatively impact evaluation performance. The variations introduced to both classes bring about certain similarities which cause overfitting, limited generalization, increased misclassifications and lastly, impose increased computational requirements. Relatively applying face alignment improved the detection accuracy by outperforming almost all the previous research, as shown in Table 3. Our research demonstrates a lower value than the 95% accuracy reported by Alam et al. [19], suggesting that alignment alone is insufficient to improve the performance of deep learning algorithms. Rather, a detailed data-centric strategy should be investigated in greater depth. Poor image quality and inadequate medical validation of the ASD patients present in the training set are additional limitations of this study.

#### 4. CONCLUSION

Our study highlights the importance of face alignment in improving the accuracy of Autism Spectrum Disorder (ASD) diagnosis using facial images. We explored the effect of alignment on the classification performance of three state-of-the-art deep learning models, and our results showed a significant improvement in prediction accuracy when using aligned faces compared to unaligned faces. Our findings suggest that accurate face alignment can improve the quality of facial features used by machine learning models, leading to more accurate and reliable predictions. The best performance was achieved with alignment only, where we achieved a prediction accuracy of 93.97% with 96.33% AUC using ResNet50V2. This is a significant improvement over previous research which has important implications for the diagnosis of ASD, where accurate and early diagnosis is crucial for effective intervention and treatment. We believe that our study opens up new avenues for future research on the use of face alignment for ASD diagnosis using facial images, and we hope that our results will contribute to the development of more innovative tools for medical professionals.

#### ACKNOWLEDGEMENT

The authors would like to express the deepest gratitude to the International Islamic University Malaysia for its support through the Tuition Fee Waiver Scheme (2021) to M.S.A.

#### REFERENCES

- [1] Ghosh T, Banna MHA, Rahman MS, Kaiser MS, Mahmud M, Hosen ASMS, Cho GH. (2021) Artificial intelligence and internet of things in screening and management of autism spectrum disorder. *Sustainable Cities and Society*, 74: 103-189. <https://doi.org/10.1016/j.scs.2021.103189>

- [2] Al Banna MH, Ghosh T, Taher KA, Kaiser MS, Mahmud M. (2020) A Monitoring System for Patients of Autism Spectrum Disorder Using Artificial Intelligence. The 13th International Conf. on Brain Informatics (BI 2020), 251-262. [https://doi.org/10.1007/978-3-030-59277-6\\_23](https://doi.org/10.1007/978-3-030-59277-6_23)
- [3] Cao, X., & Cao, J. (2023). Commentary: Machine learning for autism spectrum disorder diagnosis--challenges and opportunities--a commentary on Schulte-Rüther et al. (2022). *Journal of Child Psychology and Psychiatry*, 64(6):966–967. <https://doi.org/10.1111/jcpp.13764>
- [4] Islam, M. R., Rashid, M. M., Rahman, M. A., Mohamad, M. H. S. Bin, & others. (2022). Analysis of blockchain-based Ripple and SWIFT. *Asian Journal of Electrical and Electronic Engineering*, 2(1):1–8. <https://alambiblio.com/ojs/index.php/ajoeee/article/view/26>
- [5] Bokshi, L. R., Al Banna, M. H., Ghosh, T., Al Nahian, M. J., & Kaiser, M. S. (2022). Investigation on Heart Attack Prediction Based on the Different Machine Learning Approaches. *Rhythms in Healthcare*, 95–108. Springer. [https://doi.org/10.1007/978-981-19-4189-4\\_7](https://doi.org/10.1007/978-981-19-4189-4_7)
- [6] Ghosh, T., Banna, M. H. A., Nahian, M. J. A., Kaiser, M. S., Mahmud, M., Li, S., & Pillay, N. (2022, September). A privacy-preserving federated-mobilenet for facial expression detection from images. In *International Conf on Applied Intelligence and Informatics*, 277–292. [https://doi.org/10.1007/978-3-031-24801-6\\_20](https://doi.org/10.1007/978-3-031-24801-6_20)
- [7] Landa, R. J. (2008). Diagnosis of autism spectrum disorders in the first 3 years of life. *Nature Clinical Practice Neurology*, 4(3):138–147. <https://doi.org/10.1038/ncpneuro0731>
- [8] Ahmed, Z. A. T., Aldhyani, T. H. H., Jadhav, M. E., Alzahrani, M. Y., Alzahrani, M. E., Althobaiti, M. M., Alassery, F., Alshaflut, A., Alzahrani, N. M., & Al-madani, A. M. (2022). Facial Features Detection System To Identify Children With Autism Spectrum Disorder: Deep Learning Models. *Computational and Mathematical Methods in Medicine*, 2023:1–9. <https://doi.org/10.1155/2022/3941049>
- [9] Cowen, A. S., Keltner, D., Schroff, F., Jou, B., Adam, H., & Prasad, G. (2021). Sixteen facial expressions occur in similar contexts worldwide. *Nature*, 589(7841):251–257. <https://doi.org/10.1038/s41586-020-3037-7>
- [10] Abdollahi, B., Tomita, N., & Hassanpour, S. (2020). Data augmentation in training deep learning models for medical image analysis. *Deep Learners and Deep Learner Descriptors for Medical Applications*, 186:167–180. [https://doi.org/10.1007/978-3-030-42750-4\\_6](https://doi.org/10.1007/978-3-030-42750-4_6)
- [11] Briot, K., Pizano, A., Bouvard, M., & Amestoy, A. (2021). New Technologies as Promising Tools for Assessing Facial Emotion Expressions Impairments in ASD: A Systematic Review. *Frontiers in Psychiatry*, 12. 634756 <https://doi.org/10.3389/fpsyt.2021.634756>
- [12] Musser, M. (2020). Detecting Autism Spectrum Disorder in Children With Computer Vision. *Towards Data Science*. Available: <https://github.com/mm909/Kaggle-Autism>
- [13] Zhang, N., Luo, J., & Gao, W. (2020). Research on Face Detection Technology Based on MTCNN. *2020 International Conference on Computer Network, Electronic and Automation (ICCNEA)*, 2020:154–158. <https://doi.org/10.1109/ICCNEA50255.2020.00040>
- [14] Shorten, C., & Khoshgoftaar, T. M. (2019). A survey on Image Data Augmentation for Deep Learning. *Journal of Big Data*, 6(1):1-48 <https://doi.org/10.1186/s40537-019-0197-0>
- [15] Mujeeb Rahman, K. K., & Subashini, M. M. (2022). Identification of Autism in Children Using Static Facial Features and Deep Neural Networks. *Brain Sciences*, 12(1):94. <https://doi.org/10.3390/brainsci12010094>
- [16] He, K., Zhang, X., Ren, S., & Sun, J. (2016). Identity mappings in deep residual networks. In *Computer Vision–ECCV 2016: 14th European Conf Proceedings*, 14:630-645. [https://doi.org/10.1007/978-3-319-46493-0\\_38](https://doi.org/10.1007/978-3-319-46493-0_38)
- [17] Chollet, F. (2016). Xception: Deep Learning with Depthwise Separable Convolutions. *IEEE Conf. on Computer Vision and Pattern Recognition*, 1251–1258. <https://arxiv.org/abs/1610.02357>
- [18] Sandler, M., Howard, A., Zhu, M., Zhmoginov, A., & Chen, L.-C. (2018). MobileNetV2: Inverted Residuals and Linear Bottlenecks. *IEEE Conf. on Computer Vision and Pattern Recognition*, 4510–4520. <https://doi.org/10.48550/arXiv.1801.04381>

- [19] Alam, M. S., Rashid, M. M., Roy, R., Faizabadi, A. R., Gupta, K. D., & Ahsan, M. M. (2022). Empirical Study of Autism Spectrum Disorder Diagnosis Using Facial Images by Improved Transfer Learning Approach. *Bioengineering*, 9(11):1–18. <https://doi.org/10.3390/bioengineering9110710>
- [20] Porto, J. A., Bick, J., Perdue, K. L., Richards, J. E., Nunes, M. L., & Nelson, C. A. (2020). The influence of maternal anxiety and depression symptoms on fNIRS brain responses to emotional faces in 5-and 7-month-old infants. *Infant Behavior and Development*, 59:101447. <https://doi.org/10.1016/j.infbeh.2020.101447>
- [21] Rabbi, M. F., Hasan, S. M. M., Champa, A. I., & Zaman, M. A. (2021). A Convolutional Neural Network Model for Early-Stage Detection of Autism Spectrum Disorder. 2021 International Conf. on Information and Communication Technology for Sustainable Development, ICICT4SD – 2021:110–114. <https://doi.org/10.1109/ICICT4SD50815.2021.9397020>
- [22] Arumugam, S. R., Karuppasamy, S. G., Gowr, S., Manoj, O., & Kalaivani, K. (2021). A Deep Convolutional Neural Network based Detection System for Autism Spectrum Disorder in Facial images. Proceedings of the 5th International Conf on I-SMAC (IoT in Social, Mobile, Analytics and Cloud), I-SMAC 2021, 1255–1259. <https://doi.org/10.1109/I-SMAC52330.2021.9641046>
- [23] Jahanara, S. (2021). Detecting autism from facial image. *International Journal of Advance Research, Ideas and Innovations in Technology*, 7(2):219-225. <https://doi.org/10.13140/RG.2.2.35268.35202>
- [24] Kaur, N., & Gupta, G. (2023). Refurbished and improvised model using convolution network for autism disorder detection in facial images. *Indonesian Journal of Electrical Engineering and Computer Science*, 29(2):883–889. <https://doi.org/10.11591/ijeecs.v29.i2.pp883-889>
- [25] Akter, T., Ali, M. H., Khan, M. I., Satu, M. S., Uddin, M. J., Alyami, S. A., Ali, S., Azad, A., & Moni, M. A. (2021). Improved Transfer-Learning-Based Facial Recognition Framework to Detect Autistic Children at an Early Stage. *Brain Sciences*, 11(6):734. <https://doi.org/10.3390/brainsci11060734>
- [26] Alsaade, F. W., & Alzahrani, M. S. (2022). Classification and Detection of Autism Spectrum Disorder Based on Deep Learning Algorithms. *Computational Intelligence and Neuroscience*, 2022:1–10. <https://doi.org/10.1155/2022/8709145>
- [27] Fu, Y., Lei, Y., Wang, T., Curran, W. J., Liu, T., & Yang, X. (2020). Deep learning in medical image registration: a review. *Physics in Medicine & Biology*, 65(20), 1-50. <https://doi.org/10.1088/1361-6560/ab843e>